# Transactions of the ASME®





**Transactions of the ASME, Journal of Applied Mechanics** (ISSN 0021-8936) is published bimonthly (Jan., Mar., May, July, Sept., Nov.) The American Society of Mechanical Engineers, Three Park Avenue, New York, NY 10016. Periodicals postage paid at New York, NY and additional mailing office. POSTMASTER: Send address changes to Transactions of the ASME, Journal of Applied Mechanics, c/o THE AMERICAN SOCIETY OF MECHANICAL ENGINEERS, 22 Law Drive, Box 2300, Fairfield, NJ 07007-2300.
**CHANGES OF ADDRESS** must be received at Society headquarters seven weeks before they are to be effective. Please send old label and new address.





# Journal of Applied Mechanics

**Published Bimonthly by The American Society of Mechanical Engineers**

**VOLUME 69 • NUMBER 6 • NOVEMBER 2002**


## TECHNICAL PAPERS



## BRIEF NOTES




(Contents continued on inside back cover)

(**Contents continued**)

**Journal of Applied Mechanics** **Volume 69, Number 6** **NOVEMBER 2002**



## DISCUSSION



## ANNOUNCEMENTS AND SPECIAL NOTES

# Axisymmetric Instability of Fluid Saturated Pervious Cylinders

**J. P. Bardet**
Civil Engineering Department,
University of Southern California,
Los Angeles, CA 90089-2531

**S. Iai**
Geotechnical Earthquake Engineering Laboratory,
Port and Harbour Research Institute,
Yokosuka 239-0826, Japan

*The emergence of two-phase instability is investigated analytically for the axisymmetric cylinders made of a pervious solid matrix with pores filled with an interstitial fluid. General analytical solutions are derived for a broad range of constitutive models, and are illustrated for a few specific types of solids. For particular combinations of stresses and material moduli, saturated hypoelastic and elastoplastic solids are found to undergo two-phase instability, whereas their dry solid matrices remain stable. Two-phase instability can emerge within stable single-phase solids due to the interaction between solid matrix and fluid flow. The present analysis provides general analytical solutions useful for investigating the instabilities of axisymmetric soil samples subjected to the undrained triaxial tests of geomechanics.* [DOI: 10.1115/1.1505624]

## Introduction

Nonlinear pervious solids which have connected pores saturated with an interstitial fluid (i.e., two-phase materials), can become mechanically unstable as shown by Rice [1] for saturated dilatant hardening rocks, and Vardoulakis [2,3] for saturated contractant granular soils. The instabilities of two-phase materials have not been investigated as extensively as those of single-phase solids (e.g., Bardet [4], Biot [5], Chau [6,7], Hill and Hutchinson [8], Vardoulakis [9], and Vardoulakis and Sulem [10]). They have been analyzed using the principle of effective stress (Schrefler et al. [11]) and assuming constant-volume deformations (e.g., Darve [12], Di Prisco and Nova [13], Nova [14], and Lade [15]). These approaches, which consider two-phase materials as single-phase materials, revealed the isochoric instabilities resulting from solid nonlinearities, but neglected the effects of fluid compressibility and fluid flow throughout pervious solids. Bardet and Shiv [16] examined the two-phase instability of plane-strain rectangular samples of pervious solids with voids filled with compressible/incompressible fluids. Bardet [17] showed that two-phase instability causes numerical difficulties for the finite element solutions of plane-strain boundary value problems involving water diffusion within nonlinear solids. So far, two-phase instability has only been investigated for plane-strain problems, and not for axisymmetric conditions, which are very common in soil testing (e.g., Bardet, [18]).

This paper analyzes the two-phase instability of axisymmetric cylinders made of a pervious solid with pores filled with an interstitial fluid. It derives general analytical axisymmetric solutions for a large variety of constitutive models, examines the relations of one and two-phase instabilities, and considers the compressibility of solid and fluid constituents. The present analysis is limited to axisymmetric bifurcation modes, which are commonly observed on cylindrical samples during conventional laboratory experiments. Symmetry-breaking instabilities and antisymmetric bifurcation modes (e.g., lateral buckling and localization of strain within planar shear bands) are beyond the scope of this analysis.

Contributed by the Applied Mechanics Division of THE AMERICAN SOCIETY OF MECHANICAL ENGINEERS for publication in the ASME JOURNAL OF APPLIED MECHANICS. Manuscript received by the ASME Applied Mechanics Division, Apr. 21, 1999; final revision, Sept. 14, 1999. Associate Editor: D. A. Siginer. Discussion on the paper should be addressed to the Editor, Prof. Robert M. McMeeking, Department of Mechanical and Environmental Engineering University of California–Santa Barbara, Santa Barbara, CA 93106-5070, and will be accepted until four months after final publication of the paper itself in the ASME JOURNAL OF APPLIED MECHANICS.

## Definitions

**Problem Definition.** As shown in Fig. 1, the cylinder is made of a pervious solid matrix of height $2H$ and radius $R$, the pores of which are filled with an interstitial fluid. It is assumed that (1) the fluid is free to permeate through the connected voids of the solid matrix, (2) the lateral side and end extremities of the cylinder are impervious and frictionless, and (3) the specimen remains cylindrical when it is loaded axially in either compression or tension. Hereafter, the solid-fluid mixture is referred to as a two-phase material. The geometry of Fig. 1 is intended to represent that of soil samples subjected to the undrained triaxial testing in soil mechanics (e.g., Bardet [18]). In these tests, cylindrical soil samples are saturated with water, compressed axially through lubricated frictionless platens, and confined laterally with pressure. Similar geometries are also found in the testing of other porous solids (e.g., rocks and concrete). The boundary conditions are carefully selected so that the fluid pressure, stress, and strain can be assumed uniform and axisymmetric throughout the cylinder. At any given loading state, the Cauchy stress components anywhere within the cylinder are

$$\sigma_{rr}=\sigma_{\theta\theta} \quad \text{and} \quad \sigma_{rz}=\sigma_{r\theta}=\sigma_{z\theta}=0 \tag{1}$$

where $\sigma_{rr}$, $\sigma_{\theta\theta}$, $\sigma_{r\theta}$, $\sigma_{rz}$, and $\sigma_{z\theta}$ are the Cauchy stress components in the polar coordinates $r$, $\theta$, and $z$ of Fig. 1.

Possible departures from uniform states will be investigated by formulating a linear stability (or incremental bifurcation) problem. Starting from a given uniform state of fluid pressure, stress, and strain, we investigate the circumstances for which the rates of fluid pressure, solid stresses, and solid strains may become nonuniform within the cylinder. For a given rate of prescribed loading, the boundary conditions of the incremental bifurcation problem are as follows:

$$v_z=0, \quad \dot{t}_{rz}=0 \quad \text{and} \quad \dot{p}_{,z}=0 \quad \text{for } z=\pm H \quad \text{and} \quad 0\leqslant r\leqslant R \tag{2a}$$

$$v_r=0, \quad \dot{t}_{rz}=0 \quad \text{and} \quad \dot{p}_{,r}=0 \quad \text{for } r=R \quad \text{and} \quad -H\leqslant z\leqslant H \tag{2b}$$

where $\dot{p}$ is the time rate of fluid pressure change, $\mathbf{v}$ the solid velocity, and $\dot{\mathbf{t}}$ the rate of applied distributed force at the boundary. The partial differentiation with respect to $r$, $\theta$, and $z$ are denoted with "$,r$" "$,\theta$", and "$,z$" and the derivative with respect to time with a dot. The incremental bifurcation problem will now be completed by introducing geometric and material nonlinearities, and equilibrium equations.

**Stress States and Rates.** By definition, the distributed force vector $\mathbf{t}$ acting on the deformed surface, with area $dS_t$ and unit

  

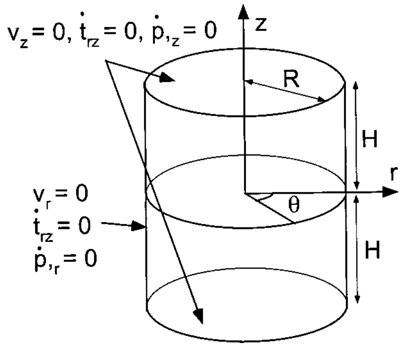


**Fig. 1 Geometry, coordinate systems, and boundary conditions of cylindrical porous solid for linear stability analysis**

normal vector $\mathbf{n}$, is related to the Cauchy stress tensor $\sigma$ and the nominal (Piola-Kirchhoff) stress tensor $\Sigma$ through

$$\mathbf{t}=\mathbf{n}\cdot\sigma dS_t=\mathbf{N}\cdot\Sigma dS_o \tag{3}$$

where $\mathbf{N}$ and $dS_o$ are the unit normal vector and area, respectively, of the reference surface. Nominal and Cauchy stresses are related through

$$\Sigma=\det(\mathbf{F})\mathbf{F}^{-1}\cdot\sigma \tag{4}$$

where $\mathbf{F}^{-1}$ is the inverse transformation of the deformation gradient $\mathbf{F}$. By definition the Kirchhoff stress tensor $\tau$ is related to $\sigma$ through

$$\tau=\det(\mathbf{F})\sigma \tag{5}$$

The rates of $\mathbf{t}$ and $\Sigma$ are

$$\dot{\mathbf{t}}=\mathbf{N}\cdot\dot{\Sigma}dS_o \quad \text{and} \quad \dot{\Sigma}=\det(\mathbf{F})\mathbf{F}^{-1}\cdot(\dot{\sigma}-\mathbf{L}\cdot\sigma+\sigma\text{trace}(\mathbf{L})) \tag{6}$$

where $\mathbf{L}$ is the velocity gradient tensor.

**Rate-Type Constitutive Models.** In the present linear stability analysis, the behavior of the solid materials is modeled with rate-type equations (Truesdell and Noll [19])

$$\hat{\tau}=\mathbf{C}\cdot\mathbf{D} \tag{7}$$

where $\hat{\tau}$ is the Jaumann rate of Kirchhoff stress $\tau$, $\mathbf{D}$ the rate of deformation, and $\mathbf{C}$ the fourth-order stiffness tensor. In general, $\mathbf{C}$ is homogeneous of degree zero in $\mathbf{D}$ and depends on the states of stress and strain. The Jaumann rate of Kirchhoff stress is

$$\hat{\tau}=\dot{\tau}-\mathbf{W}\cdot\tau+\tau\cdot\mathbf{W}. \tag{8}$$

The rate of deformation $\mathbf{D}$ and spin tensor $\mathbf{W}$ are

$$\mathbf{D}=\tfrac{1}{2}(\mathbf{L}+\mathbf{L}^T) \quad \mathbf{W}=\tfrac{1}{2}(\mathbf{L}-\mathbf{L}^T) \tag{9}$$

where the superscript "$^T$" denotes transpose. The Jaumann rate of Cauchy stress $\hat{\sigma}$, which is defined similarly to Eq. (8), is related to $\hat{\tau}$ through

$$\hat{\tau}=\det(\mathbf{F})(\hat{\sigma}+\sigma\text{trace}(\mathbf{D})). \tag{10}$$

When the present configuration is chosen as reference, the deformation gradient is approximately equal to the unity transformation $\mathbf{1}$:

$$\mathbf{F}\approx\mathbf{F}^{-1}\approx\mathbf{1} \quad \text{and} \quad \det(\mathbf{F})\approx 1. \tag{11}$$

In this condition, the nominal, Cauchy, and Kirchhoff stress tensors are identical:

$$\Sigma=\sigma=\tau \tag{12}$$

and their rates are related through

$$\hat{\tau}=\hat{\sigma}+\sigma\text{trace}(\mathbf{D}) \quad \text{and} \quad \dot{\Sigma}=\hat{\sigma}+\sigma\text{trace}(\mathbf{D})-\sigma\cdot\mathbf{W}-\mathbf{D}\cdot\sigma. \tag{13}$$

The generality of the present analysis is not affected by the choice of the Jaumann rate of Kirchhoff stress. As shown in Bardet [4], the analysis applies to other types of objective stress rates after adding stress-dependent moduli to the constitutive moduli in Equation (7).

**Axisymmetric Conditions.** In the case of axisymmetric velocity fields (i.e., $v_\theta=0$ and $v_{r,\theta}=v_{z,\theta}=0$), the nonzero terms of deformation rate and spin tensors are

$$D_{rr}=v_{r,r}, \quad D_{zz}=v_{z,z}, \quad D_{\theta\theta}=\frac{v_r}{r},$$

$$D_{rz}=\tfrac{1}{2}(v_{r,z}+v_{z,r}), \quad W_{rz}=-W_{zr}=\tfrac{1}{2}(v_{r,z}-v_{z,r}). \tag{14}$$

Hereafter, we consider the following axisymmetric constitutive equation:

$$\hat{\tau}_{rr}=C_{11}D_{rr}+C_{12}D_{\theta\theta}+C_{13}D_{zz} \tag{15a}$$

$$\hat{\tau}_{\theta\theta}=C_{12}D_{rr}+C_{11}D_{\theta\theta}+C_{13}D_{zz} \tag{15b}$$

$$\hat{\tau}_{zz}=C_{31}D_{rr}+C_{31}D_{\theta\theta}+C_{33}D_{zz} \tag{15c}$$

$$\hat{\tau}_{rz}=2C_{44}D_{rz} \tag{15d}$$

where $C_{11}$, $C_{12}$, $C_{13}$, $C_{33}$, $C_{31}$, and $C_{44}$ are constitutive moduli. This general constitutive form, which was used by Chau [6,7] will be later specified for some particular types of constitutive models.

**Equilibrium Equations.** In axisymmetric conditions and cylindrical coordinates, the stress-rate equilibrium equations for solid materials are (Hill [20]):

$$\dot{\Sigma}_{rr,r}+\dot{\Sigma}_{zr,z}+\frac{1}{r}(\dot{\Sigma}_{rr}-\dot{\Sigma}_{\theta\theta})=0$$

$$\dot{\Sigma}_{rz,r}+\dot{\Sigma}_{zz,z}+\frac{1}{r}\dot{\Sigma}_{rz}=0. \tag{16}$$

Using Eq. (13), Eq. (16) can be expressed in terms of Cauchy stress:

$$\hat{\sigma}_{rr,r}+\hat{\sigma}_{zr,z}+\frac{1}{r}(\hat{\sigma}_{rr}-\hat{\sigma}_{\theta\theta})+(\sigma_{rr}-\sigma_{zz})W_{zr,z}=0 \tag{17a}$$

$$\hat{\sigma}_{rz,r}+\hat{\sigma}_{zz,z}+\frac{1}{r}\hat{\sigma}_{rz}+(\sigma_{rr}-\sigma_{zz})\left(W_{zr,r}+\frac{1}{r}W_{zr}\right)=0. \tag{17b}$$

**Solid-Fluid Coupling.** The solid-fluid coupling is described using the following generalized effective stress principle (Schrefler et al. [11]):

$$\sigma'_{ij}=\sigma_{ij}+\alpha p\,\delta_{ij} \tag{18}$$

where $\sigma_{ij}$ is the total Cauchy stress tensor, $\sigma'_{ij}$ the effective Cauchy stress tensor, and $p$ the interstitial fluid pressure. By sign convention, both $\sigma_{ij}$ and $\sigma'_{ij}$ are positive in tension, and $p$ is positive in compression. The coefficient $\alpha$ is a positive constant that depends on the bulk modulus $K$ of the solid skeleton and the bulk modulus $K_s$ of the solid grains as (Schrefler et al. [11])

$$\alpha=1-K/K_s. \tag{19}$$

The physical parameter $\alpha$ is mathematically convenient to model the solid-fluid coupling from complete (i.e., $\alpha=1$) to none (i.e., $\alpha=0$). Hereafter, the superscript prime is omitted for effective stress because all stresses for the solid phase are effective. By substituting Eq. (18) into Eq. (17), the axisymmetric equilibrium equations for two-phase materials are

$$\hat{\sigma}_{rr,r}+\hat{\sigma}_{zr,z}+\frac{1}{r}(\hat{\sigma}_{rr}-\hat{\sigma}_{\theta\theta})+(\sigma_{rr}-\sigma_{zz})W_{zr,z}=\alpha\dot{p}_{,r} \tag{20a}$$

$$\hat{\sigma}_{rz,r}+\hat{\sigma}_{zz,z}+\frac{1}{r}\hat{\sigma}_{rz}+(\sigma_{rr}-\sigma_{zz})\left(W_{zr,r}+\frac{1}{r}W_{zr}\right)=\alpha\dot{p}_{,z}. \tag{20b}$$

The fluid pressure $p$ obeys the flow conservation equation (Schrefler et al. [11])

$$p_{,rr}+\frac{1}{r}p_{,r}+p_{,zz}=\beta\left[\alpha\left(v_{r,r}+\frac{1}{r}v_r+v_{z,z}\right)+\frac{\dot{p}}{\Theta}\right] \tag{21}$$

where the parameter $\beta$ is related to the fluid unit weight $\gamma_w$ and coefficient of permeability $k$ through

$$\beta=\gamma_w/k. \tag{22}$$

The parameter $\Theta$ is the bulk modulus of the two-phase material, which is related to the porosity $n$ and the fluid bulk modulus $K_f$ as follows (Schrefler et al. [11]):

$$\frac{1}{\Theta}=\frac{n}{K_f}+\frac{\alpha-n}{K_s}. \tag{23}$$

After introducing the following coefficients

$$d_1=C_{11}-\sigma_{rr}, \quad d_2=C_{33}-\sigma_{zz} \tag{24a}$$

$$d_3=C_{44}-\tfrac{1}{2}(\sigma_{rr}-\sigma_{zz}), \quad d_4=C_{44}+C_{13}+\tfrac{1}{2}(\sigma_{rr}+\sigma_{zz}) \tag{24b}$$

$$d_5=C_{44}+\tfrac{1}{2}(\sigma_{rr}-\sigma_{zz}), \quad d_6=C_{44}+C_{31}-\tfrac{1}{2}(\sigma_{rr}+\sigma_{zz}) \tag{24c}$$

Eqs. (20) and (21) become

$$d_1\left(v_{r,rr}+\frac{1}{r}v_{r,r}-\frac{1}{r^2}v_r\right)+d_3v_{r,zz}+d_4v_{z,rz}=\alpha\dot{p}_{,r} \tag{25a}$$

$$d_5\left(v_{z,rr}+\frac{1}{r}v_{z,r}\right)+d_2v_{z,zz}+d_6\left(v_{r,rz}+\frac{1}{r}v_{r,z}\right)=\alpha\dot{p}_{,z} \tag{25b}$$

$$\dot{p}_{,rr}+\frac{1}{r}\dot{p}_{,r}+\dot{p}_{,zz}=\beta\left[\alpha\left(\dot{v}_{r,r}+\frac{1}{r}\dot{v}_r+\dot{v}_{z,z}\right)+\frac{\ddot{p}}{\Theta}\right]. \tag{25c}$$

Equation (25) is independent of $C_{12}$ due to axisymmetric conditions. The incremental boundary value problem is finally formulated in terms of solid velocity $v_r$ and $v_z$ and fluid pressure $p$ after restating Eq. (2) as follows:

$$v_z=0, \quad v_{z,r}=0, \quad v_{r,z}=0 \quad \text{and} \quad \dot{p}_{,z}=0 \quad \text{for} \quad z=\pm H \quad \text{and} \quad 0\leqslant r\leqslant R \tag{26a}$$

$$v_r=0, \quad v_{z,r}=0, \quad v_{r,z}=0 \quad \text{and} \quad \dot{p}_{,r}=0 \quad \text{for } r=R \quad \text{and} \quad -H\leqslant z\leqslant H. \tag{26b}$$

**Trivial and Nontrivial Bifurcating Solutions.** Fields of constant solid velocity gradient and fluid pressure are obvious solutions of Eqs. (25) and (26). The nontrivial bifurcating solutions are sought in the following modes:

$$v_r=V_1J_1(\beta_1 r)\cos(\beta_2 z+\theta_2)f(t) \tag{27a}$$

$$v_z=V_2J_0(\beta_1 r)\sin(\beta_2 z+\theta_2)f(t) \tag{27b}$$

$$\dot{p}=PJ_0(\beta_1 r)\cos(\beta_2 z+\theta_2)f(t) \tag{27c}$$

where $J_n(x)$ is the Bessel function of the first kind and $n$th order, and $\theta_2$ denotes a phase shift. These modes satisfy the boundary conditions of Eq. (26) when $\beta_1$, $\beta_2$, and $\theta_2$ are selected as follows:

$$\beta_1 R=0, \quad \pm 3.832, \quad \pm 7.016, \quad \pm 10.173, \ldots \text{(roots of } J_1=0) \tag{28a}$$

$$\beta_2 H=\frac{\pi}{2}m_2 \quad \text{for } m_2 \text{ integer} \tag{28b}$$

$$\theta_2=\begin{cases} 0 & (\text{for } m_2 \text{ even}) \\ \dfrac{\pi}{2} & (\text{for } m_2 \text{ odd}) \end{cases}. \tag{28c}$$

By substituting these modes into Eq. (25) and introducing $f^*$ so that

$$f^*=\beta\frac{\dot{f}(t)}{f(t)}, \tag{29}$$

the following relations are obtained:

$$\begin{bmatrix} \beta_1^2d_1+\beta_2^2d_3 & \beta_1\beta_2d_4 & -\alpha\beta_1 \\ \beta_1\beta_2d_6 & \beta_1^2d_5+\beta_2^2d_2 & -\alpha\beta_2 \\ \alpha\beta_1 f^* & \alpha\beta_2 f^* & \beta_1^2+\beta_2^2+\dfrac{f^*}{\Theta} \end{bmatrix}\begin{Bmatrix} V_1 \\ V_2 \\ P \end{Bmatrix}=\begin{Bmatrix} 0 \\ 0 \\ 0 \end{Bmatrix}. \tag{30}$$

From the third line in Eq. (30), $f^*$ is given by

$$f^*=\frac{-(\beta_1^2+\beta_2^2)P}{\alpha(\beta_1V_1+\beta_2V_2)+\dfrac{P}{\Theta}}. \tag{31}$$

The coefficient $f^*$ is thus independent of time and space and, hence, the solution of Eq. (29) is

$$f(t)=f_0\exp(f^*t/\beta) \tag{32}$$

where $f_0$ represents an initial amplitude of the nontrivial bifurcating solution. When $f^*>0$, $f(t)$ grows exponentially with time and eventually becomes infinite. Hence, the bifurcating solution generates a material instability. When $f^*\leqslant 0$, the bifurcating solution dies out with time, and has little physical relevance. A set of nontrivial bifurcating solutions for $V_1$, $V_2$, and $P$ exist when the determinant of the matrix in Eq. (30) becomes zero. After defining the wavelength ratio of the bifurcating mode as

$$\Lambda=\frac{\beta_2}{\beta_1}, \tag{33}$$

the condition for the existence of nontrivial bifurcating solutions in Eq. (30) is

$$\frac{\alpha^2 f^*}{\beta_1^2+\beta_2^2}=\frac{N(\Lambda)}{D(\Lambda)}>0. \tag{34}$$

The numerator and denominator of the left side of Eq. (34) are

$$N(\Lambda)=a_1\Lambda^4+b_1\Lambda^2+c_1, \quad D(\Lambda)=a_2\Lambda^4+b_2\Lambda^2+c_2 \tag{35}$$

where

$$a_1=d_2d_3, \quad b_1=d_1d_2+d_3d_5-d_4d_6, \quad c_1=d_1d_5 \tag{36a}$$

$$a_2=-d_3-a_1\chi, \quad b_2=-d_1-d_2+d_4+d_6-b_1\chi, \quad c_2=-d_5-c_1\chi \tag{36b}$$

$$\chi=1/\alpha^2\Theta. \tag{36c}$$

Three types of instability and associated conditions can be defined:

$$\text{solid-fluid } (SF) \text{ instability} \quad \text{for } N(\Lambda)/D(\Lambda)>0 \tag{37a}$$

$$\text{infinite solid-fluid } (SF\infty) \text{ instability for } D(\Lambda)=0 \quad \text{and} \quad N(\Lambda)\neq 0 \tag{37b}$$

$$\text{solid } (S) \text{ instability} \quad \text{for } N(\Lambda)=0 \tag{37c}$$

The $SF$ instability is obtained when there are modes with wavelength ratios $\Lambda$ satisfying Eq. (37$a$). The $SF\infty$ instability is a particular $SF$ instability with $f^*\to+\infty$, which corresponds to an

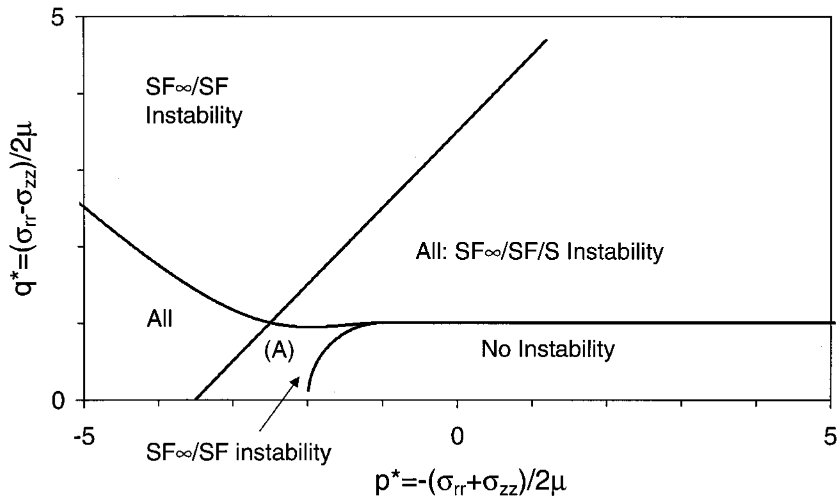


**Fig. 2 Dimensionless $p^*$-$q^*$ domains of $S$, $SF$, and $SF\infty$ instabilities for hypoelastic material with incompressible fluid ($\chi^*=0$, $\nu=0.3$)**

infinite exponential growth, and a severe solid-fluid instability. The $S$ instability is the material instability obtained for the solid alone without interstitial water. The $S$ instability is obtained by setting $\alpha=0$ in Eq. (30), fully decoupling the solid and fluid, and ignoring the interstitial fluid. $SF$ instability can be physically interpreted as the result of a rapidly growing flow of interstitial fluid through the pervious solid, which may create solid-fluid interaction forces and promote the emergence of nonuniform modes of deformation. In theory, $SF$ instability could be detected by measuring the spatial fluctuation of fluid pressure within the material specimens tested in the laboratory.

## Applications

The one and two-phase axisymmetric instabilities will be examined for three particular types of rate-type constitutive equations: (1) hypoelastic models, (2) elastoplastic models, and (3) Rudnicki pressure-sensitive models.

**Hypoelastic Model.** The constitutive moduli of isotropic hypoelastic models are (Bardet [4])

$$C_{11}=C_{33}=2\mu+\lambda,\quad C_{13}=C_{31}=\lambda\quad \text{and}\quad C_{44}=\mu \tag{38}$$

where $\mu$ is the shear modulus and λ the Lame's modulus, which are related to Poisson's ratio $\nu$ through

$$\lambda=\frac{2\nu\mu}{1-2\nu}. \tag{39}$$

It is convenient to introduce the following nondimensional stress components and coefficients:

$$p^*=-\frac{\sigma_{rr}+\sigma_{zz}}{2\mu}\quad q^*=\frac{\sigma_{rr}-\sigma_{zz}}{2\mu},\quad \text{and}\quad \chi^*=\mu\chi. \tag{40}$$

The hypoelastic model is useful for developing closed-form analytical solutions for simple linear stability problems and comparing numerical and analytical results (e.g., Bardet [17]). However, the hypoelastic model has only two material parameters, and therefore limited capabilities in modeling realistically all types of material responses.

Figures 2 to 4 show the $p^*$-$q^*$ domains of $S$, $SF$, and $SF\infty$ instability for various cases of fluid and solid compressibility. By definition, $p^*$ is positive in compression and negative in tension. These $p^*$-$q^*$ domains are symmetric about the $p^*$- axis, and are

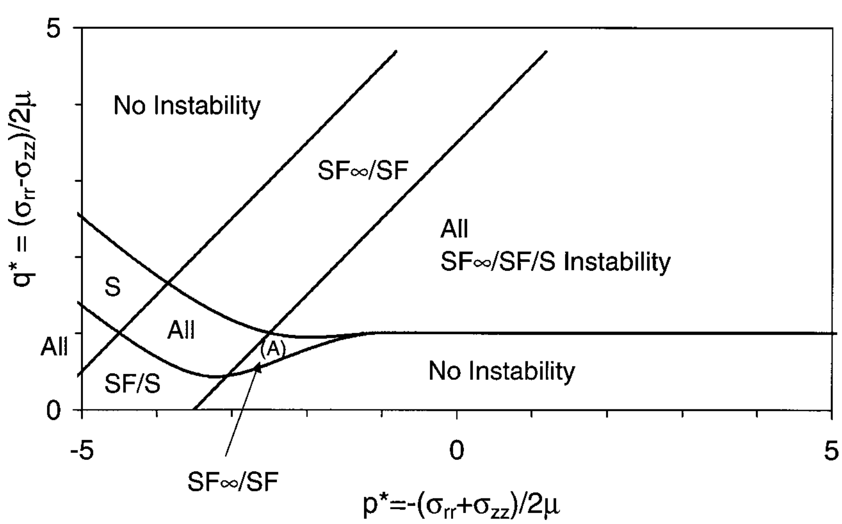


**Fig. 3 Dimensionless $p^*$-$q^*$ domains of $S$, $SF$, and $SF\infty$ instabilities for hypoelastic material with compressible fluid ($\chi^*=0.5$, $\nu=0.3$)**

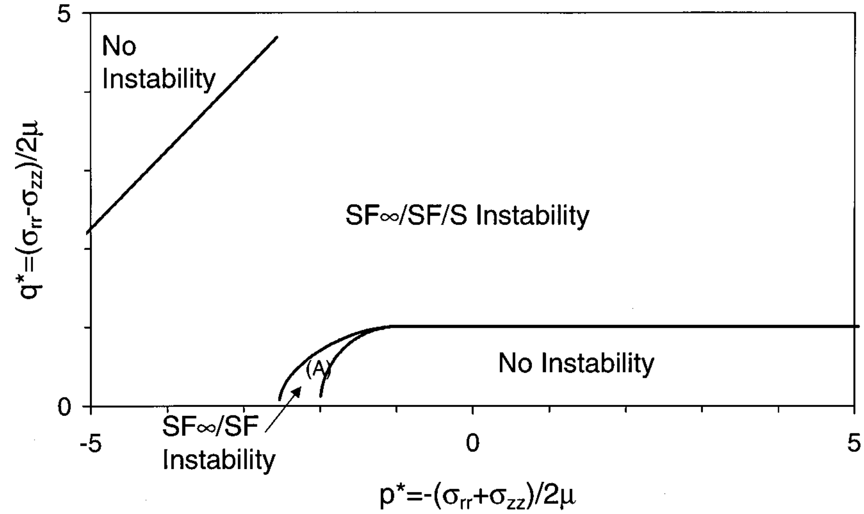


**Fig. 4 Dimensionless $p^*$-$q^*$ domains of $S$, $SF$, and $SF\infty$ instabilities for hypoelastic material with compressible fluid ($\chi^*=0.5$, $\nu=0.43$)**

only represented for positive values of $q^*$. As shown in Fig. 2 for incompressible fluid (i.e., $\chi^*=0$), zero stress states are initially stable. For $q^*=1$ and $p^*>0$, all types of instability emerge simultaneously. For $p^*<-2$, $SF$ and $SF\infty$ instabilities appear in area $A$ without $S$ instability. As shown in Fig. 3, the size of area A shrinks with the compressibility of the interstitial fluid (i.e., $\chi^*=0.5$). $SF$ and $S$ instabilities may occur simultaneously when $p^*$ decreases below 3. As shown in Fig. 4, the size of area A also shrinks as the solid becomes more incompressible (i.e., $\nu=0.43$), and vanishes for incompressible material (i.e., $\nu=0.5$). In the incompressible limit, $S$, $SF$, and $SF\infty$ instabilities may emerge simultaneously.

**Elastoplastic Mohr-Coulomb Model.** The constitutive moduli of elastoplasticity are (Hill [21] and Bardet [4])

$$C_{11}=2\mu+\lambda-\frac{1}{H'}[2\mu P_{11}+\lambda(P_{33}+2P_{11})]\times[2\mu Q_{11}+\lambda(Q_{33}+2Q_{11})],$$

$$C_{33}=2\mu+\lambda-\frac{1}{H'}[2\mu P_{33}+\lambda(P_{33}+2P_{11})]\times[2\mu Q_{33}+\lambda(Q_{33}+2Q_{11})],$$

$$C_{13}=\lambda-\frac{1}{H'}[2\mu P_{11}+\lambda(P_{33}+2P_{11})][2\mu Q_{33}+\lambda(Q_{33}+2Q_{11})],$$

$$C_{31}=\lambda-\frac{1}{H'}[2\mu P_{33}+\lambda(P_{33}+2P_{11})][2\mu Q_{11}+\lambda(Q_{33}+2Q_{11})],$$

$$C_{44}=\mu$$

$$H'=H+\lambda(P_{33}+2P_{11})(P_{33}+2P_{11})+2\mu(2P_{11}Q_{11}+P_{33}Q_{33}) \tag{41}$$

where $H$ is the plastic modulus; and $P_{ij}$ and $Q_{ij}$ are unit tensors representing the flow and yield directions, respectively. For a Mohr-Coulomb material and axisymmetric conditions, the unit tensors $P_{ij}$ and $Q_{ij}$ are related to the mobilized friction angle $\phi$ and the dilatancy angle $\psi$ as follows:

$$P_{33}=\frac{\sin\psi-2}{\sqrt{3(2+\sin^2\psi)}} \quad \text{and} \quad P_{11}=\frac{1+\sin\psi}{\sqrt{3(2+\sin^2\psi)}} \tag{42a}$$

$$Q_{33}=\frac{-2(1-\sin\phi)}{\sqrt{2(3-2\sin\phi+3\sin^2\phi)}} \quad \text{and}$$

$$Q_{11}=\frac{1+\sin\phi}{\sqrt{2(3-2\sin\phi+3\sin^2\phi)}} \tag{42b}$$

where the mobilized friction angle $\varphi$ and the dilatancy angle $\psi$ are defined by

$$\sin\phi=\left|\frac{\sigma_{zz}-\sigma_{rr}}{\sigma_{zz}+\sigma_{rr}}\right| \quad \text{and}$$

$$\sin\psi=\frac{-(d\varepsilon_{zz}^p+2d\varepsilon_{rr}^p)}{d\varepsilon_{zz}^p-d\varepsilon_{rr}^p}=\frac{-(P_{33}+2P_{11})}{P_{33}-P_{11}}. \tag{43}$$

Figure 5 shows an example of instability domain in the $\phi-H/\mu$ plane for $\nu=0.3$, $\psi=-30$ deg and $\chi^*=0$. The variations of elastoplastic moduli for fixed values of $\nu$, $\psi$, and $\chi^*$ are characterized solely by the values of $\phi$ and $H/\mu$, which are represented using the point M of coordinates $\phi-H/\mu$ in Fig. 5. When the stress states are initially isotropic at the beginning of a shear loading, the point M is initially in the upper left corner, which corresponds to an elastic state ($H\gg 1$) and no shear stress ($\phi=0$). As the shear stress increases, point M moves down from the upper left corner and intersects the SF/S boundary, or $SF\infty/SF$ boundary. If $\phi<8$ deg, point M intersects first the *SF/S* boundary for strain-softening conditions ($H<0$). In this case, $SF$ and $S$ instabilities will occur simultaneously. If $\phi>8$ deg, point M will intersect the $SF\infty/SF$ boundary for either strain-softening, strain-hardening ($H>0$), or perfectly plastic ($H=0$) conditions. This implies that $SF\infty$ and/or $SF$ instabilities may emerge without $S$ instabilities for contractant elastoplastic materials. In other words, $SF\infty$ and/or $SF$ instabilities are not necessarily generated by $S$ instabilities.

**Rudnicki Model.** In the investigation of material instability, Rudnicki [22] proposed the following rate-independent constitutive model for axisymmetric conditions, which generalizes most constitutive models used in linear stability analyses

$$C_{11}=9K/4+G_t,\quad C_{13}=9K\nu/2,\quad C_{31}=9Kr^*/4,$$

$$C_{33}=E/2+9K\nu r^*/2,\quad C_{44}=G_l, \tag{44}$$

where $K$, $E$, $\nu$, $r^*$, $G_l$, and $G_t$ are material moduli, the physical meanings of which are defined in Rudnicki [22] and Chau [7].

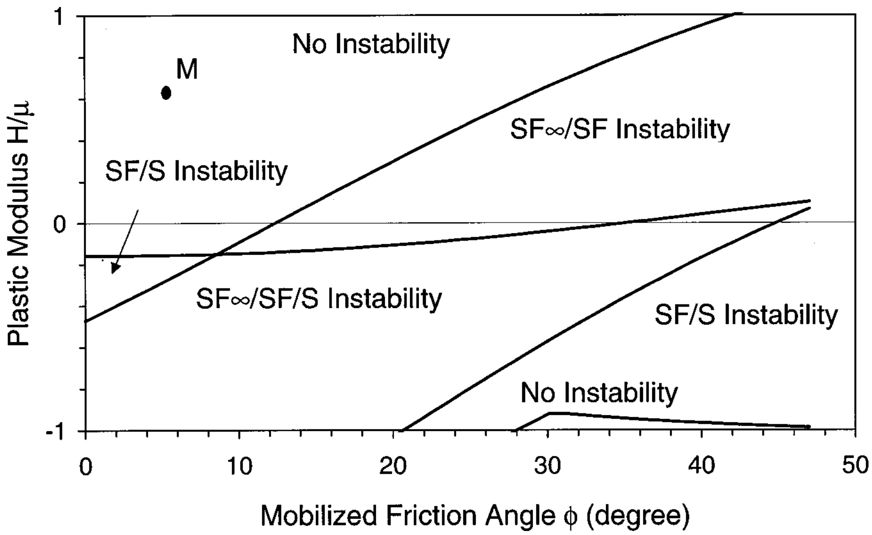


**Fig. 5 Domain of *S*, *SF*, and *SF*∞ instabilities for elastoplastic contractant Mohr-Coulomb material and incompressible fluid ($\nu$=0.3, $\psi$=−30 deg and $\chi^*$=0)**

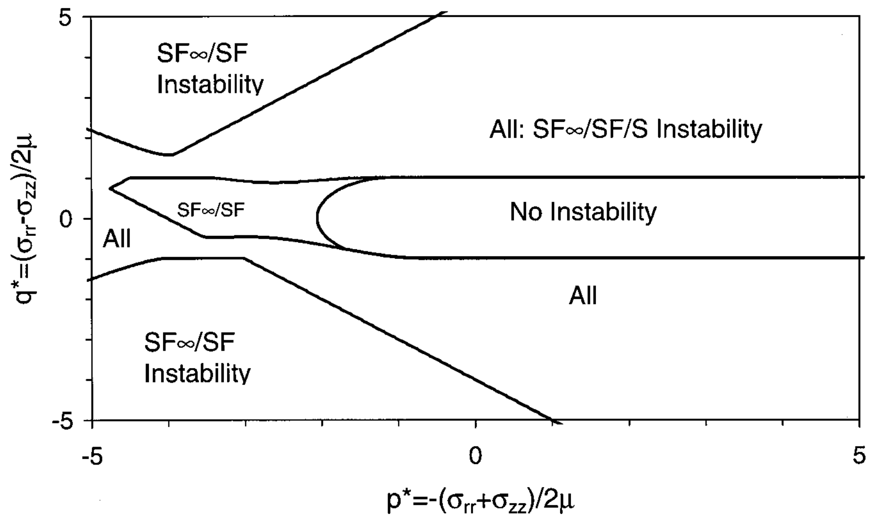


**Fig. 6 Dimensionless *p**-*q** domains of *S*, *SF*, and *SF*∞ instabilities for Rudnicki's model for incompressible fluid ($\chi^*$=0, $G_l/2G_t$=0.5, $K/2G_t$=1, $\nu$=0.3, and $r^*$=0.6)**

Figure 6 shows the domains of instability of Ruckniki's model in the $p^*-q^*$ coordinates used for the hypoelastic model of Figs. 2–4 for particular values of material parameters: $G_l/2G_t=0.5$; $K/2G_t=1$; $\nu=0.3$; $r^*=0.6$; and incompressible interstitial fluid $\chi^*=0$. For this particular selection of model parameters, the domains of $S$, $SF$, and $SF\infty$ instabilities are similar to those of Fig. 2, except for the asymmetry about the $q^*$-axis. As for hypoelastic models, $SF$ and $SF\infty$ instabilities are not generated by $S$ instability in area A.

## Discussion

A general mathematical framework and analytical solutions have been derived for studying the two-phase instability of axisymmetric cylinders made of a wide variety of pervious solids filled with a compressible/incompressible fluid. The present analysis is based on the assumptions stated in Eqs. (17), (18), and (21). The analysis holds provided that these mechanical assumptions represent the material physics, but may break down in some circumstances, e.g., when Eqs. (18) and (21) do not hold due to capillary effects and bubble formation in the interstitial fluid (Schrefler et al. [11]).

The analysis needs to be extended to nonaxisymmetric deformations (e.g., strain localization), which have been shown in the case of dry solids to become the predominant modes of instability when the axisymmetry constraints are removed (e.g., Chau [7,23]). The general framework and solutions also need to be applied to constitutive models specific to geomechanics and investigated in the context of undrained triaxial testing. There is also a need to investigate the effects of two-phase instability on the numerical solutions of liquefaction problems in geomechanics, following the approach of Bardet [17] for hypoelastic materials.

## Conclusions

The emergence of two-phase instability was investigated analytically in the case of pervious solid cylinders with voids filled with an interstitial fluid. The analysis develops a mathematical framework and analytical solutions that apply to a broad range of material models, and illustrates their application for specific types of solids including hypoelastic and elastoplastic models. For particular values of stress states and material moduli, hypoelastic and elastoplastic models were found to undergo two-phase instability, and no solid instability. Two-phase instability can emerge in stable solids due to the interaction between fluid flow and porous solid matrix. The general results of the present analysis are relevant to geomechanics for studying instabilities in undrained triaxial tests.

## Acknowledgment

The authors acknowledge the financial support of the U.S. National Science Foundation and the Science and Technology Agency, Japan.

## References

[1] Rice, J. R., 1975, ''On the Stability of Dilatant Hardening of Saturated Rock Masses,'' J. Geophys. Res., **80**, pp. 1531–1536.

[2] Vardoulakis, I., 1985, ''Stability and Bifurcation of Undrained, Plane Rectilinear Deformation on Water-Saturated Granular Soils,'' Int. J. Numer. Analyt. Meth. Geomech., **9**, pp. 399–414.

[3] Vardoulakis, I., 1986, ''Dynamic Stability Analysis of Undrained Simple Shear on Water-Saturated Granular Soils,'' Int. J. Numer. Analyt. Meth. Geomech., **10**, pp. 177–190.

[4] Bardet, J. P., 1991, ''Analytical Solutions for the Plane Strain Bifurcation of compressible solids,'' ASME J. Appl. Mech., **58**, pp. 651–657.

[5] Biot, M. A., 1965, *Mechanics of Incremental Deformation*, John Wiley and Sons, New York.

[6] Chau, K. T., 1992, ''Non-normality and Bifurcation in a Compressible Pressure-Sensitive Circular Cylinder Under Axisymmetric Tension and Compression,'' Int. J. Solids Struct., **29**, pp. 801–824.

[7] Chau, K. T., 1993, ''Antisymmetric Bifurcations in a Compressible Pressure-Sensitive Circular Cylinder Under Axisymmetric Tension and Compression,'' ASME J. Appl. Mech., **60**, pp. 282–289.

[8] Hill, R., and Hutchinson, J. W., 1975, ''Bifurcation Phenomena in the Plane Tension Test,'' J. Mech. Phys. Solids, **23**, pp. 239–264.

[9] Vardoulakis, I., 1981, ''Bifurcation Analysis of the Plane Rectilinear Deformation on Dry Sand Samples,'' Int. J. Solids Struct., **17**(11), pp. 1085–1101.

[10] Vardoulakis, I., and Sulem, J., 1995, *Bifurcation Analysis in Geomechanics*, Blackie Academic & Professional, Glasgow, UK, p. 459.

[11] Schrefler, B. A., Simoni, L., Xikui, L., and Zienkiewicz, O. C., 1990, ''Mechanics of Partially Saturated Porous Media,'' *Numerical Methods and Constitutive Modeling in Geomechanics*, C. S. Desai and G. Gioda, eds., Springer-Verlag, New York, pp. 169–209.

[12] Darve, F., 1994, ''Stability and Uniqueness in Geomaterials Constitutive Modeling,'' *Localization and Bifurcation Theory for Soils and Rocks*, R. Chambon, J. Desrues, and I. Vardoulakis, eds., A. A. Balkema, Rotterdam, The Netherlands, pp. 73–88.

[13] Di Prisco, C., and Nova, R., 1994, ''Stability Problems Related to Static Liquefaction of Loose Sand,'' *Localization and Bifurcation Theory for Soils and Rocks*, R. Chambon, J. Desrues, and I. Vardoulakis, eds., A. A. Balkema, Rotterdam, The Netherlands, pp. 59–70.

[14] Nova, R., 1991, ''A Note on Sand Liquefaction and Soil Stability,'' *Constitutive Laws for Engineering Materials*, C. S. Desai et al., ASME, New York, pp. 153–156.

[15] Lade, P. V., 1989, ''Experimental Observations of Stability, Instability and Shear Planes in Granular Materials,'' Ingenieur-Archiv, **59**, pp. 114–123.

[16] Bardet, J. P., and Shiv, A., 1995, ''Plane-Strain Instability of Saturated Porous Media,'' J. Eng. Mech. **121**(6), pp. 717–724.

[17] Bardet, J. P., 1996, ''Finite Element Analysis of Two-Phase Instability for Saturated Porous Hypoelastic Solids Under Plane Strain Loadings,'' Eng. Comput., **13**(7), pp. 29–48.

[18] Bardet, J. P., 1997, *Experimental Soil Mechanics*, Prentice-Hall, Englewood Cliffs, NJ.

[19] Truesdell, C., and Noll, W., 1965 *Nonlinear Field Theories of Mechanics* (Handbuch of Physics III/3), Springer-Verlag, Berlin.

[20] Hill, R., 1959, ''Some Basic Principles in the Mechanics of Solids Without a Natural Time,'' J. Mech. Phys. Solids, **7**, p. 209.

[21] Hill, R., 1950, *The Mathematical Theory of Plasticity*, Oxford University Press, Oxford, UK.

[22] Rudnicki, J. W., 1977, *The Effects of Stress-Induced Anisotropy on a Model of Brittle Rock Failure as Localization of Deformation*, Energy Resources and Excavation Technology, Proc. 18th US symposium on Rock Mechanics, Keystone, CO, June 22–24, pp. 3B4.1–8.

[23] Chau, K. T., 1995, ''Buckling, Barelling, and Surface Instabilities of a Finite, Transversely Isotropic Circular Cylinder,'' Q. J. Mech. Appl. Math., **53**(2), pp. 225–244.

# Motorcycle Steering Oscillations due to Road Profiling

**D. J. N. Limebeer**[1]
Department of Electrical and Electronic Engineering, Imperial College of Science Technology and Medicine, Exhibition Road, London SW7 2BT, UK

**R. S. Sharp**
School of Engineering, Cranfield University, Whittle Building, Bedford MD43 0AL, UK

**S. Evangelou**
Department of Electrical and Electronic Engineering, Imperial College of Science Technology and Medicine, Exhibition Road, London SW7 2BT, UK

*A study of the effects of regular road undulations on the dynamics of a cornering motorcycle is presented. This work is based on an enhanced version of the motorcycle model described in "A Motorcycle Model for Stability and Control Analysis" (R. S. Sharp and D. J. N. Limebeer, 2001, Multibody Syst. Dyn., Vol. 6, No. 2, pp. 123–142). We make use of root-locus and frequency response plots that were derived from a linearized version of this model; the linearization is for small perturbations from a general steady-cornering equilibrium state. The root-locus plots provide information about the damping and resonant frequencies of the key motorcycle modes at different machine speeds, while the frequency response plots are used to study the propagation of road forcing signals to the motorcycle steering system. Our results are based on the assumption that there is road forcing associated with both wheels and that there is a time delay between the front and rear wheel forcing signals—this is sometimes referred to as wheelbase filtering. As has been explained before, control systems are used in the nonlinear simulation code to establish and maintain the machine's speed and roll angle at preset values (for flat road running). These controllers are used to find the machine's equilibrium state and not to emulate a rider's control actions. The results show that at various critical cornering conditions, regular road undulations of a particular wavelength can cause severe steering oscillations. At low speeds the machine is susceptible to road forcing signals that excite the lightly damped wobble and front suspension pitch modes. At higher speeds it is the weave and front wheel hop modes that become vulnerable to road forcing. We believe that the results and theory presented here explain many of the stability related road accidents that have been reported in the popular literature and are therefore of practical import. The models used in this research make use of the multibody modelling package AUTOSIM (Autosim 2.5+ Reference Manual, 1998, Mechanical Simulation Corporation) and are available at the web site http://www.ee.ic.ac.uk/control/motorcycles/. The motorcycle and tire parameters can be found at the end of the code.* [DOI: 10.1115/1.1507768]

## 1 Introduction

It has been known for a long time that single-track vehicles can be unstable. Prior research has examined this issue in the context of small perturbations from straight running ([1–3]), and small perturbations from steady-state cornering ([4–6]). Oscillatory instabilities are clearly problematic and lightly damped resonances are commonplace. It is clear that there is a possibility that these lightly damped modes could be excited by regular road surface undulations. As we will now explain, there is a persuasive body of nontechnical evidence that suggests that these forced oscillations are an illusive source of danger for the riders of powerful motorcycles.

In the established wisdom ([7]) low-frequency weave oscillations are associated with high-speed operation, while higher-frequency wobble, or wheel shimmy resonances, are associated with lower speeds. There is some anecdotal evidence to suggest that wobble frequency steering oscillations can also occur at much higher machine speeds. Collectively, these phenomena are the basis of a notable class of accidents that involve no other road users. Although this type of accident has been known for a long time, it has proved remarkably difficult to obtain a complete understanding of the mechanics involved. There appear to be at least four reasons for this: First, single-track vehicle out-of-control accidents are usually poorly documented and are often not witnessed by independent observers. Secondly, there appears to be a tendency on the part of the investigating authorities and manufacturers to prematurely attribute them to "rider error." Thirdly, these events only occur under an unusual combination of circumstances involving the motorcycle type and setup, the speed, the lean angle, the rider's stature, and the road profile. This is consistent with the notion that the machine development process sometimes fails to reveal these behavioral problems. Finally, we will show that the underlying mechanisms are inherently complex.

A number of reports that describe these handling difficulties have appeared in the popular motorcycle press over the last ten years. Although these reports are based predominantly on anecdotal evidence, there is a compelling level of consistency between them. One example of a loss-of-control event occurred during police motorcycle training and the circumstances of this incident are summarized in the following extract from [8] "... there is a specific section of road which can cause severe handling difficulties for motorcycles being ridden at high speed ... this section of road has a series of small undulations in it at the beginning of a large sweeping right hand bend ...".

Another well-publicized event occurred at a relatively low speed under apparently benign circumstances ([9]): "... we were approaching a village at no more than 65/70 mph, on a smooth road, on a constant or trailing throttle when, for no apparent reason, the bike went wildly out of control ...". This incident and some of the associated background are described in [10–13].

A high-profile fatal accident occurred, when according to an eye witness, the machine being ridden went into a violent "tank slapper"[2] at about 60 mph as the rider was going around a gentle corner ([14]). The offending machine model was subsequently recalled in the U.S. ([15]) as well as in the U.K. ([16]). In their

[1]To whom correspondence should be addressed.

Contributed by the Applied Mechanics Division of THE AMERICAN SOCIETY OF MECHANICAL ENGINEERS for publication in the ASME JOURNAL OF APPLIED MECHANICS. Manuscript received by the ASME Applied Mechanics Division, October 21, 2001; final revision, March 6, 2002. Associate Editor: O. O'Reilly. Discussion on the paper should be addressed to the Editor, Prof. Robert M. McMeeking, Department of Mechanical and Environmental Engineering, University of California–Santa Barbara, Santa Barbara, CA 93106-5070, and will be accepted until four months after final publication of the paper itself in the ASME JOURNAL OF APPLIED MECHANICS.

[2]This expression is used to describe an oscillation that causes the handle bars to swing from lock to lock.

  

recall statement, the manufacturers said: " . . . the front wheel may oscillate, causing the handlebars to move rapidly from side to side when accelerating from a corner and/or (accelerating) over a rough road surface, commonly known as tank slapping . . . ". There was further speculation as to the possible causes of the difficulty and various tests were performed on the machine that involved changing tires, fitting a steering damper and changing the rear damper unit ([17]). Tire changes did not make a significant difference, but a new rear damper unit and a steering damper made a large improvement. One article claimed that riders who weigh over 95 kg (210 lbs) had not experienced the instability phenomena ([18]).

Resonance related difficulties are still being reported in the popular press in the context of modern motorcycles ([19]).

A remarkable video tape of a weave-type instability was taken during the 1999 Formula One Isle of Man TT race ([20]). Paul Orritt can be seen exiting the gentle left-hand bend at the top of Bray Hill on a Honda Fireblade at approximately 150 mph when for no apparent reason his machine went into an uncontrollable 2–3 Hz oscillation. His motorcycle subsequently ran wide and crashed. "It just wouldn't come out of the tank slapper," he recalled. "I was no longer in control . . . the trouble began immediately after I ran over a couple of bumps in the freshly laid road surface . . . " ([21]). Needless to say, the financial and social costs associated with a serious motorcycle accident can be high. The Metropolitan police estimate that the cost of a fatal accident involving one of their officers is approximately £1.2 M ($1.7 M) ([22]). This reason alone is sufficient that the matter should be treated as important and urgent.

The free-steering system and the associated self-steering action is fundamental to the stability and dynamic response properties of all motorcycles and it produces several lightly damped oscillatory modes: wobble, weave, cornering weave, patter, shake, and so on ([4,5,23]). For the purposes of the present study, it is convenient to distinguish straight-running motorcycle behavior from the more complex cornering case. When a motorcycle is upright and running in a substantially straight line, the in-plane motions such as bounce, pitch, and wheel hop are decoupled at first-order level from the out-of-plane motions such as the sideslip, yaw, and roll. When the machine is leaned over in cornering, the in-plane and out-of-plane motions are coupled and this cross-coupling increases with increased roll angle. As a consequence of this feature, mathematical models for the straight-running case are significantly simpler to derive than their cornering counterparts. Notwithstanding Koenen's excellent work ([5]), it seems fair to say that the effective analysis of motorcycle cornering behavior requires an automated multibody modeling software package ([4]). It is clear from the motorcycle dynamics literature that the study of motorcycle cornering effectively stagnated for almost 20 years and that computer assisted multibody modeling tools were needed to break this impasse. Such software has recently been applied to motorcycle dynamics studies ([3,4,23–25]), facilitating considerable extensions to previous knowledge.

When a motorcycle is leaned over in cornering, the coupling terms that cause the in-plane and out-of-plane motions to interact provide a signal transmission path between road undulations and lateral motions. This mechanism provides the means whereby steering oscillations can be produced by road profiling. We believe that the theory and results presented here provide an explanation for most of the behavioral observations described above. In every case it will be assumed that the machine is operating in the neighborhood of an equilibrium cornering condition and we will concentrate on the excitation of steering oscillations.

The paper is concerned with quantifying the machine response to regular road undulations through theoretical analysis. More particularly, the strength of the steering response and the associated design parameter sensitivity problem are studied. The machine condition of interest involves cornering and consequently an elaborate mathematical model of the system is needed. The existing state-of-the-art model ([4]) is extended to include road profile induced effects. The full nonlinear model is linearized for small perturbations about an equilibrium cornering state that is found from a simulation of the motorcycle-rider system on a smooth road. The linear, small perturbation, uncontrolled model is then subjected to sinusoidal road displacement forcing and the frequency responses are computed. The responses to forcing from both the front and rear wheels are considered. When studying the combined effects of front and rear wheel road forcing, a wheelbase travel time delay is introduced into the model that ensures that the two road wheel inputs are correctly phased. Section 2 contains a brief description of the mathematical model and the particular motorcycle being studied (Section 2.1), the modeling extensions required for road forcing studies (Section 2.2), a brief description of the various checks that were used to qualify the computer model (Section 2.3), and the role of the rider and the linearization process (Section 2.4). The results are presented and discussed in Section 3. Section 4 contains the conclusions and a brief commentary on the directions of future work.

## 2 The Mathematical Model

The motorcycle model used in this study is based on that given in Section 3 of [4] and the account given here will only describe the extensions needed for this study. Figure 1 shows the machine in its nominal configuration in static equilibrium with the key modeling points labeled as $p_1, \cdots, p_{14}$. The symbolic multibody modeling package AUTOSIM [26] was used to convert this conceptual model into a FORTRAN code that is used to produce the nonlinear simulation results, and a MATLAB M-file for the linearized model based studies.

The model contains the following components: a main frame with six degrees-of-freedom, a swinging arm and its associated rear suspension system, a body with a roll freedom relative to the main frame that is used to represent the upper body of the rider, a front frame with twist and steer freedoms, telescopic front forks, spinning road wheels, and dynamic tires. The road is assumed to be flat, or regularly profiled, and the motorcycle can travel anywhere in the horizontal plane.

**2.1 The Machine.** The machine and machine parameters are based on a large touring machine of an early 1980's design ([5]); some of its basic parameters are given in Table 1. The interested reader can obtain a complete set of parameters from the website http://www.ee.ic.ac.uk/control/motorcycles/.

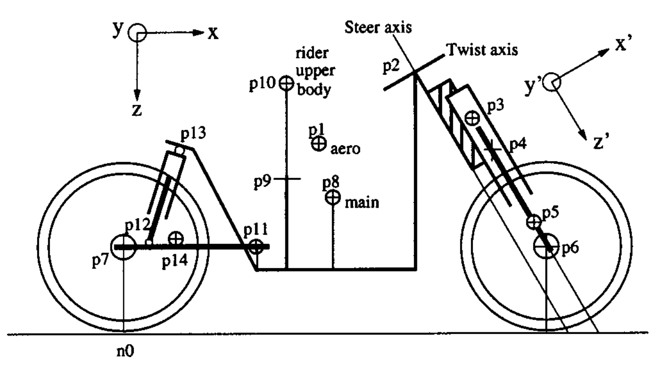


**Fig. 1 Motorcycle model in its nominal configuration**

**Table 1 Machine parameters**

| | |
|---|---|
| Total mass | 235 kg (518 lbs) |
| Maximum engine power | 65 kW (87 bhp) |
| Steering head angle | 30 deg |
| Steering offset | 0.0659 m |
| Mechanical trail | 0.0924 m |

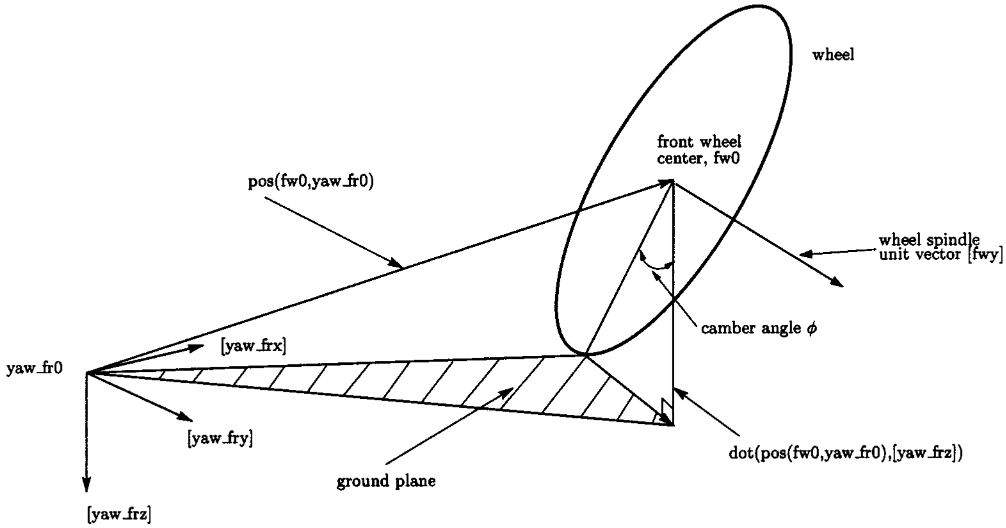


**Fig. 2 Wheel and tire geometry, showing the migration of the ground contact point**

**2.2 Road Forcing.** In order to introduce road forcing into the model, it is necessary to examine the road wheel ground contact geometry in some detail. We will assume that the road undulation amplitudes are small compared to the wheel radii and that their wavelengths are long.

The road wheel ground contact geometry is shown in detail in Fig. 2.

A vector along the line of intersection between the ground and wheel planes can be calculated via a cross product between vectors that are normal to these planes. Since the wheel spindle unit vector `[fwy]` is perpendicular to the wheel plane, and `[yaw_frz]` is a unit vector that is normal to the ground plane, we can use `cross([fwy],[yaw_frz])` to generate the plane-intersection vector. The Appendix contains a brief description of the AUTOSIM instructions used here. The vector pointing from the wheel center to the ground contact point must be perpendicular to both the wheel spindle vector and the plane intersection vector. This vector is computed using the vector triple product `cross(cross([fwy],[yaw_frz]),[fwy])`. To ensure that the triple product is a unit vector, we divide it by the sine of the angle between `[yaw_frz]` and `[fwy]` as follows:

```
cross(cross([fwy],[yaw_frz]),[fwy])/
sqrt(1-dot([fwy],[yaw_frz])**2).
```

Note that `[fwy]` is always perpendicular to `cross([fwy],[yaw_frz])` and consequently there is no need for a second normalization term. The vertical component of the vector joining the origin of the yaw frame axis system `yaw_fw0` to the front wheel center `fw0` is the height from the ground of the wheel center in the case of a smooth road and is computed as follows:

```
dot(pos(fw0,yaw_fr0),[yaw_frz]).
```

In the case of a profiled road, the height from the ground of the front wheel center is adjusted via a front wheel road height variable `uf`:

```
dot(pos(yaw_fr0,fw0),[yaw_frz])-uf.
```

Dividing the height by the camber angle gives the distance from the wheel center to the ground contact point:

```
dot(pos(yaw_fr0,fw0),[yaw_frz])-uf)/
sqrt(1-dot([fwy],[yaw_frz])**2).
```

In the nominal condition, this distance is the wheel radius, so the tire radial deflection from the nominal can be found via a tire deflection calculation and this deflection is converted into a force change via the tire carcass radial stiffness. Combining this with the unit vector defined above, one obtains a vector with the correct magnitude and direction that points from the wheel spindle axis to the ground contact point:

```
cross(cross([fwy],[yaw_frz]),[fwy])*
(dot(pos(yaw_fr0,fw0),[yaw_frz])-uf)/
(1-dot([fwy],[yaw_frz])**2).
```

The contact point can now be defined via the coordinates of this vector as a moving point on the tire circumference. This point is used to calculate the sideslip angle and it is the point of application of the load and the sideforce. A parallel set of arguments apply to the rear road wheel.

**2.3 Model Validation.** The model validation processes used here are an evolution of those described elsewhere ([3,4]). To maximize their effectiveness, they were designed to be substantially independent of the motorcycle model itself. Since we will only describe the updates to the checks described in our earlier work ([3,4]), we suggest that the interested reader consults these papers as well as the modeling code that is located at the web site http://www.ee.ic.ac.uk/control/motorcycles.

The underlying principles behind the checks are that under equilibrium conditions: (i) the external forces acting on the motorcycle rider system must match the sum of the inertial and gravitational forces, (ii) the external moments acting on the motorcycle rider system must sum to zero and (iii) the power supply and dissipation must be equal.

*The Force Balance.* The force balance check ensures that under equilibrium cornering conditions the sum of the external forces is equal to the sum of the inertial and gravitational forces. To check the balance, the force error

$$\mathbf{F}_{\mathrm{error}} = \sum_i \mathbf{F}_i^{\mathrm{ext}} + \left( \sum_j m_j \right) (\mathbf{v} \times \boldsymbol{\omega} + \mathbf{g})$$

was computed. The first sum contains the external forces, while the second sum contains the centripetal and gravitational forces. The $\mathbf{F}_i^{\mathrm{ext}}$'s include: (i) the aerodynamic lift and drag forces, (ii) the front and rear wheel normal loads, (iii) the tire side forces,

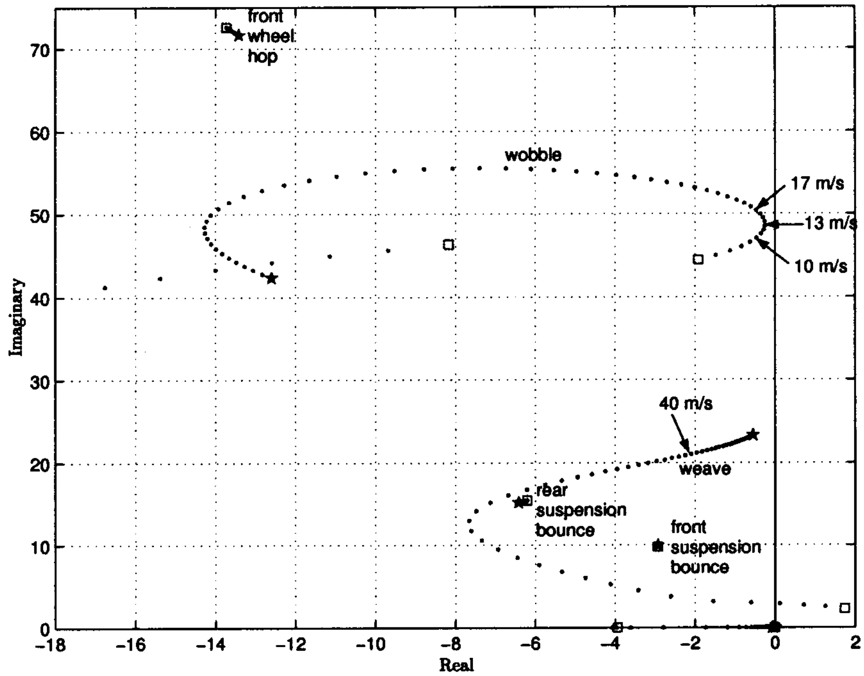


**Fig. 3 Straight running root-locus with speed the varied parameter. The speed is increased from 5 m/s (11 mph) (□) to 60 m/s (135 mph) (★).**

and (iv) the longitudinal driving and braking forces that act on the wheels at the ground contact points. In the second term, the $m_j$'s are the machine's constituent masses, $\mathbf{v}$ is the velocity of the mass center of the main body, $\boldsymbol{\omega}$ is the main body yaw rate vector, and $\mathbf{g}$ is the gravitational acceleration vector. In our experience, one should achieve $|F_{\text{error}}|<4N$, although many of the constituent forces have magnitudes of several thousands of Newtons.

*The Moment Balance.* In much the same way, it is possible to check that under equilibrium cornering conditions a moment error vector is zero. We compute

$$\mathbf{M}_{\text{error}}=\sum_i \mathbf{l}_i\times m_i(\mathbf{v}\times\boldsymbol{\omega}+\mathbf{g})+\sum_j \mathbf{l}_j\times\mathbf{F}_j+\sum_k \mathbf{M}_k .$$

The reference point for all the moment calculations is the rear-wheel ground contact point. The $\mathbf{l}_i$'s are moment arm vectors that point from the reference point to the appropriate mass centers and $m_i(\mathbf{v}\times\boldsymbol{\omega}+\mathbf{g})$ are the corresponding inertial and gravitational forces. The index $i$ ranges over each of the constituent masses. The second term contains all the external force-induced moments including: (i) the aerodynamic lift and drag forces, (ii) the front wheel normal load, (iii) the front wheel lateral tire forces and the (iv) the front tire longitudinal force. The $\mathbf{l}_j$'s are moment arms that point from the reference point to the points of application of the various forces. The third term contains the gyroscopic moments due to the rates of change of angular momentum of the spinning road wheels under cornering, and the tyre moments. In our experience, one should achieve $|M_{\text{error}}|<5$ Nm, although some of the constituent moments have magnitudes of several thousand Newton meters.

*The Power Audit.* This check is based on a ‘‘conservation of power’’ audit. The power source is the engine and the most important dissipators are the aerodynamic forces. Not surprisingly, a reliable checking process necessitates the inclusion of other effects to do with the tire forces and moments, some of which are subtle. The tires dissipate power via the longitudinal and lateral slip forces and this power dissipation is, in each case, computed via a dot product of the form $\mathbf{F}\cdot\mathbf{v}$ in which $\mathbf{F}$ is the force applied to the tread base material and $\mathbf{v}$ is the corresponding velocity.[3] The longitudinal component of this velocity is the machine velocity multiplied by the tire's longitudinal slip, while the lateral component is the machine velocity multiplied by the tangent of the tire sideslip angle. The remaining dissipation effects are associated with the tires' aligning moments. These dissipation effects can be computed using expressions of the form $\mathbf{M}\cdot\boldsymbol{\omega}$ in which the $\mathbf{M}$'s are the aligning moments and the $\boldsymbol{\omega}$'s are the wheel's angular velocity vectors. Our experience has been that the power checksum error should be no more than 1 W.

**2.4 Linearized Models and Frequency Response Calculations.** The preparation of linearized models involves a two-step procedure. In the first, AUTOSIM is used to compute, symbolically, the linearized equations of motion. In the second, the nonlinear simulation code is used to find the equilibrium state associated with the steady-state cornering condition being studied. In order to expedite the convergence of the simulation to the required condition, the drive and steering torques are controlled by feedback loops. The drive torque is controlled so that the machine maintains a preset speed, while the steering torque is adjusted to maintain a desired roll angle. In a sense, the feedback control is simply part of an algorithm that is used to solve the motorcycle's equilibrium equations of motion. We have not attempted to replicate any active rider control actions for the following reasons:

1 Individual riders have their own styles and attempting to quantify the ‘‘typical rider’’ using computer code is little more than potentially misleading speculation.

2 Our focus here is on phenomena of 2–4 Hz (weave) and 6–8 Hz (wobble). The evidence suggests that most riders would find it difficult to react consistently to an unfamiliar weave-frequency type phenomenon and rider control intervention could make matters worse. Wobble frequency effects are effectively outside the rider's bandwidth and so in this case studying the uncontrolled machine is felt appropriate. The steering damping used here, with

[3]The required velocity is that of a material point of the tire that is currently the nominal contact point. This material point changes continuously as the wheel rotates.

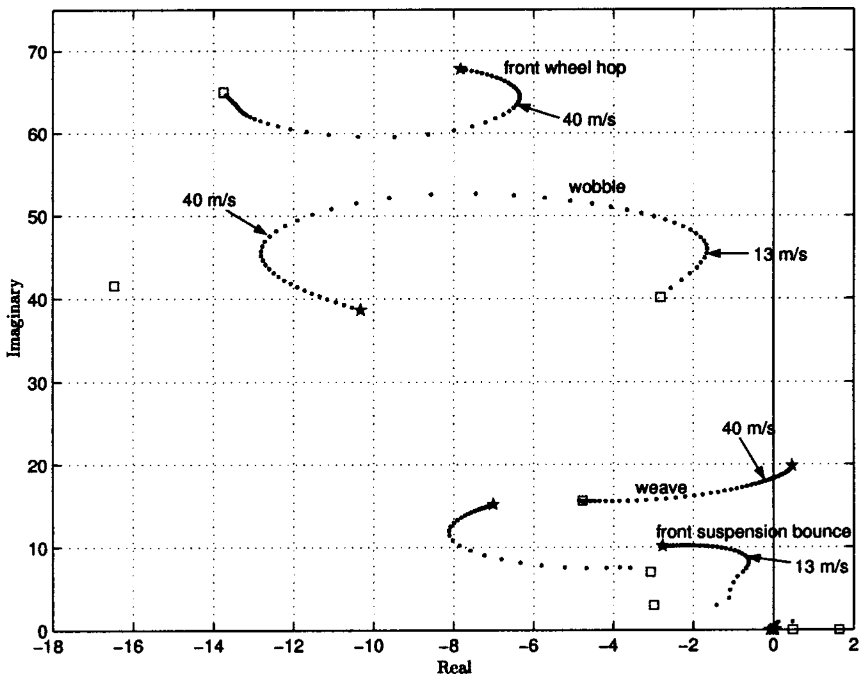


**Fig. 4 Root-locus for a fixed roll angle of 30 deg. The speed is increased from 6 m/s (□) to 60 m/s (★).**

a nominal value of 7.4 Nm/(rad/s), is predominantly due to the rider's grip on the handlebars—this represents passive rather than active control.

3 Our aim is to characterize the properties of the machine in isolation, because a well-designed vehicle should behave safely even in the hands of riders who have limited skill and experience.

We will present a number of Bode (frequency response) plots that were calculated using linearized models computed by AUTOSIM. In our case, we used two inputs $u_f$ and $u_r$ that represent changes in the road height at the front and rear wheels' ground contact points, respectively. The steering angle $\delta$ was the only output. Let us now suppose that the state-space model, generated by AUTOSIM, that corresponds to a given cornering trim condition is

$$\dot{\mathbf{x}} = A\mathbf{x} + B\mathbf{u}$$

$$\delta = C\mathbf{x}$$

in which

$$\mathbf{u} = \begin{bmatrix} u_f \\ u_r \end{bmatrix}.$$

The transfer functions that relate the front and rear road disturbance input to the steering angle are given by

$$[g_f \;\; g_r] = C(sI - A)^{-1}B$$

in which $s$ is the usual Laplace transform complex variable. One can study separately the influences of the front and rear road-wheel disturbances using $g_f(s)$ and $g_r(s)$ independently. In the case of studies of the combined influence of both wheels, the transfer function

$$g(s) = g_f(s) + e^{-sr}g_r(s)$$

is used, in which $\tau$ is the wheelbase filtering time delay given by $w_b/v$. The constant $w_b$ is the machine wheelbase and $v$ its forward speed. All our computations and plot outputs were obtained using MATLAB ([27]) M-files.

## 3 Results

**3.1 Introductory Comments.** Straight running root-loci of the type presented in Fig. 3 are well known in the motorcycle literature; see, for example, [1,2,28,29].

This plot shows that the wobble mode[4] is lightly damped at 13 m/s (29 mph) and that the associated resonant frequency is approximately 48 rad/s (7.6 Hz). This diagram also shows that the weave mode[5] becomes lightly damped at high speeds and that the resonant frequency of this mode is approximately 22 rad/s (3.5 Hz) at a machine speed of 40 m/s (90 mph). It should also be noted that the front wheel hop mode,[6] the rear suspension bounce (pitch) mode,[7] and the front suspension bounce (pitch) mode[8] are relatively insensitive to variations in the machine speed. This observation reinforces the notion that the in-plane and out-of-plane dynamics are decoupled from each other under straight running conditions. We should also observe that in-plane disturbances such as sinusoidal road undulations will not couple at first-order level into out-of-plane freedoms such as the roll and steering angles.

Let us now contrast Figs. 3 and 4 with the help of Figs. 5 and 6. Figure 4 shows the behavior of the important machine modes under cornering at different speeds at a fixed roll angle—in this case 30 deg. Figures 5 and 6 show the effect of varying the machine roll angle at two constant speed values 13 m/s (29 mph) and 40 m/s (90 mph). When one compares these plots, it can be seen that

[4]This is sometimes called the wheel shimmy mode and is associated with a front wheel castoring type oscillation.

[5]This is associated with a 2–4 Hz fish tailing motion involving the simultaneous rolling and yawing of the whole machine.

[6]This mode is associated with an oscillation that involves the compression and expansion of the fork legs and the tire carcass.

[7]This mode is associated with an oscillatory motion of the swinging arm. This movement results in the pitching, and to a lesser extent, the heaving of the machine's main body.

[8]This mode is dominated by a pitching motion that hinges around the rear wheel ground contact point and involves the oscillatory compression and expansion of the fork leg assemblies. When this mode is excited there is also a discernible heaving of the machine's main body.

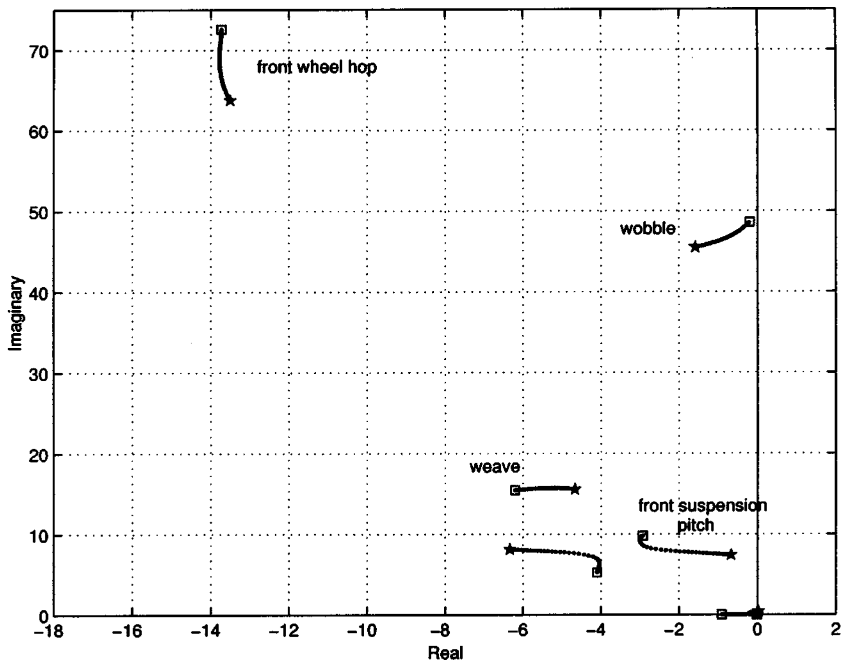


**Fig. 5 Root-locus for a fixed speed of 13 m/s (29 mph). The roll angle in increased from 0, (□) to 30 deg (★).**

1. cornering increases the damping of the wobble mode, while the speed for minimum damping remains at approximately 13 m/s (29 mph). The associated resonant frequency of this mode is essentially unaffected.
2. cornering reduces the damping of the front wheel hop mode and it is least damped at approximately 40 m/s (90 mph) with an associated resonant frequency of approximately 63 rad/s (10 Hz). This figure is lower than the straight running figure of 73 rad/s (11.6 Hz).
3. cornering tends to reduce the damping of the weave mode and in our case this mode becomes unstable at high speed; the weave mode is lightly damped at 40 m/s (90 mph).
4. cornering has a destabilizing effect on the front suspension pitch mode and it becomes particularly lightly damped at 13 m/s and 30 deg of roll angle. The resonant frequency of this mode is approximately 8 rad/s (1.27 Hz) under these conditions.

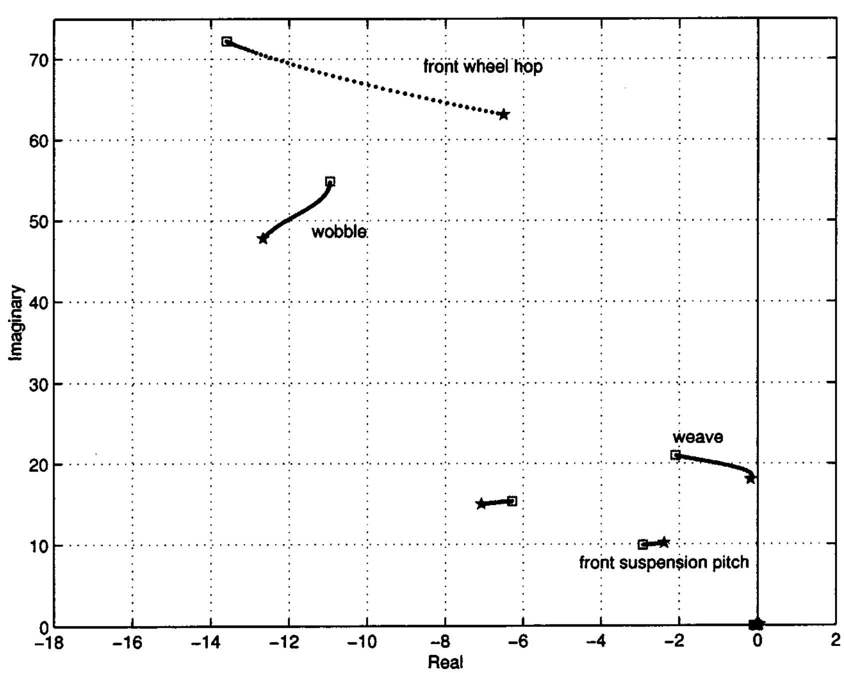


**Fig. 6 Root-locus for a fixed speed of 40 m/s (90 mph). The roll angle in increased from 0, (□) to 30 deg (★).**

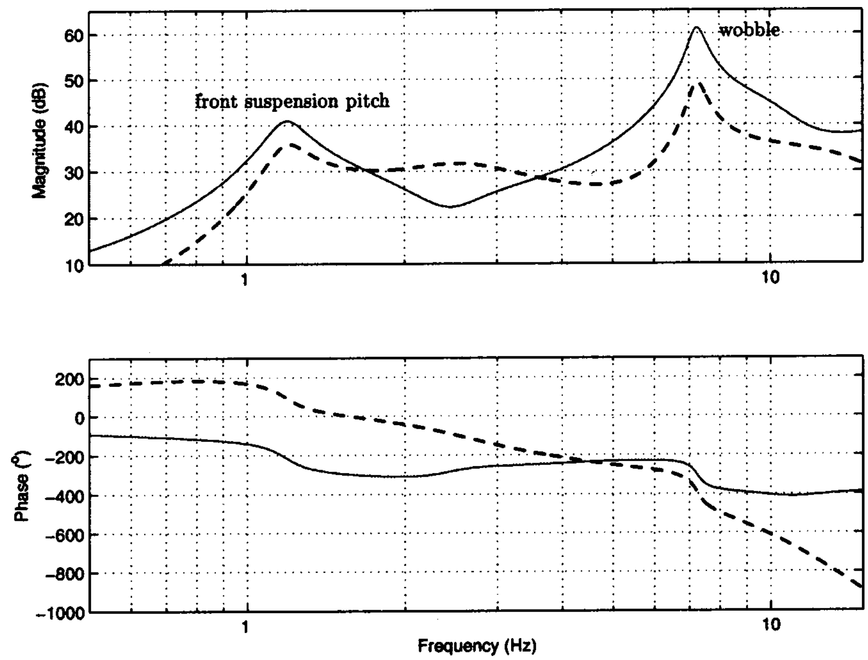


**Fig. 7 Frequency response for $g_f(s)$ (solid), and $e^{-s\tau}g_r(s)$ (dashed) (0 dB=1 deg/m). The steady-state conditions are a 30 deg roll angle and a forward speed of 13 m/s (29 mph).**

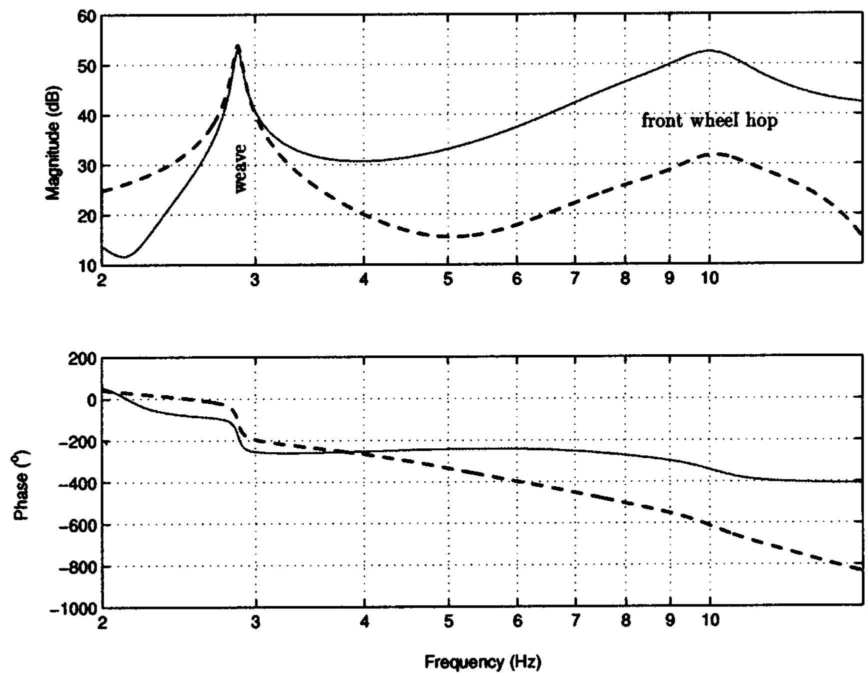


**Fig. 8 Frequency response for $g_f(s)$ (solid), and $e^{-s\tau}g_r(s)$ (dashed) (0 dB=1 deg/m). The steady-state conditions are a 30 deg roll angle and a forward speed of 40 m/s (90 mph).**

Since road forcing signals will couple into out-of-plane freedoms under cornering, these observations lead to the following hypotheses:

1. The wobble and front suspension pitch modes are exposed to resonant forcing due to road profiling at speeds of the order 13 m/s (29 mph), and
2. the weave and front wheel hop modes are similarly vulnerable at high speeds.
3. Since the coupling between road disturbances and the out-of-plane dynamics increases with roll angle, we expect to find an increase in the vulnerability of the front wheel hop mode, the weave mode, and the front suspension pitch mode with roll angle. All three modal dampings decrease with increased roll angle.
4. We expect the vulnerability of the wobble mode to reach a peak at some worst-case value of roll angle. We suggest this

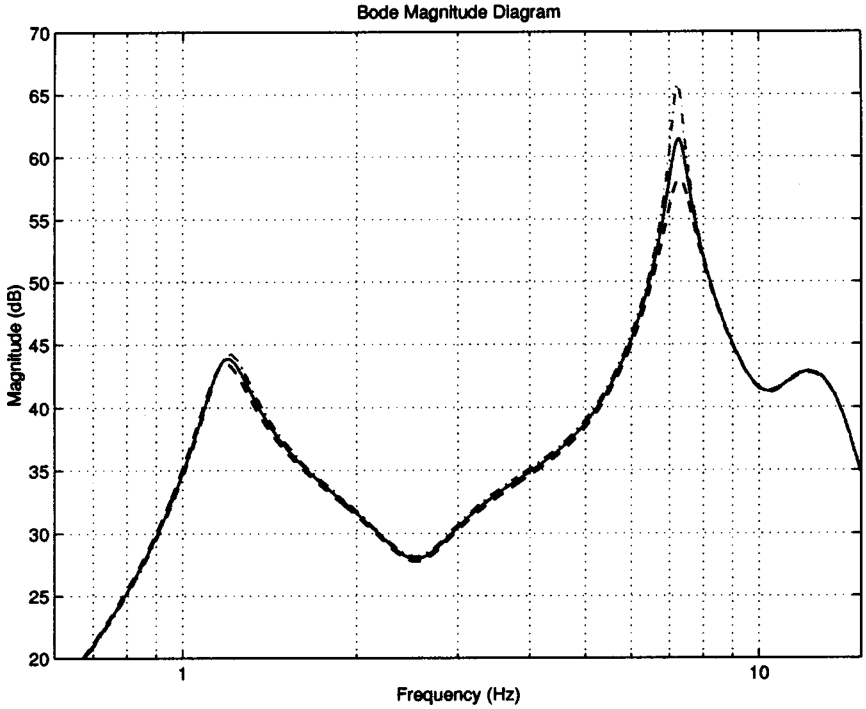


**Fig. 9 Bode magnitude plot of $g(s)$ (0 dB=1 deg/m). Nominal state: 13 m/s (29 mph), 30 deg roll angle. The solid curve represents the nominal case, the dashed one shows the effect of an increase of 20% in the steering damper setting, while the dot-dash curve shows the effect of a 20% reduction in the steering damping.**

because the interplane coupling increases with roll angle, while the damping of the wobble mode increases with roll angle.

It is the business of the remainder of this paper to investigate these conjectures.

**3.2 Individual Wheel Contributions.** Figure 7 shows Bode plots of $g_f(s)$ and $e^{-s\tau}g_r(s)$ at the relatively low speed of 13 m/s (29 mph), a roll angle of 30 deg and with nominal parameter values. It is clear from these plots that the resonant peaks for both the wobble and front suspension pitch modes are front-wheel-input dominated. The difference between the front and rear wheel excited resonant peaks for the wobble mode is 12 dB, while that for the front suspension pitch mode is approximately 5 dB. We conclude, therefore, that difficulties with either of these modes will almost certainly be ameliorated via adjustments to the front of the machine.

The situation at higher speeds is quite different as is shown in Fig. 8. At 40 m/s (90 mph) and 30 deg of roll, we see that there are resonance peaks associated with the weave and the front wheel hop modes. In the case of the weave mode, the front and rear wheel forcing signals are making equal contributions and their combined effect is a large one. Resonance difficulties with this mode are likely to be more difficult to isolate and prevent, because the problem involves potentially the geometry and parameters of the whole machine as well as the properties of both tires. The excitation of the front wheel hop mode is due almost entirely to front wheel forcing and is consequently a problem that can be isolated and tackled at the front of the bike.

At the weave mode peak, the frequency responses $g_f(s)$ and $e^{-s\tau}g_r(s)$ have a phase angle difference of approximately 56 deg. As the motorcycle speed changes, the phase shift $e^{-s\tau}$ associated with the wheelbase travel time changes. In principle, therefore, changing the speed will influence the maximum gain, not only through affecting the modal damping factor, but also through influencing the phase angle. However, changing the speed from 38 to 42 m/s (85 mph to 95 mph) only changes the phase lag, at the weave mode frequency of 18 rad/s (2.86 Hz), by about 4 deg. Quantitatively, therefore, the reinforcement/cancellation issue is a small one.

**3.3 Low-Speed Forced Oscillations.** The root-loci presented in Fig. 5 suggest that road forcing effects may cause the wobble and front suspension pitch modes to resonate at low speeds in response to regular road profiling. We begin our investigation of this possibility by referring to Fig. 9 that shows a frequency response plot that relates road forcing inputs to the vehicle's steer angle. The road profile input is in meters, while the output is in degrees. If the vehicle is traveling at 13 m/s (29 mph), road undulations with a wavelength of 1.8 m (5.85 ft), will generate a road forcing signal with a frequency of 45.4 rad/s (7.22 Hz). Since the transfer function gain is approximately 62 dB at this frequency, Fig. 9 indicates that one can expect $\pm 1.28$ deg of steering movement for road undulations with amplitude $\pm 1$ mm. If we assume that the steering head mechanism can move through approximately $\pm 20$ deg from lock to lock, the linear model would suggest that road undulations of $\pm 15$ mm will produce a sustained "tank slapping" action.[9] This figure also shows that road undulations could excite the front wheel hop mode, but the gain is only approximately 44 dB in this case.

Immediately, it is of interest to consider the influences of design and/or suspension parameter changes on the resonant peaks. Figure 9 also shows the effect of changing the steering damper setting by $\pm 1.5$ Nms/rad around the nominal value of 7.4 Nms/rad. Decreasing the steering damper setting causes the road forcing gain to increase to 66 dB, while increasing it reduces the gain to 58 dB.

The root-loci presented in Fig. 5 demonstrate an increase in the wobble mode damping with increased roll angle. As a consequence, we predicted that a reduction in roll angle could lead to an increase (rather than a decrease) in the wobble mode peak gain

[9]Note that this is only an estimate from a linearized model—see Section 3.6 for more on nonlinear effects.

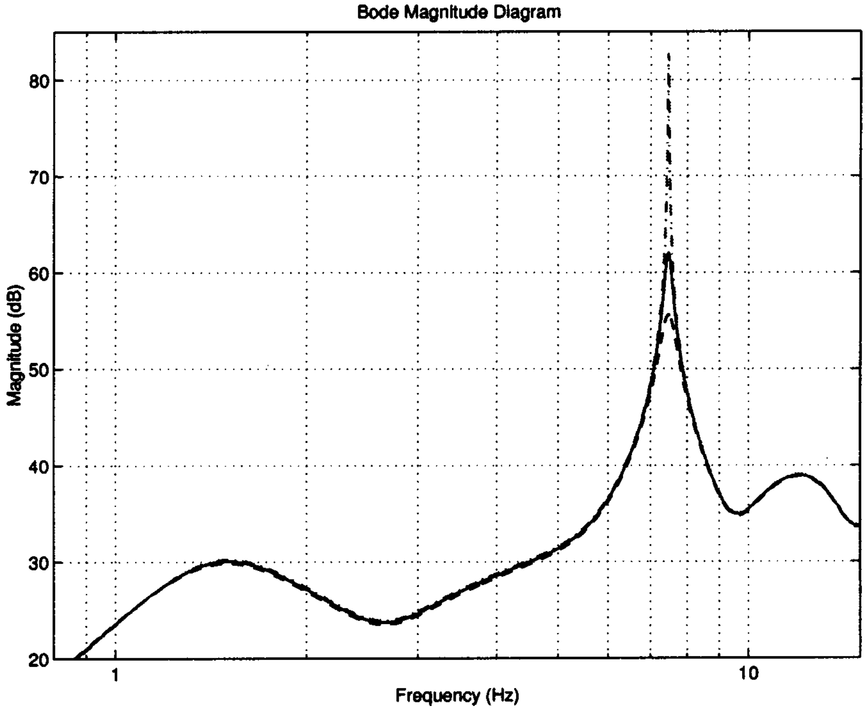


**Fig. 10** Bode magnitude plot of $g(s)$ (0 dB=1 deg/m). Nominal state: 13 m/s (29 mph), 15 deg roll angle. The solid curve represents the nominal case, the dashed one shows the effect of an increase of 20% in the steering damping, while the dot-dash curve shows the effect of a 20% decrease.

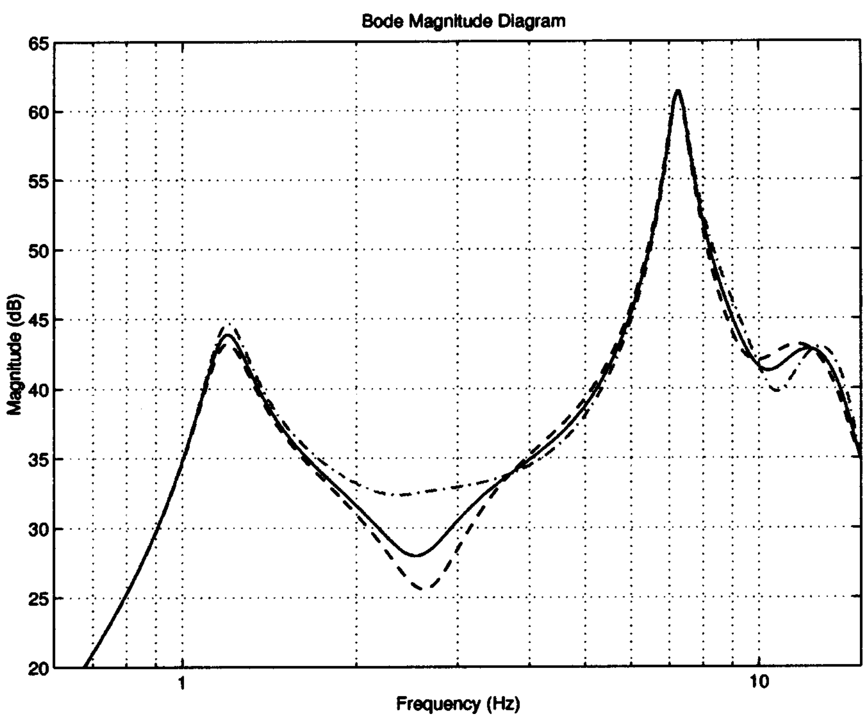


**Fig. 11** Bode magnitude plot of $g(s)$ (0 dB=1 deg/m). Nominal state: 13 m/s (29 mph), 30 deg roll angle. The solid curve represents the nominal case, the dashed one shows the effect of an increase of 40% in the rear damper setting, and the dot-dash curve shows the effect of a 40% decrease.

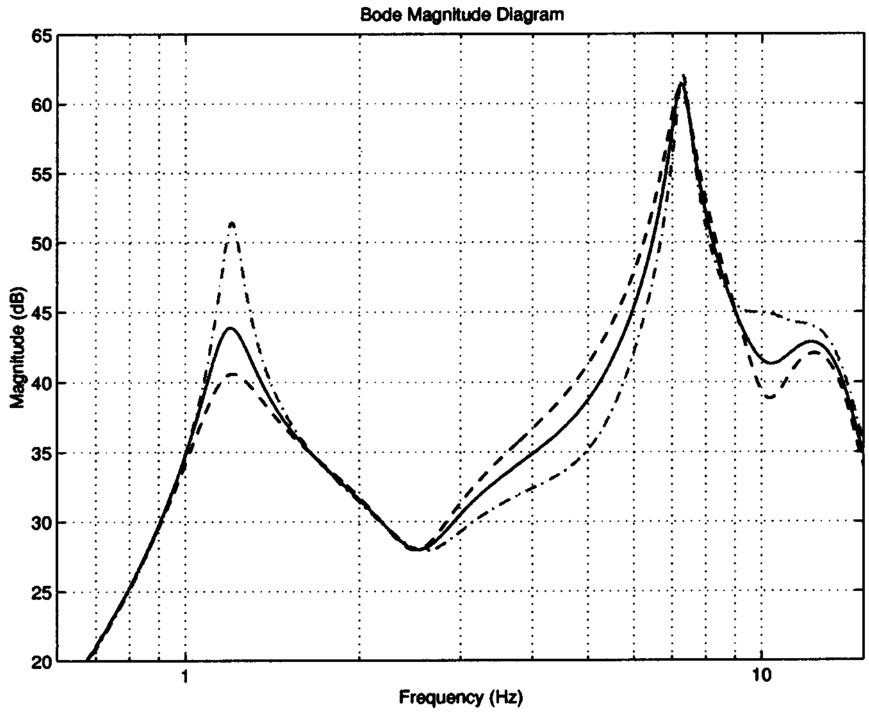


**Fig. 12 Bode magnitude plot of $g(s)$ (0 dB=1 deg/m). Nominal state: 13 m/s (29 mph), 30 deg roll angle. The solid curve represents the nominal case, the dashed one shows the effect of an increase of 40% in the front damper setting and the dot-dash curve shows the effect of a 40% decrease.**

despite an accompanying reduction in the coupling between the in-plane and out-of-plane dynamics. Figures 9 and 10 show that the peak wobble mode gain for the 15 deg and 30 deg roll angle cases are roughly equal at 62 dB for the nominal value of steering damping. An increase of 20% in the steering damping decreases the peak wobble mode gain to approximately 55 dB (rather than 58 dB in the case of 30 deg of roll). When the steering damping is decreased by 20%, the peak wobble mode gain increases to 83 dB which is substantially higher than the peak gain achieved at 30 deg of roll angle.

Figure 11 shows that changing the rear damper setting has little impact on the susceptibility of the wobble and front suspension pitch modes to road forcing. This result casts doubt on the suspected contributions of the rear damper to the wobble mode instability associated with the Suzuki TL1000 ([17]).

As one would expect, the damping of the front suspension pitch mode, and consequently the road forcing gain associated with that mode, is influenced by changes in the front suspension damper setting. Figure 12 shows the effect of changing this damper setting by $\pm 220$ Ns/m about a nominal setting of 550 Ns/m. Although the wobble mode gain is relatively unaffected by these changes, the impact on the pitch mode is significant and it can be seen that a reduction of 220 Ns/m leads to a gain increase of 8 dB over the nominal value.

**3.4 High-Speed Forced Oscillations.** At the beginning of Section 3, we argued that at high speeds the weave and front wheel hop modes are vulnerable to regular road waves of critical dimensions. The consequent forced oscillations are a significant potential threat to the motorcyclist, because it is a high-speed phenomenon and for typical motorcycle parameters, long-wavelength low-amplitude road undulations will excite these modes. Also, regular long-wavelength low-amplitude undulations are virtually impossible for the rider to see. At a speed of 40 m/s (90 mph) with the motorcycle parameters used here, the weave mode will be excited by road undulations with a wavelength of approximately 14 m (45.5 ft), while a 4 m (13 ft) wavelength will excite the front wheel hop mode.

Figure 13 show a Bode magnitude plot of the transfer function that relates the steering angle to regular road height variations. For nominal suspension and steering damper settings, the weave mode gain at 18 rad/s (2.86 Hz) is 58 dB, while the front wheel hop mode gain is 52 dB. As in the case of wobble mode excitation, this diagram shows that relatively low-amplitude road undulations will cause the rider concern. This plot also shows that an increase in the steering damper setting will make matters significantly worse. More particularly, a steering damping increase of 1.5 Nms/rad increases the road forcing gain by 10 dB, or a factor of 3.

Figure 13 also shows that the steering damper setting has little impact on the front wheel hop resonance.

Figure 14 shows the effect of changes to the rear damper setting. As with the steering damper, an increase in the rear damping increases the weave mode gain by 5 dB, while reducing this damper setting causes the peak value of weave gain to fall by 4 dB. Also, it is clear that this change has virtually no influence on the front wheel hop peak gain that remains fixed at approximately 52 dB.

Figure 15 shows the effect of changes to the front damping. In contrast to the previous two plots, this diagram shows that increasing the front damper setting has a beneficial impact on the weave and front wheel hop gain peaks. An increase of 220 Ns/m in the front damper coefficient reduces the weave gain peak and the front wheel hop gain peak by approximately 2 dB. If the front damping is reduced by a like amount, the weave mode gain peak increases by approximately 3 dB and the front wheel hop gain peak increases by approximately 6 dB.

**3.5 Influence of Rider Parameters.** There is anecdotal evidence to suggest that the weight and posture of the rider can influence the vulnerability of the motorcycle-rider system to

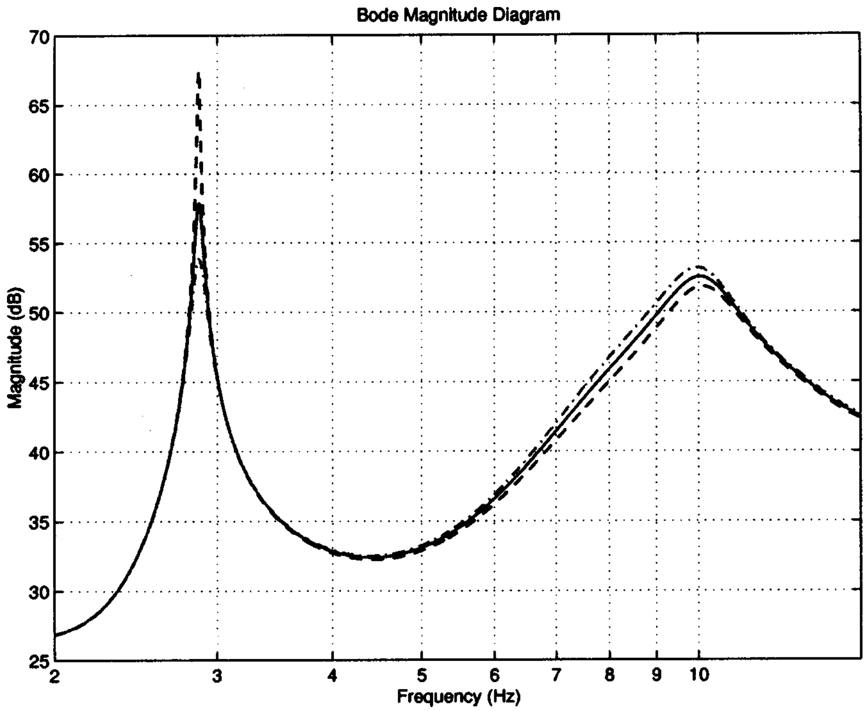


Fig. 13 Bode magnitude plot of $g(s)$ (0 dB=1 deg/m). Nominal state: 40 m/s (90 mph), 30 deg roll angle. The solid curve represents the nominal case, the dashed one shows the effect of an increase of 20% in the steering damper setting and the dot-dash curve shows the effect of a 20% decrease.

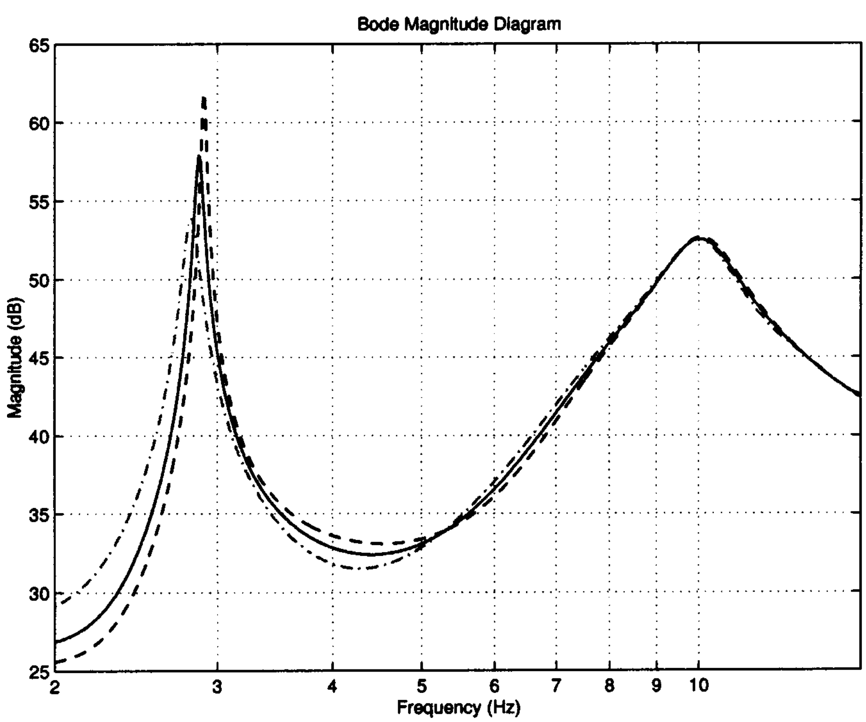


Fig. 14 Bode magnitude plot of $g(s)$ (0 dB=1 deg/m). Nominal state: 40 m/s (90 mph), 30 deg roll angle. The solid curve represents the nominal case, the dashed one shows the effect of an increase of 40% in the rear damper setting and the dot-dash curve shows the effect of a 40% decrease.

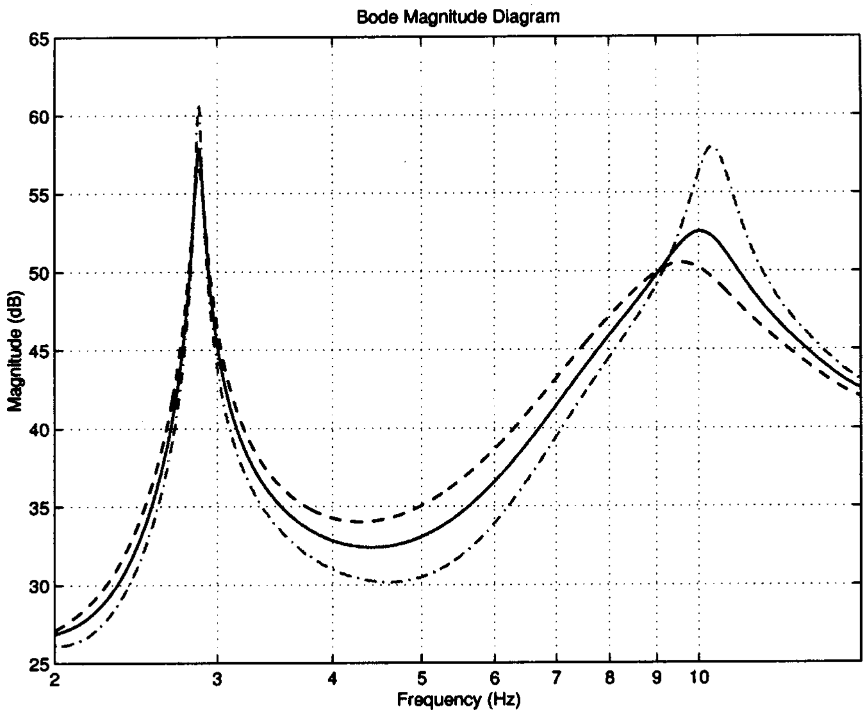


**Fig. 15** Bode magnitude plot of $g(s)$ (0 dB=1 deg/m). Nominal state: 40 m/s (90 mph), 30 deg roll angle. The solid curve represents the nominal case, the dashed one shows the effect of an increase of 40% in the front damper setting and the dot-dash curve shows the effect of a 40% decrease.

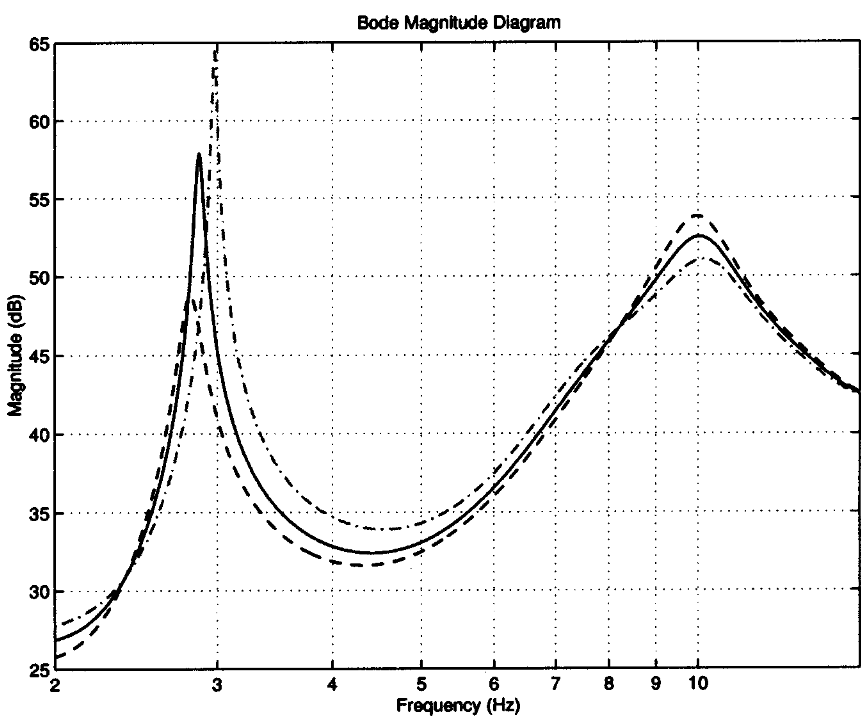


**Fig. 16** Bode magnitude plot of $g(s)$ (0 dB=1 deg/m). Nominal state: 40 m/s (90 mph), 30 deg roll angle. The solid curve represents the nominal case, the dashed one shows the effect of an increase of 20 kg (4.1 lbs) in the mass of the upper body of the rider and the dot-dash curve shows the effect of a 20 kg (4.1 lbs) decrease.

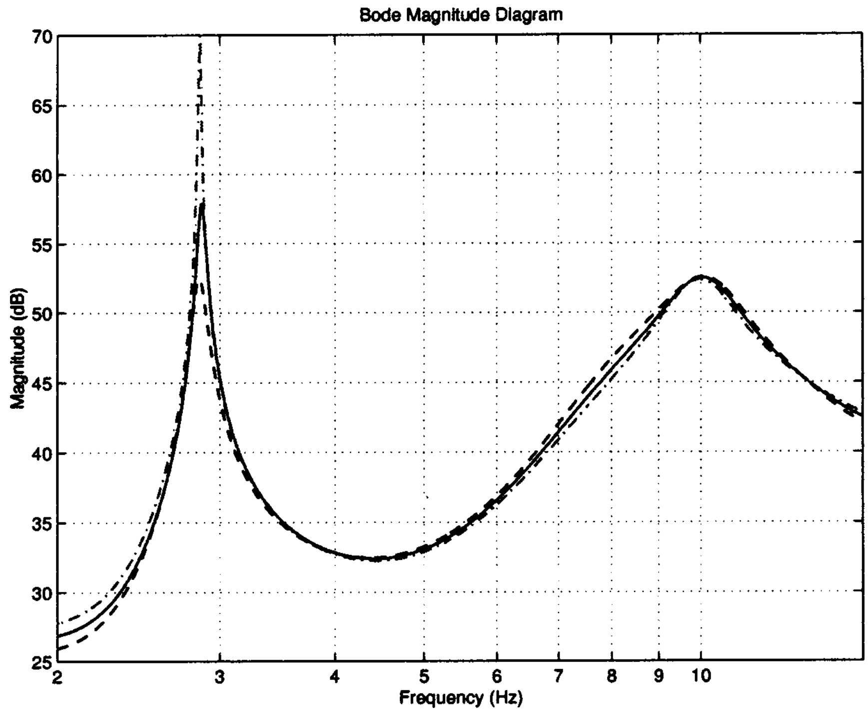


**Fig. 17** Bode magnitude plot of $g(s)$ (0 dB=1 deg/m). Nominal state: 40 m/s (90 mph), 30 deg roll angle. The solid curve represents the nominal case, the dashed one shows the effect of a forward shift of 15 cm (5.91 ins) in the center of mass of the upper body of the rider and the dot-dash curve shows the effect of a rearward shift of 15 cm (5.91 ins).

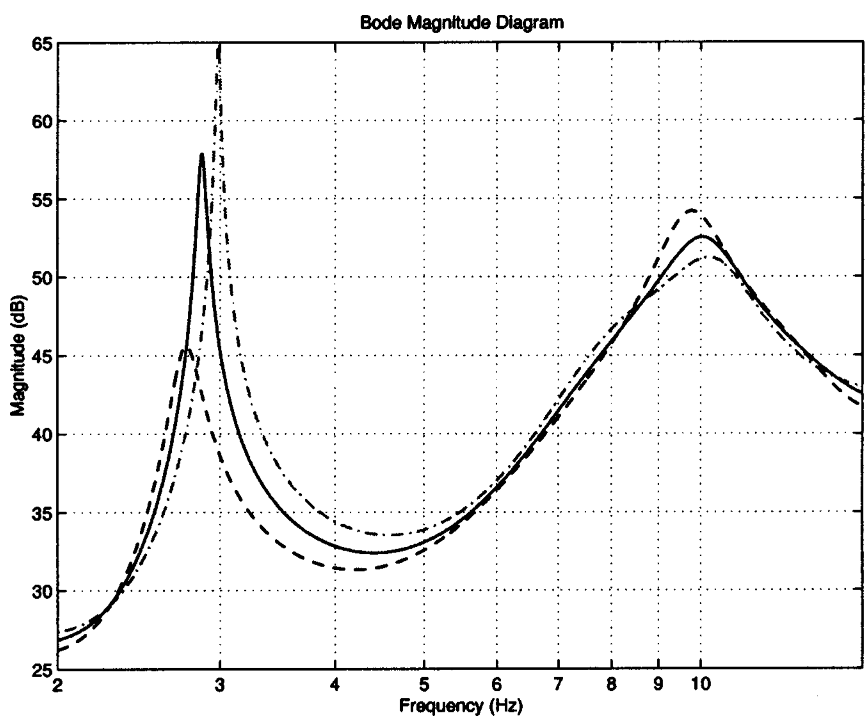


**Fig. 18** Bode magnitude plot of $g(s)$ (0 dB=1 deg/m). Nominal state: 40 m/s (90 mph), 30 deg roll angle. The solid curve represents the nominal case, the dashed one shows the effect of an upward shift of 15 cm (5.91 ins) in the center of mass of the upper body of the rider and the dot-dash curve shows the effect of a downward shift of 15 cm (5.91 ins).

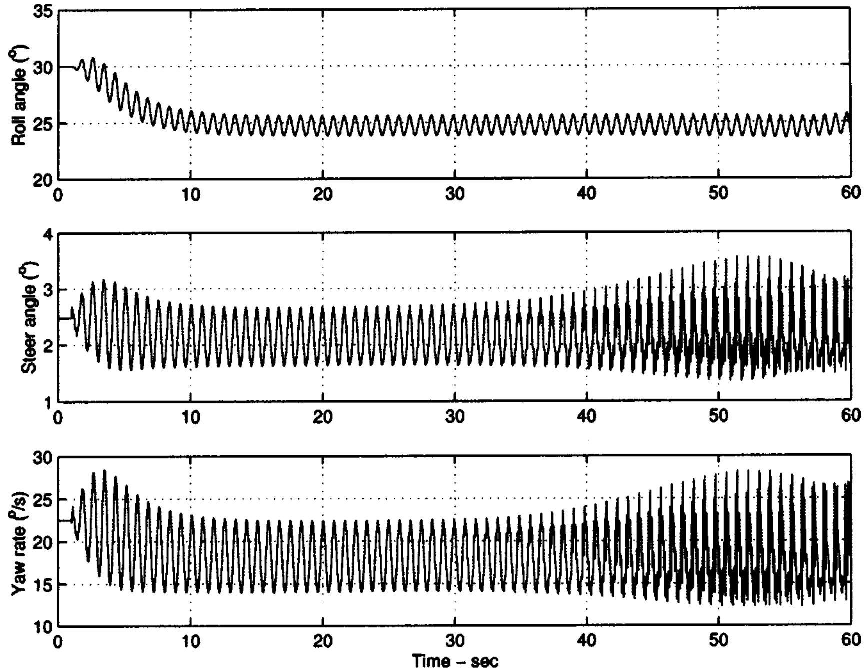


**Fig. 19 Transient behavior of the roll and steering angles, and the yaw rate in response to sinusoidal road forcing that begins at $t=1$ s and has a peak amplitude of 0.5 cm. The forcing frequency is tuned to the front suspension pitch mode. The lean angle is 30 deg and the forward speed 13 m/s (29 mph).**

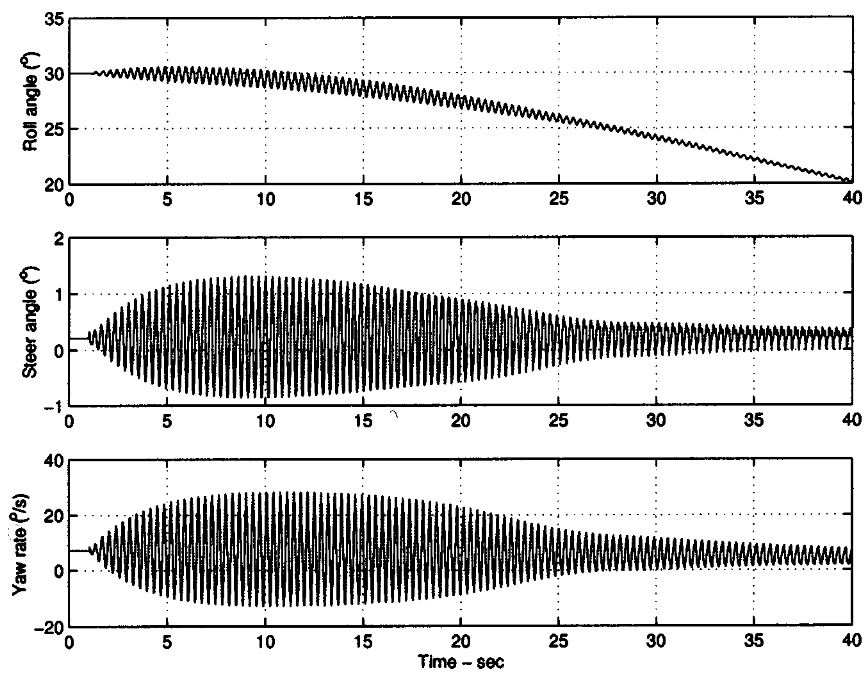


**Fig. 20 Transient behavior of the roll and steer angles and the yaw rate, in response to sinusoidal road forcing that begins at $t=1$ s and has a peak amplitude of 0.25 cm. The forcing frequency is tuned to the weave mode. The lean angle is 30 deg and the forward speed 40 m/s (90 mph).**

weave related oscillations. We will investigate the suggestion that light riders are more likely to experience difficulties with oscillatory instabilities than are heavier ones ([18,30]). We will also investigate the suggestion that the rider can attenuate weave related oscillations by lying down on the tank ([30]). We will carry out this study at a speed of 40 m/s (90 mph) and a roll angle of 30 deg, via changes in the rider's upper body mass and mass center location.

The effect of changes in the rider's upper body mass on the transfer function that maps road vertical displacement to the steering angle are studied in Fig. 16. As suggested in [18], an increase in the rider's upper body mass by 20 kg (44.1 lbs) reduces this gain peak by approximately 8 dB. In the same way, a reduction of the rider's upper body mass by 20 kg (44.1 lbs) increases the peak gain by approximately 7 dB.

The effect of variations in the longitudinal location of the rider's center of mass are studied. As suggested by the video tape ([30]), a forward shift in the rider's upper body mass appears in Fig. 17 to reduce the vulnerability of the motorcycle to weave related instabilities. In our study, we see a small reduction in the signal transmission gain peak of 5 dB for a forward shift of 15 cm (5.85 ins). If the center of mass is shifted backwards by 15 cm (5.85 ins), the transmission gain peak increases by approximately 13 dB.

The effect of variations in the (vertical) $z$-direction location of the rider's center of mass on the transfer function that maps road undulations to the steering angle are studied in Fig. 18. An upward shift of 15 cm (5.91 ins) reduces the signal transmission gain peak by 13 dB, while a corresponding downward shift increases it by approximately 7 dB.

**3.6 Nonlinear Phenomena.** Although it is not the primary purpose of this paper to study the nonlinear aspects of the road forcing problem, we do not want to conclude this account without making some introductory observations that will motivate future research. Figure 19 shows the build up of oscillations in the roll and steer angles as well as the yaw rate in response to road profiling that is tuned into the front suspension pitch mode at 7.54 rad/s (1.2 Hz). The forward speed is 13 m/s (29 mph) and the forcing amplitude is 5 mm. We can only study the very low-amplitude case here, because higher amplitude signals take the tyre model out of its domain of validity. It is evident that 7.54 rad/s (1.2 Hz) oscillations build up in 2 or 3 seconds. It can also be seen that another consequence of road forcing is a tendency for the roll angle to reduce in response to the onset of oscillations. This is possibly the result of a slow growth rate instability of the capsize type described in [1]. In practical terms, this effect will cause the vehicle to run wide, a common feature of real accidents involving oscillations. As the roll angle reduces, the road-forcing signal transmission gain will also reduce and we can see evidence of this effect in the yaw rate and steering angle oscillation amplitudes. At approximately 35 s, one can see evidence of the onset of wobble frequency oscillations. This excitation of the wobble mode is the product of nonlinear effects that remain to be analyzed.

Figure 20 shows the response of the machine to low-amplitude road undulations that are tuned into the weave mode. Again, larger amplitude profiling will take the tire model out of its domain of validity and consequently cannot be used. In common with the previous simulation result, oscillations build up in about 3 s. It is also evident that the roll angle tends to decrease. As can be seen in the video tape ([20]), weave-related instabilities cause the vehicle to run wide. It is also clear that as the roll angle reduces, the steer angle and yaw rate oscillations reduce in consequence. We believe that this is the result of transmission gain reductions that come about in response to reductions in the roll angle. At approximately 25 s, one sees evidence of waveform distortion, a product of nonlinear mechanisms.

## 4 Conclusions

A study of the effects of road profiling on motorcycle steering responses is presented. The work is based on an enhanced version of the nonlinear cornering model presented in [4]. This model has been qualified using tests that are based on the principle that under equilibrium conditions all the external forces and moments acting on the motorcycle-rider system must sum to zero. We have also checked that the drive power supplied by the engine matches that dissipated by the tires and the aerodynamic forces. An AUTOSIM code was used to generate a linearized state-space model that describes small perturbations around a general equilibrium cornering state. By introducing appropriate inputs into the model, we are able to describe the propagation of road undulation signals from the tire ground contact points to the steering angle. A particular feature of the frequency response calculations is the inclusion of the wheelbase filtering.

The results show that under cornering conditions, regular low-amplitude road undulations that would not trouble four-wheeled vehicles can be a source of considerable difficulty to motorcycle riders. At low machine speeds the wobble and front suspension pitch modes are likely to respond vigorously to resonant forcing, while at higher speeds, the weave and front wheel hop modes are similarly affected. The vigour of the oscillations is related to the previously much studied linear stability properties insofar as low damping factors lead to correspondingly high peak magnification factors. Connections between resonant responses and a class of single-vehicle loss-of-rider-control accidents have been postulated.

The work reported here has a number of practical consequences. First, it appears to explain the key features of many of the stability related road traffic accidents reported in the popular literature, and it helps to explain why motorcycles that behave perfectly well for long periods can suddenly suffer serious and dangerous oscillation problems. Such oscillations are likely to be difficult to reproduce and study in practice. Secondly, road builders and maintainers, and motorcycle manufacturers, should be aware of the possibility of strong resonant responses to small but regular undulations under certain critical running conditions. These conditions are characterized by the machine speed, the lean angle, the rider's mass and posture, and the road profile wavelength. The dynamic responses are influenced by the modal damping factors, the road profiling, and the effectiveness of the forcing from the road. For our particular motorcycle, which is representative of many large machines, the wobble mode will be excited by road undulations with a wavelength of approximately 1.7 m. This will produce a forcing signal of 7.6 Hz at a road speed of 13 m/s (approximately 30 mph). The forcing will last for 2–3 s, which is enough time for the resonance to build up, if there are 15–23 periods of undulation. If the undulation period is approximately 11.4 m, a road speed of approximately 40 m/s (90 mph) will produce forcing at the weave frequency of 3.5 Hz. In this case the forcing will last for 2–3 s if there are 7–11 periods of undulation. It will be difficult for manufacturers to establish a set of "worst case" operating conditions to be associated with new products and yet it is essential that this is done. Thirdly, the kind of theoretical analysis presented here appears to be a necessary part of determining these worst case conditions in a reliable and economical way. This type of analysis should be an essential part of the motorcycle designer's toolkit in the future.

We have studied the individual contributions to these resonances made by each of the two road wheels. Our results show that the wobble and front wheel hop resonance peaks are "front wheel dominated." In other words, difficulties with these modes are likely to be caused by the design and set up of the front of the machine. The same is true, but to a lesser extent, in the case of the front suspension pitch mode. In contrast, the weave mode resonance peak involves the road forcing to both wheels in almost equal measure. As a consequence, weave related problems appear to be more difficult to isolate and remove.

As might be anticipated, the vulnerability of the wobble mode responses to road forcing is decreased markedly by an effective steering damper, but changes to the suspension dampers are ineffectual. The front suspension pitch mode resonance, that is associated with low-speed operation, is sensitive to the front suspension damping, but is insensitive to the rear suspension and steering damping.

In the case of high-speed operation, the weave and front wheel hop modes are exposed to road profile induced oscillations due to their low modal damping. The results show that the weave mode resonant response is reduced by increasing the front suspension damping, but it is made larger by increasing the rear suspension and steering damper settings. These damping results depend, of course, on the nominal setup and will not be universally true. Increasing the front suspension damping reduces the front wheel hop resonance peak, but this peak does not respond to changes in steering damping, or rear suspension damper settings.

It has also been shown that light riders are more likely to suffer from road forced resonant weave oscillations than are heavy ones, as has been observed in practice ([18]) and on the video tape ([30]). The results indicate also that the peak gains associated with the weave mode are brought down by moving the rider upper body mass forwards and upwards. There is not sufficient practical evidence at the moment to indicate whether or not these findings coincide with experience. From the rider's perspective, a worrying feature of the road profile induced oscillations is the tendency of the uncontrolled machine to ''sit up'' and run wide. This aspect of the machine behavior can be seen on the video tape ([20]) in the case of a high-speed weave accident.

A preliminary time domain study of these resonances by motion simulations has shown the existence of interesting and essentially nonlinear phenomena, that seem to accord with practical experience. These nonlinear phenomena are worthy of further study, together with more wide-ranging investigations of design influences on the various potentially problematic running conditions.

## Appendix

**AUTOSIM Commands.** This Appendix contains a brief description of the AUTOSIM commands used in the paper. A much fuller account can be found in the AUTOSIM reference manual ([26]).

**Vector Algebra**

| Autosim code | Mathematical interpretation |
|---|---|
| `cross(v1,v2)` | the cross product between vectors $v_1$ and $v_2$ |
| `dot(v1,v2)` | inner product between vectors $v_1$ and $v_2$ |
| `pos(p1,p2)` | vector going from point p2 to point p1 |
| `[fwy]` | symbol is a unit-vector when enclosed in braces |

## References


[1] Sharp, R. S., 1971, ''The Stability and Control of Motorcycles.'' J. Mech. Eng. Sci., **13**(5), pp. 316–329.

[2] Sharp, R. S., 1994, *Vibrational Modes of Motorcycles and Their Design Parameter Sensitivities*, Vehicle NVH and Refinement, Proc Int Conf., Birmingham, May 3–5, Mech. Eng. Publications, London, pp. 107–121.

[3] Limebeer, D. J. N., Sharp, R. S., and Evangelou, S., 2001, ''The Stability of Motorcycles Under Acceleration and Braking,'' Proc. Inst. Mech. Eng., Part D (J. Automob. Eng.), **215**(C9), pp. 1095–1109.

[4] Sharp, R. S. and Limebeer, D. J. N., 2001, ''A Motorcycle Model for Stability and Control Analysis,'' Multibody Syst. Dyn., **6**(2), pp. 123–142.

[5] Koenen, C., 1983, ''The Dynamic Behavior of Motorcycles When Running Straight Ahead and When Cornering,'' Ph.D. thesis, Delft University of Technology. Delft, The Netherlands.

[6] Sharp, R. S., Limebeer, D. J. N., and Gani, M. R., 1999, ''A Motorcycle Model for Stability and Control Analysis,'' *Euromech Colloquium 404, Advances in Computational Multibody Dynamics*, J. A. C. Ambrosio and W. O. Schiehlen ed., pp. 287–312.

[7] Sharp, R. S., 1992, ''Wobble and Weave of Motorcycles With Reference to Police Usage,'' Automot. Eng., **17**(6), pp. 25–27.

[8] BMW statement to all (UK) chief constables, Dec. 14, 1993.

[9] Cutts, J., 1993, ''The Boxer Rebellion,'' Superbike, Apr., pp. 4–10.

[10] Evans, J., 1993, BMW R1100RS, Motor Cycle Int., Mar., pp. 58–64.

[11] Raymond, K., 1993, ''Could do Better,'' Perform. Bikes, Apr., pp. 34–36.

[12] ''An Interview With Dr. Goeschel,'' 1993, Motorcycle Sport, May, pp. 234–235.

[13] ''Boxer Comeback,'' 1993, Which Motorcycle, Apr., pp. 26–32.

[14] Duke, O., 1997, ''Planet Bike—Radical Thriller or Flawed Killer,'' Bike, June, pp. 14–17.

[15] ''Safety Recall Notice, American Suzuki Motor Corporation,'' 1997, Motorcycle, June 9.

[16] Farr, K., 1997, ''Suzuki TL1000 Recalled in UK,'' Motorcycle News, June 18.

[17] ''Operating Stable,'' 1997, Performance Bikes, July, pp. 44–51.

[18] Farr, K., 1997, ''Fats the Way To,'' Motorcycle News, July 2.

[19] Robinson, J., 2001, ''Wobble and Weave,'' Performance Bikes, July, pp. 83–85.

[20] Duke Marketing Ltd., 1999, ''Motorcycle Magic.''

[21] Farrar, S., 2002, ''Orritt's Story to Explain the Phenomena,'' Times Higher Educational Supplement, Feb. 15.

[22] Metropolitan Police, private communication, 2000.

[23] Sharp, R. S., 2001, ''The Stability, Control and Steering Responses of Motorcycles,'' Veh. Sys. Dyn., **35**(4–5), pp. 291–318.

[24] Breuer, T., and Pruckner, A., 1998, ''Advanced Dynamic Motorbike Analysis and Driver Simulation,'' *Proc 13th European ADAMS Users' Conference*, Paris, Nov. 1998, 20pp.

[25] Imaizumi, H., and Fujioka, T., 1996, ''Motorcycle-Rider System Dynamics by Multibody Dynamics Analysis—Effects of the Rear Load and the Suspension Assembly on Wobble and Weave Motions,'' JSAE Review, **19**(**1**), pp. 54–57.

[26] Mechanical Simulation Corporation, 1996, *Autosim 2.5+ Reference Manual*, http://www.trucksim.com.

[27] The Mathworks, Inc., 2000, *MATLAB 6 Reference Manual*, http://www.mathworks.com.

[28] Evangelou, S., and Limebeer, D. J. N., 2000, ''Lisp Programming of the ''Sharp 1971'' Motorcycle Model,'' http://www.ee.ic.ac.uk/control/motorcycles.

[29] Evangelou, S., and Limebeer, D. J. N., 2000, ''Lisp Programming of the ''Sharp 1994'' Motorcycle Model,'' http://www.ee.ic.ac.uk/control/motorcycles.

[30] Dunlop, ''Wobble and Weave Videotape,'' c1977.

**P. A. Martin**
Department of Mathematical and Computer Sciences,
Colorado School of Mines,
Golden, CO 80401-1887
e-mail: pamartin@mines.edu

**J. R. Berger**
Division of Engineering,
Colorado School of Mines,
Golden, CO 80401-1887
e-mail: jberger@mines.edu

# On Mechanical Waves Along Aluminum Conductor Steel Reinforced (ACSR) Power Lines

*The propagation of elastic waves along composite wire rope is considered. The rope is modeled as co-axial layers of cylindrically anisotropic material. Simple kinematical assumptions lead to a "rod theory" for the wire rope, consisting of three coupled one-dimensional wave equations. Solutions of these equations are found. Results for a particular aluminum conductor steel reinforced (ACSR) conductor are described in detail. The slowest mode is found to be mainly torsional and mainly nondispersive in character. The other two modes are dispersive and have small torsional components.*
[DOI: 10.1115/1.1491269]

## 1 Introduction

We are interested in the propagation of mechanical waves along overhead power lines. These are often composite structures known as aluminum conductor steel reinforced (ACSR) electrical conductors. These are composite wire ropes consisting of a central steel wire rope surrounded by several aluminum wires. Our interest stems from the potential use of mechanical waves to detect defects in ACSR power lines.

It is known that fatigue failure of strands in ACSR power lines is the most common form of damage, resulting from various forms of vibrations—aeolian, galloping, and wake-induced ([1]). Two regions of an ACSR power line can be distinguished: the region near the points of support and the region further away, "out in the span." Most fatigue damage seems to occur in the first region ([1] p. 51). In this region, the mechanical problem is very complicated and three-dimensional: one must take into account such features as interstrand slippage, suspension clamps and armor rods. Damage may also occur in the second region, sometimes induced by corrosion, and it is here that there is scope for some simpler models.

In a previous paper ([2]), we considered the propagation of torsional waves along a bimaterial elastic cylinder, composed of a steel circular cylindrical core surrounded by a co-axial aluminum cladding. The interface between the core and the cladding was assumed to be imperfect, so that some slipping was allowed. This model accounts well for the composite nature of an ACSR power line, and the imperfect-interface conditions include a parameter that may be varied. Moreover, it is possible that this model could be developed further, so as to treat the region near the points of support.

However, some features of the problem are not included, the most important of these being the anisotropy of wire rope. Thus: "The static response of axially loaded wire rope clearly points out the coupling between the axial and rotational displacements" ([3], p. 244). It follows that any plausible model of a wire rope should take this coupling into account. This paper is concerned with the development of such models for the dynamic response of wire rope.

The simplest models are based on a strength-of-materials approach, in which one writes

$$F = A_1\varepsilon + A_2\chi \quad \text{and} \quad M = A_3\varepsilon + A_4\chi, \tag{1}$$

where $F$ is the axial force acting at an arbitrary cross section of the wire rope, $M$ is the axial twisting moment, $\varepsilon$ is the axial strain, $\chi$ is the rotation per unit length, and $A_1$, $A_2$, $A_3$, and $A_4$ are constants ([4]). This model has been used for the static response of ACSR cables by McConnell and Zemke [5], and it has been extended to include bending moments ([6,7]).

Equation (1) is a constitutive relation for the wire rope. Clearly, the coefficients $A_i$ will depend on the details of the rope's construction. Much effort has been directed at obtaining analytical expressions for $A_i$; see, for example, [4,8], and references therein. For ACSR applications, see [4], Section 3.9 and [5]. One can also attempt to determine $A_i$ experimentally ([9,5]). The diagonal coefficients $A_1$ (relating two axial quantities) and $A_4$ (relating two rotational quantities) may be obtained using standard test equipment, but the off-diagonal coefficients $A_2$ and $A_3$ require more specialized techniques. A third option is to adopt a hybrid scheme, whereby $A_1$ and $A_4$ are determined by analytical approximations or static experiments, but $A_2$ and $A_3$ are found using information obtained from dynamic experiments. This option will be mentioned in Section 2.

One question that arises is: does $A_2 = A_3$? Costello [4], Section 3.9, has calculated $A_i$ for a particular ACSR cable, and found that $A_1 = 1.21\times10^6$ lb, $A_2 = 1.69\times10^4$ in lb, $A_3 = 1.61\times10^4$ in lb, and $A_4 = 5.55\times10^2$ in$^2$ lb, with $A_2/A_3 \simeq 1.05$. For a steel wire rope used in marine applications, Samras et al. [9] found experimentally that $A_1 = 4.44\times10^6$ lb, $A_2 = 2.23\times10^5$ in lb, $A_3 = 2.36\times10^5$ in lb, and $A_4 = 1.43\times10^4$ in$^2$ lb, with $A_2/A_3 \simeq 0.94$. Thus, it is reasonable to assume that $A_2 = A_3$. Moreover, this equality follows from the assumption that the wire rope is genuinely elastic; it seems to be a good approximation for real wire ropes, where constituent wires may slip, for example.

Following on from Eq. (1), one can write down equations of motion, in the form of two coupled wave equations for the axial displacement ($w$) and the angular rotation ($\phi$),

$$A_1\frac{\partial^2 w}{\partial z^2} + A_2\frac{\partial^2 \phi}{\partial z^2} = m\,\frac{\partial^2 w}{\partial t^2}, \tag{2}$$

$$A_3\frac{\partial^2 w}{\partial z^2} + A_4\frac{\partial^2 \phi}{\partial z^2} = I\,\frac{\partial^2 \phi}{\partial t^2}, \tag{3}$$

where $m$ is the mass per unit length and $I$ is the mass moment of inertia per unit length about the central axis. (Further details and references are given in Section 2.) These equations permit wave motion, and this is investigated in Section 2. There are two wave speeds. In general, each torsional wave is accompanied by a longitudinal wave of the same shape but with a different amplitude.

Contributed by the Applied Mechanics Division of THE AMERICAN SOCIETY OF MECHANICAL ENGINEERS for publication in the ASME JOURNAL OF APPLIED MECHANICS. Manuscript received by the ASME Applied Mechanics Division, Sept. 6, 2001; final revision, Jan. 9, 2002. Associate Editor: A. K. Mal. Discussion on the paper should be addressed to the Editor, Prof. Robert M. McMeeking, Department of Mechanical and Environmental Engineering University of California–Santa Barbara, Santa Barbara, CA 93106-5070, and will be accepted until four months after final publication of the paper itself in the ASME JOURNAL OF APPLIED MECHANICS.

  

In Section 3, we develop an alternative theory, based on the exact stress equations of motion for a composite anisotropic elastic cylinder. The cylinder consists of co-axial layers, each of which is made of a cylindrically anisotropic elastic material. Simple kinematical assumptions are made, leading to a system of three coupled one-dimensional wave equations:

$$A_1\frac{\partial^2 w}{\partial z^2}+A_2\frac{\partial^2 \phi}{\partial z^2}+A_5\frac{\partial^2 u}{\partial z^2}+B_1\frac{\partial u}{\partial z}=m\,\frac{\partial^2 w}{\partial t^2}, \tag{4}$$

$$A_2\frac{\partial^2 w}{\partial z^2}+A_4\frac{\partial^2 \phi}{\partial z^2}+A_6\frac{\partial^2 u}{\partial z^2}+B_2\frac{\partial u}{\partial z}=I\,\frac{\partial^2 \phi}{\partial t^2}, \tag{5}$$

$$A_5\frac{\partial^2 w}{\partial z^2}+A_6\frac{\partial^2 \phi}{\partial z^2}+A_7\frac{\partial^2 u}{\partial z^2}-B_1\frac{\partial w}{\partial z}-B_2\frac{\partial \phi}{\partial z}-B_3u=I\,\frac{\partial^2 u}{\partial t^2}. \tag{6}$$

Here, $u$ gives the radial displacement. In general, this $3\times3$ system does not reduce to the $2\times2$ system, Eqs. (2) and (3), when $u=0$, which is an underlying assumption in the derivation of the $2\times2$ system. On the other hand, the $3\times3$ system does reduce to well known equations for the approximate description of waves in *isotropic* elastic rods ([10] Section 8.3).

Our model for the wire rope is called *semi-continuous* by Cardou and Jolicoeur [11] in their thorough review article: all the strands in each co-axial layer of the rope are ''homogenized'' into an elastic continuum. This idea was first used by Hobbs and Raoof [12]; they regarded each layer as a thin orthotropic sheet. It has been developed further by Cardou and his students ([13–15]). They do not regard the layers as thin, and they permit the orthotropy axes of the material of each layer to be aligned in directions that differ from the global cylindrical polar coordinate axes. We have extended this model to dynamic situations.

The coefficients occurring in Eqs. (4)–(6) are given in terms of certain integrals of the elastic stiffnesses of each layer over a typical cross section. Once these are known, wave propagation along the wire rope can be studied. For an example, we present some numerical results for a simple seven-wire ACSR conductor. Three distinct modes are found. The slowest mode is mainly torsional and mainly nondispersive in character. Such a mode could be excited by a device (transducer) designed to launch torsional waves. The two other modes are dispersive and have small torsional components.

## 2 The Samras-Skop-Milburn (SSM) Equations of Motion

Let $z$ be distance along the wire rope and let $t$ be the time. Let $w$ be the axial displacement and let $\phi$ be the angular rotation. We use the constitutive relations (1), in which $\varepsilon=\partial w/\partial z$ and $\chi=\partial\phi/\partial z$, whence

$$F=A_1\frac{\partial w}{\partial z}+A_2\frac{\partial \phi}{\partial z} \quad\text{and}\quad M=A_3\frac{\partial w}{\partial z}+A_4\frac{\partial \phi}{\partial z}. \tag{7}$$

Then, a balance of forces and moments acting on an elementary slice of the wire rope gives Eqs. (2) and (3), which are approximate, one-dimensional equations of motion for the wire rope. They were derived by Samras, Skop, and Milburn [9]; we call Eqs. (2) and (3) the *SSM system*. This $2\times2$ system has been used in several subsequent papers, including [3,16–18].

It is of interest to obtain solutions to the SSM system. If we eliminate $\phi$, say, we obtain a single fourth-order linear partial differential equation for $w$,

$$mI\,\frac{\partial^4 w}{\partial t^4}-(IA_1+mA_4)\,\frac{\partial^4 w}{\partial t^2\partial z^2}+(A_1A_4-A_2A_3)\,\frac{\partial^4 w}{\partial z^4}=0. \tag{8}$$

This has traveling-wave solutions of the form $w(z,t)=f(z-ct)$, where $f$ is an arbitrary function (with four continuous derivatives) and there are four possible wavespeeds $c$, given by the roots of

$$mIc^4-c^2(IA_1+mA_4)+A_1A_4-A_2A_3=0; \tag{9}$$

these roots are given by

$$c^2=\{IA_1+mA_4\pm\sqrt{(IA_1-mA_4)^2+4mIA_2A_3}\}/(2mI). \tag{10}$$

We observe that these are the eigenvalues of the matrix

$$\mathbf{A}_2=\begin{pmatrix} A_1/m & A_2/m \\ A_3/I & A_4/I \end{pmatrix}.$$

Thus, we obtain two positive values of $c$ and two negative values. The positive values correspond to different wavespeeds for waves propagating in the positive $z$ direction; we will denote these by $c_1$ and $c_2$.

We can rewrite Eq. (9) as $A_2A_3=(mc^2-A_1)(Ic^2-A_4)$. If we assume that $A_2=A_3$ and we have good estimates for $A_1$ and $A_4$ (perhaps obtained from fairly standard static measurements on the wire rope), $m$ and $I$, we could then calculate $A_2$ using a measurement of wavespeed $c$ along the rope.

Returning to Eqs. (2) and (3), we could eliminate $w$ instead of $\phi$. This shows that $\phi$ satisfies exactly the same equation as $w$, namely Eq. (8), and so admits the same wavespeeds.

Next, let us look for solutions of Eqs. (2) and (3) in the form

$$w(z,t)=f(\xi) \quad\text{and}\quad \phi(z,t)=g(\xi), \tag{11}$$

where $\xi=z-ct$ and $c$ solves Eq. (9). We obtain

$$\left.\begin{aligned}(A_1-mc^2)f''+A_2g''=0,\\ A_3f''+(A_4-Ic^2)g''=0,\end{aligned}\right\}$$

so that $(f'',g'')^T$ is an eigenvector of $\mathbf{A}_2$ corresponding to the eigenvalue $c^2$. Integrating twice, we see that

$$f(z-ct)=G(c)g(z-ct), \tag{12}$$

where the factor $G$ is given by $G(c)=A_2/(mc^2-A_1)=(Ic^2-A_4)/A_3$. (When we integrated, we discarded terms of the form $C_1\xi+C_2$, where $C_1$ and $C_2$ are constants of integration. Such terms do satisfy Eqs. (2) and (3), as do any functions that are linear in both $z$ and $t$, but they are not usually of interest.)

Equation (12) shows that if there is a torsional wave, $\phi$, propagating at speed $c$, then it will be accompanied by an axial wave, $w$, propagating at the same speed and with the same shape, but with a different amplitude. For this conclusion to be valid, we require that there is actual coupling between axial and torsional motions; for a solid isotropic rod, we would have $A_2=A_3=0$, and then the axial and torsional waves can exist independently (as Eqs. (2) and (3) decouple).

This completes our study of the SSM system. In the next section, we attempt to give a more rational derivation of one-dimensional wave equations modeling the wire rope. We shall see that the SSM system should be replaced by a $3\times3$ system, in general.

## 3 An Approximate Theory for Waves in a Wire Rope

**3.1 Stress Equations of Motion.** In cylindrical polar coordinates $(r,\theta,z)$, the exact stress equations of motion are ([10], p. 600)

$$\frac{\partial}{\partial r}\tau_{rr}+\frac{1}{r}\frac{\partial}{\partial\theta}\tau_{r\theta}+\frac{\partial}{\partial z}\tau_{rz}+\frac{1}{r}(\tau_{rr}-\tau_{\theta\theta})=\rho\,\frac{\partial^2 u_r}{\partial t^2}, \tag{13}$$

$$\frac{\partial}{\partial r}\tau_{r\theta}+\frac{1}{r}\frac{\partial}{\partial\theta}\tau_{\theta\theta}+\frac{\partial}{\partial z}\tau_{\theta z}+\frac{2}{r}\tau_{r\theta}=\rho\,\frac{\partial^2 u_\theta}{\partial t^2}, \tag{14}$$

$$\frac{\partial}{\partial r}\tau_{rz}+\frac{1}{r}\frac{\partial}{\partial\theta}\tau_{\theta z}+\frac{\partial}{\partial z}\tau_{zz}+\frac{1}{r}\tau_{rz}=\rho\,\frac{\partial^2 u_z}{\partial t^2}, \tag{15}$$

where $(u_r,u_\theta,u_z)$ is the displacement, $\rho$ is the mass density, and $\tau_{ij}$ are the stress components. We seek approximate solutions of these equations for a wire rope.

We model the wire rope as a circular cylinder of radius $a$. The cylinder consists of a cylindrical core, $0 \leq r < a_0$, and $N$ co-axial layers, $a_{i-1} < r < a_i$, $i = 1,2,\ldots,N$, with $a_N = a$. Thus, there are $N$ interfaces, $r = a_{i-1}$, $i = 1,2,\ldots,N$. The outer surface is free of tractions,

$$\tau_{rr} = \tau_{r\theta} = \tau_{rz} = 0 \quad \text{on} \quad r = a. \tag{16}$$

In general, the $N$ interfaces may be imperfect: Slippage may occur. They could be modeled using one of several available models of imperfect interfaces; see [2] or [19].

In order to develop a "rod theory" for wire rope, we begin with some kinematical assumptions. Thus, we assume that

$$u_r = r u(z,t), \quad u_\theta = r\phi(z,t) \quad \text{and} \quad u_z = w(z,t), \tag{17}$$

where $u$, $\phi$ and $w$ are to be found. Here, the approximations for $u_r$ and $u_z$ are usually made for longitudinal motions ([10], p. 511), whereas the approximation for $u_\theta$ means that cross sections can rotate about the central axis at $r=0$. One consequence of Eq. (17) is that the $\theta$-derivative terms in Eqs. (13)–(15) are zero.

We are going to integrate Eqs. (13)–(15) across an arbitrary cross section $\mathcal{C}$ of the wire rope. We have

$$\int_0^a r\frac{\partial}{\partial r}\tau_{rz}dr = \sum_{i=0}^{N}\int_{a_{i-1}}^{a_i} r\frac{\partial}{\partial r}\tau_{rz}dr = \sum_{i=0}^{N}\left\{[r\tau_{rz}]_{a_{i-1}}^{a_i} - \int_{a_{i-1}}^{a_i}\tau_{rz}dr\right\} = I_z - \int_0^a \tau_{rz}dr,$$

where $a_{-1} = 0$, we have used Eq. (16),

$$I_z = \sum_{i=0}^{N-1} a_i[\tau_{rz}(a_i,z,t)]$$

and

$$[f(a_i,z,t)] = \lim_{r\to a_i^-} f(r,z,t) - \lim_{r\to a_i+} f(r,z,t)$$

gives the jump in a quantity $f$ across an interface at $r = a_i$. Thus, integrating Eq. (15) across $\mathcal{C}$, we obtain

$$\frac{\partial}{\partial z}\int_{\mathcal{C}}\tau_{zz}dA + 2\pi I_z = m\frac{\partial^2 w}{\partial t^2} \tag{18}$$

where $dA = r\,dr\,d\theta$ and $m = \int_{\mathcal{C}}\rho dA$ is the mass per unit length of the wire rope.

We use a similar procedure with Eqs. (13) and (14), the difference being that we multiply both by $r$ before integrating over $\mathcal{C}$. We obtain

$$\frac{\partial}{\partial z}\int_{\mathcal{C}} r\tau_{rz}dA - \int_{\mathcal{C}}(\tau_{rr}+\tau_{\theta\theta})dA + 2\pi I_r = I\frac{\partial^2 u}{\partial t^2} \tag{19}$$

and

$$\frac{\partial}{\partial z}\int_{\mathcal{C}} r\tau_{\theta z}dA + 2\pi I_\theta = I\frac{\partial^2\phi}{\partial t^2}, \tag{20}$$

where

$$I_r = \sum_{i=0}^{N-1} a_i^2[\tau_{rr}(a_i,z,t)], \quad I_\theta = \sum_{i=0}^{N-1} a_i^2[\tau_{r\theta}(a_i,z,t)]$$

and $I = \int_{\mathcal{C}}\rho r^2 dA$ is the mass moment of inertia per unit length about the central axis.

Note that if the wire rope was a solid circular cylinder of radius $a$, with constant density and welded interfaces, then we would have $I_r = I_\theta = I_z = 0$, $I = (1/2)ma^2$ and $m = \pi\rho a^2$.

The quantities $I_r$, $I_\theta$, and $I_z$ give the total contributions from the possible discontinuities in the traction across each of the $N$ interfaces. We assume that

$$I_r = I_\theta = I_z = 0. \tag{21}$$

This simplifies the analysis, of course, but it also turns out to be realistic ([1], p. 54):

> Real conductors do not have frictionless strands, and, for the small amounts of flexure experienced due to vibration waves out in the span, the friction present between strands is normally great enough to prevent gross sliding between them. The relative axial movements of the strands are absorbed in largely elastic shear strains around the small areas of interstrand contact. The amounts of movement are not great enough to build up tractions that exceed the threshold of sliding.

On the other hand, the assumption (21) cannot be justified near the points of support.

**3.2 Cylindrically Anisotropic Materials.** Next, we need constitutive relations for the materials of the wire rope. We assume that each layer is composed of a cylindrically anisotropic elastic solid. Letting $(r,\theta,z) = (1,2,3)$, Hooke's law becomes

$$\tau_{ij} = C_{ijkl}\varepsilon_{kl}, \tag{22}$$

where $\varepsilon_{ij}$ are the strain components, and we emphasize that the stiffnesses $C_{ijkl}$ are referred to cylindrical polar coordinates; see [20] and [21] for more details. We assume further that each layer of the wire is homogeneous, so that the stiffnesses are constant within each layer. Thus, $C_{ijkl} = C_{ijkl}(r)$ are piecewise-constant functions of $r$.

The strains are given as follows ([20], p. 2399):

$$\varepsilon_{rr} = \frac{\partial u_r}{\partial r} = u, \quad \varepsilon_{\theta\theta} = \frac{1}{r}\frac{\partial u_\theta}{\partial\theta} + \frac{u_r}{r} = u,$$

$$\varepsilon_{zz} = \frac{\partial u_z}{\partial z} = \frac{\partial w}{\partial z}, \quad \varepsilon_{r\theta} = \frac{1}{2}\left(\frac{1}{r}\frac{\partial u_r}{\partial\theta} + \frac{\partial u_\theta}{\partial r} - \frac{u_\theta}{r}\right) = 0,$$

$$\varepsilon_{rz} = \frac{1}{2}\left(\frac{\partial u_z}{\partial r} + \frac{\partial u_r}{\partial z}\right) = \frac{1}{2}r\frac{\partial u}{\partial z},$$

$$\varepsilon_{\theta z} = \frac{1}{2}\left(\frac{\partial u_\theta}{\partial z} + \frac{1}{r}\frac{\partial u_z}{\partial\theta}\right) = \frac{1}{2}r\frac{\partial\phi}{\partial z}.$$

The corresponding stresses are given by Eq. (22) as

$$\tau_{ij} = C_{ij11}\varepsilon_{rr} + C_{ij22}\varepsilon_{\theta\theta} + C_{ij33}\varepsilon_{zz} + 2C_{ij12}\varepsilon_{r\theta} + 2C_{ij23}\varepsilon_{\theta z} + 2C_{ij13}\varepsilon_{rz} = (C_{ij11}+C_{ij22})u + C_{ij33}\frac{\partial w}{\partial z} + C_{ij23}r\frac{\partial\phi}{\partial z} + C_{ij13}r\frac{\partial u}{\partial z}.$$

Thus

$$\tau_{rz} = \tau_{13} = (C_{15}+C_{25})u + C_{35}\frac{\partial w}{\partial z} + C_{45}r\frac{\partial\phi}{\partial z} + C_{55}r\frac{\partial u}{\partial z},$$

$$\tau_{\theta z} = \tau_{23} = (C_{14}+C_{24})u + C_{34}\frac{\partial w}{\partial z} + C_{44}r\frac{\partial\phi}{\partial z} + C_{45}r\frac{\partial u}{\partial z},$$

$$\tau_{r\theta} = \tau_{12} = (C_{16}+C_{26})u + C_{36}\frac{\partial w}{\partial z} + C_{46}r\frac{\partial\phi}{\partial z} + C_{56}r\frac{\partial u}{\partial z},$$

$$\tau_{zz} = \tau_{33} = (C_{13}+C_{23})u + C_{33}\frac{\partial w}{\partial z} + C_{34}r\frac{\partial\phi}{\partial z} + C_{35}r\frac{\partial u}{\partial z},$$

$$\tau_{rr} = \tau_{11} = (C_{11}+C_{12})u + C_{13}\frac{\partial w}{\partial z} + C_{14}r\frac{\partial\phi}{\partial z} + C_{15}r\frac{\partial u}{\partial z},$$

$$\tau_{\theta\theta} = \tau_{22} = (C_{12}+C_{22})u + C_{23}\frac{\partial w}{\partial z} + C_{24}r\frac{\partial\phi}{\partial z} + C_{25}r\frac{\partial u}{\partial z},$$

where we have used the usual contracted notation $C_{\alpha\beta}$ for $C_{ijkl}$ ([22], Section 2.3). Note that these expressions make use of 20 of the 21 stiffnesses, the exception being $C_{66}$.

**3.3 One-Dimensional Equations of Motion.** We use the expressions above for $\tau_{ij}$ in Eqs. (18), (19), and (20), together with Eq. (21), and obtain Eqs. (4)–(6), wherein

$$A_1=\int_{\mathcal{C}} C_{33}dA, \quad A_2=\int_{\mathcal{C}} rC_{34}dA, \quad A_4=\int_{\mathcal{C}} r^2C_{44}dA,$$

$$A_5=\int_{\mathcal{C}} rC_{35}dA, \quad A_6=\int_{\mathcal{C}} r^2C_{45}dA, \quad A_7=\int_{\mathcal{C}} r^2C_{55}dA,$$

$$B_1=\int_{\mathcal{C}} (C_{13}+C_{23})dA, \quad B_2=\int_{\mathcal{C}} r(C_{14}+C_{24})dA,$$

$$B_3=\int_{\mathcal{C}} (C_{11}+C_{22}+2C_{12})dA.$$

Note that these expressions make use of 13 different elastic stiffnesses.

Equations (4)–(6) are three coupled one-dimensional wave equations for $u$, $\phi$, and $w$, defined by Eq. (17). This $3\times 3$ system should be compared with the $2\times 2$ SSM system (which was derived by strength-of-materials arguments). We do this next.

**3.4 Comparison With the Samras-Skop-Milburn (SSM) System.** We see immediately that Eqs. (4) and (5) reduce to Eqs. (2) and (3), respectively, if $u\equiv 0$ (no radial displacement). Then, the third equation, Eq. (6), becomes

$$A_5\frac{\partial^2 w}{\partial z^2}+A_6\frac{\partial^2 \phi}{\partial z^2}-B_1\frac{\partial w}{\partial z}-B_2\frac{\partial \phi}{\partial z}=0. \tag{23}$$

Now, we know that the SSM system has traveling-wave solutions, given by Eqs. (11) and (12). When these are substituted in Eq. (23), we obtain an ordinary differential equation for $g(\xi)$, with solution $g(\xi)=e^{\gamma\xi}$ where $\gamma=(B_1G+B_2)/(A_5G+A_6)$, provided $A_5$ and $A_6$ are not both zero. This particular exponential solution is not of interest to us, as we want to consider the propagation of bounded pulses along the wire rope; therefore, we discard this solution. If $A_5=A_6=0$ (this case will arise in Section 4.1), Eq. (23) reduces to $B_1G+B_2=0$. This may be satisfied for one value of $c^2$ given by Eq. (10), but not both.

Another way to satisfy Eq. (23) identically is to require that the stiffnesses are such that

$$A_5=A_6=B_1=B_2=0. \tag{24}$$

These conditions involve the stiffnesses and radius of each concentric layer of the composite cylinder. They will be satisfied if the material in each layer satisfies $C_{35}=C_{45}=0$, $C_{13}=-C_{23}$ and $C_{14}=-C_{24}$.

We conclude that, in very special circumstances, our $3\times 3$ system reduces to the SSM system, together with $u\equiv 0$.

Let us also calculate the forces and moments acting on a cross section $\mathcal{C}$ of the wire rope. The axial force is given by

$$F=\int_{\mathcal{C}} \tau_{zz}dA=A_1\frac{\partial w}{\partial z}+A_2\frac{\partial \phi}{\partial z}+A_5\frac{\partial u}{\partial z}+B_1u \tag{25}$$

and the axial twisting moment is given by

$$M=\int_{\mathcal{C}} r\tau_{\theta z}dA=A_2\frac{\partial w}{\partial z}+A_4\frac{\partial \phi}{\partial z}+A_6\frac{\partial u}{\partial z}+B_2u.$$

Both of these reduce to Eq. (7), provided $u\equiv 0$ *or* Eq. (24) holds.

**3.5 Waves.** Before looking for solutions of Eqs. (4)–(6), it is convenient to introduce dimensionless variables. Let $c_0$ be a typical wave speed for elastic waves in the rope. For a length scale, we shall use $a$, the outer radius of the rope's cross section. (Phillips and Costello [17] use the length of the rope.) Define

$$z'=\frac{z}{a}, \quad t'=\frac{c_0t}{a}, \quad u'=u\sqrt{\frac{I}{ma^2}},$$

$$\phi'=\phi\sqrt{\frac{I}{ma^2}} \text{ and } w'=\frac{w}{a}, \tag{26}$$

where the primes signify dimensionless quantities. Then, Eqs. (4)–(6) become

$$A_1'\frac{\partial^2 w'}{\partial z'^2}+A_2'\frac{\partial^2 \phi'}{\partial z'^2}+A_5'\frac{\partial^2 u'}{\partial z'^2}+B_1'\frac{\partial u'}{\partial z'}=\frac{\partial^2 w'}{\partial t'^2}, \tag{27}$$

$$A_2'\frac{\partial^2 w'}{\partial z'^2}+A_4'\frac{\partial^2 \phi'}{\partial z'^2}+A_6'\frac{\partial^2 u'}{\partial z'^2}+B_2'\frac{\partial u'}{\partial z'}=\frac{\partial^2 \phi'}{\partial t'^2}, \tag{28}$$

$$A_5'\frac{\partial^2 w'}{\partial z'^2}+A_6'\frac{\partial^2 \phi'}{\partial z'^2}+A_7'\frac{\partial^2 u'}{\partial z'^2}-B_1'\frac{\partial w'}{\partial z'}-B_2'\frac{\partial \phi'}{\partial z'}-B_3'u'=\frac{\partial^2 u'}{\partial t'^2}, \tag{29}$$

where

$$A_1'=\frac{A_1}{mc_0^2}, \quad A_2'=\frac{A_2}{c_0^2\sqrt{mI}}, \quad A_4'=\frac{A_4}{c_0^2I}, \quad A_5'=\frac{A_5}{c_0^2\sqrt{mI}},$$

$$A_6'=\frac{A_6}{c_0^2I}, \quad A_7'=\frac{A_7}{c_0^2I}, \quad B_1'=\frac{aB_1}{c_0^2\sqrt{mI}}, \quad B_2'=\frac{aB_2}{c_0^2I},$$

$$\text{and } B_3'=\frac{a^2B_3}{c_0^2I}.$$

Henceforth, we drop all the primes.

The scaling introduced above may seem complicated but it has *three* beneficial consequences. First, all equations and coefficients are *dimensionless*. Second, it will lead to a *Hermitian* coefficient matrix when we seek solutions proportional to $\exp\{ik(z-\alpha t)\}$ (see Eq. (32) below) and, third, the wave speed $\alpha$ will be determined by solving an eigenvalue problem (rather than a *generalized* eigenvalue problem).

Thus, we seek solutions in the form

$$u=u_0e^{ik\xi}, \quad \phi=\phi_0e^{ik\xi} \text{ and } w=w_0e^{ik\xi}, \tag{30}$$

where $\xi=z-\alpha t$, $u_0$, $\phi_0$, and $w_0$ are constants, $k$ is a nonzero dimensionless real wave number, and $\alpha$ is a dimensionless wave speed; the actual wave speed is $\alpha c_0$ and the actual wavelength is $2\pi a/k$. Substituting Eq. (30) in Eqs. (27)–(29) gives

$$(\mathbf{A}-\alpha^2\mathbf{I})\mathbf{x}=\mathbf{0}, \tag{31}$$

where

$$\mathbf{A}=\begin{pmatrix} A_1 & A_2 & A_5-iB_1/k \\ A_2 & A_4 & A_6-iB_2/k \\ A_5+iB_1/k & A_6+iB_2/k & A_7+B_3/k^2 \end{pmatrix} \tag{32}$$

and $\mathbf{x}^T=(w_0,\phi_0,u_0)$. Equation (31) will have a nontrivial solution provided that

$$\det(\mathbf{A}-\alpha^2\mathbf{I})=0, \tag{33}$$

which is a cubic in $\alpha^2$. The three solutions for $\alpha^2$ are all real. This follows by noting that $\mathbf{A}$ is a complex Hermitian matrix so that $\overline{\mathbf{x}}^T\mathbf{A}\mathbf{x}$ is real (where the overbar denotes complex conjugation).

We would like to know that the real solutions for $\alpha^2$ are *all positive*, so that we have six real solutions for $\alpha$. With $\lambda=\alpha^2$, we can write Eq. (33) as

$$f(\lambda)\equiv\lambda^3+d_2\lambda^2+d_1\lambda+d_0=0, \tag{34}$$

where the coefficients $d_i$ are known in terms of the entries of $\mathbf{A}$. We know that $f(\lambda)=0$ has real roots only, so elementary considerations (such as sketching the graph of $f(\lambda)$) will lead to conditions on $d_i$ that are sufficient to guarantee that all the roots are positive. For example, we must have $f(0)<0$, which yields $\det(\mathbf{A})>0$. We must also have two positive turning points, and this yields $d_2<0$.

Let us make three further remarks. First, despite the appearance of first derivatives with respect to $z$, the system (27)–(29) is symmetric in $z$. In other words, if there is a solution proportional to $e^{ikz}$, then there is another proportional to $e^{-ikz}$, with the same value of $\alpha$. For $\det(\bar{\mathbf{A}}-\alpha^2\mathbf{I})=\det(\mathbf{A}-\alpha^2\mathbf{I})$, as $\mathbf{A}$ is Hermitian. Second, as $\mathbf{A}$ depends on $k$, so too does $\alpha$: the waves are *dispersive*, unlike the solutions of the SSM system. Third, having found the eigenvalues $\alpha^2$, the relative displacement amplitudes are given by the corresponding eigenvector $\mathbf{x}=(w_0,\phi_0,u_0)^T$ of $\mathbf{A}$.

## 4 Cylindrically Orthotropic Materials

The theory developed in Section 3 is fairly general. As a special case, we can suppose that the material of each layer is cylindrically orthotropic. For such materials, there are nine nontrivial stiffnesses, namely $C_{11}$, $C_{12}$, $C_{13}$, $C_{22}$, $C_{23}$, $C_{33}$, $C_{44}$, $C_{55}$, and $C_{66}$. It follows that $A_2=A_5=A_6=B_2=0$, so that the torsional component $\phi$ decouples from $u$ and $w$. Equation (28) reduces to $A_4\partial^2\phi/\partial z^2=\partial^2\phi/\partial t^2$, the one-dimensional wave equation with wavespeed $\sqrt{A_4}$. Equations (27) and (29) reduce to

$$A_1\frac{\partial^2 w}{\partial z^2}+B_1\frac{\partial u}{\partial z}=\frac{\partial^2 w}{\partial t^2}, \tag{35}$$

$$A_7\frac{\partial^2 u}{\partial z^2}-B_1\frac{\partial w}{\partial z}-B_3 u=\frac{\partial^2 u}{\partial t^2}. \tag{36}$$

These can be solved, using Eq. (30). However, we do not pursue this here, as we are interested mainly in situations where the torsional motions do *not* decouple.

We remark that for *isotropic* materials, we can show that Eqs. (35) and (36) reduce to Eq. (8.3.148) in [10].

**4.1 Rotated Coordinate Systems.** Above, we considered a material with cylindrical orthotropy, where the principal axes are aligned with the cylindrical-polar coordinate axes. We saw that torsional motions decoupled from axial and radial motions.

Suppose, now, that the material of each layer is cylindrically orthotropic with respect to a different coordinate system, $(r',\theta',z')$, with nine nontrivial elastic stiffnesses $C'_{\alpha\beta}$ ([14,15]). We want to express $C_{\alpha\beta}$ in terms of $C'_{\alpha\beta}$. (This is a standard calculation in tensor analysis.) Specifically, at a typical point $P$, the cylinder has three coordinate directions, namely, $1\equiv r$, $2\equiv\theta$ and $3\equiv z$. At the same point, the material has three principal directions, namely, $1'\equiv r'$, $2'\equiv\theta'$, and $3'\equiv z'$. We suppose that the $r$ and $r'$ directions coincide (at $P$), and that the $(\theta,z)$ directions are obtained by rotating the $(\theta',z')$ directions by an angle $\beta$ about the $r$-direction. The stiffnesses transform according to

$$C_{ijkl}(\beta)=\Omega_{ip}\Omega_{jq}\Omega_{kr}\Omega_{ls}C'_{pqrs},$$

where

$$\Omega_{ij}(\beta)=\begin{pmatrix}1&0&0\\0&\cos\beta&\sin\beta\\0&-\sin\beta&\cos\beta\end{pmatrix}.$$

Explicit calculations show that the (symmetric) stiffness matrix referred to coordinates $(r',\theta',z')$, which has the structure

$$\mathbf{C}'=\begin{pmatrix}C'_{11}&C'_{12}&C'_{13}&0&0&0\\&C'_{22}&C'_{23}&0&0&0\\&&C'_{33}&0&0&0\\&&&C'_{44}&0&0\\&&&&C'_{55}&0\\&&&&&C'_{66}\end{pmatrix},$$

is transformed into a (symmetric) stiffness matrix referred to coordinates $(r,\theta,z)$ with the structure

$$\mathbf{C}=\begin{pmatrix}C_{11}&C_{12}&C_{13}&C_{14}&0&0\\&C_{22}&C_{23}&C_{24}&0&0\\&&C_{33}&C_{34}&0&0\\&&&C_{44}&0&0\\&&&&C_{55}&C_{56}\\&&&&&C_{66}\end{pmatrix}. \tag{37}$$

Explicit expressions for $C_{\alpha\gamma}$ in terms of $C'_{\alpha\gamma}$ are given in Appendix A. A consequence of this structure of $\mathbf{C}$ is that $A_5=A_6=0$, leading to a slight simplification of the analysis in Section 3.

**4.2 Transverse Isotropy.** Transverse isotropy is a special case of cylindrical orthotropy. For such materials, there are five nontrivial stiffnesses; the (unrotated) stiffness matrix can be written as

$$\mathbf{C}'=\begin{pmatrix}C'_{11}&C'_{12}&C'_{13}&0&0&0\\&C'_{11}&C'_{13}&0&0&0\\&&C'_{33}&0&0&0\\&&&C'_{44}&0&0\\&&&&C'_{44}&0\\&&&&&\frac{1}{2}(C'_{11}-C'_{12})\end{pmatrix}.$$

In order to use the results in [14,15], it is convenient to introduce engineering constants. These are the longitudinal Young's modulus $E_L$, the transverse Young's modulus $E_T$, the longitudinal Poisson's ratio $\nu_L$, the transverse Poisson's ratio $\nu_T$, and the longitudinal shear modulus $G_L$. Then, using [15] (Eq. (2)) and [23] (Eqs. (2.25) and (2.36)), we obtain

$$C'_{11}=\frac{1-\gamma\nu_L^2}{\Delta}E_T,\quad C'_{12}=\frac{\nu_T+\gamma\nu_L^2}{\Delta}E_T,$$

$$C'_{13}=\frac{\nu_L(1+\nu_T)}{\Delta}E_L,\quad C'_{33}=\frac{1-\nu_T^2}{\Delta}E_L$$

and $C'_{44}=G_L$; here, $\gamma=E_L/E_T$ and $\Delta=1-\nu_T^2-2\gamma\nu_L^2(1+\nu_T)$. Note that $C'_{66}=(1/2)E_T/(1+\nu_T)$. After rotation, one obtains a matrix $\mathbf{C}$ with the same structure as Eq. (37).

For an isotropic material, $E_L=E_T=E$, $\nu_L=\nu_T=\nu$ and $G_L=\mu=(1/2)E/(1+\nu)$.

Following Jolicoeur and Cardou [14,15], we shall use this constitutive model (rotated transverse isotropy) for a composite wire rope. A specific example of a simple ACSR electrical conductor is considered in the next section.

## 5 A Simple Example of an Aluminum Conductor Steel Reinforced (ACSR) Conductor

In order to use the foregoing theory, we have to specify the physical characteristics of the wire rope and we have to estimate the elastic constants. Methods for doing this have been described by Jolicoeur and Cardou [14,15] in their analysis of the static loading of wire rope. We follow their method closely, making use of some calculations of Costello ([4], Section 3.9). Thus, we consider a very simple ACSR conductor, consisting of six aluminum wires helically wound around a single straight steel-wire core. The steel wire has radius $r_s = 1.70$ mm (0.067 in.). All the aluminum wires have radius $r_a = 1.68$ mm (0.066 in.). In terms of the model described in Section 3, we have $N=1$, $a_0 = r_s$ and $a_1 = a = r_s + 2r_a$. The aluminum wires have a helical radius of $h = r_s + r_a$ and a helical angle of $\beta = 10$ deg. (These parameters are approximately those of the so-called Raven 6/1 ACSR conductor; see [24], Table 1–6).

**Mass per Unit Length.** Taking a cross section of the wire rope, we see that each aluminum wire has an approximately elliptical cross section, with a semi-minor axis of length $r_a$ and a semi-major axis of length $r_a \sec\beta$; see [4], Fig. 3.1. Thus, each wire has a mass per unit length of $\pi\rho_a r_a^2 \sec\beta = m_a$, say, where $\rho_a$ is the density of aluminum. Hence, if $\rho_s$ is the density of steel,

$$\frac{m}{\pi\rho_a a^2} = \frac{\rho_s}{\rho_a}\left(\frac{r_s}{a}\right) + 6\left(\frac{r_a}{a}\right)^2 \sec\beta = 0.998, \tag{38}$$

where we have used $\rho_s = 7800$ kg/m$^3$ and $\rho_a = 2700$ kg/m$^3$. Note that the mass of the wire rope is almost the same as that of a solid aluminum cylinder of the same diameter. Note also that our calculated value for $m$ is consistent with the tabulated value of 216 kg/km for the Raven ACSR conductor; see [24], Table 1–6.

**Moment of Inertia.** The moment of inertia of an ellipse about an axis through its center (and perpendicular to its plane) is $(1/4)M(a^2+b^2)$, where $M$ is its mass and $a$ and $b$ are the lengths of the semi-major and semi-minor axes. Then, using the parallel-axes theorem, we obtain

$$I = \frac{1}{2}\pi\rho_s r_s^4 + 6\left\{ m_a h^2 + \frac{1}{4} m_a r_a^2 (1+\sec^2\beta)\right\}.$$

Hence, $I = 0.357 m a^2$; about 95% of this comes from the aluminum wires. (For comparison, a solid composite cylinder composed of a steel core of radius $a_0$ surrounded by an aluminum cladding of outer radius $a$ has $I = 0.422 m a^2$.)

**Stiffnesses.** The steel core is isotropic with Young's modulus $E_s$ and Poisson's ratio $\nu_s = 0.25$. Thus $E_L = E_T = E_s$, $\nu_L = \nu_T = \nu_s$ and $G_L = 0.4E_s$. The corresponding stiffnesses are $C_{11} = C_{33} = 1.2E_s$ and $C_{12} = C_{13} = C_{44} = C_{66} = 0.4E_s$.

Let aluminum have Young's modulus $E_a$ and Poisson's ratio $\nu_a = 0.33$. Then, from Eqs. (3), (9), and (12)–(14) in [15], the aluminum wires may be modeled using

$$\frac{E_L}{E_a} = \frac{3}{2}\frac{r_a}{h}\sec\beta = 0.756,$$

$$\frac{\nu_L}{\nu_a} = \frac{E_T}{E_L} = \frac{1}{\gamma}, \quad \frac{\nu_T}{\nu_a} = \frac{E_T}{E_a},$$

$$\frac{G_L}{E_a} = \frac{r_a^2(E_L/E_a)}{2(1+\nu_a)(r_a^2+h^2)(1+\cos^2\beta)} = 0.0285$$

and

$$\frac{1}{E_T} = \frac{C_E}{\pi}\left\{ \log\frac{\pi(r_s+r_a)}{X_c C_E} - \frac{1}{3}\right\},$$

where $X_c$ is the contact force per unit length and, from [25], Table 33,

$$C_E = \frac{1-\nu_s^2}{E_s} + \frac{1-\nu_a^2}{E_a} = \frac{1.204}{E_a},$$

using $E_s = 3E_a$. The calculation of $X_c$ is described in Appendix B, using the method of Costello [4]. From Eq. (*B*6), we obtain

$$\pi(r_s+r_a)/(X_c C_E) = 790.4 h^2 E_a/F,$$

where $F$ is the (static) axial force on the wire rope. As an example, let us take $F = 5000$ N (1124 lb). We take $E_a = 7\times 10^{10}$ N/m$^2$ whence $E_T = 0.229E_a$. (Evidently, $E_T$ will increase if $F$ is increased, but the increase is not linear; in fact, $E_T$ depends logarithmically on $F$, so that large changes in $F$ will induce moderate changes in $E_T$.) Hence $\nu_T = 0.08$, $\nu_L = 0.10$, $\gamma = 3.3$, and $\Delta = 0.92$. Then, from Section 4.2, we obtain $C'_{11} = 0.241E_a$, $C'_{12} = 0.028E_a$, $C'_{13} = 0.089E_a$, $C'_{33} = 0.816E_a$, $C'_{44} = 0.029E_a$ and $C'_{66} = 0.106E_a$. Finally, the rotated stiffnesses are given by

$$\mathbf{C} = E_a \begin{pmatrix} 0.24 & 0.03 & 0.09 & 0.01 & 0 & 0 \\ & 0.23 & 0.11 & 0.01 & 0 & 0 \\ & & 0.78 & 0.11 & 0 & 0 \\ & & & 0.05 & 0 & 0 \\ & & & & 0.03 & -0.01 \\ & & & & & 0.10 \end{pmatrix},$$

using the relations given in Appendix A.

**Averaged Stiffnesses.** The coefficients $A_1$, $A_2$, $A_4$, $A_5$, $A_6$, $A_7$, $B_1$, $B_2$, and $B_3$ are defined in Section 3.3 by certain integrals of the stiffnesses over a cross section of the wire rope. Dimensionless versions of these coefficients are defined in Section 3.5, making use of $m$, $I$ and a typical wave speed $c_0$, which we shall take to be the speed of shear waves in aluminum: $c_0^{-2} = 2\rho_a(1+\nu_a)/E_a$. Thus, $mc_0^2 = 0.375\pi E_a a^2$, using $\nu_a = 0.33$ and Eq. (38). Then

$$A_1 = \frac{1}{mc_0^2}\int_{\mathcal{C}} C_{33}\,dA = \frac{\pi E_a a^2}{mc_0^2}\left\{ \left(\frac{r_s}{a}\right)^2 \frac{E_s}{E_a}\frac{C_{33}^s}{E_s} + \left[1 - \left(\frac{r_s}{a}\right)^2\right]\frac{C_{33}^a}{E_a}\right\},$$

where the superscripts on $C_{33}$ denote steel or aluminum, as appropriate. We have $r_s/a = 0.337$, $E_s/E_a = 3$, $C_{33}^s/E_s = 1.2$ and $C_{33}^a/E_a = 0.78$ whence $A_1 = 2.94$. The other coefficients are obtained similarly. Thus, we find that

$$A_1 = 2.94, \quad A_2 = 0.32, \quad A_4 = 0.24, \quad A_5 = A_6 = 0,$$

$$A_7 = 0.17, \quad B_1 = 2.00, \quad B_2 = 0.096 \quad \text{and} \quad B_3 = 11.61.$$

**Waves.** Having specified the mechanical properties of the ACSR conductor, we can now calculate the allowable wave modes, according to the theory described in Section 3.5. For a given dimensionless wave number $k$, the dimensionless wavespeeds $\alpha$ are given by solving Eq. (33), which can be written as a cubic in $\lambda = \alpha^2$, namely Eq. (34), in which

$$d_2 = -(3.35 + 11.61k^{-2}), \quad d_1 = 1.14 + 32.91k^{-2} \quad \text{and}$$

$$d_0 = -(0.103 + 6.14k^{-2}).$$

As $d_0$ and $d_2$ are both negative, for all $k^2$, the cubic has only positive real roots, so that all the wave speeds are real.

**Numerical Results.** We have solved Eq. (34) for $\alpha^2$. In Fig. 1, we have plotted the three positive values of $\alpha$, as a function of $k$. Evidently, we can denote these three values by $\alpha_i(k)$, $i = 1, 2, 3$, with $0 < \alpha_1 < \alpha_2 < \alpha_3$. We see that $\alpha_i(k)$ is a decreasing function of $k$. In fact, the lowest wave speed, $\alpha_1$, is almost independent of $k$: for example, $\alpha_1(1) \simeq 0.448$ and $\alpha_1(10) \simeq 0.447$. Thus, the wave corresponding to $\alpha_1$ is almost nondispersive: it travels with a speed of approximately $0.45c_0$, where $c_0$ is the speed of shear waves in aluminum.

Figure 1 also suggests that $\alpha_2(k) - \alpha_1(k) \to 0$ as $k \to \infty$. This is false. To see this, let $k \to \infty$ in $\mathbf{A}$, and put $A_5 = A_6 = 0$. Then, using the notation of Abramowitz and Stegun [26], Section 3.8.2, we calculate $q^3 + r^2$, where $q = (1/3)d_1 - (1/9)d_2^2$ and $r = (1/6)(d_1 d_2 - 3d_0) - (1/27)d_2^3$. We find that

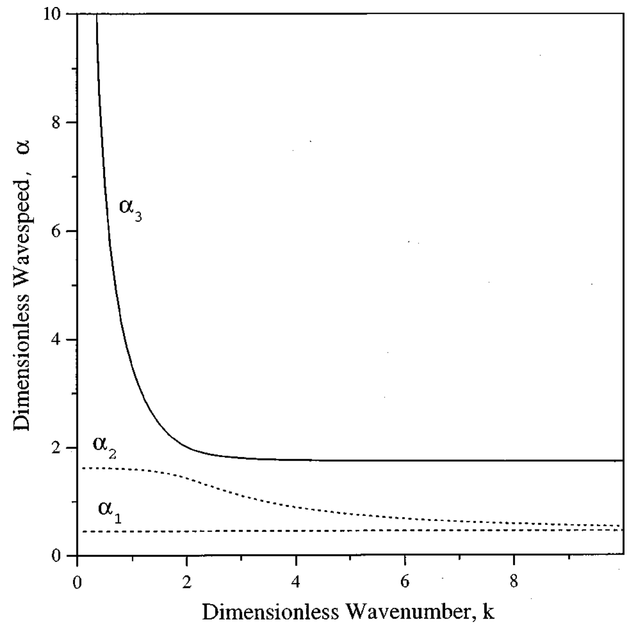


**Fig. 1 The dimensionless wave speeds $\alpha_i$ as functions of dimensionless wave number $k$**

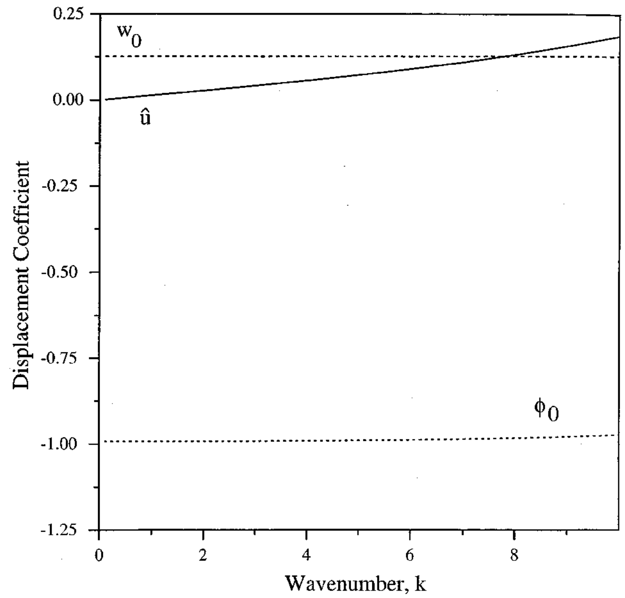


**Fig. 2 The components of the dimensionless eigenvector $\mathbf{x}_1 = (w_0, \phi_0, i\hat{u})$ corresponding to the dimensionless wave speed $\alpha_1$, as functions of dimensionless wave number $k$. This is the quasi-torsional mode.**

$$q^3+r^2=-\frac{1}{108}\{(A_1-A_4)^2+4A_2^2\}\{A_2^2+(A_1-A_7)(A_7-A_4)\}^2,$$

which is negative, confirming that all the roots are real (when $k=\infty$). However, for our particular values of $A_i$, we obtain $q^3+r^2\simeq-0.02$, which is small, and so $\alpha_1$ and $\alpha_2$ will differ by a small but finite amount for large $k$. In fact, we find $\alpha_2(10)\simeq 0.523$ and $\alpha_3(10)\simeq 1.73$.

Next, we have calculated the eigenvectors $\mathbf{x}_i$ of $\mathsf{A}$, corresponding to $\alpha_i$, where $\mathbf{x}=(w_0,\phi_0,u_0)^T$. We can arrange that $|\mathbf{x}|=1$ and, as $A_5=A_6=0$, it follows from Eq. (31) that we can take $w_0$ and $\phi_0$ to be real and $u_0$ to be pure imaginary, $u_0=i\hat{u}$, say. Then, taking the real part of Eq. (30), we obtain

$$u=-\hat{u}\sin k\xi,\quad \phi=\phi_0\cos k\xi \quad \text{and} \quad w=w_0\cos k\xi,$$

where $\xi=z-\alpha t$. Thus, the radial component is out of phase with the axial and torsional components. Then, the normalized eigenvectors show the physical character of each mode.

The three components of $\mathbf{x}_1$, corresponding to the lowest wavespeed $\alpha_1$, are shown in Fig. 2, as a function of $k$. We see that this mode is a quasi-torsional mode: The axial and radial components are small. This weakly dispersive mode is the most important in the context of our application to ACSR conductors, because our transducers are designed to launch torsional waves.

The components of the eigenvector $\mathbf{x}_2$, corresponding to the wave speed $\alpha_2$, are shown in Fig. 3, whereas $\mathbf{x}_3$ is shown in Fig. 4. We see that both of these modes have small torsional components. For $\mathbf{x}_2$, the axial component decreases with $k$ and the radial component dominates, whereas the opposite situation occurs with $\mathbf{x}_3$.

## 6 Conclusions

In this paper, we have attempted to give a rational model for the propagation of elastic waves along composite wire ropes. The goal was to obtain one-dimensional differential equations of wave-equation type, with coefficients obtained from certain integrals over the cross section of the wire rope. Such equations are well known for waves in isotropic rods. We used simple kinematical assumptions, Eq. (17), but it is clear that various expansions in $r$ could be used; see Boström [27] for a recent discussion of such methods.

We derived a set of three coupled partial differential equations, Eqs. (4)–(6). The coefficients in these equations are given as integrals involving the elastic stiffnesses of each layer of the composite wire rope, when regarded as a solid with cylindrical anisotropy. A basic difficulty is how to determine these stiffnesses. We have used a method described by Jolicoeur and Cardou [15]. This leads to a logical inconsistency: one of the Young's moduli, $E_T$, was calculated from a knowledge of the contact forces between individual wires within the rope, and these forces were estimated using Costello's theory ([4]); the inconsistency is that the latter theory gives Eq. (1) for $F$ whereas we obtain Eq. (25) (wherein

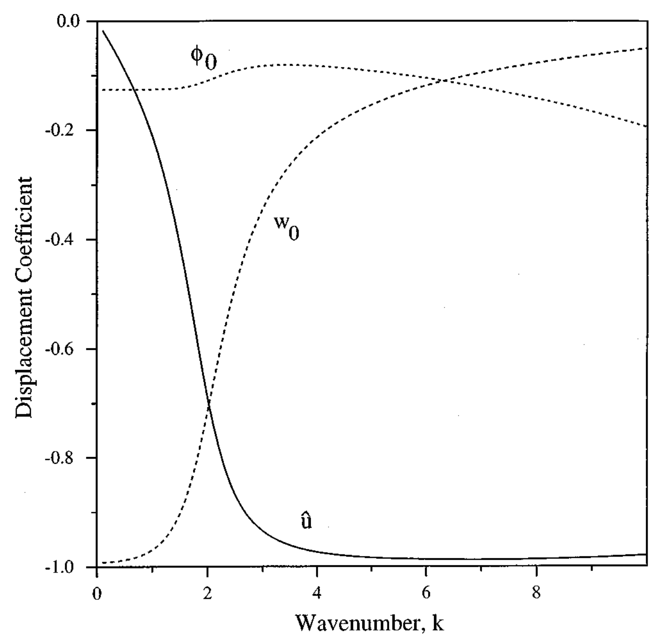


**Fig. 3 The components of the dimensionless eigenvector $\mathbf{x}_2$ corresponding to the dimensionless wave speed $\alpha_2$.**

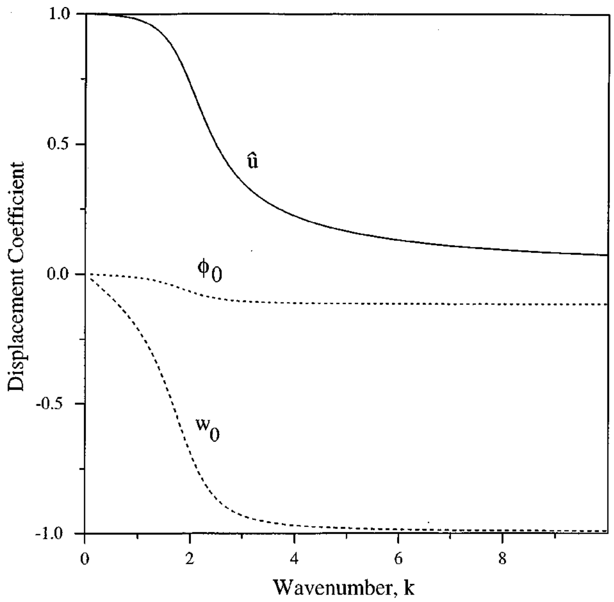


**Fig. 4 The components of the dimensionless eigenvector $x_3$ corresponding to the dimensionless wave speed $\alpha_3$.**

$A_5=0$). In fact, we applied a static tension, determined the contact forces, and then superimposed a wave motion. In the absence of a better algorithm, we feel that the present approach is adequate; we note that the modulus $E_T$ depends weakly on the actual magnitude of the contact forces, so that a rough estimate should suffice.

One aspect not considered here is that of *damping*: experimentally, it is observed that wave amplitude decays with distance along the wire rope. The precise cause of this phenomenon is unknown. For a wire rope under static tension $F$, it is known that interwire slippage is not responsible ([28]), although the damping does vary with $F$ and with the number of wires comprising the rope; see [29] for a review. Further work is needed so as to develop a predictive model for damping.

## Acknowledgments


This work was partially supported by the Center for Advanced Control of Energy and Power Systems, a National Science Foundation Industry/University Cooperative Research Center, at the Colorado School of Mines. We are grateful for many discussions with the Center's Director, Rahmat Shoureshi, and with other colleagues and students. We have also benefited from comments and reprints from A. Cardou and M. Raoof.


## Appendix A

**Rotated Stiffnesses.** A material with cylindrical orthotropy has elastic stiffnesses $C'_{\alpha\gamma}$ when referred to principal axes. Rotation about the radial axis by an angle $\beta$ leads to stiffnesses $C_{\alpha\gamma}$, defined as follows:

$$C_{11}=C'_{11}, \quad C_{12}=C'_{12}\cos^2\beta+C'_{13}\sin^2\beta,$$

$$C_{13}=C'_{13}\cos^2\beta+C'_{12}\sin^2\beta,$$

$$C_{14}=\frac{1}{2}(C'_{13}-C'_{12})\sin 2\beta, \quad C_{22}=C'_{22}\cos^4\beta+\frac{1}{2}C'_{23}\sin^2 2\beta,$$

$$C_{23}=C'_{23}(\cos^4\beta+\sin^4\beta)+\left(\frac{1}{4}C'_{22}+\frac{1}{4}C'_{33}-C'_{44}\right)\sin^2 2\beta,$$

$$C_{24}=\frac{1}{2}(C'_{44}+C'_{23})\sin 4\beta+\frac{1}{2}(C'_{33}\sin^2\beta-C'_{22}\cos^2\beta)\sin 2\beta,$$

$$C_{33}=C'_{33}\cos^4\beta+C'_{22}\sin^4\beta+\left(C'_{44}+\frac{1}{2}C'_{23}\right)\sin^2 2\beta,$$

$$C_{34}=\frac{1}{2}(C'_{33}\cos^2\beta-C'_{22}\sin^2\beta)\sin 2\beta-\frac{1}{2}\left(C'_{44}+\frac{1}{2}C'_{23}\right)\sin 4\beta,$$

$$C_{44}=C'_{44}\cos^2 2\beta+\frac{1}{4}(C'_{33}+C'_{22}-2C'_{23})\sin^2 2\beta,$$

$$C_{55}=C'_{55}\cos^2\beta+C'_{66}\sin^2\beta,$$

$$C_{56}=\frac{1}{2}(C'_{55}-C'_{66})\sin 2\beta \quad \text{and} \quad C_{66}=C'_{66}\cos^2\beta+C'_{55}\sin^2\beta.$$

## Appendix B

**Contact Stresses.** In order to calculate $E_T$, we have to calculate the contact stresses between the aluminum wires and the steel core. Specifically, we require $X_c$, the contact force per unit length acting along the line of contact. Thus, we apply a static load to the wire rope; the axial force $F$, axial twisting moment $M$, axial strain $\varepsilon$, and rotation per unit length $\chi$ are related by Eq. (1). The theory in [4] yields expressions for $A_1-A_4$, and also for $X$, the contact force per unit length along the centerline of the rope. Then, $X_c$ is given by [4], Eqs. (3.10) and (3.114), as

$$X_c=-X\{\cos^2\beta+(r_s/h)^2\sin^2\beta\}^{-1/2}=-1.011X, \qquad (B1)$$

using $\beta=10$ deg and $r_s/h=0.503$ for our ACSR conductor.

The total axial force acting on the wire rope is $F=F_0+F_1$, where $F_0$ and $F_1$ are the axial forces in the steel core and aluminum wires, respectively. We have $F_0=\pi E_s r_s^2\varepsilon$. For $F_1$ and $X$, we have the following equations from [4], Section 3.9:

$$F_1=6(T\cos\beta+N\sin\beta),$$

$$hX=(N\cos\beta-T\sin\beta)\sin\beta,$$

$$hN=(H\sin\beta-G\cos\beta)\sin\beta,$$

$$hG=\frac{1}{4}\pi E_a r_a^4(\Lambda\sin^2\beta-\alpha_1\sin 2\beta),$$

$$hH=\frac{1}{4}\pi(1+\nu_a)^{-1}E_a r_a^4(\Lambda\sin\beta\cos\beta-\alpha_1\cos 2\beta),$$

with $T=\pi E_a r_a^2\xi_1$ and $h\Lambda=\nu_s r_s\varepsilon+\nu_a r_a\xi_1$. We also have

$$\xi_1+\alpha_1\tan\beta=\varepsilon, \qquad (B2)$$

$$\xi_1\tan\beta-\alpha_1+\Lambda\tan\beta=h\chi. \qquad (B3)$$

Comparing our notation with that used in [4], we have $F_1=F_2$, $G=G'_2$, $H=H'_2$, $N=N'_2$, $T=T'_2$, $X=X_2$, $\alpha_1=\Delta\alpha_2$, $r_a=R_2$, $r_s=R_1$, $\beta=(1/2)\pi-\alpha_2$, $h=r_2$, $\chi=\tau_s$ and $\xi_1=\xi_2$. Also, $m_2=6$.

We can solve Eqs. ($B2$) and ($B3$) for $\xi_1$ and $\alpha_1$:

$$\xi_1=\Omega^{-1}\{\varepsilon(h\cos^2\beta-\nu_s r_s\sin^2\beta)+\chi h^2\sin\beta\cos\beta\},$$

$$\alpha_1=\Omega^{-1}\{\varepsilon(h+\nu_s r_s+\nu_a r_a)\sin\beta\cos\beta-\chi h^2\cos^2\beta\},$$

where $\Omega=h+\nu_a r_a\sin^2\beta$. We can then substitute back, so as to obtain an expression for $F$ in terms of $\varepsilon$ and $\chi$.

Let us suppose that the wire rope is subject to a prescribed static load $F$ and that the moment $M$ is adjusted so that the rope does not rotate ($\chi=0$). Then, we find that

$$T=\pi E_a r_a^2\varepsilon\Omega^{-1}(h\cos^2\beta-\nu_s r_s\sin^2\beta),$$

$$hG=\frac{1}{4}\pi E_a r_a^4\varepsilon\Omega^{-1}\{\nu_s r_s-(2h+2\nu_s r_s+\nu_a r_a)\cos^2\beta\}\sin^2\beta,$$

$$hH=\frac{1}{4}\pi(1+\nu_a)^{-1}E_a r_a^4 \varepsilon \Omega^{-1}\{(2h+2\nu_s r_s+\nu_a r_a)\sin^2\beta$$

$$-h\}\sin\beta\cos\beta.$$

If we take $\nu_s=0.25$ and $\nu_a=0.33$, we find that

$$G=-0.0259E_a r_a^3\varepsilon, \quad H=-0.0462E_a r_a^3\varepsilon,$$

$$T=3.019E_a r_a^2\varepsilon \text{ and } N=0.00151E_a r_a^2\varepsilon.$$

We can take $E_s=3E_a$, whence

$$F_0=1.07E_a a^2\varepsilon \text{ and } F_1=1.96E_a a^2\varepsilon, \tag{B4}$$

and so $F=3.03\,E_a a^2\varepsilon$. Thus, given the static load $F$, this equation determines the axial strain $\varepsilon$, whence

$$N=(5.5\times10^{-5})F, \quad T=0.11F \text{ and } hX=-0.0033F. \tag{B5}$$

Finally, we deduce from Eq. $(B1)$ that

$$hX_c=0.0033F. \tag{B6}$$

The fact that $N$ is much smaller than $T$ suggests that asymptotic approximations valid for small $\beta$ should be useful. With errors of $O(\beta^2)$ as $\beta\to0$, we easily obtain $\Omega=h$, $\xi_1=\varepsilon$, $T=\pi E_a r_a^2\varepsilon$, $G=O(\beta^2)$, $H=O(\beta)$, $N=O(\beta^3)$,

$$F_1/(E_a a^2\varepsilon)=6\pi(r_a/a)^2=2.07$$

(which should be compared with the "exact" result Eq. $(B4)$) and

$$hX\sim-\pi\beta^2 r_a^2 E_a\varepsilon\sim-0.0032F,$$

using $\beta=0.17$. This result for $X$ is in error by about 3%.

## References


[1] Rawlins, C. B., 1979, "Fatigue of Overhead Conductors," *Transmission Line Reference Book: Wind-Induced Conductor Motion*, Electric Power Research Institute, Palo Alto, CA, pp. 51–81.

[2] Berger, J. R., Martin, P. A., and McCaffery, S. J., 2000, "Time-Harmonic Torsional Waves in a Composite Cylinder With an Imperfect Interface," J. Acoust. Soc. Am., **107**, pp. 1161–1167.

[3] Butson, G. J., Phillips, J. W., and Costello, G. A., 1980, "Stresses in Wire Rope due to Dynamic Loads Associated With Deep Shaft Hoisting Systems," *Proc. First Annual Wire Rope Symposium*, Denver, CO, Engineering Extension Service, Washington State University, Pullman, WA, pp. 243–273.

[4] Costello, G. A., 1997, *Theory of Wire Rope*, 2nd Ed., Springer, New York.

[5] McConnell, K. G., and Zemke, W. P., 1982, "A Model to Predict the Coupled Axial Torsion Properties of ACSR Electrical Conductors," Exp. Mech., **22**, pp. 237–244.

[6] Lanteigne, J., 1985, "Theoretical Estimation of the Response of Helically Armored Cables to Tension, Torsion, and Bending," ASME J. Appl. Mech., **52**, pp. 423–432.

[7] Sathikh, S., Rajasekaran, S., Jayakumar, and Jebaraj, C., 2000, "General Thin Rod Model for Preslip Bending Response of Strand," J. Eng. Mech., **126**, pp. 132–139.

[8] Raoof, M., and Kraincanic, I., 1994, "Critical Examination of Various Approaches Used for Analysing Helical Cables," J. Strain Anal., **29**, pp. 43–55.

[9] Samras, R. K., Skop, R. A., and Milburn, D. A., 1974, "An Analysis of Coupled Extensional-Torsional Oscillations in Wire Rope," J. Eng. Ind., **96**, pp. 1130–1135.

[10] Graff, K. F., 1991, *Wave Motion in Elastic Solids*, Dover, New York.

[11] Cardou, A., and Jolicoeur, C., 1997, "Mechanical Models of Helical Strands," Appl. Mech. Rev., **50**, pp. 1–14.

[12] Hobbs, R. E., and Raoof, M., 1982, "Interwire Slippage and Fatigue Prediction in Stranded Cables for TLP Tethers," *Proceedings, 3rd Intl. Conf. Behavior of Offshore Structures*, Hemisphere, Washington, DC, pp. 77–92.

[13] Blouin, F., and Cardou, A., 1989, "A Study of Helically Reinforced Cylinders Under Axially Symmetric Loads and Application to Strand Mathematical Modelling," Int. J. Solids Struct., **25**, pp. 189–200.

[14] Jolicoeur, C., and Cardou, A., 1994, "Analytical Solution for Bending of Coaxial Orthotropic Cylinders," J. Eng. Mech., **120**, pp. 2556–2574.

[15] Jolicoeur, C., and Cardou, A., 1996, "Semicontinuous Mathematical Model for Bending of Multilayered Wire Strands," J. Eng. Mech., **122**, pp. 643–650.

[16] Skop, R. A., and Samras, R. K., 1975, "Effects of Coupled Extensional-Torsional Oscillations in Wire Rope During Ocean Salvage and Construction Operations," J. Eng. Ind., **97**, pp. 485–492.

[17] Phillips, J. W., and Costello, G. A., 1977, "Axial Impact of Twisted Wire Cables," ASME J. Appl. Mech., **44**, pp. 127–131.

[18] Raoof, M., Huang, Y. P., and Pithia, K. D., 1994, "Response of Axially Preloaded Spiral Strands to Impact Loading," Comput. Struct., **51**, pp. 125–135.

[19] Martin, P. A., 1992, "Boundary Integral Equations for the Scattering of Elastic Waves by Elastic Inclusions With Thin Interface Layers," J. Nondestruct. Eval., **11**, pp. 167–174.

[20] Ting, T. C. T., 1996, "Pressuring, Shearing, Torsion and Extension of a Circular Tube or Bar of Cylindrically Anisotropic Material," Proc. R. Soc. London, Ser. A, **452**, pp. 2397–2421.

[21] Martin, P. A., and Berger, J. R., 2001, "Waves in Wood: Free Vibrations of a Wooden Pole," J. Mech. Phys. Solids, **49**, pp. 1155–1178.

[22] Ting, T. C. T., 1996, *Anisotropic Elasticity*, Oxford University Press, Oxford, UK.

[23] Jones, R. M., 1999, *Mechanics of Composite Materials*, 2nd Ed., Taylor & Francis, Philadelphia, PA.

[24] Doocy, E. S., and Hard, A. R., 1979, "Introduction," *Transmission Line Reference Book: Wind-Induced Conductor Motion*, Electric Power Research Institute, Palo Alto, CA, pp. 1–50.

[25] Young, W. C., 1989, *Roark's Formulas for Stress and Strain*, 6th Ed., McGraw-Hill, New York.

[26] Abramowitz, M., and Stegun, I. A., eds., 1965, *Handbook of Mathematical Functions*, Dover, New York.

[27] Boström, A., 2000, "On Wave Equations for Elastic Rods," Z. Angew. Math. Mech., **80**, pp. 245–251.

[28] Labrosse, M., Nawrocki, A., and Conway, T., 2000, "Frictional Dissipation in Axially Loaded Simple Straight Strands," J. Eng. Mech., **126**, pp. 641–646.

[29] Fang, J., and Lyons, G. J., 1996, "Structural Damping of Tensioned Pipes With Reference to Cables," J. Sound Vib., **193**, pp. 891–907.

# Hamiltonian Mechanics for Functionals Involving Second-Order Derivatives

**B. Tabarrok**[1]
Department of Mechanical Engineering,
University of Victoria,
British Columbia, V8W 3P6, Canada

**C. M. Leech**
Department of Mechanical Engineering,
UMIST,
Manchester M60 1QD, UK
Fellow ASME

*Hamilton's principle was developed for the modeling of dynamic systems in which time is the principal independent variable and the resulting equations of motion are second-order differential equations. This principle uses kinetic energy which is functionally dependent on first-order time derivatives, and potential energy, and has been extended to include virtual work. In this paper, a variant of Hamiltonian mechanics for systems whose motion is governed by fourth-order differential equations is developed and is illustrated by an example invoking the flexural analysis of beams. The variational formulations previously associated with Newton's second-order equations of motion have been generalized to encompass problems governed by energy functionals involving second-order derivatives. The canonical equations associated with functionals with second order derivatives emerge as four first-order equations in each variable. The transformations of these equations to a new system wherein the generalized variables and momenta appear as constants, can be obtained through several different forms of generating functions. The generating functions are obtained as solutions of the Hamilton-Jacobi equation. This theory is illustrated by application to an example from beam theory the solution recovered using a technique for solving nonseparable forms of the Hamilton-Jacobi equation. Finally whereas classical variational mechanics uses time as the primary independent variable, here the theory is extended to include static mechanics problems in which the primary independent variable is spatial.* [DOI: 10.1115/1.1505626]

## 1 Introduction

Hamilton's principle and his celebrated canonical equations are based on Newton's second-order differential equations of motion. The same is true for the further development of this analytical approach to mechanics culminating in the celebrated Hamilton-Jacobi equation. Excellent accounts of the theory are available in texts in classical mechanics, e.g., Lanczos [1], Goldstein [2], Whittaker [3], Pars [4], Synge [5], and Logan [6]. Classical variational mechanics invokes kinetic energy functions, which are expressed in terms of momenta or velocities. This theory is then developed where the first derivative is the highest temporal derivative. It is of interest to examine the extension of this theory to cases when the Lagrangian involves second-order derivatives; such circumstances arise in spatial mechanics, and for such functionals the Euler-Lagrange equations are fourth order. Accordingly, the generalization of Hamiltonian theory for such systems is ideally suited to problems of beam flexure. In this generalization the mathematical structure of the Hamiltonian theory remains essentially in tact; the change in the independent variable from time to space implies a change in the physics of the problem from determining trajectories of particles in time to finding deflected configurations of beams in space.

Rund [7,8] examined the theory of functionals depending on second-order derivatives and in particular identified some difficulties when the functional is not a positive definite function in the second derivative terms. Analogous difficulties would have arisen in Hamilton's principle in dynamics had the kinetic energy not been a positive definite function in velocities. Rodrigues [9] considered Lagrangians that contained second-order differentials, and developed the corresponding Hamilton equations; since the formulation is dynamic, he did not suggest the source of these high derivatives. In the following a theory for the Hamiltonian mechanics of systems described by fourth-order differential equations is developed and is illustrated by an example invoking the flexural analysis of beams.

## 2 Functionals Involving Second-order Derivatives

Consider the following functional:

$$\delta\int_{x_1}^{x_2} L(x,y,y_x,y_{xx})dx=0 \tag{1}$$

where

$$y_x=\frac{\partial y}{\partial x} \quad \text{and} \quad y_{xx}=\frac{\partial^2 y}{\partial x^2}.$$

The Euler-Lagrange equation of this functional is given by

$$\frac{\partial L}{\partial y}-\frac{d}{dx}\left(\frac{\partial L}{\partial y_x}\right)+\frac{d^2}{dx^2}\left(\frac{\partial L}{\partial y_{xx}}\right)=0. \tag{2}$$

Now in analogy with classical mechanics a modified momentum is defined,

$$r\overset{\text{def}}{=}\frac{\partial L(x,y,y_x,y_{xx})}{\partial y_{xx}}, \tag{3}$$

with this definition, Eq. (2) may be written as

$$\frac{\partial L}{\partial y}=\frac{d}{dx}\left[\frac{\partial L}{\partial y_x}-\frac{dr}{dx}\right]. \tag{4}$$

If a modified momentum $p$ is also defined as

[1]Deceased.

Contributed by the Applied Mechanics Division of THE AMERICAN SOCIETY OF MECHANICAL ENGINEERS for publication in the ASME JOURNAL OF APPLIED MECHANICS. Manuscript received by the ASME Applied Mechanics Division, April 21, 2001; final revision, Feb. 28, 2002. Associate Editor: M. Ortiz. Discussion on the paper should be addressed to the Editor, Prof. Robert M. McMeeking, Department of Mechanical and Environmental Engineering University of California–Santa Barbara, Santa Barbara, CA 93106-5070, and will be accepted until four months after final publication of the paper itself in the ASME JOURNAL OF APPLIED MECHANICS.

  

$$p \stackrel{\text{def}}{=} \left[\frac{\partial L}{\partial y_x} - \frac{dr}{dx}\right] \tag{5}$$

then Eq. (4) may be expressed as

$$\frac{\partial L}{\partial y} = \frac{dp}{dx}. \tag{6}$$

This equation resembles Lagrange's equation in dynamics, the differences being the definition of the momenta and also the fact that in dynamics the independent variable is time $t$ instead of the space variable $x$. Again in analogy with classical dynamics we can see that if $y$ does not appear in the Lagrangian, i.e., $\partial L/\partial y = 0$, then $y$ will be ignorable with a conserved modified momentum, i.e., $p = c$.

The modified momentum, $p$ shown above is used here to distinguish it from generalized momentum. This definition for modified momentum is reserved here for use within the theory of spatial mechanics whereas the generalized momentum $p = \partial L/\partial y_t$ is conventionally associated with temporal mechanics. This distinction is made so that the following development can be compared with those associated with classical Hamiltonian theory. Finally the modified momentum $r$ defined above is now relabeled hyper momentum since it is the derivative with respect to $y_{xx}$ and not $y_x$; the second temporal derivative $y_{tt}$ is not intrinsic in classical Hamiltonian mechanics.

Now consider the total derivative of $L$ with respect to $x$,

$$\frac{dL}{dx} = \frac{\partial L}{\partial x} + \frac{\partial L}{\partial y} y_x + \frac{\partial L}{\partial y_x} y_{xx} + \frac{\partial L}{\partial y_{xx}} y_{xxx}. \tag{7}$$

Substituting for $\partial L/\partial y$ in Eq. (7) from Eqs. (3) and (4), yields

$$\frac{\partial L}{\partial x} = \frac{d}{dx}\left[L - y_x\left\{\frac{\partial L}{\partial y_x} - \frac{d}{dx}\left(\frac{\partial L}{\partial y_{xx}}\right)\right\} - y_{xx}\frac{\partial L}{\partial y_{xx}}\right]$$

and after simplification,

$$\frac{d}{dx}[L - y_x p - y_{xx} r] = \frac{\partial L}{\partial x}. \tag{8}$$

If $x$ does not appear explicitly in $L$, then Eq. (8) may be integrated resulting in

$$-L + p y_x + r y_{xx} = H, \quad \text{a constant} \tag{9}$$

where $H$ is the Hamiltonian the system. The first two terms resemble the form of the Hamiltonian for dynamics. The inclusion of the second-order term in the functional in Eq. (1) modifies the Hamiltonian through the third term above.

**Example.** In order to illustrate the application of the developments in this paper, an example is included and is revisited after various developments in this paper. A prismatic bar is subjected to an inline compressive axial force $F$ and to a lateral distributed load $q(x)$. For small deflection theory, the Lagrangian for this system is

$$L = \frac{EI}{2} y_{xx}^2 - q(x) y - \frac{F}{2} y_x^2$$

and the associated Euler-Lagrange equation is

$$EI y_{xxxx} + F y_{xx} = q. \tag{10}$$

The hyper momentum, the bending moment, is

$$r = \frac{\partial L}{\partial y_{xx}} = EI y_{xx}$$

and the modified momentum, the effective shear, becomes

$$p = \frac{\partial L}{\partial y_x} - \frac{dr}{dx}$$

or

$$p = -F y_x - \frac{d}{dx}(EI y_{xx}).$$

If $q(x) = 0$, $y$ will not appear in $L$ and is therefore ignorable, the associated momentum namely

$$p = -F y_x - EI y_{xxx}$$

will then be constant across the beam. If $EI$ and $q$ are constants, then $x$ will not appear explicitly in $L$ and the Hamiltonian $H = p y_x + r y_{xx} - L$, will have a constant value across the beam. In this case

$$H = \frac{EI}{2} y_{xx}^2 + q y - \frac{F}{2} y_x^2 - EI y_{xxx} y_x$$

and

$$\frac{dH}{dx} = (EI y_{xxxx} + F y_{xx} - q) y_x$$

which vanishes by virtue of Eq. (10). It is interesting to note that in contrast to the case of classical dynamics the energy terms appearing in the Lagrangian that define the problem, are not sufficient to describe the Hamiltonian, i.e., an additional energy term is needed for definition of Hamiltonian in this case.

At this point the general solution of Eq. (10) is stated, for use in a later section,

$$y = A + Bx + C \sin \lambda x + D \cos \lambda x + \frac{q x^2}{2\lambda^2 EI} \tag{11}$$

where

$$\lambda^2 = \frac{F}{EI} \tag{12}$$

and $A$, $B$, $C$, and $D$ are constants to be determined from the boundary conditions.

## 3 The Canonical Equations

The second-order Newtonian equations of motion yield two first-order canonical equations; for the present fourth-order system, four first-order canonical equations arise. To derive these equations, Eq. (3) is inverted,

$$y_{xx} = \psi(x, y, y_x, r).$$

Here it is assumed tacitly that $y_{xx}$ appears in $L$ in such a fashion that the above inversion can be carried out.

The Hamiltonian is now constructed,

$$H(x,y,y_x,p,r) = -L(x,y,y_x,\psi(x,y,y_x,r)) + p y_x + r\psi(x,y,y_x,r)$$

and leads to the canonical equations

$$\frac{\partial H}{\partial y} = -\frac{\partial L}{\partial y} - \frac{\partial L}{\partial \psi}\frac{\partial \psi}{\partial y} + r\frac{\partial \psi}{\partial y} = -\frac{\partial L}{\partial y} + \left(r - \frac{\partial L}{\partial \psi}\right)\frac{\partial \psi}{\partial y} = -\frac{\partial L}{\partial y}$$

since the term in the brackets on the right hand side vanishes by definition of $r$.

Now noting Eq. (6), the first canonical equation becomes

$$\frac{\partial H}{\partial y} = -\frac{dp}{dx}.$$

Similarly

$$\begin{aligned}\frac{\partial H}{\partial y_x} &= -\frac{\partial L}{\partial y_x} - \frac{\partial L}{\partial \psi}\frac{\partial \psi}{\partial y_x} + p + r\frac{\partial \psi}{\partial y_x} \\ &= p + \left(r - \frac{\partial L}{\partial \psi}\right)\frac{\partial \psi}{\partial y_x} - \frac{\partial L}{\partial y_x} \\ &= \left[\frac{\partial L}{\partial y_x} - \frac{d}{dx}\left(\frac{\partial L}{\partial y_{xx}}\right)\right] - \frac{\partial L}{\partial y_x} = -\frac{d}{dx}\left(\frac{\partial L}{\partial y_{xx}}\right).\end{aligned}$$

Again referring to Eq. (3), the second canonical equation becomes

$$\frac{\partial H}{\partial y_x} = -\frac{dr}{dx}.$$

The third and fourth canonical equations are obtained readily as

$$\frac{\partial H}{\partial y_x} = \frac{dy}{dx} \quad \text{and} \quad \frac{\partial H}{\partial r} = \frac{dy_x}{dx}.$$

The four canonical equations are thus tabulated:

$$\frac{\partial H}{\partial y} = -\frac{dp}{dx} \qquad \frac{\partial H}{\partial p} = \frac{dy}{dx}$$

$$\frac{\partial H}{\partial y_x} = -\frac{dr}{dx} \qquad \frac{\partial H}{\partial r} = \frac{dy_x}{dx}.$$

Now consider the total derivative of $H$:

$$\frac{d}{dx}H(x,y,y_x,p,r) = \frac{\partial H}{\partial x} + \frac{\partial H}{\partial y}y_x + \frac{\partial H}{\partial y_x}y_{xx} + \frac{\partial H}{\partial p}p_x + \frac{\partial H}{\partial r}r_x.$$

Substituting the canonical equations into the right-hand side, and simplifying gives

$$\frac{d}{dx}H = \frac{\partial H}{\partial x}.$$

**Example.** Consider again the prismatic beam under the inline compressive load and recall the Lagrangian

$$L = \frac{EI}{2}y_{xx}^2 - q(x)y - \frac{F}{2}y_x^2$$

and the Hamiltonian

$$H = L - py_x + ry_{xx}$$

where $r = EIy_{xx}$.

Eliminating $y_{xx}$ from the Hamiltonian results in the following:

$$H = -\frac{EI}{2}\frac{r^2}{EI^2} + qy + \frac{F}{2}y_x^2 + py_x + \frac{r^2}{EI}$$

or

$$H = \frac{1}{2}\frac{r^2}{EI} + qy + \frac{F}{2}y_x^2 + py_x$$

The canonical equations are then

$$\frac{\partial H}{\partial y} = q = -\frac{dp}{dx} \tag{13}$$

$$\frac{\partial H}{\partial y_x} = Fy_x + p = -\frac{dr}{dx} \tag{14}$$

$$\frac{\partial H}{\partial p} = y_x = \frac{dy}{dx} \tag{15}$$

$$\frac{\partial H}{\partial r} = \frac{r}{EI} = \frac{dy_x}{dx}. \tag{16}$$

Combining (13) and (15) to eliminate $r$ results in the equilibrium equation

$$Fy_x + p = -EIy_{xxx}$$

and now substituting into (12) to eliminate $p$ gives

$$q = (Fy_x + EIy_{xxx})_x$$

the static equilibrium equation.

## 4 Generalization of the Principle of Least Action

In analytical dynamics the principle of Least Action, attributed to Maupertuis and described by Tabarrok and Rimrott [10], is stated as

$$\Delta\int_{t_1}^{t_2}\sum p_i q_i dt = 0.$$

In this principle the independent variable time $t$, the generalized displacements $q_i$ and the momenta $p_i$ are subject to variations. The principle is subject to two constraints. These are the conservation of the Hamiltonian and the coterminations of the displacements (but not time) at $t_1$ and $t_2$, i.e.,

$$H(P_i, q_i) = C$$

$$\Delta q_i = \delta q_i + q_i \delta t = 0 \quad \text{at } t_1, t_2.$$

Generalization of this principle to functionals depending on second-order derivatives results in

$$\Delta\int_{x_1}^{x_2}(py_x + ry_{xx})dx = 0 \tag{17}$$

or

$$\int_{x_1}^{x_2}\delta(py_x + ry_{xx})dx + (py_x + ry_{xx})(\delta x)\Big|_{x_1}^{x_2} = 0.$$

Integrating the terms under the integral we write this equation as

$$\int_{x_1}^{x_2}\left(-\frac{dp}{dx}\delta y - \frac{dr}{dx}\delta y_x + \frac{dy}{dx}\delta p + y_{xx}\delta r\right)dx + p(\delta y + y_x\delta x)\Big|_{x_1}^{x_2}$$

$$+ r(\delta y_x + y_{xx}\delta x)\Big|_{x_1}^{x_2} = 0. \tag{18}$$

Now as in the case of dynamics we impose the constraints

$$H(y, y_x, p, r) = C$$

and

$$\Delta y = \Delta y_x = 0 \quad \text{at } x_1, x_2.$$

Thus in Eq. (29) the last two terms drop out by virtue of the second set of constraints. It remains to show that the integrand in Eq. (17) also vanishes by virtue of constancy of $H$.

Now

$$\delta H = \frac{\partial H}{\partial y}\delta y + \frac{\partial H}{\partial y_x}\delta y_x + \frac{\partial H}{\partial p}\delta p + \frac{\partial H}{\partial r}\delta r = 0.$$

In terms of the canonical equations, this equation becomes

$$\delta H = -p_x\delta y - r_x\delta y_x + y_x\delta p + y_{xx}\delta r = 0$$

the integrand in Eq. (17)

## 5 Canonical Transformations

Assembling the variables $(y, y_x, p, r)$ as a state vector $\sigma$ and transforming to a new state vector $\Sigma$ whose components are $(Y, Y_x, P, O)$ that is

$$Y=Y(y,y_x,p,r,x)$$
$$Y_x=Y_x(y,y_x,p,r,x)$$
$$P=P(y,y_x,p,r,x)$$
$$R=R(y,y_x,p,r,x),$$

it is now required to develop the canonical equations in the new system, so that they are of the same format as those in the old coordinates; the Lagrangian in these new coordinates is thus

$$L=PY_x+RY_{xx}-K$$

where $K$ is the new Hamiltonian; that is

$$\frac{\partial K}{\partial Y}=-\frac{dP}{dx}\qquad \frac{\partial K}{\partial P}=\frac{dY}{dx}$$
$$\frac{\partial K}{\partial Y_x}=-\frac{dR}{dx}\qquad \frac{\partial K}{\partial R}=\frac{dY_x}{dx}.$$

The two Lagrangians can differ at most by the total derivative of an arbitrary function $S$; that is

$$L-\hat{L}=(py_x+ry_{xx}-H)-(PY_x+RY_{xx}-K)=\frac{dS}{dx} \qquad (19)$$

or

$$\int_{x_1}^{x_2}(L-\hat{L})dx=\int_{x_1}^{x_2}(py_x+ry_{xx}-H)dx-\int_{x_1}^{x_2}(PY_x+RY_{xx}-K)dx=\int_{x_1}^{x_2}\frac{dS}{dx}dx=S(x_2)-S(x_1). \qquad (20)$$

To effect this transformation $S$, the generating function must be a function of both the old $(p,r,y,y_x)$ and the new $(P,R,Y,Y_x)$ state variables. Thus $S$ besides being a function of $x$ must depend on the eight variables $(p,r,y,y_x)$ and $(P,R,Y,Y_x)$; however, only four of these can be independent since the two sets of state variables are related by the four mapping functions. The generating function may now be written as a function of four independent variables in one of 56 possible ways.

Consider for example the following four generating function forms:

$$S_1=S_1(y,y_x,Y,Y_x,x)$$
$$S_2=S_2(y,y_x,P,R,x)$$
$$S_3=S_3(p,r,P,R,x)$$
$$S_4=S_4(p,r,Y,Y_x,x)$$

and specifically the first form,

$$(py_x+ry_{xx}-H)-(PY_x+RY_{xx}-K)=\frac{dS_1}{dx}=\frac{\partial S_1}{\partial x}+\frac{\partial S_1}{\partial y}y_x+\frac{\partial S_1}{\partial y_x}y_{xx}+\frac{\partial S_1}{\partial Y}Y_x+\frac{\partial S_1}{\partial Y_x}Y_{xx}. \qquad (21)$$

Now matching the coefficients results in

$$\frac{\partial S_1}{\partial y}=p,\quad \frac{\partial S_1}{\partial y_x}=r,\quad \frac{\partial S_1}{\partial Y}=-P. \qquad (22)$$

$$\frac{\partial S_1}{\partial Y_x}=-R,\quad \text{and}\quad K=\frac{\partial S_1}{\partial x}+H. \qquad (23)$$

If the second form is used,

$$\frac{\partial S_2}{\partial y}=p,\quad \frac{\partial S_2}{\partial y_x}=r,\quad \frac{\partial S_2}{\partial P}=Y \qquad (24)$$

$$\frac{\partial S_2}{\partial R}=Y_x\quad \text{and}\quad K=\frac{\partial S_2}{\partial x}+H. \qquad (25)$$

## 6 The Hamilton-Jacobi Equation

Now let $(P,R,Y,Y_x)$ be the *initial* state vector[2], that is

$$y=y(y_0,y_{x0},p_0,r_0,x)$$
$$y_x=y_x(y_0,y_{x0},p_0,r_0,x)$$
$$p=p(y_0,y_{x0},p_0,r_0,x)$$
$$r=r(y_0,y_{x0},p_0,r_0,x).$$

To ensure that $y_0$ and $y_{x0}$ are constant, set $K=0$. Then $\partial K/\partial y_0=dp_0/dx=0$ and thus $p_0$ is constant.

If $S_2$ is the generating function, the Hamilton-Jacobi equation can be written

$$\frac{\partial S_2}{\partial x}+H=0$$

or

$$\frac{\partial S_2(x,y,y_x,P,R)}{\partial x}+H\left(x,y,y_x,\frac{\partial S_2}{\partial y},\frac{\partial S_2}{\partial y_x}\right)=0.$$

The variables in this nonlinear partial differential equation are $x$, $y$ and $y_x$; $P$ and $R$ are constants since $K=0$. Now

$$\frac{dS_2}{dx}=\frac{\partial S_2}{\partial x}+\frac{\partial S_2}{\partial y}y_x+\frac{\partial S_2}{\partial y_x}y_{xx}+\frac{\partial S_2}{\partial P}P_x.$$

The last term vanishes since $P$ is a constant and

$$\frac{dS_2}{dx}=-H+py_x+ry_{xx}$$

or

$$S_2=\int L\,dx+\text{constant}.$$

**Example.** The prismatic beam with in-line axial load

$$L=\frac{EI}{2}y_{xx}^2-\frac{F}{2}y_x^2-qy$$

where

$$r=\frac{\partial L}{\partial y_{xx}}=EIy_{xx}$$

and the Hamiltonian becomes

$$H=\frac{r^2}{2EI}+\frac{F}{2}y_x^2+qy+py_x,$$

the Hamilton-Jacobi equation takes the form

$$\frac{\partial S_2}{\partial x}+H=0$$

or

$$\frac{\partial S_2}{\partial x}+\frac{r^2}{2EI}+\frac{F}{2}y_x^2+qy+py_x=0$$

or

[2] $y_0$, $y_{x0}$, $p_0$, and $r_0$ are known constants, from the initial conditions when $x=0$.

$$\frac{\partial S_2}{\partial x}+\frac{1}{2EI}\left(\frac{\partial S_2}{\partial y_x}\right)^2+\left(\frac{1}{2}Fy_x+\frac{\partial S_2}{\partial y}\right)y_x+qy=0. \tag{26}$$

The above equation must now be solved for $S_2(x,y,y_x)$, from which the specific form of $y(x)$ can be developed. In texts on theoretical mechanics ([1–10]), solutions for few examples of Hamilton-Jacobi equation are obtained by splitting the generating function into separate additive parts, i.e.,

$$S_2=S_{2x}(x)+S_{2y}(y)+S_{2y_x}(y_x). \tag{27}$$

Denham and Buch [11] used a separable product for $S$, that is $S(q,t)=S_q(q)S_t(t)$ where in this case $t$, time is the independent variable and $q(t)$ is the generalized coordinate. Other forms for $S$ have been used, for example Saletan and Cromer [12], Benton [13], and Sanz-Serna and Calvo [14]. The aim is to represent the Hamilton-Jacobi partial differential equation by decoupled ordinary differential equations but the assumed form of the principal function $S_2$, Eq. (26) will not yield decoupled equations. A new scheme for solving some nonseparable forms of the Hamilton-Jacobi equation has been suggested by the present authors ([15,16]). In this approach the generating function is formed by a polynomial in terms of the primary variables. Thus a solution of the following form is assumed for Eq. (25):

$$S_2=a(x)y_x^2+b(x)y_xy+c(x)y^2+d(x)y_x+e(x)y+f(x). \tag{28}$$

Using this form for $S_2$ in Eq. (25) we find

$$\frac{da}{dx}y_x^2+\frac{db}{dx}y_xy+\frac{dc}{dx}y^2+\frac{dd}{dx}y_x+\frac{de}{dx}y$$
$$+\frac{df}{dx}+\frac{1}{2EI}(2ay_x+by+d)^2+(by_x+2cy+e)y_x$$
$$+\frac{F}{2}y_x^2+qy=0.$$

Collecting the various polynomial terms

$$y_x^2:\quad \frac{da}{dx}+\frac{2a^2}{EI}+b+\frac{F}{2}=0 \tag{29}$$

$$y_xy:\quad \frac{db}{dx}+\frac{2ab}{EI}+2c=0 \tag{30}$$

$$y^2:\quad \frac{dc}{dx}+\frac{b^2}{2EI}=0 \tag{31}$$

$$y_x:\quad \frac{dd}{dx}+\frac{2ad}{EI}+e=0 \tag{32}$$

$$y:\quad \frac{de}{dx}+\frac{bd}{EI}+q=0 \tag{33}$$

$$\text{constant:}\quad \frac{df}{dx}+\frac{d^2}{2EI}=0. \tag{34}$$

The first three of these equations are coupled in $a$, $b$ and $c$; these variables form the *kernel functions*, (Leech and Tabarrok [15] and Leech [16]). The solutions to the first three equations are not unique and the constants of integration may be set arbitrarily. A solution for these equations subjected to $a(0)=b(0)=c(0)=0$ is presented.

The kernel functions $a$, $b$, and $c$ generate the solution for the *primary system functions* $d(x)$ and $e(x)$. The latter, determined from the last two differential equations are solved for the initial conditions $d(0)=\alpha_2$ and $e(0)=\alpha_1$ where $\alpha_1$ and $\alpha_2$ are constants associated with the initial momenta $P$ and $R$. Finally the *secondary system function* $f(x)$ is determined by quadrature from the last equation subject to the initial condition $f(0)=0$.

One solution for the kernel functions is

$$a=\frac{j}{2}\sqrt{FEI}=\frac{EI}{2}\omega,\quad b=c=0\ \text{ where }\ j=\sqrt{-1}.$$

The loading, $q(x)$ is known "a priori" and from this the following functions are defined as follows:

$$Q(x)=\int_0^x q(s)ds$$

and

$$E(x)=\int_0^x e^{\omega s}Q(s)ds$$

where $\omega=2a/EI=j\sqrt{F/EI}$ and $s$ is a dummy integration variable.

Then from Eqs. (32) and (33) it follows that

$$e(x)=-\int_0^x q(s)ds=\alpha_1-O(x) \tag{35}$$

and

$$d(x)=\alpha_2e^{-\omega x}-\frac{\alpha_1}{\omega}(1-e^{-\omega x})+e^{-\omega x}E(x) \tag{36}$$

where $\alpha_1$ and $\alpha_2$ the previously defined constants of integration are associated with the initial momenta. Finally the secondary system function can now be determined from Eq. (29) as

$$f(x)=-\frac{1}{2EI}\int_0^x d^2ds$$
$$=-\frac{1}{2EI}\int_0^x e^{-2\omega s}\left[\alpha_2-\frac{\alpha_1}{\omega}(e^{\omega s}-1)+E(s)\right]^2ds.$$

Since the constants $\alpha_1$ and $\alpha_2$ are ignorable ([1,2]), there are constants of motion $\beta_i$ given as follows:

$$\beta_i=\frac{\partial S_2}{\partial \alpha_i}\quad i=1,2 \tag{37a}$$

where $\beta_1$ may be associated with the initial displacement $Y$ and $\beta_2$ with the initial slope $Y_x$.

Using the assumed form for $S_2$, then

$$\beta_i=\frac{\partial d(x)}{\partial \alpha_i}y_x+\frac{\partial e(x)}{\partial \alpha_i}y+\frac{\partial f(x)}{\partial \alpha_i}\quad i=1,2 \tag{37b}$$

since $a(x)$, $b(x)$, and $c(x)$ do not depend on $\alpha_i$. To facilitate the evaluation of the constants of motion $\beta_i$, the following derivatives of $f(x)$ are established:

$$\frac{\partial f}{\partial \alpha_1}=\frac{1}{EI\omega}\int_0^x e^{-\omega s}E(s)(1-e^{-\omega s})ds+\frac{\alpha_2[1-e^{-\omega x}]^2}{2EI\omega^2}$$
$$-\frac{\alpha_1[1+2\omega x-(2-e^{-\omega x})^2]}{2EI\omega^3}$$

and

$$\frac{\partial f}{\partial \alpha_2}=-\frac{1}{EI}\int_0^x e^{-2\omega s}E(s)ds-\frac{\alpha_2[1-e^{-2\omega x}]}{2EI\omega}+\frac{\alpha_1[1-e^{-\omega x}]^2}{2EI\omega^2}.$$

Introducing the following integrals $F(x)=\int_0^x e^{-\omega s}E(s)ds$ and $G(x)=\int_0^x e^{-2\omega s}E(s)ds$ into the above equations yields

$$\frac{\partial f}{\partial \alpha_1}=\frac{F(x)-G(x)}{EI\omega}+\frac{\alpha_2[1-e^{-\omega x}]^2}{2EI\omega^2}$$
$$-\frac{\alpha_1[1+2\omega x-(2-e^{-\omega x})^2]}{2EI\omega^3}$$

and

$$\frac{\partial f}{\partial \alpha_2} = -\frac{G(x)}{EI} - \frac{\alpha_2[1-e^{-2\omega x}]}{2EI\omega} + \frac{\alpha_1[1-e^{-\omega x}]^2}{2EI\omega^2}. \tag{38}$$

The constants of motion thus become, by substituting the partial derivatives equations above into the two equations (36b),

$$\beta_1 = y - \frac{(1-e^{-\omega x})}{\omega} y_x + \frac{F(x)-G(x)}{EI\omega} + \frac{\alpha_2}{2EI\omega^2}(1-e^{-\omega x})^2 - \frac{\alpha_1}{2EI\omega^3}(2\omega x + 1 - [2-e^{-\omega x}]^2) \tag{39a}$$

and

$$\beta_2 = e^{-\omega x} y_x - \frac{G(x)}{EI} - \frac{\alpha_2}{2EI\omega}(1-e^{-2\omega x}) + \frac{\alpha_1}{2EI\omega^2}(1-e^{-\omega x})^2. \tag{39b}$$

These two equations can be solved for $y$, first by solving for $y_x$ in the second equation above (38$b$), in terms of $\beta_2$

$$y_x = \beta_2 e^{\omega x} + \frac{G(x)e^{\omega x}}{EI} + e^{\omega x}\frac{\alpha_2}{2EI\omega}(1-e^{-2\omega x}) - e^{\omega x}\frac{\alpha_1}{2EI\omega^2}(1-e^{-\omega x})^2$$

and then substituting in the above (38$a$) for $y_x$; this yields

$$y = \beta_1 + \frac{(1-e^{-\omega x})}{\omega}\left(\beta_2 e^{\omega x} + \frac{G(x)e^{\omega x}}{EI} + e^{\omega x}\frac{\alpha_2}{2EI\omega}(1-e^{-2\omega x}) - e^{\omega x}\frac{\alpha_1}{2EI\omega^2}(1-e^{-\omega x})^2\right) - \frac{F(x)-G(x)}{EI\omega} - \frac{\alpha_2}{2EI\omega^2} \times (1-e^{-\omega x})^2 + \frac{\alpha_1}{2EI\omega^3}(2\omega x + 1 - [2-e^{-\omega x}]^2)$$

which can be simplified using conventional beam functions to

$$y = \beta_1 + \frac{(e^{\omega x}-1)}{\omega}\beta_2 - \frac{F(x)-G(x)e^{\omega x}}{EI\omega} + \frac{\alpha_2}{EI\omega^2}(\cosh \omega x - 1) + \frac{\alpha_1}{EI\omega^3}(\omega x - \sinh \omega x). \tag{40}$$

For the specific beam configuration, built in at $x=0$, where the boundary conditions become $y=y_x=0$, then both $\beta_1$ and $\beta_2$ are zero and the solution for $y(x)$ is

$$y = -\frac{F(x)-G(x)e^{\omega x}}{EI\omega} + \frac{\alpha_2}{EI\omega^2}(\cosh \omega x - 1) + \frac{\alpha_1}{EI\omega^3}(\omega x - \sinh \omega x). \tag{41a}$$

Also from the second equation above the solution for

$$y_x = \frac{G(x)e^{\omega x}}{EI} + \frac{\alpha_2}{EI\omega}\sinh \omega x - e^{\omega x}\frac{\alpha_1}{2EI\omega^2}(1-e^{-\omega x})^2 = \frac{G(x)e^{\omega x}}{EI} + \frac{\alpha_2}{EI\omega}\sinh \omega x - \frac{\alpha_1}{EI\omega^2}(\cosh \omega x - 1) \tag{41b}$$

is the differential of the above equation for $y(x)$ even though it was generated as an independent generalized coordinate as the second part of Eq. (36$b$).

## 7 Concluding Comments

In the foregoing the variational formulations associated with Newton's second-order equations of motion have been generalized to encompass problems governed by fourth-order ordinary differential equations. This new formulation is applied, as an example in the analysis of Euler-Bernoulli beams. The mathematical structure of the Hamiltonian theory remains intact and its further extension to functionals depending on, say, third-order derivatives, becomes largely self-evident.

The canonical equations associated with functionals with second-order derivatives emerge as four first-order equations in each variable. The transformations of these equations to a new system wherein the generalized variables and momenta appear as constants, can be obtained through several different forms of generating functions. The generating functions are obtained as solutions of the Hamilton-Jacobi equation. This theory is illustrated by application to an example from beam theory the solution recovered using a technique for solving nonseparable forms of the Hamilton-Jacobi equation.

Finally it is considered important to emphasize that in this paper, classical variational mechanics that uses time as the primary independent variable is extended to include static mechanics problems in which the primary independent variable is spatial.

## References


[1] Lanczos, C., 1966, *Variational Principles of Mechanics*, 3rd Ed., University of Toronto Press, Toronto, pp. 229–243.
[2] Goldstein, H., 1980, *Classical Mechanics*, 2nd Ed., Addison-Wesley, Reading, MA, pp. 438–457.
[3] Whittaker, E. T., 1964, *Analytical Dynamics of Particles and Rigid Bodies*, Cambridge University Press, Cambridge, UK.
[4] Pars, L. A., 1965, *A Treatise on Analytical Dynamics*, Heinemann Educational Books, London, pp. 268–286.
[5] Synge, J. L., 1960, *Classical Dynamics in Encyclopedia of Physics, 3/1*, S. Flügge, ed., Springer, Berlin, pp. 125–130.
[6] Logan, J. D., 1977, *Invariant Variational Principles*, Academic Press, San Diego, CA, pp. 56–58.
[7] Rund, H., 1961, "The Theory of Problems in the Calculus of Variations Whose Lagrangian Function Involves Second-Order Derivatives: A New Approach," Ann. Mat. Pure. Appl., **55**, pp. 77–104.
[8] Rund, H., 1966, *The Hamilton-Jacobi Theory in the Calculus of Variations*, Van Nostrand, New York.
[9] Rodrigues, P. R., 1976, "Géométrie Différentielle—Sur les Systèmes Méchaniques Généralisés," C.R. Seances Acad. Sci., Ser. A, **282**, pp. 1307–1309.
[10] Tabarrok, B., and Rimrott, F. P. J., 1994, *Variational Methods and Complementary Formulations in Dynamics*, Kluwer, Dordrecht, The Netherlands.
[11] Denman, H. H., and Buch, L. H., 1973, "Solution of the Hamilton-Jacobi Equation for Certain Dissipative Mechanical Systems," J. Math. Phys., **14**(3), pp 326–329.
[12] Saletan, E. J., and Cromer, A. H., 1971, *Theoretical Mechanics*, John Wiley and Sons, New York, pp. 225–258.
[13] Benton S. H., Jr., 1977, *The Hamilton-Jacobi Equation: A Global Approach* (Mathematics in Science and Engineering, Vol. 131), Academic Press, San Diego, CA, pp 8–13.
[14] Sanz-Serna, J. M., and Calvo, M. P., 1994, *Numerical Hamiltonian Problems* (Applied Mathematics and Mathematical Computation 7), Chapman and Hall, London, pp. 129–153.
[15] Leech, C. M., and Tabarrok, B., 1997, "Nonseparable Solutions to the Hamilton-Jacobi Equation," ASME J. Appl. Mech., **64**, pp. 636–641.
[16] Leech, C. M., 1997, "The Hamilton-Jacobi Equation applied to Continuum," ASME J. Appl. Mech., **64**, pp. 658–663.

C. Garion[1]
B. Skoczen[2]
CERN, European Organization
for Nuclear Research,
LHC Division,
CH-1211 Geneva 23,
Switzerland

# Modeling of Plastic Strain-Induced Martensitic Transformation for Cryogenic Applications

*A simplified model of martensitic transformation in stainless steels at cryogenic temperatures is proposed. The constitutive modeling of plastic flow under cryogenic conditions is based on the assumption of small strains (≤0.2). The hardening law for the biphase material ($\alpha'$ martensite platelets embedded in the $\gamma$ austenite matrix) has been obtained from the Mori-Tanaka homogenization. A mixed hardening with combined isotropic and kinematic contributions is proposed. The constitutive model, containing a reasonable number of parameters, has been numerically implemented and checked with respect to experimental data. Finally, the model is applied to compute the martensite evolution in thin-walled corrugated shells designed for cryogenic temperatures (mechanical compensation system of the Large Hadron Collider at CERN).* [DOI: 10.1115/1.1509485]

## 1 Introduction

Fe-Cr-Ni stainless steels are commonly used to manufacture components of superconducting magnets and cryogenic transfer lines since they retain their ductility at low temperatures and are paramagnetic. The nitrogen strengthened stainless steels of series 300 belong to the group of metastable austenitic alloys. Under certain conditions the steels undergo martensitic transformation at cryogenic temperatures that lead to a considerable evolution of material properties and to a ferromagnetic behavior. The martensitic transformations are induced mainly by plastic strain fields and amplified by high magnetic fields. Spontaneous transformations due to the cooling process—identified with respect to some alloys—are not observed in the most often used grades 304L, 304LN, 316L, and 316LN. The series 300 stainless steels show at room temperature a classical $\gamma$-phase of face centered cubic austenite (FCC). This phase may transform either to $\alpha'$ phase of body centered tetragonal ferrite (BCT) or to a hexagonal $\varepsilon$-phase. The most often occurring $\gamma$-$\alpha'$ transformation leads to formation of martensite sites dispersed in the surrounding austenite matrix. In the course of the strain induced transformation the martensite platelets modify the FCC lattice leading to local distortions. The amount of martensite depends on the chemical composition, temperature, stress state, plastic strains, and exposure to a magnetic field. It is well known that the solutes like Ni, Mn, and N considerably stabilize the $\gamma$-phase. For instance, the strain-induced martensitic content in the grades 304LN, 316LN at low temperatures is much lower than in the grades 304L, 316L for the same level of plastic strain ([1]).

The increase in martensite fraction promoted by plastic deformation can be detected by measuring the magnetic permeability $\mu$. The evolution of $\mu$ at low temperature corresponding to monotonic straining as well as to the cyclic loads for 304L and 316L stainless steels was investigated by Suzuki et al. [2]. Tensile properties of stainless steels at low temperatures are strongly influenced by the plastic strain-induced martensitic transformation. As a result of the transformation the initially homogenous $\gamma$-phase loses its homogeneity because of the inclusions of the harder martensite phase. The martensite platelets embedded in the soft austenite matrix provoke local stress concentration and block the movement of dislocations. Therefore the onset of martensitic transformation leads to an increase in strain hardening. Results showing the increase of $\alpha'$ martensite with strain for 304L and 304LN stainless steel at 77 K have been reported by Morris et al. [1]. Similar studies for 304L and 316L stainless steels at 77 K and at 4 K were carried out by Suzuki et al. [2].

Transformation kinetics has been developed by Olson and Cohen [3]. The authors attribute the strain-induced martensite nucleation sites to the shear-band intersections (the shear bands being in the form of $\varepsilon'$ martensite, mechanical twins or stacking-fault bundles). The analysis leads to the following equation for the volume fraction of martensite versus plastic strain:

$$\xi_{\alpha'} = 1 - \exp\{-\beta[1-\exp(-\alpha\varepsilon^p)]^n\} \tag{1}$$

where $\alpha$ represents the rate of shear band formation, $\beta$ represents the probability that a shear-band intersection will become a martensite site, and $n$ is a fixed exponent. The transformation curves (volume fraction of martensite versus plastic strain) show a typical sigmoidal shape with saturation levels below 100 percent (Fig. 1).

Constitutive modeling of steels exhibiting strain-induced martensitic transformation was initiated by Narutani, Olson, and Cohen [4]. The approach was based on the Voigt model with equal repartition of strains in both phases of the two-phase composite. A more complex constitutive model has been developed by Stringfellow, Parks, and Olson [5]. Here an isotropic hypoelastic formulation based on large strains was used. The inelastic stretching was decomposed into two parts: slip in the austenite and martensite phases and the nucleation component resulting from the transformation process. Local and global stress and strain components were linked by using the Eshelby solutions for incompressible spherical inclusions in an infinite, incompressible isotropic matrix. The model was successfully validated on the Angel [6] set of data. The next complex constitutive modeling has been developed by Levitas, Idesman, and Olson [7]. The phase transformation model is based on the mesoscopic continuum thermodynamics. Generalization of the Prandtl-Reuss equations with isotropic hardening to the case of large strains for elastoplastic isotropic materials was

[1]On leave from LaRama, Blaise Pascal University, Clermont-Ferrand, France.
[2]On leave from Cracow University of Technology, Cracow, Poland.

Contributed by the Applied Mechanics Division of THE AMERICAN SOCIETY OF MECHANICAL ENGINEERS for publication in the ASME JOURNAL OF APPLIED MECHANICS. Manuscript received by the Applied Mechanics Division, June 19, 2001; final revision, Apr. 3, 2002. Associate Editor: M.-J. Pindera. Discussion on the paper should be addressed to the Editor, Prof. Robert M. McMeeking, Chair, Department of Mechanics and Environmental Engineering, University of California–Santa Barbara, Santa Barbara, CA 93106-5070, and will be accepted until four months after final publication in the paper itself in the ASME JOURNAL OF APPLIED MECHANICS.

  

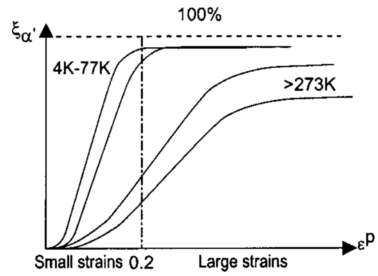


**Fig. 1 Volume fraction of martensite versus plastic strain at cryogenic temperatures**

used. The deformation gradient was decomposed into three parts: elastic, plastic, and the transformation one. Elastic strains were assumed small when compared to inelastic strains. A difference between phase transformation under displacement and stress controlled boundary conditions was demonstrated. Some further recent constitutive modeling of TRIP steels for the temperature above 77 K can be found in ([8–11]).

The constitutive modeling mentioned above was based on the assumption of large inelastic strains. However, if the strain-induced transformation occurs at very low temperatures (liquid nitrogen 77 K, liquid helium 4.5 K) then the steep part of the transformation curves (see Fig. 1) remains in the domain of relatively small strains (below 0.2). In such a case, constitutive modeling can be considerably simplified and remains within the scope of the classical theories of plasticity. The relevant elastoplastic model with linear mixed (isotropic/kinematic) hardening including the effect of strain-induced martensitic transformation is developed in the present paper.

## 2 Transformation Kinetics

Olson and Cohen [3] developed a one-dimensional model for the kinetics of martensitic transformation, called the OC model. The evolution of the volume fraction of martensite as a function of plastic strain is derived by considering shear band formation, probability of shear-band intersections and probability of an intersection generating a martensitic embryo. In this model, only temperature and plastic strain control martensite evolution. Different improvements have been brought to this model, covering the influence of stress state ([5]) and strain rate ([7]). However, a considerable number of parameters has to be identified for these models.

In the present paper, a simplified model will be developed for cryogenic applications. Generally, the volume fraction of martensite $\xi$ can be presented in the following form:

$$\xi=\xi(p,T,\dot{\boldsymbol{\varepsilon}}^p,\boldsymbol{\sigma}) \tag{2}$$

where $p$ is the accumulated plastic strain defined by

$$p=\int_0^t\sqrt{\frac{2}{3}\dot{\boldsymbol{\varepsilon}}^p:\dot{\boldsymbol{\varepsilon}}^p}d\tau \tag{3}$$

with $\dot{\boldsymbol{\varepsilon}}^p$ the plastic strain rate and $\boldsymbol{\sigma}$ the stress tensor.

Under isothermal conditions and for a given strain rate, the classical sigmoidal curve is shown in Fig. 2.

The curve may be decomposed into three regions:

- region I that corresponds to a nonlinear increase of the martensitic content with strain (primary phase),
- region II where the $\alpha'$ volume fraction ($\xi$) is linearly related to plastic deformation ($\varepsilon^p$) ([12]) (secondary phase), and
- region III that corresponds to a saturation effect (tertiary phase).

A simplified evolution law for the martensite content may be proposed for region II as follows:

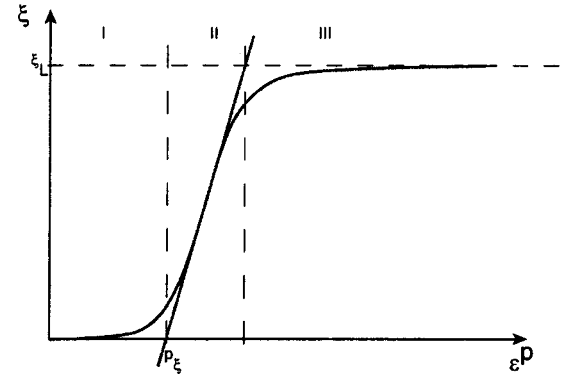


**Fig. 2 Volume fraction of martensite $\xi$ versus plastic strain $\varepsilon^p$**

$$\dot{\xi}=A(T,\boldsymbol{\sigma},\dot{\boldsymbol{\varepsilon}}^p)\dot{p}H((p-p_\xi)(\xi_L-\xi)) \tag{4}$$

where

- $A$ is a function of temperature, stress state, and strain rate,
- $p_\xi$ is the accumulated plastic strain threshold (to trigger the formation of martensite),
- $\xi_L$ is the martensite content limit, over which the martensitic transformation rate is considered equal to 0. $H$ represents the Heavyside function.

The three regions shown above are thus simplified in the following way:

- region I: no martensitic transformation until $p_\xi$ is reached.
- region II: the volume fraction of martensite ($\xi$) is linearly related to accumulated plastic strain ($p$) until $\xi_L$ is reached.
- region III: no martensitic transformation above $\xi_L$.

Stringfellow and et al. [5] show that the stress state dependence is best represented by the triaxiality $\Sigma$, defined as the ratio of the hydrostatic stress and the equivalent stress.

$$\Sigma=\frac{1}{3}\frac{\mathrm{tr}[\boldsymbol{\sigma}]}{\sigma_e} \tag{5}$$

with $\sigma_e=\sqrt{3/2\mathbf{s}:\mathbf{s}}$, where $\mathbf{s}$ is the deviatoric stress

$$\mathbf{s}=\boldsymbol{\sigma}-\frac{1}{3}\mathrm{tr}[\boldsymbol{\sigma}]\mathbf{I} \tag{6}$$

and $\mathbf{I}$ is the identity tensor.

## 3 Constitutive Modeling of Plastic Flow at Cryogenic Temperatures

The present section aims at developing a mesoscopic model, capable of representing the hardening work and the evolution of martensite content for the material under different types of loads (monotonic or cyclic). The model is sufficiently simple to be easily integrated into a finite element code.

The constitutive model is based on a classical approach to the plastic flow, that is on linear mixed hardening. Since the material (stainless steel), containing a limited amount of martensite, can be described as a ductile austenitic matrix ($\gamma$-phase) containing rigid inclusions ($\alpha'$-phase), dispersed in the whole volume of the RVE (representative volume element), it is obvious that the material retains its ductility also at cryogenic temperatures. As long as the plastic flow mechanism is based mainly on the motion of dislocations (no serrated yielding), classical models can be applied.

**3.1 Constitutive Formulation.** Generally, the model is based on the following assumptions:

1. The rate of increase of the volume fraction of the martensitic phase, $\dot{\xi}$, is given by

$$\dot{\xi}=A(T,\Sigma,\dot{\boldsymbol{\varepsilon}}^p)\dot{p}H((p-p_\xi)(\xi_L-\xi)). \tag{7}$$

2. Small strains are considered (linear additive rule). The total strain is given by

$$\boldsymbol{\varepsilon}=\boldsymbol{\varepsilon}^e+\boldsymbol{\varepsilon}^p+\boldsymbol{\varepsilon}^{th}+\xi\boldsymbol{\varepsilon}^{bs} \tag{8}$$

where $\boldsymbol{\varepsilon}^e$ denotes elastic strain, and $\boldsymbol{\varepsilon}^p$ and $\boldsymbol{\varepsilon}^{th}$ stand for plastic and thermal strain tensors, respectively. $\boldsymbol{\varepsilon}^{bs}$ is free deformation called bain strain. It can be expressed in terms of relative volume change $\Delta v$, due to the phase transformation, as

$$\boldsymbol{\varepsilon}^{bs}=\frac{1}{3}\Delta v\mathbf{I} \tag{9}$$

with

$$\Delta v=\frac{V_m-V_a}{V_a} \tag{10}$$

where $V_a$ and $V_m$ represent the unstressed specific volumes occupied by the austenite and the martensite, respectively. The value of $\Delta v$ is about 0.02–0.05, depending on the alloy composition ([13]).

The expression for the thermal strain is given as a function of the dilatation tensor of the biphase material $\boldsymbol{\alpha}$, by the general formula

$$d\boldsymbol{\varepsilon}^{th}=\boldsymbol{\alpha}(T,\xi)dT. \tag{11}$$

Considering both phases isotropic and under the assumption of global isotropy of the material, the tensor $\boldsymbol{\alpha}$ can be reduced to

$$\boldsymbol{\alpha}=\alpha^h\mathbf{I} \tag{12}$$

with $\alpha^h$ the homogenized dilatation coefficient.

3. The constitutive law is given by

$$\boldsymbol{\sigma}=\boldsymbol{E}:(\boldsymbol{\varepsilon}-\boldsymbol{\varepsilon}^p-\boldsymbol{\varepsilon}^{th}-\xi\boldsymbol{\varepsilon}^{bs}). \tag{13}$$

For isotropic material, the elastic stiffness tensor $\boldsymbol{E}$ is expressed in the form:

$$\boldsymbol{E}=3k\boldsymbol{J}+2\mu\boldsymbol{K} \tag{14}$$

with

$$\begin{cases} J_{ijkl}=\frac{1}{3}\delta_{ij}\delta_{kl} \\ \boldsymbol{K}=\boldsymbol{I}-\boldsymbol{J} \quad \text{and} \quad I_{ijkl}=\frac{1}{2}(\delta_{ik}\delta_{jl}+\delta_{il}\delta_{jk}) \end{cases} \tag{15}$$

and where $\mu=E/2(1+v)$, $k=E/3(1-2v)$ are shear and bulk moduli, respectively. To simplify the equations, we assume that the elastic properties of the biphase material are not modified by the martensitic transformation (the elastic properties of the martensite and of the austenite are quite similar). Nevertheless, the elastic properties of the austenite +martensite structure, i.e., the elastic coefficients, can be obtained by homogenization.

4. The yield surface is defined as

$$f_c(\boldsymbol{\sigma},\mathbf{X},R)=J_2(\boldsymbol{\sigma}-\mathbf{X})-\sigma_y-R=0 \tag{16}$$

where

$$J_2(\boldsymbol{\sigma}-\mathbf{X})=\sqrt{\frac{3}{2}(\mathbf{s}-\mathbf{X}):(\mathbf{s}-\mathbf{X})} \tag{17}$$

is the second invariant of the stress tensor. $\mathbf{X}$ is the back stress tensor and $\sigma_y$, $R$ stand for the yield point and the isotropic hardening parameter, respectively.

5. It is assumed that the material obeys the normality rule with the yield function postulated as the plastic potential. The plastic flow rate is given by

$$d\boldsymbol{\varepsilon}^p=\frac{3}{2}\frac{\mathbf{s}-\mathbf{X}}{J_2(\boldsymbol{\sigma}-\mathbf{X})}d\lambda \tag{18}$$

where $\lambda$ is the plastic multiplier. Furthermore, it is assumed that the yield surface of the biphase material is smooth and convex. This assumption is justified by the fact that the martensite inclusions are considered elastic and the austenitic matrix is elastoplastic with a smooth and convex form of the yield surface. Neither instabilities of Drucker type nor the serrated yielding (discontinuous in terms of $d\sigma/d\varepsilon$) are considered in the constitutive model. Thus, a combination of elastoplastic matrix with elastic inclusions (biphase composite) preserves convexity and regularity of the yield surface.

6. The hardening variables $R$ and $\mathbf{X}$ are altered by the presence of martensite and the corresponding evolution laws are postulated in the following general form:

$$dR=F(\xi)dp \tag{19}$$

$$d\mathbf{X}=d\mathbf{X}_a+d\mathbf{X}_{a+m}=\frac{2}{3}Cd\boldsymbol{\varepsilon}^p+G(\xi)d\boldsymbol{\varepsilon}^p. \tag{20}$$

Here, we assume that the back stress increment is the sum of a classical term which corresponds to the behavior of the austenitic phase $d\mathbf{X}_a$ and a new term related to the presence of martensite in the austenitic matrix $(d\mathbf{X}_{a+m})$.

**3.2 Hardening Law for the Biphase Material.** The BCC martensite is much harder than the FCC austenite. The martensite platelets do not have the same orientation as the initial lattice. If the movement of the dislocations occurs (plastic flow) then the dislocations are mobile in the austenitic matrix and are supposed to be stopped by the martensite inclusions. Thus, an elastoplastic matrix and elastic inclusions are the principal components that constitute the biphase material model.

A simple linear kinematic hardening law may be used to model the plastic behavior of the pure austenite phase:

$$d\mathbf{X}_{a0}=\frac{2}{3}C_0d\boldsymbol{\varepsilon}^p. \tag{21}$$

Here $C_0$ represents the hardening modulus for the austenitic phase without the presence of martensite. For the biphase material, the hardening modulus $C_0$ is replaced by the modulus $C$. The coefficient $C$ is higher than $C_0$ because of the interactions between the dislocations in the austenite and the martensite inclusions. Generally, a function $\varphi(\xi)$ is defined:

$$C=C_0\varphi(\xi) \quad \text{for } 0\leqslant\xi\leqslant\xi_L \tag{22}$$

with $\varphi(0)=1$ (see Fig. 3).

For the sake of simplicity, the function $\varphi(\xi)$ has been linearized and takes the form:

$$\varphi(\xi)=h\xi+1 \tag{23}$$

where $h$ is a parameter that depends on the material. The function $\varphi(\xi)$ represents the part of the hardening process that is related to the increase in volume fraction of martensitic inclusions and enhanced probability that a dislocation will be stopped by an inclusion. Here, the martensite platelets are regarded as infinitely rigid small objects, embedded into $\gamma$-phase, that act as the stoppers of motion of dislocations. Thus, the amount of plastic work corresponding to the same total strain considerably increases. Thus, the back stress increment can be subdivided into two components:

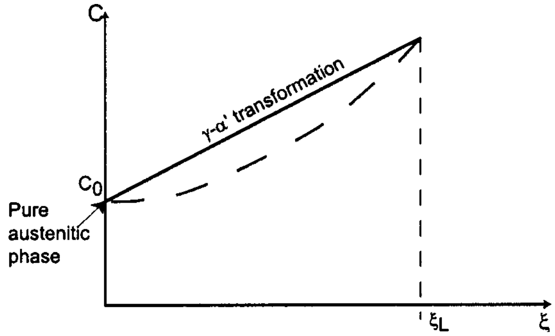


**Fig. 3 Evolution of the hardening modulus as a function of the martensite content**

$$d\mathbf{X}_a = d\mathbf{X}_{a0} + d\mathbf{X}_{a\xi} = \frac{2}{3}C_0 d\boldsymbol{\varepsilon}^p + \frac{2}{3}C_0 h\xi d\boldsymbol{\varepsilon}^p \tag{24}$$

where $d\mathbf{X}_{a\xi}$ corresponds to the interaction between the dislocations into the austenitic matrix and the martensite inclusions.

For the pure austenitic phase, a linearization of the constitutive equations of plastic flow in the vicinity of the current state leads to the following formula (provided that the process of plastic flow is active)

$$\Delta\boldsymbol{\sigma}_a = \boldsymbol{E_t}:\Delta\boldsymbol{\varepsilon} \tag{25}$$

where $\boldsymbol{E_t}$ denotes the tangent stiffness tensor.

If the same strain increment is applied to the austenite/martensite structure, the stress increment is obtained by homogenization:

$$\Delta\boldsymbol{\sigma}_{a+m} = \boldsymbol{E_H}:\Delta\boldsymbol{\varepsilon}. \tag{26}$$

The increment of hardening (for the biphase material) implied by the presence of the martensite is given by

$$\Delta\boldsymbol{\sigma} = \Delta\boldsymbol{\sigma}_{a+m} - \Delta\boldsymbol{\sigma}_a = (\boldsymbol{E_H} - \boldsymbol{E_t}):\Delta\boldsymbol{\varepsilon}. \tag{27}$$

The homogenization theory has been developed for elastic materials (matrix and inclusions) ([14]). The matrix is considered isotropic. In the domain of plastic deformation (active processes) the linearization in the vicinity of the current state allows us to apply the homogenisation technique. Thus, over one load increment the matrix ($\gamma$-phase) is represented by the corresponding tangent modulus:

$$\boldsymbol{E_{ta}} = 3k_{ta}\boldsymbol{J} + 2\mu_{ta}\boldsymbol{K} \tag{28}$$

where

$$\mu_{ta} = \frac{E_t}{2(1+v)}, \quad k_{ta} = \frac{E_t}{3(1-2v)} \quad \text{and} \quad E_t = \frac{EC}{E+C}.$$

It is assumed that the inclusions are isotropic and elastic. The corresponding modulus of elasticity is given by

$$\boldsymbol{E_m} = 3k_m\boldsymbol{J} + 2\mu_m\boldsymbol{K} \tag{29}$$

where

$$\mu_m = \frac{E}{2(1+v)} \quad \text{and} \quad k_m = \frac{E}{3(1-2v)}.$$

Furthermore, the inclusions are supposed to be spherical and uniformly distributed in the austenite matrix. The Mori Tanaka homogenization (it is assumed that the interactions between inclusions are reduced to a homogeneous strain field in the inclusion) reads ([14,15])

$$\boldsymbol{E_H} = \boldsymbol{E_{MT}} = 3k_{MT}\boldsymbol{J} + 2\mu_{MT}\boldsymbol{K} \tag{30}$$

with $\boldsymbol{E_{MT}}$ obtained from

$$[\boldsymbol{E_{MT}} + \boldsymbol{E}^*]^{-1} = \sum_{i=a,m} f_i[\boldsymbol{E_i} + \boldsymbol{E}^*]^{-1} \tag{31}$$

where $f_i$ denotes volume fraction of the constituant "$i$" and $\boldsymbol{E}^*$ stands for the Hill influence tensor.

Finally, the following equations are derived:

$$3k_{MT} + 3k^* = \left[\frac{1-\xi}{3(k_{ta}+k^*)} + \frac{\xi}{3(k_m+k^*)}\right]^{-1}$$

$$2\mu_{MT} + 2\mu^* = \left[\frac{1-\xi}{2(\mu_{ta}+\mu^*)} + \frac{\xi}{2(\mu_m+\mu^*)}\right]^{-1}, \tag{32}$$

$$k^* = \frac{4}{3}\mu_{ta} \quad \text{and} \quad 2\mu^* = \frac{\mu_{ta}(9k_{ta}+8\mu_{ta})}{3(k_{ta}+2\mu_{ta})} \tag{32}$$

In what follows, it is assumed that the strain increment is mainly due to the plastic strains: $\Delta\boldsymbol{\varepsilon} \cong \Delta\boldsymbol{\varepsilon}^p$. Thus, Eq. (27) becomes

$$\Delta\boldsymbol{\sigma} = (\boldsymbol{E_{MT}} - \boldsymbol{E_t}):\Delta\boldsymbol{\varepsilon}^p. \tag{33}$$

As the plastic strains are represented by a deviatoric tensor (the trace is equal to 0) then

$$\boldsymbol{J}:\Delta\boldsymbol{\varepsilon}^p = \boldsymbol{0} \quad \text{and} \quad \boldsymbol{K}:\Delta\boldsymbol{\varepsilon}^p = \Delta\boldsymbol{\varepsilon}^p.$$

Finally, the hardening due to martensite formation becomes

$$\Delta\boldsymbol{\sigma} = 2(\mu_{MT} - \mu_{ta})\Delta\boldsymbol{\varepsilon}^p. \tag{34}$$

In order to obtain a sound response under cyclic loads, hardening has to be expressed in terms of plastic variables: $R$ is the isotropic hardening parameter and $\mathbf{X}$ is the kinematic hardening (back stress).

If pure kinematic hardening is considered, the increment of the back stress due to the mixture of martensite and austenite fraction (biphase material) is obtained by

$$\Delta\mathbf{X}_{a+m} = \Delta\boldsymbol{\sigma} \tag{35}$$

which leads to the equation

$$d\mathbf{X}_{a+m} = 2(\mu_{MT} - \mu_{ta})d\boldsymbol{\varepsilon}^p. \tag{36}$$

If pure isotropic hardening is considered, the increment of the hardening parameter is obtained by the second invariant of the stress tensor:

$$\Delta R = \Delta R_{a+m} = J_2(\Delta\boldsymbol{\sigma}) = 3(\mu_{MT} - \mu_{ta})\Delta p \tag{37}$$

with

$$\Delta p = \sqrt{\frac{2}{3}\Delta\boldsymbol{\varepsilon}^p:\Delta\boldsymbol{\varepsilon}^p}.$$

Hence, one obtains

$$dR = dR_{a+m} = 3(\mu_{MT} - \mu_{ta})dp. \tag{38}$$

This formulation is valid exclusively for a small martensite content (at the beginning of the strain-induced transformation). Since the region II at cryogenic temperatures corresponds approximately to $\varepsilon^p \leqslant 0.2$ and the saturation level of the martensite content is reached, a more general formulation of isotropic hardening has to be applied. The generalization leads to the following model:

$$dR = (R_\infty(\xi) - R)dp. \tag{39}$$

This approach is compatible with the model of isotropic hardening with a saturation level $R_\infty$ included, as proposed by Chaboche [16]. The linearization of Eq. (39) in the vicinity of the initial state leads back to Eq. (38). The contributions from kinematic and isotropic hardening are controlled by the Baushinger parameter $\beta$ defined by $0 \leqslant \beta \leqslant 1$.

Therefore, for mixed hardening, the following model is postulated:

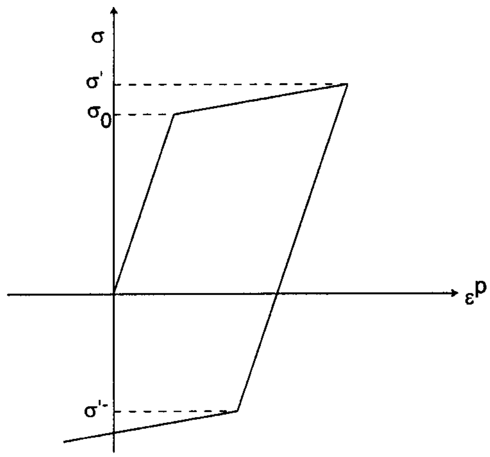


**Fig. 4 Illustration of the unloading and the reverse loading processes**

$$d\mathbf{X}=2b(\xi)\beta(\mu_{MT}-\mu_{ta})d\boldsymbol{\varepsilon}^p \tag{40}$$

$$dR=b(\xi)(1-\beta)(R_\infty(\xi)-R)dp. \tag{41}$$

Or in expanded form

$$d\mathbf{X}=2\beta(1-\xi)(\mu_{MT}-\mu_{ta})d\boldsymbol{\varepsilon}^p \tag{42}$$

$$dR=(1-\xi)(1-\beta)(3(\mu_{MT}-\mu_{ta})-R)dp. \tag{43}$$

Here, the term $b(\xi)=1-\xi$ is added in order to compensate for the strong assumption that the martensite inclusions are elastic. It tends to 0 for high content of martensite. In reality, the martensite inclusions shall rather be considered elasto-plastic. Therefore their contribution to the hardening of the biphase material is slightly smaller. Also, it is assumed that when $\xi=1$ ($\gamma$ phase entirely replaced by the $\alpha'$ phase) the process of hardening linked to the phase transformation is terminated. For the sake of simplicity the relevant function $b(\xi)$ describing these effects has been linearized.

The experimental curves, obtained under kinematically controlled cycling ([2,17]) show that, for symmetric strain loading, the compressive stresses are higher than tensile. This indicates a strong Bauschinger effect that can be described in terms of the parameter introduced by Zyczkowski [18]. The parameter $\beta$ is related to the stress level at unloading ($\sigma'$) and the stress level associated with the reverse active process ($\sigma'^-$), see Fig. 4. It is defined by the following formula:

$$\beta=\frac{\sigma'+\sigma'^-}{2(\sigma'-\sigma_0)}. \tag{44}$$

It varies between 0 for the isotropic hardening (no Bauschinger effect) and 1 for the kinematic hardening (perfect Bauschinger effect). Thus, it allows to describe the ratio between isotropic and kinematic hardening. This parameter has to be determined experimentally (see Table 1).

**3.3 Final Set of the Constitutive Equations.** The final set of the constitutive equations reduces to (incremental formulation has been replaced by time derivatives):

**Table 1 Set of data for the 304L at 77 K (* obtained from Suzuki's data)**

| $E$ [GPa] | $\nu$ | $\sigma_y$ [MPa] | $C_0$ [MPa] | $h$ | $A$ | $p_\xi$ | $\xi_L$ | $\beta$* | $\Delta v$ |
|---|---|---|---|---|---|---|---|---|---|
| 190.0 | 0.3 | 580.0 | 750.0 | 1.9 | 4.23 | 0.004 | 0.9 | 0.45 | 0.05 |

- Kinetics of the martensitic transformation:

$$\dot{\xi}=A(T,\Sigma,\dot{\boldsymbol{\varepsilon}}^p)\dot{p}H((p-p_\xi)(\xi_L-\xi)) \tag{45}$$

- The constitutive law:

$$\boldsymbol{\sigma}=\boldsymbol{E}:(\boldsymbol{\varepsilon}-\boldsymbol{\varepsilon}^p-\boldsymbol{\varepsilon}^{th}-\xi\boldsymbol{\varepsilon}^{bs}) \tag{46}$$

- The yield surface:

$$f_c(\boldsymbol{\sigma},\mathbf{X},R)=\sqrt{\frac{3}{2}(\mathbf{s}-\mathbf{X}):(\mathbf{s}-\mathbf{X})}-\sigma_y-R=0 \tag{47}$$

- The normality rule:

$$\dot{\boldsymbol{\varepsilon}}^p=\frac{3}{2}\frac{\mathbf{s}-\mathbf{X}}{J_2(\boldsymbol{\sigma}-\mathbf{X})}\dot{\lambda} \tag{48}$$

- The hardening laws:

$$\begin{cases}\dot{\mathbf{X}}=\dfrac{2}{3}(C+3\beta(1-\xi)(\mu_{MT}(\xi)-\mu_{ta}))\dot{\boldsymbol{\varepsilon}}^p\\ \dot{R}=(1-\xi)(1-\beta)(3(\mu_{MT}(\xi)-\mu_{ta})-R)\dot{p}\end{cases} \tag{49}$$

## 4 Implementation of the Constitutive Model

**4.1 Numerical Versus Experimental Results.** The model has been implemented in a finite element code. The method of the type "radial return," originally proposed by Wilkins [19], is used to integrate the constitutive equations for an active plastic process. The radial return algorithm is based on the elastic-plastic split, by first integrating the elastic equations to obtain an elastic predictor, which is used as initial condition for the plastic return ([20]). The numerical algorithm can be illustrated in the following way:

- current state variables at the step $n$: $\boldsymbol{\sigma}_n$, $\boldsymbol{\varepsilon}_n^p$, $\mathbf{X}_n$, $R_n$, $\xi_n$, $p_n$.
- elastic predictor (iteration 0 for the step $n+1$) obtained from a total strain increment: $\boldsymbol{\sigma}_{n+1}^0$, $\boldsymbol{\varepsilon}_{n+1}^{p^0}=\boldsymbol{\varepsilon}_n^p$, $\mathbf{X}_{n+1}^0=\mathbf{X}_n$, $R_{n+1}^0=R_n$, $\xi_{n+1}^0=\xi_n$, $p_{n+1}^0=p_n$.
- test if the new state is elastic or not.
- if not ($f_{c_{n+1}}^0>0$), the increments $\Delta p$ and $\Delta\boldsymbol{\varepsilon}^p$ are computed.
- the increment $\Delta\xi=A\Delta p$ is calculated.
- the state variables $q=\{\boldsymbol{\sigma},\boldsymbol{\varepsilon}^p,\mathbf{X},R,\xi,p\}$ are updated from the evolution law ($q_{n+1}^{i+1}=q_{n+1}^i+\Delta q$).
- the condition $\xi_{n+1}^{i+1}\leqslant\xi_L$ is checked. If $\xi_{n+1}^{i+1}>\xi_L$, no further accumulation of martensite takes place.
- the iterative process stops for $f_{c_{n+1}}^{i+1}\leqslant 0$.

For initial validation, the model has been compared to the experimental results obtained on 304L samples tested at 77 K (cf. Morris et al. [1]) under tensile monotonic loading (Fig. 5). Identification of the material parameters is based on two curves: stress versus strain (tensile test) and volume fraction of martensite versus plastic strain. The first curve is obtained from a simple tensile test at a given temperature. Simultaneously, the magnetic permeability of the sample is measured under a predefined magnetic field. A correlation between the volume fraction of martensite ($\alpha'$ martensite is ferromagnetic) and the magnetic permeability of the sample provides the necessary information for construction of the second curve: volume fraction of martensite versus plastic strain.

The numerical simulation is terminated just after having reached the strain level 0.2 which—in this case corresponds approximately to the martensite content saturation level (end of region II). Figure 6 shows that the model is equally applicable to cyclic loads, even if the full set of experimental data allowing determination of the material parameters is not yet available. The results presented in Figs. 5 and 6 were obtained from the following set of data (Table 1).

Next, the model has been compared to the experimental data of Iwamoto et al. [21]. Figure 7 shows the comparison between the numerical and experimental results for monotonic loading of

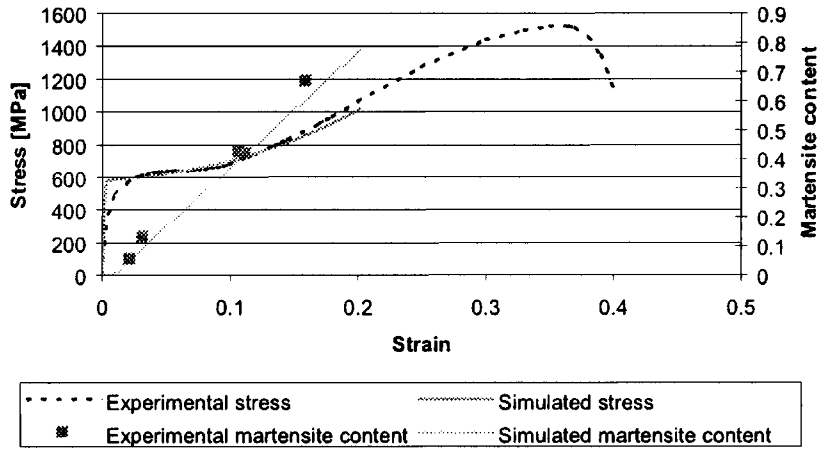


**Fig. 5** Stress and martensite content versus strain for the grade 304L stainless steel at 77 K

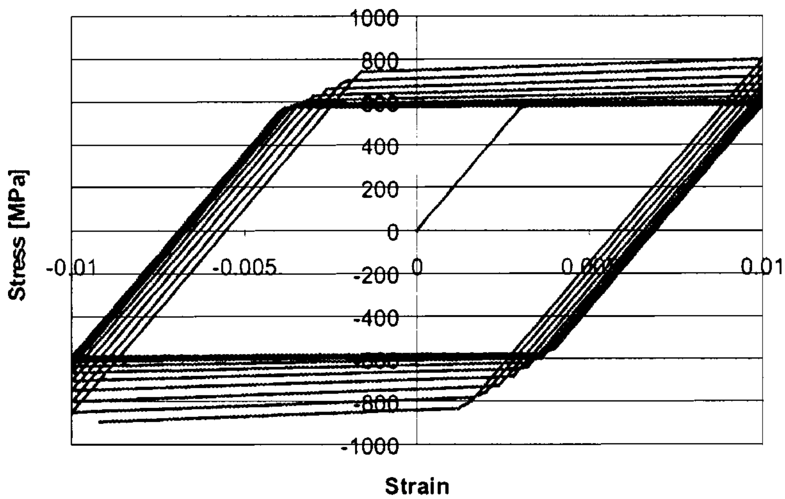


**Fig. 6** Hysteresis loops under cyclic loading

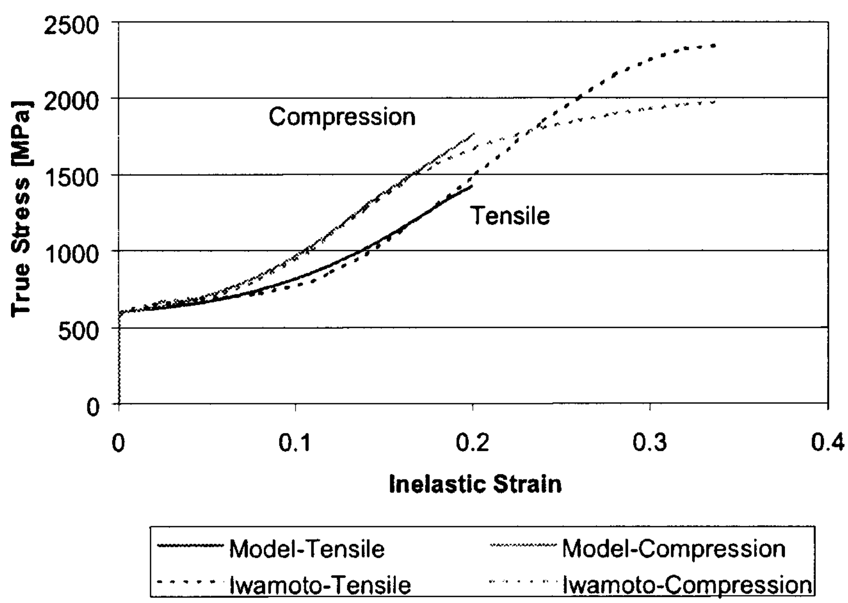


**Fig. 7** True stress as a function of the inelastic strain for grade 304 stainless steel at 128 K

**Table 2 Set of data for the stainless steel 304 at 128 K (corresponding to Iwamoto's data) (*T* stands for tension and *C* stands for compression)**

| $E$ [GPa] | $\nu$ | $\sigma_y$ [MPa] | $H$ | $\beta$ | $C_0$ [MPa] | $\Delta v$ | $\xi_L$ | $A$ | | $p_\xi(\%)$ | |
|---|---|---|---|---|---|---|---|---|---|---|---|
| | | | | | | | | $T$ | $C$ | $T$ | $C$ |
| 190.0 | 0.3 | 600 | 1.8 | 0.45 | 1200 | 0.05 | 0.97 | 6.3 | 6.3 | 2.8 | 0.5 |

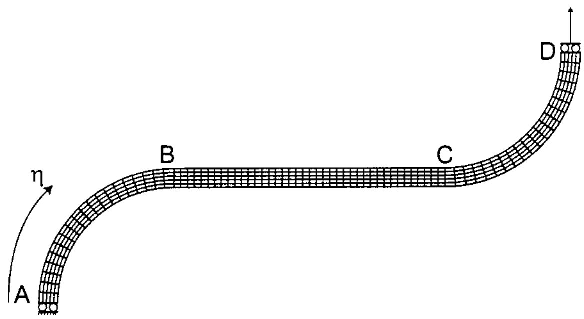


**Fig. 8 Model of half-convolution of a cryogenic bellows**

SUS304 samples, tested at 128 K. Here, inelastic strain corresponds to the plastic strain $\varepsilon^p$ and the bain strain $\xi\varepsilon^{bs}$.

The results shown in Fig. 7 were obtained from the set of data in Table 2.

In both cases (Fig. 5, Fig. 7) the numerical model shows good correlation with experimental data for total strain not exceeding 0.2.

**4.2 Application: LHC Bellows Expansion Joints.** The model has been used to determine the evolution of martensite content and its impact on the behavior of thin-walled corrugated shells (316L bellows expansion joints) used in the mechanical compensation system of the Large Hadron Collider (CERN, Geneva). These cryogenic bellows are subjected to particularly severe thermomechanical loads (cooldown/warmup between 293 K and 1.9 K and pressure loads). Analysis of evolution of martensite content in the initially austenitic structure turns out to be of particular importance for the bellows remaining in direct proximity of the beams of particles (protons, ions) or close to the extremities of the supraconducting magnets (in their stray field). Since the $\alpha'$ martensite is ferromagnetic a massive phase transformation (above 50%) may have a serious impact on the magnetization of these thin-walled components. Therefore, failure of the expansion joint is related on one hand to the state of inelastic strain in the convolutions, evolution of damage and propagation of a macro-crack. On the other hand, magnetic permeability exceed-

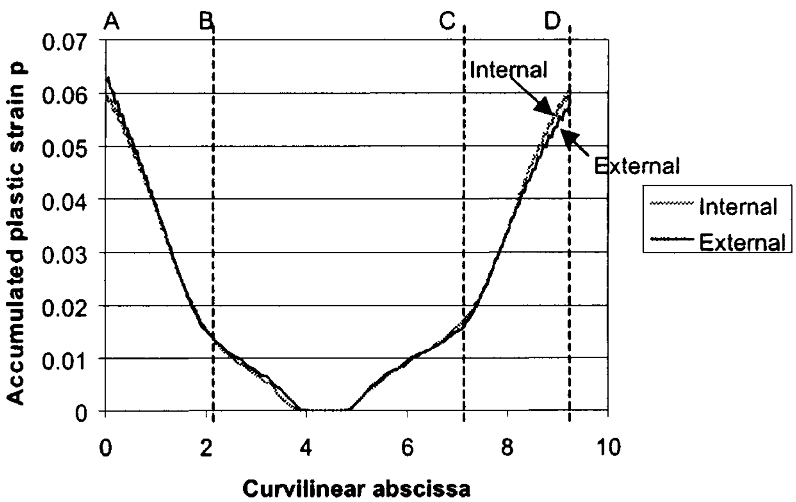


**Fig. 9 Accumulated plastic strain along the half-convolution of cryogenic bellows (at 77 K)**

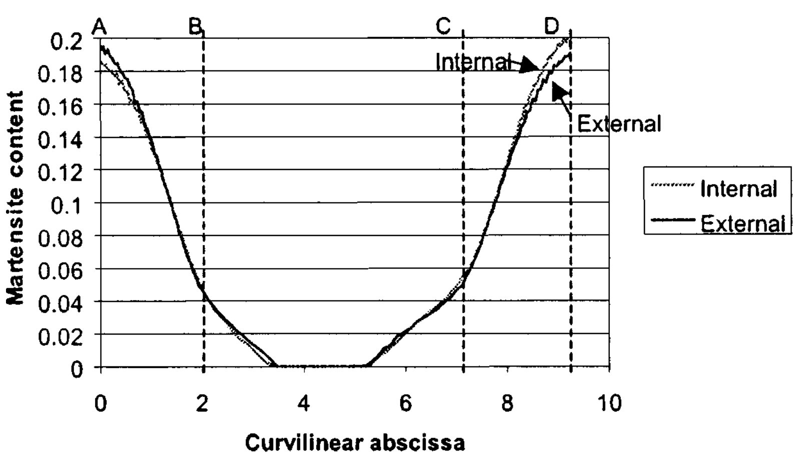


**Fig. 10 Martensite content along the half-convolution of cryogenic bellows (at 77 K)**

ing a predefined level is also classified as a magnetic failure. For this reason, a constitutive model that gives a good prediction of the evolution of volume fraction of martensite is useful in prediction of the magnetic failure of the structure.

Axisymmetric analysis of half-convolution of a typical bellows, with the corresponding boundary conditions, (Fig. 8), subjected to axial displacements at low temperatures (for instance 77 K), allows to determine the plastic strain fields and the corresponding martensite content.

The numerically computed accumulated plastic strain $p$, corresponding to an axial displacement equal to 185 percent of the bellows length, is shown as a function of the curvilinear abscissa $\eta$ in Fig. 9.

The maximum accumulated plastic strain occurs at the root and at the crest of the convolution because of particularly strong flexure in these zones. The martensite content has the same distribution as the accumulated plastic strain since the martensite evolution law (45) is linear. The numerically computed martensite content along the bellows profile, corresponding to strain induced martensitic transformation at 77 K, is shown in Fig. 10. As expected, the most intense martensitic transformation occurs at the root and at the crest of bellows convolution.

In this particular case, the volume fraction of martensite remains below 20%, far from the magnetic failure of the structure. On the other hand, impact of the phase transformation on the axial stiffness of the bellows is equal to 0.5% and is rather negligible.

## 5 Conclusions

A simplified model of the transformation kinetics, corresponding to phase II of martensitic transformation in stainless steels at cryogenic temperatures, has been proposed. The model is based on a linear relation between the rate of martensite content and the accumulated plastic strain rate.

The set of constitutive Eqs. (45) through (49), presented in Section 3.3, has the following advantages:

- The equations are based on the classical theory of plasticity with mixed kinematic/isotropic hardening.
- The approach based on small strain ($\varepsilon^p \leqslant 0.2$) turns out to be sufficient to describe region II of the martensitic transformation at cryogenic temperatures.
- The model can be implemented in any finite element code.
- The approach is uncoupled therefore the increment of volume fraction of martensite ($\Delta\xi$) for a given load step can be computed during postprocessing.
- The constitutive equations were verified using two different sources of experimental data ([1,21]) and seem to yield coherent results.
- The model is easily applicable in structural analysis developed for cryogenic conditions (superconducting accelerators, cryogenic transfer lines).
- Both kinematic and isotropic hardening are obtained from the theory of homogenisation applied to biphase material composed of the austenitic matrix ($\gamma$ phase) and the martensitic inclusions ($\alpha'$ phase).

The applicability of the presented model to cyclic loads remains to be shown. Also, further research covering the multiaxial stress states and complex paths in the strain space seems to be necessary and will certainly throw some more light on the process of strain induced martensitic transformation.


## Acknowledgments

The authors wish to express their gratitude to D. Marquis (IFMA/Clermont-Ferrand) and S. Calloch (ENS/Cachan) for many valuable discussions and suggestions which were helpful in preparing the paper.


## References


[1] Morris, J. W., Chan, J. W., and Mei, Z., 1992, "The Influence of Deformation-Induced Martensite on the Cryogenic Behavior of 300-Series Stainless Steels," Cryogenics, **32**, pp. 78–85.

[2] Suzuki, K., Fukakura, J., and Kashiwaya, H., 1988, *Cryogenic Fatigue Properties of 304L and 316L Stainless Steels Compared to Mechanical Strength and Increasing Magnetic Permeability*, American Society for Testing and Materials, pp. 190–197.

[3] Olson, G. B., and Cohen, M., 1975, "Kinetics of Strain-Induced Martensitic Nucleation," Metall. Trans. A, **6A**, Apr., pp. 791–795.

[4] Narutani, T., Olson, G. B., and Cohen, M., 1982, "Constitutive Flow Relations for Austenitic Steels During Strain-Induced Martensitic Transformation," J. de Phys., Colloque C4, Supplément au No. 12, **43**, pp. 429–434.

[5] Stringfellow, R. G., Parks, D. M., and Olson, G. B., 1992, "Constitutive Model for Transformation Plasticity Accompanying Strain-Induced Martensitic Transformations in Metastable Austenitic Steels," Acta Metall. Mater., **40(7)**, pp. 1703–1716.

[6] Angel, T., 1954, "Formation of Martensite in Austenitic Stainless Steel," J. Iron Steel Inst., **177**, pp. 165–174.

[7] Levitas, V. I., Idesman, A. V., and Olson, G. B., 1999, "Continuum Modeling of Strain-Induced Martensitic Transformation at Shear Band Intersections," Acta Mater., **47**(1), pp. 219–233.

[8] Lebedev, A. A., and Kosarchuk, V. V., 2000, "Influence of Phase Transformation on the Mechanical Properties of Austenitic Stainless Steels," Int. J. Plast., **16**, pp. 749–767.

[9] Fisher, F. D., Reisner, G., Werner, E., Tanaka, K., Cailletaud, G., and Antretter, T., 2000, "A New View on Transformation Induced Plasticity (TRIP)," Intl. J. Plasticity, **16**, pp. 723–748.

[10] Cherkaoui, M., Berveiller, M., and Lemoine, X., 2000, "Couplings Between Plasticity and Martensitic Phase Transformation: Overall Behavior of Polycrystalline TRIP Steels," Intl. J. Plasticity, **16**, pp. 1215–1241.

[11] Tomita, Y., and Iwamoto, T., 2001, "Computational Prediction of Deformation Behavior of TRIP Steels Under Cycling Loading," Int. J. Mech. Sci., **43**, pp. 2017–2034.

[12] Reed, R. P., "Martensitic phase transformations," *Material at Low Temperatures*, American Society for Metals.

[13] Tomita, Y., and Iwamoto, T., 1995, "Constitutive Modeling of TRIP Steel and Its Application to the Improvement of Mechanical Properties," Int. J. Mech. Sci., **37**(12), pp. 1295–1305.

[14] Bornert, M., Bretheau, T., and Gilormini, P., 2001, *Homogénéisation en mécanique des matériaux 1: Matériaux aléatoires élastiques et milieux périodiques*, Hermès, Paris.

[15] Mori, T., and Tanaka, K., 1973, "Average Stress in Matrix and Average Elastic Energy of Materials With Misfitting Inclusions," Acta Metall. Mater., **21**, pp. 597–629.

[16] Chaboche, J.-L., 1993, "Cyclic Viscoplastic Constitutive Equations, Part I: A Thermodynamically Consistent Formulation," ASME J. Appl. Mech., **60**, pp. 813–828.

[17] Sadough-Vanini, A., and Lehr, P., 1994, "Comportement en fatigue oligocyclique de l'acier inoxydable Z3CN18-10 à 20 et −196°C," *La revue de métallurgie-CIT/Science et Génie des matériaux*, May, pp. 781–788.

[18] Zyczkowski, M., 1981, *Combined Loadings in the Theory of Plasticity*, Scientific Publication, Warsaw.

[19] Wilkins, M. L., 1964, "Calculation of Elastic-Plastic Flow," Methods Comput. Phys., **3**, pp. 211–263.

[20] Ortiz, M., and Simo, J. C., 1986, "An Analysis of a New Class of Integration Algorithms for Elastoplastic Constitutive Equations," Int. J. Numer. Methods Eng., **23**, pp. 1353–1366.

[21] Iwamoto, T., Tsuta, T., and Tomita, Y., 1998, "Investigation on Deformation Mode Dependence of Strain-Induced Martensitic Transformation in TRIP Steels and Modeling of Transformation Kinetics," Int. J. Mech. Sci., **40**(2–3), pp. 173–182.

# Analysis of Belt-Drive Mechanics Using a Creep-Rate-Dependent Friction Law

**M. J. Leamy**
Department of Civil and Mechanical Engineering,
United States Military Academy,
West Point, NY 10996
e-mail: im8022@usma.edu

**T. M. Wasfy**
Advanced Science and Automation Corporation,
113 Derosa Drive
Hampton, VA 23666
e-mail: tamer@ascience.com

*An analysis of the frictional mechanics of a steadily rotating belt drive is carried out using a physically appropriate creep-rate-dependent friction law. Unlike in belt-drive mechanics analyzed using a Coulomb friction law, the current analysis predicts no adhesion zones in the belt-pulley contact region. Regardless of this finding, for the limiting case of a creep-rate law approaching a Coulomb law, all predicted response quantities (including the extent of belt creep on each pulley) approach those predicted by the Coulomb law analysis. Depending on a slope parameter governing the creep-rate profile, one or two sliding zones exist on each pulley, which together span the belt-pulley contact region. Closed-form expressions are obtained for the tension distribution, the sliding-zone arc magnitudes, and the frictional and normal forces per unit length exerted on the belt. A sample two-pulley belt drive is analyzed further to determine its pulley angular velocity ratio and belt-span tensions. Results from this analysis are compared to a dynamic finite element solution of the same belt drive. Excellent agreement in predicted results is found. Due to the presence of arbitrarily large system rotations and a numerically friendly friction law, the analytical solution presented herein is recommended as a convenient comparison test case for validating friction-enabled dynamic finite element schemes.*
[DOI: 10.1115/1.1488663]

## 1 Introduction

Belt drives are widely used to transmit power between machine elements. Common applications include drives transmitting power from electric motors to rotational elements in home appliances such as washing machines, vacuum cleaners, and tape drives; from gas engines to cutting elements in lawn and garden equipment such as lawnmowers, rototillers, and snow blowers; and from the crankshaft pulley to accessory pulleys in automobiles and other transportation vehicles, where the accessories include alternators, air conditioning compressors, and power-steering pumps. The life of the belt drive in all these applications depends critically on the tension magnitudes in the belt spans and the extent of belt creep on the pulley.

Even in a belt drive transmitting a constant torque between machine elements, the translating belt is subjected to cyclic tension variations as its tension transitions from a larger to a smaller tension on the driver pulley, and then from a smaller to a larger tension on each driven pulley, before returning again to the driver pulley. As a result, fatigue of the belt, and the subsequent permanent set and loss of compliance, is a large consideration in belt-drive design. Additionally, the belt is subjected to sliding wear as the belt creeps against the pulley during tension transitions. This wear can have a detrimental effect on the belt's friction characteristics as the belt surface deteriorates, and can lead to gross slip and noisy operation. These considerations motivate the need for a thorough understanding of belt-drive mechanics, and the need for belt-drive models which can accurately predict belt-span tensions and belt creep.

The earliest studies of belt-drive mechanics include Leonard Euler's study ([1]) of a belt wrapped around a fixed pulley or capstan, and Grashof's study ([2]) of the frictional mechanics of belt drives under steady operating conditions. A comprehensive review of studies on belt-drive mechanics after Grashof and up to 1981 is given by Fawcett [3]. The aforementioned studies of Euler and Grashof developed the classical creep theory of belt-drive operation. In this theory, a Coloumb law governs the belt-pulley frictional contact, and the belt is treated as a string which adheres to the pulley in an initial adhesion arc, and creeps against the pulley in a subsequent slip arc. Classical creep theory was reviewed by Johnson [4], and recently updated with new inertial effects by Bechtel et al. [5]. Other studies have considered the mechanics of the belt-drive with belt shear effects, including Firbank [6] and Gerbert [7,8]. Gerbert [7,8] also included seating/unseating and radial compliance effects in his analysis. Townsend and Salisbury [9] derived the power loss expression and the efficiency limit of a belt drive assuming the validity of the classical creep theory.

Much recent emphasis of belt-drive studies has been on the dynamic response of automotive *serpentine* belt drives to crankshaft excitation. Serpentine belt drives include an automatic tensioner which attempts to take up belt slack in the drive system. These studies have considered both the rotational response of the pulleys, and/or the transverse response of the axially moving belt, and have simplified the belt-pulley contact to linear stretching and viscous damping models. Barker [10] studied belt-drive tensions resulting from rapid engine acceleration, Hwang et al. [11] studied the periodic rotational response of the serpentine belt drive, and Beichman et al. [12–14] studied the coupled rotational and transverse response of a three-pulley prototypical serpentine belt drive. Leamy et al. [15,16] included a Coulomb dry friction damper to the tensioner arm element, and also studied the serpentine drive's rotational response. Kraver et al. [17] linearized the dry friction in the tensioner arm and developed a complex modal approach to analyze the drive's rotational response.

The two groups of studies reviewed above, namely belt-drive mechanics studies and serpentine belt-drive dynamic response studies, have had little connection to each other due to the lack of dynamic excitation in the belt-drive mechanics studies, and the lack of true frictional belt-pulley modeling in the serpentine belt-drive studies. Leamy et al. [18–20] attempted to bridge this gap

Contributed by the Applied Mechanics Division of THE AMERICAN SOCIETY OF MECHANICAL ENGINEERS for publication in the ASME JOURNAL OF APPLIED MECHANICS. Manuscript received by the Applied Mechanics Division, May 30, 2001; final revision, Sept. 25, 2001. Associate Editor: R. C. Benson. Discussion on the paper should be addressed to the Editor, Prof. Robert M. McMeeking, Chair, Department of Mechanics and Environmental Engineering, University of California–Santa Barbara, Santa Barbara, CA 93106-5070, and will be accepted until four months after final publication in the paper itself in the ASME JOURNAL OF APPLIED MECHANICS.

  

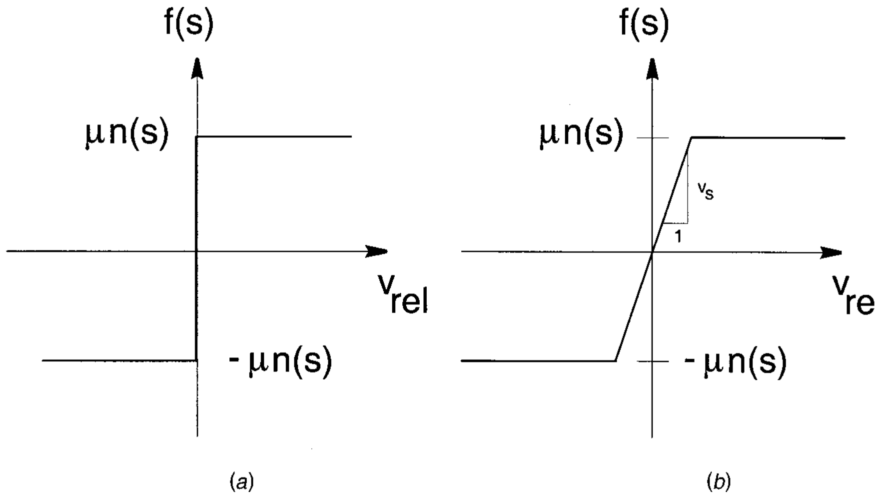


**Fig. 1 Friction laws used in the belt-drive analysis: (*a*) Coulomb law, (*b*) creep-rate-dependent law. The three linear regions of the creep-rate law are referred to as the left-most, middle, and right-most sliding regions.**

by studying simplified dynamic models for small ([18]) and large ([19,20]) rotational speeds. These studies considered individual pulleys only, and did not calculate the global response of the entire belt drive. Furthermore, the case of medium rotational speeds was not addressed.

A true modeling of the belt-pulley contact and the rotational response of a two-pulley spring-supported belt drive has recently been completed by Leamy and Wasfy [21]. In the latter study, a dynamic finite element model of the belt drive was developed using truss elements for the belt, rigid constraints for the pulleys, and a penalty formulation to model the belt-pulley contact. No restrictions on the rotational speed were made. The model is general enough to consider arbitrary excitation at the pulleys, and is capable of capturing rotational pulley and belt transverse response. A trilinear creep-rate-dependent law ([22–24]) shown in Fig. 1 and defined in Section 3, was chosen to govern the contact friction due to its physical relevance ([23]), particularly for small sliding velocities ([22]), and its numerical friendliness. By appropriate choice of a friction profile parameter $v_s$, this law can be made to approach a Coulomb friction law.

The present study considers the belt drive studied by Leamy and Wasfy [21] and analyzes its *steady* operation (constant angular velocities and constant applied torques). An exact belt-drive solution for the trilinear frictional creep-rate law is developed, and explored for several values of the friction profile parameter $v_s$. The resulting sliding regions, their tension distributions, and their locations on the pulley are discussed. Comparisons to the dynamic finite element model of [21] are made.

## 2 Review of Mechanics Resulting From a Coulomb Friction Law

Before focusing attention on the creep-rate-dependent friction law, belt-drive mechanics associated with the Coulomb friction law are reviewed first. A steadily rotating (constant applied torques and angular velocities) belt drive with belt-pulley contact governed by a Coulomb friction law develops a single *adhesion* and *slip zone* on each pulley. Together, the adhesion and slip zones span the entire belt-pulley contact region. As depicted in the example two-pulley belt-drive of Fig. 2, the uninterrupted adhesion zone begins at the point of contact of the pulley with the incoming belt span, and terminates at the beginning of the slip zone. The slip zone then extends to the point of loss of contact between the belt and the pulley. As the name suggests, the belt adheres to the pulley throughout the adhesion zone. The arguments for the existence of only a single adhesion zone and not multiple, as well as for its location at the inlet, are discussed in [4].

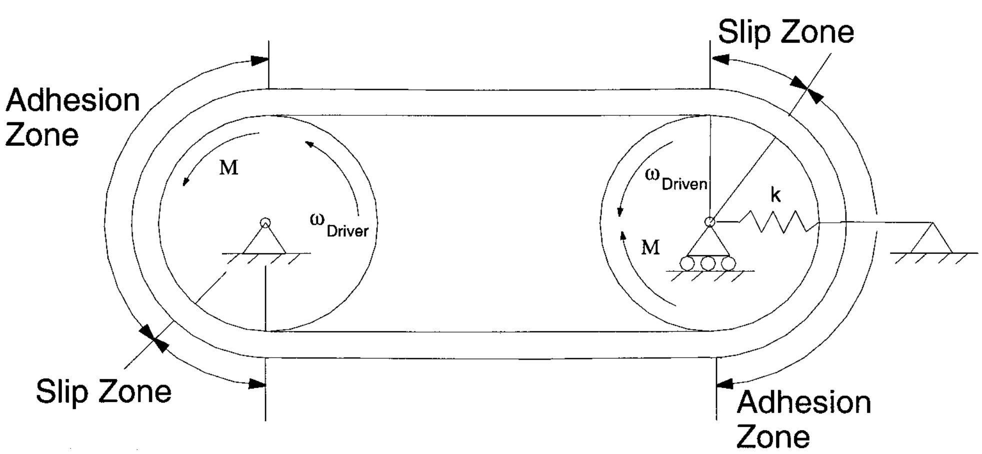


**Fig. 2 Location of adhesion and slip zones on the driver and driven pulley using a Coulomb friction law**

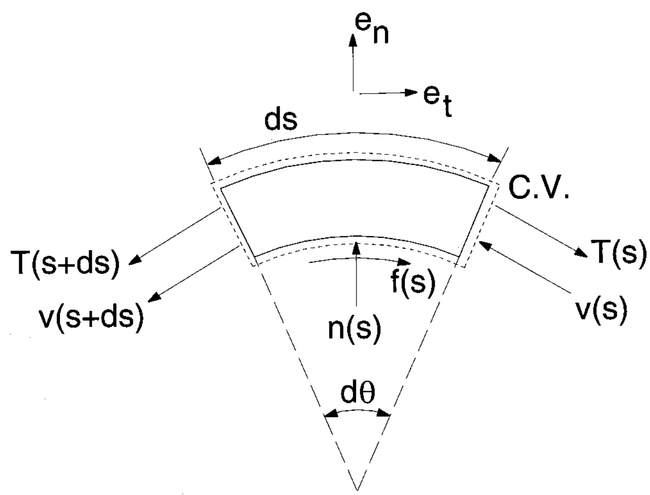


**Fig. 3 Belt element with control volume**

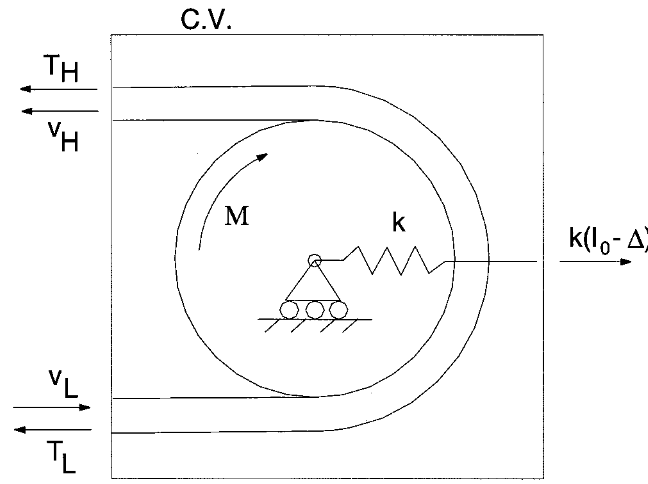


**Fig. 4 Control volume of driven pulley in the deformed configuration**

If the pulley is assumed to be rigid and the belt stretching is assumed to be isothermal, the adhesion condition implies the belt must maintain a constant strain in the adhesion zone. This further implies that the belt tension is also constant throughout this region, and thus no frictional forces are supported by, or exerted on, the belt. In contrast, the belt *creeps* against the pulley in the slip zone as its strain increases (or decreases) and the tension transitions from low (high) to high (low) tension. Coulomb's law dictates that, for a nonzero creep rate of the belt relative to the pulley, equal and opposite fully developed frictional forces per unit belt length of the form $\mu^* n$ act on the belt and the pulley, where $\mu$ denotes a coefficient of friction and $n$ denotes the normal force per unit belt length.

The steadily rotating belt drive has recently been re-addressed by Bechtel et al. [5] and their analysis has updated the known analytical solution to include previously undocumented effects due to belt velocity changes in the slip zone. Their work, which assumes a Coulomb friction law, is reviewed here before analyzing the belt drive with a creep-rate-dependent friction law. The review analysis differs from Bechtel et al. [5] in that a spring support has been added to the driven pulley, and a more exact belt length compatibility relationship replaces their assumption of an equally distributed tension difference $\Delta T$ in the belt spans.

The tension distribution $T(s)$ at any distance $s$ along the pulley arc can be derived using the element control volume shown in Fig. 3. A momentum balance in the tangential and normal directions yields the relationships

$$\frac{d}{ds}T - f(s) = G\frac{d}{ds}v(s), \tag{1}$$

$$n(s) = \frac{T(s) - Gv(s)}{R}, \tag{2}$$

where $f(s)$ denotes a friction force per unit length, $v(s)$ denotes the belt velocity, $n(s)$ denotes the normal force per unit length, $R$ denotes the pulley radius, and

$$G = \rho(s)v(s)A(s) = \rho_{\mathrm{ref}} v_{\mathrm{ref}} A_{\mathrm{ref}} = \text{constant}, \tag{3}$$

denotes the belt mass flow rate. The quantities $\rho(s)$ and $A(s)$ refer to the belt density and cross-sectional area, respectively, while a subscript ref refers to a convenient (fictitious) reference state defined as quantities evaluated at zero belt strain. The friction force per unit length exerted on the belt is governed by a Coulomb law (see Fig. 1) evaluated in conjunction with the isothermal adhesion and slip zone conditions,

$$f(s) = \begin{cases} -\mu n(s); & \text{slip zone (driver)} \\ \mu n(s); & \text{slip zone (driven)}, \\ 0; & \text{stick zone} \end{cases} \tag{4}$$

where $\mu$ denotes the coefficient of friction. A linear constitutive law relates the belt tension to the strain $\varepsilon(s)$,

$$T(s) = K\varepsilon(s), \tag{5}$$

where $K = EA_{\mathrm{ref}}$ denotes the belt modulus and $E$ denotes the belt material elastic modulus.

Conservation of mass applied to belt material entering and leaving the control volume in Fig. 4 yields an expression for the belt velocity in terms of the tension,

$$v(s) = v_{\mathrm{ref}}(1+\varepsilon(s)) = v_{\mathrm{ref}}\left(1 + \frac{T(s)}{K}\right), \tag{6}$$

while conservation of linear and angular momentum yield the relationships

$$-T_L - T_H + k(l_0 - \Delta) = -G(v_L + v_H), \tag{7}$$

$$(T_H - T_L)R + GR(v_L - v_H) = M, \tag{8}$$

where subscripts $L$ and $H$ refer to quantities evaluated for the high and low tension spans, $M$ denotes the externally applied moment on the pulleys, $k$ denotes the support spring's stiffness, $l_0$ denotes the initial spring deflection, and $\Delta$ denotes the displacement of the driven pulley's center from its initial position. A physical initial state, denoted by subscript 0, corresponds to the initial belt drive configuration of zero belt velocity, zero belt strain, zero applied moment, and initial spring deflection $l_0$. Due to the presence of $l_0$, this state is *not* an equilibrium state.

The adhesion condition at the inlet of the belt-pulley contact region leads to boundary conditions relating the pulleys' angular velocities to the span tensions,

$$v_H = R\omega_{\mathrm{Driver}} = v_{\mathrm{ref}}(1 + T_H/K), \tag{9}$$

$$v_L = R\omega_{\mathrm{Driven}} = v_{\mathrm{ref}}(1 + T_L/K), \tag{10}$$

where $\omega_{\mathrm{Driver}}$, $\omega_{\mathrm{Driven}}$ denote the driver and driven pulley angular velocities, respectively. A final relationship equates the reference belt length $L_{\mathrm{ref}}^{\mathrm{belt}}$ calculated from the geometry of the deformed (or operating) configuration to the geometrical belt length in the undeformed initial state $L_0^{\mathrm{belt}}$,

$$\left(\oint \frac{dl}{1+\varepsilon(l)} = L_{\mathrm{ref}}^{\mathrm{belt}}\right) = (2L_0^{\mathrm{span}} + 2\pi R = L_0^{\mathrm{belt}}), \tag{11}$$

where $dl$ is an element of length in the deformed configuration, and $L_0^{\text{span}}$ denotes the initial span length. The deformed span length $L^{\text{span}}$ is related to the initial span length $L_0^{\text{span}}$ through the driven pulley displacement $\Delta$,

$$L^{\text{span}} = L_0^{\text{span}} + \Delta, \tag{12}$$

and is used in the calculation of the closed integral in (11). Equation (11) is an exact relationship not utilized by Bechtel et al. [5], and together with Eq. (8) replaces their assumption that the tension difference $\Delta T$ required to balance an externally applied moment on the pulleys is distributed equally to the low-tension and high-tension belt spans.

Evaluation of Eqs. (1)–(6) leads to an expression for the driver pulley belt tension in the slip region

$$T_{\text{Driver}}(s) = \frac{K\rho_{\text{ref}} v_{\text{ref}}^2 A_{\text{ref}}}{K - \rho_{\text{ref}} v_{\text{ref}}^2 A_{\text{ref}}} + C_1 e^{-(\mu/R)S}, \tag{13}$$

where $0 < s < R\phi$, and where Eq. (4) has been evaluated using the driver-pulley slip-zone expression and arc measure $s$ has been taken to be zero at the start of the slip arc. The integration constant $C_1$ can be obtained using the boundary condition $T_{\text{Driver}}(0) = T_H$, while the slip arc metric $\phi$ can be obtained with the boundary condition $T_{\text{Driver}}(R\phi) = T_L$, yielding

$$T_{\text{Driver}}(s) = \frac{T_H K - \rho_{\text{ref}} v_{\text{ref}}^2 A_{\text{ref}}(T_H + K)}{K - \rho_{\text{ref}} v_{\text{ref}}^2 A_{\text{ref}}} e^{-(\mu/R)S} + \frac{K\rho_{\text{ref}} v_{\text{ref}}^2 A_{\text{ref}}}{K - \rho_{\text{ref}} v_{\text{ref}}^2 A_{\text{ref}}}, \tag{14}$$

$$\phi = \frac{1}{\mu} \ln\left( \frac{T_H K - \rho_{\text{ref}} v_{\text{ref}}^2 A_{\text{ref}}(T_H + K)}{T_L K - \rho_{\text{ref}} v_{\text{ref}}^2 A_{\text{ref}}(T_L + K)} \right). \tag{15}$$

A similar procedure yields the *driven* pulley slip arc tension,

$$T_{\text{Driven}}(s) = \frac{T_L K - \rho_{\text{ref}} v_{\text{ref}}^2 A_{\text{ref}}(T_L + K)}{K - \rho_{\text{ref}} v_{\text{ref}}^2 A_{\text{ref}}} e^{(\mu/R)S} + \frac{K\rho_{\text{ref}} v_{\text{ref}}^2 A_{\text{ref}}}{K - \rho_{\text{ref}} v_{\text{ref}}^2 A_{\text{ref}}}, \tag{16}$$

where the *driven* pulley slip arc metric is again given by (15). The *adhesion* zone expressions for each pulley are simply given as $T_{\text{Driver}}(s) = T_H$ and $T_{\text{Driven}}(s) = T_L$ for $-R(\pi - \phi) < s < 0$.

Knowing the belt's reference density ($\rho_{\text{ref}}$), reference cross-sectional area ($A_{\text{ref}}$), and modulus ($K$), the spring's constant ($k$) and initial deflection ($l_0$), as well as the externally applied torque ($M$), the pulley radius ($R$), the operating speed of the driver pulley ($\omega_{\text{Driver}}$), the friction coefficient ($\mu$), and the initial span length ($L_0^{\text{span}}$), the unknown quantities remaining to be found consist of the span tensions ($T_L, T_H$), the driven pulley's angular velocity ($\omega_{\text{Driven}}$), the reference velocity ($v_{\text{ref}}$), and the spring displacement ($\Delta$). Specifying numerical values for the known physical quantities described above, a numerical solution of Eqs. (3), (7–12), (14–16) yields the remaining unknown quantities. These equations are easily reduced to a single equation for $T_H$, for which a root solver can be employed. This solution strategy is followed for an example belt drive in Section 4. Note that Eq. (11) is an Eulerian description of belt compatibility, and requires an integral calculation over the entire closed *deformed* belt length. As such, Eq. (11) includes terms arising from the belt spans, the slip zones, and the adhesion zones.

A second model can be developed when Eqs. (8) and (11) are supplanted by the approximate equations used by Bechtel et al. [5]. Their equations (adapted to the spring-supported belt drive in this study) are as follows:

$$T_L = T_e - \frac{M}{2R}, \quad T_H = T_e + \frac{M}{2R}, \quad T_e = \frac{K}{L_0^{\text{span}}} \Delta_e, \tag{17}$$

$$-2T_e + k(l_0 - \Delta_e) = 2Gv_e, \tag{18}$$

$$v_e = v_{\text{ref}}\left(1 + \frac{T_e}{K}\right), \tag{19}$$

where $T_e$, $(l_0 - \Delta_e)$, and $v_e$ are the span tension, spring deflection, and belt velocity in an *equilibrium* configuration corresponding to zero applied moment and nonzero belt velocity. Equation (17) is an assumption stating that the applied external moment causes a redistribution of tension such that the required tension difference is split equally between the high and low tension spans. Equation (18) follows from Eq. (7) evaluated for the equilibrium configuration, while Eq. (19) follows similarly from Eq. (6). This solution is also explored numerically with the example belt drive of Section 4.

## 3 Mechanics Resulting From a Creep-Rate-Dependent Friction Law

An analysis of the belt drive depicted in Fig. 2, using a piecewise linear creep-rate friction law, as shown in column (*b*) of Fig. 1, retains most of the governing equations (Eqs. (1–3), (5–8), (11), (12)) derived in Section 2. In addition, the creep-rate-dependent friction law replaces the Coulomb friction law (Eq. (4)),

$$f = \begin{cases} -\mu n(s), & v_{\text{rel}} \leqslant -\dfrac{\mu n(s)}{v_s} \\[2ex] v_s v_{\text{rel}}, & -\dfrac{\mu n(s)}{v_s} < v_{\text{rel}} < \dfrac{\mu n(s)}{v_s}, \\[2ex] \mu n(s), & v_{\text{rel}} \geqslant \dfrac{\mu n(s)}{v_s} \end{cases} \tag{20}$$

where $v_s$ denotes the slope of the friction profile for sliding velocities $v_{\text{rel}}$ near the origin. The sliding velocity $v_{\text{rel}}$ for the belt drive is defined as

$$v_{\text{rel}} \equiv v(s) - R\omega, \tag{21}$$

where $\omega$ takes subscripts Driven or Driver. Note that the contact boundary conditions of Section 2, Eqs. (9)–(10), are no longer valid for the present analysis due to the absence of an adhesion zone (for reasons to be shown below) on the driven and driver pulleys.

**3.1 Single Sliding Zone on Each Pulley—Small $v_s$.** For small values of the friction slope parameter $v_s$, the velocity difference between the belt and the pulleys for any arc measure $s$ will lie in the middle zone of the friction profile. Thus, for all $s$,

$$f(s) = v_s v_{\text{rel}} = v_s(v(s) - R\omega). \tag{22}$$

Two possibilities exist for the existence of adhesion and slip arcs: (1) a first possibility analogous to the state arising in the Coulomb analysis—an adhesion arc starts at the inlet of the contact region and is followed by a slip arc, or (2) a second possibility in which a single slip arc spans the entire contact region. A third possibility in which a slip arc begins at the contact region inlet and is followed by an adhesion arc cannot occur since increasing arc metric $s$ always results in movement on the friction profile away from the origin, and thus away from the possibility of having an adhesion arc. This is true regardless of the magnitude of the friction slope parameter $v_s$. The aforementioned movement constraint can be seen most clearly by example: if the belt is moving slower [faster] than the pulley, the friction force will be negative [positive], which will tend to decrease [increase] the tension and thus decrease [increase] the belt velocity by Eq. (6), which will ultimately result in a more negative [positive] velocity difference $v_{\text{rel}}$ and thus movement along the friction profile away from the origin.

The first of the two adhesion/slip arc possibilities would appear to be most likely since the creep-rate law shares with the Coulomb law the same zero friction point at zero relative velocity. This would allow the belt to move in the adhesion zone with the same velocity as the rigid pulley, and thus to maintain a constant strain and to experience no friction forces, as in the Coulomb analysis.

To examine this possibility, Eqs. (1–3), (5), (6), (21), (22) are evaluated for the driver pulley in order to determine the driver pulley's tension distribution in the slip zone:

$$T_{\mathrm{Driver}}(s)=C_1e^{v_s v_{\mathrm{ref}}/(K-Gv_{\mathrm{ref}})s}+K\left(\frac{R\omega_{\mathrm{Driver}}}{v_{\mathrm{ref}}}-1\right), \tag{23}$$

where $C_1$ denotes an integration constant. The arc metric $s$ can be chosen to be zero at the start of the slip zone, without loss of generality. Thus, using the boundary conditions

$$T_{\mathrm{Driver}}(0)=T_H, \quad v_{\mathrm{Driver}}(0)=v_{\mathrm{ref}}(1+T_{\mathrm{Driver}}(0)/K)=R\omega_{\mathrm{Driver}} \tag{24}$$

to calculate $C_1$ and $v_{\mathrm{ref}}$, it is found that

$$v_{\mathrm{ref}}=\frac{K\omega_{\mathrm{Driver}}}{(1+T_H/K)}, \quad C_1=T_H-K\left(\frac{R\omega_{\mathrm{Driver}}}{v_{\mathrm{ref}}}-1\right)=0, \tag{25}$$

with the result that $T_{\mathrm{driver}}(s)=T_H$ throughout the sliding region. As a result, the tension is a constant $T_H$ over the entire belt-pulley contact region, and hence an unacceptable prediction is made that no torque is transmitted by the driver pulley, violating Eq. (8). A similar violation occurs for an analysis of the driven pulley, and more generally, for any proposed solution which includes an adhesion zone anywhere on either pulley. Therefore only solutions proposed with no adhesion arcs appearing on the pulleys are valid—an unexpected result considering the existence of adhesion arcs in the Coulomb analysis.

In light of the previous discussion, only the second possible solution remains plausible, and is examined next. The tension distribution given by Eq. (23) now holds for the entire contact region, $0<s<R\pi$, with boundary conditions:

$$T_{\mathrm{Driver}}(0)=T_H, \tag{26}$$

$$T_{\mathrm{Driver}}(R\pi)=T_L. \tag{27}$$

Satisfaction of Eq. (26) gives an expression for $C_1$, and thus the tension distribution:

$$T_{\mathrm{Driver}}(s)=\left[T_H-K\left(\frac{R\omega_{\mathrm{Driver}}}{v_{\mathrm{ref}}}-1\right)\right]e^{[v_s v_{\mathrm{ref}}/(K-Gv_{\mathrm{ref}})]s}+K\left(\frac{R\omega_{\mathrm{Driver}}}{v_{\mathrm{ref}}}-1\right). \tag{28}$$

Satisfaction of Eq. (27) also gives an expression for the reference velocity $v_{\mathrm{ref}}$, but not in a convenient closed form. This expression will be evaluated numerically for an example belt drive in Section 4.

A similar analysis for the driven pulley with the boundary conditions

$$T_{\mathrm{Driven}}(0)=T_L, \quad T_{\mathrm{Driven}}(R\pi)=T_H \tag{29}$$

yields the tension distribution and the driven pulley angular velocity

$$T_{\mathrm{Driven}}(s)=\left[T_L-K\left(\frac{R\omega_{\mathrm{Driven}}}{v_{\mathrm{ref}}}-1\right)\right]e^{[v_s v_{\mathrm{ref}}/(K-Gv_{\mathrm{ref}})]s}+K\left(\frac{R\omega_{\mathrm{Driven}}}{v_{\mathrm{ref}}}-1\right), \quad 0<s<R\pi, \tag{30}$$

$$\omega_{\mathrm{Driven}}=\frac{v_{\mathrm{ref}}}{KR(e^{[v_s v_{\mathrm{ref}}/(K-Gv_{\mathrm{ref}})]\pi R}-1)}[(T_L+K)\times e^{[v_s v_{\mathrm{ref}}/(K-Gv_{\mathrm{ref}})]\pi R}-(T_H+K)]. \tag{31}$$

Expressions for the normal force and belt velocities for each pulley $(n_{\mathrm{Driver}}(s),n_{\mathrm{Driven}}(s),v_{\mathrm{Driver}}(s),v_{\mathrm{Driven}}(s))$ follow from Eqs. (2) and (6), respectively.

**3.2 Single Sliding Zone on Driven Pulley, Dual Sliding Zones on Driver Pulley—Moderate $v_s$.** At larger values of the friction slope parameter $v_s$, the transition from high to low tension on the driver pulley cannot be compensated for by a single sliding zone, and movement along the friction profile (as arc metric $s$ is increased) results in development of a second sliding zone composed of fully developed frictional forces lying in the left-most zone of the friction profile. The driven pulley boundary conditions, angular velocity, and tension distribution of Section 3.1 (Eqs. (29)–(31)) *remain* valid. A further discussion on the above is given in Section 3.4. The tension distribution for the driver pulley must here be divided into a distribution for the middle sliding region, represented by $T_{DR,1}(s)$, and a distribution for the left-most sliding region, represented by $T_{DR,2}(s)$. Solution of Eqs. (1–3), (5), (6) (20) results in the driver pulley tension distributions:

$$T_{DR,1}(s)=C_2e^{[v_s v_{\mathrm{ref}}/(K-Gv_{\mathrm{ref}})]s}+K\left(\frac{R\omega_{\mathrm{Driver}}}{v_{\mathrm{ref}}}-1\right), \quad 0<s<R\phi_{DR1}, \tag{32}$$

$$T_{DR,2}(s)=\frac{KGv_{\mathrm{ref}}}{K-Gv_{\mathrm{ref}}}+C_3e^{-\mu/Rs}, \quad 0<s<R\phi_{DR2}, \tag{33}$$

where to reduce complexity, the arc metric $s$ is initialized to zero at the start of each sliding region, and where $(\phi_{DR1},\phi_{DR2})$ denote slip arc magnitudes for the two distributions. The updated boundary conditions for the driver pulley are expressed as

$$T_{DR,1}(0)=T_H, \quad T_{DR,1}(R\phi_{DR1})=T_{DR1}=T_{DR,2}(0), \quad T_{DR,2}(R\phi_{DR2})=T_L, \tag{34}$$

$$v_s(v_{DR,1}(R\phi_{DR1})-R\omega_{\mathrm{Driver}})=-\mu n_{DR,1}(R\phi_{DR1}), \tag{35}$$

$$\phi_{DR1}+\phi_{DR2}=\pi, \tag{36}$$

where Eq. (34) represents tension boundary conditions and $T_{DR1}$ denotes the tension at the transition between the two sliding regions, Eq. (35) expresses a friction force matching condition, and Eq. (36) insures that the two sliding regions span the entire contact region. Satisfaction of Eqs. (34), (35) yields the integration constants $(C_2,C_3)$ and final expressions for the tension distributions, the transition tension $T_{DR1}$, and the slip arc magnitudes $(\phi_{DR1},\phi_{DR2})$:

$$T_{DR,1}(s)=\left[T_H-K\left(\frac{R\omega_{\mathrm{Driver}}}{v_{\mathrm{ref}}}-1\right)\right]e^{[v_s v_{\mathrm{ref}}/(K-Gv_{\mathrm{ref}})]s}+K\left(\frac{R\omega_{\mathrm{Driver}}}{v_{\mathrm{ref}}}-1\right), \tag{37}$$

$$T_{DR,2}(s)=\frac{KGv_{\mathrm{ref}}}{K-Gv_{\mathrm{ref}}}+\left[T_{DR1}-\frac{KGv_{\mathrm{ref}}}{K-Gv_{\mathrm{ref}}}\right]e^{-\mu/Rs}, \tag{38}$$

$$T_{DR1}=\frac{K[v_sR^2\omega_{\mathrm{Driver}}-v_sRv_{\mathrm{ref}}+\mu Gv_{\mathrm{ref}}]}{v_sRv_{\mathrm{ref}}+\mu K-\mu Gv_{\mathrm{ref}}}, \tag{39}$$

$$\phi_{DR1}=\frac{K-Gv_{\mathrm{ref}}}{v_sRv_{\mathrm{ref}}}\ln\left[\frac{R\omega_{\mathrm{Driver}}-v_{\mathrm{ref}}\left(1+\frac{T_{DR1}}{K}\right)}{R\omega_{\mathrm{Driver}}-v_{\mathrm{ref}}\left(1+\frac{T_H}{K}\right)}\right], \tag{40}$$

$$\phi_{DR2}=\frac{1}{\mu}\ln\left[\frac{T_{DR1}-Gv_{\mathrm{ref}}-\frac{Gv_{\mathrm{ref}}}{K}T_{DR1}}{T_L-Gv_{\mathrm{ref}}-\frac{Gv_{\mathrm{ref}}}{K}T_L}\right]. \tag{41}$$

The final boundary condition (Eq. (36)) is evaluated numerically for an example belt drive in Section 4 in order to determine the reference velocity $v_{\mathrm{ref}}$.

**3.3 Dual Sliding Zones on Each Pulley—Large $v_s$.** For still larger values of the friction slope parameter $v_s$, the driven pulley also develops a second sliding zone composed of fully developed frictional forces, similar to the driver pulley of Section 3.2, but with frictional forces lying in the right-most zone of the friction profile. The driver pulley boundary conditions, slip arc magnitudes, and tension distribution of Section 3.2 (Eqs. (32)–(41)) *remain* valid. The tension distribution for the driven pulley must here be divided into a distribution for the middle sliding region, represented by $T_{DN,1}(s)$, and a distribution for the right-most sliding region, represented by $T_{DN,2}(s)$. Solution of Eqs. (1)–(3), (5), (6), (20) results in the driven pulley tension distributions:

$$T_{DN,1}(s)=C_4e^{(v_s v_{\mathrm{ref}}/K-Gv_{\mathrm{ref}})s}+K\left(\frac{R\omega_{\mathrm{Driven}}}{v_{\mathrm{ref}}}-1\right),\quad 0<s<R\phi_{DN1}, \tag{42}$$

$$T_{DN,2}(s)=\frac{KGv_{\mathrm{ref}}}{K-Gv_{\mathrm{ref}}}+C_5e^{(\mu/R)s},\quad 0<s<R\phi_{DN2}, \tag{43}$$

where the arc metric $s$ is once again initialized to zero at the start of each sliding region, and where $(\phi_{DN1},\phi_{DN2})$ denote driven pulley slip arc magnitudes for the two distributions. The updated boundary conditions for the driven pulley are expressed as

$$T_{DN,1}(0)=T_L,T_{DN,1}(R\phi_{DN1})=T_{DN1}=T_{DN,2}(0),\quad T_{DN,2}(R\phi_{DN2})=T_H, \tag{44}$$

$$v_s(v_{DN,1}(R\phi_{DN1})-R\omega_{\mathrm{Driven}})=\mu n_{DN,1}(R\phi_{DN1}), \tag{45}$$

$$\phi_{DN1}+\phi_{DN2}=\pi, \tag{46}$$

where $T_{DN1}$ denotes the tension at the transition between the two sliding regions. Satisfaction of Eqs. (44), (45) yields the integration constants $(C_4,C_5)$ and final expressions for the tension distributions, the transition tension $T_{DN1}$, and the slip arc magnitudes $(\phi_{DN1},\phi_{DN2})$:

$$T_{DN,1}(s)=\left[T_L-K\left(\frac{R\omega_{\mathrm{Driven}}}{v_{\mathrm{ref}}}-1\right)\right]e^{[v_s v_{\mathrm{ref}}/(K-Gv_{\mathrm{ref}})]s}+K\left(\frac{R\omega_{\mathrm{Driven}}}{v_{\mathrm{ref}}}-1\right), \tag{47}$$

$$T_{DN,2}(s)=\frac{KGv_{\mathrm{ref}}}{K-Gv_{\mathrm{ref}}}+\left[T_{DN1}-\frac{KGv_{\mathrm{ref}}}{K-Gv_{\mathrm{ref}}}\right]e^{(\mu/Rs)}, \tag{48}$$

$$T_{DN1}=\frac{K[-v_sR^2\omega_{\mathrm{Driven}}+v_sRv_{\mathrm{ref}}+\mu Gv_{\mathrm{ref}}]}{v_sRv_{\mathrm{ref}}-\mu K+\mu Gv_{\mathrm{ref}}}, \tag{49}$$

$$\phi_{DN1}=\frac{K-Gv_{\mathrm{ref}}}{v_sRv_{\mathrm{ref}}}\ln\left[\frac{R\omega_{\mathrm{Driven}}-v_{\mathrm{ref}}\left(1+\dfrac{T_{DN1}}{K}\right)}{R\omega_{\mathrm{Driven}}-v_{\mathrm{ref}}\left(1+\dfrac{T_L}{K}\right)}\right], \tag{50}$$

$$\phi_{DN2}=\frac{1}{\mu}\ln\left[\frac{T_H-Gv_{\mathrm{ref}}-\dfrac{Gv_{\mathrm{ref}}}{K}T_H}{T_{DN1}-Gv_{\mathrm{ref}}-\dfrac{Gv_{\mathrm{ref}}}{K}T_{DN1}}\right]. \tag{51}$$

The final boundary condition (Eq. (46)) is evaluated numerically for an example belt drive in Section 4 in order to determine the driven pulley angular velocity $\omega_{\mathrm{Driven}}$.

**3.4 Discussion on the Existence of Multiple Sliding Zones.** As mentioned in Sections 3.2 and 3.3, a second sliding zone appears on the driver and driven pulleys for larger values of $v_s$. This value of $v_s$ can be analyzed for each pulley from closer inspection of Eqs. (35), (45).

Specifically, the critical value of $v_s$ for which a second sliding zone appears on the driver pulley can be determined from Eq. (35) by setting $\phi_{DR1}=\pi$ and noting that then $T_{DR,1}(\phi_{DR1})=T_L$ and $v_{DR,1}(\phi_{DR1})=v_L$,

$$v_{s,cr}^{\mathrm{Driver}}=\frac{\mu(T_L-Gv_L)}{R(R\omega_{\mathrm{Driver}}-v_L)}, \tag{52}$$

where $v_{s,cr}^{\mathrm{Driver}}$ denotes the critical profile slope required for the existence of two sliding regions on the driver pulley. Similarly, an expression for the critical value of $v_s$ for the driven pulley results from setting $\phi_{DN1}=\pi$, $T_{DN,1}(\phi_{DN1})=T_H$ and $v_{DN,1}(\phi_{DN1})=v_H$ in Eq. (45),

$$v_{s,cr}^{\mathrm{Driven}}=\frac{\mu(T_H-Gv_H)}{R(v_H-R\omega_{\mathrm{Driven}})}, \tag{53}$$

where $v_{s,cr}^{\mathrm{Driven}}$ denotes the critical profile slope required for the existence of two sliding regions on the driven pulley. Due to the appearance of $T_L$ in the numerator of Eq. (52) versus $T_H$ in the numerator of Eq. (53), a smaller value of $v_{s,cr}^{\mathrm{Driver}}$ than $v_{s,cr}^{\mathrm{Driven}}$ is generally required for two sliding regions to exist on the driver pulley as opposed to the driven pulley. The denominators of Eqs. (52), (53) are close in magnitude due to the need to transition over the same tension difference, and to thus occupy nearly equal relative velocity domain measures on the friction profile.

## 4 Results and Discussion for an Example Belt Drive

A sample two-pulley belt drive, as defined in Table 1, is analyzed further to determine important system parameters such as the high and low belt tensions, the number of slip arcs present on each pulley and their extent, the friction and normal forces per unit belt length, and the driven pulley's angular velocity. Although the analysis considers a two-pulley belt drive, the solution procedure is easily generalized to consider multipulley drives with an arbitrary number of pulleys.

As discussed in Section 3, the magnitude of the friction profile parameter $v_s$ determines whether or not multiple slip zones exist on each pulley. Each of the three possible slip-zone combinations (Sections 3.1–3.3) are illustrated by evaluating solutions for $v_s=4.0\mathrm{E}+3, 1.0\mathrm{E}+5, 8.0\mathrm{E}+5$, respectively. In addition to the closed-form expressions for most of the response quantities given in Section 3, the conservation of angular momentum yields a closed-form expression for the low tension:

$$T_L=\frac{RT_H(K-Gv_{\mathrm{ref}})-KM}{R(K-Gv_{\mathrm{ref}})}. \tag{54}$$

The only remaining response quantities to be determined (numerically) are then $(T_H,v_{\mathrm{ref}})$ in Section 3.1, computed using Eq. (11) and the final unevaluated boundary condition, Eq. (27); $(T_H,v_{\mathrm{ref}})$ in Section 3.2, computed using Eq. (11) and Eq. (36); and $(T_H,v_{\mathrm{ref}},\omega_{\mathrm{Driven}})$ in Section 3.3, computed using Eqs. (11), (36) and Eq. (46). A numerical solution of the Coulomb law example is also evaluated using the solution procedure for $T_H$ described in Section 2. Results are given in Table 1 and Figs. 5–6.

The friction forces and normal forces per unit length are compared in Fig. 5 for each value of $v_s$, and the computed driven pulley angular velocities are given in Table 1. For convenience,

**Table 1 Left two columns of table: parameter space assigned to the example two-pulley belt drive. Right five columns of table: computed drive parameters using the creep-rate law and the Coulomb law.**

| Belt Drive Parameter | Assigned Value | Belt Drive Parameter | $v_s=4.0\mathrm{E}+3$ | $v_s=1.0\mathrm{E}+5$ | $v_s=8.0\mathrm{E}+5$ | Coulomb Law |
|---|---|---|---|---|---|---|
| $\rho_{\mathrm{ref}}$ | 1036 kg/m$^3$ | $T_L$ | 165.18 | 168.3 | 169.57 | 169.47 N |
| $A_{\mathrm{ref}}$ | 1.0E-4 m$^2$ | $T_H$ | 719.1 | 722.2 | 723.48 | 723.38 N |
| $K$ | 80.068 kN | $\omega_{\mathrm{Driven}}$ | 106.63 | 119.09 | 119.177 | 119.177 rad/s |
| $k$ | 150 kN/m | $v_{\mathrm{ref}}$ | 9.1564 | 9.659 | 9.66269 | 9.66270 m/s |
| $l_0$ | 0.01 m | $V_L$ | 9.175 | 9.679 | 9.68315 | 9.68315 m/s |
| $M$ | 45 N-m | $v_H$ | 9.24 | 9.746 | 9.750 | 9.750 m/s |
| $\omega_{\mathrm{Driver}}$ | 120 rad/s | $\Delta$ | 4.22E-3 | 4.19E-3 | 4.176E-3 | 4.177E-3 m |
| $\mu$ | 1.2 | $\phi$ | N/A | N/A | N/A | 1.247 rad |
| $R$ | 0.08125 m | $\phi_{DR1}$ | N/A | 2.516 | 2.013 rad | N/A |
| $L_0^{\mathrm{span}}$ | 0.5105 m | $\phi_{DR2}$ | N/A | 0.624 | 1.128 rad | N/A |
| | | $\phi_{DN1}$ | N/A | N/A | 2.033 rad | N/A |
| | | $\phi_{DN2}$ | N/A | N/A | 1.108 rad | N/A |
| | | $G$ | 0.985 | 1.0006 | 1.001055 | 1.001056 kg/s |
| | | $\dfrac{\omega_{\mathrm{Driven}}}{\omega_{\mathrm{Driver}}}$ | 0.8886 | 0.9924 | 0.9931 | 0.9931 |

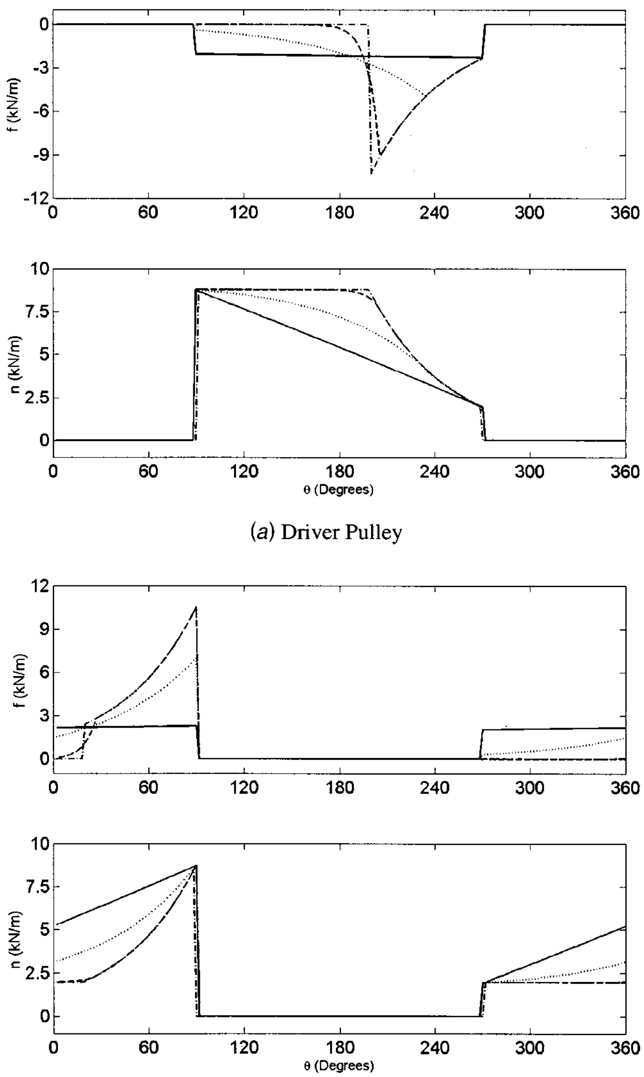


(*a*) Driver Pulley

(*b*) Driven Pulley

**Fig. 5 Friction and normal forces per unit belt length for (*a*) driver and (*b*) driven pulleys. Values of $v_s$ represented: 4.0E+3 (_), 1.0E+5 (· · · ·), 8.0E+5 (— — —). The Coulomb law solution is represented by (—·—·—·—.).**

the pulley location is given by an angle $\theta$ measured counterclockwise from the right-horizontal (or three o'clock) position on each pulley. For small values of $v_s$, represented by $v_s=4.0\mathrm{E}+3$, the friction and normal force profiles have a nearly constant slope over the entire belt-pulley contact region. As the value of $v_s$ is increased, these forces become increasingly more exponential (in appearance) and begin to approach the profiles for the Coulomb law analysis, as expected. Note that for $v_s=8.0\mathrm{E}+5$, the profiles are nearly identical to the Coulomb profiles, even though no adhesion zone exists on the pulley and the first sliding-zone arc measures over two radians (see $\phi_{DR1}$ in Table 1). But, the relative velocities are small enough for the friction forces to be near zero throughout this entire zone, as shown in the figure. Also, as the slope profile parameter is increased, the driven pulley's angular velocity increases, until it is nearly equal to that using a Coulomb law. Smaller values of $v_s$ require a large amount of initial slip between the belt and the pulley in order for the friction forces to transition the tension from $T_L$ to $T_H$.

Using the belt-drive parameter space of Table 1 and Eqs. (3), (7), (9), (10), (17)–(19), the assumption of a constant tension difference $\Delta T$ in each belt span can be evaluated for its appropriateness. A numerical solution yields $T_e=500.8$ N, $T_L=223.9$ N, $T_H=777.7$ N, $v_e=9.716$ m/s, $v_{\mathrm{ref}}=9.656$ m/s, $v_L=9.683$ m/s, $v_H=9.75$ m/s, and $\Delta\cong\Delta_e=3.148\mathrm{E}-3$ m. Based on the above computed parameters and those computed for the Coulomb analysis (Table 1), for this belt drive the assumed tension difference results in tension errors of 7.5 percent for the high-tension span and 32 percent error for the low-tension span. It is not shown here, but it is remarked that these errors decrease with decreasing externally applied torque $M$. Based on these results, it is suggested that the more exact compatibility relationship be used for belt drives transmitting large external torques.

A final comparison is made between the analytical solution presented herein and a finite element solution of the same drive, as detailed in [21]. Figure 6 depicts the friction and normal force distributions of both solutions for each value of $v_s$. For comparison's sake, the distribution is shown as nodal forces, where the analytical force per unit length is converted to the necessary nodal force through multiplication with the numerical model's element belt length. As evidenced by the figure, a high degree of correlation between the two solutions is found, confirming the predictions of the analytical solution.

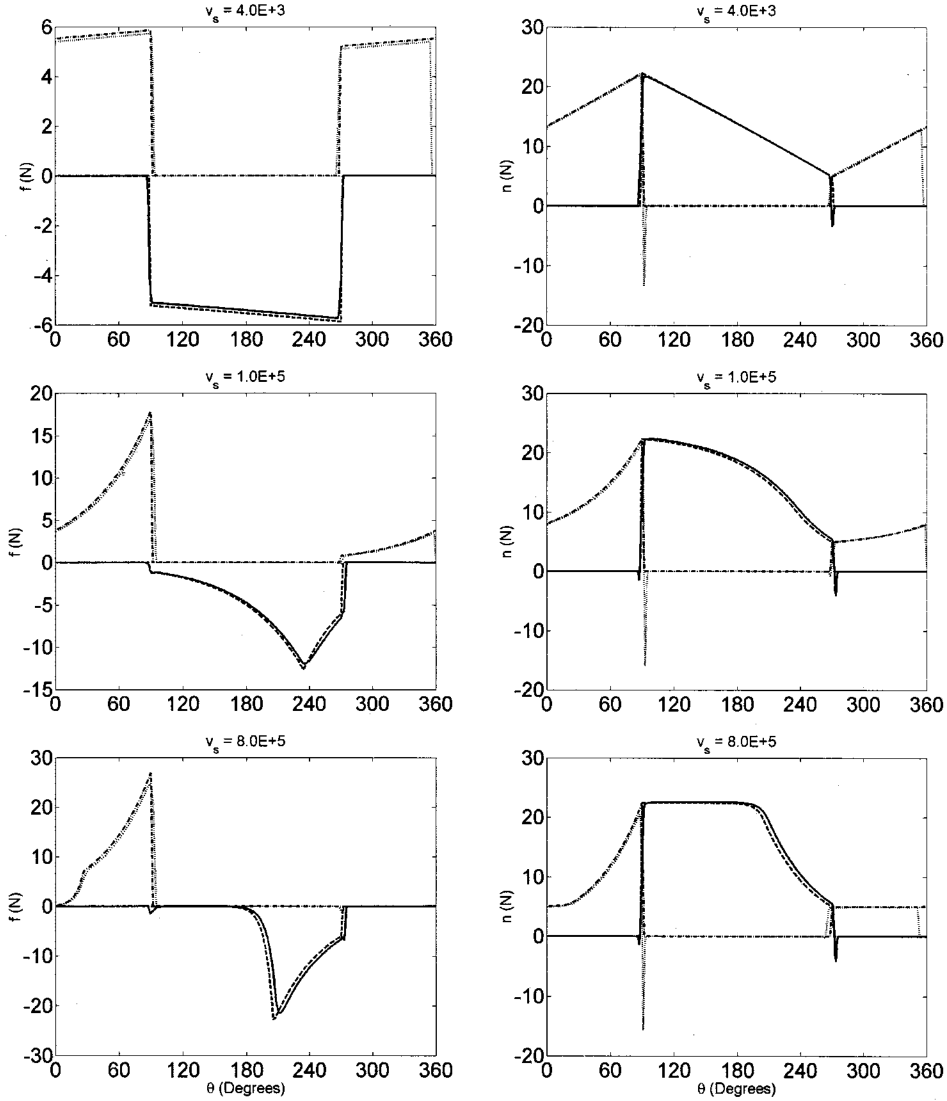


**Fig. 6 Comparisons of analytical and finite element predicted frictional and normal forces at belt nodes for several values of the slope profile parameter $v_s$. Results are for a discretization of 100 belt elements per half pulley. In all plots, the finite element driver solutions are represented by (_), finite element driven by (· · · ·), analytical driver by (— — —), and analytical driven by (—·—·—·—).**

## 5 Conclusions

Belt-drive mechanics associated with a physically appropriate creep-rate-dependent friction law have been analyzed. The analysis shows no adhesion zones can exist on the pulleys, in contrast to the existence of adhesion zones in belt-drive analyses with a Coulomb friction law. Two types of slip zones have been identified, and the existence of one or both slip zones on the pulleys has been shown to depend on the magnitude of the friction profile slope $v_s$. Closed-form expressions have been generated for the location and magnitude of the slip zones, the associated tension distributions, and the frictional and normal forces per unit length exerted on the belt by the pulleys. The analytical solution was applied to an example belt drive and then compared to a dynamic finite element solution of the same drive. Excellent agreement was found when predicted quantities from each solution were compared over a large range of $v_s$.

## References


[1] Euler, M. L., 1762, "Remarques sur l'effect du frottement dans l'equilibre," Mém. Acad. Sci., Berlin, pp. 265–278.

[2] Grashof, B. G., 1883, *Theoretische Maschinenlehre, Bd 2*, Leopold Voss, Hamburg.

[3] Fawcett, J. N., 1981, "Chain and Belt Drives—A Review," Shock Vib. Dig., **13**(5), pp. 5–12.

[4] Johnson, K. L., 1985, *Contact Mechanics*, Cambridge University Press, London, Chap. 8.

[5] Bechtel, S. E., Vohra, S., Jacob, K. I., and Carlson, C. D., 2000, "The Stretching and Slipping of Belts and Fibers on Pulleys," ASME J. Appl. Mech., **67**, pp. 197–206.

[6] Firbank, T. C., 1970, "Mechanics of the Belt Drive," Int. J. Mech. Sci., **12**, pp. 1053–1063.

[7] Gerbert, G. G., 1991, "On Flat Belt Slip," *Vehicle Tribology* (Tribology Series 16), Elsevier, Amsterdam, pp. 333–339.

[8] Gerbert, G. G., 1996, "Belt Slip—A Unified Approach," ASME J. Mech. Des., **118**, pp. 432–438.

[9] Townsend, W. T., and Salisbury, J. K., 1988, "The Efficiency Limit of Belt and Cable Drives," ASME J. Mech., Transm., Autom. Des., **110**, pp. 303–307.

[10] Barker, C. R., Oliver, L. R., and Brieg, W. F., 1991, "Dynamic Analysis of Belt Drive Tension Forces During Rapid Engine Acceleration," *SAE Congress*, Detroit, MI, Paper No. 910687, pp. 239–254.

[11] Hwang, S. J., Perkins, N. C., Ulsoy, A. G., and Meckstroth, R. J., 1994, "Rotational Response and Slip Prediction of Serpentine Belt Drive Systems," ASME J. Vibr. Acoust., **116**, pp. 71–78.

[12] Beikmann, R. S., Perkins, N. C., and Ulsoy, A. G., 1996, "Free Vibration of Serpentine Belt Drive Systems," ASME J. Vibr. Acoust., **118**, pp. 406–413.

[13] Beikmann, R. S., Perkins, N. C., and Ulsoy, A. G., 1996, "Nonlinear Coupled

Vibration Response of Serpentine Belt Drive Systems,'' ASME J. Vibr. Acoust., **118**, pp. 567–574.
[14] Beikmann, R. S., Perkins, N. C., and Ulsoy, A. G., 1997, ''Design and Analysis of Automotive Serpentine Belt Drive Systems for Steady State Performance,'' ASME J. Mech. Des., **119**, pp. 162–168.
[15] Leamy, M. J., Perkins, N. C., Barber, J. R., and Meckstroth, R. J., 1997, ''The Influence of Tensioner Friction on Accessory Drive Dynamics,'' *1997 SAE Noise & Vibration Conference and Expedition*, Traverse City, MI, May 20–22, Paper No. 97NV103.
[16] Leamy, M. J., and Perkins, N. C., 1998, ''Nonlinear Periodic Response of Engine Accessory Drives With Dry Friction Tensioners,'' ASME J. Vibr. Acoust., **120**, pp. 909–916.
[17] Kraver, T. C., Fan, G. W., and Shah, J. J., 1996, ''Complex Modal Analysis of a Flat Belt Pulley System With Belt Damping and Coulomb-Damped Tensioner,'' ASME J. Mech. Des., **118**, pp. 306–311.
[18] Leamy, M. J., Barber, J. R., and Perkins, N. C., 1998, ''Distortion of a Harmonic Elastic Wave Reflected From a Dry Friction Support,'' ASME J. Appl. Mech., **65**, pp. 851–857.
[19] Leamy, M. J., Barber, J. R., and Perkins, N. C., 1998, ''Dynamics of Belt/Pulley Frictional Contact,'' *IUTAM Symposium on Unilateral Multibody Contacts*, Proceedings, Munich, Aug. 3–7, Kluwer Academic Press, Dordrecht, The Netherlands, pp. 277–286.
[20] Leamy, M. J., 1998, ''The Influence of Dry Friction in the Dynamic Response of Accessory Belt Drive Systems,'' *doctoral dissertation*, The University of Michigan.
[21] Leamy, M. J., and Wasfy, T., 2001, ''Dynamic Finite Element Modeling of Belt Drives,'' 18th Biennial Conference on Mechanical Vibration and Noise, ASME International 2001 DETC.
[22] Oden, J. T., and Martins, J. A. C., 1985, ''Models and Computational Methods for Dynamic Friction Phenomena,'' Comput. Methods Appl. Mech. Eng., **52**, pp. 527–634.
[23] Makris, N., and Constantinou, M. C., 1991, ''Analysis of Motion Resisted by Friction. II. Velocity-Dependent Friction,'' Mech. Struct. Mach., **19**(4), pp. 501–526.
[24] Begley, C. J., and Virgin, L. N., 1997, ''A Detailed Study of the Low-Frequency Periodic Behavior of a Dry Friction Oscillator,'' ASME J. Dyn. Syst., Meas., Control, **119**, pp. 491–497.

**R. M. Christensen**
Honorary Mem. ASME
Lawrence Livermore National Laboratory,
Livermore, CA 94550;
and Stanford University,
Stanford, CA 94305

# A Possible Limiting Case Behavior for Brittle Material Fracture

*The self-consistent scheme is used to model the state of an elastic material with a very high density of nearly connected cracks. Then fracture mechanics is used to pose the problem of the complete and final failure of the material under uniaxial and eqibiaxial tension. These failure states are taken to be those of the extreme case of brittle fracture. A specific form for the resulting extreme brittle failure criterion is given.*
[DOI: 10.1115/1.1483835]

This communication is concerned with the type of homogeneous, isotropic materials that exhibit highly brittle behavior when stressed to failure. The limit of extreme brittle behavior is taken to be that of fracture when the elastic material is so heavily damaged by a concentrated distribution of cracks that it is near to causing a state of disintegration under load. The problem will be studied in the two-dimensional context, although three-dimensional behavior will be inferred.

Classical fracture mechanics was first developed to treat the failure inducing behavior of a single isolated and thereby noninteractive crack in an elastic medium under load. The methodology was enormously successful and much effort has been given over to solving more complex problems involving crack interactions, both for determining the effective elastic properties (Kachanov [1]) and for the overall fracture-induced failure problem (Kanninen and Popelar [2]). If the behavior of the single, isolated crack represents one limit of the fracture problem, the question arises as to what the appropriate characterization may be for the other possible limit of the fracture problem involving a dense population of highly interactive cracks. The self-consistent scheme (SCS) will be used to deduce possible fracture behavior at this other limit condition.

The SCS for isotropic cracked media has been criticized as being too severe compared with other crack models that give the effective moduli as vanishing only when the crack density becomes unboundedly large, the SCS does so at a finite value of the crack density. However, there probably is no single crack model appropriate for all purposes. In any case, the SCS is ideally suited for the present purpose of studying behavior as the crack density severely degrades the elastic properties approaching the state of vanishing properties.

The SCS for cracked media was developed by Budiansky and O'Connell [3] in the three-dimensional isotropic context. In this method a single crack is embedded in a medium of the unknown elastic properties which are to be determined. In the limit of vanishing crack density the effective properties must revert to the properties of the given starter material. The problem is well posed and yields an explicit result for $E$ and $\nu$, the effective isotropic properties as a function of the crack density and the base or matrix material properties, $E_m$ and $\nu_m$. The problem was further considered by Laws and Brokenbrough [4], and two-dimensional problems of certain crack types were considered by Gottesman et al. [5]. Crack problems of this general type were very extensively treated by Kachanov [1], including the two-dimensional case of randomly oriented cracks modeled by the SCS as well as by other methods.

The problem of interest here is that of the two-dimensional cracked medium modeled by the SCS. Following Kachanov [1], the solution for the effective isotropic properties $E$ and $\nu$ are given by

$$\frac{E}{E_m}=1-\frac{\rho}{\rho_o} \tag{1}$$

$$\frac{\nu}{\nu_m}=1-\frac{\rho}{\rho_o} \tag{2}$$

where the crack density $\rho$ is given by

$$\rho=\frac{1}{A}\sum_i l_i^2 \tag{3}$$

for cracks of lengths $2l_i$ within area, $A$. At a crack density of $\rho=\rho_o$ the cracks form an interconnective network and material collapse occurs. The SCS solution gives the crack density at material disintegration as

$$\rho_o=\frac{1}{\pi}=0.318 \tag{4}$$

where perfectly elastic deformations have been assumed. The properties (1) and (2) are for two-dimensional plane stress conditions. For plane-strain conditions these properties must be reinterpreted as the corresponding plane-strain forms.

Not only are the expressions (1)–(4) the correct forms for a dilute distribution of cracks, they are rigorously the full range form obtained from the SCS idealization and solution.

It is interesting to compare the crack density at collapse (4) with the corresponding crack densities for a regular pattern of connected cracks forming hexagonal and equilateral triangular cells. The latter two values are given by

$$\rho_H=\frac{1}{2\sqrt{3}}=0.289 \quad \text{(hexagonal)} \tag{5}$$

and

$$\rho_T=\frac{\sqrt{3}}{2}=0.866 \quad \text{(triangular)}. \tag{6}$$

Comparing (4) and (5) it is seen that the SCS is in close proximity to the response expected from a hexagonal network of cracks.

Contributed by the Applied Mechanics Division of THE AMERICAN SOCIETY OF MECHANICAL ENGINEERS for publication in the ASME JOURNAL OF APPLIED MECHANICS. Manuscript received by the ASME Applied Mechanics Division, January 2, 2001; final revision, October 19, 2001. Associate Editor: K. Ravi-Chandar. Discussion on the paper should be addressed to the Editor, Prof. Robert M. McMeeking, Department of Mechanical and Environmental Engineering University of California–Santa Barbara, Santa Barbara, CA 93106-5070, and will be accepted until four months after final publication of the paper itself in the ASME JOURNAL OF APPLIED MECHANICS.

  

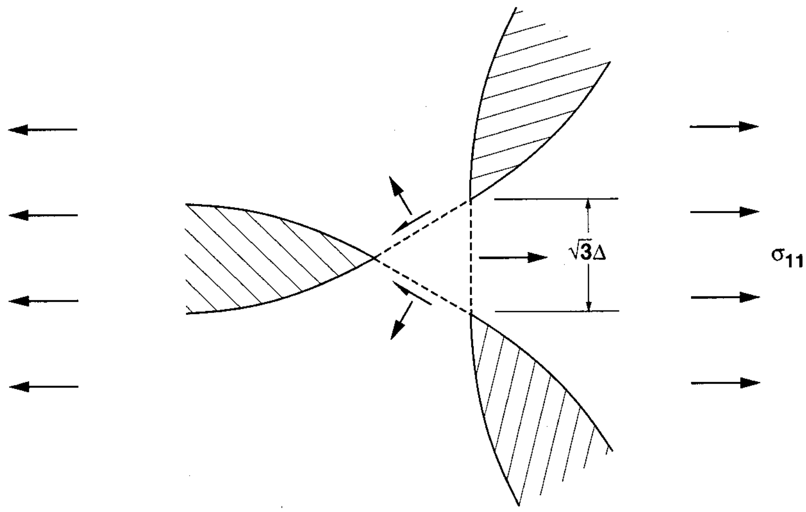


**Fig. 1 Uniaxial stress fracture pattern**

While such a pattern and corresponding behavior is highly idealized, its relationship to the SCS may be helpful toward the present objective of modeling brittle fracture.

Take the case of single size cracks and with $l=a$ establishing the crack connectivity network. Then $\rho$ and $\rho_o$ become

$$\rho=\frac{nl^2}{A} \tag{7}$$

and

$$\rho_o=\frac{na^2}{A} \tag{8}$$

where $n$ is the number of density of the cracks. With (7) and (8) there results from (1) and (2)

$$\frac{E}{E_m}=\frac{\nu}{\nu_m}=1-\left(\frac{l}{a}\right)^2. \tag{9}$$

Let $\Delta$ be the gap size where

$$l=a-\Delta. \tag{10}$$

Thus $\Delta$ is the dimensional size needed to establish continuity of the cracks. With (10), (9) takes the form

$$\frac{E}{E_m}=\frac{\nu}{\nu_m}=\left(\frac{\Delta}{a}\right)\left[2-\left(\frac{\Delta}{a}\right)\right]. \tag{11}$$

Initial consideration here will be with the fracture behavior for uniaxial tension, $\sigma_{11}$. Interest here is in the case of $(\Delta/a)$ being very small because fracture behavior near the condition of material collapse is what is being sought. Thus, only the first term in (11) need be retained as

$$\frac{E}{E_m}=\frac{\nu}{\nu_m}=2\left(\frac{\Delta}{a}\right)+O\left(\left(\frac{\Delta}{a}\right)^2\right). \tag{12}$$

The strain energy density is conveniently expressed through the effective property (12) as

$$U=\frac{\sigma_{11}^2}{4\left(\frac{\Delta}{a}\right)E_m}. \tag{13}$$

The strain energy per crack is needed at this point. From the definitions of $\rho$ and thereby $\rho_o$ and the value of $\rho_o$ from (4), the area per crack is given by

$$A=\pi a^2. \tag{14}$$

Then the strain energy per crack is

$$\hat{U}=\frac{\pi a^2\sigma_{11}^2}{4\left(\frac{\Delta}{a}\right)E_m}. \tag{15}$$

Now consider the surface energy needed to cause total material fracture under stress $\sigma_{11}$. Take the fracture pattern as shown by the dashed lines in Fig. 1. This pattern is that suggested by hexagonal symmetry, with three initial cracks near to joining at 120-deg angular intervals. The fracture pattern is taken as that which presumably has the greatest strain energy release rate as the fracture process commences. This involves crack opening under normal stress components, leading to complete material disintegration. The surface energy or work to create surface energy per initial crack follows from Fig. 1 as

$$W=4\sqrt{3}\Gamma\Delta \tag{16}$$

where $\Gamma$ is the surface energy per unit length for each surface of the newly created cracks.

Take the classical fracture condition such that the strain energy lost balances the surface energy gained by the fracture process. Then equating (15) and (16) gives

$$\sigma_{11}=\frac{4(3)^{\frac{1}{4}}}{(\pi)^{\frac{1}{2}}}\left(\frac{\Delta}{a}\right)\sqrt{\frac{E_m\Gamma}{a}}. \tag{17}$$

The result (17) in addition to requiring the characteristic crack size $l\cong a$, also requires the relative crack size for ultimate crack connectivity, specified through $(\Delta/a)$.

Now consider the state of eqibiaxial tension, $\sigma_{11}=\sigma_{22}=\sigma$. Accordingly, the properties $E$ and $\nu$ must be converted to the proper two-dimensional bulk modulus form. The identity for this conversion is given by

$$K=\frac{E}{2(1-\nu)} \tag{18}$$

where $K$ is the two-dimensional bulk modulus. Using $E$ and $\nu$ from (11) in (18) and keeping only the lowest order term in $(\Delta/a)$ gives

$$\frac{K}{E_m}=\left(\frac{\Delta}{a}\right)+O\left(\left(\frac{\Delta}{a}\right)^2\right). \tag{19}$$

The strain energy density $U=\sigma^2/2K$ then becomes

$$U=\frac{\sigma^2}{2\left(\frac{\Delta}{a}\right)E_m}. \tag{20}$$

Now using (14) the strain energy per crack is given by

$$\hat{U}=\frac{\pi a^2\sigma^2}{2\left(\frac{\Delta}{a}\right)E_m} \tag{21}$$

The hydrostatic tensile stress state has the maximum degree of symmetry. In coordination with this, take the resulting fracture pattern as also having the maximum possible degree of symmetry and similitude. Specifically for the region of initial crack confluence in Fig. 1, take the three cracks as co-linearly extending inward by distance $\Delta$ to the joining point, causing crack continuity and material collapse. The work to create the surface energy per initial crack is then given by

$$W=4\Gamma\Delta. \tag{22}$$

Forming the energy balance by equating (21) and (22) gives the eqibiaxial stress to cause fracture as

$$\sigma=2\left(\frac{2}{\pi}\right)^{1/2}\left(\frac{\Delta}{a}\right)\sqrt{\frac{E_m\Gamma}{a}}. \tag{23}$$

The two fracture criteria (17) and (23) for uniaxial and eqibiaxial stress states are thus given by

$$\sigma_{11}=2.970\left(\frac{\Delta}{a}\right)\sqrt{\frac{E_m\Gamma}{a}}$$

and

$$\sigma_{11}=\sigma_{22}=1.596\left(\frac{\Delta}{a}\right)\sqrt{\frac{E_m\Gamma}{a}}. \tag{24}$$

These two results have followed from the SCS methodology. Now, a generalization will be given.

Observe that the general form

$$\sigma_{ii}=k \quad (i,j=1,2) \tag{25}$$

very nearly includes the specific results (24). Form (25) when optimally taken to fit the results in (24) does so with a deviation of only 3.6%. This limit form, mean normal stress fracture criterion, (25), is the main result presented here. If in the derivations of the two results in (24) the fracture events were taken to be initiated by just one of the three surfaces in each case, rather than all three surfaces, then each result in (24) would be scaled by the same factor and the conclusion leading to (25) would be unchanged. Although there is some uncertainty involved with the assumed fracture patterns, the major effect is that the strain energy to be released is half as much for the uniaxial case as for the eqibiaxial case at the same stress levels, thus giving a lower fracture stress for the eqibiaxial case.

It is not implied that brittle fragmentation occurs in the highly idealized hexagonal pattern. The SCS and its relationship to the hexagonal pattern case merely provides a convenient mechanism for examining brittle behavior. The significant thing here is not the explicit formulas in (24) but rather that their ratio leads to (25). There probably would be other mechanistic ways to approach this criterion rather than through the SCS, but it is possible, but not proven, that all physical methods would approach the same limit form. Further research in this area would be of considerable interest. Although the present results are for the two dimensional case, the same general theme would appear to apply in three-dimensional form although the SCS in that case is more complex.

The very brittle material fracture criterion (25) sometimes has been used on an ad hoc basis for generally brittle materials. The present derivation, however, shows that it should only be used with considerable caution. It is intended to represent limiting case behavior, whereas most brittle materials would not be near the limit condition and would require a more comprehensive fracture criterion.

It is conceptually interesting that in the present treatment, the limiting brittle behavior for homogeneous isotropic elastic materials (under positive normal stresses) is fracture type, dilatational stress controlled. In the limiting ductile case, it is well understood that the controlling mechanism is of the yielding type, distortional stress. Thus, stress related behavior at one extreme is here suggested to be distortionally limited while the other extreme is dilatationally limited. These two opposite extreme cases would comprise a mechanistically balanced and complementary behavior.

## Acknowledgment

This work was performed under the auspices of the U.S. Department of Energy by University of California Lawrence Livermore National Laboratory under contract No. W-7405-Eng-48 and with support from the Office of Naval Research, Dr. Y. D. S. Rajapakse, program monitor.

## References

[1] Kachanov, M., 1992, ''Effective Elastic Properties of Cracked Solids: Critical Review of Some Basic Concepts,'' Appl. Mech. Rev., **45**, pp. 304–335.
[2] Kanninen, M. F., and Popelar, C. H., 1985, *Advanced Fracture Mechanics*, Oxford University Press, Oxford.
[3] Budiansky, B., and O'Connell, R. J., 1976, ''Elastic Moduli of a Cracked Solid,'' Int. J. Solids Struct., **12**, pp. 81–97.
[4] Laws, N., and Brockenbrough, J. R., 1987, ''The Effect of Microcrack Systems on Loss of Stiffness of Brittle Solids,'' Int. J. Solids Struct., **23**, pp. 1247–1268.
[5] Gottesman, T., Hashin, Z., and Brull, M. A., 1980, ''Effective Elastic Moduli of Cracked Fiber Composite Materials,'' *Advances in Composite Materials*, Proc. ICCM 3, Bunsell et al., eds., Pergamon, Oxford, pp. 749–758.

# Scattering From an Elliptic Crack by an Integral Equation Method: Normal Loading

**T. K. Saha**
Department of Mathematics,
Surendranath College,
24/2 M. G. Road,
Calcutta 700 009, India
e-mail: tksaha@cubmb.ernet.in

**A. Roy**
Department of Applied Mathematics,
University of Calcutta,
92 A. P. C. Road,
Calcutta 700 009, India
e-mail: aroy@cucc.ernet.in

*The scattering of normally incident elastic waves by an embedded elliptic crack in an infinite isotropic elastic medium has been solved using an analytical numerical method. The representation integral expressing the scattered displacement field has been reduced to an integral equation for the unknown crack-opening displacement. This integral equation has been further reduced to an infinite system of Fredholm integral equation of the second kind and the Fourier displacement potentials are expanded in terms of Jacobi's orthogonal polynomials. Finally, proper use of orthogonality property of Jacobi's polynomials produces an infinite system of algebraic equations connecting the expansion coefficients to the prescribed dynamic loading. The matrix elements contains singular integrals which are reduced to regular integrals through contour integration. The first term of the first equation of the system yields the low-frequency asymptotic expression for scattering cross section analytically which agrees completely with previous results. In the intermediate and high-frequency scattering regime the system has been truncated properly and solved numerically. Results of quantities of physical interest, such as the dynamic stress intensity factor, crack-opening displacement scattering cross section, and back-scattered displacement amplitude have been given and compared with earlier results.*
[DOI: 10.1115/1.1483834]

## 1 Introduction

Quantitative nondestructive evaluation (NDE)/quantitative nondestructive testing (NDT) is becoming the state of the art in detecting and locating cracks in material structures by the observation of the crack's effect on an externally applied ultrasonic field. To promote this to a full-fledged technology requires the solution of the direct scattering problem, i.e., calculating the response due to applied dynamic load on the structure with a known crack embedded in it. But except for highly idealized cases it is almost impossible to obtain analytical solutions to the problems. This handicap has resulted in the evolution of various numerical modeling techniques for solving scattering problems. Such techniques have been reviewed by Bond [1]. De Hoop [2] has also noted that except for the cannonical problems whose solution can be expressed in terms of analytical functions of a not too complicated nature, and for analytic approximation techniques, wave propagation and scattering problems in elastodynamics have to be addressed with the aid of numerical methods. Here we will present an analytical-numerical technique for the solution of the title problem which may be treated as a benchmark to test all numerical methods when applied to such problems of scattering from elliptic cracks.

Scattering of elastic waves from an embedded planar crack often occurs in ultrasonic nondestructive evaluation. But there are only a limited number of rigorous solutions and these have been obtained almost exclusively for the special case of scattering from penny-shaped cracks. For a brief review of the previous works related to scattering from a penny-shaped crack, one can refer to Martin and Wickham [3]. For planar cracks other than penny-shaped cracks, previous works were mostly restricted to the case of long-wavelength scattering. Most of these works were concerned with scattering from an elliptic crack (e.g., see Roy [4,5], Lin and Keer [6], Hirose [7], and Shifrin [8]). But Visscher [9] concluded that only very accurate experiments can distinguish a flat crack of general shape from a penny-shaped crack by long-wavelength elastic-wave scattering. Hence the need for mid and high-frequency scattering solution. Recently the numerical boundary integral equation method has developed into a discipline of its own and a surge of interest has been seen for solving problems of high-frequency scattering by planar cracks applying this method. Other numerical methods, like the boundary element method, variational-difference method, etc., have also been applied in parallel to solve such problems. In the recent past few work in this field has been reported in the literature and these works involve both scattering from elliptic and rectangular cracks. For details one may refer to Budreck and Achenbach [10], Nishimura and Kobayashi [11], Zhang and Gross [12], Alves and Ha Duong [13], Schafbuch et al. [14], Itou [15], Guan and Norris [16], and Glushkov and Glushkova [17] for the solution of scattering from elliptic and rectangular cracks. Also one may refer to Bostrom and Eriksson [18] for the solution of crack scattering in anisotropic and layered media.

In the present study our interest is confined to problems of scattering from embedded elliptic cracks only, and here we present an analytical-numerical method which is best suited to solve such problems in mid and high-frequency regime. A recently developed integral equation method of Roy and Chatterjee [19] has been used here for the present method. The method is to reduce the integral equation obtained from the representation integral expressing the scattered displacement field into an infinite system of algebraic equations by the judicious expansion of the Fourier displacement potentials in terms of Jacobi's orthogonal polynomials and the application of the orthogonality property of Jacobi's polynomials. The first term of the first equation of the infinite algebraic system does yield the low-frequency asymptotic for a scattering cross section which has been evaluated analytically and these results agree completely with the existing results. The algebraic system is then solved numerically for the expansion coefficients after properly truncating it. Each term of the truncated

Contributed by the Applied Mechanics Division of THE AMERICAN SOCIETY OF MECHANICAL ENGINEERS for publication in the ASME JOURNAL OF APPLIED MECHANICS. Manuscript received by the ASME Applied Mechanics Division, November 22, 2000; final revision, October 22, 2001. Associate Editor: A. K. Mal. Discussion on the paper should be addressed to the Editor, Professor Robert M. McMeeking, Department of Mechanical and Environmental Engineering University of California–Santa Barbara, Santa Barbara, CA 93106-5070, and will be accepted until four months after final publication of the paper itself in the ASME JOURNAL OF APPLIED MECHANICS.

  

matrix contains an improper integral with singularity which is reduced to a more suitable integral for numerical computation through the contour integration technique of Mal [20] and Krenk and Schmidt [21]. The complex valued expansion coefficients have been computed for a normally incident plane longitudinal wave in the mid and high-frequency regime. The quantities of physical interest, namely, the dynamic stress intensity factor, crack-opening displacement, and scattering cross section are computed for both an embedded penny-shaped crack and elliptic crack and are compared with previous results given by Mal [22], Krenk and Schmidt [21], Martin and Wickham [3], Keogh [23], Budreck and Achenbach [10], Zhang and Gross [12], and Alves and Ha Duong [13]. The convergence of the system has been tested by increasing the order of the truncated matrix step by step starting with a fourth-order truncated system and going upto a 12th-order truncated system. The crack-opening displacement for a particular crack with incident wave having a fixed frequency have been computed with results from these different truncated systems and the plots of these results reveal the convergence of the system.

## 2 The Integral Equation

Consider a homogeneous, isotropic, infinite three-dimensional elastic solid containing a finite planar crack $S$ of the elliptic shape embedded in it (Fig. 1). The crack occupies the region

$$S: \frac{x^2}{a^2}+\frac{y^2}{b^2}\leqslant 1, \quad z=0 \tag{1}$$

where '$a$' and '$b$' are the semi-major and semi-minor axis of the elliptic crack, respectively. Suppose a time-harmonic plane longitudinal wave, of angular frequency $\omega$, is the incident normally on the crack surface $S$. The time-harmonic factor is omitted throughout this paper. Let $u_i$ and $\tau_{ij}$ be the scattered displacement and stress field, respectively. Then we are to determine the scattered displacement field $\mathbf{u}$ satisfying the elastodynamic equation of motion

$$k_1^{-2}\,\text{grad div}\,\mathbf{u}-k_2^{-2}\text{curl curl}\;\;\mathbf{u}+\mathbf{u}=0 \tag{2}$$

where the wave numbers $k_1$ and $k_2$ are defined by

$$\rho\omega^2=(\lambda+2\mu)k_1^2=\mu k_2^2 \tag{3}$$

and $\lambda$, $\mu$ are Lamé constants, $\rho$ is the density of the medium, and the boundary condition on the crack faces are

$$n_j\tau_{ij}(\mathbf{x})=-n_j\tau_{ij}^{(i)}(\mathbf{x})\forall\mathbf{x}\in S^{\pm} \tag{4}$$

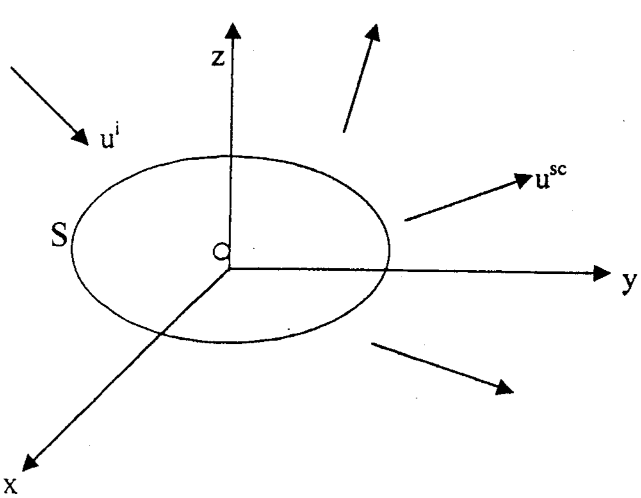


**Fig. 1 Scattering geometry of an elliptic crack. $u^i$ is the incident displacement field and $u^{sc}$ is the scattered field.**

where $\mathbf{n}$ is the unit normal vector, $\tau_{ij}^{(i)}$ is the incident stress field and $S^+$, $S^-$ are the two opposite faces of the elliptic crack.

Since the material is isotropic the elastic tensor is given by

$$C_{ijkl}=\lambda\,\delta_{ij}\delta_{kl}+\mu(\delta_{ik}\delta_{jl}+\delta_{il}\delta_{jk}) \tag{5}$$

where $\delta_{ij}$ is the Kronecker delta.

The scattered displacement field for a crack of general orientation can be expressed by the following representation integral (Martin, [24]):

$$u_k(\mathbf{x}_q)=\int\int_S u_i(\mathbf{x})\tau_{ijk}^f(\mathbf{x};\mathbf{x}_q)n_j dS-\int\int_S G_{ik}^f(\mathbf{x};\mathbf{x}_q)\tau_{ij}(\mathbf{x})n_j dS \tag{6}$$

where $\mathbf{x}_q$ is the position vector of the observation point, $\mathbf{x}$ denotes the position vector of the source point, and $\tau_{ijk}^f$ is the stress tensor corresponding to fundamental Green's tensor $G_{ij}^f$ given by

$$G_{ij}^f(\mathbf{x};\mathbf{x}_q)=\mu^{-1}\left\{\delta_{ij}\Psi+k_2^{-2}\frac{\partial^2}{\partial x_i\partial x_j}(\Psi-\Phi)\right\} \tag{7}$$

$$\Phi=\frac{e^{ik_1R}}{4\pi R},\quad \Psi=\frac{e^{ik_2R}}{4\pi R},\quad R=|\mathbf{x}-\mathbf{x}_q|, \tag{8}$$

$$\tau_{ij}(\mathbf{x})=C_{ijkl}\frac{\partial u_l(\mathbf{x})}{\partial x_k} \tag{9}$$

and

$$\tau_{ijm}^f(\mathbf{x};\mathbf{x}_q)=C_{ijkl}\frac{\partial G_{lm}^f(\mathbf{x};\mathbf{x}_q)}{\partial x_k}. \tag{10}$$

Now, since $\tau_{ij}$, $G_{ij}^f$, $\tau_{ijk}^f$ are continuous across $S$, we get

$$u_k(\mathbf{x}_q)=\int\int_S [u_i(\mathbf{x})]\tau_{ijk}^f(\mathbf{x};\mathbf{x}_q)n_j dS \tag{11}$$

where $[u_i(\mathbf{x})]=u_i^+(\mathbf{x})-u_i^-(\mathbf{x})$ is the crack-opening displacement.

Applying the boundary condition then reduces the determination of $[u_i(\mathbf{x})]$ to the solution of the following integro-differential equation:

$$-n_k\tau_{kl}^{(i)}(\mathbf{x}')=n_kC_{klmn}\frac{\partial}{\partial x_m}\int\int_S[u_i(\mathbf{x})]\tau_{ijn}^f(\mathbf{x};\mathbf{x}_q)n_j dS|\mathbf{x}_q=\mathbf{x}'. \tag{12}$$

Equation (12) is valid for any arbitrary crack surface $S$, but we are interested in scattering from elliptic cracks only. In this case Eq. (12) partially decouples and the normal displacement discontinuity satisfies the following integro-differential equation (Roy [5]):

$$4\left[\left(\frac{\partial^2}{\partial x^2}+\frac{\partial^2}{\partial y^2}\right)^2+k_2^2\left(\frac{\partial^2}{\partial x^2}+\frac{\partial^2}{\partial y^2}\right)\right]\int\int_S\frac{[u_z]}{4\pi R}(e^{ik_1R}-e^{ik_2R})dS$$
$$+k_2^4\int\int_S\frac{[u_z]}{4\pi R}e^{ik_1R}dS=\frac{\tau_{zz}^{(i)}}{\mu}. \tag{13}$$

Now, we have the well-known integral representation:

$$\frac{e^{ik_jR}}{R}=\frac{1}{2\pi}\int_{-\infty}^{\infty}\int_{-\infty}^{\infty}\frac{\exp[i\xi(x-x')+i\eta(y-y')]}{\nu_j}d\xi d\eta$$
$$(j=1,2) \tag{14}$$

where

$$R=[(x-x')^2+(y-y')^2]^{1/2}$$

and

$$\nu_j=(\xi^2+\eta^2-k_j^2)^{1/2},\quad \text{Re}(\nu_j)>0(j=1,2). \tag{15}$$

Substituting (14) in (13) we get the following integral equation:

$$\frac{1}{2\pi}\int_{-\infty}^{\infty}\int_{-\infty}^{\infty}\int\int_{S}[u_z]\frac{(2\lambda_0^2-k_2^2)^2-4\lambda_0^2\nu_1\nu_2}{2\nu_1}$$
$$\times\exp[i\{\xi(x-x')+\eta(y-y')\}]dx'dy'd\xi d\eta$$
$$=\frac{2\pi\tau_{zz}^{(i)}(x,y)}{\mu} \tag{16}$$

where

$$\lambda_0=(\xi^2+\eta^2)^{1/2}. \tag{17}$$

Now, we introduce a normalized crack-opening displacement related to $[u_z(x',y')]$ through the relation

$$w(x',y')=k_2^2(1-\sigma^2)^2[u_z(x',y')] \tag{18}$$

where

$$\sigma=\frac{k_1}{k_2}=\frac{c_2}{c_1} \tag{19}$$

where $c_1$, $c_2$ are the $P$ and $S$ wave velocities, respectively, given by

$$c_1=\left(\frac{\lambda+2\mu}{\rho}\right)^{1/2},\quad c_2=\left(\frac{\mu}{\rho}\right)^{1/2}. \tag{20}$$

We get the integral equation in the form

$$\frac{1}{2\pi}\int_{-\infty}^{\infty}\int_{-\infty}^{\infty}\int\int_{S}\lambda_0[1+F(\xi,\eta)]w(x',y')$$
$$\times\exp[i\{\xi(x-x')+\eta(y-y')\}]dx'dy'd\xi d\eta$$
$$=-\frac{2\pi\tau_{zz}^{i}(x,y)}{\mu} \tag{21}$$

where

$$1+F(\xi,\eta)=-\frac{(2\lambda_0^2-k_2^2)^2-4\lambda_0^2\nu_1\nu_2}{2k_2^2(1-\sigma^2)^2\nu_1\lambda_0}. \tag{22}$$

## 3 Fredholm's Integral Equations of the Second Kind

Fredholm's integral equations of the second kind are obtained following the reduction procedure of Roy and Chatterjee [19].

The Cartesian coordinate system is transformed to cylindrical polar coordinate system through the following set of transformations:

$$(x,y)=(ar\cos\theta,br\sin\theta)$$
$$(x',y')=(a\rho\cos\phi,b\rho\sin\phi). \tag{23}$$

We assume that the normalized crack-opening displacement $w(x',y')$ and the prescribed stress $\tau_{zz}^{(i)}(x,y)$ have complete Fourier series expansion of the form

$$[w(x',y'),\tau_{zz}^{(i)}(x',y')]=\sum_{n=0}^{\infty}[w_n(\rho),t_n(\rho)]\cos n\phi$$
$$+\sum_{n=1}^{\infty}[\overline{w}_n(\rho),\overline{t}_n(\rho)]\sin n\phi. \tag{24}$$

The following transformation is also made:

$$(\xi a,\eta b)=(k\cos\chi,k\sin\chi)\quad(0<k<\infty;0\leqslant\chi\leqslant 2\pi). \tag{25}$$

Use of standard representation for $\exp(\pm iz\cos\theta)$ in terms of Bessel function and application of the orthogonality property of trigonometric functions then gives rise to infinite systems of integral equations involving $w_n(\rho)$, $\overline{w}_n(\rho)$. Further reduction is affected by relating $w_n(\rho)$, $\overline{w}_n(\rho)$ to displacement potentials $\Phi_n(t)$, $\overline{\Phi}_n(t)$ through the following Abelian transformations:

$$[w_n(\rho),\overline{w}_n(\rho)]=\rho^nA_n[t^{-n}\{\Phi_n(t),\overline{\Phi}_n(t)\};\rho] \tag{26}$$

and

$$[\Phi_n(t),\overline{\Phi}_n(t)]=t^nA_n^{-1}[\rho^{-n}\{w_n(\rho),\overline{w}_n(\rho)\};t] \tag{27}$$

where

$$A_n[f(t);\rho]=\frac{2}{\pi}\int_{\rho}^{1}\frac{f(t)dt}{(t^2-\rho^2)^{1/2}}$$

and

$$A_n^{-1}[g(\rho);t]=-\frac{d}{dt}\int_{t}^{1}\frac{\rho g(\rho)d\rho}{(\rho^2-t^2)^{1/2}}.$$

Using standard results on Bessel functions (Roy and Chatterjee, [19]) one finally obtains the following sets of Fredholm integral equations of the second kind: $\forall s=0,1,2,\ldots,\infty$, $(n+s)$ even; $\xi\in[0,1]$

$$\begin{pmatrix}I_{s,s}^{c}\Phi_s(\xi)\\ I_{s,s}^{s}\overline{\Phi}_s(\xi)\end{pmatrix}+\sum_{\substack{n=0\\ n\neq s}}^{\infty}\int_0^1L_{n,s}(\xi,t)\begin{pmatrix}I_{n,s}^{c}\Phi_n(t)\\ I_{n,s}^{s}\overline{\Phi}_n(t)\end{pmatrix}dt$$
$$+\sum_{n=0}^{\infty}\begin{pmatrix}K_{n,s}[\Phi_n(t)]\\ \overline{K}_{n,s}[\overline{\Phi}_n(t)]\end{pmatrix}=\begin{pmatrix}F_s(\xi)\\ \overline{F}_s(\xi)\end{pmatrix} \tag{28}$$

where

$$\begin{pmatrix}I_{n,s}^{c}\\ I_{n,s}^{s}\end{pmatrix}=\frac{1}{2}i^s(-i)^n\int_0^{2\pi}(1-k_0^2\cos^2\chi)^{1/2}\begin{pmatrix}\cos n\chi\cos s\chi\\ \sin n\chi\sin s\chi\end{pmatrix}d\chi \tag{29}$$

$$k_0^2=\left(1-\frac{b^2}{a^2}\right) \tag{30}$$

$$L_{n,s}(\xi,t)=(\xi t)^{1/2}\int_0^{\infty}kJ_{n+1/2}(kt)J_{s+1/2}(k\xi)dk \tag{31}$$

$$\begin{pmatrix}K_{n,s}[\Phi_n(t)]\\ \overline{K}_{n,s}[\overline{\Phi}_n(t)]\end{pmatrix}=\frac{1}{2}i^s(-i)^n\int_0^{\infty}\int_0^{2\pi}\int_0^1k(\xi t)^{1/2}$$
$$\times F(k,\chi)(1-k_0^2\cos^2\chi)^{1/2}$$
$$\times J_{n+1/2}(kt)J_{s+1/2}(k\xi)$$
$$\times\begin{pmatrix}\Phi_n(t)\cos n\chi\cos s\chi\\ \overline{\Phi}_n(t)\sin n\chi\sin s\chi\end{pmatrix}dtd\chi dk \tag{32}$$

$$\begin{pmatrix}F_s(\xi)\\ \overline{F}_s(\xi)\end{pmatrix}=-\frac{\pi b\xi^{-s}}{\mu\epsilon_s}\int_0^{\xi}\frac{r^{s+1}}{(\xi^2-r^2)^{1/2}}\begin{pmatrix}t_s(r)\\ \overline{t}_s(r)\end{pmatrix}dr. \tag{33}$$

## 4 Reduction to Algebraic Systems of Equations

Part of the reduction follows from Roy and Saha [25]. The displacement potentials are expanded in term of Jacobi polynomials as

$$[\Phi_n(t),\overline{\Phi}_n(t)]=\sum_{j=0}^{\infty}[W_j^n,\overline{W}_j^n]t^{s+1}P_j^{(s+1/2,0)}(1-2t^2). \tag{34}$$

Then following Roy and Saha [25], Eq. (28) reduces to

$\forall s=0,1,2,\ldots,\infty$, $(n+s)$ even; $\xi,r\in[0,1]$

$$\sum_{n=0}^{\infty}\sum_{j=0}^{\infty}\begin{pmatrix}I_{n,s}^{c}W_j^n\\ I_{n,s}^{s}\overline{W}_j^n\end{pmatrix}\xi^{s+1}P_{j-(s-n)/2}^{(s+1/2,0)}(1-2\xi^2)+\sum_{n=0}^{\infty}\begin{pmatrix}K_{n,s}[\Phi_n(t)]\\ \overline{K}_{n,s}[\overline{\Phi}_n(t)]\end{pmatrix}$$
$$=\begin{pmatrix}F_s(\xi)\\ \overline{F}_s(\xi)\end{pmatrix}. \tag{35}$$

For $K_{n,s}[.]$ and $\overline{K}_{n,s}[.]$, the following transformation is made:

$$(k\cos\chi, k\sin\chi)=(au\cos\psi, bu\sin\psi). \tag{36}$$

Then, writing

$$p=(1-k_0^2\sin^2\psi)^{1/2}, \tag{37}$$

and after making use of the following result (Gradshteyn and Ryzhik, [26])

$$\int_0^1 t^{n+3/2}P_j^{(n+1/2,0)}(1-2t^2)J_{n+1/2}(aput)dt=\frac{J_{2j+n+3/2}(apu)}{apu}, \tag{38}$$

both sides of (35) are multiplied by $\xi P_m^{(s+1/2,0)}(1-2\xi^2)$ and integrated with respect to $\xi$ between 0 and 1 and the following orthogonality property of Jacobi's polynomial is used (Gradshteyn and Ryzhik, [26]):

$$\int_0^1 t^{2s+2}P_j^{(s+1/2,0)}(1-2t^2)P_k^{(s+1/2,0)}(1-2t^2)dt=\frac{\delta_{jk}}{2s+4j+3} \tag{39}$$

to obtain the following set of algebraic equations:

$\forall s=0,1,2,\ldots,\infty,\ (n+s)$ even

$$\sum_{n=0}^{s-2}\begin{pmatrix} I^c_{n,s}W^n_{m+(s-n)/2}\\ I^s_{n,s}\overline{W}^n_{m+(s-n)/2}\end{pmatrix}+\begin{pmatrix} I^c_{s,s}W^s_m\\ I^s_{s,s}\overline{W}^s_m\end{pmatrix}+\sum_{n=s+2}^{2m+s}\begin{pmatrix} I^c_{n,s}W^n_{m-(n-s)/2}\\ I^s_{n,s}\overline{W}^n_{m-(n-s)/2}\end{pmatrix}$$

$$+(4m+2s+3)\sum_{n=0}^{\infty}\sum_{j=0}^{\infty}\frac{1}{2}i^s(-i)^n\frac{b^2}{a^2}\int_0^{2\pi}\int_0^{\infty}p^{-3}u^{-1}$$

$$\times F(u)J_{2j+n+3/2}(apu)J_{2m+s+3/2}(apu)$$

$$\times\begin{pmatrix} W^n_j\cos[n\tan^{-1}(\frac{b}{a}\tan\psi)]\cos[s\tan^{-1}(\frac{b}{a}\tan\psi)]\\ \overline{W}^n_j\sin[n\tan^{-1}(\frac{b}{a}\tan\psi)]\sin[s\tan^{-1}(\frac{b}{a}\tan\psi)]\end{pmatrix}dud\psi$$

$$=(4m+2s+3)\int_0^1\xi^{s+1}P_m^{(s+1/2,0)}(1-2\xi^2)\begin{pmatrix}F_s(\xi)\\ \overline{F}_s(\xi)\end{pmatrix}d\xi \tag{40}$$

where

$$F(u)=-1-\frac{(2u^2-k_2^2)^2-4u^2(u^2-k_1^2)^{1/2}(u^2-k_2^2)^{1/2}}{2uk_2^2(1-\sigma^2)^2(u^2-k_1^2)^{1/2}}. \tag{41}$$

Let

$$I=\int_0^{\infty}\left[-\frac{1}{u}-\frac{4}{2k_2^2(1-\sigma^2)^2}\left\{\frac{\left(u^2-\frac{1}{2}k_2^2\right)^2}{u^2(u^2-k_1^2)^{1/2}}-(u^2-k_2^2)^{1/2}\right\}\right]$$

$$\times J_{w+1/2}(apu)J_{x+1/2}(apu)du \tag{42}$$

where $w=2j+n+1$ and $x=2m+s+1$.

This integral can be recast into a form more suitable for numerical integration. The principle is to extend the integrand into the complex half-plane $\mathrm{Re}\{u\}\geqslant 0$ and to use contour integration. The procedure is taken from Mal [20] and Krenk and Schmidt [21].

For $w\geqslant x$, the result is

$$I=\frac{1}{\sigma^2(1-\sigma^2)^2}\int_0^1\left[\frac{i(2\sigma^2\xi^2-1)^2}{2\xi^2(1-\xi^2)^{1/2}}J_{w+1/2}(apk_1\xi)\right.$$

$$\left.\times H^{(2)}_{x+1/2}(apk_1\xi)+\frac{1}{\pi(2w+1)}\frac{\delta_{wx}}{\xi^2(1-\xi^2)^{1/2}}\right]d\xi+\frac{2i}{(1-\sigma^2)^2}$$

$$\times\int_0^1(1-\xi^2)^{1/2}J_{w+1/2}(apk_2\xi)H^{(2)}_{x+1/2}(apk_2\xi)d\xi$$

$$-\frac{8_{j+n-s/2,m}}{(4m+2s+3)}. \tag{43}$$

For $w<x$ one must interchange $w$ and $x$ in (43).

Substituting (43) in (40) and noting that

$$\frac{1}{2}i^s(-i)^n\frac{b^2}{a^2}\int_0^{2\pi}(1-k_0^2\sin^2\psi)^{-3/2}$$

$$\times\begin{pmatrix}\cos[n\tan^{-1}(\frac{b}{a}\tan\psi)]\cos[s\tan^{-1}(\frac{b}{a}\tan\psi)]\\ \sin[n\tan^{-1}(\frac{b}{a}\tan\psi)]\sin[s\tan^{-1}(\frac{b}{a}\tan\psi)]\end{pmatrix}d\psi$$

$$=\begin{pmatrix}I^c_{n,s}\\ I^s_{n,s}\end{pmatrix}. \tag{44}$$

Eq. (40) may be written as

$\forall s=0,1,2,\ldots,\infty,\ (n+s)$ even and $\forall m\geqslant 0$

$$\sum_{n=0}^{\infty}\sum_{j=0}^{\infty}\frac{1}{2}(-1)^{3(n+s)/2}\frac{b^2}{a^2}\int_0^{2\pi}p^{-3}$$

$$\times\begin{pmatrix} W^n_j\cos[n\tan^{-1}(\frac{b}{a}\tan\psi)]\cos[s\tan^{-1}(\frac{b}{a}\tan\psi)]\\ \overline{W}^n_j\sin[n\tan^{-1}(\frac{b}{a}\tan\psi)]\sin[s\tan^{-1}(\frac{b}{a}\tan\psi)]\end{pmatrix}$$

$$\times C^{ns}_{jm}(\psi)d\psi=\int_0^1\xi^{s+1}P_m^{(s+1/2,0)}(1-2\xi^2)\begin{pmatrix}F_s(\xi)\\ \overline{F}_s(\xi)\end{pmatrix}d\xi \tag{45}$$

where $C^{ns}_{jm}(\psi)$ is obtained from (43) by deleting the last term and replacing the values of $w$ and $x$. The detailed calculation of $C^{ns}_{jm}(\psi)$ is given in the Appendix.

## 5 Low-Frequency Asymptotic for Scattering Cross Section

In the present and subsequent discussions we take the incident stress field corresponding to the normally incident plane $P$-wave as

$$\tau^i_{zz}=ik_1(\lambda+2\mu)A_0 \tag{46}$$

so that

$$t_0(r)=ik_1(\lambda+2\mu)A_0$$
$$t_s(r)=\overline{t_s}(r)\equiv 0\,\forall s\geqslant 1. \tag{47}$$

Hence, in the present situation

$$\overline{W}^n_j\equiv 0\,\forall n\geqslant 1\ \text{ and }\ j\geqslant 0, \tag{48}$$

so there is no contribution to the physical quantities from the second algebraic system of Eq. (45). All subsequent results are obtained under this incident field with $A_0=1/ik_1$.

Here we obtain an analytical expression of the low-frequency asymptotic for scattering cross-section.

Putting $s=0$, $m=0$, $n=0$, $j=0$ in the first algebraic system of Eq. (45) we get

$$\frac{1}{2}\frac{b^2}{a^2}\int_0^{2\pi}p^{-3}W^0_0C^{00}_{00}(\psi)d\psi=\int_0^1\xi P_0^{(1/2,0)}(1-2\xi^2)F_0(\xi)d\xi. \tag{49}$$

Using the expression for $t_0(r)$ from (47) we get

$$\text{right-hand side of }(49)=-\frac{\pi b}{3}\frac{2(1-\nu)}{(1-2\nu)}. \tag{50}$$

For the left-hand side of (49) we retain terms in $C^{00}_{00}(\psi)$ up to $k_i^3$, $(i=1,2)$ only because the $k_i$s are small. Hence, after some simplification we get

$$C^{00}_{00}(\psi)=\frac{1}{3}-\frac{a^2p^2k_1^2(2-4\sigma^2+3\sigma^4)+a^2p^2k_2^2\sigma^2}{30\sigma^2(1-\sigma^2)^2}$$
$$+i\frac{a^3p^3k_1^3(15-40\sigma^2+32\sigma^4)+8a^3p^3k_2^3\sigma^2}{135\pi\sigma^2(1-\sigma^2)^2}. \tag{51}$$

Substituting this value of $C_{00}^{00}(\psi)$ at the left-hand side of (49) and noting that $W_0^0$ is complex valued we obtain, after separating the real and imaginary parts from both sides of (49), and solve

$$\text{real part of } W_0^0 = -\frac{3\pi b}{4\sigma^2 E^2(k_0)}\left[\frac{2}{3}E(k_0) + \frac{b^2\{k_1^2(2-4\sigma^2+3\sigma^4)+k_2^2\sigma^2\}}{15\sigma^2(1-\sigma^2)^2}F(k_0)\right] \quad (52)$$

and

$$\text{imaginary part of } W_0^0 = \frac{3\pi a b^3 k_2^4}{4k_1 E^2(k_0)}\left[\frac{8+15\sigma-40\sigma^3+32\sigma^5}{135\sigma(1-\sigma^2)^2}\right]. \quad (53)$$

Now, a scattering cross section is a measure of an obstacle's ability to scatter the incident field. Following Budreck and Achenbach [10] the normal displacement of the far-field scattered longitudinal wave has the form

$$u_3^{sc}(\mathbf{x}) \sim u(\psi)\frac{\exp(ik_1 r)}{4\pi r} \text{ as } r\to\infty, \quad (54)$$

where $\psi$ is the angle of observation in the $(x_\alpha, x_3)$-plane ($\alpha=1,2$) as measured from the $x_3$-axis, $|\mathbf{x}|=r$ and

$$u(\psi) = -ik_1[2\sigma^2\cos^2\psi + (1-2\sigma^2)] \times \cos\psi \int\int_S \exp(-ik_1 \sin\psi) w(x',y')\,dS. \quad (55)$$

For normal observation, $\psi=0$, so that

$$u(0) = -ik_1\int\int_S w(x',y')\,dS. \quad (56)$$

For an elliptic crack

$$\int\int_S w(x',y')\,dS = \frac{4ab}{3}W_0^0. \quad (57)$$

Now, the scattering cross section is given by

$$\Sigma_P = \mathrm{Re}[u(0)]. \quad (58)$$

Hence the dimensionless scattering cross section for an elliptic crack is

$$\frac{\Sigma_P}{\pi ab} = \mathrm{Re}\left[-\frac{4}{3\pi}ik_1 W_0^0\right] \quad (59)$$

which is also the expression of dimensionless scattering cross section for a circular crack. Hence applying the expression for the imaginary part of $W_0^0$ from (53) in the above expression we get the low-frequency asymptotic for the dimensionless scattering cross section as

$$\frac{\Sigma_P}{\pi ab} = \frac{ab^3k_2^4(8+15\sigma-40\sigma^3+32\sigma^5)}{135\sigma(1-\sigma^2)^2E^2(k_0)} \quad (60)$$

which agrees exactly with the same expressions given earlier by Roy [4]. Putting $a=b$ in this expression and noting that $E(k_0)=\pi/2$ for $a=b$ we get back the result of the scattering cross section for a penny-shaped crack given earlier by Robertson [27] and Piau [28]. Thus we conclude that the present method does yield the known asymptotic approximation analytically.

## 6 Quantities of Physical Interest

We give here the formulas for computing the quantities of physical interest, namely, the dynamic crack-opening displacement, dynamic stress intensity factor, scattering cross section, and back-scattered displacement amplitude for an elliptic crack in the mid and high-frequency regime in terms of the unknown displacement coefficients $W_j^n$.

**6.1 Dynamic Crack-Opening Displacement.** Using the following results (Gradshteyn and Ryzhik, [26])

$$P_j^{(n+1/2,0)}(1-2t^2) = (-1)^j F\left(j+n+\frac{3}{2},-j;1;1-t^2\right) \quad (61)$$

and

$$\int_0^1 (1-x)^{\mu-1}x^{\nu-1}F(a_1,a_2;\nu;ax)\,dx = \frac{\Gamma(\mu)\Gamma(\nu)}{\Gamma(\mu+\nu)}F(a_1,a_2;\mu+\nu;a) \quad (62)$$

$$(\mathrm{Re}\ \mu>0, \mathrm{Re}\ \nu>0 \ \text{ and } \ |a|<1)$$

where $F(.,.;.;.)$ is the hypergeometric function, the normalized dynamic crack-opening displacement for an elliptic crack is obtained from (18) as

$$w(x',y') \equiv w(\rho,\phi) = \frac{2}{\pi}\sum_{n=0}^{\infty}\rho^n\sqrt{1-\rho^2}\left[\sum_{j=0}^{\infty}(-1)^j W_j^n \times F\left(j+n+\frac{3}{2},-j;\frac{3}{2};1-\rho^2\right)\right]\cos n\phi. \quad (63)$$

Now applying the result (Gradshteyn and Ryzhik [26])

$$C_{2n+1}^{\lambda}(t) = \frac{(-1)^n 2t}{B(\lambda,n+1)}F\left(-n,n+\lambda+1;\frac{3}{2};t^2\right) \quad (64)$$

where $C_n^{\lambda}(.)$ is the Gegenbauer polynomial and $B(.,.)$ is the beta function, and noting that for $s$ even, $n$ is even, we get

$$w(x',y') \equiv w(\rho,\phi) = \frac{1}{\pi}\sum_{m=0}^{\infty}\sum_{j=0}^{\infty}W_j^{2m}\frac{j!\,\Gamma\left(2m+\frac{1}{2}\right)}{\Gamma\left(2m+j+\frac{3}{2}\right)} \times C_{2j+1}^{2m+1/2}((1-\rho^2)^{1/2})\rho^{2m}\cos 2m\phi \quad (65)$$

which coincides with the result for static crack-opening displacement for an elliptic crack given by Martin [29], except for a constant.

The normalized dynamic crack-opening displacement for a circular crack is given by

$$w(x',y') = \frac{2}{\pi}\sqrt{1-\rho^2}\sum_{j=0}^{\infty}(-1)^j W_j^0 F\left(j+\frac{3}{2},-j;\frac{3}{2};1-\rho^2\right). \quad (66)$$

It must be noted that $W_j^n$ are complex valued so that $w(x',y')$ is also so.

The exact solution of the static crack-opening displacement for a circular crack has been given by Sneddon [30]. So that the dimensionless dynamic crack-opening displacement for circular crack is

$$\frac{(1-2\nu)\pi}{4a(1-\nu)}|w(x',y')|. \quad (67)$$

Similarly the dimensionless dynamic crack-opening displacement for an elliptic crack is given by

$$\frac{(1-2\nu)E(k_0)}{2b(1-\nu)}|w(x',y')| \tag{68}$$

where $w(x',y')$ is given above, and now the exact solution of the static problem for an elliptic crack is obtained from Mura [31].

**6.2 Dynamic Stress Intensity Factor.** Following Roy and Chatterjee [19], the dynamic stress intensity factor for an elliptic crack is given by

$$K_I(\phi)=\frac{2\mu}{\pi(1-\nu)b}\left(\frac{b}{a}\right)^{1/2}(a^2\sin^2\phi+b^2\cos^2\phi)^{1/4} \times\left[\sum_{n=0}^{\infty}\Phi_n(1)\cos n\phi+\sum_{n=1}^{\infty}\bar{\Phi}_n(1)\sin n\phi\right] \tag{69}$$

which in the present case reduces to

$$K_I(\phi)=\frac{2\mu}{\pi(1-\nu)b}\left(\frac{b}{a}\right)^{1/2}(a^2\sin^2\phi+b^2\cos^2\phi)^{1/4} \times\sum_{n=0}^{\infty}\sum_{j=0}^{\infty}(-1)^jW_j^n\cos n\phi. \tag{70}$$

The corresponding expression for a circular crack is

$$K_I(\phi)=\frac{2\mu}{\pi(1-\nu)\sqrt{a}}\sum_{j=0}^{\infty}(-1)^jW_j^0. \tag{71}$$

Hence the nondimensional dynamic stress intensity factor for an elliptic and circular crack, obtained by dividing the norm of $K_I(\phi)$ by the corresponding static value $K_I^s$, are respectively,

$$\frac{(1-2\nu)E(k_0)}{\pi b(1-\nu)}\left|\sum_{n=0}^{\infty}\sum_{j=0}^{\infty}(-1)^jW_j^n\cos n\phi\right| \tag{72}$$

and

$$\frac{(1-2\nu)}{2a(1-\nu)}\left|\sum_{j=0}^{\infty}(-1)^jW_j^0\right|. \tag{73}$$

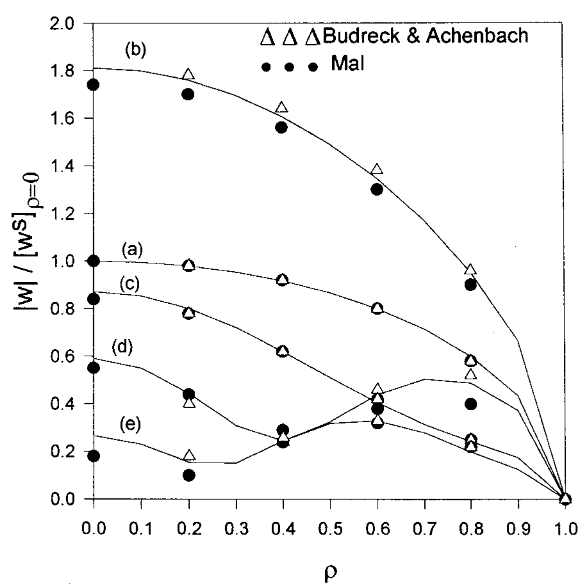


**Fig. 2 Present method (lines), BIEM (triangles), and Mal (bullets) nondimensional dynamic crack-opening displacement for circular crack for $k_2a$ equal to (*a*) 0.0; (*b*) 1.4; (*c*) 3.2; (*d*) 4.4; and (*e*) 6.0.**

**6.3 Scattering Cross Section and Back-Scattered Displacement Amplitude.** The expression for dimensionless scattering cross section for both elliptic and circular cracks are given by the single expression of Eq. (59).

The norm of the dimensionless back-scattered displacement amplitude is given by

$$\left|\frac{u(0)}{A}\right|,$$

i.e.,

$$\left|-\frac{4ik_1}{3\pi}W_0^0\right|, \tag{74}$$

where $A$ represents the area of the crack surface.

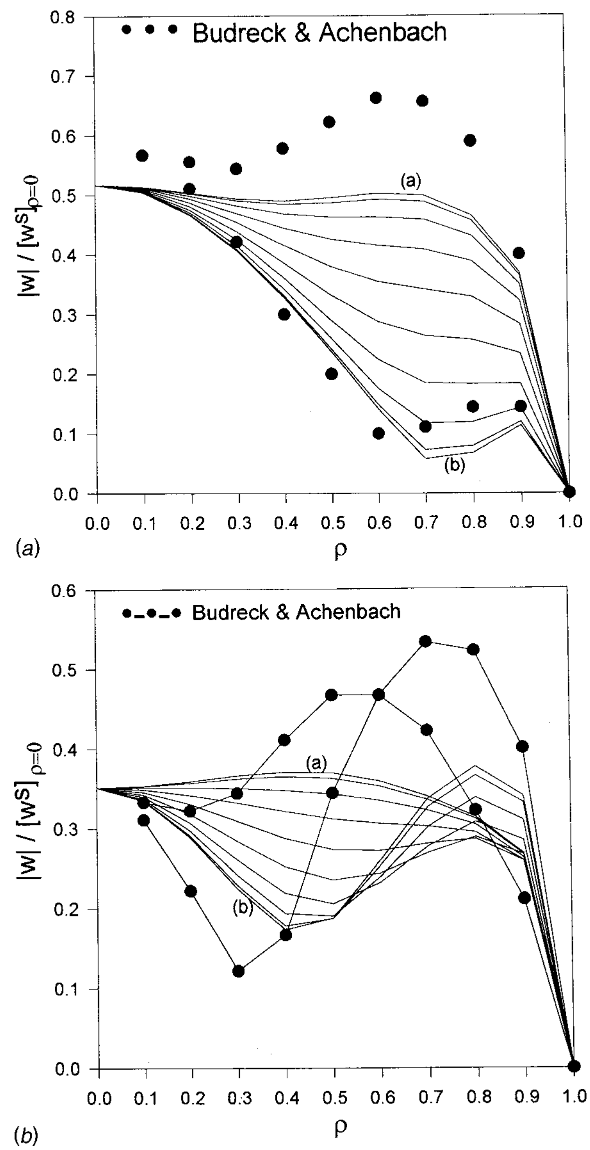


**Fig. 3 (*a*) Dimensionless crack-opening displacement of an 1:1/$\sqrt{2}$ elliptic crack with $k_2a$ equal to 4.5. (*b*) Dimensionless crack-opening displacement of an 1:1/$\sqrt{2}$ elliptic crack with $k_2a$ equal to 5.5.**

## 7 Numerical Results

Numerical results of various quantities of physical interest, which are given in the previous section, are presented for both penny-shaped and elliptic cracks in the mid and high-frequency regime.

**7.1 Dynamic Crack-Opening Displacement.** Figure 2 shows the ratio of the norm of the complex normalized crack-opening displacement for a circular crack and the corresponding (i.e., due to the same stress amplitude) static crack-opening displacement evaluated at the crack's center. The results are for Poisson's ratio 0.25 and for $k_2a=0.0$, 1.4, 3.2, 4.4, and 6.0.

The dimensionless crack-opening displacements for a circular crack computed by the present method are compared to those presented by Mal [22] and Budreck and Achenbach [10]. It is seen that the present results match well with the results of Mal [22] and Budreck and Achenbach [10]. Oscillations in the curves at mid frequencies indicate multiple reflections inside the crack as interpreted by Mal [22]. At low frequency the dynamic crack-opening displacement is greater than that for the static case but at mid frequencies this goes down below the static crack-opening displacement.

In Fig. 3 the same quantity of Fig. 2 has been plotted against $\rho$ for an elliptic crack of aspect ratio $1:1/\sqrt{2}$. It shows plottings for two distinct frequencies viz. $k_2a=4.5$ and 5.5. Due to the symmetric nature of the crack-opening displacement with respect to the $x$ and $y$-axis in this case, results are presented for only the first quarter of the crack. The lines marked (a) and (b) represent data for $\phi=0$ deg and $\phi=90$ deg, respectively, and these are compared with those presented by Budreck and Achenback [10]. The plottings given by us and Budreck and Achenbach [10] differ significantly. This may be due to the fact that the data of Budreck and Achenbach [10] were obtained at the centroid of each element into which the crack was meshed. The question that now naturally arises is whether the present scheme converges or not. A theoretical discussion regarding the convergence of the present scheme is out of scope of the present study. We expect to persue it later. However, for the present we verify the convergence of the scheme through a numerically particular example. The data plotted in Fig. 3($b$) are replotted in Fig. 4 for $\phi=0$ deg and $\phi=90$ deg after truncating the infinite system to a fourth order, sixth order, and eight-order matrix equation, respectively. It is obvious from the plotting that the present scheme does converge.

Figure 5 shows the same quantity plotted against $\rho$ as in Fig. 3 except that now the plotting is for two distinct frequency viz. $k_2a=4.5$ and 5.5 with the elliptic crack having aspect ratio 1:1/2. The markings in Figs. 5($a$) and ($b$) represent data between $\phi=0$ deg and $\phi=90$ deg, i.e., along the $x$-axis and $y$-axis, respectively. The dependence of the crack-opening displacement on the shape of the crack and on the frequency of the incident wave is clear from the figures. The highest value of the crack-opening displacement is attained along the major axis. Also the general trend is the higher the frequency lower the crack-opening displacement.

**7.2 Dynamic Stress Intensity Factor.** Figure 6 shows the results of a nondimensional dynamic stress intensity factor for a

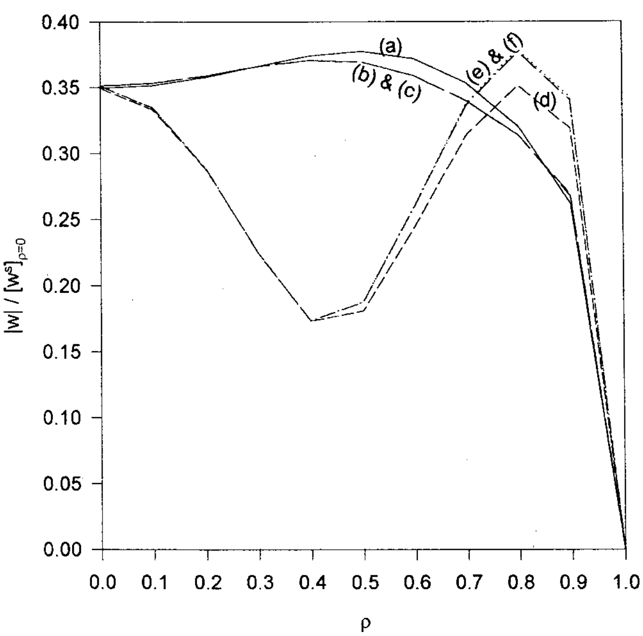


**Fig. 4 Dimensionless crack-opening displacement of an $1:1/\sqrt{2}$ elliptic crack with $k_2a$ equal to 5.5 ($a$) fourth-order system $\phi=0$ deg; ($b$) sixth-order system $\phi=0$ deg; ($c$) eighth-order system $\phi=0$ deg; ($d$) fourth-order system $\phi=90$ deg; ($e$) sixth-order system $\phi=90$ deg; ($f$) eighth-order system $\phi=90$ deg**

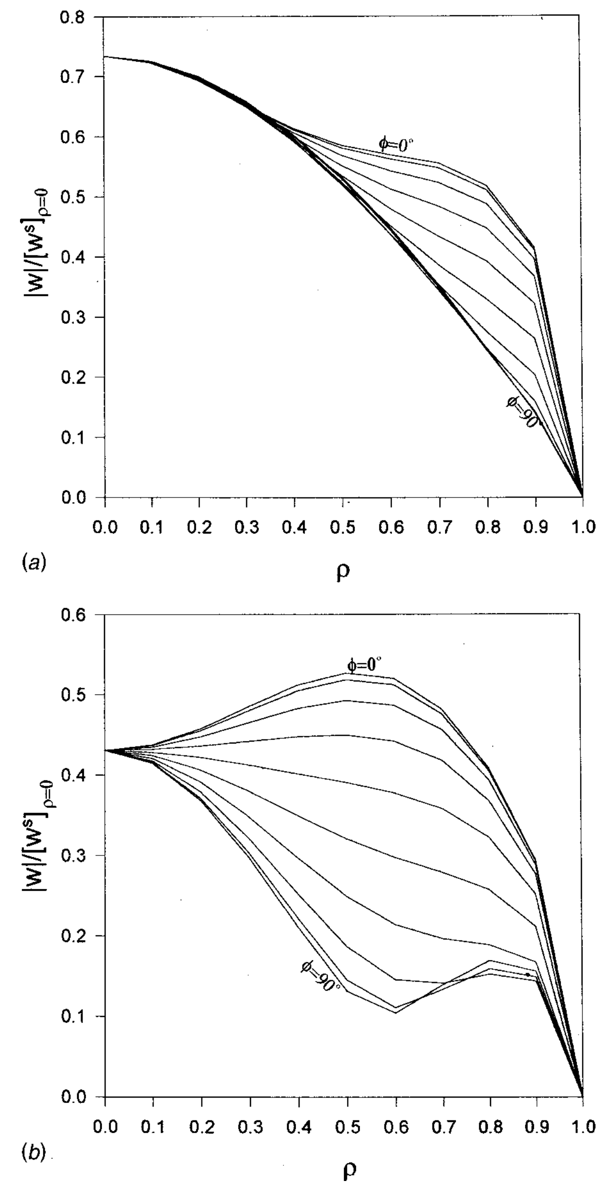


**Fig. 5 ($a$) Dimensionless crack-opening displacement of an 1:1/2 elliptic crack with $k_2a$ equal to 4.5. ($b$) Dimensionless crack-opening displacement of an 1:1/2 elliptic crack with $k_2a$ equal to 5.5.**

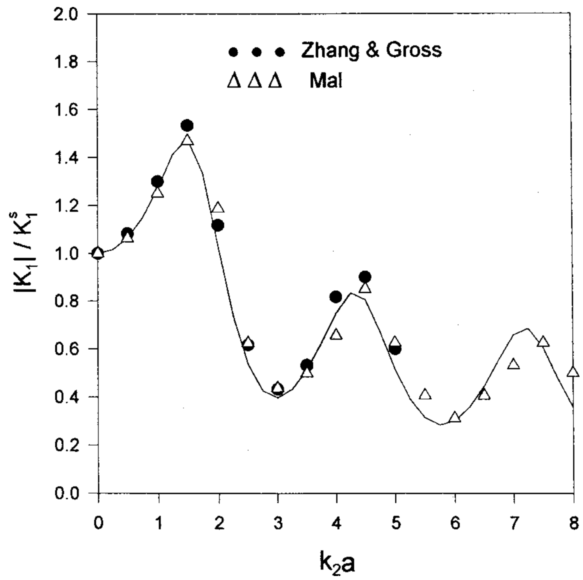


**Fig. 6 Present method (lines), Zhang and Gross (bullets) and Mall (triangles) nondimensional dynamic stress intensity factor for a circular crack for $\nu$=0.25**

circular crack with Poisson's ratio 0.25, and these results are compared with the existing results of Mal [22] and Zhang and Gross [12]. The results are seen to match well with the existing results, except at the peaks. The peaks are attained at frequencies $k_2a=1.5$, 4.25, 7.25 which are nearer to the resonant frequencies $k_2a=1.44$, 4.33, 7.22, … . The result reveals that the amplification of the stress intensity factor is within $k_2a=0$ and $k_2a=2$. For the rest of the higher frequencies the result is only that of shielding, although it is of oscillatory nature. Hence the crack, if propagating will start its propagation for the value of $k_2a$ near 1.5.

Figure 7 shows the results of a nondimensional dynamic stress intensity factor for elliptic crack with aspect ratios 1:1/2 and 1:1/5. The Poisson ratio is now taken to be 0.3 for the sake of comparing the present results with those presented by Zhang and Gross [12]. Here the stress intensity factor has been computed at the two points $\phi=0$ deg and $\phi=90$ deg of the crack edge. For results of the 1:1/2 elliptic crack, comparison with results presented by Zhang and Gross [12] shows that there is almost no difference in the two results. The peaks of the curves are related to resonant frequencies. It is observed that maximum amplification of the stress intensity factor is attained at the edge of the minor axis and hence crack propagation, if initiated, will initiate at the blunt edge of the elliptic crack. Also it may be noted that the narrower the crack, the higher the frequency required to reach the maximum amplification.

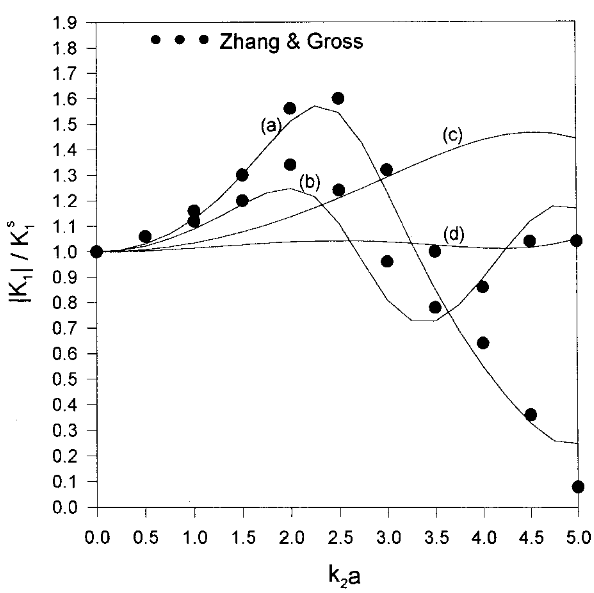


**Fig. 7 Present method (lines) and Zhang and Gross (bullets) nondimensional dynamic stress intensity factor for elliptic cracks with aspect ratio (*a*) 1:1/2, $\phi$=90 deg; (*b*) 1:1/2, $\phi$=0 deg; (*c*) 1:1/5, $\phi$=90 deg; (*d*) 1:1/5, $\phi$=0 deg. $\nu$=0.3.**

**Table 1 Dimensionless scattering cross section for normal incidence of a longitudinal wave on a penny-shaped crack as computed by [21], [23], [3], and [10] and the present method**

| $k_2a$ | Krenk and Schmidt [21] | Keogh [23] | Martin and Wickham [3] | Budreck and Achenbach [10] | Present Method |
|---|---|---|---|---|---|
| 1 | 0.214 | - | 0.214 | 0.262 | 0.224 |
| 2 | 2.894 | 3.066 | 2.895 | 3.066 | 3.030 |
| 3 | 1.910 | 1.836 | 1.910 | 1.904 | 1.999 |
| 4 | 1.655 | 1.612 | 1.600 | 1.649 | 1.673 |
| 5 | 2.106 | 2.364 | 2.314 | 2.342 | 2.422 |
| 6 | 1.801 | 1.851 | 1.877 | 1.890 | 1.969 |
| 7 | 1.987 | 1.770 | 1.831 | 1.920 | 1.887 |
| 8 | 1.941 | 2.212 | 2.208 | 2.207 | 2.341 |

**7.3 Scattering Cross-Section and Back-Scattered Displacement Amplitude.** Another important parameter is the scattering cross section of the crack. Table 1 lists the dimensionless scattering cross section for normally incident *P*-wave on a penny-shaped crack as computed by Krenk and Schmidt [21], Keogh [23], Martin and Wickham [3], Budreck and Achenbach [10], and the present method. The computations are done for $\nu=0.25$.

In Fig. 8 the nondimensional scattering cross section $\Sigma_P/A$ ($A$ being the area of the crack surface) has been plotted as a function of the dimensionless wave number $k_2a$. Figure 9 shows the results of the norm of the dimensionless back-scattered displacement field given by $|u(0)/A|$ plotted against the dimensionless wave number. Both the results of Figs. 8 and 9 have been compared with existing results of Budreck and Achenbach [10] and Alves and Ha Duong [13]. It is found that the present result matches well with both the results of Budreck and Achenbach [10] and

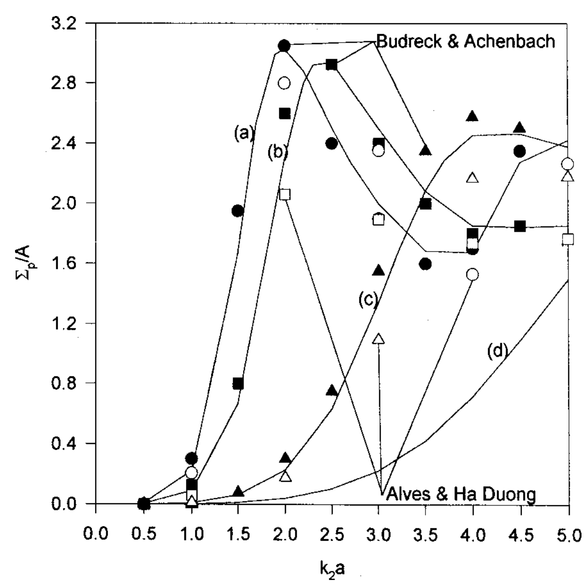


**Fig. 8 Scattering cross section of (*a*) 1:1; (*b*) 1:1/$\sqrt{2}$; (*c*) 1:1/3, and (*d*) 1:1/5 elliptic cracks under normal incidence of a longitudinal wave**

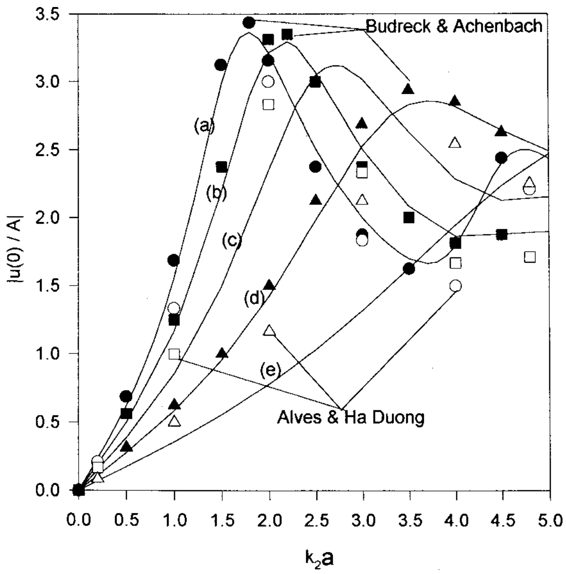


**Fig. 9 Back-scattered displacement amplitudes of (*a*) 1:1; (*b*) 1:1/√2; (*c*) 1:1/2; (*d*) 1:1/3, and (*e*) 1:1/5 elliptic cracks under normal incidence of a longitudinal wave**

Alves and Ha Duong [13]. The peaks of the curves in the figures are related to resonant wave motion on the faces of the crack. The interesting features of the figures are that the first peaks become lower as the crack becomes narrower starting from the penny-shaped crack, and also the narrower the crack the higher the frequency required to reach the first peak.

## 8 Conclusion

The problem of the scattering of the normally incident compressional wave by a plane elliptic crack has been solved in an analytical numerical way in the intermediate and high-frequency domain. An infinite system of algebraic equations is obtained, each element of whose coefficient matrix contain a singular integral which is converted by contour integration into a suitable form amenable for numerical computation. The expression for low-frequency asymptotic of scattering cross section has been obtained analytically, which agrees exactly with previous known results. The system has been truncated suitably for computational work. Results have been obtained for the dynamic crack-opening displacement, dynamic stress intensity factor, scattering cross section, and norm of the back-scattered displacement amplitude for both circular and elliptic cracks of various aspect ratios. The computational work has been carried out with the help of a personal computer. Even retaining only six terms ($s=0$, 2, 4, $m=0$, 1, $n=0$, 2, 4, and $j=0$, 1) in the truncated system has yielded results which are accurate enough to match with the existing results by the boundary integral equation method. The convergence of the results has been tested numerically and this has been demonstrated by plotting results of the crack-opening displacement for a test case obtained from the fourth-order, sixth-order, and eighth-order truncated systems, respectively. This method may be looked upon as an alternative to the boundary integral equation method for solving three-dimensional scattering problems. We do not claim that this is the best method or the most general method to solve such types of problems, but its importance lies in the fact that it is an analytical method. The solutions obtained from this method may be used to validate the various numerical methods which are used by most of the researchers to solve such a type of elliptic crack problems. The method can be easily extended to a variety of problems including crack interaction problems under dynamic loading and solutions can be obtained without heavy computational work as required by the other methods. The problem of scattering of shear waves by an elliptic crack is under consideration and will be communicated shortly.

## Acknowledgment

The constructive comments of the three reviewers are greatfully acknowledged.

## Appendix

We demonstrate here the evaluation of $C_{jm}^{ns}(\psi)$ in Eq. (45). For this we begin with Eq. (42).

$$I=\int_0^\infty\left[-\frac{1}{u}-\frac{4}{2k_2^2(1-\sigma^2)^2}\left\{\frac{\left(u^2-\frac{1}{2}k_2^2\right)^2}{u^2(u^2-k_1^2)^{1/2}}-(u^2-k_2^2)^{1/2}\right\}\right]$$

$$\times J_{w+1/2}(apu)J_{x+1/2}(apu)du \qquad (A1)$$

where $w=2j+n+1$ and $x=2m+s+1$.

We have (Gradshteyn and Ryzhik [26])

$$\int_0^\infty -\frac{1}{u}J_{w+1/2}(apu)J_{x+1/2}(apu)du=-\frac{\delta_{wx}}{(2w+1)}. \qquad (A2)$$

For the remaining part of ($A1$) we extend the argument of the integrand to the complex half-plane $\mathrm{Re}\,z=u\geqslant 0$ and follow the following steps.

Let

$$G(z)=\frac{\left(z^2-\frac{1}{2}k_2^2\right)^2}{z^2(z^2-k_1^2)^{1/2}}-(z^2-k_2^2)^{1/2}. \qquad (A3)$$

For $w\geqslant x$, we write

$$J_{w+1/2}(apz)J_{x+1/2}(apz)=\frac{1}{2}J_{w+1/2}(apz)$$

$$\times[H_{x+1/2}^{(1)}(apz)+H_{x+1/2}^{(2)}(apz)]. \qquad (A4)$$

Then we have the following asymptotic relations as $z\to 0$ (in the complex plane):

$$G(z)J_{w+1/2}(apz)H_{x+1/2}^{(1)}(apz)$$

$$=(apz)^{w-x}\left[-\frac{2(2x-1)!!}{4\pi(2w+1)!!}\frac{k_2^4}{k_1}\frac{1}{z^2}+\sum_{j=0}^{\infty}c_jz^j\right] \qquad (A5)$$

where $c_j$ are constants. Similarly,

$$G(z)J_{w+1/2}(apz)H_{x+1/2}^{(2)}(apz)$$

$$=(apz)^{w-x}\left[\frac{2(2x-1)!!}{4\pi(2w+1)!!}\frac{k_2^4}{k_1}\frac{1}{z^2}+\sum_{j=0}^{\infty}c_jz^j\right]. \qquad (A6)$$

Now, choosing the different contours following Krenk and Schmidt [21] and noting that the larger quarter-circles and the small semicircles make no contribution to the integral in either case we find that as $z\to 0$ the only contribution from the smaller quarter-circles is due to the term (since $w\geqslant x$, the only contribution is for $w=x$)

$$\mp\frac{2(2x-1)!!}{4\pi(2w+1)!!}\frac{k_2^4}{k_1}(ap)^{w-x}z^{w-x-2}. \qquad (A7)$$

Hence, the second part of the singular integral $I$ reduces to the following regular integral:

$$\int_0^{\infty}\left[\frac{\left(u^2-\frac{1}{2}k_2^2\right)^2}{u^2(u^2-k_1^2)^{1/2}}-(u^2-k_2^2)^{1/2}\right]J_{w+1/2}(apu)J_{x+1/2}(apu)du$$

$$=-i\int_0^{k_1}\frac{\left(u^2-\frac{1}{2}k_2^2\right)^2}{u^2(k_1^2-u^2)^{1/2}}J_{w+1/2}(apu)H_{x+1/2}^{(2)}(apu)du$$

$$-i\int_0^{k_2}(k_2^2-u^2)^{1/2}J_{w+1/2}(apu)H_{x+1/2}^{(2)}(apu)du$$

$$-\frac{k_2^4}{2\pi k_1}\frac{\delta_{wx}}{(2w+1)\epsilon} \qquad (A8)$$

where $\epsilon$ is the radius of both the smaller quarter circles of the contours choosen.

Making the transformations $u=k_1\xi$ in the first integral and $u=k_2\xi$ in the second integral and noting by Krenk and Schmidt [21]

$$\lim_{\epsilon\to 0}\frac{1}{k_1\epsilon}=\int_0^1\frac{d\xi}{k_1^2\xi^2(1-\xi^2)^{1/2}} \qquad (A9)$$

we finally get (43).

Now, replacing $w$ by $(2j+n+1)$ and $x$ by $(2m+s+1)$ and substituting this result of (43) in (40) and noting the result (44) and the following result,

$$\sum_{n=0}^{\infty}\sum_{j=0}^{\infty}\begin{pmatrix} I_{n,s}^c W_j^n \\ I_{n,s}^s \overline{W}_j^n \end{pmatrix}\delta_{j+(n-s)/2,m}=\sum_{n=0}^{2m+s}\begin{pmatrix} I_{n,s}^c W_{m-(n-s)/2}^n \\ I_{n,s}^s \overline{W}_{m-(n-s)/2}^n \end{pmatrix}, \quad (A10)$$

we ultimately get the Eq. (45) with the expression for $C_{jm}^{ns}(\psi)$ obtained from (43) after deleting the last term.

## References


[1] Bond, L. J., 1990, ''Numerical Technique and Their Use to Study Wave Propagation and Scattering—A Review,'' *Elastic Waves and Ultrasonic Nondestructive Evaluation*, S. K. Datta, J. D. Achenbach, and Y. S. Rajapakse, eds., North-Holland, Amsterdam.

[2] De Hoop, A. T., 1990, ''Reciprocity, Discretization, and the Numerical Solution of Elastodynamic Propagation and Scattering Problems,'' *Elastic Waves and Ultrasonic Nondestructive Evaluation*, S. K. Datta, J. D. Achenbach, and Y. S. Rajapakse, eds., North-Holland, Amsterdam.

[3] Martin, P. A., and Wickham, G. R., 1983, ''Diffraction of Elastic Waves by a Penny-Shaped Crack: Analytical and Numerical Results,'' Proc. R. Soc. London, Ser. A, **390**, pp. 91–129.

[4] Roy, A., 1984, ''Diffraction of Elastic Waves by an Elliptic Crack,'' Int. J. Eng. Sci., **22**, pp. 729–739.

[5] Roy, A., 1987, ''Diffraction of Elastic Waves by an Elliptic Crack—II,'' Int. J. Eng. Sci., **25**, pp. 155–169.

[6] Lin, W., and Keer, L. M., 1987, ''Scattering by a Planar Three-Dimensional Crack,'' J. Acoust. Soc. Am., **82**, pp. 1442–1448.

[7] Hirose, S., 1989, ''Scattering From an Elliptic Crack by the Time-Domain Boundary Integral Equation Method,'' *Advances in Boundary Elements, Vol 3: Stress Analysis*, C. A. Brebbia, and J. J. Connor, eds, Computational Mechanics Publications, Southampton, UK, pp. 99–110.

[8] Shifrin, E. I., 1996, ''Semi-Analytical Solution of the Problem of Elastic Wave Scattering by Elliptical Cracks,'' Z. Angew. Math. Mech., **76**, pp. 471–472.

[9] Visscher, W. M., 1983, ''Theory of Scattering of Elastic Waves From Flat Cracks of Arbitrary Shape,'' Wave Motion, **5**, pp. 15–32.

[10] Budreck, D. E., and Achenbach, J. D., 1988, ''Scattering From Three-Dimensional Planar Cracks by the Boundary Integral Equation Method,'' ASME J. Appl. Mech., **55**, pp. 405–412.

[11] Nishimura, N., and Kobayashi, S., 1989, ''A Regularized Boundary Integral Equation Method for Elastodynamic Crack Problems,'' Comput. Mech., **4**, pp. 319–328.

[12] Zhang, Ch., and Gross, D., 1998, *On Wave Propagation in Elastic Solids With Cracks*, Computational Mechanics Publications, Southampton, UK.

[13] Alves, C., and Duong, T. Ha, 1995, ''Numerical Resolution of the Boundary Integral Equations for Elastic Scattering by a Plane Crack,'' Int. J. Numer. Methods Eng., **38**, pp. 2347–2371.

[14] Schafbuch, P. J., Thompson, R. B., and Rizzo, F. J., 1990, ''Application of the Boundary Element Method to Elastic Wave Scattering by Irregular Defects,'' J. Nondestruct. Eval., **9**, pp. 113–127.

[15] Itou, S., 1980, ''Dynamic Stress Concentration Around a Rectangular Crack in an Infinite Elastic Medium,'' Z. Angew. Math. Mech., **60**, pp. 317–322.

[16] Guan, L., and Norris, A., 1992, ''Elastic Wave Scattering by Rectangular Cracks,'' Int. J. Solids Struct., **29**, pp. 1549–1565.

[17] Glushkov, Y. V., and Glushkova, N. V., 1996, ''Diffraction of Elastic Waves by Three-Dimensional Cracks of Arbitrary Shape in a Plane,'' Appl. Math. Mech., **60**, pp. 277–283.

[18] Bostrom, A., and Eriksson, A. S., 1993, ''Scattering by Two Penny-Shaped Cracks With Spring Boundary Conditions,'' Proc. R. Soc. London, Ser. A, **443**, pp. 183–201.

[19] Roy, A., and Chatterjee, M., 1994, ''Interaction Between Coplanar Elliptic Cracks—I. Normal Loading,'' Int. J. Solids Struct., **31**, pp. 127–144.

[20] Mal, A. K., 1968, ''Dynamic Stress Intensity Factor for an Axisymmetric Loading of the Penny Shaped Crack,'' Int. J. Eng. Sci., **6**, pp. 623–629.

[21] Krenk, S., and Schmidt, H., 1982, ''Elastic Wave Scattering by a Circular Crack,'' Philos. Trans. R. Soc. London, Ser. A, **A308**, pp. 167–198.

[22] Mal, A. K., 1970, ''Interaction of Elastic Waves With a Penny-Shaped Crack,'' Int. J. Eng. Sci., **8**, pp. 381–388.

[23] Keogh, P. S., 1983, Ph.D. thesis, University of Manchester.

[24] Martin, P., 1981, ''Diffraction of Elastic Waves by a Penny-Shaped Crack,'' Proc. R. Soc. London, Ser. A, **A378**, pp. 263–285.

[25] Roy, A., and Saha, T. K., 2000, ''Weight Function for an Elliptic Crack in an Infinite Medium. I. Normal Loading,'' Int. J. Fracture, **103**, pp. 227–241.

[26] Gradshteyn, I. S., and Ryzhik, I. M., 1980, *Tables of Integrals, Series and Products*, Corrected and Enlarged Ed., Academic Press, San Diego, CA (English translation: A. Jeffrey, ed.).

[27] Robertson, I. A., 1967, ''Diffraction of a Plane Longitudinal Wave by a Penny-Shaped Crack,'' Proc. Cambridge Philos. Soc., **63**, pp. 229–238.

[28] Piau, M., 1979, ''Attenuation of a Plane Compressional Wave by a Random Distribution of Thin Circular Cracks,'' Int. J. Eng. Sci., **17**, pp. 151–167.

[29] Martin, P. A., 1986, ''Orthogonal Polynomial Solutions for Pressurized Elliptical Cracks,'' Q. J. Mech. Appl. Math., **39**, pp. 269–287.

[30] Sneddon, I. N., 1951, *Fourier Transforms*, McGraw-Hill, New York.

[31] Mura, T., 1982, *Micromechanics of Defects in Solids*, Martinus Nijhoff, The Hague.

**P. Tong**[1]
Mechanical Engineering Department,
Hong Kong University of Science and Technology,
Clearwater Bay, Hong Kong, P. R. China
e-mail: pintong@ust.hk

**W. Huang**
Assistant Project Scientist,
Department of Bioengineering,
University of California, San Diego,
La Jolla, CA 92093-0412

# Large Deflection of Thin Plates in Pressure Sensor Applications

*The present paper examines the large deflections of a clamped circulate thin plate for pressure sensor applications and establishes a simple solution using the singular perturbation technique. The perturbation solution for the slope of the lateral deflection is in a closed form in terms of the load-induced radial stress resultant. The nonlinearity has a strong stiffened effect. The nondimensional load-induced stress resultants are functions of the nondimensional initial stress resultant, lateral load, and Poisson's ratio.*
[DOI: 10.1115/1.1507767]

## 1 Introduction

Silicon-based thin films are frequently used in microelectronics for the measurement of pressure, temperature, and other physical quantities. The film is often under initial tension and its thickness is of the order microns. The tension can be as large as 1 GPa ([1]). Sheplak and Dugunji [2] examined the large deflection characteristics of circular plates in detail by integrating the full set of the nonlinear equations of motion. The present paper re-examines the problem and establishes a simpler solution using the singular perturbation technique. The results compare well with those of Sheplak and Dugunji [2].

## 2 Basic Equations

Consider a circular plate of radius $a$ and thickness $h$ under initial tension $N_0$. The plate is stretched initially by a uniform load $N_0$ and then subjected to a uniform pressure $P$. The equilibrium equations are ([2,3])

$$\frac{dN_r}{dr}+\frac{N_r-N_\theta}{r}=0, \tag{1}$$

$$\frac{dN_\theta}{dr}-\frac{N_r-N_\theta}{r}+\frac{Eh}{2r}\left(\frac{dW}{dr}\right)^2=0, \tag{2}$$

$$D\left(\frac{d^3W}{dr^3}+\frac{1}{r}\frac{d^2W}{dr^2}-\frac{1}{r^2}\frac{dW}{dr}\right)-N_r\frac{dW}{dr}=\frac{Pr}{2}, \tag{3}$$

where $N_r, N_\theta$ are the in-plane stress resultants, $r$ is the radius, $W$ is the lateral deflection, and

$$D=\frac{Eh^3}{12(1-\nu^2)}$$

is the bending rigidity with $E$, $\nu$ being Young's modulus and Poisson's ratio, respectively.

We define

$$N_r(r)=N_0+S_r(x),\quad N_\theta(r)=N_0+S_\theta(x),$$

and the following nondimensional quantities:

$$w=\frac{W}{h},\quad x=\frac{r}{a},\quad \left(\frac{Pa^4}{Eh^4}\right)^{1/3}\theta=\frac{dw}{dx},$$

$$n_0=N_0/(EP^2a^2h)^{1/3},\quad s_r=S_r/(EP^2a^2h)^{1/3},$$

$$s_\theta=S_\theta/(EP^2a^2h)^{1/3},$$

$$p=\frac{Pa^4}{Eh^4},\quad 1/\varepsilon=\sqrt{12(1-\nu^2)}p^{1/3},\quad k=p^{1/3}\sqrt{12(1-\nu^2)n_0},$$

$$k_e=p^{1/3}\sqrt{12(1-\nu^2)[n_0+s_r(1)]},$$

where $S_r, S_\theta$ are the in-plane stress resultants induced by the lateral load that

$$S_r=N_r-N_0,\quad S_\theta=N_\theta-N_0. \tag{4}$$

Only two of the parameters $n_0$, $p$, $\varepsilon$, $k$, and $k_e$ are independent. The value of the different parameters controls different characteristics of the plate and thus are used for the specific circumstances.

The present definitions of the nondimensional stress resultants $s_r, s_\theta$ differ slightly from that of Sheplak and Dugunji [2], who defined them as $p^{2/3}s_r, p^{2/3}s_\theta$. The choice here is for mathematical convenience. However, it does make the physical interpretation of $s_r, s_\theta, n_0$ somewhat indirect as they involve both stress resultants and lateral load. The present definition leads to constant asymptotic values for $s_r, s_\theta$ at higher values of $p$ as shown later in the results. The definitions for $p$ and $k$ are the same as those of [2].

In nondimensional form, Eqs. (1)–(3) become

$$\frac{ds_r}{dx}+\frac{s_r-s_\theta}{x}=0, \tag{5}$$

$$\frac{ds_\theta}{dx}-\frac{s_r-s_\theta}{x}+\frac{\theta^2}{2x}=0, \tag{6}$$

$$\varepsilon^2\left(\frac{d^2\theta}{dx^2}+\frac{1}{x}\frac{d\theta}{dx}-\frac{\theta}{x^2}\right)-[n_0+s_r(x)]\theta=\frac{1}{2}x. \tag{7}$$

The boundary conditions are

$$\theta=0,\quad s_r=s_\theta\quad \text{at } x=0, \tag{8}$$

$$\theta=0,\quad s_\theta-\nu s_r=0\quad \text{at } x=1. \tag{9}$$

The governing equations depend on the non-dimensional initial stress resultant $n_0$ and $\varepsilon$. Poisson's ratio appears only in the boundary condition.

## 3 Solution

The parameter $k_e[=\sqrt{n_0+s_r(1)}/\varepsilon]$ characterizes the behavior of the plate. If $k_e \gg 1$, it indicates that the plate is either very thin or the in-plane stress resultant is large that the membrane behavior is dominant. In this case, we can construct the solution by the singular perturbation method ([4]).

---

[1] To whom correspondence should be addressed. Also visiting Professor of Bioengineering, University of California, San Diego, CA.

Contributed by the Applied Mechanics Division of THE AMERICAN SOCIETY OF MECHANICAL ENGINEERS for publication in the ASME JOURNAL OF APPLIED MECHANICS. Manuscript received by the ASME Applied Mechanics Division, September 19, 2001; final revision, June 8, 2002. Associate Editor: R. C. Benson. Discussion on the paper should be addressed to the Editor, Prof. Robert M. McMeeking, Department of Mechanical and Environmental Engineering University of California–Santa Barbara, Santa Barbara, CA 93106-5070, and will be accepted until four months after final publication of the paper itself in the ASME JOURNAL OF APPLIED MECHANICS.

  

We first construct the outer solution that is valid everywhere except near $x=1$. The zeroth-order outer solution for $\theta$ is obtained from Eq. (7) by neglecting the terms proportional to $\varepsilon^2$, i.e.:

$$\theta=-\frac{x}{2[n_0+s_r(x)]}+O(\varepsilon^2) \tag{10}$$

for sufficiently small $\varepsilon$ (or large $k_e$).

In principle, we can determine the zeroth-order solution for $s_r$ and $s_\theta$ from Eqs. (5) and (6) by numerical integration subjected to the boundary conditions Eqs. (8) and (9). The solution depends only on the nondimensional parameter $n_0$ and Poisson's ratio $\nu$. Unfortunately, the outer solution for $\theta$ does not satisfy the boundary condition Eq. (9) at $x=1$. The integrated $s_\theta$ will give incorrect result at $x=1$. Thus the solution is not good near the boundary, but valid everywhere else. This is also the reason that $\theta$ given in Eq. (10) is called the outer solution.

Let us construct the solution valid near $x=1$ and call it the inner solution. We introduce the inner variable

$$Y=\varepsilon(1-x) \tag{11}$$

and the perturbation solution in the form

$$\begin{aligned}\theta(x)&=\theta_0(Y)+\varepsilon\theta_1(Y)+O(\varepsilon^2)\\ s_r(x)&=s_{r0}(Y)+\varepsilon s_{r1}(Y)+O(\varepsilon^2)\\ s_\theta(x)&=s_{\theta 0}(Y)+\varepsilon s_{\theta 1}(Y)+O(\varepsilon^2)\end{aligned} \tag{12}$$

near $x=1$. Substituting the perturbation solution into Eqs. (5), (6), and (7) and collecting terms of the same order of $\varepsilon$, we find the zeroth-order equations

$$\frac{d}{dY}s_{r0}(Y)=0,\quad \frac{d}{dY}s_{\theta 0}(Y)=0,$$

$$\frac{d^2\theta_0}{dY^2}-[n_0+s_{r0}(0)]\theta_0=\frac{1}{2[n_0+s_{r0}]},$$

and the first-order equations

$$\frac{d}{dY}s_{r1}(Y)=s_{r0}-s_{\theta 0},\quad \frac{d}{dY}s_{\theta 1}(Y)=s_{\theta 0}-s_{r0}+\frac{1}{2}\theta_0^2,$$

$$\frac{d^2\theta_1}{dY^2}-[n_0+s_{r0}(0)]\theta_1=s_{r1}\theta_0+\frac{d\theta_0}{dY}-\frac{1}{2}Y.$$

The zeroth-order solution is

$$s_{\theta 0}=\nu s_{r0}=\nu s_{r0}=\text{constant}, \tag{13}$$

$$\theta_0=-\frac{1-\exp(-\sqrt{b}Y)}{2b}, \tag{14}$$

and the first order solution is

$$s_{r1}=(1-\nu)s_{r0}Y \tag{15}$$

$$s_{\theta 1}=-(1-\nu)s_{r0}Y+\frac{1}{8b^2}\left(Y+\frac{2}{\sqrt{b}}e^{-\sqrt{b}Y}-\frac{1}{2\sqrt{b}}e^{-2\sqrt{b}Y}-\frac{3}{2\sqrt{b}}\right) \tag{16}$$

$$\theta_1=\frac{1}{4}\left[\frac{Y}{b}-\frac{1}{2b}(1-\nu)s_{r0}\left(\frac{Y^2}{\sqrt{b}}+\frac{Y}{b}\right)\right]e^{-\sqrt{b}Y}+\frac{1}{2}\left[(1-\nu)\frac{s_{r0}}{b}+1\right]\frac{Y}{b} \tag{17}$$

where

$$b=n_0+s_{r0}.$$

We shall first establish a uniformly valid solution for $\theta$. By matching the inner solution given by Eq. (12) and the outer solution given by Eqs. (5), (6), and (10), we can show that

$$s_{r0}=s_r(1)$$

and the common part of the inner and outer solutions of $\theta$ is

$$-\frac{1}{2b}+\frac{\varepsilon}{2}\left[(1-\nu)\frac{s_{r0}}{b}+1\right]\frac{Y}{b}.$$

Thus the uniformly valid solution (the sum of the inner and outer solutions minus their common part) for $\theta$ is thus

$$\theta_u=-\frac{x}{2[n_0+s_r(x)]}+\frac{e^{k_e(x-1)}}{4b}\times\left\{3-x+\frac{(1-\nu)(1-x)[(1-x)k_e+1]s_{r0}}{2b}\right\}+O(\varepsilon^2).$$

This solution does not equal zero at $x=0$ but is exponentially small for small $\varepsilon$. Without invalid the solution, we may add a small term to $\theta_u$ making it exactly zero at the origin. Thus

$$\theta_u=-\frac{x}{2[n_0+s_r(x)]}+\frac{e^{k_e(x-1)}}{4b}\times\left\{3-x+\frac{(1-\nu)(1-x)[(1-x)k_e+1]s_{r0}}{2b}\right\}+c(x-1)+O(\varepsilon^2) \tag{18}$$

where

$$c=\frac{e^{-k_e}}{4b}\left[3+\frac{(1-\nu)(k_e+1)s_{r0}}{2b}\right].$$

The deflection $w$ is obtain by integrating Eq. (18) with respect to $x$:

$$\begin{aligned}\frac{w}{p^{1/3}}=&\int_x^1\frac{x\,dx}{2[n_0+s_r(x)]}+\frac{c(1-x)^2}{2}+\frac{1}{4bk_e}\left[\frac{3(1-\nu)s_{r0}}{2bk_e}-2-\frac{1}{k_e}\right]+\frac{e^{k_e(x-1)}}{4bk_e}\\ &\times\left\{3-x+\frac{1}{k_e}-\frac{1}{2}\left[(1-x)^2k_e+3(1-x)+\frac{3}{k_e}\right]\frac{(1-\nu)s_{r0}}{b}\right\}.\end{aligned} \tag{19}$$

Thus $w$ is proportional to $p^{1/3}$ for $n_0, s_r$ being of the order 1. For small ratio of $s_r(r)/n_0$, the induced stress resultant can be neglected to give the linear solution for $w$ and $\theta$. We obtain the linearized solution for $w$ by setting $s_r=s_{r0}=0$ and $k_e=k$ in Eq. (19):

$$\frac{w}{p^{1/3}}=\frac{1}{2n_0}\left[\frac{1-x^2}{2}-\frac{1}{k}-\frac{1}{2k^2}+\frac{e^{k(x-1)}}{2k}\left(3-x+\frac{1}{k}\right)+\frac{3e^{-k}}{4}(1-x)^2\right]. \tag{20}$$

We may obtain the uniformly valid solutions of $s_r$ and $s_\theta$ as that for $\theta$. However, it will be more direct to integrate the following set of equations:

$$\frac{ds_r}{dx}+\frac{s_r-s_\theta}{x}=0, \tag{21}$$

$$\frac{ds_\theta}{dx}-\frac{s_r-s_\theta}{x}+\frac{\theta_u^2}{2x}=0. \tag{22}$$

We shall change the independent variable $x$ to

$$y=1-x,$$

and integrate the equations with respect to $y$ is from 0 to 1 with the boundary conditions

$$s_\theta = \nu s_r \quad \text{at } y=0, \tag{23}$$

$$s_r = s_\theta \quad \text{at } y=1. \tag{24}$$

The reason for starting the integration from $y=0$ (i.e., $x=1$) rather than $y=1$ (i.e., $x=0$) is because $\theta_u$ depends explicitly on the value of $s_r$ at $y=0$.

Equations (21) and (22) have a removable singularity at $y=1$. We can numerically integrate the equations only to a point, $y_0$, which is close 1. Thus we have to modify the boundary conditions Eq. (24) as

$$s_\theta = s_r - \frac{(1-y_0)^2}{64(n_0+s_r)} \quad \text{at } y=y_0, \tag{25}$$

which is obtained by expanding Eqs. (21) and (22) around $y=y_0$. We normally choose $y_0=0.99$. We integrate Eqs. (21) and (22) by the choosing appropriate value of $s_r$ at $y=0$ to satisfy Eq. (25).

## 4 Results

The solution depends of three nondimensional parameters, namely $n_0$, $p$, and $\nu$. All results given are for $\nu=0.3$. Figure 1 gives the induced radial stress resultant ratios $s_r/n_0$ at the center and at the boundary versus $n_0$. The solid and dotted curves are $s_r(0)/n_0, s_r(1)/n_0$, respectively, for $p=1000$. The points "○" and "□" are $s_r(0)/n_0, s_r(1)/n_0$ for $p=100$. The figure shows that $s_r(0)/n_0, s_r(1)/n_0$ decrease rapidly as $n_0$ increases. The magnitude of the ratio is an indication of the importance of nonlinearity. For small ratio, we can approximate the solution by linear approximation. The values of $s_r(0)/n_0, s_r(1)/n_0$ for $p=100$ are smaller than those for $p=1000$, an indication of less nonlinear effect as $p$ reduces. Results of the nonlinear solutions for $\log[s_r(0)]$ (solid curve) and $\log[s_r(1)]$ (dash curve) versus $\log(p)$ for $k=5$, 10, 20 are given in Fig. 2. We see that $s_r(0)$ and $s_r(1)$ are proportional to $p^{4/3}$ at low loadings and approaches 0.43 and 0.331, respectively, as $p$ approaches infinite. Thus $S_r(0)$ and $S_r(1)$ are proportional to $p^2$ at small $p$ and to $p^{2/3}$ for large $p$, which are the same as those of Sheplak and Dugunji [2]. A higher value of $k$ delays the transition.

Figures 3 and 4 plot $s_r$ and $s_\theta$, respectively, for different $p$. The top three curves are for $n_0=0.0$ and the lower three for $n_0=0.5$ with solid, dot and dash curves for $p=100$, 1000, and 10,000, respectively. The former case corresponds to $k=0$ and $k_e=7.2$, 17.6, 39.6 and the latter case corresponds to $k=10.8$, 23.4 50.3 and $k_e=11.6$, 25.5, 53.4. The two figures show the influence of initial stress resultant on the induced ones. Generally the smaller the initial stress resultant, the larger are the induced stress resultants for the same lateral load. The top three curves are for $k=0$, which compare well with those of Sheplak and Dugunji [2] in Figs. 13 and 14.

Figure 5 denotes $\log[w(0)]$ versus $\log(p)$. Curves are the present results for $k=5$ (solid), 10 (dot), 20 (dash); points are from Ref.

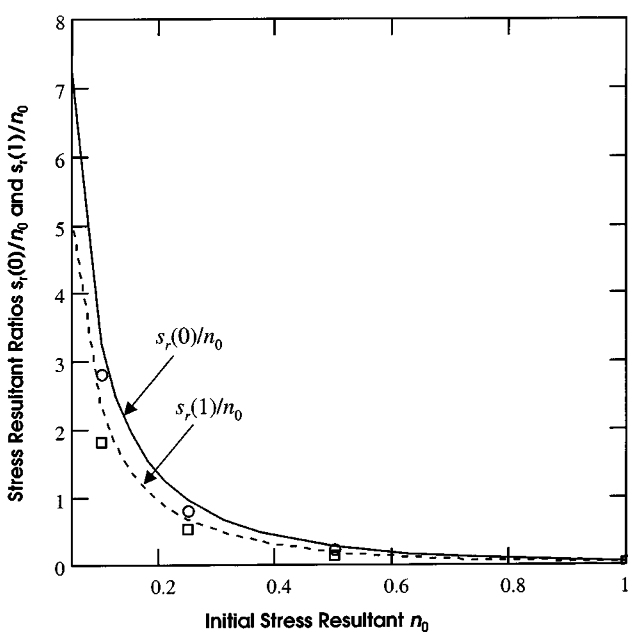


**Fig. 1 Induced radial stress resultant to initial stress resultant ratios at $x=0$ (solid curve) and 1 (dot curve) for $p=1000$; correspondingly points "○" and "□" are for $p=100$**

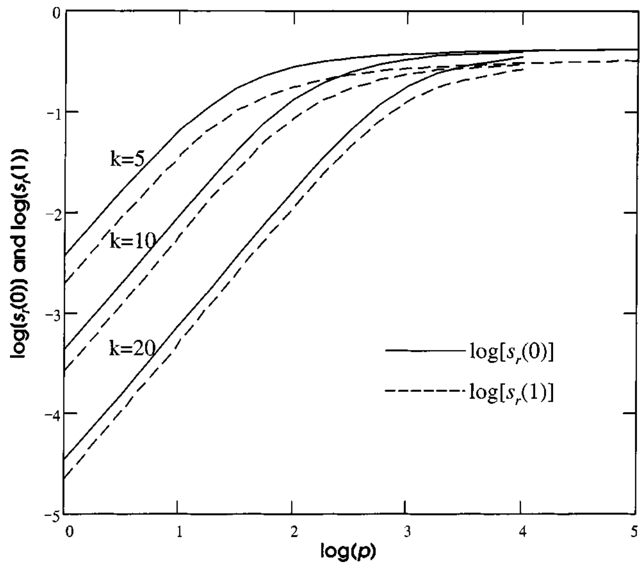


**Fig. 2 $\log[s_r(0)]$ (solid curve) and $\log[s_r(1)]$ (dash curve) versus $\log(p)$ for $k=5$, 10, 20**

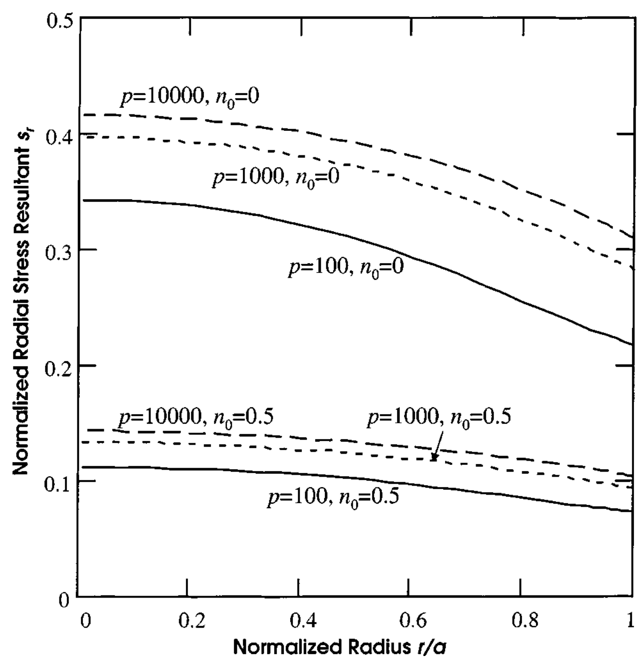


**Fig. 3 Induced stress resultant $s_r$. The top three curves are for $n_0=0$ and the lower three for $n_0=0.5$ with $p=100$ (solid), 1000 (dot), 10000 (dash), respectively. The former case corresponds to $k=0$ and $k_e=7.2$, 17.6, 39.6 and the latter case corresponds to $k=10.8$, 23.4, 50.3 and $k_e=11.6$, 25.5, 53.4.**

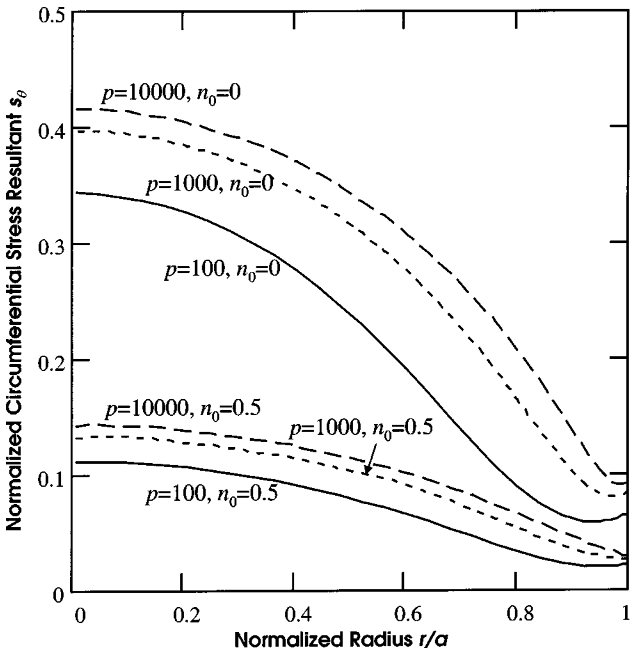


**Fig. 4 Induced stress resultant $s_\theta$. The top three curves are for $n_0=0$ and the lower three for $n_0=0.5$ with $p=100$ (solid), 1000 (dot), 10000(dash), respectively. The former case corresponds to $k=0$ and $k_e=7.2$, 17.6, 39.6 and the latter case corresponds to $k=10.8$, 23.4 50.3 and $k_e=11.6$, 25.5, 53.4.**

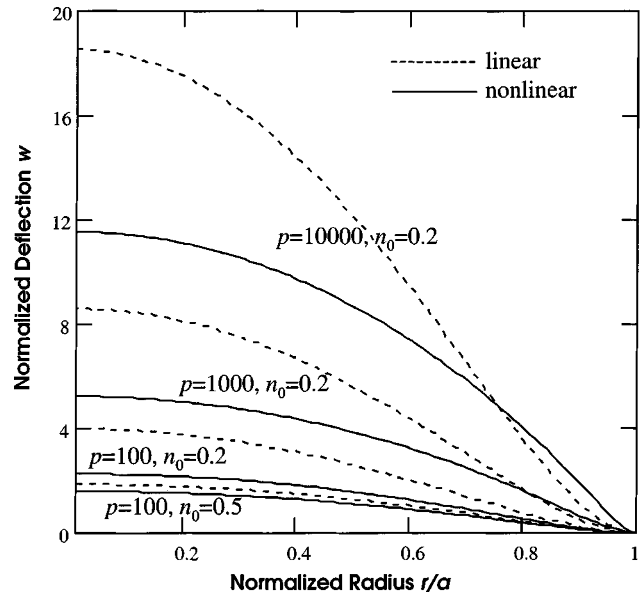


**Fig. 6 Linear (dot) and nonlinear (solid) normalized deflections $w$. The lowest pair of curves are for $n_0=0.5$ and $p=100$. The top three pairs of curves are for $n_0=0.2$ and $p=10000$, 1000, and 100, respectively.**

[2] for $k=5(\bigcirc)$, $10(+)$, 20 ($\square$). At low loadings and $n_0 \gg s_r$, $w(0)$ is linearly proportional to $p$ as given by the linear theory. Note that $n_0=k^2/[12(1-\nu^2)p^{2/3}]$. For higher $p$ and $n_0 \ll s_r$, the nonlinear stiffened effect from the normalized induced radial stress resultant $s_r$ is significant and $w(0)\approx p^{1/3}$. A large $k$ delays the transition from linear to nonlinear behavior. The results compare well with those given by Sheplak and Dugunji [2] who integrated the full nonlinear Eqs. (5)–(7).

Figure 6 illustrates the distribution of the deflection $w$. The solid curves are the nonlinear solution and the dotted curves are the linear solution. The lowest pair of curves are the deflection $w$ for $n_0=0.5$ and $p=100$. The difference between the linear and nonlinear solutions is minimum. The top three pairs of curves are for $n_0=0.2$ and $p=10{,}000$, 1000, and 100, respectively. The difference between linear and nonlinear solutions is much larger than the previous case of larger $n_0$. The difference is more pronounce for higher load (e.g., the top pair of curves). The top three pairs of curves show, as expected, increasing deflection with increasing load. Comparing the lowest two pair of curves, one sees that the initial stress $n_0$ makes the plate stiffer. Similar characteristics can be seen in the slopes of $w$ shown in Fig. 7. In Fig. 7, the top pair of curves is for the linear (dash-dot) and nonlinear (solid) solutions with $n_0=0.5$ and $p=100$. The next three curves are for $n_0$

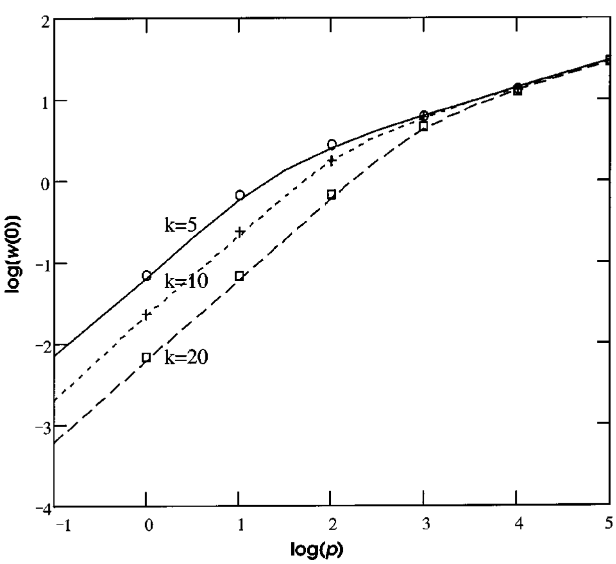


**Fig. 5 Center deflection versus nondimensional pressure. Curves are the present results for $k=5$ (solid), 10 (dot), 20 (dash); points are from Ref. [2] for $k=5(\bigcirc)$, $10(+)$, 20 ($\square$).**

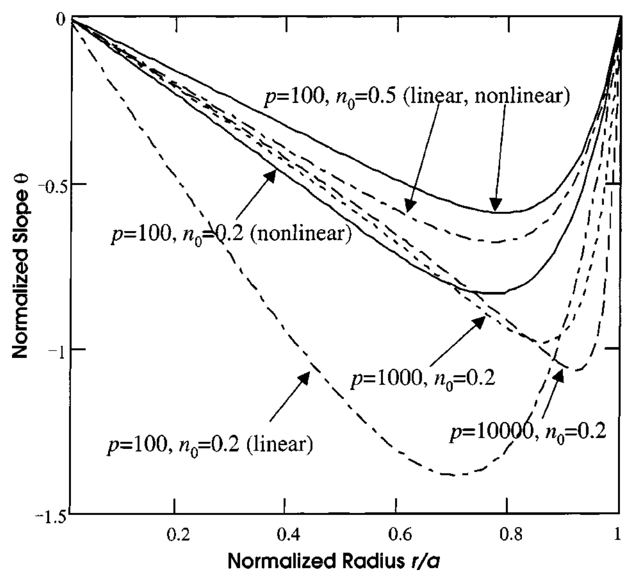


**Fig. 7 Normalized slope $\theta$. The top two curves are the linear (dash-dot) and nonlinear (solid) solutions for $n_0=0.5$ and $p=100$. The next three curves are for $n_0=0.2$ and $p=10000$ (dash), 1000 (dot), and 100 (solid). The lowest curve (dash-dot) is the linear solution for $n_0=0.2$ and $p=100$.**

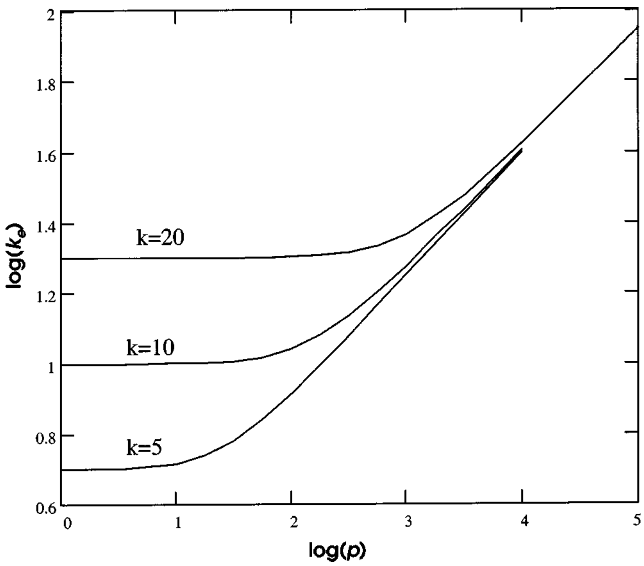


**Fig. 8 log($k_e$) and log($p$) for $k=5,$ 10, 20**

$=0.2$ and $p=10{,}000$ (dash), 1000 (dot), and 100 (solid). The lowest curve (dash-dot) is the linear solution for $n_0=0.2$ and $p=100$. The slope $\theta$ is very much like a linear line except near the boundary where the slope changes rapidly to become zero at $x=1$, more so for higher values of $p$ (e.g., $p=1000$ and 10,000). This is the phenomenon of the boundary layer in which bending effect becomes dominant making $\theta$ satisfy the boundary condition. The size of the boundary layer is proportional to $\varepsilon/\sqrt{n_0+s_r(1)}$ $[=p^{-1/3}/\sqrt{12(1-\nu^2)(n_0+s_r(1))}]$, which is precisely the inverse of $k_e$. The top solid curve is for $k_e=11.6$. The lower solid curve and the dotted and dash-dotted curves are for $k_e=9$, 20.6, and 45.4, respectively. The lowest dash-dotted curve is the linear solution for $k_e=9$.

As pointed out before, only two of the five parameters $n_0$, $p$, $\varepsilon$, $k$, and $k_e$ are independent. Figure 8 shows the relationship between log($k_e$) and log($p$) for $k=5$, 10, 20. For small $p$, $k_e$ approximately equals to $k$. For large $p$, $k_e$ is proportional to $p^{1/3}$.

## 5 Remarks

The deflection of plate is characterized by nondimensional parameters, such as the nondimensional initial stress resultant $n_0$, the nondimensional pressure load $p$ and Poisson's ratio $\nu$. We establish the singular perturbation solution on the basis that $\varepsilon[=\sqrt{n_0+s_r(1)}/k_e]$ is small. For reasonably large $k_e$ (see Fig. 6), the slope of the deflection is dominated by membrane behavior everywhere except the small region near the boundary. Using the singular perturbation technique, one first obtains a uniformly valid solution for the slope $\theta_u$ in terms of the load-induced radial stress resultant $s_r$. One then integrates numerically two simple first-order nonlinear ordinary differential equations to determine both $s_r$ and $s_\theta$ in terms of $\theta_u$. Since $\theta_u$ depends explicitly on the value of $s_r$ at the boundary, it is more convenient to integrate the equations for $s_r$ and $s_\theta$ from the boundary $(x=1)$ to the center $(x=0)$ of the plate. The uniformly valid perturbation solution for $w$ can be integrated directly from $\theta_u$. The perturbation solution (Fig. 2) shows that $s_r(0)$ and $s_r(1)$ are proportional to $p^{4/3}$ at low loadings and approach 0.43 and 0.331, respectively, as $p$ approaches infinite. In other words, $S_r(0)$ and $S_r(1)$ are proportional to $p^2$ for small $p$ and to $p^{2/3}$ for large $p$. The perturbation solution (Fig. 5) shows also that $w$ is proportional to $p^{1/3}$ for large $p$ and proportional to $p$ for small $p$. The nonlinear effect generally stiffens the plate. A higher value of $k$ delays the transition. The results compare well with those of Sheplak and Dugunji [2] who obtained the solution by integrating the full set of nonlinear differential equations Eqs. (5) and (7) for $k_e>5$ (Fig. 5).


## Acknowledgment

This work was supported by a grant from the RGC of Hong Kong. W. Huang was supported by the National Heart, Lung, and Blood Institute of the National Institutes of Health Grant HL 43026. The authors wish to thank Professor Dugundji for his valuable comments and suggestions.


## References


[1] Cho, S. T., Najafi, K., and Wise, K. D., 1992, "Internal Stress Compensation and Scaling in Ultra-Sensitive Silicon Pressure Sensors," IEEE Trans. Electron Devices, **99**(4), pp. 836–842.

[2] Sheplak, M., and Dugundji, J., 1998, "Large Deflections of Clamped Circular Plates Under Initial Tension and Transitions to Membrane Behavior," ASME J. Appl. Mech., **65**, pp. 107–115.

[3] Fung, Y. C., and Tong, P., 2001, *Classical and Computational Solid Mechanics*, World Scientific, Singapore.

[4] O'Malley, R. E., 1991, *Singular Perturbation Methods for Ordinary Differential Equations*, Spring-Verlag, New York.

J. B. Dafedar

Y. M. Desai[1]
Associate Professor
e-mail: desai@civil.iitb.ac.in

Department of Civil Engineering,
Indian Institute of Technology Bombay,
Powai, Mumbai 400 076, India

# Thermomechanical Buckling of Laminated Composite Plates Using Mixed, Higher-Order Analytical Formulation

*A novel, analytical mixed theory based on the potential energy principle has been presented in this paper to investigate buckling response of laminated composite plates subjected to mechanical and hygrothermal loads. Two sets of higher-order mixed models have been proposed on the basis of an individual layer as well as equivalent single layer theories by selectively incorporating nonlinear components of Green's strain tensor. Displacements, as well as transverse stress continuities, have been enforced in the formulation of models by incorporating displacements and transverse stresses as the degrees-of-freedom. The modal transverse stresses have been obtained as eigenvectors and thus their separate calculations have been advantageously avoided. Solutions from the models have been shown to be in excellent agreement with the available three-dimensional elasticity solutions. Few benchmark solutions have also been presented for the bi-axial compression-tension loading.* [DOI: 10.1115/1.1490372]

## Introduction

Increasing use of composite materials in high-performance structures has created a need to understand their structural behavior under different conditions. Mechanical buckling has been identified to be a primary mode of failure for layered composite plates subjected to in-plane compressive loads. Laminates may also experience thermal buckling due to change in temperature, and hygroscopic buckling due to change in moisture concentrations.

Accurate prediction of the buckling response can be made by the three-dimensional elasticity analysis. However, solution of three-dimensional elasticity equations may be intractable, especially for thick plates with a large number of layers. Equivalent single layer (ESL) approaches using displacement-based higher-order shear deformation theories, on the other hand, have been widely used for buckling analysis of laminated plates. Reddy and Phan [1], for example, presented analytical solutions for the plate buckling problem by using the higher-order theory ([2]) with stress-free boundaries at the top and bottom surfaces of plates. Senthilnathan et al. [3] derived closed-form solutions for the plate buckling problem by using the higher order theory ([2]) and by employing Von Karman nonlinear strains. Results for isotropic, orthotropic, and two-layered antisymmetric crossply (0 deg/90 deg) and angle ply (45 deg/−45 deg) square plates under uniaxial compression were presented. Khdeir [4] had also used Reddy's ([2]) higher-order theory for buckling of crossply laminated plates by adopting the Levy-type solutions of the governing equations. Different combinations of simply supported, clamped, and free boundary conditions were considered. Later, Khdeir [5] extended the work to consider antisymmetrical angle-ply laminates. Buckling loads of laminated composite plates were also evaluated analytically by Doong [6], Doong et al. [7], Ren and Owen [8], Savithri and Varadhan [9], Matsunaga [10], and Kant and Swaminathan [11].

All the ESL theories mentioned above were displacement based, where one set of Cartesian coordinates was invariably located on the mid surface of the entire laminate and the global displacement fields were assumed to be of first-order or high-order polynomial series, across the entire laminate thickness. Although the continuity of the displacement field through thickness was satisfied, continuity of the transverse stresses at the interface could not be enforced. Thus, these theories may yield poor results for thick or moderately thick laminates. Furthermore, pointwise recalculations are required by integrating the equilibrium equations, to evaluate transverse stress distribution through the thickness of a laminate.

Pagano [12,13] illustrated that the displacement functions of laminated plates can be represented by piecewise continuous high-order polynomial series, layer by layer, in the thickness direction. Subsequently, Wu and Chen [14] proposed a local higher-order theory to determine natural frequencies and buckling loads of laminated composite plates. The displacement continuity conditions at an interface between laminae were introduced into the Lagrangian functional of the laminate, by the Lagrange multiplier method. However, the fundamental elasticity relations could not be satisfied exactly, as the stress fields were assumed independent of the displacement fields. Further, analytical solutions to buckling problems were presented only for a simple loading condition of uni-axial buckling, except Khedir [4], who presented analytical solutions for a bi-axial compressive loading condition. No analytical solutions by using higher-order theories are available in the literature, to the author's knowledge, for buckling loads due to bi-axial compression-tension loading, thermal loading, and also due to the change in moisture concentrations. The same has been presented in this paper by employing a unified analytical approach based on mixed theory.

Mixed formulation has been developed by considering six degrees-of-freedom, viz. three displacement components, $u$, $v$, and $w$ (along the $x$, $y$ and $z$-directions, respectively) and three transverse stress components, $\tau_{xz}$, $\tau_{yz}$, and $\sigma_z$. These transverse

[1]To whom correspondence should be addressed.

Contributed by the Applied Mechanics Division of THE AMERICAN SOCIETY OF MECHANICAL ENGINEERS for publication in the ASME JOURNAL OF APPLIED MECHANICS. Manuscript received by the ASME Applied Mechanics Division, July 11, 2001; final revision, Dec. 5, 2001. Associate Editor: M.-J. Pindera. Discussion on the paper should be addressed to the Editor, Prof. Robert M. McMeeking, Department of Mechanical and Environmental Engineering University of California–Santa Barbara, Santa Barbara, CA 93106-5070, and will be accepted until four months after final publication of the paper itself in the ASME JOURNAL OF APPLIED MECHANICS.

  

stresses have been invoked from the assumed displacement fields by using constitutive law. Equilibrium equations have been derived by using the minimum potential energy principle. Thus, the method presented here differs from the higher-order theories available in the literature in following ways:

(i) A novel analytical approach using mixed theory has been presented that is based on minimum potential energy principle.
(ii) Fundamental elasticity relations between stress and displacement fields have been maintained at all points of an elastic continuum. It is a distinct feature of the present formulation that the stress-displacement relations are satisfied at the beginning of the formulation itself.
(iii) The method explicitly satisfies the requirements of through-thickness continuity of transverse stress components and continuous displacement fields as both are incorporated in the degrees-of-freedom.
(iv) Modal stresses (transverse stress components) have been directly evaluated as eigenvectors, as the same have been considered to be basic degrees-of-freedom.

Two sets of mixed models HYF1 and HYF2 have been presented in this paper by selectively incorporating nonlinear components of Green's strain tensor. Individual layer models HYF1 have been formulated by considering a local Cartesian coordinate system at the mid surface of each individual layer. Six degrees-of-freedom are assigned to the bottom as well as the top surfaces of each individual layer. Therefore, the total number of degrees-of-freedom in HYF1 always equals $[(N+1)\times 6]$ for the $N$ layered laminate. On the other hand, the global mixed models HYF2 have been formulated by considering the Cartesian coordinate system at the mid surface of the entire laminate and by assigning six degrees-of-freedom to the bottom as well as the top surface of the entire laminate. Hence, the total number of degrees-of-freedom always remains 12 in HYF2 models. The condition of the traction-free surface is not enforced in the case of HYF2 for a consistent comparison with the data available in the literature.

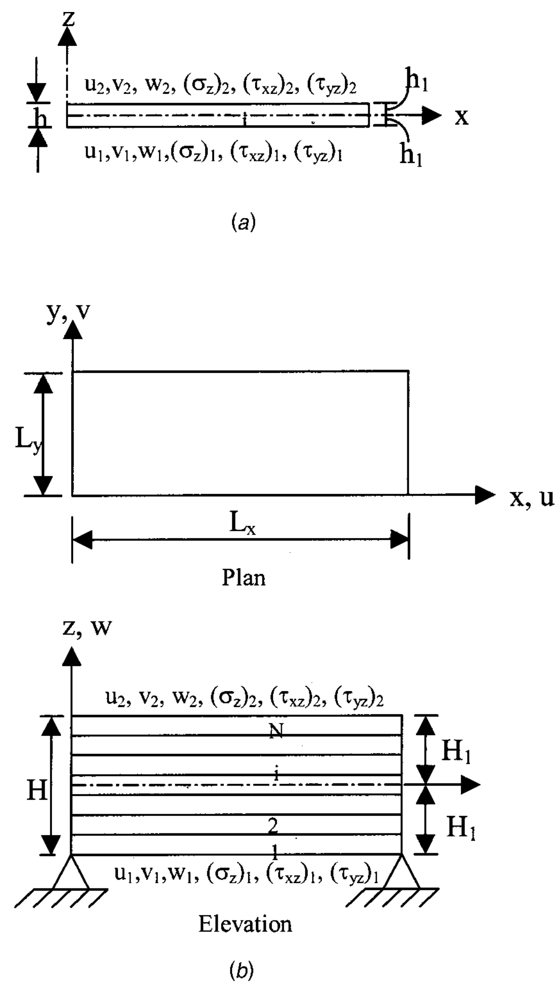


**Fig. 1 Laminated plate geometry, coordinate axes and degrees-of-freedom for (*a*) *i*th layer of a laminated plate in conjunction with HYF1 model, (*b*) laminated plate**

## Formulation

A rectangular laminated plate of plan dimensions $L_x$ by $L_y$ and thickness $H$ has been considered as shown in Fig. 1. The plate is composed of uniform thickness layers of homogeneous and orthotropic material. Three-displacement components $u(x,y,z)$, $v(x,y,z)$ and $w(x,y,z)$ at any point in a lamina can be expanded in terms of the thickness coordinate, $z$, by using the Taylor's series expansion as

$$u_k(x,y,z)=\sum_{i=0}^{3} z^i a_{ki}(x,y). \tag{1}$$

Here, $u_k$ $(k=1,2,3)$ represents three displacement components, $u$, $v$, $w$, respectively, and $a_{ki}$ indicate the generalized coordinates.

**Constitutive Law.** Each lamina in a laminate has been considered to be in a three-dimensional state of stress. Constitutive relations for a typical $i$th specially orthotropic lamina can be expressed as

$$\begin{Bmatrix}\sigma_x\\ \sigma_y\\ \sigma_z\\ \tau_{xy}\\ \tau_{xz}\\ \tau_{yz}\end{Bmatrix}^i=\begin{bmatrix}C_{11} & C_{12} & C_{13} & 0 & 0 & 0\\ & C_{22} & C_{23} & 0 & 0 & 0\\ & & C_{33} & 0 & 0 & 0\\ & & & C_{44} & 0 & 0\\ & \text{sym.} & & & C_{55} & 0\\ & & & & & C_{66}\end{bmatrix}^i \times\begin{Bmatrix}\varepsilon_x-\alpha_x\Delta T-\beta_x\Delta m\\ \varepsilon_y-\alpha_y\Delta T-\beta_y\Delta m\\ \varepsilon_z-\alpha_z\Delta T-\beta_z\Delta m\\ \gamma_{xy}\\ \gamma_{xz}\\ \gamma_{yz}\end{Bmatrix}^i \tag{2a}$$

$$\{\sigma\}^i=[C]^i\{\varepsilon\}^i. \tag{2b}$$

Here, $\{\sigma\}^i$ and $\{\varepsilon\}^i$ are stresses and the linear strain components, respectively, referred to the lamina coordinates and $C_{mn}$ $(m,n=1,2,3)$ are the elastic constants of the $i$th lamina. Further, $\alpha_j$ and $\beta_j$ $(j=x,y,z)$ represent the coefficients of thermal expansion and coefficients of moisture variations, respectively, in the three principal material directions of an $i$th lamina. $\Delta T$ and $\Delta m$, on the other hand, indicate changes in temperature and moisture concentration, respectively.

**Green's Strain Tensor.** Components of Green's strain tensor are

$$\varepsilon_x=\frac{\partial u}{\partial x}+\frac{\delta_1}{2}\left(\frac{\partial u}{\partial x}\right)^2+\frac{\delta_2}{2}\left(\frac{\partial v}{\partial x}\right)^2+\frac{\delta_3}{2}\left(\frac{\partial w}{\partial x}\right)^2$$

$$\varepsilon_y=\frac{\partial v}{\partial y}+\frac{\delta_1}{2}\left(\frac{\partial u}{\partial y}\right)^2+\frac{\delta_2}{2}\left(\frac{\partial v}{\partial y}\right)^2+\frac{\delta_3}{2}\left(\frac{\partial w}{\partial y}\right)^2$$

$$\varepsilon_z=\frac{\partial w}{\partial z}+\frac{1}{2}\left(\frac{\partial u}{\partial z}\right)^2+\frac{1}{2}\left(\frac{\partial v}{\partial z}\right)^2+\frac{1}{2}\left(\frac{\partial w}{\partial z}\right)^2 \qquad (3a)$$

$$\gamma_{xy}=\frac{\partial u}{\partial y}+\frac{\partial v}{\partial x}+\delta_1\left(\frac{\partial u}{\partial x}\frac{\partial u}{\partial y}\right)+\delta_2\left(\frac{\partial v}{\partial x}\frac{\partial v}{\partial y}\right)+\delta_3\left(\frac{\partial w}{\partial x}\frac{\partial w}{\partial y}\right)$$

$$\gamma_{yz}=\frac{\partial w}{\partial y}+\frac{\partial v}{\partial z}+\frac{\partial u}{\partial y}\frac{\partial u}{\partial z}+\frac{\partial v}{\partial y}\frac{\partial v}{\partial z}+\frac{\partial w}{\partial y}\frac{\partial w}{\partial z}$$

$$\gamma_{xz}=\frac{\partial u}{\partial z}+\frac{\partial w}{\partial x}+\frac{\partial u}{\partial x}\frac{\partial u}{\partial z}+\frac{\partial v}{\partial x}\frac{\partial v}{\partial z}+\frac{\partial w}{\partial x}\frac{\partial w}{\partial z}$$

$$\{\varepsilon\}=\{\varepsilon\}_L+\{\varepsilon\}_{NL}. \qquad (3b)$$

The linear part of strain-displacement relations $\{\varepsilon\}_L$ has been used to derive the lamina property matrices. On the other hand, the nonlinear strain-displacement relations $\{\varepsilon\}_{NL}$ have been employed to derive the geometric property matrices of a lamina. The $\delta$s are not included deliberately in the third, fifth, and sixth, of Eq. (3$a$) as laminates do not buckle under the application of external stresses in the $z$-direction ($\sigma_z$) and the transverse shear stresses $\tau_{xz}$ and $\tau_{yz}$. Therefore, the nonlinear terms from the strains $\varepsilon_z$, $\gamma_{xz}$, and $\gamma_{yz}$ will not contribute to the work done by external stresses. Different hybrid models are defined based on values of the Kronecker deltas $\delta_1$ to $\delta_3$ used in Eq. (3$a$).

**Various Mixed Models.** Contributions of nonlinear strains terms related with the $u$ and $v$ displacements have been neglected in most higher-order theories available in the literature to simplify analysis. Following HYF1 and HYF2 hybrid models have been proposed, based on $\delta_1$ to $\delta_3$, to evaluate the influence of these terms on buckling loads of the laminates.

HYF13 and HYF23—all nonlinear strain terms are incorporated in the formulation,

$$\text{i.e.,}\quad \delta_1=\delta_2=\delta_3=1.$$

HYF12 and HYF22—nonlinear strain terms related with $v$ displacements are neglected,

$$\text{i.e.,}\quad \delta_2=0, \quad \text{but}\quad \delta_1=\delta_3=1.$$

HYF11 and HYF21—nonlinear strain terms related with $u$ displacements are neglected,

$$\text{i.e.,}\quad \delta_1=0, \quad \text{but}\quad \delta_2=\delta_3=1.$$

HYF10 and HYF20—nonlinear strain terms related with both $u$ and $v$ displacements are neglected,

$$\text{i.e.,}\quad \delta_1=\delta_2=0, \quad \text{but}\quad \delta_3=1.$$

It can be noted from Eq. (3$a$) that Von Karman strain-displacement relations are utilized in models HYF10 and HYF20.

**Kinematics.** The stress-displacement expressions have been derived by substituting Eq. (1) in the linear part of the strain-displacement relations from Eq. (3$a$) and substituting the resulting equation into the stress-strain relations from Eq. (2$a$). Consequently, equations for the stress degrees-of-freedom can be derived by substituting, $z=\pm\zeta$ in the resulting equations. Here, $\zeta$ is half the thickness of the $i$th lamina ($h_1$) for all individual layer mixed models (HYF1), or half the thickness of entire laminate ($H_1$) for all HYF2 models. Similarly, the equations for displacement degrees-of-freedom can be derived by substituting $z=\pm\zeta$ in Eq. (1). By solving two sets of equations simultaneously, the displacement field can be expressed in terms of degrees-of-freedom as

$$\begin{Bmatrix} u \\ v \\ w \end{Bmatrix}=[N_1]\{q\}+[N_2]\{q\}'+[N_3]\{q\}^*+[N_4]\{q_c\}. \qquad (4)$$

Here, $[N_1]$, $[N_2]$, $[N_3]$, and $[N_4]$ are $3\times12$ shape function matrices and are defined more conveniently in the Appendix. On the other hand, $\{q\}$ and $\{q_c\}$ are

$$\{q\}=\{u_r\ (\tau_{xz})_r\ w_r\ (\sigma_z)_r\ v_r\ (\tau_{yz})_r\ u_s\ (\tau_{xz})_s\ w_s\ (\sigma_z)_s\ v_s\ (\tau_{yz})_s\}^t \qquad (5a)$$

$$\{q_c\}=[\{q_{cr}\}^t\{q_{cs}\}^t]^t_{(1\times12)}$$

$$\{q_{cj}\}=\{\alpha_{xj}\Delta T\ \beta_{xj}\Delta m\ \alpha_{yj}\Delta T\ \beta_{yj}\Delta m\ \alpha_{zj}\Delta T\ \beta_{zj}\Delta T\}^t,\quad j=r,s. \qquad (5b)$$

The prime (′) and star (*) appearing in Eq. (4) represent derivatives of vector $\{q\}$ with respect to the $x$ and $y$-coordinates, respectively. Subscripts $r$ and $s$, in Eq. (5$a$) indicate the bottom and top surface of the $i$th layer in the HYF1 models. However, they represent the bottom and top surfaces of the entire laminate in the HYF2 models.

**Strain-Displacement Relations.** Substitution of Eq. (4) in the linear part of Eq. (3$a$) yields the linear strain-displacement equation

$$\{\varepsilon\}_L=[a]\{q\}+[b]\{q\}'+[d]\{q\}''+[e]\{q\}^*+[f]\{q\}^{**}+[g]\{q\}^{*\prime}+[t]\{q_c\} \qquad (6)$$

where $[a]$, $[b]$, $[d]$, $[e]$, $[f]$, $[g]$, and $[t]$ are $6\times12$ nodal strain-displacement matrices. Nonzero coefficients of these matrices have been presented in the Appendix. Equations (4), (6), and (7) are the general equations representing displacements, linear strains, and the relevant nonlinear strains, respectively, at any point in the laminate. $\{q\}$ in these equations represents the matrix of the degrees-of-freedom given by Eq. (5$a$). By substituting Eqs. (4) in the nonlinear part of Eqs. (3$a$), the relevant nonlinear strain terms can be expressed as

$$\left(\frac{\partial u_k}{\partial x}\right)^2=[\{N_{1k}\}\{q\}'+\{N_{2k}\}\{q\}''+\{N_{3k}\}\{q\}^{*\prime}]^2$$
$$\left(\frac{\partial u_k}{\partial y}\right)^2=[\{N_{1k}\}\{q\}^*+\{N_{2k}\}\{q\}'^*+\{N_{3k}\}\{q\}^{**}]^2 \qquad (7)$$

where $\{N_{jk}\}$ $(j,k=1,2,3)$ indicate the elements of the $k$th row of the $j$th shape function matrix presented in the Appendix.

**Potential Energy of a Lamina.** The potential energy, $\Pi^i$ of a typical $i$th lamina enclosing a space volume, $V$, can be expressed as

$$\Pi^i=U^i-W^i \qquad (8)$$

where $U^i$ represents the strain energy stored in the lamina and $W^i$ indicates the work done by externally applied stresses, $\sigma_x^{pi}$ and $\sigma_y^{pi}$ acting in the $x$ and $y$-directions, respectively. By substituting the expressions for strain energy and the work done in Eq. (8), the potential energy of a lamina can be written as

$$\Pi^i=\frac{1}{2}\int_v\{\varepsilon\}_L^T[C]^i\{\varepsilon\}_L dv-\left[\int_v\sigma_x^{pi}(\varepsilon_x)_{NL}dv+\int_v\sigma_y^{pi}(\varepsilon_y)_{NL}dv\right]. \qquad (9)$$

**Lamina Equilibrium Equations.** The following trial solutions have been considered, which satisfy simple support conditions.

$$
\begin{aligned}
u_j &= A_j \cos \lambda_1 x \sin \lambda_2 y \qquad (\tau_{xz})_j = B_j \cos \lambda_1 x \sin \lambda_2 y \\
w_j &= C_j \sin \lambda_1 x \sin \lambda_2 y \qquad (\sigma_z)_j = D_j \sin \lambda_1 x \sin \lambda_2 y \\
v_j &= E_j \sin \lambda_1 x \cos \lambda_2 y \qquad (\tau_{yz})_j = F_j \sin \lambda_1 x \cos \lambda_2 y, \\
&\qquad j = r, s.
\end{aligned} \tag{10}
$$

Here, $\lambda_1 = m\pi/L_x$, $\lambda_2 = n\pi/L_y$, $m$ and $n$ are the wave numbers indicating a specific buckling mode.

By substituting Eq. (10) by Eq. (9), the ensuing equilibrium equation can be obtained by applying variational principle as

$$[[K]^i - \sigma_x^{pi}[K_{G1}]^i - \sigma_y^{pi}[K_{G2}]^i]\{q_a\} = 0 \tag{11}$$

where

$$\{q_a\} = \{A_1 B_1 C_1 D_1 E_1 F_1 A_2 B_2 C_2 D_2 E_2 F_2\}^t. \tag{12a}$$

The property matrix $[K]^i$ and the geometric property matrices $[K_{G1}]^i$ and $[K_{G2}]^i$ of the $i$th lamina are given by

$$
[K] = \begin{bmatrix}
[S_{aa}] + \lambda_1([\overline{S_{ab}}] - [\overline{S_{ba}}]) - \lambda_1^2([S_{ad}] + [S_{da}] - [S_{bb}]) + \lambda_2([\overline{S_{ae}}] - [\overline{S_{ea}}]) \\
-\lambda_2^2([S_{af}] + [S_{fa}] - [S_{ee}]) + \lambda_1\lambda_2([\overline{S_{ag}}] + [\overline{S_{ga}}] - [\overline{S_{be}}] - [\overline{S_{eb}}]) \\
+\lambda_1^3([\overline{S_{db}}] - [\overline{S_{bd}}]) + \lambda_1^2\lambda_2([\overline{S_{gb}}] - [\overline{S_{bg}}] + [\overline{S_{de}}] - [\overline{S_{ed}}]) + \lambda_1^4[S_{dd}] \\
+\lambda_1^2\lambda_2^2([S_{df}] + [S_{fd}] + [S_{gg}]) + \lambda_1^3\lambda_2([\overline{S_{dg}}] + [\overline{S_{gd}}]) + \lambda_2^3([\overline{S_{fe}}] - [\overline{S_{ef}}]) \\
+\lambda_1\lambda_2^2([\overline{S_{fb}}] - [\overline{S_{bf}}] - [\overline{S_{eg}}] + [\overline{S_{ge}}]) + \lambda_2^4[S_{ff}] + \lambda_1\lambda_2^3([\overline{S_{fg}}] + [\overline{S_{gf}}])
\end{bmatrix} \tag{12b}
$$

$$
\begin{aligned}
[K_{G1}] &= \sum_{j=1}^{3} \sigma_j \begin{bmatrix} \lambda_1^2[G_{bbj}] + \lambda_1^4[G_{aaj}] + \lambda_1^2\lambda_2^2[G_{ccj}] + \lambda_1^3([\overline{G_{abj}}] - [\overline{G_{baj}}]) \\ +\lambda_1^2\lambda_2([\overline{G_{cbj}}] - [\overline{G_{bcj}}]) + \lambda_1^3\lambda_2([\overline{G_{acj}}] + [\overline{G_{caj}}]) \end{bmatrix} \\
[K_{G2}] &= \sum_{j=1}^{3} \delta_j \begin{bmatrix} \lambda_2^2[G_{bbj}] + \lambda_1^2\lambda_2^2[G_{aaj}] + \lambda_2^4[G_{ccj}] + \lambda_1\lambda_2^2([\overline{G_{abj}}] - [\overline{G_{baj}}]) \\ +\lambda_2^3([\overline{G_{cbj}}] - [\overline{G_{bcj}}]) + \lambda_1\lambda_2^3([\overline{G_{acj}}] + [\overline{G_{caj}}]) \end{bmatrix}.
\end{aligned} \tag{12c}
$$

Layerwise property matrices $[S_{aa}]$, $[S_{ab}]$, etc., and geometric property matrices $[G_{aa}]$, $[G_{ab}]$, etc., are presented in the Appendix. The signs of the few elements of the matrices would get modified due to the substitution of Eq. (10) into Eq. (9). Such matrices have been represented with bars atop them. Further, superscript $i$ has been omitted in Eqs. (12) for convenience.

**Laminate/Global Equilibrium Equations.**

*HYF1—Individual Layer Models.* Matrices $[K]^i$ and $[K_G]^i$ of various laminae are assembled by enforcing continuities of the displacements and transverse stresses at the interfaces of the laminae to form the global matrices $[K]$ and $[K_G]$ for the entire laminate. The global equilibrium equations can then be written as

$$[K] - \lambda_{cr}[K_G] = [0] \tag{13a}$$

where

$$[K_G] = \sigma_x^p[K_{G1}] + \sigma_y^p[K_{G2}]. \tag{13b}$$

The critical buckling coefficient $\lambda_{cr}$ can be evaluated by employing a generalized eigenvalue solver. Subsequently, the buckling stresses can be expressed as $\sigma_{xcr}^p = \lambda_{cr}\sigma_x^p$ and $\sigma_{ycr}^p = \lambda_{cr}\sigma_y^p$.

*HYF2—Equivalent Single-Layer Models.* Global matrices of the entire laminate are evaluated by summing the respective matrices of all the laminae for HYF2 models as

$$[K] = \sum_{i=1}^{N} [K]^i \quad \text{and} \quad [K_G] = \sum_{i=1}^{N} [K_G]^i. \tag{14}$$

By substituting these global matrices in Eq. (13*a*), the critical buckling coefficient $\lambda_{cr}$ can be evaluated.

**Hygrothermal Buckling.** A general formulation was presented in the preceding sections for stability analysis of laminates subjected to mechanical as well as hygrothermal loads. When a laminate is subjected to change in temperature or moisture, stresses are developed at the supports due to the restriction to free expansion or contraction. These stresses may be evaluated by simply performing a prebuckling analysis of laminates with the help of the nonhomogeneous equation

$$[K]\{q\} = \{F\} \tag{15}$$

where $\{F\}$ represents the load vector associated with the given change in temperature or moisture concentration. Because isotropic and orthotropic laminates are in a state of plane stress due to temperature or moisture changes, only $\sigma_x^p$ and $\sigma_y^p$ would develop at the supports. These in-plane stresses can be evaluated by using the plane stress-strain relations. Such an approach has been employed for the first time here for thermal buckling analysis of laminated plates.

**Shear Buckling.** Laminates may also buckle under the action of externally applied in-plane shear stresses $\tau_{xy}^p$. However, the presence of derivatives, such as $\partial^4 w/\partial x^3 \partial y$ or $\partial^4 w/\partial x \partial y^3$ prevent separation of variables (Narita and Leissa [15]). Therefore, the problem of shear buckling cannot be solved with the help of an assumed trial solution. Instead, the series solutions satisfying the boundary condition can be used. Such solutions, however, have not been attempted here. Thus, the Kronecker deltas were not shown in the expressions for transverse strain components in Eq. (3).

## Illustrative Examples

Various mixed models were applied to compute buckling loads of simply supported, isotropic, orthotropic, as well as laminated plates. Discretization of each layer of a laminated plate into ten sublayers was found to yield converging solutions for the HYF1 models. However, such divisions did not improve results when HYF2 models were used. Critical buckling loads were computed for uni-axial compression, bi-axial compression, bi-axial compression-tension, and thermal and hygroscopic loading conditions. Results were validated by comparing them with three-dimensional elasticity and other analytical solutions available in the literature.

**Table 1 Various material property sets used in the illustrative examples**

| Material Set | Properties |
|---|---|
| 1 | $C_{12}/C_{11}=0.233190$, $C_{13}/C_{11}=0.010776$, $C_{22}/C_{11}=0.543103$, $C_{23}/C_{11}=0.098276$, $C_{33}/C_{11}=0.530172$, $C_{44}/C_{11}=0.262931$, $C_{55}/C_{11}=0.159914$, $C_{66}/C_{11}=0.266810$ (Source: Srinivas and Rao [17]) |
| 2 | $E_1/E_2=3$ to 40, $E_3=E_2$, $G_{12}/E_2=G_{13}/E_2=0.60$, $G_{23}/E_2=0.50$, $\nu_{12}=\nu_{23}=\nu_{13}=0.25$ (Source: Noor [18]) |
| 3 | $E_1/E_2=40$, $E_3=E_2$, $G_{12}/E_2=G_{13}/E_2=0.50$, $G_{23}/E_2=0.20$, $\nu_{12}=\nu_{23}=\nu_{13}=0.25$ |
| 4 | $E_1/E_2=15$, $E_3=E_2$, $G_{12}/E_2=G_{13}/E_2=0.50$, $G_{23}/E_2=0.3356$, $\nu_{12}=\nu_{13}=0.30$, $\nu_{23}=0.49$, $\alpha_1/\alpha_0=0.015$, $\alpha_2/\alpha_0=\alpha_3/\alpha_0=1.00$ (Source: Noor [20]) |
| 5 | Elastic moduli graphite epoxy lamina at different moisture concentrations $C$ (%), $E_1=130$ GPa, $G_{13}=G_{12}=6.0$ GPa, $G_{23}=0.5\,G_{12}$, $\nu_{12}=\nu_{23}=\nu_{13}=0.3$, $\beta_1=0$ and $\beta_2=\beta_3=0.44$. (Source: Sai-Ram, and Sinha [21]) |

| $C$ (%) | 0.00 | 0.25 | 0.50 | 0.75 | 1.00 | 1.25 | 1.50 |
|---|---|---|---|---|---|---|---|
| $E_2$ GPa | 9.5 | 9.25 | 9.0 | 8.75 | 8.5 | 8.5 | 8.5 |

Different material property sets considered in the illustrative examples are tabulated under Table 1. Buckling loads have been expressed in terms of the following nondimensional parameters for facilitating comparison.

$$\text{(i)} \qquad \lambda = H\sqrt{(\sigma_{xcr}\lambda_1^2+\sigma_{ycr}\lambda_2^2)/\eta} \tag{16}$$

where $\sigma_{xcr}$, $\sigma_{ycr}$ represent critical stresses in the $x$ and $y$-directions of a plate, referred in Example 1, and $\eta$ indicates normalization factor that is equal to $G$ for isotropic plates and $C_{11}$ for orthotropic plates.

$$\text{(ii)} \qquad \lambda_U=\lambda_B=\lambda_{CT}=\frac{\sigma_{xcr}L_y^2}{E_2H^2} \tag{17}$$

where $\lambda_U$, $\lambda_B$, and $\lambda_{CT}$ are, respectively, the uni-axial, bi-axial, and compression-tension bi-axial buckling stress parameters.

$$\text{(iii)} \qquad \lambda_T=\alpha_0 T_{cr} \tag{18}$$

where $\lambda_T$ represents the thermal buckling parameter, $\alpha_0$ indicates normalization factor for the coefficient of thermal expansion, and $T_{cr}$ refers to the critical temperature.

**Example 1—Orthotropic Plate Subjected to Uni-axial and Bi-axial Compression.** Buckling load parameters $\lambda$ for an orthotropic plate (Material 1) for various values of $(L_y/H)$ have been tabulated under Table 2. The table is applicable for uni-axial (either $\sigma_{xcr}=0$ or $\sigma_{ycr}=0$) as well as bi-axial loading conditions. It can be observed from Table 2 that results obtained by using the HYF13 model are in excellent agreement with the three-dimensional elasticity solutions presented in [16] and [17]. It is evident from the table that the values of $\lambda$ estimated by the HYF10 model are inferior to those estimated by other HYF1 models as the nonlinear strain-displacement terms related with $u$ as well as $v$ displacements have been neglected in the HYF10 model. However, results from the HYF12 model are inferior to those from the HYF11 model for an orthotropic plate. Numerical experimentation show that the difference in the results of two models (HYF12 and HYF11) go on increasing as the degree of orthotropy $(E_1/E_2)$ increases, particularly for thick plates. Further, it has been observed that the results from HYF12 and HYF11 models are identical for an isotropic plate. However, these numerical results are not presented here for brevity. Thus, it can be tentatively concluded that the contribution of nonlinear strain-displacement terms related with $v$ displacement is significant in buckling response, probably due to the Poisson's effect.

Variation of stresses and displacements (evaluated by using the HYF13 model) across a thickness for a homogeneous, orthotropic square plate (Material 1) are also in excellent agreement with the three-dimensional elasticity results presented by Srinivas and Rao [17]. However, the results are not presented for brevity.

**Example 2—Crossply Laminated Plate Subjected to Uni-axial Compression.** Uni-axial buckling load parameters $\lambda_U$ for crossply, antisymmetric laminated plates (Material 2) have been presented in Table 3. Results are compared with the three-dimensional elasticity solutions by Noor [18] and with the following analytical solutions by using displacement-based higher-order theories: (i) Putcha and Reddy [19]—higher order shear deformation theory (HSDT); and (ii) Wu and Chen [14]—displacement-based local higher-order shear deformation theory (LHSDT).

It can be seen from Table 3 that the HSDT overestimate buckling loads compared to the results from the present study and the

**Table 2 Buckling load parameters λ for an orthotropic plate in Example 1**

| | | HYF1 | | | | HYF2 | | | |
|---|---|---|---|---|---|---|---|---|---|
| $L_y/H$ | 3-D Elast.[a] | HYF13 | HYF12 | HYF11 | HYF10 | HYF23 | HYF22 | HYF21 | HYF20 |
| 2.0 | 0.70338 | 0.70338 | 0.72473 | 0.70653 | 0.72879 | 0.70406 | 0.72553 | 0.70726 | 0.72965 |
| 2.5 | 0.51342 | 0.51342 | 0.52680 | 0.51676 | 0.53067 | 0.51368 | 0.52710 | 0.51704 | 0.53100 |
| 10/3 | 0.33200 | 0.33200 | 0.33858 | 0.33473 | 0.34153 | 0.33207 | 0.33866 | 0.33480 | 0.34161 |
| 5 | 0.16942 | 0.16942 | 0.17141 | 0.17070 | 0.17275 | 0.16942 | 0.17142 | 0.17071 | 0.17276 |
| 10 | 0.04742 | 0.04742 | 0.04760 | 0.04758 | 0.04776 | 0.04742 | 0.04760 | 0.04758 | 0.04776 |

[a]Srinivas and Rao [17]

**Table 3 Buckling load parameter $\lambda_U$ for square, antisymmetric crossply laminate in Example 2 when $L_x/H=10$**

| $N$ | $E_1/E_2$ | 3-D Elast.[a] | HYF1 | | | | HYF23 | HSDT[b] | LHSDT[c] |
|---|---|---|---|---|---|---|---|---|---|
| | | | HYF13 | HYF12 | HYF11 | HYF10 | | | |
| | 3 | 4.6948 | 4.6953 | 4.7385 | 4.7385 | 4.7824 | 4.6960 | 4.7749 | 4.6953 |
| | 10 | 6.1181 | 6.1202 | 6.1881 | 6.1881 | 6.2575 | 6.1300 | 6.2721 | 6.1202 |
| 2 | 20 | 7.8196 | 7.8237 | 7.9128 | 7.9128 | 8.0038 | 7.8727 | 8.1151 | 7.8238 |
| | 30 | 9.3746 | 9.3809 | 9.4867 | 9.4867 | 9.5949 | 9.4952 | 9.8695 | 9.3809 |
| | 40 | 10.8167 | 10.8253 | 10.9454 | 10.9454 | 11.0681 | 11.0262 | 11.5630 | 10.8254 |
| | 3 | 5.1738 | 5.1739 | 5.2139 | 5.2139 | 5.2545 | 5.1788 | 5.2523 | 5.1739 |
| | 10 | 9.0164 | 9.0176 | 9.0858 | 9.0858 | 9.1550 | 9.0607 | 9.2315 | 9.0176 |
| 4 | 20 | 13.7429 | 13.7461 | 13.8405 | 13.8405 | 13.9361 | 13.8944 | 14.2540 | 13.7461 |
| | 30 | 17.7829 | 17.7886 | 17.8993 | 17.8993 | 18.0114 | 18.0771 | 18.6670 | 17.7886 |
| | 40 | 21.2796 | 21.2879 | 21.4089 | 21.4089 | 21.5313 | 21.7342 | 22.5790 | 21.2880 |
| | 3 | 5.2673 | 5.2674 | 5.3067 | 5.3067 | 5.3466 | 5.2711 | 5.3420 | 5.2674 |
| | 10 | 9.6051 | 9.6057 | 9.6724 | 9.6724 | 9.7401 | 9.6296 | 9.7762 | 9.6057 |
| 6 | 20 | 15.0014 | 15.0030 | 15.0949 | 15.0949 | 15.1878 | 15.0802 | 15.3520 | 15.0031 |
| | 30 | 19.6394 | 19.6425 | 19.7489 | 19.7489 | 19.8565 | 19.7901 | 20.2010 | 19.6425 |
| | 40 | 23.6689 | 23.6734 | 23.7881 | 23.7881 | 23.9038 | 23.9008 | 24.4600 | 23.6735 |
| | 3 | 5.3159 | 5.3159 | 5.3548 | 5.3548 | 5.3943 | 5.3189 | 5.3882 | 5.3159 |
| | 10 | 9.9134 | 9.9136 | 9.9794 | 9.9794 | 10.0461 | 9.9281 | 10.0560 | 9.9136 |
| 10 | 20 | 15.6685 | 15.6692 | 15.7593 | 15.7593 | 15.8505 | 15.7116 | 15.9140 | 15.6692 |
| | 30 | 20.6347 | 20.6360 | 20.7398 | 20.7398 | 20.8446 | 20.7149 | 20.9860 | 20.6360 |
| | 40 | 24.9636 | 24.9654 | 25.0763 | 25.0763 | 25.1882 | 25.0855 | 25.4220 | 24.9654 |

[a]Noor [18]
[b]Putcha and Reddy [19]
[c]Wu and Chen [14]

LHSDT. The shortcomings of the HSDT can be attributed to two facts: (i) the theory is two-dimensional equivalent single-layer theory; and (ii) the nonlinear strain terms related with $u$ as well as $v$ displacements have been neglected while evaluating the external work in this theory. Thus, it can be summarized that the ESL theories cannot predict buckling loads accurately for a large degree of orthotropy and for large difference in material properties of different layers in a laminate. Individual layer theories would certainly be required in such situations. Further, the nonlinear strain-displacement terms related with at least $v$ displacement should be incorporated in the external work equations for better accuracy.

Though the buckling load parameters obtained by LHSDT and the present HYF13 model are the same, the present mixed approach has many advantages over the LHSDT. The LHSDT is a displacement-based layerwise theory while the present HYF1 is a layerwise theory that is based on the mixed approach. Continuity of transverse stresses between the laminae is to be specifically satisfied through Lagrange multipliers in the LHSDT. However, in the HYF1 the transverse stress continuity is inherently satisfied as these stresses are incorporated in the degrees-of-freedom. Moreover, in the HYF1 the transverse stresses are evaluated directly as eigenvectors. Therefore, pointwise recalculation of stresses is not required in the present approach.

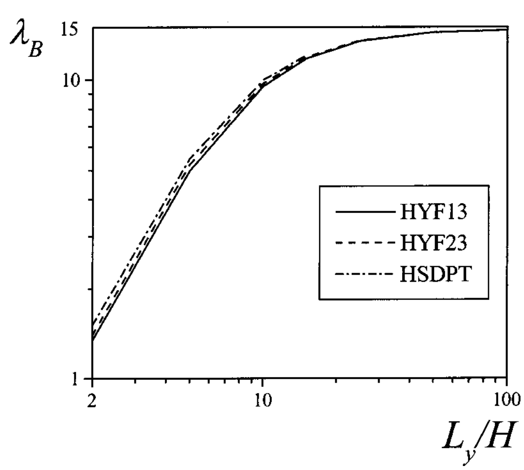


**Fig. 2 Variation of biaxial buckling load parameter $\lambda_B$ with $L_y/H$ for a crossply [0 deg/90 deg/0 deg] laminated plate considered in Example 3**

**Example 3—Crossply Laminated Plate Subjected to Bi-axial Compression.** The buckling load parameter $\lambda_B$ for a square, crossply (0 deg/90 deg/0 deg) laminate (Material 2 with $E_1/E_2=40$) under bi-axial compressive loading ($\sigma_x^p=1$ and $\sigma_y^p=1$) are presented in Fig. 2. Results are compared with the analytical solutions by Khdeir [4]. The minimum buckling loads in the table correspond to a buckling mode $m=1$ and $n=2$. It is observed that the results obtained by Khdeir [4] (HSDPT) are close to those obtained by the global HYF20 model and are higher compared to the HYF13 model due to the reasons cited above.

Modal stresses and displacements have been plotted in Figs. 3($a$) to 3($f$) for the bi-axial compressive loading condition ($\sigma_x^p=1$ and $\sigma_y^p=1$) with $E_1/E_2=40$ and $L_x/H=10$. Pointwise recalculation of modal stresses and displacements is required when ESL theories are used. On the other hand, the local mixed HYF13 model directly provides these parameters as eigenvectors, which is a distinct advantage of the mixed theory presented here. Soundness and applicability of the proposed formulation has been further demonstrated through the continuity of the transverse modal stresses and displacements.

**Example 4—Orthotropic Plate Subjected to Bi-axial Compression-Tension Loading.** Few analytical benchmark solutions for the buckling load parameters $\lambda_{CT}$ for a bi-axial compression-tension loading condition have been presented in Table 4 for an orthotropic plate (Material 3). Buckling load parameters $\lambda_U$ and $\lambda_B$ are also presented for comparison. Angle $\theta$ in Table 4 represents the angle made by the fiber direction of the orthotropic plate with respect to the $x$-axis. It can be observed from the table that the buckling parameter $\lambda_{CT}$ for thin plates is comparatively higher for bi-axial compression-tension loading when the compressive load is applied along the fibers and the tensile load in the transverse direction. Such behavior can be attributed to: (i) the restraining action provided by the applied tensile stress in the transverse direction; and to (ii) the Poisson's effect. On the other hand, buckling load increases only marginally when the tensile load is applied along the fiber and compressive

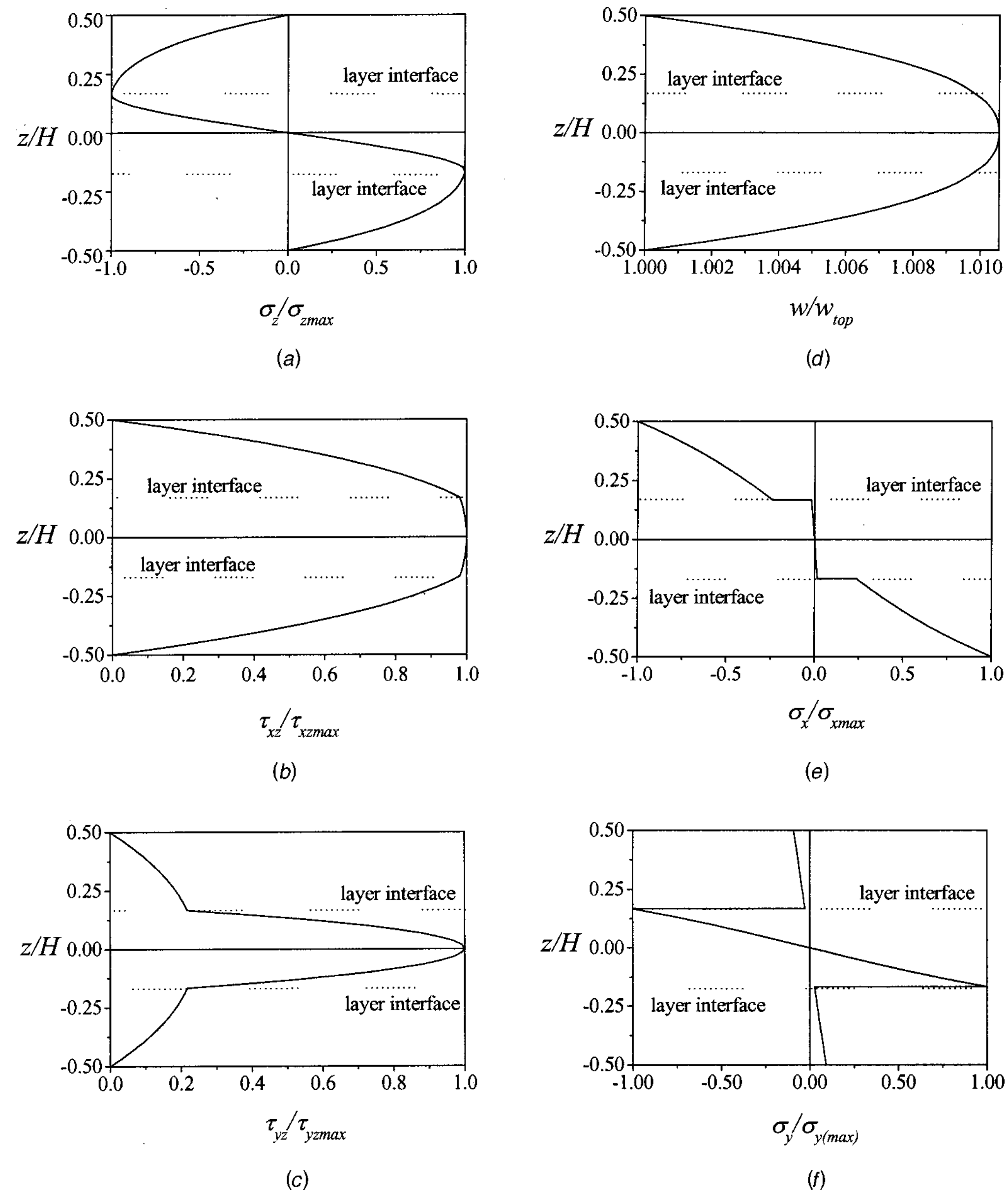


**Fig. 3 Variation of normalized (*a*) transverse normal stress ($\sigma_z/\sigma_{z\,\max}$); (*b*) transverse shear stress ($\tau_{xz}/\tau_{xz\,\max}$); (*c*) transverse shear stress ($\tau_{yz}/\tau_{yz\,\max}$); (*d*) transverse displacement ($w/w_{\mathrm{top}}$); (*e*) in-plane stress ($\sigma_x/\sigma_{x\,\max}$) and (*f*) in-plane stress ($\sigma_y/\sigma_{y\,\max}$) for a (0 deg/90 deg/0 deg) crossply laminated plate in Example 3 under bi-axial compressive loading with $P_x = P_y = 1$**

load in the transverse direction because the Poisson's ratio in the transverse direction ($\upsilon_{TL}$) is very small compared to the one in the longitudinal direction ($\upsilon_{LT}$). However, the value of $\lambda_{CT}$ is comparable to $\lambda_U$ for a thick plate regardless of the value of $\theta$ considered in the present analysis as the applied tensile stress is insignificant to create an appreciable restraining action in the transverse direction. Further, thick plates buckle in higher modes, especially when they are subjected to bi-axial compression-tension loads.

**Example 5 Laminates Subjected to Thermal Loads.** Thermal buckling parameters $\lambda_T$ for a laminate having ten orthotropic layers (Material 4) have been presented in Table 5. These results are also in excellent agreement with the three-dimensional elasticity results ([20]) for thin as well as for thick plates. Critical temperatures for the laminate corresponds to the buckling mode $m = 1$. $n = 2$, because laminates subjected to change in temperature are essentially subjected to the biaxial loading condition. It can be observed from Table 5 that the thin laminates buckle, as expected, at very low temperatures compared to thick laminates.

**Example 6 Effect of Change in Moisture Concentration on Uni-axial Buckling Load.** Few analytical benchmark solutions on the effects of change in moisture concentrations on the uni-axial buckling load parameter $\lambda_U$ of a crossply $[(0/90)_s]$ laminated plate (Material 5) have been tabulated under Table 6. Reduction in material properties with the increase in moisture concentration ([21]) has been considered to evaluate the buckling loads. The parameter $(E_2)_{c=0.0\%}$ has been used to evaluate the buckling load parameter $\lambda_U$ from Eq. (17). $\lambda_U$ obtained by the HYF13 model for different $L_y/H$ ratios have been plotted in Fig. 4. It can be seen from Fig. 4 that the buckling parameter reduces rapidly in thin plates compared to thick plates. However, the reduction is almost linear for thin as well as thick plates. Further,

**Table 4 Buckling load parameters for an orthotropic square plate in Example 4**

| $\theta$ | Theory | $L_x/H=100$ | | | $L_x/H=10$ | | | $L_x/H=2$ | | |
|---|---|---|---|---|---|---|---|---|---|---|
| | | $\lambda_U$ | $\lambda_B$ | $\lambda_{CT}$ | $\lambda_U$ | $\lambda_B$ | $\lambda_{CT}$ | $\lambda_U$ | $\lambda_B$ | $\lambda_{CT}$ |
| 0 deg | HYF13 | 35.5487 | 10.7932 | 173.2168 | 20.2128 | 6.5163 | 43.2361 | 1.9515 | 0.7395 | 1.9875 |
| | HYF12 | 35.5516 | 10.7968 | 173.2310 | 20.3521 | 6.6562 | 43.4668 | 1.9710 | 0.7486 | 1.9880 |
| | HYF11 | 35.5516 | 10.7941 | 173.2703 | 20.2632 | 6.5308 | 43.2983 | 1.9520 | 0.7397 | 1.9877 |
| | HYF10 | 35.5549 | 10.7977 | 173.2845 | 20.4032 | 6.6713 | 43.5298 | 1.9716 | 0.7489 | 1.9882 |
| | HYF23 | 35.5487 | 10.7932 | 173.2168 | 20.2163 | 6.5177 | 43.5593 | 2.0043 | 0.7610 | 2.0056 |
| | HYF20 | 35.5545 | 10.7976 | 173.2845 | 20.4068 | 6.6728 | 43.8604 | 2.0282 | 0.7748 | 2.0066 |
| | $(m,n)$ | (1,1) | (1,2) | (2,1) | (1,1) | (1,2) | (3,1) | (3,1) | (1,5) | (19,1) |
| 90 deg | HYF13 | 13.0327 | 10.7932 | 14.6617 | 7.6985 | 6.5163 | 8.6608 | 0.7582 | 0.7395 | 0.7649 |
| | HYF12 | 13.0337 | 10.7941 | 14.6629 | 7.7133 | 6.5308 | 8.6774 | 0.7583 | 0.7486 | 0.7650 |
| | HYF11 | 13.0422 | 10.7968 | 14.6725 | 7.9603 | 6.6562 | 8.9553 | 0.7649 | 0.7397 | 0.7709 |
| | HYF10 | 13.0433 | 10.7977 | 14.6737 | 7.9762 | 6.6713 | 8.9732 | 0.7651 | 0.7489 | 0.7710 |
| | HYF23 | 13.0327 | 10.7932 | 14.6617 | 7.7017 | 6.5177 | 8.6644 | 0.7904* | 0.7610 | 0.7996 |
| | HYF20 | 13.0433 | 10.7976 | 14.6737 | 7.9797 | 6.6728 | 8.9772 | $0.7999^{+}$ | 0.7748 | 0.8016 |
| | $(m,n)$ | (3,1) | (2,1) | (3,1) | (3,1) | (2,1) | (3,1) | (9,1) | (5,1) | (14,1) |

*indicates $(m=7,\ n=1)$ and $^{+}$indicates $(m=6,\ n=1)$.

**Table 5 Thermal buckling parameter $(\lambda_T=\alpha_0 T_{cr})$ of a square orthotropic plate in Example 5 when $N=10$, and $m=1$, $n=2$**

| $L_x/H$ | 3-D Elast.[a] | HYF1 | | | | HYF23 |
|---|---|---|---|---|---|---|
| | | HYF13 | HYF12 | HYF11 | HYF10 | |
| 100.0000 | $0.7463\times10^{-3}$ | $0.7463\times10^{-3}$ | $0.7466\times10^{-3}$ | $0.7464\times10^{-3}$ | $0.7466\times10^{-3}$ | $0.7463\times10^{-3}$ |
| 20.0000 | $0.1739\times10^{-1}$ | $0.1739\times10^{-1}$ | $0.1752\times10^{-1}$ | $0.1742\times10^{-1}$ | $0.1755\times10^{-1}$ | $0.1739\times10^{-1}$ |
| 10.0000 | $0.5782\times10^{-1}$ | $0.5782\times10^{-1}$ | $0.5926\times10^{-1}$ | $0.5805\times10^{-1}$ | $0.5951\times10^{-1}$ | $0.5782\times10^{-1}$ |
| 6.6667 | 0.1029 | 0.1029 | 0.1073 | 0.1034 | 0.1078 | 0.1030 |
| 5.0000 | 0.1436 | 0.1436 | 0.1515 | 0.1442 | 0.1522 | 0.1438 |
| 4.0000 | 0.1777 | 0.1777 | 0.1886 | 0.1783 | 0.1894 | 0.1782 |
| 3.3333 | 0.2057 | 0.2057 | 0.2187 | 0.2063 | 0.2194 | 0.2066 |

[a]Noor and Burton [20]

**Table 6 Effect of moisture change on critical buckling load parameter $\lambda_U$ of a square, $[(0/90)_s]$ crossply laminated plate in Example 6**

| $L_x/H$ | $C$ (%) | HYF1 | | | | HYF23 |
|---|---|---|---|---|---|---|
| | | HYF13 | HYF12 | HYF11 | HYF10 | |
| 40 | 0.0 | 14.4529 | 14.4602 | 14.4600 | 14.4673 | 14.4627 |
| | 0.5 | 10.0180 | 10.0254 | 10.0254 | 10.0324 | 10.0278 |
| | 1.0 | 6.0708 | 6.0781 | 6.0778 | 6.0851 | 6.0805 |
| | 1.5 | 1.9523 | 1.9596 | 1.9593 | 1.9666 | 1.9620 |
| 20 | 0.0 | 13.6835 | 13.7106 | 13.7070 | 13.7342 | 13.7180 |
| | 0.5 | 12.5247 | 12.5517 | 12.5517 | 12.5752 | 12.5591 |
| | 1.0 | 11.4879 | 11.5147 | 11.5112 | 11.5381 | 11.5221 |
| | 1.5 | 10.4582 | 10.4851 | 10.4816 | 10.5085 | 10.4924 |
| 10 | 0.0 | 11.3466 | 11.4275 | 11.3956 | 11.4772 | 11.4362 |
| | 0.5 | 11.0183 | 11.0990 | 11.0671 | 11.1485 | 11.1076 |
| | 1.0 | 10.7205 | 10.8009 | 10.7691 | 10.8502 | 10.8093 |
| | 1.5 | 10.4631 | 10.5435 | 10.5117 | 10.5928 | 10.5519 |
| | 0.0 | 6.9932 | 7.1383 | 7.0279 | 7.1746 | 7.1092 |
| 5 | 0.5 | 6.8911 | 7.0365 | 6.9257 | 7.0726 | 7.0069 |
| | 1.0 | 6.7963 | 6.9420 | 6.8309 | 6.9781 | 6.9121 |
| | 1.5 | 6.7320 | 6.8776 | 6.7665 | 6.9138 | 6.8477 |

Fig. 4 indicates a trend that thin plates may buckle without any external forces, solely due to small change in moisture concentration.

## Conclusions

A novel, analytical mixed formulation has been developed by using the minimum potential energy principle for stability analysis of laminated composite plates. Continuity of displacements as well as transverse stresses through the thickness of a plate has been explicitly satisfied in the formulation. The modal transverse stresses and displacements have been obtained as eigenvectors so that the stresses need not be evaluated separately. Further, a simple approach has been presented for thermal buckling analysis of laminated plates. From the extensive parametric investigation, the local higher-order mixed model (HYF13) has been found to yield results that are in excellent agreement with the three-dimensional elasticity solutions as compared to the commonly used displacement-based equivalent single-layer, higher-order theories. It is recommended that, at least, the nonlinear strain-displacements terms related with in-plane $v$ displacements should be incorporated along with those terms related without plane displacement to evaluate the potential energy functional, i.e., in Eq. (3$a$) at least $\delta_2$ along with $\delta_3$ shall be taken as unity.

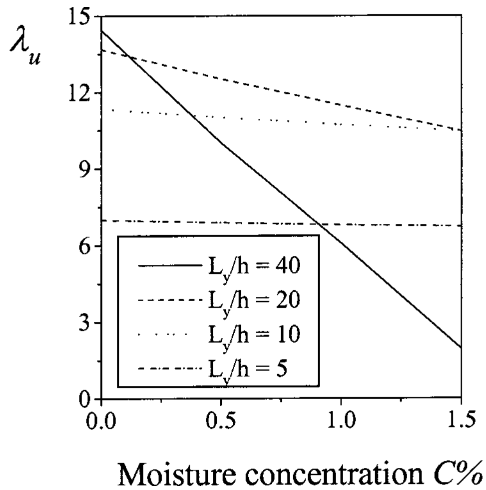


**Fig. 4 Effect of moisture change on uni-axial buckling load parameter $\lambda_U$ computed by using the HYF13 model for a square $[(0/90)_s]$ crossply laminated plate in Example 6**

## Appendix

**Shape Function Matrices.** The shape function matrices $[N_1]$, $[N_2]$, $[N_3]$, and $[N_4]$ of Eq. (4$a$) are of size $3\times 12$. These matrices can be written rowwise as follows:

$$[N_j]=[\{N_{j1}\}\quad \{N_{j2}\}\quad \{N_{j3}\}]^t,\quad j=1,2,3,4. \tag{A1}$$

Nonzero elements of shape function matrices are presented matrixwise as follows:

$$N_1(1,1)=f_1;\quad N_1(1,2)=\frac{f_3}{C^r_{55}};\quad N_1(1,7)=f_2;$$

$$N_1(1,8)=\frac{f_4}{C^s_{55}};$$

$$N_1(2,5)=f_1;\quad N_1(2,6)=\frac{f_3}{C^r_{66}};\quad N_1(2,11)=f_2;$$

$$N_1(2,12)=\frac{f_4}{C^s_{66}};$$

$$N_1(3,3)=f_1;\quad N_1(3,4)=\frac{f_3}{C^r_{33}};\quad N_1(3,9)=f_2;$$

$$N_1(3,10)=\frac{f_4}{C^s_{33}}.$$

$$N_2(1,3)=-f_3;\quad N_2(1,9)=-f_4;$$

$$N_2(3,1)=-\frac{C^r_{13}}{C^r_{33}}f_3;\quad N_2(3,7)=-\frac{C^s_{13}}{C^s_{33}}f_4.$$

$$N_3(2,3)=-f_3;\quad N_3(2,9)=-f_4;$$

$$N_3(3,5)=-\frac{C^r_{23}}{C^r_{33}}f_3;\quad N_3(3,11)=-\frac{C^s_{23}}{C^s_{33}}f_4$$

$$N_4(3,1)=\frac{C^r_{13}}{C^r_{33}}f_3;\quad N_4(3,2)=\frac{C^r_{13}}{C^r_{33}}f_3;$$

$$N_4(3,3)=\frac{C^r_{23}}{C^r_{33}}f_3;\quad N_4(3,4)=\frac{C^r_{23}}{C^r_{33}}f_3;$$

$$N_4(3,5)=f_3\quad N_4(3,6)=f_3\quad N_4(3,7)=\frac{C^s_{13}}{C^s_{33}}f_4;$$

$$N_4(3,8)=\frac{C^s_{13}}{C^s_{33}}f_4;$$

$$N_4(3,9)=\frac{C^s_{23}}{C^s_{33}}f_4\quad N_4(3,10)=\frac{C^s_{23}}{C^s_{33}}f_4$$

$$N_4(3,11)=f_4;\quad N_4(3,12)=f_4.$$

Superscripts $r$ and $s$ indicate, respectively, the bottom and top surfaces of the $l$th lamina for all HYF1 models. Therefore, $r=s=i$. On the other hand $r=1$, $s=N$ for all HYF2 models.

**Strain-Displacement Matrices.** Nonzero elements of $6\times 12$ strain-displacement matrices $[a]$, $[b]$, $[d]$, $[e]$, $[f]$, $[g]$, and $[t]$ appearing in Eq. (6) are

$$a(3,3)=\overline{f_1};\quad a(3,4)=\frac{\overline{f_3}}{C^r_{33}};\quad a(3,9)=\overline{f_2};\quad a(3,10)=\frac{\overline{f_4}}{C^s_{33}};$$

$$a(5,1)=\overline{f_1};\quad a(5,2)=\frac{\overline{f_3}}{C^r_{55}};\quad a(5,7)=\overline{f_2};\quad a(5,8)=\frac{\overline{f_4}}{C^s_{55}};$$

$$a(6,5)=\overline{f_1};\quad a(6,6)=\frac{\overline{f_3}}{C^r_{66}};\quad a(6,11)=\overline{f_2};\quad a(6,12)=\frac{\overline{f_4}}{C^s_{66}}.$$

$$b(1,1)=f_1;\quad b(1,2)=N_1(1,2);\quad b(1,7)=f_2;$$

$$b(1,8)=N_1(1,8);$$

$$b(3,1)=-\frac{C^r_{13}}{C^r_{33}}\overline{f_3};\quad b(3,7)=-\frac{C^s_{13}}{C^s_{33}}\overline{f_4};\quad e(4,1)=f_1;$$

$$e(4,7)=f_2;$$

$$b(4,5)=f_1;\quad b(4,6)=N_1(2,6);\quad b(4,11)=f_2;$$

$$b(4,12)=N_1(2,12);$$

$$b(5,3)=f_1-\overline{f_3};\quad b(5,4)=N_1(3,4);\quad b(5,9)=f_2-\overline{f_4};$$

$$b(5,10)=N_1(3,10);$$

$$d(1,3)=-f_3;\quad d(1,9)=-f_4;\quad d(5,1)=N_2(3,1);$$

$$d(5,7)=N_2(3,7).$$

$$e(2,5)=f_1;\quad e(2,6)=b(4,6);\quad e(2,11)=f_2;$$

$$e(2,12)=b(4,12);$$

$$e(3,5)=-\frac{C^r_{23}}{C^r_{33}}\overline{f_3};\quad e(3,11)=-\frac{C^s_{23}}{C^s_{33}}\overline{f_4};$$

$$e(4,2)=b(1,2);\quad e(4,8)=b(1,8);$$

$$e(6,3)=b(5,3);\quad e(6,4)=b(5,4);\quad e(6,9)=b(5,9);$$

$$e(6,10)=b(5,10);$$

$$f(2,3)=-f_3;\quad f(2,9)=-f_4;\quad f(6,5)=-\frac{C^r_{23}}{C^r_{33}}f_3;$$

$$f(6,11)=-\frac{C^s_{23}}{C^s_{33}}f_4;$$

$$g(4,3)=-2\,f_3;\quad g(4,9)=-2\,f_4;\quad g(5,5)=f(6,5);$$

$$g(5,11)=f(6,11);$$

$$g(6,1)=d(5,1); \quad g(6,7)=d(5,7)$$

$$t(3,1)=-b(3,1); \quad t(3,2)=-b(3,1);$$

$$t(3,3)=-e(3,5); \quad t(3,4)=-e(3,5);$$

$$t(3,5)=\overline{f_3}; \quad t(3,6)=\overline{f_3}; \quad t(3,7)=-b(3,7);$$

$$t(3,8)=-b(3,7);$$

$$t(3,9)=-e(3,11); \quad t(3,10)=-e(3,11);$$

$$t(3,11)=\overline{f_4} \quad t(3,12)=\overline{f_4}.$$

Here, $f_1$, $f_2$, $f_3$, and $f_4$ are the interpolation functions, $\overline{f_1}$, $\overline{f_2}$, $\overline{f_3}$, and $\overline{f_4}$ being their derivatives with respect to the $z$-direction. The interpolation functions are

$$f_1=\frac{1}{4}(2-3\xi+\xi^3) \quad f_2=\frac{1}{4}(2+3\xi-\xi^3)$$
$$f_3=\frac{\zeta}{4}(1-\xi-\xi^2+\xi^3) \quad f_4=\frac{\zeta}{4}(-1-\xi+\xi^2-\xi^3). \tag{A2}$$

Here, $\xi=z/\zeta$ and $\zeta=h_1$, for the HYF1 models and $\zeta=H_1$ for the HYF2 models.

**Property Matrices.** Different property matrices in Eq. (12$b$) for a lamina can be evaluated as

$$[S_{\alpha\beta}]=\int_{-h_1}^{h_1}[\alpha]^t[C][\beta]dz \tag{A3}$$

where $[\alpha],[\beta]=[a],[b],[c],[d],[e],[f],[g],[t]$.

**Geometric Property Matrices.** Various geometric property matrices in Eq. (12$c$) can be obtained from

$$[G_{\alpha\beta j}]=\int_{-h_1}^{h_1}\{N_{\gamma j}\}^t\{N_{\eta j}\}dz, \quad j=1,2,3; \quad \alpha,\beta=a,b,c. \tag{A4}$$

Here, $\alpha=a,b,c$ for $\gamma=2,1,3$, respectively, and $\beta=a,b,c$ for $\eta=2,1,3$, respectively.

## References


[1] Reddy, J. N., and Phan, N. D., 1985, ‘‘Stability and Vibration of Isotropic. Orthotropic and Laminated Plates According to a Higher-Order Shear Deformation Theory,’’ J. Sound Vib., **98**, pp. 157–170.

[2] Reddy, J. N., 1984, ‘‘A Simple Higher-Order Theory for Laminated Composite Plates,’’ ASME J. Appl. Mech., **51**(4), pp. 745–752.

[3] Senthilnathan, N. R., Lim, S. P., Lee, K. H., and Chow, S. T., 1987, ‘‘Buckling of Shear Deformable Plates,’’ AIAA J., **25**, pp. 1268–1271.

[4] Khdeir, A. A., 1988, ‘‘Free Vibration and Buckling of Symmetric Cross-Ply Laminated Plates by an Exact Method,’’ J. Sound Vib., **126**, pp. 447–461.

[5] Khdeir, A. A., 1989, ‘‘Stability of Anti-Symmetric Angle-Ply Laminated Plates,’’ J. Eng. Mech., **115**, pp. 952–962.

[6] Doong, J. L., 1987, ‘‘Vibration and Stability of an Initially Stressed Thick Plate According to a Higher-Order Deformation Theory,’’ J. Sound Vib., **113**, pp. 425–440.

[7] Doong, J. L., Lee, C., and Fung, C. P., 1991, ‘‘Vibration and Stability of Laminated Plates Based on a Modified Plate Theory,’’ J. Sound Vib., **151**, pp. 193–201.

[8] Ren, J. G., and Owen, D. R. J., 1989, ‘‘Vibration and Buckling of Laminated Plates,’’ Int. J. Solids Struct., **25**, pp. 95–106.

[9] Savithri, S., and Varadhan, T. K., 1990, ‘‘Free Vibration and Stability of Cross-Ply Laminated Plates,’’ J. Sound Vib., **141**, pp. 516–520.

[10] Matsunaga, H., 2000, ‘‘Vibration and Stability of Cross-Ply Laminated Composite Plates According to a Global Higher-Order Plate Theory,’’ Compos. Struct., **48**, pp. 234–244.

[11] Kant, T., and Swaminathan, K., 2000, ‘‘Analytical Solutions Using a Higher Order Refined Theory for The Stability Analysis of Laminated Composite and Sandwich Plates,’’ Struct. Eng. Mech., **10**(4), pp. 337–357.

[12] Pagano, N. J., 1969, ‘‘Exact Solutions for Composite Laminates in Cylindrical Bending,’’ J. Compos. Mater., **3**, pp. 398–411.

[13] Pagano, N. J., 1970, ‘‘Exact Solutions for Rectangular Bi-Directional Composites,’’ J. Compos. Mater., **4**, pp. 20–34.

[14] Wu, C. P., and Chen, W. Y., 1994, ‘‘Vibration and Stability of Laminated Plates Based on a Local High Order Plate Theory,’’ J. Sound Vib., **177**(4), pp. 503–520.

[15] Narita, Y., and Leissa, A. W., 1990, ‘‘Buckling Studies for Simply Supported Symmetrically Laminated Rectangular Plates,’’ Int. J. Mech. Sci., **32**(11), pp. 909–924.

[16] Srinivas, S., 1970, ‘‘Three-Dimensional Analysis of Some Plates and Laminates and a Study of Thickness Effects,’’ Ph.D. thesis, Department of Aeronautical Engineering, Indian Institute of Science Banglore, India.

[17] Srinivas, S., and Rao, A. K., 1970, ‘‘Bending, Vibration and Buckling of Simply Supported Thick Orthotropic Rectangular Plates and Laminates,’’ Int. J. Solids Struct., **6**, pp. 1463–1481.

[18] Noor, A. K., 1975, ‘‘Stability of Multilayered Composite Plates,’’ Fibre Sci. Technol., **8**(2), pp. 81–89.

[19] Putcha, N. S., and Reddy, J. N., 1986, ‘‘Stability and Natural Vibration Analysis of Laminated Plates by Using a Mixed Element Based on a Refined Plate Theory,’’ J. Sound Vib., **104**(2), pp. 285–300.

[20] Noor, A. K., and Burton, W. S., 1992, ‘‘Three-Dimensional Solutions for Thermal Buckling of Multilayered Anisotropic Plates,’’ J. Eng. Mech., **118**(4), pp. 683–701.

[21] Sai Ram, K. S., and Sinha, P. K., 1992, ‘‘Hygro-Thermal Effects on the Buckling of Laminated Composite Plates,’’ Compos. Struct., **21**, pp. 233–247.

# On the Singularity Induced by Boundary Conditions in a Third-Order Thick Plate Theory

**C. S. Huang**
Associate Professor,
Department of Civil Engineering,
National Chiao Tung University,
1001 Ta-Hsueh Road,
Taiwan 30050, R. O. C.
e-mail: cshuang@cc.nctu.edu.tw

*This paper thoroughly examines the singularity of stress resultants of the form $r^{-\xi}F(\theta)$ for $0<\xi\leqslant 1$ as $r\rightarrow 0$ (Williams-type singularity) at the vertex of an isotropic thick plate; the singularity is caused by homogeneous boundary conditions around the vertex. An eigenfunction expansion is applied to derive the first known asymptotic solution for displacement components, from the equilibrium equations of Reddy's third-order shear deformation plate theory. The characteristic equations for determining the singularities of stress resultants are presented for ten sets of boundary conditions. These characteristic equations are independent of the thickness of the plate, Young's modulus, and shear modulus, but some do depend on Poisson's ratio. The singularity orders of stress resultants for various boundary conditions are expressed in graphic form as a function of the vertex angle. The characteristic equations obtained herein are compared with those from classic plate theory and first-order shear deformation plate theory. Comparison results indicate that different plate theories yield different singular behavior for stress resultants. Only the vertex with simply supported radial edges (S(I)_S(I) boundary condition) exhibits the same singular behavior according to all these three plate theories.*
[DOI: 10.1115/1.1490371]

## Introduction

Obtaining accurate numerical solutions to many elasticity problems requires knowledge of the singular behavior of stress components in the neighborhood of singular points in the domain of the problem under consideration. For example, analyzing crack (or V-notch) problems using finite element approaches usually involves shape functions to describe correctly the singular behavior of stresses at the crack tip ([1,2]). The admissible functions of the Ritz method include the corner functions that precisely describe the moment singularities at the notches or corners in vibration problems of thin plates with V-notches or with re-entrant corners, to accelerate convergence and increase the accuracy of the solution ([3,4]).

Many papers have addressed the stress singularities at sharp corners based on plane elasticity theory (i.e., [5–8]) and three-dimensional elasticity theory ([9,10]). However, the stress singularities for different plate theories have received lesser attention. Williams [11] first investigated the stress singularities due to boundary conditions in the angular corner of isotropic thin plates under bending. Williams and Owens [12] and Williams and Chapkis [13] extended this work to thin plates with varying flexural rigidity and with polarly orthotropic material properties, respectively. Rao [14] considered the singularities at the interface corners for bi-material thin plates, and Ojikutu, Low, and Scott [15] investigated stress singularities at the apex of a laminated composite thin plate with simply supported radial edges. Huang et al. [16] discussed the singularities of moments and shear forces at the apex of a sector plate with simply supported radial edges in an exact solution for vibrations of such a plate. Sinclair [17] considered logarithmic stress singularities in thin plate theory.

Based on the first-order shear deformation plate theory, Burton and Sinclair [18] investigated the stress singularities at corners due to six sets of homogeneous boundary conditions by introducing a stress potential. Huang et al. [19] examined the singularities of moments and shear forces at the vertex of a Mindlin sector plate with simply supported radial edges, by establishing an exact solution in terms of Bessel functions for the vibrations of such a plate. Recently, Huang [20] comprehensively investigated the stress singularities of moments and shear forces at corners caused by ten sets of homogeneous boundary conditions by adopting Xie and Chaudhuri's technique ([10]) to directly solve the equilibrium equations in terms of displacement components. Comparing the results with the exact solution given by Huang et al. [19] reveals that the singularity orders for moments and shear forces in Huang's results ([20]) are consistent with those in the exact solution for a simply supported corner, while the solution proposed by Burton and Sinclair [18] is consistent only for moment singularities but not for shear force singularities.

Comparing published work based on classical plate theory and on first-order shear deformation plate theory reveals that different singularity orders for moments and shear forces are suggested by different plate theories. Consequently, this study aims primarily to investigate for the first time, what results are suggested by the third-order shear deformation thick plate theory. This study applies Reddy's refined plate theory ([21]). The theory is equivalent to other third-order shear deformation plate theories proposed by Schmidt [22] and Krishna Murty [23]. This work considers only the Williams-type stress singularities at a corner caused by various boundary conditions but does not consider logarithmic stress singularities as the former singularities are more often encountered than the latter. The eigenfunction expansion methodology proposed by Hartranft and Sih [9] for three-dimensional elasticity problems is adopted to determine the asymptotic displacement field around the corner by solving the equilibrium equations in terms of displacement components in Reddy's refined plate theory. The characteristic equations for determining the singularity orders of stress resultants are established for ten sets of boundary conditions around a corner. Finally, the singular behavior of stress resultants obtained in this investigation is compared with those determined from the classic plate theory, first-order shear deformation plate theory, and three-dimensional elasticity theory.

Contributed by the Applied Mechanics Division of THE AMERICAN SOCIETY OF MECHANICAL ENGINEERS for publication in the ASME JOURNAL OF APPLIED MECHANICS. Manuscript received by the ASME Applied Mechanics Division, July 11, 2001; final revision, Feb. 28, 2002. Associate Editor: R. C. Benson. Discussion on the paper should be addressed to the Editor, Prof. Robert M. McMeeking, Department of Mechanical and Environmental Engineering University of California–Santa Barbara, Santa Barbara, CA 93106-5070, and will be accepted until four months after final publication of the paper itself in the ASME JOURNAL OF APPLIED MECHANICS.

  

## Basic Formulation

For a sector plate with cylindrical coordinates shown in Fig. 1, the displacement field for the third-order plate theory proposed by Reddy [21] is given as

$$u=z\left[\psi_r-\frac{4}{3}\left(\frac{z}{h}\right)^2(\psi_r+w_{,r})\right], \tag{1}$$

$$v=z\left[\psi_\theta-\frac{4}{3}\left(\frac{z}{h}\right)^2\left(\psi_\theta+\frac{1}{r}w_{,\theta}\right)\right], \tag{2}$$

$$w=w(r,\theta), \tag{3}$$

where the subscript ",$j$" refers to a partial differential with respect to independent variable $j$; $u$, $v$, and $w$ denote the displacements of a point ($r$, $\theta$, $z$) along the $r$, $\theta$, and $z$ directions, while $\psi_r$ and $\psi_\theta$ are the rotations of the midplane normal in the radial and circumferential directions, respectively. This displacement field leads to zero shear stresses, $\sigma_{zr}$ and $\sigma_{z\theta}$, on the plate top and bottom surfaces.

By using the variational method, one can develop the equilibrium equations and consistent boundary conditions. The equilibrium equations without external loading in terms of the stress resultants are

$$C_1\left(P_{r,rr}+\frac{2}{r}P_{r,r}+\frac{1}{r^2}P_{\theta,\theta\theta}-\frac{1}{r}P_{\theta,r}+\frac{2}{r}P_{r\theta,r\theta}+\frac{2}{r^2}P_{r\theta,\theta}\right)+\frac{\bar{Q}_r}{r}$$
$$+\bar{Q}_{r,r}+\frac{1}{r}\bar{Q}_{\theta,\theta}=0, \tag{4}$$

$$\bar{M}_{r,r}+\frac{\bar{M}_r}{r}-\frac{\bar{M}_\theta}{r}+\frac{1}{r}\bar{M}_{r\theta,\theta}-\bar{Q}_r=0, \tag{5}$$

$$\frac{1}{r}\bar{M}_{\theta,\theta}+\bar{M}_{r\theta,r}+\frac{2\bar{M}_{r\theta}}{r}-\bar{Q}_\theta=0, \tag{6}$$

$C_1=4/3h^2$, $C_2=4/h^2$, $\bar{M}_{r\theta}=M_{r\theta}-C_1P_{r\theta}$, $\bar{M}_\beta=M_\beta-C_1P_\beta$, $\bar{Q}_\beta=Q_\beta-C_2R_\beta$, $h$ is the thickness of plate and subscript $\beta$ denotes $r$ or $\theta$. Furthermore, the radial boundary conditions (at $\theta=\alpha$) should specify

$$\psi_\theta \text{ or } \bar{M}_\theta,\quad \psi_r \text{ or } \bar{M}_{r\theta},$$
$$w \text{ or } \bar{Q}_\theta+C_1\left(\frac{2}{r}P_{r\theta}+2P_{r\theta,r}+\frac{1}{r}P_{\theta,\theta}\right),\ \text{and}\ \frac{w_{,\theta}}{r} \text{ or } P_\theta. \tag{7}$$

The circumferential boundary conditions (at $r=R$) should prescribe

$$\psi_\theta \text{ or } \bar{M}_{r\theta},\quad \psi_r \text{ or } \bar{M}_r,$$
$$w \text{ or } \bar{Q}_r+C_1\left(\frac{P_r}{r}+P_{r,r}+\frac{2}{r}P_{r\theta,\theta}-\frac{P_\theta}{r}\right),\ \text{and}\ w_{,r} \text{ or } P_r. \tag{8}$$

The details of derivation for the equilibrium equations and boundary conditions in Cartesian coordinates can be found in Reddy's book [24]. The stress resultants in above equations are related to stress components by

$$\begin{Bmatrix}Q_\beta\\R_\beta\end{Bmatrix}=\int_{-h/2}^{h/2}\sigma_{\beta z}\begin{Bmatrix}1\\z\end{Bmatrix}dz, \tag{9a}$$

$$\begin{Bmatrix}M_\beta\\P_\beta\end{Bmatrix}=\int_{-h/2}^{h/2}\sigma_{\beta\beta}\begin{Bmatrix}z\\z^3\end{Bmatrix}dz, \tag{9b}$$

$$\begin{Bmatrix}M_{r\theta}\\P_{r\theta}\end{Bmatrix}=\int_{-h/2}^{h/2}\sigma_{r\theta}\begin{Bmatrix}z\\z^3\end{Bmatrix}dz. \tag{9c}$$

For an isotropic and elastic plate, the relationships between the stress resultants and displacement components are established by using strain-displacement and stress-strain relationships. They are

$$Q_r=\frac{2Gh}{3}(\psi_r+w_{,r}),\quad Q_\theta=\frac{2Gh}{3}\left(\psi_\theta+\frac{1}{r}w_{,\theta}\right),$$

$$R_r=\frac{Gh^3}{30}(\psi_r+w_{,r}),\quad R_\theta=\frac{Gh^3}{30}\left(\psi_\theta+\frac{1}{r}w_{,\theta}\right),$$

$$M_{r\theta}=Gh^3\left[\frac{1}{12}\left(\psi_{\theta,r}-\frac{1}{r}\psi_\theta+\frac{1}{r}\psi_{r,\theta}\right)\right.$$
$$\left.-\frac{1}{60r}\left(-\psi_\theta-\frac{2}{r}w_{,\theta}+\psi_{r,\theta}+2w_{,r\theta}+r\psi_{\theta,r}\right)\right],$$

$$M_r=\frac{Eh^3}{1-\nu^2}\left\{\left(\frac{1}{15}\psi_{r,r}-\frac{1}{60}w_{,rr}\right)\right.$$
$$\left.+\frac{\nu}{r}\left[\frac{1}{15}(\psi_r+\psi_{\theta,\theta})-\frac{1}{60}\left(w_{,r}+\frac{1}{r}w_{,\theta\theta}\right)\right]\right\},$$

$$M_\theta=\frac{Eh^3}{1-\nu^2}\left\{\frac{1}{r}\left[\frac{1}{15}(\psi_r+\psi_{\theta,\theta})-\frac{1}{60}\left(w_{,r}+\frac{1}{r}w_{,\theta\theta}\right)\right]\right.$$
$$\left.+\nu\left(\frac{1}{15}\psi_{r,r}-\frac{1}{60}w_{,rr}\right)\right\},$$

$$P_{r\theta}=\frac{Gh^5}{1680}\left[16\psi_{\theta,r}-\frac{16}{r}\psi_\theta+\frac{16}{r}\psi_{r,\theta}-\frac{10}{r}\left(w_{,r\theta}-\frac{w_{,\theta}}{r}\right)\right],$$

$$P_r=\frac{Eh^2}{(1-\nu^2)}\left\{\frac{\psi_{r,r}}{105}-\frac{w_{,rr}}{336}\right.$$
$$\left.+\frac{\nu}{r}\left[\frac{1}{80}(\psi_r+\psi_{\theta,\theta})-\frac{1}{336}\left(\psi_{\theta,\theta}+\psi_r+w_{,r}+\frac{w_{,\theta\theta}}{r}\right)\right]\right\},$$

$$P_\theta=\frac{Eh^5}{(1-\nu^2)}\left\{\frac{1}{r}\left[\frac{1}{105}(\psi_r+\psi_{\theta,\theta})-\frac{1}{336}\left(w_{,r}+\frac{w_{,\theta\theta}}{r}\right)\right]\right.$$
$$\left.+\nu\left(\frac{\psi_{r,r}}{105}-\frac{w_{,rr}}{336}\right)\right\}, \tag{10}$$

where $E$ is Young's modulus; $G$ is the shear modulus, and $\nu$ is Poisson's ratio.

Substituting Eq. (10) into Eqs. (4)–(6) with careful arrangement yields the equilibrium equations in terms of the displacement components:

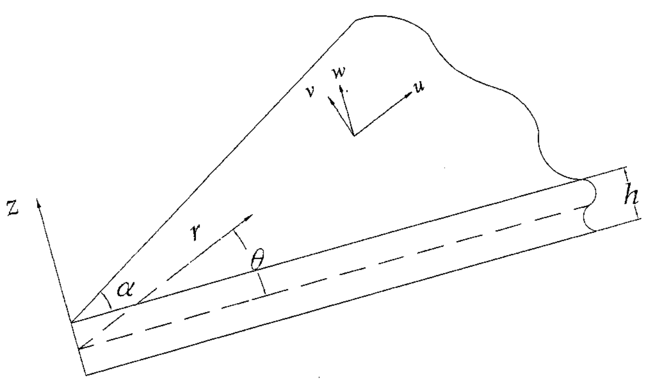


**Fig. 1 Coordinate system and positive displacement components for a sector plate**

$$\psi_{r,rrr}+\frac{2}{r}\psi_{r,rr}+\frac{1}{r^2}\psi_{r,r\theta\theta}+\frac{1}{r^3}\psi_{r,\theta\theta}-\frac{1}{r^2}\psi_{r,r}+\frac{1}{r^3}\psi_r+\frac{1}{r^3}\psi_{\theta,\theta\theta\theta}+\frac{1}{r}\psi_{\theta,rr\theta}-\frac{1}{r^2}\psi_{\theta,r\theta}+\frac{1}{r^3}\psi_{\theta,\theta}-\frac{5}{16}\left(w_{,rrrr}+\frac{2}{r}w_{,rrr}+\frac{2}{r^2}w_{,rr\theta\theta}-\frac{1}{r^2}w_{,rr}-\frac{2}{r^3}w_{,r\theta\theta}+\frac{1}{r^3}w_{,r}+\frac{1}{r^4}w_{,\theta\theta\theta\theta}+\frac{4}{r^4}w_{,\theta\theta}\right)+\frac{21(1-\nu)}{h^2}\left(\psi_{r,r}+\frac{1}{r}\psi_r+\frac{1}{r}\psi_{\theta,\theta}+w_{,rr}+\frac{1}{r}w_{,r}+\frac{1}{r^2}w_{,\theta\theta}\right)=0, \tag{11}$$

$$\psi_{r,rr}+\left(\frac{1}{r}\psi_r\right)_{,r}+\frac{1-\nu}{2}\frac{1}{r^2}\psi_{r,\theta\theta}-\frac{3-\nu}{2}\frac{1}{r^2}\psi_{\theta,\theta}+\frac{1+\nu}{2}\frac{1}{r}\psi_{\theta,r\theta}-\frac{4}{17}\left(w_{,rrr}+\frac{1}{r}w_{,rr}+\frac{1}{r^2}w_{,r\theta\theta}-\frac{1}{r^2}w_{,r}-\frac{2}{r^3}w_{,\theta\theta}\right)-\frac{84(1-\nu)}{17h^2}(\psi_r+w_{,r})=0, \tag{12}$$

$$\frac{1+\nu}{2}\frac{1}{r}\psi_{r,r\theta}+\frac{3-\nu}{2}\frac{1}{r^2}\psi_{r,\theta}+\frac{1-\nu}{2}\psi_{\theta,rr}+\frac{1-\nu}{2}\left(\frac{1}{r}\psi_\theta\right)_{,r}+\frac{1}{r^2}\psi_{\theta,\theta\theta}-\frac{4}{17}\left(\frac{1}{r}w_{,rr\theta}+\frac{1}{r^2}w_{,r\theta}+\frac{1}{r^3}w_{,\theta\theta\theta}\right)-\frac{84(1-\nu)}{17h^2}\left(\psi_\theta+\frac{1}{r}w_{,\theta}\right)=0. \tag{13}$$

## Construction of Series Solution

The eigenfunction expansion approach proposed by Hartranft and Sih [9] for three-dimensional elasticity problems is adopted herein to find the solution of Eqs. (11)–(13). The displacement components can be expressed in terms of the following series:

$$w(r,\theta)=\sum_{m=0}^{\infty}\sum_{n=0,2,}^{\infty}r^{\lambda_m+n+1}W_n^{(m)}(\theta,\lambda_m), \tag{14a}$$

$$\psi_r(r,\theta)=\sum_{m=0}^{\infty}\sum_{n=0,2,}^{\infty}r^{\lambda_m+n}\Psi_n^{(m)}(\theta,\lambda_m), \tag{14b}$$

$$\psi_\theta(r,\theta)=\sum_{m=0}^{\infty}\sum_{n=0,2,}^{\infty}r^{\lambda_m+n}\Phi_n^{(m)}(\theta,\lambda_m), \tag{14c}$$

where the characteristic values $\lambda_m$ are assumed to be constants and can be complex numbers. Notably, odd $n$ in Eqs. (14) will not produce any additional solution such that they are not considered in Eqs. (14).

The real part of $\lambda_m$ must exceed zero to satisfy the regularity conditions at the vertex of the sector plate. The regularity conditions require that $\psi_\theta$, $\psi_r$, $w$, and $w_{,r}$ are finite as $r$ approaches zero. As a result, the solution form given in Eqs. (14) with the real part of $\lambda_m$ less than one leads to singularities of $M_r$, $M_\theta$, $M_{r\theta}$, $P_r$, $P_\theta$, and $P_{r\theta}$, which is observed from the relationships between stress resultants and displacement components given in Eq. (10). However, no singularity for shear forces ($Q_r$ and $Q_\theta$), $R_r$ and $R_\theta$ will be produced from the solution.

Substituting Eqs. (14) into Eqs. (11)–(13) yields

$$\sum_{m=0}^{\infty}\sum_{n=0,2,}^{\infty}r^{\lambda_m+n-3}\Big\{(\lambda_m n+1)\Psi_{n,\theta\theta}^{(m)}+(\lambda_m+n-1)^2(\lambda_m+n+1)\times\Psi_n^{(m)}+\Phi_{n,\theta\theta\theta}^{(m)}+(\lambda_m+n-1)^2\Phi_{n,\theta}^{(m)}-\frac{5}{16}[(\lambda_m+n-1)^2+(\lambda_m+n+1)^2W_n^{(m)}+2((\lambda_m+n)^2+1)W_{n,\theta\theta}^{(m)}+W_{n,\theta\theta\theta\theta}^{(m)}]\Big\}+\frac{21(1-\nu)}{h^2}r^{\lambda_m+n-1}\{(\lambda_m+n+1)\Psi_n^{(m)}+\Phi_{n,\theta}^{(m)}+W_{n,\theta\theta}^{(m)}+(\lambda_m+n+1)^2W_n^{(m)}\}=0 \tag{15}$$

$$\sum_{m=0}^{\infty}\sum_{n=0,2,}^{\infty}r^{\lambda_m+n-2}\left\{\frac{1-\nu}{2}\Psi_{n,\theta\theta}^{(m)}+[(\lambda_m+n)^2-1)\right]\Psi_n^{(m)}+\left[\frac{1+\nu}{2}(\lambda_m+n)-\frac{3-\nu}{2}\right]\Phi_{n,\theta}^{(m)}-\frac{4}{17}[(\lambda_m+n+1)^2\times(\lambda_m+n-1)W_n^{(m)}+(\lambda_m+n-1)W_{n,\theta\theta}^{(m)}]-\frac{84(1-\nu)}{17h^2}r^{\lambda_m+n}\{\Psi_n^{(m)}+(\lambda_m+n+1)W_n^{(m)}\}=0, \tag{16}$$

$$\sum_{m=0}^{\infty}\sum_{n=0,2,}^{\infty}r^{\lambda_m+n-2}\left\{\left[\frac{1+\nu}{2}(\lambda_m+n)+\frac{3-\nu}{2}\right]\Psi_{n,\theta}^{(m)}+\Phi_{n,\theta\theta}^{(m)}+\frac{1-\nu}{2}[(\lambda_m+n)^2-1)\right]\Phi_n^{(m)}-\frac{4}{17}[(\lambda_m+n+1)^2W_{n,\theta}^{(m)}+W_{n,\theta\theta\theta}^{(m)}]\}-\frac{84(1-\nu)}{17h^2}r^{\lambda_m+n}\{\Phi_n^{(m)}+W_{n,\theta}^{(m)}\}=0. \tag{17}$$

Satisfying Eqs. (15)–(17) leads to the coefficients of $r$ with different orders equal to zero. Subsequently, a set of recurrent relationships among $W_n^{(m)}$, $\Psi_n^{(m)}$, $\Phi_n^{(m)}$ and their previous values can be attained and expressed as

$$(\lambda_m+n+3)\Psi_{n+2,\theta\theta}^{(m)}+(\lambda_m+n+1)^2(\lambda_m+n+3)\Psi_{n+2}^{(m)}+\Phi_{n+2,\theta\theta\theta}^{(m)}+(\lambda_m+n+1)^2\Phi_{n+2,\theta}^{(m)}-\frac{5}{16}[(\lambda_m+n+1)^2(\lambda_m+n+3)^2\times W_{n+2}^{(m)}+2((\lambda_m+n+2)^2+1)W_{n+2,\theta\theta}^{(m)}+W_{n+2,\theta\theta\theta\theta}^{(m)}]=-\frac{21(1-\nu)}{h^2}\{(\lambda_m+n+1)\Psi_n^{(m)}+\Phi_{n,\theta}^{(m)}+W_{n,\theta\theta}^{(m)}+(\lambda_m+n+1)^2W_n^{(m)}\}, \tag{18}$$

$$[(\lambda_m+n+2)^2-1]\Psi_{n+2}^{(m)}+\frac{1-\nu}{2}\Psi_{n+2,\theta\theta}^{(m)}-\frac{3-\nu}{2}\Phi_{n+2,\theta}^{(m)}+\frac{1+\nu}{2}(\lambda_m+n+2)\Phi_{n+2,\theta}^{(m)}-\frac{4}{17}[(\lambda_m+n+3)^2\times(\lambda_m+n+1)W_{n+2}^{(m)}+(\lambda_m+n+1)W_{n+2,\theta\theta}^{(m)}]=\frac{84(1-\nu)}{17h^2}[\Psi_n^{(m)}+(\lambda_m+n+1)W_n^{(m)}], \tag{19}$$

$$\left[\frac{1+\nu}{2}(\lambda_m+n+2)+\frac{3-\nu}{2}\right]\Psi_{n+2,\theta}^{(m)}+\frac{1-\nu}{2}[(\lambda_m+n+2)^2-1]\times\Phi_{n+2}^{(m)}+\Phi_{n+2,\theta\theta}^{(m)}-\frac{4}{17}[(\lambda_m+n+3)^2W_{n+2,\theta}^{(m)}+W_{n+2,\theta\theta\theta}^{(m)}]=\frac{84(1-\nu)}{17h^2}(\Phi_n^{(m)}+W_{n,\theta}^{(m)}). \tag{20}$$

Furthermore, one can establish the following equations from the coefficients of the lowest order of $r$ in Eqs. (15)–(17):

$$(\lambda_m+1)\Psi^{(m)}_{0,\theta\theta}+(\lambda_m-1)^2(\lambda_m+1)\Psi^{(m)}_0+\Phi^{(m)}_{0,\theta\theta\theta}+(\lambda_m-1)^2\Phi^{(m)}_{0,\theta}$$
$$-\frac{5}{16}[(\lambda_m-1)^2(\lambda_m+1)^2W^{(m)}_0+2(\lambda_m^2+1)W^{(m)}_{0,\theta\theta}+W^{(m)}_{0,\theta\theta\theta\theta}]$$
$$=0, \tag{21}$$

$$(\lambda_m^2-1)\Psi^{(m)}_0+\frac{1-\nu}{2}\Psi^{(m)}_{0,\theta\theta}-\frac{3-\nu}{2}\Phi^{(m)}_{0,\theta}+\frac{(1+\nu)\lambda_m}{2}\Phi^{(m)}_{0,\theta}$$
$$-\frac{4}{17}[(\lambda_m+1)^2(\lambda_m-1)W^{(m)}_0+(\lambda_m-1)W^{(m)}_{0,\theta\theta}]=0, \tag{22}$$

$$\left(\frac{(1+\nu)\lambda_m}{2}+\frac{3-\nu}{2}\right)\Psi^{(m)}_{0,\theta}+\frac{1-\nu}{2}(\lambda_m^2-1)\Phi^{(m)}_0+\Phi^{(m)}_{0,\theta\theta}$$
$$-\frac{4}{17}[(\lambda_m+1)^2W^{(m)}_{0,\theta}+W^{(m)}_{0,\theta\theta\theta}]=0. \tag{23}$$

It is easy to find that the general solution for the set of ordinary differential equations given by Eqs. (21)–(23) is

$$\Phi^{(m)}_0(\theta,\lambda_m)=B_0\cos(\lambda_m+1)\theta+B_1\sin(\lambda_m+1)\theta$$
$$+B_2\cos(\lambda_m-1)\theta+B_3\sin(\lambda_m-1)\theta, \tag{24a}$$

$$\Psi^{(m)}_0(\theta,\lambda_m)=-B_1\cos(\lambda_m+1)\theta+B_0\sin(\lambda_m+1)\theta$$
$$+A_2\cos(\lambda_m-1)\theta+A_3\sin(\lambda_m-1)\theta, \tag{24b}$$

$$W^{(m)}_0(\theta,\lambda_m)=A_0\cos(\lambda_m+1)\theta+A_1\sin(\lambda_m+1)\theta$$
$$+(k_1A_2+k_2B_3)\cos(\lambda_m-1)\theta$$
$$+(k_1A_3-k_2B_2)\sin(\lambda_m-1)\theta, \tag{24c}$$

where

$$k_1=\frac{17}{16\lambda_m}\left(\frac{(1+\nu)\lambda_m}{2}+\frac{3-\nu}{2}\right),$$
$$k_2=\frac{17}{16\lambda_m}\left(\frac{(1+\nu)\lambda_m}{2}-\frac{3-\nu}{2}\right),$$

and $A_i$ and $B_i$ ($i=1,2,3,4$) are coefficients to be determined from boundary conditions.

To establish the complete series solution for equilibrium equations (i.e., Eqs. (11)–(13)), one has to determine $\lambda_m$ and the relations among $A_i$ and $B_i$ in Eqs. (24) from the boundary conditions along radial edges. Then, one finds the solutions for $\Phi^{(m)}_n$, $\Psi^{(m)}_n$, and $W^{(m)}_n$ with $n>1$ from Eqs. (18)–(20) and boundary conditions.

Notably, one may construct the series solution by starting with assuming the following solution form:

$$w(r,\theta)=\sum_{m=0}^{\infty}\sum_{n=0,2,}^{\infty}r^{\lambda_m+n+l_1}\bar{W}^{(m)}_n(\theta,\lambda_m), \tag{25a}$$

$$\psi_r(r,\theta)=\sum_{m=0}^{\infty}\sum_{n=0,2,}^{\infty}r^{\lambda_m+n+l_2}\bar{\Psi}^{(m)}_n(\theta,\lambda_m), \tag{25b}$$

$$\psi_\theta(r,\theta)=\sum_{m=0}^{\infty}\sum_{n=0,2,}^{\infty}r^{\lambda_m+n+l_3}\bar{\Phi}^{(m)}_n(\theta,\lambda_m), \tag{25c}$$

where $l_i$ ($i=1,2,3$) can be arbitrary integers, but at least one of them is zero. Following the above procedure, one will find the solution form given by Eqs. (14) is the only one that may yield Williams-type stress singularities. Furthermore, there are possible solutions involving logarithmic function of $r$ leading to logarithmic singularities for stress resultants at the vertex of a sector plate, which are out of the scope of this work and will not be investigated here. The readers who are interested in the logarithmic singularities may refer to Dempsey and Sinclair [7] and Sinclair [17].

## Characteristic Equations and Corner Functions

To determine Williams-type stress singularities at the vertex of a sector plate caused by homogeneous boundary conditions, one only needs the asymptotic solution with the lowest order of $r$ in the series solution of Eqs. (14). Consequently, only the solution with $n=0$ in Eqs. (14) needs to be considered. Let

$$\psi^{(m)}_{\theta 0}=r^{\lambda_m}\Phi^{(m)}_0(\theta,\lambda_m),\quad \psi^{(m)}_{r0}=r^{\lambda_m}\Psi^{(m)}_0(\theta,\lambda_m),\ \text{and}$$
$$w^{(m)}_0=r^{\lambda_m+1}W^{(m)}_0(\theta,\lambda_m). \tag{26}$$

Furthermore, as well known, the stress singularities are affected by the boundary conditions along radial edges only.

In the following, we will consider four types of homogeneous boundary conditions along a radial edge, say $\theta=\alpha$, namely,

$$\text{clamped:}\quad w=\psi_r=\psi_\theta=\frac{w_{,\theta}}{r}=0, \tag{27a}$$

$$\text{free:}\quad \bar{M}_\theta=\bar{M}_{r\theta}=\bar{Q}_\theta+C_1\left(\frac{2}{r}P_{r\theta}+2P_{r\theta,r}+\frac{1}{r}P_{\theta,\theta}\right)=P_\theta=0, \tag{27b}$$

$$\text{type I simply supported:}\quad w=\psi_r=\bar{M}_\theta=P_\theta=0, \tag{27c}$$

$$\text{type II simply supported:}\quad w=\bar{M}_\theta=\bar{M}_{r\theta}=P_\theta=0. \tag{27d}$$

For simplicity, C and F are used to present the clamped and free boundary conditions, respectively, while S(I) and S(II) denote type I and type II simply supported boundary conditions.

For the sake of demonstration, we will describe the procedure for obtaining the characteristic equation for $\lambda_m$, and the corresponding asymptotic displacement field for describing the singular behavior of stress resultants in the vicinity of a corner. Consider a sector plate with vertex angle equal to $\alpha$ and having clamped and free boundary conditions along two radial edges, respectively. For the free radial edge at $\theta=\alpha$, substituting Eq. (26) into Eq. (27$b$) and using the relations given in Eq. (10) leads to the following equations for the lowest order of $r$:

$$a_{11}A_0+a_{12}A_1+a_{13}A_2+a_{14}A_3+a_{15}B_0+a_{16}B_1+a_{17}B_2+a_{18}B_3$$
$$=0, \tag{28a}$$

$$a_{21}A_0+a_{22}A_1+a_{23}A_2+a_{24}A_3+a_{25}B_0+a_{26}B_1+a_{27}B_2+a_{28}B_3$$
$$=0, \tag{28b}$$

$$a_{31}A_0+a_{32}A_1+a_{33}A_2+a_{34}A_3+a_{35}B_0+a_{36}B_1+a_{37}B_2+a_{38}B_3$$
$$=0, \tag{28c}$$

$$a_{41}A_0+a_{42}A_1+a_{43}A_2+a_{44}A_3+a_{45}B_0+a_{46}B_1+a_{47}B_2+a_{48}B_3$$
$$=0, \tag{28d}$$

where lengthy expression for $a_{ij}$ is given in the Appendix. Similarly, one also obtains four equations for $A_i$ and $B_i$ from the clamped edge at $\theta=0$:

$$B_0+B_2=0, \tag{29a}$$

$$-B_1+A_2=0, \tag{29b}$$

$$A_0+k_1A_2+k_2B_3=0, \tag{29c}$$

$$(\lambda_m+1)A_1+(\lambda_m-1)(k_1A_3-k_2B_2)=0. \tag{29d}$$

Equations (28) and (29) construct a set of linear homogeneous algebraic equations for $A_i$ and $B_i$. To have nontrivial solution for $A_i$ and $B_i$ yields the characteristic equations for $\lambda_m$,

$$\sin^2 \lambda_m \alpha = \frac{4-\lambda_m^2(1+\nu)^2 \sin^2 \alpha}{(3-\nu)(1+\nu)}, \tag{30a}$$

$$\sin^2 \lambda_m \alpha = \frac{4-\lambda_m^2(1-\nu)^2 \sin^2 \alpha}{(3+\nu)(1-\nu)}. \tag{30b}$$

Then, one can find the relations among $A_i$ and $B_i$ from Eqs. (29) and (28*a*)–(28*c*). Consequently, $\psi_{\theta 0}^{(m)}$, $\psi_{r0}^{(m)}$, and $w_0^{(m)}$ in Eq. (26) are expressed as

$$\psi_{r0}^{(m)}(r,\theta) = B_3 r^{\lambda_m}\left\{ \frac{1+\lambda_m}{\lambda_m-1}\cos(\lambda_m+1)\theta - \eta_2 \sin(\lambda_m+1)\theta - \frac{1+\lambda_m}{\lambda_m-1}\cos(\lambda_m-1)\theta + \eta_1 \sin(\lambda_m-1)\theta \right\}, \tag{31a}$$

$$\psi_{\theta 0}^{(m)}(r,\theta) = B_3 r^{\lambda_m}\left\{ -\frac{1+\lambda_m}{\lambda_m-1}\sin(\lambda_m+1)\theta - \eta_2 \cos(\lambda_m+1)\theta + \sin(\lambda_m-1)\theta + \eta_2 \cos(\lambda_m-1)\theta \right\}, \tag{31b}$$

$$w_0^{(m)}(r,\theta) = B_3 r^{\lambda_m+1}\left\{ \left( \frac{k_1(1+\lambda_m)}{\lambda_m-1} - k_2 \right)\cos(\lambda_m+1)\theta + \frac{(1-\lambda_m)}{\lambda_m+1}(k_1\eta_1 - k_2\eta_2)\sin(\lambda_m+1)\theta + \left( -\frac{(1+\lambda_m)k_1}{\lambda_m-1} + k_2 \right)\cos(\lambda_m-1)\theta + (k_1\eta_1 - k_2\eta_2)\sin(\lambda_m-1)\theta \right\}, \tag{31c}$$

where $\eta_1$ and $\eta_2$ are given in Table 1. Since $\psi_{\theta 0}^{(m)}$, $\psi_{r0}^{(m)}$, and $w_0^{(m)}$ are the smallest order of $r$ in the series solution given in Eqs. (14) for different $\lambda_m$, they characterize the asymptotic behavior of the series solution in the vicinity of the vertex. Furthermore, they are the displacement field describing the singular behavior of stress resultants at the vertex when the positive real part of $\lambda_m$ is less than one. The asymptotic displacement field will be called as corner functions below.

By following the procedure given above, one can develop the characteristic equations for $\lambda_m$ and the corresponding corner functions for different boundary conditions along radial edges. Tables 1 and 2, respectively, summarize the characteristic equations for $\lambda_m$ and the corresponding corner functions for ten different combinations of boundary conditions. To take advantage of the problem's symmetry, the corner functions for the identical boundary conditions along two radial edges were determined by considering the range, $-\alpha/2 \leq \theta \leq \alpha/2$, which is also indicated in Table 1.

Notably, using trigonometric identities, the characteristic equations for S(I)_S(I) in Table 2 are found equivalent to

$$\cos(\lambda_m-1)\alpha/2 = 0 \quad \text{or} \quad \cos(\lambda_m+1)\alpha/2 = 0, \tag{32a}$$

and

$$\sin(\lambda_m-1)\alpha/2 = 0 \quad \text{or} \quad \sin(\lambda_m+1)\alpha/2 = 0, \tag{32b}$$

for symmetric and antisymmetric cases, respectively. Consequently, the corner functions corresponding to the roots of $\lambda_m$ for different equations are separately listed in Table 1. Similar situation also happens to the cases with S(II)_S(II) and S(I)_S(II) boundary conditions.

## Singularity of Stress Resultants

The relations between displacements and stress resultants given in Eq. (10) indicate that the smallest orders of $r$ for moments $(M_r, M_\theta, M_{r\theta})$ and $P_r$, $P_\theta$, and $P_{r\theta}$ are the same, and they are less than those for rotation components ($\psi_r$ and $\psi_\theta$) and $w$ by one and two, respectively. Consequently, the root $\lambda_m$ of the characteristic equations with a positive real part below one leads to singular behavior of moments and $P_r$, $P_\theta$, and $P_{r\theta}$, described by $r^{\lambda_m-1}$ as $r$ approaches zero. Moreover, the singular behavior of stress components, $\sigma_{rr}$, $\sigma_{\theta\theta}$, and $\sigma_{r\theta}$, can also be found according to the relationship between stresses and displacement components in elasticity. Notably, the characteristic equations listed in Table 2 reveal that the thickness of the plate is unrelated to these characteristic equations, and Poisson's ratio is the single material property that can affect the singularity order of stress resultants.

As stated earlier, the real part of $\lambda_m$ (Re($\lambda_m$)) must exceed zero to meet the regularity conditions for the displacement components, as $r$ approaches zero. Figure 2 displays the minimum positive values of Re($\lambda_m$) versus the vertex angle ($\alpha$) for various boundary conditions. These minimum values of Re($\lambda_m$) were determined by solving the characteristic equations in Table 2 with $\nu$ equal to 0.3. Notably, some different boundary conditions around a corner produce the same minimum Re($\lambda_m$) within certain ranges of vertex angles. Boundary conditions S(I)_S(I), S(I)_S(II), and S(II)_S(II) give the same minimum Re($\lambda_m$), while boundary conditions S(I)_F and S(II)_F yield the same minimum Re($\lambda_m$) except for 180deg$<\alpha<$270deg. Boundary conditions C_C and F_F have the same minimum Re($\lambda_m$) when $\alpha$ exceeds 180 deg. Boundary conditions C_F and C_S(II) show the same minimum Re($\lambda_m$) for $\alpha$ below about 128 deg. When $\alpha$ is between 180 deg and 270 deg, boundary condition S(I)_C yield a minimum Re($\lambda_m$) equal to that for S(I)_F and C_S(II).

Figure 2 indicates that no singularities of moments and $P_r$, $P_\theta$, and $P_{r\theta}$ occur if $\alpha$ is less than 60 deg, regardless of the boundary conditions around the corner. However, such singularities are always present if $\alpha$ exceeds 180 deg. A corner with S(I)_S(I), S(I)_S(II), S(II)_S(II), S(I)_F, S(II)_F, or S(I)_C boundary conditions exhibit a singularity when $\alpha$ exceeds 90 deg. Boundary conditions C_F and C_S(II) cause the strongest singularity of the stress resultants at the vertex for $\alpha$ between 60 deg and approximately 105 deg; S(I)_S(I), S(I)_S(II), and S(II)_S(II) boundary conditions result in the strongest singularity for other vertex angles. C_C and F_F boundary conditions cause a singularity in stress resultants for $\alpha$ exceeding 180 deg. This singularity is weaker than that due to other boundary conditions.

Figure 2 also indicates that singularities generally become more severe as the vertex angle increases, except in those cases with S(I)_S(I), S(I)_S(II), S(II)_S(II), C_F, or C_S(II) boundary conditions. For the C_F and C_S(II) cases, the minimum positive Re($\lambda_m$) increases with $\alpha$ for $\alpha$ between 122 deg and 130 deg in which region the roots of the characteristic equations change from real to complex numbers. The minimum positive Re($\lambda_m$) for S(I)_S(I), and S(II)_S(II) was determined from different characteristic equations for different ranges of $\alpha$. That is, from Eqs. (32), when $\alpha \leq \pi$, the minimum positive Re($\lambda_m$) is determined from $\cos(\lambda_m+1)\alpha/2=0$, while for $\pi<\alpha\leq 3\pi/2$ and for $3\pi/2 \leq \alpha < 2\pi$, the minimum positive Re($\lambda_m$) is determined from $\cos(\lambda_m-1)\alpha/2=0$ and $\sin(\lambda_m+1)\alpha/2=0$, respectively. As $\alpha$ approaches $2\pi$, the singularity order for moments and $P_r$, $P_\theta$, and $P_{r\theta}$ due to S(I)_S(I), S(I)_S(II), and S(II)_S(II) boundary conditions approaches $r^{-1}$, while F_F and C_C boundary conditions lead to an order of $r^{-1/2}$. Other boundary conditions yield an order of $r^{-3/4}$.

Most of the characteristic equations listed in Table 2 can also be found in either classic plate theory (CPT) or first-order shear deformation plate theory (FSDPT). Williams [11] obtained those characteristic equations marked with a superscript, "#," in Table 2, from the classic plate theory. Burton and Sinclair [18] and Huang [20] found those characteristic equations marked with superscript "*" in Table 2, based on FSDPT using different solution approaches. The characteristic equations pertaining to the S(II) boundary condition given in Table 2 cannot find the corresponding ones in classic plate theory because no S(II) boundary condition

**Table 1 Corner functions**

| Case No. | Boundary Conditions | Corner Functions |
|---|---|---|
| 1 | S(I)-S(I) $\left(-\frac{\alpha}{2}\leqslant\theta\leqslant\frac{\alpha}{2}\right)$ | (1) for $\cos(\lambda_m-1)\alpha/2=0$<br>$\psi_{r0}^{(m)}(r,\theta)=A_2 r^{\lambda_m}\cos(\lambda_m-1)\theta,\quad \psi_{\theta 0}^{(m)}(r,\theta)=B_3 r^{\lambda_m}\sin(\lambda_m-1)\theta,\ w_0^{(m)}(r,\theta)=(k_1A_2+k_2B_3)r^{\lambda_m+1}\cos(\lambda_m-1)\theta$<br>(2) for $\cos(\lambda_m+1)\alpha/2=0$<br>$\psi_{r0}^{(m)}(r,\theta)=-B_1 r^{\lambda_m}\cos(\lambda_m+1)\theta,\quad \psi_{\theta 0}^{(m)}(r,\theta)=B_1 r^{\lambda_m}\sin(\lambda_m+1)\theta,\ w_0^{(m)}(r,\theta)=A_0 r^{\lambda_m+1}\cos(\lambda_m+1)\theta$<br>(3) for $\sin(\lambda_m-1)\alpha/2=0$<br>$\psi_{r0}^{(m)}(r,\theta)=A_3 r^{\lambda_m}\sin(\lambda_m-1)\theta,\quad \psi_{\theta 0}^{(m)}(r,\theta)=B_2 r^{\lambda_m}\cos(\lambda_m-1)\theta,\ w_0^{(m)}(r,\theta)=(k_1A_3+k_2B_2)r^{\lambda_m+1}\sin(\lambda_m-1)\theta$<br>(4) for $\sin(\lambda_m+1)\alpha/2=0$<br>$\psi_{r0}^{(m)}(r,\theta)=B_0 r^{\lambda_m}\sin(\lambda_m+1)\theta,\quad \psi_{\theta 0}^{(m)}(r,\theta)=B_0 r^{\lambda_m}\cos(\lambda_m+1)\theta,\ w_0^{(m)}(r,\theta)=A_1 r^{\lambda_m+1}\sin(\lambda_m+1)\theta$ |
| 2 | C-F $(0\leqslant\theta\leqslant\alpha)$ | $\psi_{r0}^{(m)}(r,\theta)=B_3 r^{\lambda_m}\left\{\frac{1+\lambda_m}{\lambda_m-1}\cos(\lambda_m+1)\theta-\eta_2\sin(\lambda_m+1)\theta-\frac{1+\lambda_m}{\lambda_m-1}\cos(\lambda_m-1)\theta+\eta_1\sin(\lambda_m-1)\theta\right\}$<br>$\psi_{\theta 0}^{(m)}(r,\theta)=B_3 r^{\lambda_m}\left\{-\frac{1+\lambda_m}{\lambda_m-1}\sin(\lambda_m+1)\theta-\eta_2\cos(\lambda_m+1)\theta+\sin(\lambda_m-1)\theta+\eta_2\cos(\lambda_m-1)\theta\right\}$<br>$w_0^{(m)}(r,\theta)=B_3 r^{\lambda_m+1}\left\{\left(\frac{k_1(1+\lambda_m)}{\lambda_m-1}-k_2\right)\cos(\lambda_m+1)\theta+\frac{(1-\lambda_m)}{\lambda_m+1}(k_1\eta_1-k_2\eta_2)\sin(\lambda_m+1)\theta+\left(-\frac{(1+\lambda_m)k_1}{\lambda_m-1}+k_2\right)\cos(\lambda_m-1)\theta\right.$ $\left.+(k_1\eta_1-k_2\eta_2)\sin(\lambda_m-1)\theta\right\}$<br>$\eta_1=\frac{(\lambda_m+1)[(3+\nu+\nu\lambda_m-\lambda_m)\cos(\lambda_m-1)\alpha+(1+\lambda_m)(1-\nu)\cos(\lambda_m+1)\alpha]}{(\lambda_m-1)[(3+\nu+\nu\lambda_m-\lambda_m)\sin(\lambda_m-1)\alpha-(1-\lambda_m)(1-\nu)\sin(\lambda_m+1)\alpha]}$<br>$\eta_2=\frac{(3+\nu+\nu\lambda_m-\lambda_m)\cos(\lambda_m-1)\alpha+(1+\lambda_m)(1-\nu)\cos(\lambda_m+1)\alpha}{(3+\nu+\nu\lambda_m-\lambda_m)\sin(\lambda_m-1)\alpha-(1-\lambda_m)(1-\nu)\sin(\lambda_m+1)\alpha}$ |
| 3 | S(I)-F $(0\leqslant\theta\leqslant\alpha)$ | $\psi_{r0}^{(m)}(r,\theta)=B_2 r^{\lambda_m}\left\{\eta_3\sin(\lambda_m+1)\theta+\frac{\lambda_m+1}{\lambda_m-1}\sin(\lambda_m-1)\theta\right\},\quad \psi_{\theta 0}^{(m)}(r,\theta)=B_2 r^{\lambda_m}\{\eta_3\cos(\lambda_m+1)\theta+\cos(\lambda_m-1)\theta\}$<br>$w_0^{(m)}(r,\theta)=B_2 r^{\lambda_m+1}\left\{\eta_4\sin(\lambda_m+1)\theta+\left[\frac{(\lambda_m+1)k_1}{\lambda_m-1}-k_2\right]\sin(\lambda_m-1)\theta\right\}$<br>$\eta_3=-\frac{(3+\nu-\lambda_m+\nu\lambda_m)}{(\nu-1)(\lambda_m-1)}\frac{\sin(\lambda_m-1)\alpha}{\sin(\lambda_m+1)\alpha},\quad \eta_4=\frac{17}{4(\lambda_m+1)}\eta_3$ |
| 4 | S(I)-C $(0\leqslant\theta\leqslant\alpha)$ | $\psi_{r0}^{(m)}(r,\theta)=B_0 r^{\lambda_m}\left\{\sin(\lambda_m+1)\theta-\frac{\sin(\lambda_m+1)\alpha}{\sin(\lambda_m-1)\alpha}\sin(\lambda_m-1)\theta\right\}$<br>$\psi_{\theta 0}^{(m)}(r,\theta)=B_0 r^{\lambda_m}\left\{\cos(\lambda_m+1)\theta-\frac{\cos(\lambda_m+1)\alpha}{\cos(\lambda_m-1)\alpha}\cos(\lambda_m-1)\theta\right\}$<br>$w_0^{(m)}(r,\theta)=B_0 r^{\lambda_m+1}\left\{\eta_5\sin(\lambda_m+1)\theta+\left[-\frac{k_1\sin(\lambda_m+1)\alpha}{\sin(\lambda_m-1)\alpha}+\frac{k_2\cos(\lambda_m+1)\alpha}{\cos(\lambda_m-1)\alpha}\right]\sin(\lambda_m-1)\theta\right\}$<br>$\eta_5=k_1-\frac{k_2(\sin 2\lambda_m\alpha-\sin 2\alpha)}{(\sin 2\lambda_m\alpha+\sin 2\alpha)}$ |
| 5 | F-F $\left(-\frac{\alpha}{2}\leqslant\theta\leqslant\frac{\alpha}{2}\right)$ | (1) Symmetric case<br>$\psi_{r0}^{(m)}(r,\theta)=B_3 r^{\lambda_m}\left\{\eta_7\cos(\lambda_m+1)\theta+\frac{1+\lambda_m}{1-\lambda_m}\cos(\lambda_m-1)\theta\right\},\quad \psi_{\theta 0}^{(m)}(r,\theta)=B_3 r^{\lambda_m}\{-\eta_7\sin(\lambda_m+1)\theta+\sin(\lambda_m-1)\theta\}$<br>$w_0^{(m)}(r,\theta)=B_3 r^{\lambda_m+1}\left\{\eta_6\cos(\lambda_m+1)\theta+\left(\frac{(1+\lambda_m)k_1}{1-\lambda_m}+k_2\right)\cos(\lambda_m-1)\theta\right\}$<br>$\eta_6=\frac{17\eta_7}{4(1+\lambda_m)},\quad \eta_7=\frac{3+\nu-\lambda_m+\lambda_m\nu}{(-1+\nu)(\lambda_m-1)}\frac{\cos(\lambda_m-1)\alpha/2}{\cos(\lambda_m+1)\alpha/2},$<br>(2) Antisymmetric case<br>$\psi_{r0}^{(m)}(r,\theta)=B_2 r^{\lambda_m}\left\{-\eta_9\sin(\lambda_m+1)\theta+\frac{\lambda_m+1}{\lambda_m-1}\sin(\lambda_m-1)\theta\right\},\ \psi_{\theta 0}^{(m)}(r,\theta)=B_2 r^{\lambda_m}\{-\eta_9\cos(\lambda_m+1)\theta+\cos(\lambda_m-1)\theta\}$ |

**Table 1 (*continued*)**

| Case No. | Boundary Conditions | Corner Functions |
|---|---|---|
| | | $w_0^{(m)}(r,\theta)=B_2r^{\lambda_m+1}\left\{-\eta_8\sin(\lambda_m+1)\theta+\left[\frac{k_1(\lambda_m+1)}{\lambda_m-1}-k_2\right]\sin(\lambda_m-1)\theta\right\}$<br>$\eta_8=\frac{17}{4(\lambda_m+1)}\eta_9,\quad \eta_9=\frac{(3+\nu-\lambda_m+\nu\lambda_m)}{(\nu-1)(\lambda_m-1)}\frac{\sin(\lambda_m-1)\alpha/2}{\sin(\lambda_m+1)\alpha/2}$ |
| 6 | C-C $\left(-\frac{\alpha}{2}\leqslant\theta\leqslant\frac{\alpha}{2}\right)$ | (1) Symmetric case:<br>$\psi_{r0}^{(m)}(r,\theta)=B_1r^{\lambda_m}\left\{-\cos(\lambda_m+1)\theta+\frac{\cos(\lambda_m+1)\alpha/2}{\cos(\lambda_m-1)\alpha/2}\cos(\lambda_m-1)\theta\right\}$<br>$\psi_{\theta0}^{(m)}(r,\theta)=B_1r^{\lambda_m}\left\{\sin(\lambda_m+1)\theta-\frac{\sin(\lambda_m+1)\alpha/2}{\sin(\lambda_m-1)\alpha/2}\sin(\lambda_m-1)\theta\right\}$<br>$w_0^{(m)}(r,\theta)=B_1r^{\lambda_m+1}\left\{\left[-k_1+\frac{k_2(\sin\lambda_m\alpha+\sin\alpha)}{\sin\lambda_m\alpha-\sin\alpha}\right]\cos(\lambda_m+1)\theta+\left[\frac{k_1\cos(\lambda_m+1)\alpha/2}{\cos(\lambda_m-1)\alpha/2}-\frac{k_2\sin(\lambda_m+1)\alpha/2}{\sin(\lambda_m-1)\alpha/2}\right]\cos(\lambda_m-1)\theta\right\}$<br>(2) Antisymmetric case:<br>$\psi_{r0}^{(m)}(r,\theta)=B_0r^{\lambda_m}\left\{\sin(\lambda_m+1)\theta-\frac{\sin(\lambda_m+1)\alpha/2}{\sin(\lambda_m-1)\alpha/2}\sin(\lambda_m-1)\theta\right\}$<br>$\psi_{\theta0}^{(m)}(r,\theta)=B_0r^{\lambda_m}\left\{\cos(\lambda_m+1)\theta-\frac{\cos(\lambda_m+1)\alpha/2}{\cos(\lambda_m-1)\alpha/2}\cos(\lambda_m-1)\theta\right\}$<br>$w_0^{(m)}(r,\theta)=B_0r^{\lambda_m+1}\left\{\left[k_1-\frac{k_2(\sin\lambda_m\alpha-\sin\alpha)}{\sin\lambda_m\alpha+\sin\alpha}\right]\sin(\lambda_m+1)\theta+\left[-\frac{k_1\sin(\lambda_m+1)\alpha/2}{\sin(\lambda_m-1)\alpha/2}+\frac{k_2\cos(\lambda_m+1)\alpha/2}{\cos(\lambda_m-1)\alpha/2}\right]\sin(\lambda_m-1)\theta\right\}$ |
| 7 | S(II)-S(II) $\left(-\frac{\alpha}{2}\leqslant\theta\leqslant\frac{\alpha}{2}\right)$ | (1) Symmetric case:<br>When $\cos(\lambda_m-1)\alpha/2=0$,<br>$\psi_{r0}^{(m)}(r,\theta)=A_2r^{\lambda_m}\cos(\lambda_m-1)\theta,\quad \psi_{\theta0}^{(m)}(r,\theta)=B_3r^{\lambda_m}\sin(\lambda_m-1)\theta,\quad w_0^{(m)}(r,\theta)=(k_1A_2+k_2B_3)r^{\lambda_m+1}\cos(\lambda_m-1)\theta.$<br>When $\cos(\lambda_m+1)\alpha/2=0$,<br>$\psi_{r0}^{(m)}(r,\theta)=-B_1r^{\lambda_m}\cos(\lambda_m+1)\theta,\quad \psi_{\theta0}^{(m)}(r,\theta)=B_1r^{\lambda_m}\sin(\lambda_m+1)\theta,\quad w_0^{(m)}(r,\theta)=A_0r^{\lambda_m+1}\cos(\lambda_m+1)\theta.$<br>When $\lambda_m\sin\alpha+\sin\lambda_m\alpha=0$, the corner functions are the same as those for F-F.<br>(2) Antisymmetric case:<br>When $\sin(\lambda_m-1)\alpha/2=0$,<br>$\psi_{r0}^{(m)}(r,\theta)=A_3r^{\lambda_m}\sin(\lambda_m-1)\theta,\quad \psi_{\theta0}^{(m)}(r,\theta)=B_2r^{\lambda_m}\cos(\lambda_m-1)\theta,\quad w_0^{(m)}(r,\theta)=(k_1A_3-k_2B_2)r^{\lambda_m+1}\sin(\lambda_m-1)\theta.$<br>When $\sin(\lambda_m+1)\alpha/2=0$,<br>$\psi_{r0}^{(m)}(r,\theta)=B_0r^{\lambda_m}\sin(\lambda_m+1)\theta,\quad \psi_{\theta0}^{(m)}(r,\theta)=B_0r^{\lambda_m}\cos(\lambda_m+1)\theta,\quad w_0^{(m)}(r,\theta)=A_1r^{\lambda_m+1}\sin(\lambda_m+1)\theta.$<br>When $\lambda_m\sin\alpha-\sin\lambda_m\alpha=0$, the corner functions are the same as those for F-F. |
| 8 | C-S (II) $(0\leqslant\theta\leqslant\alpha)$ | The corner functions are the same as those for C_F. |
| 9 | S(I)-S(II) $(0\leqslant\theta\leqslant\alpha)$ | When $\sin 2\alpha\lambda_m=\lambda_m\sin 2\alpha$, the corresponding corner functions are the same as those for S(I)_F.<br>For $\cos 2\alpha\lambda_m=-\cos 2\alpha$,<br>when $\sin(\lambda_m-1)\alpha=0$,<br>$\psi_{r0}^{(m)}(r,\theta)=A_3r^{\lambda_m}\sin(\lambda_m-1)\theta,\quad \psi_{\theta0}^{(m)}(r,\theta)=B_2r^{\lambda_m}\cos(\lambda_m-1)\theta,$<br>$w_0^{(m)}(r,\theta)=(k_1A_3-k_2B_2)r^{\lambda_m+1}\sin(\lambda_m-1)\theta;$<br>when $\sin(\lambda_m+1)\alpha=0$,<br>$\psi_{r0}^{(m)}(r,\theta)=B_0r^{\lambda_m}\sin(\lambda_m+1)\theta,\quad \psi_{\theta0}^{(m)}(r,\theta)=B_0r^{\lambda_m}\cos(\lambda_m+1)\theta,\quad w_0^{(m)}(r,\theta)=A_1r^{\lambda_m+1}\sin(\lambda_m+1)\theta.$ |
| 10 | S(II)-F $\left(-\frac{\alpha}{2}\leqslant\theta\leqslant\frac{\alpha}{2}\right)$ | $\psi_{r0}^{(m)}(r,\theta)=B_3r^{\lambda_m}\left\{\eta_7\cos(\lambda_m+1)\theta+\eta_{11}\sin(\lambda_m+1)\theta-\frac{\lambda_m+1}{\lambda_m-1}\cos(\lambda_m-1)\theta-\frac{(\lambda_m+1)\cos(\lambda_m-1)\alpha/2}{(\lambda_m-1)\sin(\lambda_m-1)\alpha/2}\sin(\lambda_m-1)\theta\right\}$<br>$\psi_{\theta0}^{(m)}(r,\theta)=B_3r^{\lambda_m}\left\{\eta_{11}\cos(\lambda_m+1)\theta-\eta_7\sin(\lambda_m+1)\theta-\frac{\cos(\lambda_m-1)\alpha/2}{\sin(\lambda_m-1)\alpha/2}\cos(\lambda_m-1)\theta+\sin(\lambda_m-1)\theta\right\}$<br>$w_0^{(m)}(r,\theta)=B_3r^{\lambda_m+1}\left\{\eta_6\cos(\lambda_m+1)\theta+\eta_{10}\sin(\lambda_m+1)\theta+\left(-\frac{k_1(\lambda_m+1)}{\lambda_m-1}+k_2\right)\cos(\lambda_m-1)\theta\right.$<br>$\left.+\frac{\cos(\lambda_m-1)\alpha/2}{\sin(\lambda_m-1)\alpha/2}\left(-\frac{k_1(\lambda_m+1)}{\lambda_m-1}+k_2\right)\sin(\lambda_m-1)\theta\right\}$<br>$\eta_{10}=\frac{17}{4(\lambda_m+1)}\eta_{11},\quad \eta_{11}=\frac{(3+\nu+\lambda_m\nu-\lambda_m)\cos(\lambda_m-1)\alpha/2}{(\lambda-1)(\nu-1)\sin(\lambda_m+1)\alpha/2}$ |

exists in classic plate theory. This comparison concludes that different plate theories can lead to different singularity orders for moments at the corner.

To show the stress resultant distributions corresponding to the corner function with the smallest positive value of $\mathrm{Re}(\lambda_m)$, Fig. 3 exhibits the distributions of $M_r$ and $M_\theta$ along $\theta=0$deg for the symmetric case of a wedge with free radial edges, while Fig. 4 plots the distributions at $\theta=150$deg for a wedge with C_F bound-

**Table 2 Characteristic equations for high-order shear deformation plate theory**

| Case No. | Boundary Conditions | Characteristic Equations |
|---|---|---|
| 1 | S(I)-S(I) | Symmetric: $\cos\lambda_m\alpha=-\cos\alpha$*,# <br> Antisymmetric: $\cos\lambda_m\alpha=+\cos\alpha$*,# |
| 2 | C_F | $\sin^2\lambda_m\alpha=\dfrac{4-\lambda_m^2(1+\nu)^2\sin^2\alpha}{(3-\nu)(1+\nu)}$* <br> $\sin^2\lambda_m\alpha=\dfrac{4-\lambda_m^2(1-\nu)^2\sin^2\alpha}{(3+\nu)(1-\nu)}$# |
| 3 | S(I)_F | $\sin 2\lambda_m\alpha=\lambda_m\sin 2\alpha$* <br> $\sin 2\lambda_m\alpha=\dfrac{\lambda_m(1-\nu)}{-3-\nu}\sin 2\alpha$# |
| 4 | S(I)_C | $\sin 2\lambda_m\alpha=\dfrac{\lambda_m(1+\nu)}{-3+\nu}\sin 2\alpha$* <br> $\sin 2\lambda_m\alpha=\lambda_m\sin 2\alpha$# |
| 5 | F_F | Symmetric: <br> $\sin\lambda_m\alpha=-\lambda_m\sin\alpha$,* <br> $\sin\lambda_m\alpha=-\dfrac{\lambda_m(1-\nu)}{-3-\nu}\sin\alpha$# <br> Antisymmetric: <br> $\sin\lambda_m\alpha=\lambda_m\sin\alpha$,* <br> $\sin\lambda_m\alpha=\dfrac{\lambda_m(1-\nu)}{-3-\nu}\sin\alpha$# |
| 6 | C_C | Symmetric: <br> $\sin\lambda_m\alpha=-\dfrac{\lambda_m(1+\nu)}{-3+\nu}\sin\alpha$,* <br> $\sin\lambda_m\alpha=-\lambda_m\sin\alpha$# <br> Antisymmetric: <br> $\sin\lambda_m\alpha=\dfrac{\lambda_m(1+\nu)}{-3+\nu}\sin\alpha$,* <br> $\sin\lambda_m\alpha=\lambda_m\sin\alpha$# |
| 7 | S(II)_S(II) | Symmetric: <br> $\sin\lambda_m\alpha=-\lambda_m\sin\alpha$,* $\cos\lambda_m\alpha=-\cos\alpha$ <br> Antisymmetric: <br> $\sin\lambda_m\alpha=\lambda_m\sin\alpha$,* $\cos\lambda_m\alpha=\cos\alpha$ |
| 8 | C_S(II) | $\sin^2\lambda_m\alpha=\dfrac{4-\lambda_m^2(1+\nu)^2\sin^2\alpha}{(3-\nu)(1+\nu)}$* <br> $\sin 2\lambda_m\alpha=\lambda_m\sin 2\alpha$ |
| 9 | S(I)_S(II) | $\sin 2\lambda_m\alpha=\lambda_m\sin 2\alpha$* <br> $\cos 2\lambda_m\alpha=\cos 2\alpha$ |
| 10 | S(II)_F | $\sin\lambda_m\alpha=\pm\lambda_m\sin\alpha$* <br> $\sin 2\lambda_m\alpha=\dfrac{\lambda_m(-1+\nu)}{3+\nu}\sin 2\alpha$ |

Note:* means that the equation can be recovered in FSDPT.
# means that the equation can be recovered in CPT.

ary condition around the vertex. In both cases, $\alpha=300$deg and $\nu=0.3$. The value of $\lambda_m$ is real in the case of the F_F boundary condition, and $\lambda_m$ is complex for the C_F condition. The stress resultants were computed by substituting the corresponding corner functions given in Table 1 into Eq. (10) and setting the undetermined coefficients (such as $B_3$ in Table 1) in the corner functions equal to unity. Notably, when $\lambda_m$ is a complex number, the corresponding stress resultants are also complex functions. Figure 4 only presents the distributions for the imaginary parts of the stress resultants. In Fig. 4, the superscripts "+" and "−" in the legend of the vertical axis are the signs for the stress resultants. Positive stress resultants were plotted as $\mathrm{Log}|M^+/D|$ versus $\mathrm{Log}r$ and negative stress resultants were plotted as $\mathrm{Log}|M^-/D|$ versus $\mathrm{Log}r$, where $D$ is the flexural rigidity.

Figure 3 shows that the magnitudes of the stress resultants from the present solution monotonically approach infinity as $r$ approaches zero, because $\lambda_m$ is a positive real number and smaller than unity. Figure 3 also displays the stress resultant distributions obtained by CPT and by FSDPT. The stress resultant distributions for FSDPT were computed using the corner functions given in [20], and the distributions for CPT were obtained from the corner functions given in [25] and [26]. The coefficients to be determined in the corner functions for CPT and FSDPT were obtained by requiring that the values of $M_r$ at $r=10^{-5}$ for CPT and FSDPT should be identical to that from the present solution. The value of $r$ was arbitrarily chosen. Consequently, the distribution of $M_r$ for FSDPT coincides with that for the theory used here because both theories have the same $\lambda_m$ in this case. However, the distributions of $M_\theta$ for these two theories are not coincident (Fig. 3). In fact, the distributions of stress resultants along various values of $\theta$, determined by these two theories, are generally not coincident, which fact is not depicted here. Therefore, although the theory used here and FSDPT have the same $\lambda_m$ for the case shown in Fig. 3, the stress resultants approach infinity at different rates for each theory as $r$ approaches zero. This may be due to the fact that $M_{r\theta}$ is required to equal zero along a free edge in FSDPT, whereas $M_{r\theta}$ for the theory used here still approaches infinity as $r$ approaches zero, even along a free edge. The stress resultants for CPT approach infinity more slowly than those for FSDPT and the theory used here as $r$ approaches zero, since the value of $\lambda_m$ for CPT exceeds those for the other two theories.

Figure 4 reveals that the stress resultants from the present solution oscillate toward infinitely as $r$ goes to zero because $\lambda_m$ is complex. Figure 4 also plots the distributions of stress resultants for CPT and FSDPT. The corner function for FSDPT given in [20] and the corner function for CPT given in [4] and [26] were used to determine these distributions. The undetermined coefficients in these corner functions were obtained in the same way as for Fig. 3. Notably, $\lambda_m$ for CPT equals that for the theory used here in the case of Fig. 4. Figure 4 indicates that the distributions of stress resultants from the present solution coincide with those for CPT. Stress resultant functions of $M_r$, $M_\theta$, and $M_{r\theta}$ from the present solution can be shown to be exactly the same as those for CPT in this case. The value of $\lambda_m$ for FSDPT is also a complex number but differs from those for CPT and the theory used here. Accordingly, the distributions of stress resultants for FSDPT significantly differ from those for CPT and the theory used here.

The present solution involves no singularities for shear forces or $R_\beta$, which is attributable to the regularity conditions at $r=0$ and the relations between stress resultants and displacement components. The regularity conditions require $\psi_\theta$, $\psi_r$, $w$, and $w_{,r}$ to remain finite as $r$ approaches zero. The relations in Eq. (10) suggest that the shear forces and $R_\beta$ either have the same order of $r$ as $\psi_\theta$ or $\psi_r$, or one order lower than $w$. Consequently, shear forces and $R_\beta$ cannot exhibit singular behavior as $r$ approaches zero, regardless of the boundary conditions around the vertex. Notably, this finding markedly differs from that observed in CPT and FSDPT. Since shear deformation is not considered in CPT, shear forces are determined from equilibrium equations such that the singularity of shear forces is always stronger than that for moments. Huang [20] found the characteristic equations for the singularity of shear forces in first-order shear deformation plate theory, according to which the singularity order of shear forces also depends on both the boundary conditions and the vertex angle.

Comparing the singular behavior in various plate theories with that in elasticity theory yields interesting results. Hartranft and Sih [9] developed the characteristic equations for a completely free

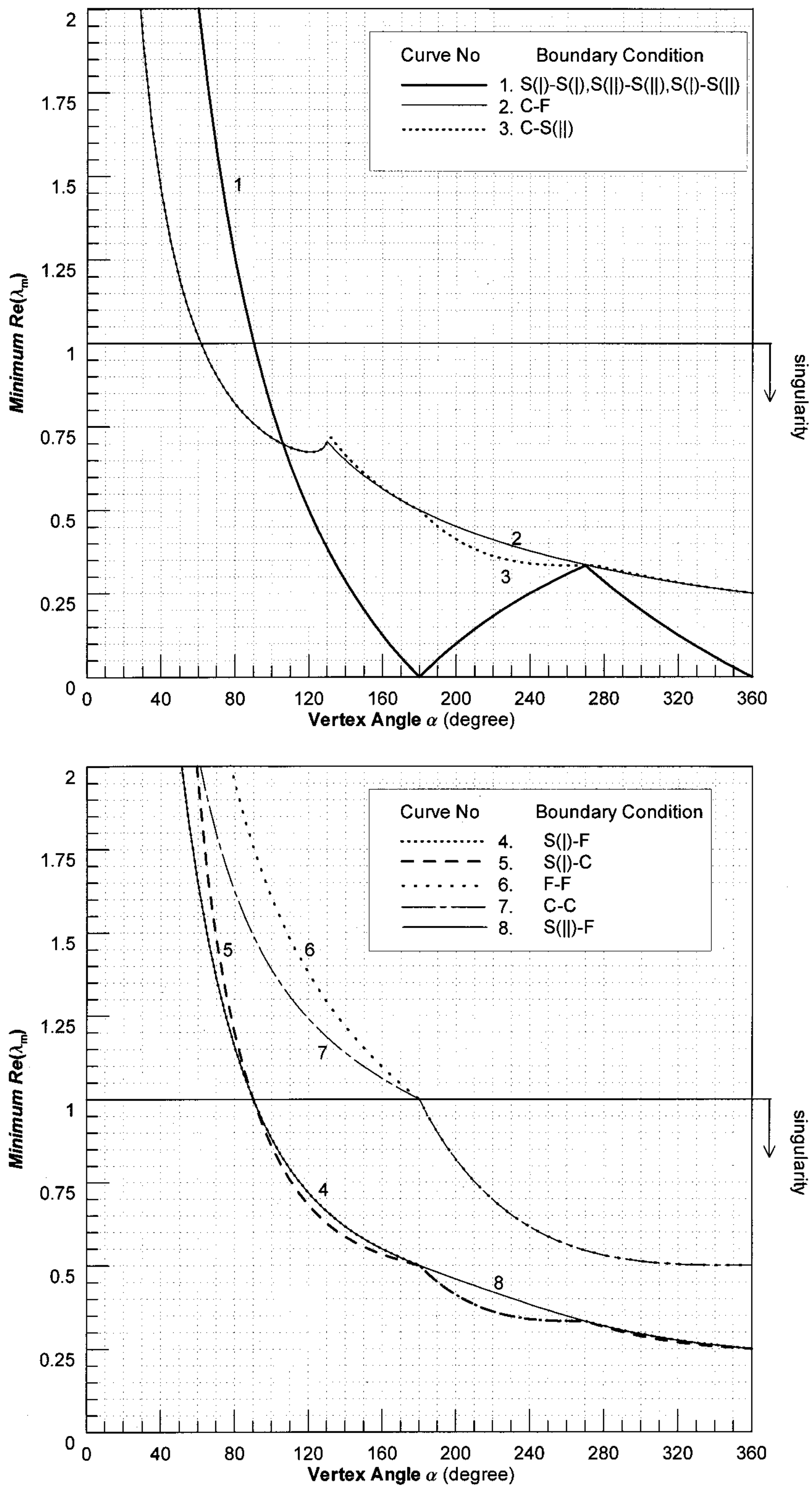


**Fig. 2 Variation of minimum Re($\lambda_m$) with vertex angle**

wedge based on a three-dimensional elasticity approach. According to their results, the stress singularity order of $r$ at the vertex of the wedge is $\lambda_m - 1$, where $\lambda_m$ is determined by

$$\sin \lambda_m \alpha = \lambda_m \sin \alpha, \tag{33a}$$

$$\sin \lambda_m \alpha = -\lambda_m \sin \alpha, \tag{33b}$$

$$\text{or } \lambda_m = (2m+1)\pi/\alpha, \tag{33c}$$

where $m = 0,1,2,3 \ldots$ . The first two equations also appear in the present work for F_F boundary conditions (Table 2), while none of these equations are found in CPT [11]. However, all three equations are also found in FSDPT [20]. The third equation characterizes the singular behavior of shear forces in FSDPT.

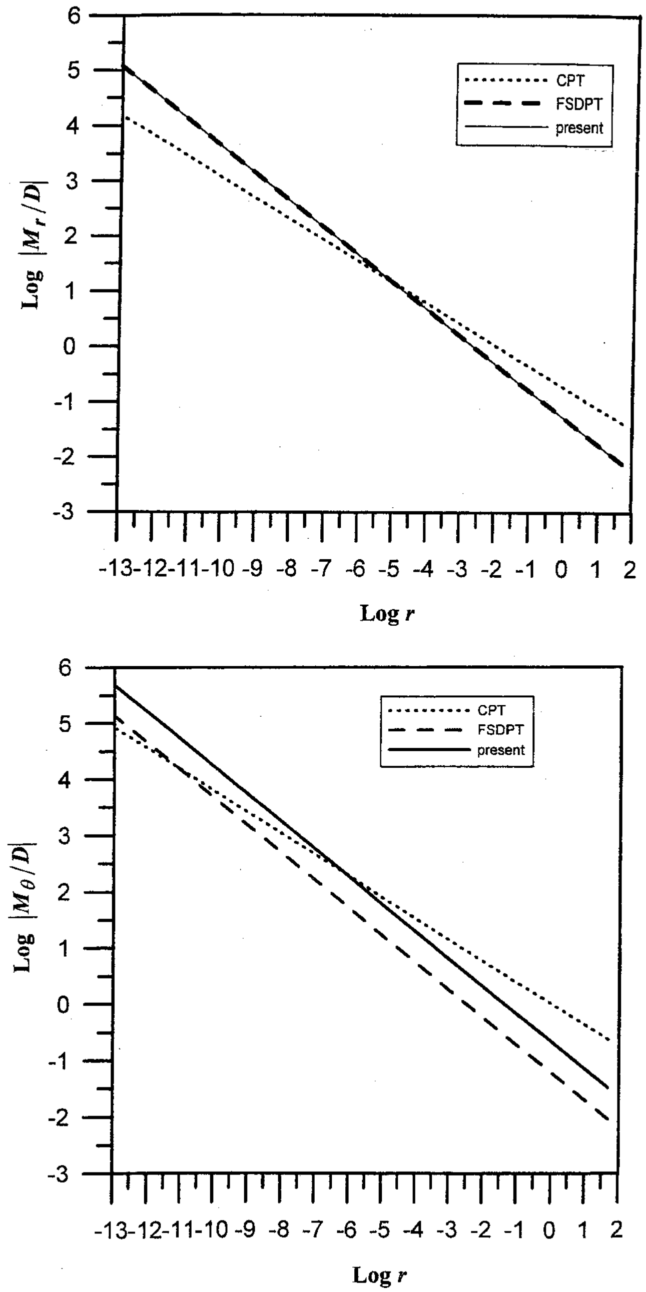


**Fig. 3 Distribution of $M_r$ and $M_\theta$ along the symmetric axis for a wedge with free radial edges**

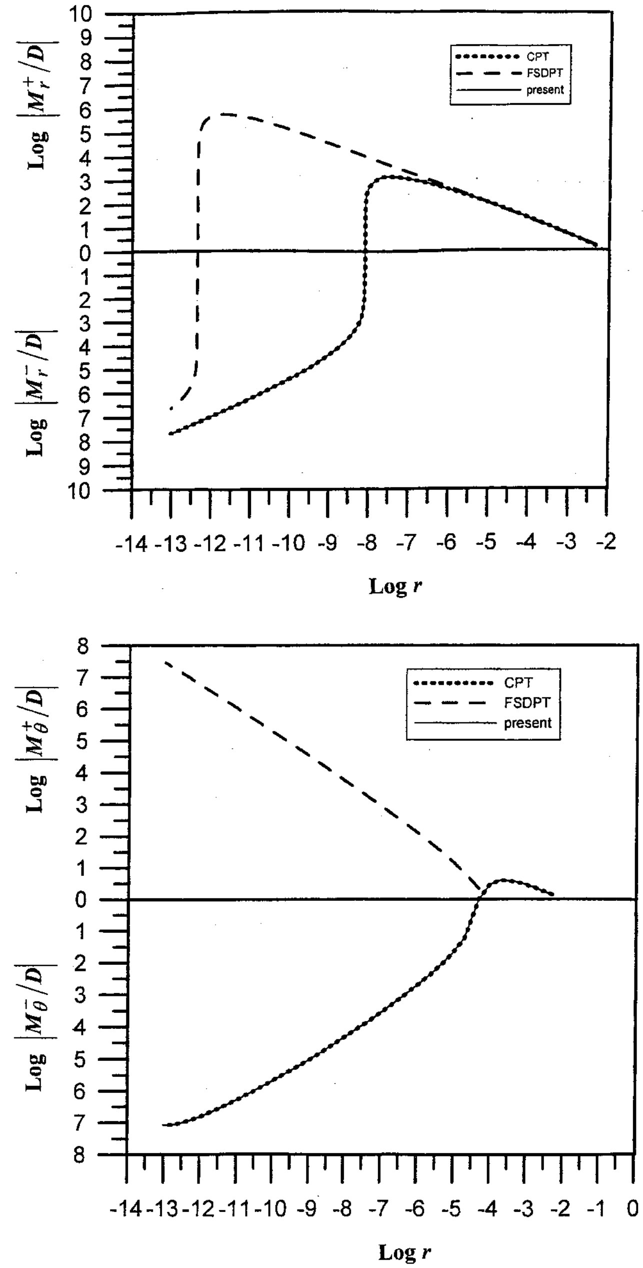


**Fig. 4 Distributions of $M_r$ and $M_\theta$=$\alpha$/2 for a wedge with C_F boundary conditions**

## Concluding Remarks

This study has established the asymptotic displacement field to describe the singular behavior of stress resultants at the vertex of a sector thick plate based on Reddy's third-order thick plate theory. The solution was obtained using an eigenfunction expansion approach to solve the equilibrium equations in terms of displacement components. The characteristic equations for determining Williams-type singularities of stress resultants were also developed for ten sets of boundary conditions around the vertex. These characteristic equations do not involve the thickness of plate. Poisson's ratio is the single material property that could possibly influence the singular behavior of stress resultants. Notably, unlike the singularity of shear forces found in classic plate theory and first-order shear deformation plate theory, no such singularity is involved in Reddy's plate theory.

The characteristic equations for determining the singular behavior of $M_r$, $M_\theta$, $M_{r\theta}$, $P_r$, $P_\theta$, and $P_{r\theta}$ in this work include the characteristic equations for classic plate theory and first-order shear deformation plate theory. For the same boundary conditions, different plate theories usually lead to different singularity orders for stress resultants, except for the case with S(I)_S(I) boundary conditions. For a plate with $\nu=0.3$, no singularity occurs when the vertex angle is less than 60 deg, while a singularity is always present when the vertex angle exceeds 180 deg. C_F boundary conditions result in the strongest singularity among the ten sets of boundary conditions considered in this study when the vertex angle is less than approximately 105 deg, while S(I)_S(I), S(II)_S(II), and S(I)_S(II) boundary conditions lead to the strongest singularity for other angles. F_F and C_C boundary conditions cause the weakest singularity.

The singularity orders for stress resultants and the corresponding corner functions given in this investigation are important for developing singularity elements in finite element approach for complex thick plate problems involving corner stress singularities. Furthermore, the corner functions for various corner boundary conditions provided herein are also very valuable for applying the Ritz method to solve thick plate problems with reentrant corners like the work by McGee et al. [4] and Leissa et al. [3] for thin plate problems.

## Acknowledgments

This work reported herein was supported by the National Science Council, R.O.C. through research grant no. NSC90-2211-E-009-035. The supported is gratefully acknowledged. The appreciation is also extended to author's graduate students, Mr. M. J. Chang and Mr. I. P. Hung, for preparing the figures shown in the paper.

## Appendix

The coefficients for Eqs. (28) are

$$a_{11}=5\lambda_m(1+\lambda_m)\cos(1+\lambda_m)\alpha,$$

$$a_{12}=5\lambda_m(1+\lambda_m)\sin(1+\lambda_m)\alpha,$$

$$a_{13}=\frac{\rho_1}{\nu-1}\cos(1-\lambda_m)\alpha,\quad a_{14}=-\frac{\rho_1}{\nu-1}\sin(1-\lambda_m)\alpha,$$

$$a_{15}=-16\lambda_m\sin(1+\lambda_m)\alpha,$$

$$a_{16}=16\lambda_m\cos(1+\lambda_m)\alpha,\quad a_{17}=\frac{\rho_2}{\nu-1}\sin(1-\lambda_m)\alpha,$$

$$a_{18}=\frac{\rho_2}{\nu-1}\cos(1-\lambda_m)\alpha$$

$$a_{21}=(\nu-1)\lambda_m(1+\lambda_m)\cos(1+\lambda_m)\alpha,$$

$$a_{22}=(\nu-1)\lambda_m(1+\lambda_m)\sin(1+\lambda_m)\alpha$$

$$a_{23}=\delta_1\cos(1-\lambda_m)\alpha,\quad a_{24}=-\delta_1\sin(1-\lambda_m)\alpha,$$

$$a_{25}=-4(\nu-1)\lambda_m\sin(1+\lambda_m)\alpha,$$

$$a_{26}=4(\nu-1)\lambda_m\cos(1+\lambda_m)\alpha,\quad a_{27}=\delta_2\sin(1-\lambda_m)\alpha,$$

$$a_{28}=\delta_2\cos(1-\lambda_m)\alpha,$$

$$a_{31}=8\lambda_m(1+\lambda_m)\sin(1+\lambda_m)\alpha,$$

$$a_{32}=-8\lambda_m(1+\lambda_m)\cos(1+\lambda_m)\alpha,$$

$$a_{33}=-(\lambda_m-1)(-17+8k_1\lambda_m)\sin(1-\lambda_m)\alpha,$$

$$a_{34}=-(\lambda_m-1)(-17+8k_1\lambda_m)\cos(1-\lambda_m)\alpha,$$

$$a_{35}=34\lambda_m\cos(1+\lambda_m)\alpha,\quad a_{36}=34\lambda_m\sin(1+\lambda_m)\alpha,$$

$$a_{37}=(\lambda_m-1)(17+8k_2\lambda_m)\cos(1-\lambda_m)\alpha,$$

$$a_{38}=-(\lambda_m-1)(17+8k_2\lambda_m)\sin(1-\lambda_m)\alpha$$

$$a_{41}=-\gamma_1\sin(1+\lambda_m)\alpha,\quad a_{42}=\gamma_1\cos(1+\lambda_m)\alpha,$$

$$a_{43}=-\gamma_2\sin(1-\lambda_m)\alpha,$$

$$a_{44}=-\gamma_2\cos(1-\lambda_m)\alpha,\quad a_{45}=-\gamma_3\cos(1+\lambda_m)\alpha,$$

$$a_{46}=-\gamma_3\sin(1+\lambda_m)\alpha,$$

$$a_{47}=-\gamma_4\cos(1-\lambda_m)\alpha,\quad a_{48}=\gamma_4\sin(1-\lambda_m)\alpha$$

$$\rho_1=-16(1+\nu\lambda_m)+5k_1\lambda_m(3+\nu-\lambda_m+\nu\lambda_m),$$

$$\rho_2=16+(-16+5(3+\nu)k_2)\lambda_m+5(\nu-1)k_2\lambda_m^2,$$

$$\delta_1=-4(1+\nu\lambda_m)+(3+\nu-\lambda_m+\nu\lambda_m)k_1\lambda_m,$$

$$\delta_2=4+(-4+(3+\nu)k_2)\lambda_m+(\nu-1)k_2\lambda_m^2,$$

$$\gamma_1=5(\nu-1)E\lambda_m(1+\lambda_m)(1-\lambda_m),$$

$$\gamma_2=E(\lambda_m-1)\lambda_m[2(-1+\nu)(-8+5k_1\lambda_m)+16(1+\nu\lambda_m)$$
$$-5k_1\lambda_m(3+\nu-\lambda_m+\nu\lambda_m)],$$

$$\gamma_3=16(\nu-1)E\lambda_m(1-\lambda_m),$$

$$\gamma_4=E(\lambda_m-1)[16+(-16+15k_2+5\nu k_2-16(\nu-1))\lambda_m$$
$$-5(\nu-1)k_2\lambda_m^2].$$

## References


[1] Rice, J. R., and Tracy, D. M., 1973, "Computational Fracture Mechanics," *Numerical and Computer Methods in Structural Mechanics*, S. J. Fenves et al., eds., Academic Press, San Diego, CA, pp. 585–623.

[2] Aminpour, M. A., and Holsapple, K. A., 1991, "Finite Element Solutions for Propagating Interface Cracks With Singularity Elements," Eng. Fract. Mech., **39**(3), pp. 451–468.

[3] Leissa, A. W., McGee, O. G., and Huang, C. S., 1993, "Vibrations of Sectorial Plates Having Corner Stress Singularities," ASME J. Appl. Mech., **60**, pp. 134–140.

[4] McGee, O. G., Leissa, A. W., and Huang, C. S., 1992, "Vibrations of Cantilevered Skewed Plates With Corner Stress Singularities," Int. J. Numer. Methods Eng., **35**(2), pp. 409–424.

[5] William, M. L., 1952, "Stress Singularities Resulting From Various Boundary Conditions in Angular Corners of Plates in Extension," ASME J. Appl. Mech., **19**, pp. 526–528.

[6] Hein, V. L., and Erdogan, F., 1971, "Stress Singularities in a Two-Material Wedge," Int. J. Fract. Mech., **7**(3), pp. 317–330.

[7] Dempsey, J. P., and Sinclair, G. B., 1979, "On the Stress Singularities in the Plate Elasticity of the Composite Wedge," J. Elast., **9**(4), pp. 373–391.

[8] Ting, T. C. T., and Chou, S. C., 1981, "Edge Singularities in Anisotropic Composites," Int. J. Solids Struct., **17**(11), pp. 1057–1068.

[9] Hartranft, R. J., and Sih, G. C., 1969, "The Use of Eigenfunction Expansions in the General Solution of Three-Dimensional Crack Problems," J. Math. Mech., **19**(2), pp. 123–138.

[10] Xie, M., and Chaudhuri, R. A., 1998, "Three-Dimensional Stress Singularity at a Bimaterial Interface Crack Front," Compos. Struct., **40**(2), pp. 137–147.

[11] William, M. L., 1952, "Stress Singularities Resulting From Various Boundary Conditions in Angular Corners of Plates Under Bending," *Proceedings of 1st U.S. National Congress of Applied Mechanics*, ASME, New York, pp. 325–329.

[12] Williams, M. L., and Owens, R. H., 1954, "Stress Singularities in Angular Corners of Plates Having Linear Flexural Rigidities for Various Boundary Conditions," *Proceedings of 2nd U.S. National Congress of Applied Mechanics*, ASME, New York, pp. 407–411.

[13] William, M. L., and Chapkis, R. L., 1958, "Stress Singularities for a Sharp-Notched Polarly Orthotropic Plate," *Proceedings of 3rd U.S. National Congress of Applied Mechanics*, ASME, New York, pp. 281–286.

[14] Rao, A. K., 1971, "Stress Concentrations and Singularities at Interfaces Corners," Z. Angew. Math. Mech., **51**, pp. 395–406.

[15] Ojikutu, I. O., Low, R. O., and Scott, R. A., 1984, "Stress Singularities in Laminated Composite Wedge," Int. J. Solids Struct., **20**(8), pp. 777–790.

[16] Huang, C. S., Leissa, A. W., and McGee, O. G., 1993, "Exact Analytical Solutions for the Vibrations of Sectorial Plates With Simply-Supported Radial Edges," ASME J. Appl. Mech., **60**, pp. 478–483.

[17] Sinclair, G. B., 2000, "Logarithmic Stress Singularities Resulting From Various Boundary Conditions in Angular Corners of Plates Under Bending," ASME J. Appl. Mech., **67**, pp. 219–223.

[18] Burton, W. S., and Sinclair, G. B., 1986, "On the Singularities in Reissner's Theory for the Bending of Elastic Plates," ASME J. Appl. Mech., **53**, pp. 220–222.

[19] Huang, C. S., McGee, O. G., and Leissa, A. W., 1994, "Exact Analytical Solutions for the Vibrations of Mindlin Sectorial Plates With Simply Supported Radial Edges," Int. J. Solids Struct., **31**(11), pp. 1609–1631.

[20] Huang, C. S., 2001, "Stress Singularities at Angular Corners in First-Order Shear Deformation Plate Theory," Int. J. Mech. Sci., submitted for publication.

[21] Reddy, J. N., 1999, *Theory and Analysis of Elastic Plates*, Taylor and Francis, London.

[22] Schmidt, R., 1977, "A Refined Nonlinear Theory for Plates With Transverse Shear Deformation," J. Indust. Math. Soc., **27**(1), pp. 23–38.

[23] Krishna Murty, A. V., 1977, "Higher Order Theory for Vibration of Thick Plates," AIAA J., **15**(2), pp. 1823–1824.

[24] Reddy, J. N., 1984, *Energy and Variational Methods in Applied Mechanics*, John Wiley and Sons, New York.

[25] Leissa, A. W., McGee, O. G., and Huang, C. S., 1993, "Vibrations of Circular Plates Having V-Notches or Sharp Radial Cracks," J. Sound Vib., **161**(2), pp. 227–239.

[26] Huang, C. S., 1991, "Singularities in Plate Vibration Problems," Ph.D. dissertation, The Ohio State University.

# Transient Ultrasonic Waves in Multilayered Superconducting Plates

**A. J. Niklasson**
Department of Applied Mechanics,
Chalmers University of Technology,
SE-412 96 Göteborg, Sweden

**S. K. Datta**
Department of Mechanical Engineering,
University of Colorado,
Boulder, CO 80309-0427
Fellow ASME

*Transient response of multilayered superconducting tapes has been studied in this paper. These tapes are usually composed of layers of a superconducting material (like $YBa_2Cu_3O_{7-\delta}$, or YBCO, for simplicity) alternating between layers of a metallic material (like nickel or silver). The tapes are thin, in the range of 100–200 μm. The superconducting layer is orthotropic with a thickness of 5–10 μm. In applications, tapes are long and have a finite width. In this paper, attention has been focused on the transient response of homogeneous and three-layered tapes assuming that the width is infinite and that the thickness of the superconducting layer is much smaller than the metal layer. The problem considered here is of general interest for understanding the effect of anisotropy of thin coating or interface layers in composite plate structures on ultrasonic guided waves. Three plate geometries are considered as prototype examples: a homogeneous nickel (Ni) layer, a three-layered YBCO/Ni/YBCO, and a three-layered Ni/YBCO/Ni. Transient response due to a line force applied normal to the surface of the tape has been studied by means of Fourier transforms and direct numerical integration. Numerical results are presented using an exact model and a first-order approximation to the thin YBCO layer. The first-order approximation simplifies the problem to that of a homogeneous isotropic plate subject to effective boundary conditions representing the thin anisotropic layers. Both are seen to agree well (except when the center frequency of the force is high) and capture the coupling of the longitudinal, S, (or flexural, A) motion and the shear-horizontal (SH) motion. Detailed analysis of the influence of the thin layers, especially their anisotropy, on this coupling and the transient response shows significant differences among the three cases. The model results provide insight into the coupling phenomenon and indicate the feasibility of careful experiments to exploit the significant changes in the transient response caused by coupling for the determination of the in-plane elastic constants of thin coating or interface layers.* [DOI: 10.1115/1.1505627]

## 1 Introduction

In this paper, our attention is focused on the transient response of a plate with *thin* anisotropic layers. As a particular technologically important problem, we consider the anisotropic layers to be superconducting. Two specific examples are considered. In one, the thin layers are on the outer surfaces of a homogeneous isotropic core layer and in the other, a thin layer is sandwiched between two identical homogeneous isotropic layers. The motivation for this study is to develop a fundamental understanding of ultrasonic guided waves in tapes that are fabricated for commercial high-current applications. The tapes are composites consisting of a brittle superconducting phase and a ductile metal phase. Various mechanical processes are used to get the crystallographic texture most favorable to high current capacity of the tapes. Such processes coupled with thermal cycling cause microcracking of the brittle oxide layer(s), which limits the current carrying capacity. The degree of current carrying capacity reduction is a strong function of the crystallographic texture of the oxide layer and the nature of microcracking, which is also a function of the texture. These effects influence the mechanical responses such as ultrasonic guided waves along the tapes. Exploitation of the connection between the electrical and mechanical responses may prove to be an efficient means of nondestructive material property characterization during and after the processing of the tapes.

There is now a large body of literature on ultrasonics in superconducting bulk materials. It is known that for superconductors, the elastic constants can be linked to the superconducting transition temperature $T_C$ through the Debye temperature $\Theta_D$ and the electron-phonon coupling parameter $\lambda$ ([1,2]). A review of various ultrasonic measurements of elastic properties can be found in [3]. Investigation of *in situ* mechanical behavior and properties of thin superconducting layers has been limited. Since the properties are highly dependent upon external and internal stress fields, interface properties and porosity, to name a few, the motivation for this work is to understand the basic problem of guided wave propagation in an anisotropic three-layered tape.

Dispersion of guided waves along a direction of material symmetry of the orthotropic oxide layer(s) in a three-layered (Ni/YBCO/Ni and YBCO/Ni/YBCO) was studied by Pan and Datta [4]. Transient response of such a plate to a line force orthogonal to the symmetry axis and applied to the surface of the tape was also reported in [4]. In this example, the motion (P-SV) in the plane of symmetry containing the symmetry axis is uncoupled from the motion (SH) perpendicular to the plane. Thus, the former problem is one of plane strain. Niklasson, Datta, and Dunn [5,6] considered dispersion of guided waves along an arbitrary direction in a three-layered plate. In this case, P-SV motion is coupled with shear-horizontal (SH) motion so that the displacement has all the three components. It was shown that because of this coupling symmetric SH mode is coupled with the extensional (S) mode and the antisymmetric SH mode is coupled with the flexural (A) mode. As a consequence, for propagation in directions not aligned with the symmetry axes, there are bands of frequency when a predomi-

Contributed by the Applied Mechanics Division of THE AMERICAN SOCIETY OF MECHANICAL ENGINEERS for publication in the ASME JOURNAL OF APPLIED MECHANICS. Manuscript received by the ASME Applied Mechanics Division, July 6, 2001; final revision, Mar. 21, 2002. Associate Editor: A. K. Mal. Discussion on the paper should be addressed to the Editor, Prof. Robert M. McMeeking, Department of Mechanical and Environmental Engineering, University of California–Santa Barbara, Santa Barbara, CA 93106-5070, and will be accepted until four months after final publication of the paper itself in the ASME JOURNAL OF APPLIED MECHANICS.

  

nantly symmetric SH mode ($q\mathrm{SH}_{(2n)}$, $n=0,1,2,\ldots$) changes to a predominantly extensional (qS) mode and vice versa. Similarly, there are different frequency bands when an antisymmetric SH mode ($q\mathrm{SH}_{(2n+1)}$, $n=0,1,2,\ldots$) changes to a predominantly flexural (qA) mode. These mode interchanges occur within narrow frequency bands, the widths of which depend on the *thickness* and in-plane anisotropy of the anisotropic layer. This suggests the possibility that with appropriate choice of narrow-band pulsed excitation the mode interchange can be captured in the time domain response of the plate.

The objective of this paper is to analyze the transient response of the three-layered plate in order to understand this mode interchange and to suggest experiments that would lead to the determination of the in-plane anisotropic properties efficiently. The attention has been focused primarily on the coupling of the $\mathrm{SH}_0$ and $\mathrm{S}_0$ modes which is observed first at a relatively low frequency. However, the analysis could be easily extended to coupling of other modes at high frequencies.

The layout of the paper is as follows. In the next section, the calculation of the exact Green's function due to a line force applied to the surface of a layered anisotropic plate is outlined. Since the approach taken here may be found in previous works, the procedure is only briefly outlined and references are made to earlier works. In Section 3, approximations of the Green's function are derived. Two examples of three-layered plates are considered as illustration: (1) a line force located on the surface of a plate made of a thick isotropic core coated symmetrically on both surfaces by identical thin anisotropic layers, and (2) a line force located on the surface of a plate made of a thin anisotropic layer sandwiched between two identical thick isotropic layers. The approximations are obtained by means of effective boundary and interface conditions, respectively, as described in [5,6]. In Section 4, the exact and approximate Green's functions are compared for particular cases. Features due to mode coupling are described which may be useful for ultrasonic material characterization.

## 2 Exact Green's function

In this section, we derive the exact Green's function due to a line force applied to the surface of an anisotropic multilayered plate. The solution is presented for a layered plate consisting of an arbitrary number of layers of general anisotropy. The details concerning the approach taken here, the so-called global matrix method, may be found elsewhere (see, for example, [7] and [8]). Only a brief outline is presented in this section.

Consider an infinite plate consisting of $N$ anisotropic layers, each of thickness $b^{(j)}$, $j=1,\ldots,N$ (see Fig. 1). All quantities with superscript $(j)$ are associated with layer $j$ and this superscript is dropped when no ambiguity is possible. The equations governing the exact time-harmonic Green's function $G_{jm}(x_1,x_3;\xi_1)$ due to a line force at $x_1=\xi$, $x_3=0$ in the $x_m$ direction and parallel to the $x_2$-direction are

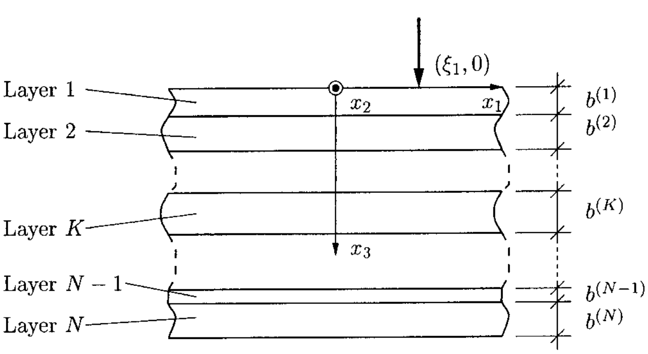


**Fig. 1 An anisotropic layered plate**

$$\partial_\alpha \Sigma^{(r)}_{\alpha jm}+\rho^{(r)}\omega^2 G^{(r)}_{jm}=0,\quad d^{(r-1)}<x_3<d^{(r)},\quad r=1,\ldots,N, \tag{1}$$

with the boundary and interface conditions (perfect bonds)

$$\Sigma^{(1)}_{3jm}=-\delta(x_1-\xi_1)\delta_{jm},\quad x_3=0, \tag{2a}$$

$$\Sigma^{(N)}_{3jm}=0,\quad x_3=d^{(N)}, \tag{2b}$$

$$G^{(r)}_{jm}=G^{(r+1)}_{jm},\quad \Sigma^{(r)}_{3jm}=\Sigma^{(r+1)}_{3jm},\quad x_3=d^{(r)},\quad r=1,\ldots,N-1, \tag{2c}$$

where $d^{(r)}$ is the thickness of the first $r$ layers, i.e., $d^{(r)}=\Sigma_{j=1}^{r}b^{(j)}$. Note that the fields are independent of the $x_2$-coordinate. The summation convention is used throughout this paper, unless otherwise indicated, with lowercase Roman indices taking on the values 1, 2, and 3 and lowercase Greek indices taking on the values 1 and 3. $\delta_{jm}$ is the Kronecker delta, $\delta(x)$ is the Dirac delta function and the notation $\partial_j$ means $\partial/\partial x_j$. In Eqs. (1) and (2), $\Sigma_{jmn}$ is the stress tensor corresponding to the displacement $G_{jm}$, $\rho$ the density, and $\omega$ the circular frequency. Component $(j,m)$ of the Green's function is thus component $j$ of the displacement field in the plate at $(x_1,x_3)$ due to a line force in the $x_m$-direction at $(\xi_1,0)$ (the line force when $m=3$ is shown in Fig. 1). In Voigt's abbreviated notation, the Green's stress tensor may be written as (see Auld [9])

$$\begin{pmatrix}\Sigma_{11m}\\ \Sigma_{22m}\\ \Sigma_{33m}\\ \Sigma_{32m}\\ \Sigma_{31m}\\ \Sigma_{21m}\end{pmatrix}=\begin{pmatrix}C_{11}&C_{12}&C_{13}&C_{14}&C_{15}&C_{16}\\ C_{12}&C_{22}&C_{23}&C_{24}&C_{25}&C_{26}\\ C_{13}&C_{23}&C_{33}&C_{34}&C_{35}&C_{36}\\ C_{14}&C_{24}&C_{34}&C_{44}&C_{45}&C_{46}\\ C_{15}&C_{25}&C_{35}&C_{45}&C_{55}&C_{56}\\ C_{16}&C_{26}&C_{36}&C_{46}&C_{56}&C_{66}\end{pmatrix}\times\begin{pmatrix}\partial_1 G_{1m}\\ 0\\ \partial_3 G_{3m}\\ \partial_3 G_{2m}\\ \partial_3 G_{1m}+\partial_1 G_{3m}\\ \partial_1 G_{2m}\end{pmatrix}. \tag{3}$$

The problem is solved by applying a spatial Fourier transform in $x_1$,

$$\hat{f}(k)=\int_{-\infty}^{\infty} f(x_1)e^{-ikx_1}dx_1,\quad f(x_1)=\frac{1}{2\pi}\int_{-\infty}^{\infty}\hat{f}(k)e^{ikx_1}dk, \tag{4}$$

to the equations of motion and the interface and boundary conditions. The transformed system of equations is solved by means of the so-called global matrix method described by Ju and Datta [7] and Mal [8]. The procedure is briefly as follows in our case. First we obtain a general solution in each of the $N$ layers by reformulating the transformed Eq. (1) as a first-order system of ordinary differential equations in the displacement-traction vector $(\hat{G}_{1m}\hat{G}_{2m}\hat{G}_{3m}\hat{\Sigma}_{31m}\hat{\Sigma}_{32m}\hat{\Sigma}_{33m})^T$. These systems are then solved by assuming that the solutions are in the form $A\mathbf{v}e^{ik_3x_3}$, where $A$ is a constant, $\mathbf{v}$ is the 6-by-1 polarization vector and $k_3$ is the wave number in the $x_3$-direction. The wave numbers $k_3$ and the polarization vectors $\mathbf{v}$ are obtained by solving a generalized eigenvalue problem in each layer. The constants are determined by inserting the general solutions into Eq. (2) and forming a sparse banded global system of equations (which will have three-right hand sides, one for each value of $m$). Once the constants have been determined, the inverse Fourier transform may be applied to obtain the exact Green's function. Inversion of the Fourier transform, i.e., the computation of the integral numerically is discussed in Section 4.

Another alternative to the global matrix method is the Thomson-Haskell or transfer matrix method (see, for example, Nayfeh [10]). By using this method, one only deals with 6-by-6 transfer matrices (one for each layer), their sizes being independent of the number of layers $N$. One drawback of the Thomson-Haskell method is that it requires stabilization in order to be useful numerically. This makes it less straightforward to use than the global matrix method.

## 3 Approximations of the Green's Function

In this section, we derive approximations of the line force Green's function for two specific configurations. The first system considered consists of a thick isotropic core and two identical anisotropic (superconducting) coatings (see Fig. 2), and the second consists of a thin anisotropic (superconducting) layer sandwiched between two identical thick isotropic layers (see Fig. 3). The approximations are obtained by replacing the thin layers by effective boundary and interface conditions.

**3.1 A Coated Plate.** In this section, we derive an approximation to the line force Green's function for a coated plate. The plate consists of a thick isotropic core and two identical thin anisotropic coatings perfectly bonded to the core (see Fig. 2). Note that we have located the origin of the coordinate system in the middle of the plate since the configuration is then symmetric with respect to the $x_1x_2$-plane. The approximation of the Green's function is denoted by $g_{jm}(x_1,x_3;\xi_1)$. Furthermore, we denote the material properties of the anisotropic coatings by $C_{JM}$ (the elastic constants in abbreviated form) and $\rho_L$ (the density) and the material properties of the isotropic substrate by $\lambda$, $\mu$ (the Lamé constants) and $\rho$ (the density).

If we assume that the thickness of the coatings, $h$, is small compared to all wavelengths involved, we can replace the coatings by the effective boundary conditions used by Niklasson et al. [5]. The equations governing $g_{jm}$ inside the core ($|x_3|<a$) are then given by

$$\partial_\alpha \sigma_{\alpha jm} + \rho\omega^2 g_{jm} = 0, \quad -a<x_3<a, \tag{5a}$$

$$\sigma_{jmn} = \lambda\,\delta_{jm}\partial_r g_{rn} + \mu(\partial_j g_{mn} + \partial_m g_{jn}), \quad -a<x_3<a, \tag{5b}$$

$$\boldsymbol{\tau}_m - h(A_u\mathbf{g}_m + A_\sigma\boldsymbol{\tau}_m) = 0, \quad x_3 = a, \tag{5c}$$

$$\boldsymbol{\tau}_m + h(A_u\mathbf{g}_m + A_\sigma\boldsymbol{\tau}_m) = -\,\delta(x_1-\xi_1)\mathbf{I}_m, \quad x_3 = -a, \tag{5d}$$

where $\mathbf{g}_m = (g_{1m}, g_{2m}, g_{3m})^T$, $\boldsymbol{\tau}_m = (\sigma_{31m}, \sigma_{32m}, \sigma_{33m})^T$, and $\mathbf{I}_m = (\delta_{1m}, \delta_{2m}, \delta_{3m})^T$. The nonzero elements of the matrices $A_u$ and $A_\sigma$ are (see [5])

$$\begin{aligned}
(A_u)_{11} &= \rho_L\omega^2 + (C_{11} - C_{13}^2/C_{33})\partial_1^2,\\
(A_u)_{12} &= (A_u)_{21} = (C_{16} - C_{13}C_{36}/C_{33})\partial_1^2,\\
(A_u)_{22} &= \rho_L\omega^2 + (C_{66} - C_{36}^2/C_{33})\partial_1^2, \quad (A_u)_{33} = \rho_L\omega^2,\\
(A_\sigma)_{13} &= C_{13}\partial_1/C_{33}, \quad (A_\sigma)_{23} = C_{36}\partial_1/C_{33}, \quad (A_\sigma)_{31} = \partial_1.
\end{aligned} \tag{6}$$

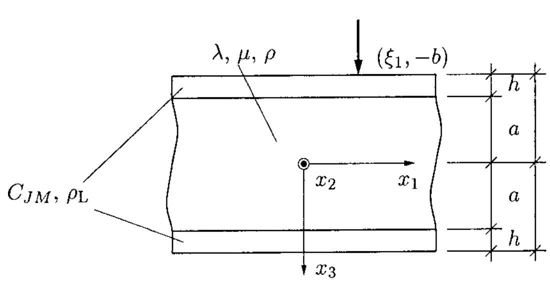

Fig. 2 A coated plate

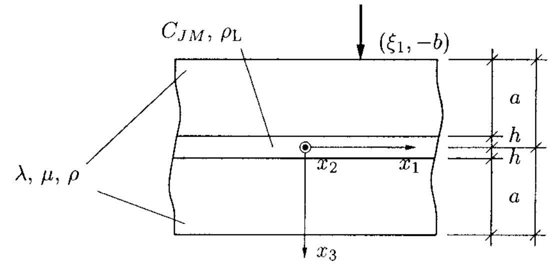

Fig. 3 A sandwich plate

In order to obtain the field in the entire plate ($|x_3|<b$), a continuation of $g_{jm}$ obtained as the solution to Eq. (5) is made. This continuation is obtained as a series expansion in $x_3$ keeping up to the linear term in $|x_3|-a$

$$g_{jm}(x_1,x_3;\xi_1) \approx g_{jm}(x_1,\pm a;\xi_1) + (x_3 \mp a) \times(\partial_3 g_{jm}(x_1,x_3;\xi_1))_{x_3=\pm a}, \quad \pm a \lesseqgtr x_3 \lesseqgtr \pm b. \tag{7}$$

When solving the equations stated above, we start by finding a general solution. This is very straightforward since, due to the introduction of the effective boundary conditions, the waves are now propagating in a homogeneous isotropic plate. First, we apply the spatial Fourier transform (4) to the equations and then solve the resulting system of ordinary differential equations. The general solution may be written as (see, for example, Achenbach [11])

$$\hat{\mathbf{g}}_m = \nabla\Phi_m + \nabla\times\boldsymbol{\Psi}_m, \quad \nabla\cdot\boldsymbol{\Psi}_m = 0, \tag{8a}$$

$$\Phi_m = A_{m0}\sin px_3 + B_{m0}\cos px_3, \quad p = \sqrt{k_p^2 - k^2}, \quad k_p = \omega/c_p, \tag{8b}$$

$$(\boldsymbol{\Psi}_m)_n = A_{mn}\sin qx_3 + B_{mn}\cos qx_3, \quad q = \sqrt{k_s^2 - k^2}, \quad k_s = \omega/c_s, \tag{8c}$$

where $m,n = 1,2,3$, and $c_p = \sqrt{(\lambda+2\mu)/\rho}$ and $c_s = \sqrt{\mu/\rho}$ are the pressure and shear wave speeds of the isotropic core, respectively. The integration constants (six for each $m$ if we use the condition $\nabla\cdot\boldsymbol{\Psi}_m = 0$) are determined by applying the boundary conditions to the general solution Eq. (8). It should be noted here that the problem described by Eq. (5) can be split into a symmetric and an antisymmetric problem (with respect to the $x_3$-coordinate). This will reduce the set of six equations for the six unknowns into two sets of three equations for three unknowns. This has been done but the explicit equations are not given here for brevity.

**3.2 A Sandwich Plate.** The second approximation considered, is derived for a system consisting of a thin anisotropic layer sandwiched between two identical isotropic layers (see Fig. 3). As in the previous section, the approximation of the Green's function is denoted by $g_{jm}(x_1,x_3;\xi_1)$. Note again that we have located the origin of the coordinate system in the middle of the plate. We denote the material properties of the anisotropic layer by $C_{JM}$ and $\rho_L$, and the material properties of the isotropic layers by $\lambda$, $\mu$, and $\rho$ as before.

If we assume that the thickness of the sandwiched layer, $2h$, is small compared to the wavelengths involved, we can replace the thin anisotropic layer by the effective interface conditions used by Niklasson et al. [6] and Rokhlin and Huang [12]. The equations governing $g_{jm}$ inside the isotropic layers ($h<|x_3|<b$) are given by

$$\partial_\alpha \sigma^{\pm}_{\alpha jm} + \rho\omega^2 g^{\pm}_{jm} = 0, \quad \pm h \lesseqgtr x_3 \lesseqgtr \pm b, \tag{9a}$$

$$\sigma^{\pm}_{jmn} = \lambda\,\delta_{jm}\partial_r g^{\pm}_{rn} + \mu(\partial_j u^{\pm}_{mn} + \partial_m u^{\pm}_{jn}), \quad \pm h \lesseqgtr x_3 \lesseqgtr \pm b, \tag{9b}$$

$$(\mathbf{T}_m^+)_{x_3=h}+h(D\mathbf{T}_m^+)_{x_3=h}=(\mathbf{T}_m^-)_{x_3=-h}-h(D\mathbf{T}_m^-)_{x_3=-h}, \tag{9c}$$

$$\sigma_{3jm}^+=0, \quad x_3=b, \tag{9d}$$

$$\sigma_{3jm}^-=-\delta(x_1-\xi_1)\delta_{jm}, \quad x_3=-b, \tag{9e}$$

where $\mathbf{T}_m^{\pm}=(g_{1m}^{\pm},g_{2m}^{\pm},g_{3m}^{\pm},\sigma_{31m}^{\pm},\sigma_{32m}^{\pm},\sigma_{33m}^{\pm})^T$, and the matrix $D$ is given by

$$D=\begin{pmatrix} A_\sigma^T & B_\sigma \\ A_u & A_\sigma \end{pmatrix}. \tag{10}$$

The matrices $A_u$ and $A_\sigma$ are as before, and the nonzero elements of $B_\sigma$ are

$$\begin{aligned}(B_\sigma)_{11}&=-C_{44}/\delta, \quad (B_\sigma)_{22}=-C_{55}/\delta,\\ (B_\sigma)_{12}&=(B_\sigma)_{21}=C_{45}/\delta, \quad (B_\sigma)_{33}=-1/C_{33},\end{aligned} \tag{11}$$

where $\delta=C_{44}C_{55}-C_{45}^2$. The superscripts $\pm$ are used to indicate if we refer to the field below or above the interface layer, i.e., $f^+(x_3)=f(x_3),\ x_3>h$, and $f^-(x_3)=f(x_3),\ x_3<-h$.

In order to obtain the field in the entire plate ($|x_3|<b$), a continuation of $g_{jm}$ obtained as the solution to Eq. (9) is made. This continuation is obtained as a series expansion in $x_3$ keeping up to the linear term in $h-|x_3|$

$$\begin{aligned}g_{jm}^{\pm}(x_1,x_3;\xi_1)&\approx g_{jm}^{\pm}(x_1,\pm h;\xi_1)+(x_3\mp h)\\ &\quad\times(\partial_3 g_{jm}^{\pm}(x_1,x_3;\xi_1))_{x_3=\pm h}, \quad 0\leqslant x_3\leqslant \pm h.\end{aligned} \tag{12}$$

When solving the equations stated above, we start by finding a general solution in each of the two isotropic layers. These solutions are in the same form as in the previous section

$$\hat{\mathbf{g}}_m^{\pm}=\nabla\Phi_m^{\pm}+\nabla\times\mathbf{\Psi}_m^{\pm}, \quad \nabla\cdot\mathbf{\Psi}_m^{\pm}=0, \tag{13a}$$

$$\Phi_m^{\pm}=A_{m0}^{\pm}\sin px_3+B_{m0}^{\pm}\cos px_3, \tag{13b}$$

$$(\mathbf{\Psi}_m^{\pm})_n=A_{mn}^{\pm}\sin qx_3+B_{mn}^{\pm}\cos qx_3. \tag{13c}$$

The constants are determined by applying the boundary conditions at $x_3=\pm b$ and the interface conditions at $x_3=\pm h$. It should be noted here as well that the problem described by Eq. (9) can be split into a symmetric and an antisymmetric problem (with respect to the $x_3$-coordinate). This will, for each $m$, reduce the original set of twelve equations for the 12 unknown integration constants (if the equations $\nabla\cdot\mathbf{\Psi}_m^{\pm}=0$ already have been used) into two sets of six equations for six unknowns. These sets of equations are omitted in this paper for brevity. In order to recover the Green's function, the solutions to the symmetric and antisymmetric subproblems are added.

## 4 Numerical Examples

Here, we present some numerical examples using the exact and approximate solutions, derived above in this paper, for the line force Green's function. In all the examples $G_{33}(x_0,0;0)$ or $g_{33}(x_0,-b;0)$ are shown with $x_0=5.0$ mm (see Figs. 2 and 3 for the definition of $b$). Note once again that different coordinate systems are used for $G_{33}$ and $g_{33}$, $x_3=0$ is the top surface for $G_{33}$ and $x_3=-b$ is the top surface for $g_{33}$. Only $G_{33}$ and $g_{33}$ are considered since they are of most interest from an experimental point of view. The main objective is to investigate the influence of the anisotropy of the thin layers on the Green's function at low frequencies. A second objective is to investigate the usefulness of the approximate solutions.

We consider two different superconducting tapes in the examples: one coated three-layered plate and one three-layered sandwiched plate. The isotropic material in both tapes is nickel (Ni) and the thin layers are made of the orthotropic superconductor $YBa_2Cu_3O_{7-\delta}$ (YBCO). The material properties of YBCO are given in Table 1 (from [1]) and the properties used for nickel are $\lambda=129.5$ GPa, $\mu=84.71$ GPa, and $\rho=8910$ kg/m$^3$. Note that only the nonzero elastic constants are included in the table. The prime on the elastic constants means that they are given in the materials crystal axes system, denoted by $(x_1',x_2',x_3')$. The orientation of the crystal axes system relative to the $(x_1,x_2,x_3)$ system is given by the angle $\phi$ as shown in Fig. 4. The transformation from the crystal axes system to this latter system is given by Auld [9]. The dimensions of both tapes are given by $a=50\ \mu$m and $h=5\ \mu$m (see Figs. 2 and 3). The two configurations considered here have recently been studied by Pan and Datta [4]. In [4], however, only the plane-strain Green's function is presented and the propagation is thus restricted to a plane of elastic symmetry. In addition to the layered tapes, examples are given for a pure Ni tape of thickness 110 $\mu$m ($a=b=55\ \mu$m, $h=0\ \mu$m).

**Table 1 Material properties of YBCO ($C'_{JM}$ in GPa and $\rho$ in kg/m$^3$)**

| $C'_{11}$ | $C'_{22}$ | $C'_{33}$ | $C'_{44}$ | $C'_{55}$ | $C'_{66}$ | $C'_{12}$ | $C'_{13}$ | $C'_{23}$ | $\rho$ |
|---|---|---|---|---|---|---|---|---|---|
| 268 | 231 | 186 | 37 | 49 | 95 | 132 | 95 | 71 | 6333 |

In order to calculate the expressions for the Green's function, the inverse Fourier transform must be computed. Since all integrands (the exact and approximate) have got a large number of poles along the real $k$-axis, great care need be taken. In order to remove the singularities (poles) from the integrands, the integration paths are deformed in the complex $k$-plane. The integrations are performed along

$$k(s)=s(1-i\alpha e^{-\beta|s|}), \quad 0\leqslant s<\infty, \tag{14}$$

instead of along the real $k$-axis. Symmetries of $\hat{G}_{jm}$ and $\hat{g}_{jm}$ with respect to $k$ have been used as well to reduce the integration interval from $(-\infty,\infty)$ to $[0,\infty)$. Suitable values for the parameters $\alpha$ and $\beta$ have been determined from numerical tests and $\alpha=0.1$ and $\beta=1/2|k_s|$ have been used in the examples below. When the integration contours have been deformed as described above, the singularities are no longer present in the integrands. The integrands do, however, still experience highly irregular behavior which makes the numerical evaluation very difficult. We, therefore, use adaptive integration schemes to evaluate these integrals. We use the adaptive scheme by Xu and Mal [13] for the finite part $0\leqslant s\leqslant s_c$ and the scheme by Xu and Mal [14] for the remaining semi-infinite part $s_c<s<\infty$. For the finite part, we use polynomial approximations of fourth and eighth order and for the semi-infinite part, we approximate the integrand by polynomials of fourth order. The value of $s_c$ is determined numerically from the desired accuracy of the approximation of the semi-infinite part of the integral. When the approximate Green's functions are computed, the finite part is calculated by means of the approximations derived in Section 3 and the tail is computed by means of the exact Green's function derived in Section 2. This is done since the

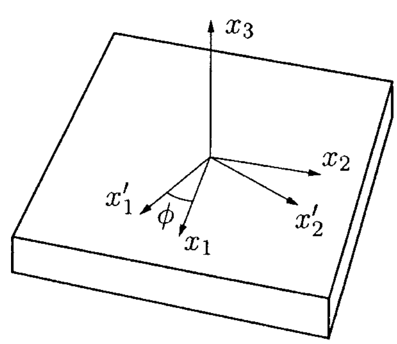


**Fig. 4 The orientation of the crystal axes system**

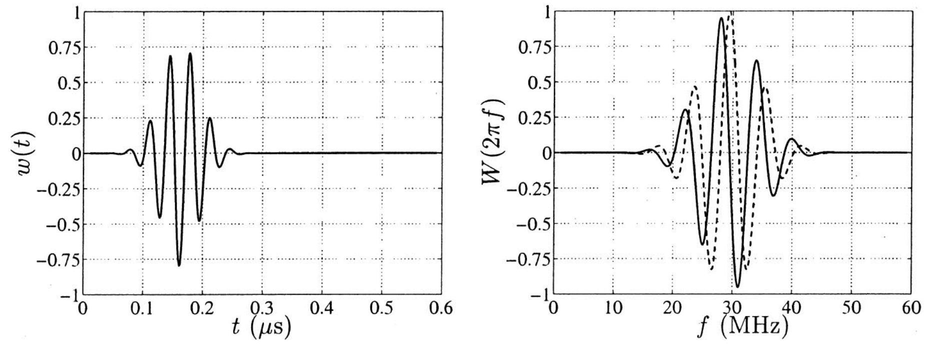


(a) The time response.

(b) The frequency spectrum. Solid line is the real part and dashed the imaginary part.

**Fig. 5 The time response and frequency spectrum of the line force when $f_c = 29.4$ MHz**

approximations break down for large $kh$. Still, since the tail is computed using very few points, the approximations are much faster to compute than the exact Green's function.

When the time-harmonic Green's function is obtained, it is multiplied by a frequency spectrum $W(\omega)$ and to this product, the inverse temporal Fourier transform is applied. The result is the Green's function in the time domain from a line force with a frequency spectrum given by $W(\omega)$. In all the examples, $W(\omega)$ is taken as the temporal transform of the function

$$w(t) = \sqrt{\frac{2}{\pi}} e^{-c_s^2(t-t_0)^2/8a^2} \sin(\omega_c t), \qquad (15)$$

with $t_0 = 0.16\ \mu$s, $a = 50\ \mu$m, and $c_s$ is the shear speed of Ni. The remaining parameter $\omega_c = 2\pi f_c$ (the center frequency) is varied in the examples below. For the specific value $f_c = 29.4$ MHz, the time response $w(t)$, Eq. (15), and the frequency spectrum $W(\omega) = W(2\pi f)$ are shown in Fig. 5. As is seen in the Fig. 5, the line force is essentially zero outside an interval of width 30 MHz centered around $f_c$. The chosen value of $f_c$ is close to the point where the mode interchange between $S_0$ and $SH_0$ occurs for the sandwich plate. In all the examples below, we will keep the center frequency close to the point of mode interchange for the sandwich and coated plates. The main reasons for this choice is that, since the mode interchange is due to the anisotropy, its effect is expected to be amplified in this region. The function Eq. (15) has been used by, for example, Pan and Datta [4]. Finally, we employ the exponential windowing technique when inverting the temporal Fourier transform (see, for example, [4]).

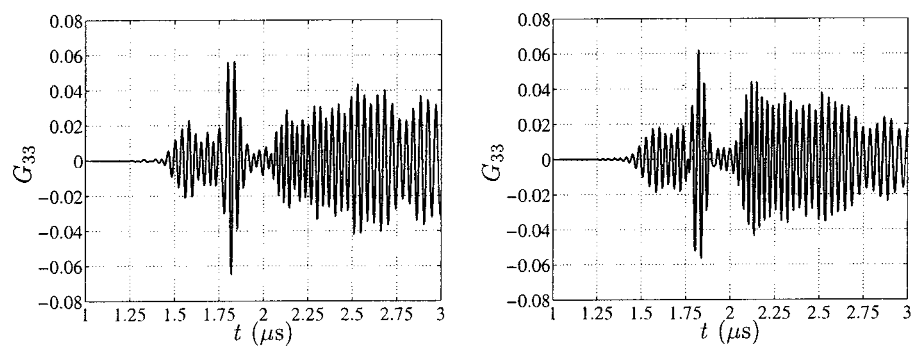


(a) $f_c = 27.0$ MHz.

(b) $f_c = 29.4$ MHz.

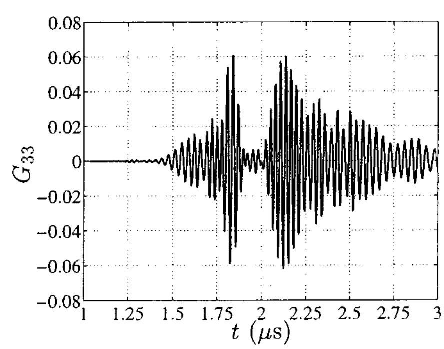


(c) $f_c = 31.9$ MHz.

**Fig. 6 $G_{33}$ for a 110-$\mu$m thick Ni plate**

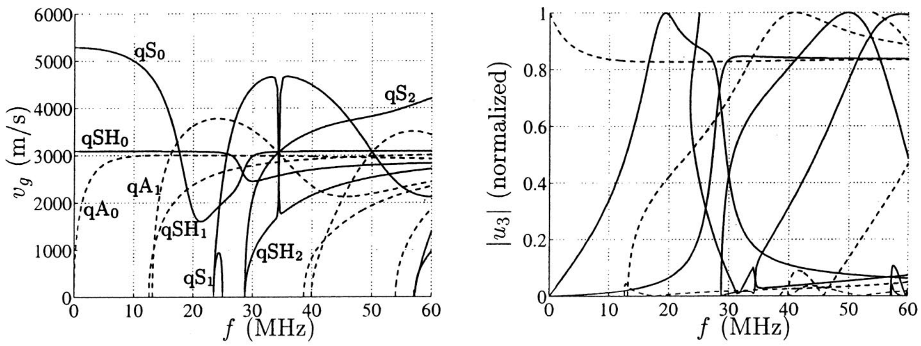


(a) Group velocity.

(b) $|u_3|$ on the top surface.

**Fig. 7 Group velocity and vertical displacement for a 30 deg Ni/YBCO/Ni plate. Solid lines are the symmetric modes and dashed the antisymmetric modes.**

**4.1 The Ni Tape.** First, we consider a pure Ni plate of thickness 110 $\mu$m ($a=b=55\,\mu$m, $h=0\,\mu$m). This plate is included mainly as a comparison to the layered plates. The thickness of the Ni plate is the same as the total thicknesses of the layered plates thus eliminating the thickness effect.

In Fig. 6(a), $G_{33}$ is shown for $f_c=27.0$ MHz. The distinct responses in the figures correspond to the $A_1$ mode mixed with the $S_1$ mode at $t\approx 1.6\,\mu$s and the $A_0$ mode at $t\approx 1.85\,\mu$s. The $S_0$ mode, however, is not clearly seen in the figure.

The center frequency is increased to $f_c=29.4$ MHz in Fig. 6($b$). The main difference from Fig. 6($a$) is that the $S_0$ mode is now visible (mixed with the $S_2$ mode). $S_0$ is seen to arrive at $t\approx 2.15\,\mu$s which corresponds well to the arrival time computed from the group velocity.

The final example for the Ni plate is shown in Fig. 6($c$). Here, the center frequency is increased even further to $f_c=31.9$ MHz. Now, it is hard to identify the $A_1$ and $S_1$ modes but the $S_0$ mode mixed with the $S_2$ mode is even more pronounced. The $A_0$ mode is still easy to identify.

**4.2 The Sandwich Tape.** The second example considered is a tape made of a thin YBCO layer sandwiched between two thick identical isotropic layers made of nickel (Ni). The total thickness of the plate is 110 $\mu$m ($a=50\,\mu$m, $h=5\,\mu$m) as in all examples.

In Fig. 7, the group velocities and the $x_3$-component of the mode displacements on the upper surface are shown for a rotated middle layer ($\phi$=30 deg). Here, the specific choices of center frequency $f_c$ become evident. The point of our interest is when the mode interchange between the $qS_0$ and $qSH_0$ modes occur. From the figure, it is seen that this location is $f_c\approx 28$ MHz. In the examples below, $f_c$ is varied but kept close to this point.

The first example is for propagation in a symmetry plane ($\phi$=0 deg). The resulting signal when $f_c=29.4$ MHz is shown in Fig. 8. Since the propagation is in a symmetry plane, no mode interchange occurs (the SH modes are not present at all in this case). If the figures are compared to the corresponding ones for the pure Ni plate (Fig. 6($b$)), the main difference lies in the part of the signal arriving after the $A_0$ mode.

In Fig. 9, the propagation is no longer in a symmetry plane ($\phi$=30 deg) and the mode interchange shown in Fig. 7 takes place. Here, the center frequency is $f_c=27.0$ MHz which is slightly below the point of mode interchange. If this figure is compared to Fig. 6($a$) it is seen that the signals are quite different. The most notable feature is that it is now much easier to identify the arrival of the lowest modes.

In Fig. 10, the exact and approximate Green's functions for the off-angle case $\phi$=30 deg are compared when $f_c=29.4$ MHz. As is seen from the figures, the approximation works very well and captures all the features of the signal. The signals show that the arrival of the modes is even more pronounced in this case and especially the signal arriving at $t\approx 2.0\,\mu$s is of interest to us. The corresponding group velocity, taking the time delay into account, is $v_g\approx 2700$ m/s. From Fig. 7, it is seen that this corresponds to the location of the mode interchange between the $qS_0$ and $qSH_0$ modes. We note that this signal is not seen in the case when $\phi$=0 deg nor for the pure Ni plate. This is expected, since no mode interchange takes place in those cases. The signal is also seen when $f_c=27.0$ MHz (Fig. 9), but not as clearly as in Fig. 10.

Finally, in Fig. 11 the case when $\phi$=60 deg and $f_c=29.4$ MHz is shown. If the signal is compared to Fig. 10, we find that they are very different. The difference lies in the anisotropy of the interface layer and especially the signal due to the mode interchange is now much weaker. If the group velocity and mode shape graphs (not shown here) are studied, it is seen that the mode

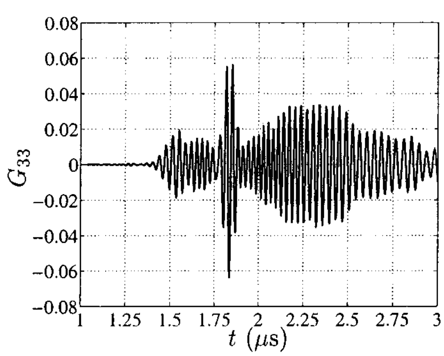


**Fig. 8 $G_{33}$ for a 0 deg Ni/YBCO/Ni plate when $f_c=29.4$ MHz**

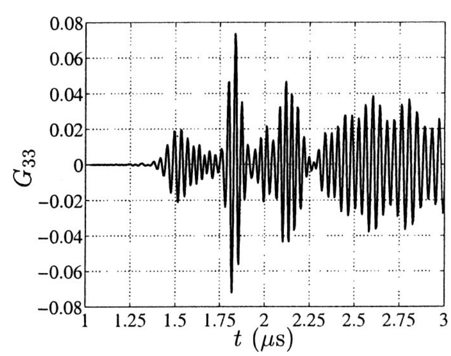


**Fig. 9 $G_{33}$ for a 30 deg Ni/YBCO/Ni plate when $f_c=27.0$ MHz**

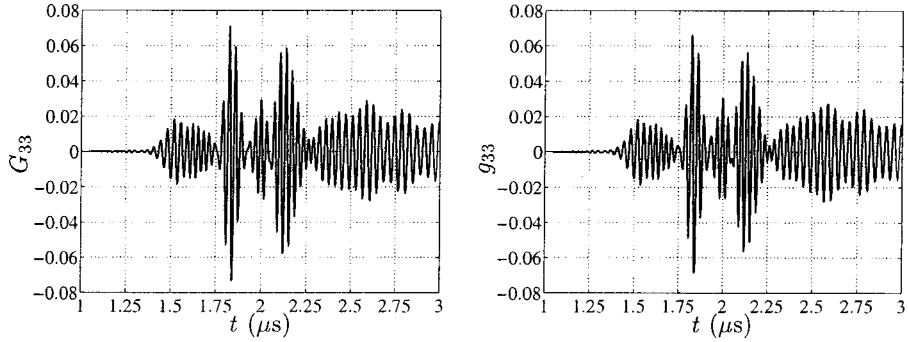


(a) Exact solution. (b) Approximate solution.

**Fig. 10 $G_{33}$ and $g_{33}$ for a 30 deg Ni/YBCO/Ni plate when $f_c = 29.4$ MHz**

interchange takes place during a much narrower frequency interval. Therefore, the mixing of the modes is hardly seen. Also, the signal arriving at $t \approx 2.15$ $\mu$s in Fig. 10 is no longer as distinct in Fig. 11.

**4.3 The Coated Tape.** In this section, we consider the tape made of a thick Ni layer coated with two identical thin YBCO layers. Once again, the total thickness of the plate is 110 $\mu$m ($a = 50$ $\mu$m, $h = 5$ $\mu$m).

In Fig. 12, the group velocities and the $x_3$-component of the mode displacements on the upper surface are shown for rotated coating layers ($\phi = 60$ deg). Here, the frequency of mode interchange between the $qS_0$ and $qSH_0$ modes is higher than for the sandwich plate. From the figure, it is seen that this location is $f_c \approx 32$ MHz.

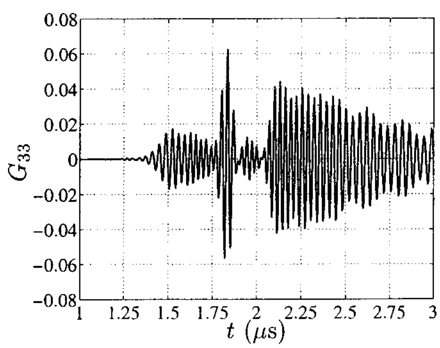


**Fig. 11 $G_{33}$ for a 60 deg Ni/YBCO/Ni plate when $f_c = 29.4$ MHz**

Figure 13 shows the exact and approximate Green's functions for the 60-deg coated tape when $f_c = 31.9$ MHz. In the figures, the $qA_0$ and $qS_0$ modes are clearly seen. If the figures are compared to Fig. 6($c$) (the pure Ni tape), the big difference lies in the part from the $qS_0$ mode. This is mainly a result of the mode interchange that occurs in the coated tape. We also see that the approximation does not work very well in this case (compared to the sandwich tape). One reason is that the center frequency is higher now and that the approximation loses accuracy for high frequencies.

## 5 Concluding Remarks

This paper was devoted to the transient response of a layered anisotropic plate due to an ultrasonic line force of finite bandwidth applied to the surface of the plate. In two earlier papers [5,6], dispersion of guided elastic waves in three-layered plates, one composed of a core elastic isotropic material surrounded by symmetric thin anisotropic coating layers and the other made of thin anisotropic interface layer sandwiched between two identical thick isotropic material, was studied. Simplified boundary and interface conditions were derived taking into account the small thickness of the coating and interface layers, respectively. Detailed analysis of the effect of anisotropy on the mode coupling for propagation along directions deviating from the symmetry directions revealed the existence of mode interchanges in certain finite ranges of the frequency of the guided waves. Furthermore, it was shown that the dispersion behavior of the coated plate was quite different than the sandwich plate with a thin interface layer. Here, a model study of time-dependent line force Green's function was presented with an objective to bring out the mode interchange behavior as depicted by the shapes and arrival times of different

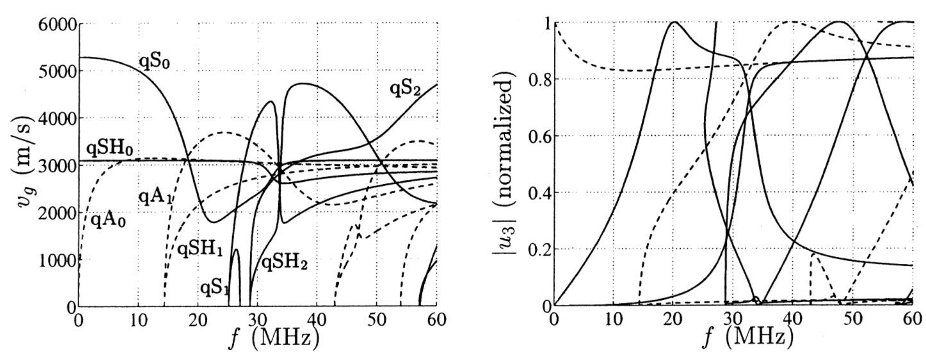


(a) Group velocity. (b) $|u_3|$ on the top surface.

**Fig. 12 Group velocity and vertical displacement for a 60 deg YBCO/Ni/YBCO plate. Solid lines are the symmetric modes and dashed the antisymmetric modes.**

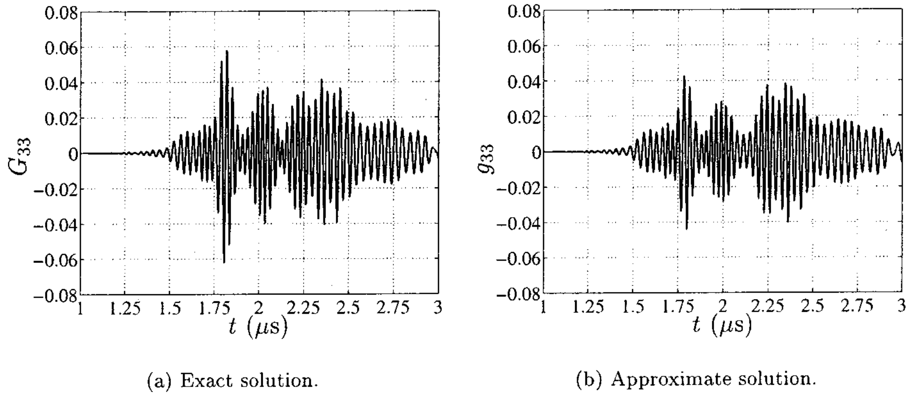


**Fig. 13 $G_{33}$ and $g_{33}$ for a 60 deg YBCO/Ni/YBCO plate when $f_c$=31.9 MHz**

pulses. Particular attention was focused on the coupling of the first symmetric extensional ($S_0$) and antiplane shear ($SH_0$) modes since it occurs at a relatively low frequency. The study showed that when the center frequency of the narrow band source was close to the frequency of strong coupling pulse shapes changed markedly. A new wave form, which was the mode converted SH, was seen to emerge. The arrival time of this wave was predicted well by the group velocity of the mode. Since this mode interchange strongly depended upon the in-plane anisotropy and thickness of the thin layer, it would be possible to measure these properties ultrasonically with judicious choice of the frequency band of the excitation source.

This investigation also validated the thin layer approximation for studying time-dependent line force Green's function for coated and sandwich plates. It should be emphasized that although the study was for the case of a plate with superconducting layers as a model, the conclusions would be generally valid for other types of anisotropic layers.

## Acknowledgments

The work of the first author (AJN) was made possible primarily through the financial support provided by the Swedish Foundation for International Cooperation in Research and Higher Education (STINT). The authors also gratefully acknowledge the support provided by the Department of Energy, Office of Basic Energy Sciences, Division of Materials Science and Engineering (grant # DE-FG03-97ER14738).

## References


[1] Lei, M., Sarrao, J. L., Visscher, W. M., Bell, T. M., Thompson, J. D., Migliori, A., Welp, U. W., and Veal, B. W., 1993, "Elastic Constants of a Monocrystal of Superconducting $YBa_2Cu_3O_{7-\delta}$," Phys. Rev. B, **47**, pp. 6154–6156.

[2] Shindo, Y., Ledbetter, H., and Nozaki, H., 1995, "Elastic Constants and Microcracks in $YBa_2Cu_3O_7$," J. Mater. Res., **10**, pp. 7–10.

[3] Levy, M., ed., 1993, *Ultrasonics of High-$T_c$ and Other Unconventional Superconductors* (Physical Acoustics, Vol. 20), Academic Press, New York.

[4] Pan, E., and Datta, S. K., 1999, "Ultrasonic Waves in Multilayered Superconducting Plates," J. Appl. Phys., **86**, pp. 543–551.

[5] Niklasson, A. J., Datta, S. K., and Dunn, M. L., 2000, "On Approximating Guided Waves in Thin Anisotropic Coatings by Means of Effective Boundary Conditions," J. Acoust. Soc. Am., **108**, pp. 924–933.

[6] Niklasson, A. J., Datta, S. K., and Dunn, M. L., 2000, "On Ultrasonic Guided Waves in a Thin Anisotropic Layer Lying Between Two Isotropic Layers," J. Acoust. Soc. Am., **108**, pp. 2005–2011.

[7] Ju, T. H., and Datta, S. K., 1992, "Dynamics of a Laminated Composite Plate With Interface Layers," J. Nondestruct. Eval., **11**, pp. 227–235.

[8] Mal, A. K., 1988, "Wave Propagation in Layered Composite Laminates Under Periodic Surface Loads," Wave Motion, **10**, pp. 257–266.

[9] Auld, B. A., 1990, *Acoustic Fields and Waves in Solids*, **1**, Krieger, Melbourne, FL.

[10] Nayfeh, A. H., 1995, *Wave Propagation in Layered Anisotropic Media With Applications to Composites* (Applied Mathematics and Mechanics, Vol. 39), Elsevier, Amsterdam.

[11] Achenbach, J. D., 1973, *Wave Propagation in Elastic Solids*, North-Holland, Amsterdam.

[12] Rokhlin, S. I., and Huang, W., 1993, "Ultrasonic Wave Interaction With a Thin Anisotropic Layer Between Two Anisotropic Layers. II. Second-Order Asymptotic Boundary Conditions," J. Acoust. Soc. Am., **94**, pp. 3405–3420.

[13] Xu, P.-C., and Mal, A. K., 1985, "An Adaptive Integration Scheme for Irregularly Oscillatory Functions," Wave Motion, **7**, pp. 235–243.

[14] Xu, P.-C., and Mal, A. K., 1987, "Calculation of the Inplane Green's Functions for a Layered Viscoelastic Solid," Bull. Seismol. Soc. Am., **77**, pp. 1823–1837.

# Wave Propagation in a Piezoelectric Coupled Solid Medium

**Q. Wang**
Mem. ASME
Department of Civil Engineering,
National University of Singapore,
Singapore 119260,
Republic of Singapore

*Shear horizontal (SH) wave propagation in a semi-infinite solid medium surface bonded by a layer of piezoelectric material abutting the vacuum is investigated in this paper. The dispersive characteristics and the mode shapes of the deflection, the electric potential, and the electric displacements in the thickness direction of the piezoelectric layer are obtained theoretically. Numerical simulations show that the asymptotic phase velocities for different modes are the Bleustein surface wave velocity or the shear horizontal wave velocity of the pure piezoelectric medium. Besides, the mode shapes of the deflection, electric potential, and electric displacement show different distributions for different modes and different wave number. These results can be served as a benchmark for further analyses and are significant in the modeling of wave propagation in the piezoelectric coupled structures.* [DOI: 10.1115/1.1488662]

## 1 Introduction

Wave propagation and vibration in a pure piezoelectric medium have received considerable attention ([1–4]). In order to achieve the time delay effect in acoustic applications, the surface wave propagation in the piezoelectric plate is of importance and has arisen interests by Viktorov [5,6], Curtis and Redwood [7], and Cheng and Sun [8,9]. Sun and Cheng [9] presented acoustic surface wave propagating around a piezoelectric cylinder with metallic overlay. Their results show that a thin metallic film placed on the top of a piezoelectric substrate can change the propagation characteristics of the surface waves. So the electromechanical effect by a layer of metal should be modeled.

Nowadays, the study of piezoelectric coupled structures over the last two decades spans from the simple mechanics model ([10]) to the more recent finite element model ([11]). The use of piezoelectric layers both surface bonded and embedded sensor and actuator patches have been widely studied ([12–15]). Such embedded and surface-mounted sensor and actuator patches have been used in applications such as aerospace engineering, mechanical engineering, civil engineering, and even in bioengineering.

A potential of piezoelectric materials as actuators and sensors is the health monitoring of structures by use of the interdigital transducer (IDT). This application requires a piezoelectric layer surface bonded on the structures to be health monitored, and the IDT is used to excite a wave propagating in the piezoelectric coupled structure to study the wave signal for the purpose of damage detection of the host structure. Some methods and experimental works on the rapid monitoring of structures using IDT to excite Lamb wave have been attempted ([16,17]) in some plate-like structures. In this study, an accurate analytical model of wave propagation in the piezoelectric coupled structures with piezoelectric coupling effects fully modeled is a key to the design of the wavelength of the IDT and the excitation of the wave propagation in the structure. Wang et al. [18] studied the shear horizontal (SH) wave propagation in a semi-infinite solid medium surface bonded by a piezoelectric layer with electrodes shortly connected in their analyses. The wave excitation of such SH wave propagation in a plate-like structure by use of IDT is proposed in [19].

This paper is an attempt on the wave propagation in the piezoelectric coupled structures based on the above background of the application of the piezoelectric material in health monitoring of structures. The dispersive characteristics of the wave propagation in a semi-infinite solid medium surface mounted by a piezoelectric layer abutting the vacuum are presented in the paper. The distributions of the deflection, the electric potential and the electric displacement in the thickness direction of the piezoelectric are thus studied thereafter. The result of this paper can be used as benchmark for the study of the wave propagation in the piezoelectric coupled structures and is significant in the design of wave propagation in the piezoelectric coupled structures as well.

## 2 Mechanics Model

We consider a metal half-space $x_2>0$ covered by a piezoelectric layer of thickness $h$ $(-h<x_2<0)$ as shown in Fig. 1. The poling direction is in its transverse $x_3$-direction so that only the SH wave will be studied in this layered structure.

The propagation of an SH wave in the host structure is governed by

$$c'_{44}\nabla^2 u'_3=\rho'\frac{\partial^2 u'_3}{\partial t^2} \tag{1}$$

where $c'_{44}=2G=E/(1+\nu')$ is the shear module, $\rho'$ is the mass density, $\nu'$ is the Poisson ration, $E$ is the Young's module of the host plate, $u'_3$ is the deflection in the host medium, and the Laplace operator is $\nabla^2=\partial/\partial x_1+\partial/\partial x_2$.

The shear stress in the host semi-infinite medium is then written as

$$\sigma'_{23}=c'_{44}\frac{\partial u'_3}{\partial x_1} \tag{2}$$

The coupling equation for piezoelectric layer is written as

$$c_{44}\nabla^2 u_3+e_{15}\nabla^2\phi=\rho\frac{\partial^2 u_3}{\partial t^2} \tag{3a}$$

$$e_{15}\nabla^2 u_3-\Xi_{11}\nabla^2\phi=0 \tag{3b}$$

Contributed by the Applied Mechanics Division of THE AMERICAN SOCIETY OF MECHANICAL ENGINEERS for publication in the ASME JOURNAL OF APPLIED MECHANICS. Manuscript received by the ASME Applied Mechanics Division, Apr. 27, 2001; final revision, Dec. 17, 2001. Associate Editor: A. K. Mal. Discussion on the paper should be addressed to the Editor, Prof. Robert M. McMeeking, Department of Mechanical and Environmental Engineering University of California–Santa Barbara, Santa Barbara, CA 93106-5070, and will be accepted until four months after final publication of the paper itself in the ASME JOURNAL OF APPLIED MECHANICS.

  

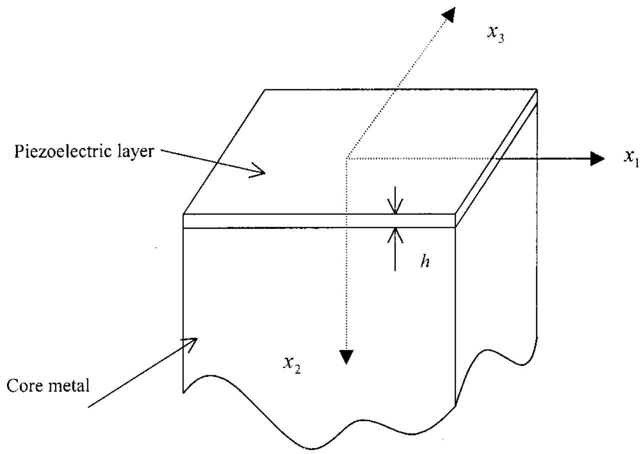


**Fig. 1 A Semi-infinite metal medium surface covered by a layer of piezoelectric material**

where $c_{44}$ is the elastic module, $e_{15}$ is piezoelectric coefficient, $\Xi_{11}$ is the dielectric constant, $\rho$ is mass density of the piezoelectric layer, $u_3$ is the deflection in the piezoelectric layer, and $\phi$ is the electric potential.

The shear force, electric field, and electric displacement in the piezoelectric layer are then written as

$$\sigma_{23}=c_{44}\frac{\partial u_3}{\partial x_2}+e_{15}\frac{\partial \phi}{\partial x_2} \tag{4a}$$

$$E_2=-\frac{\partial \phi}{\partial x_2} \tag{4b}$$

$$D_2=e_{15}\frac{\partial u_3}{\partial x_2}+\Xi_{11}E_2=e_{15}\frac{\partial u_3}{\partial x_2}-\Xi_{33}\frac{\partial \phi}{\partial x_2}. \tag{4c}$$

Consider the case when no electrodes are covered on the surfaces of the piezoelectric layer, and the piezoelectric layer abuts the air. In this case, the electric potential at the interface of the piezoelectric layer and the core metal will be zero. However, the electric potential and the electric displacement of the piezoelectric layer at the upper surface will be referenced by the field variables in the vacuum. The continuity conditions of the shear stress and the deflection at the interface and condition of free traction for the piezoelectric layer at the upper surface should also be modeled as in the following.

In view of the above, the boundary conditions for this piezoelectric coupled structure are then expressed by the following equations:

at $x_2=0$:

$$u_3=u_3' \tag{5a}$$

$$\sigma_{23}=\sigma_{23}' \tag{5b}$$

$$\phi=0 \tag{5c}$$

at $x_2=-h$:

$$\sigma_{23}=0 \tag{6a}$$

$$D_2=D' \tag{6b}$$

$$\phi=\phi' \tag{6c}$$

where $\phi'$ and $D'$ are the corresponding variables in a vacuum.

Because only wave propagation in the $x_1$-direction is considered in this paper, we can write the solutions of $u_3'$ by the following equation:

$$u_3'=f'(x_2)e^{i\omega(t-x_1/c)} \tag{7}$$

where $c$ is the phase velocity of the wave propagation and $\omega$ is the frequency.

Substituting Eq. (7) into Eq. (1) yields

$$\frac{d^2f'}{dx_2^2}-\chi'^2f'=0 \tag{8}$$

with the solution of the deflection shown as follows:

$$u_3'=Ae^{-\chi' x_2}e^{i\omega(t-x_1/c)} \tag{9}$$

where

$$\chi'=\frac{\omega}{c}\sqrt{1-\left(\frac{c}{v'}\right)^2},\quad v'^2=c_{44}'/\rho'.$$

The above solution is the kind of surface wave solution under the assumption that $c<v'$. When $c>v'$, such a wave would represent the kind of plane wave solution and this type of wave carries the energy away from the layer. Such a wave system would quickly lose its energy and not be of significance at any distance, and thus is beyond the scope of this paper.

By assuming

$$\psi=\phi-\frac{e_{15}}{\Xi_{11}}u_3, \tag{10}$$

Eq. (3) changes to the following equation:

$$\nabla^2\psi=0 \tag{11}$$

whose solution is as follows:

$$\psi=(B_1e^{-\xi x_2}+B_2e^{\xi x_2})e^{i\omega(t-x_1/c)} \tag{12}$$

where $\xi=\omega/c$ is the wave number of motion.

Substituting Eq. (3*b*) into (3*a*) gives

$$\overline{c_{44}}\nabla^2u_3=\rho\frac{\partial^2u_3}{\partial t^2} \tag{13}$$

where

$$\overline{c_{44}}=c_{44}+\frac{e_{15}^2}{\Xi_{11}}.$$

The solution of Eq. (13) is obtained,

$$u_3=(A_1e^{-\chi_2x_2}+A_2e^{\chi_2x_2})e^{i\omega(t-x_1/c)}\quad \text{when } c<v \tag{14a}$$

$$u_3=(A_1\cos\chi_2x_2+A_2\sin\chi_2x_2)e^{i\omega(t-x_1/c)}\quad \text{when } v'>c>v \tag{14b}$$

where

$$\chi_2=\frac{\omega}{c}\sqrt{\left|1-\left(\frac{c}{v}\right)^2\right|},\quad v^2=\frac{\overline{c_{44}}}{\rho}.$$

Substituting Eq. (12) and Eqs. (14*a*)–(14*b*), we can have the expression for variable $\phi$ and $D_2$,

$$\phi=\left[(B_1e^{-\xi x_2}+B_2e^{\xi x_2})+\frac{e_{15}}{\Xi_{11}}(A_1e^{-\chi_2x_2}+A_2e^{\chi_2x_2})\right]e^{i\omega(t-x_1/c)} \tag{15a}$$

$$D_2=-\Xi_{11}[\xi(-B_1e^{-\xi x_2}+B_2e^{\xi x_2})]e^{i\omega(t-x_1/c)}, \tag{15b}$$

when $c<v$, and

$$\phi=\left[(B_1e^{-\xi x_2}+B_2e^{\xi x_2})+\frac{e_{15}}{\Xi_{11}}(A_1\cos\chi_2x_2+A_2\sin\chi_2x_2)\right]e^{i\omega(t-x_1/c)} \tag{15c}$$

$$D_2=-\Xi_{11}[\xi(B_1e^{-\xi x_2}-B_2e^{\xi x_2})]e^{i\omega(t-x_1/c)}, \tag{15d}$$

when $v'>c>v$.

Substituting Eq. (9), Eqs. (14$a$)–(14$b$), and Eqs. (15$a$)–(15$d$) into Eqs. (2) and (4), we have

$$\sigma'_{23}=c'_{44}(-\chi')Ae^{-\chi' x_2} \tag{16}$$

$$\sigma_{23}=[(-\chi_2)\overline{c_{44}}(A_1e^{-\chi_2x_2}-A_2e^{\chi_2x_2})+(-\xi)e_{15}(B_1e^{-\xi x_2} -B_2e^{\xi x_2})]e^{i\omega(t-x_1/c)} \tag{17a}$$

when $c<v$, and

$$\sigma_{23}=[(-\chi_2)\overline{c_{44}}(A_1\sin\chi_2x_2-A_2\cos\chi_2x_2)+(-\xi)e_{15}(B_1e^{-\xi x_2} -B_2e^{\xi x_2})]e^{i\omega(t-x_1/c)} \tag{17b}$$

when $v'>c>v$.

The potential $\phi'$ in the vacuum can be found by solving the electronic Maxwell equation,

$$\nabla^2\phi'=0, \tag{18}$$

and seeking the solution which remains finite as $x_2\to-\infty$. Such a solution for $\phi'$ and $D'$ can be obtained as

$$\phi'=C_1e^{\xi x_2}e^{i\omega(t-x_1/c)} \tag{19a}$$

$$D'=-\Xi_0\xi C_1e^{\xi x_2}e^{i\omega(t-x_1/c)}. \tag{19b}$$

## 3 Dispersion Characteristics

The dispersive characteristics may be obtained by the solution of an eigenvalue problem when substituting the solutions from Eqs. (14$a$)–(19$b$) into the boundary conditions in Eq. (5$a$)–(6$c$).

For the case when $c<v$, Eqs. (5$a$)–(5$c$) give

$$A=A_1+A_2 \tag{20a}$$

$$(-\chi_2)\overline{c_{44}}(A_1-A_2)+(-\xi)e_{15}(B_1-B_2)=(-\chi')c'_{44}A \tag{20b}$$

$$B_1+B_2+\frac{e_{15}}{\Xi_{11}}(A_1+A_2)=0. \tag{20c}$$

From Eqs. (6$a$)–(6$c$), we have

$$(-\chi_2)\overline{c_{44}}(A_1e^{\chi_2h}-A_2e^{-\chi_2h})+(-\xi)e_{15}(B_1e^{\xi h}-B_2e^{-\xi h})=0 \tag{21a}$$

$$(B_1e^{\xi h}+B_2e^{-\xi h})+\frac{e_{15}}{\Xi_{11}}(A_1e^{\chi_2h}+A_2e^{-\chi_2h})=C_1e^{-\xi h} \tag{21b}$$

$$-\Xi_{11}(-\xi B_1e^{\xi h}+\chi_1B_2e^{-\xi h})=-\Xi_0\xi C_1e^{-\xi h}. \tag{21c}$$

Variables $B_1$ and $B_2$ can be obtained from Eqs. (20$a$)–(20$c$) as

$$B_1=(N_1A_1+N_2A_2)/2 \tag{22a}$$

$$B_2=(N_3A_1+N_4A_2)/2 \tag{22b}$$

where

$$N_1=-\frac{\chi_2\overline{c_{44}}}{\xi e_{15}}+\frac{\chi'c'_{44}}{\xi e_{15}}-\frac{e_{15}}{\Xi_{11}},$$

$$N_2=\frac{\chi_2\overline{c_{44}}}{\xi e_{15}}+\frac{\chi'c'_{44}}{\xi e_{15}}-\frac{e_{15}}{\Xi_{11}},$$

$$N_3=\frac{\chi_2\overline{c_{44}}}{\xi e_{15}}-\frac{\chi'c'_{44}}{\xi e_{15}}+\frac{e_{15}}{\Xi_{11}},$$

$$N_4=-\frac{\chi_2\overline{c_{44}}}{\xi e_{15}}-\frac{\chi'c'_{44}}{\xi e_{15}}-\frac{e_{15}}{\Xi_{11}}.$$

Investigation of Eqs. (21$a$)–(21$c$) gives

$$B_1=(N_5A_1+N_6A_2)/2 \tag{23a}$$

$$B_2=(N_7A_1+N_8A_2)/2 \tag{23b}$$

where

$$N_5=\left(-\frac{\chi_2\overline{c_{44}}}{\xi e_{15}}+\frac{\chi_2\overline{c_{44}}\Xi_{11}}{\xi e_{15}\Xi_0}-\frac{e_{15}}{\Xi_{11}}\right)e^{(\chi_2-\xi)h},$$

$$N_6=\left(\frac{\chi_2\overline{c_{44}}}{\xi e_{15}}-\frac{\chi_2\overline{c_{44}}\Xi_{11}}{\xi e_{15}\Xi_0}-\frac{e_{15}}{\Xi_{11}}\right)e^{-(\xi+\chi_2)h},$$

$$N_7=\left(\frac{\chi_2\overline{c_{44}}}{\xi e_{15}}+\frac{\chi_2\overline{c_{44}}\Xi_{11}}{\xi e_{15}\Xi_0}-\frac{e_{15}}{\Xi_{11}}\right)e^{(\xi+\chi_2)h},$$

$$N_8=\left(-\frac{\chi_2\overline{c_{44}}}{\xi e_{15}}+\frac{\chi_2\overline{c_{44}}\Xi_{11}}{\xi e_{15}\Xi_0}+\frac{e_{15}}{\Xi_{11}}\right)e^{(\xi-\chi_2)h}.$$

Comparisons of Eqs. (22$a$)–(23$b$) result in the following expression:

$$\begin{bmatrix}N_1-N_5 & N_2-N_6\\ N_3-N_7 & N_4-N_8\end{bmatrix}\begin{Bmatrix}A_1\\ A_2\end{Bmatrix}=\begin{Bmatrix}0\\ 0\end{Bmatrix}. \tag{24}$$

The dispersion characteristics for this piezoelectric coupled structure can then be obtained by considering the condition for the existence of the nontrivial solution for $A_1$ and $A_2$, which finally comes to the eigenvalue solution as follows:

$$\begin{vmatrix}N_1-N_5 & N_2-N_6\\ N_3-N_7 & N_4-N_8\end{vmatrix}=0. \tag{25}$$

For the case when $v'>c>v$, Eqs. (5$a$)–(5$c$) change to

$$A=A_1 \tag{26a}$$

$$(-\chi_2)\overline{c_{44}}(-A_2)+(-\xi)e_{15}(B_1-B_2)=(-\chi')c'_{44}A \tag{26b}$$

$$B_1+B_2+\frac{e_{15}}{\Xi_{11}}(A_1)=0. \tag{26c}$$

Equations (6$a$)–(6$c$) become,

$$(-\chi_2)\overline{c_{44}}(-A_1\sin\chi_2h-A_2\cos\chi_2h)+(-\xi)e_{15}(B_1e^{\xi h} -B_2e^{-\xi h})=0 \tag{27a}$$

$$(B_1e^{\xi h}+B_2e^{-\xi h})+\frac{e_{15}}{\Xi_{11}}(A_1\cos\chi_2h-A_2\sin\chi_2h)=C_1e^{-\xi h} \tag{27b}$$

$$-\Xi_{11}\xi(-B_1e^{\xi h}+B_2e^{-\xi h})=-\Xi_0\xi C_1e^{-\xi h}. \tag{27c}$$

Similar to the above analyses, from Eqs. (26$a$)–(26$c$), we have

$$B_1=(L_1A_1+L_2A_2)/2 \tag{28a}$$

$$B_2=(L_3A_1+L_4A_2)/2 \tag{28b}$$

where

$$L_1=\frac{\chi'c'_{44}}{\xi e_{15}}-\frac{e_{15}}{\Xi_{11}},\quad L_2=\frac{\chi_2\overline{c_{44}}}{\xi e_{15}},$$

$$L_3=-\frac{\chi'c'_{44}}{\xi e_{15}}-\frac{e_{15}}{\Xi_{11}},\quad L_4=-\frac{\chi_2\overline{c_{44}}}{\xi e_{15}}.$$

Investigation of Eq. (27$a$)–(27$c$) gives

$$B_1=(L_5A_1+L_6A_2)/2 \tag{29a}$$

$$B_2=(L_7A_1+L_8A_2)/2 \tag{29b}$$

where

$$L_5=\left(\frac{\chi_2\overline{c_{44}}}{\xi e_{15}}\sin\chi_2h-\frac{\chi_2\overline{c_{44}}\Xi_{11}}{\xi e_{15}\Xi_0}\sin\chi_2h-\frac{e_{15}}{\Xi_{11}}\cos\chi_2h\right)e^{-\xi h}$$

$$L_6=\left(\frac{\chi_2\overline{c_{44}}}{\xi e_{15}}\cos\chi_2h-\frac{\chi_2\overline{c_{44}}\Xi_{11}}{\xi e_{15}\Xi_0}\cos\chi_2\,h+\frac{e_{15}}{\Xi_{11}}\sin\chi_2h\right)e^{-\xi h}$$

$$L_7=\left(-\frac{\chi_2\overline{c}_{44}}{\xi e_{15}}\sin\chi_2 h-\frac{\chi_2\overline{c}_{44}\Xi_{11}}{\xi e_{15}\Xi_0}\sin\chi_2 h-\frac{e_{15}}{\Xi_{11}}\cos\chi_2 h\right)e^{\xi h}$$

$$L_8=\left(-\frac{\chi_2\overline{c}_{44}}{\xi e_{15}}\cos\chi_2 h-\frac{\chi_2\overline{c}_{44}\Xi_{11}}{\xi e_{15}\Xi_0}\cos\chi_2 h+\frac{e_{15}}{\Xi_{11}}\sin\chi_2 h\right)e^{\xi h}.$$

The dispersion characteristics of the structure is again obtained by

$$\begin{vmatrix} L_1-L_5 & L_2-L_6 \\ L_3-L_7 & L_4-L_8 \end{vmatrix}=0. \tag{30}$$

## 4 Mode Shape Analysis in Piezoelectric Layer

The mode shapes of the deflection, the electric potential, and the electric displacement in thickness direction of piezoelectric layer may be obtained from the characteristic equation of this piezoelectric coupled medium obtained in the above section. The final expressions are shown below.

For the case when $c<v$, the mode shapes (denoted by an overbar) are expressed by

$$\overline{u}_3=A_1(e^{-\chi_2 x_2}+M_1 e^{\chi_2 x_2}) \tag{31a}$$

$$\overline{\phi}=A_1\left\{(N_1+N_2M_1)e^{-\xi x_2}+(N_3+N_4M_1)e^{\xi x_2}+\frac{2e_{15}}{\Xi_{11}}(e^{-\chi_2 x_2}+M_1 e^{\chi_2 x_2})\right\} \tag{31b}$$

$$\overline{D}_2=A_1\{(N_1+N_2M_1)e^{-\xi x_2}+(N_3+N_4M_1)e^{\xi x_2}\} \tag{31c}$$

where

$$M_1=-\frac{N_2-N_6}{N_1-N_5}.$$

For the case when $v'>c>v$, we have

$$\overline{u}_3=A_1(\cos\chi_2 x_2+M_2\sin\chi_2 x_2) \tag{32a}$$

$$\overline{\phi}=A_1\left\{(L_1+L_2M_2)e^{-\xi x_2}+(L_3+L_4M_2)e^{\xi x_2}+\frac{2e_{15}}{\Xi_{11}}(\cos\chi_2 x_2+M_2\sin\chi_2 x_2)\right\} \tag{32b}$$

$$\overline{D}_2=A_1\{(L_1+L_2M_2)e^{-\xi x_2}+(L_3+L_4M_2)e^{\xi x_2}\} \tag{32c}$$

where

$$M_2=-\frac{L_2-L_6}{L_1-L_5}.$$

Next, numerical simulations will be conducted to give the dispersion curves of the SH wave propagation in the structure mentioned above, and to present the variations of the mode shapes in the piezoelectric layer for different wave modes and wave numbers.

## 5 Numerical Simulations

Table 1 lists the material properties that will be used in the following numerical simulations. The bulk shear wave velocities for the host material used by steel and the piezoelectric layer used by PZT 4 are obtained as $v'|_{\mathrm{steel}}=3281$ m/s, $v|_{\mathrm{PZT4}}=2351$ m/s. The Bleustein-Gulyayev surface wave velocities in the PZT4 for the case when no electrodes are surface bonded on it can be determined by the expression ([4,6,9])

$$v_B=v\sqrt{1-\frac{k_{15}^4}{2(1+k_{15}^2)^2(1+\Xi_{11}/\Xi_0)^2}},$$

**Table 1 Material properties**

| | Host Structure (Steel) | Piezoelectric Layer (PZT4) |
|---|---|---|
| Young's modulus (N/m$^2$) | $E=210\times10^9$ | $c_{11}=132\times10^9$ |
| | | $c_{44}=8.5\times10^9$ |
| Mass density (kg/m$^3$) | $7.8\times10^3$ | $7.5\times10^3$ |
| $e_{15}$ (C/m$^2$) | $\cdots$ | 10.5 |
| $e_{31}$ (C/m$^2$) | $\cdots$ | −4.1 |
| $\Xi_0$ ($F$/m) | $\cdots$ | $8.854\times10^{-12}$ |
| $\Xi_{11}/\Xi_0$ | $\cdots$ | 800 |
| $\Xi_{33}/\Xi_0$ | $\cdots$ | 660 |

where

$$k_{15}^2=\frac{e_{15}^2}{c_{44}\Xi_{11}}$$

and $\Xi_{11}$ and $\Xi_0$ are dielectric constants for the piezoelectric layer and the air. For $\Xi_{11}\gg\Xi_0$, we usually have $v_B\approx v|_{\mathrm{PZT4}}$ ([20]).

The nondimensional phase velocity is taken as $\overline{c}=c/v|_{\mathrm{PZT4}}$ and the nondimensional wave number is used by $\overline{\xi}=\xi h/2\pi$. The dispersive characteristics for the first seven modes are shown in Fig. 2. The curves show that the phase velocities for all these modes start from the shear velocity of the host steel semi-infinite medium at a smaller wave number. This result is reasonable as the Love wave velocity in a semi-infinite medium is always less than the velocity of the buck shear horizontal wave in the substrate, which can also been seen from Eq. (9). Another investigation of the figure shows that the curves approach the Bleustein-Gulyaev (B-G) wave velocity or the shear horizontal (SH) wave velocity of the piezoelectric layer at higher wave number. This result is here compared with that obtained for the same structure but with the electrodes shortly connected on the piezoelectric layer ([18]). When the electrodes are shortly connected, the asymptotic velocity of the first mode tends towards the B-G wave velocity, whereas the velocities of other modes tend towards the SH wave velocity. This is due to the fact that for the first mode the surface wave for the piezoelectric layer will become dominant when the wavelength is short compared with the thickness of the layer ([18]). However, the B-G wave velocity and the SH velocity are almost the same in the current study when the piezoelectric layer (without electrodes bonded on it) abutting the vacuum, was also claimed by Parton [20]. Thus, it is with no doubt that the asymptotic velocities of all the modes for the case when the piezoelectric layer abuts the vacuum tend to one value as shown in Fig. 2. It also shows that the higher modes can only exist beyond certain values of the wave numbers, for example, the second mode begins around $\overline{\xi}=0.5$.

The mode shapes of the deflection, the electric potential, and the electric displacement in the piezoelectric layer are plotted in Figs. 3–6. Figures 3–4 show the first mode shapes with the wave number assigned at the values of 0.1 and 1.0, respectively. The mode shape of the electric potential and electric displacement display their smooth curves at a small wave number as seen in Fig. 3, and change to curves with higher curvatures with a zero node at a higher wave number as shown in Fig. 4. This phenomenon is not surprising. As the wave number increases, the difference in the properties of the two media (air and steel) on the two surfaces of the piezoelectric layer becomes important. However, it can be seen from the figures that the mode shape of the deflection remains almost a straight line for the two wave numbers. Different from the result in this paper, the electric potential in the piezoelectric layer shows an approximate quadratic variation for the case

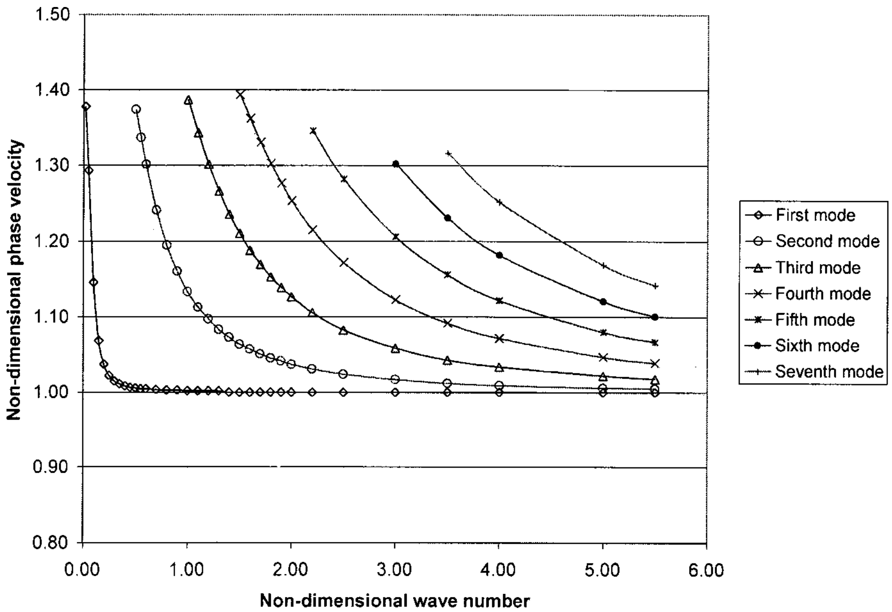


**Fig. 2 Dispersion curves for a PZT 4 coupled structure**

when the piezoelectric layer is shortly connected with electrodes on it ([18]).

Figures 5–6 show the second mode shapes and the third mode shapes of the deflection, the electric potential, and the electric displacement in the piezoelectric layer at a wave number of 1.0. Both curves for the electric potential and the electric displacement have more zero nodes compared to the results in the first mode shape seen from Figs. 3–4. Surprisingly, the mode shapes of the deflection displays a curve, instead of a straight line, with one zero node for the second mode and two zero nodes for the third

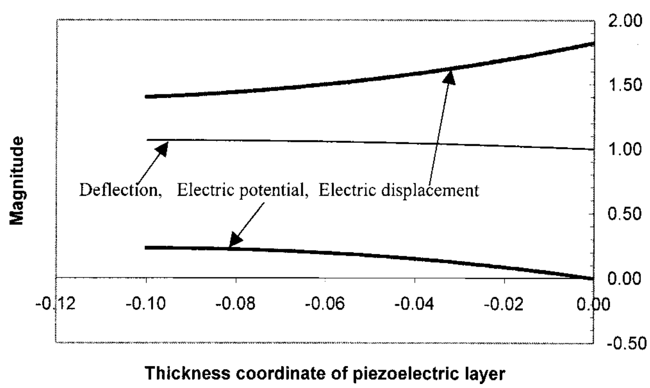


**Fig. 3 First mode shapes in a piezoelectric layer at wave number 0.1**

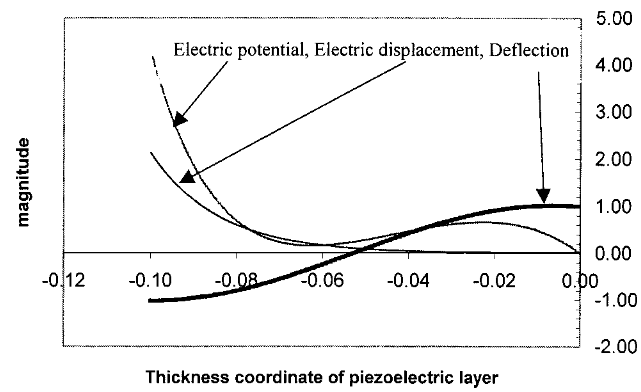


**Fig. 5 Second mode shapes in a piezoelectric layer at nondimensional wave number 1.0**

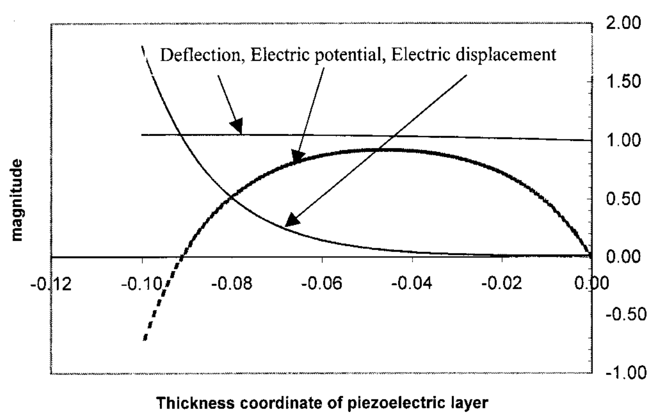


**Fig. 4 First mode shapes in a piezoelectric layer at nondimensional wave number 1.0**

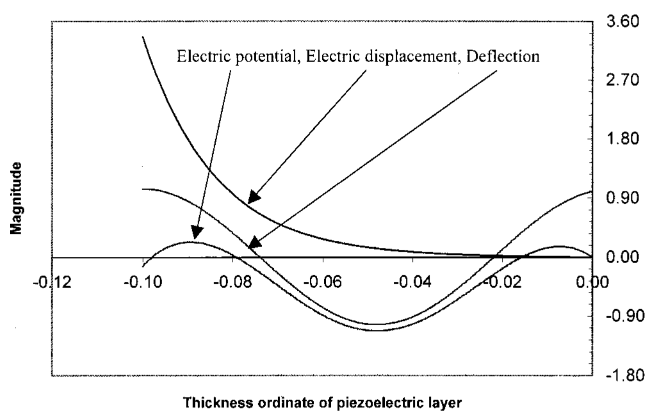


**Fig. 6 Third mode shapes in a piezoelectric layer at nondimensional wave number 1.0**

mode. This investigation indicates that for higher modes the mode shapes of deflection, electric potential, and electric displacement contain more zero nodes.

## 6 Concluding Remarks

This paper presents the study of wave propagation in the piezoelectric coupled solid medium. The dispersive characteristics for the piezoelectric couple structure are first obtained. The results show that the phase velocity starts from the shear wave velocity of the host material and approaches the B-G velocity or SH wave velocity at higher wave numbers. The piezoelectric effects thus dominate the dispersive characteristics of this piezoelectric coupled structure at higher wave numbers. The mode shapes of the deflection, the electric potential, and the electric displacement display normal uniform distribution with no zero nodes at lower modes, but take a skew shape with zero nodes at higher modes.

This paper provides the analytical model for the wave propagation in the piezoelectric couple structures. The results in this paper may be used as the benchmark for the wave propagation in the piezoelectric coupled structure with no electrodes on the piezoelectric layer and may be helpful in the design of the piezoelectric coupled structures. The possible potential of this research lies in the surface wave application in health monitoring of structures.


## Acknowledgment

The author appreciates the valuable comments from the reviewer.


## References


[1] Mindlin, R. D., 1952, "Forced Thickness-Shear and Flexural Vibrations of Piezoelectric Crystal Plates," J. Appl. Phys., **23**, pp. 83–88.

[2] Tiersten, H. F., 1963, "Thickness Vibrations of Piezoelectric," J. Acoust. Soc. Am., **35**, pp. 53–58.

[3] Tiersten, H. F., 1963, "Wave Propagation in an Infinite Piezoelectric Plate," J. Acoust. Soc. Am., **35**, pp. 234–239.

[4] Bleustein, J. L., 1969, "Some Simple Modes of Wave Propagation in Infinite Piezoelectric Plates," J. Acoust. Soc. Am., **45**, pp. 614–620.

[5] Viktorov, I. A., 1967, *Rayleigh and Lamb Waves*, Plenum, New York.

[6] Viktorov, I. A., 1981, *Surface Waves in Solids*, Nauka, Moscow (in Russian).

[7] Curtis, R. G., and Redwood, M., 1973, "Transverse Surface Waves in Piezoelectric Materials Carrying a Metal Layer of Finite Thickness," J. Appl. Phys., **44**, pp. 2002–2007.

[8] Cheng, N. C., and Sun, C. T., 1975, "Wave Propagation in Two-Layered Piezoelectric Plates," J. Acoust. Soc. Am., **57**, pp. 632–638.

[9] Sun, C. T., and Cheng, N. C., 1974, "Piezoelectric Waves on a Layered Cylinder," J. Appl. Phys., **45**, pp. 4288–4294.

[10] Bailey, T., and Hubbard, J. E., Jr., 1985, "Distributed Piezoelectric Polymer Active Vibration Control of a Cantilever Beam," J. Guid. Control Dyn., **8**, pp. 605–611.

[11] Kim, J., Varadan, V. V., Varadan, V. K., and Bao, X. Q., 1996, "Finite Element Modeling of a Smart Cantilever Plate and Comparison With Experiments," Smart Mater. Struct., **5**, pp. 165–170.

[12] Crawley, E. F., and de Luis, Javier, 1987, "Use Of Piezoelectric Actuators as Elements of Intelligent Structures," AIAA J., **25**, pp. 1373–1385.

[13] Lee, C. K., and Moon, F. C., 1989, "Laminated Piezopolymer Plates for Torsion and Bending Sensors and Actuators," J. Acoust. Soc. Am., **85**, pp. 2432–2439.

[14] Sun, C. T., and Zhang, X. D., 1995, "Use of Thickness Shear Mode in Adaptive Sandwich Structures," Smart Mater. Struct., **4**, pp. 202–206.

[15] Varadan, V. K., Lim, Y. H., and Varadan, V. V., 1996, "Close Loop Finite Element Modeling of Active/Passive Damping in Structural Vibration Control," Smart Mater. Struct., **5**, pp. 685–694.

[16] Badcock, R. A., and Birt, E. A., 2000, "The Use of 0-3 Piezocomposite Embedded Lamb Wave Sensors for Detection of Damage in Advanced Fibre Composites," Smart Mater. Struct., **9**, pp. 291–297.

[17] Monkhouse, R. S. C., Wilcox, P. W., Dalton, R. P., and Cawley, P., 2000, "The Rapid Monitoring of Structures Using Interdigital Lamb Wave Transducers," Smart Mater. Struct., **9**, pp. 304–309.

[18] Wang, Q., Quek, S. T., and Varadan, V. K., 2001, "Love Wave Propagation in Piezoelectric Coupled Media," Smart Mater. Struct., **10**, pp. 380–388.

[19] Wang, Q., and Varadan, V. K., 2001, "Wave Propagation in Piezoelectric Coupled Plates by Use of Interdigital Transducer Part 2: Wave Excitation by Interdigital Transducer," Int. J. Solids Struct., in press.

[20] Parton, V. Z., and Kudryavtser, B. A., 1988, *Electromagnetoelasticity*, Gordon & Breach, New York.

**X. C. Yin**
Department of Applied Mechanics,
Nanjing University of Science and Technology,
Nanjing 210014, P. R. China
e-mail: yinxch@mail.njust.edu.cn

**Z. Q. Yue**[1]
Department of Civil Engineering,
The University of Hong Kong,
Pokfulam Road,
Hong Kong, P. R. China
e-mail: yueqzq@hkucc.hku.hk

# Transient Plane-Strain Response of Multilayered Elastic Cylinders to Axisymmetric Impulse

*This paper presents an exact solution and an approximate solution, using the expansion of transient wave functions in a series of eigenfunctions, for the transient response of an infinitely long and multilayered circular cylinder subjected to uniformly distributed dynamic pressures at the boundaries. Numerical results are given to illustrate the effects of the layer properties on the interfacial stresses and the spatial and temporal variations of the displacement and stresses. In particular, the exact solution is used to examine the applicability of the thin shell theories to the transient response of multilayered cylinders.*
[DOI: 10.1115/1.1505625]

## 1 Introduction

Multilayered, specially two-layered, elastic circular cylinders and cylindrical shells are common elements in structural and machinery applications. The dynamic behaviors of multilayered cylinders and shells have received a continuously increased attention in applied mechanics community due to their growing usefulness in structural and mechanical engineering [1]. Over the past three decades, considerable publications available in the relevant literature, as shown in the reviewing articles and research reports [1–6], deal with the steady-state behaviors such as the propagation of steady-state waves and free vibrations. The dispersion phenomenon of wave propagation in cylinders and shells has been a particular subject investigated in details by many researchers using shell theories and the three-dimensional theory of elasticity.

As an impulse acts, the propagation of the mechanical disturbance with wave speeds makes a multilayered cylinder respond immediately to the impulse at the place of wave incident, and respond later at other places. After the forcing impulse has subsided, and over a long time in comparison with the time of the wave propagating through the whole wall, the multilayered cylinder turns out to vibrate freely and then rests finally due to the external resistance and interior friction in the material. The dynamic stresses, however, play a more substantial rule in structural failure. They can reach their maximum values at the early time when the transient effects of the impulse are significant. In this case, the importance of the transient-state behavior is well recognized.

In order to get some simple, but practical results of the transient responses, some thin shell theories, developed using the simplified assumptions of the Kirchhoff-Love hypotheses and their refinements considering shear deformation and rotary and/or longitudinal inertia effects, have been applied to finite and infinitely long, isotropic and anisotropic circular cylindrical shells with a single layer [7–16]. The numerical results showed that the transient effects are influenced by impact loadings (Christoforou and Swanson [7]), sizes of cylindrical shells (Chonan [8], and Humphreys and Winter [9]), elasticity of materials (Chonan [8]), and material damping (Sivadas and Ganesan [10]).

The dynamic effects can also play important roles in some stability problems. When a cylindrical shell is subjected to a traveling load, there are some critical load speeds to cause the deflection unbounded [11]. Jones and Bhuta [12] found that a bending resonance can occur at a very low speed in an infinitely long and isotropic cylindrical shell. Mangrum and Burns [13] found that there are five critical load speeds in an infinitely long and orthotropic cylindrical shell. As an impulsive pressure is suddenly developed, unstable plane-strain responses may take place in an isotropic circular cylindrical shell, and result in shell buckling [14]. Goodier and McIvor [15] and Lovell and McIvor [16] discussed, respectively, such unstable responses by linear and nonlinear strain-displacement relationships. Their results showed that the cyclic energy may exchange between the in-and-out ''breathing'' mode and the one or two high flexural modes.

As discussed by Loy and Lam [17], the refined thin shell theories may be still inadequate to model moderately thick and thick circular cylindrical shells with a single layer. In contrast to the steady-state response, the transient response depends upon the dynamic loading applied to the boundary surfaces, which causes more complexity to both the solutions and the computations.

An exact three-dimensional elastodynamic analysis of circular cylindrical shells with a single layer is a very important subject, but, has much greater difficulties in mathematical formulation. It seems that there are only a limited number of papers available in the relevant literature dealing with some plane-stain problems and three-dimensional problems by approximate analyses [18–30]. Svärdh [18] analyzed an end load problem for an axially symmetric semi-infinite hollow cylinder by using the asymptotic solutions. Chong, Lee, and Cakmak [19] examined the problem in Svärdh [18] previously by considering only three modes: the first radial, longitudinal, and shear modes. Experiments on the end problems had also been conducted to measure pulse dispersions [20–21] and dispersion curves [22] through the measurements of transient waves. In addition, by using two and three-dimensional finite element methods, Rabern and Lewis [23] simulated the dynamic stresses and strains excited by moving pressure fronts in gun tubes. Using the finite Hankel transform techniques, Cinell [24] presented a solution of axisymmetric transient stresses for infinitely long and isotropic thick hollow cylinders. As pointed out by Gong and Wang [25], the solution presented in Cinell [24] does not coincide with the nonzero stress boundary conditions. In the equation of the radial stress with frequency equation, it can be observed that the radial stresses always vanish at the inner and outer boundary surfaces where nonzero pressures are imposed on. Wang and Gong [26] refined Cinell's solution. Wang [27] and Cho and Kardomateas and Valle [28] further applied the refined solution to thermal shock problems. Gong and Wang [25] also pre-

[1]To whom correspondence should be addressed.

Contributed by the Applied Mechanics Division of THE AMERICAN SOCIETY OF MECHANICAL ENGINEERS for publication in the ASME JOURNAL OF APPLIED MECHANICS. Manuscript received by the ASME Applied Mechanics Division, June 20, 2001; final revision, Mar. 6, 2002. Associate Editor: A. K. Mal. Discussion on the paper should be addressed to the Editor, Prof. Robert M. McKeeking, Department of Mechanical and Environmental Engineering University of California—Santa Barbara, Santa Barbara, CA 93106-5070, and will be accepted until four months after final publication of the paper itself in the ASME JOURNAL OF APPLIED MECHANICS.

  

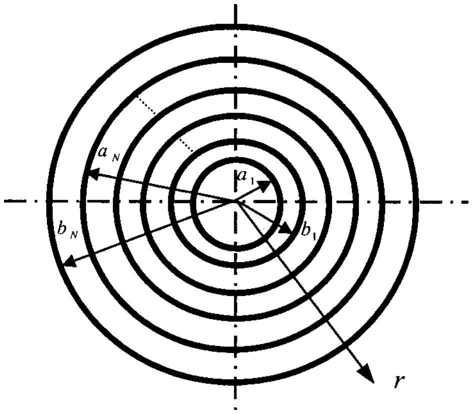


**Fig. 1 Geometry and coordinate system of the multilayered cylinder**

sented another type of the exact solution by the expansion of transient wave function in a series of eigenfunctions. This eigenfunction approach has been further applied to the problems of internal multiple impacts by Yin [29] and Yin and Wang [30].

For multilayered circular cylinders subjected to axially uniform distributed pressures, Wang and Gong [31] and Wang [32] examined the transient responses using the finite Hankel transforms. The presence of the interfacial pressures in a multilayered circular cylinder causes an additional difficulty in the mathematical formulation of the analytical solutions. For solving the problem, Wang and Gong [31] and Wang [32] tried to divide the radial displacement into two parts: the equistate and dynamic parts. Furthermore, they used two additional assumptions. The first assumption is that the radial displacement of the equistate part within each circular layer can be expressed in the form similar to Lame's static solution associated with two unknown constants and time-dependent applied pressures. The second is that the radial stress of the dynamic part vanishes at the inner and outer boundary surfaces of each circular layer. The second assumption can offer a facility for the direct application of the method that has been used for solving a circular hollow cylinder with a single layer. Nevertheless, the combination of the two assumptions may lead a doubtful result of the interfacial pressures, which can be explained using a multilayered circular cylinder that is only subject to an interior pressure. At the interfaces, because the radial stresses of the dynamic part are zero, the radial stresses are just those of the equistate part, which varies in the time history of the interior pressure. It becomes clear that the above approach in Wang and Gong [31] and Wang [32] is not suitable for general cases.

In this paper, the expansion of the transient wave functions in a series of eigenfunctions is used to obtain an exact solution for the transient response of an infinitely long and multilayered circular cylinder subjected to uniformly distributed dynamic pressures. Numerical results are then given for several typical examples of multilayered circular cylinders under dynamic loading. In particular, the present solution is compared numerically with an approximate solution based on the method suggested by Eringen and Suhubi [33]. The present solution is further applied to the verifications of the use of the thin shell theories in the axisymmetric plain-strain transient responses of multilayered circular cylindrical shells. It is considered that the present method can be extended for the examination of the transient wave propagation along composite cylinders.

## 2 Formulation of Solutions

**2.1 The Initial and Boundary Value Problem.** We consider the transient response of an infinitely long, multilayered circular and elastic cylinder under dynamic loading at the inner and outer boundaries. As shown in Fig. 1, the multilayered cylinder consists of arbitrary number of coaxial layers with different material properties. Each coaxial layer is made of homogenous, isotropic, and elastic solid. The total number of the coaxial layers is an integer $N$. From the center of the coaxial layers, the layers are consequently numbered as 1,2, . . . , and $N$. The inner radius is $a_1$ and outer radius $b_N$. The $i$th layer has the inner radius $a_i$, the outer radius $b_i$, the wall thickness $h_i(=b_i-a_i)$ and the radial wave speed $c_i$. The radial wave speed $c_i$, the speed of the longitudinal wave traveling along the radial direction, can be expressed as $c_i=[(\lambda_i+2\mu_i)/\rho_i]^{1/2}$, where $\lambda_i$ and $\mu_i$ are the Lame's material constants of the $i$th layer and $\rho_i$ the mass density.

As body force vanishes, Navier's equation for axisymmetric plane-strain motion is

$$\frac{\partial^2 u_i(r,t)}{\partial r^2}+\frac{1}{r}\frac{\partial u_i(r,t)}{\partial r}-\frac{u_i(r,t)}{r^2}=\frac{1}{c_i^2}\frac{\partial^2 u_i(r,t)}{\partial t^2} \tag{1}$$

where $a_i \leqslant r \leqslant b_i$; $i=1,2,\ldots,$ and $N$; $u_i(r,t)$ is the radial displacement of the $i$th layer; and the subscript $i$ stand for the $i$th layer.

If the interior and external boundary surfaces of the multilayered cylinder are subjected to uniformly distributed dynamic pressures $p_1(t)$ and $p_2(t)$, the stress boundary conditions, the displacement, and stress continuity across the interfaces and the initial conditions can be expressed as follows:

$$\sigma_{r1}(a_1,t)=-p_1(t) \tag{2a}$$

$$\sigma_{rN}(b_N,t)=-p_2(t) \tag{2b}$$

$$\sigma_{ri}(b_i,t)=\sigma_{r(i+1)}(a_{i+1},t) \tag{2c}$$

$$u_i(b_i,t)=u_{i+1}(a_{i+1},t) \tag{2d}$$

$$u_i(r,0)=u_{0i}(r) \tag{2e}$$

$$v_i(r,0)=v_{0i}(r) \tag{2f}$$

where $\sigma_{ri}(r,t)$, $u_{0i}(r)$, and $v_{0i}(r)$ are the radial stress, the initial distributions of radial displacement and the velocity of the $i$th layer, respectively.

**2.2 Exact Solution.** To find an exact solution for the initial and boundary value problem described above, we firstly divide the dynamic radial displacement $u_i(r,t)$ of the $i$th layer into the quasi-static part $u_{si}(r,t)$ and the dynamic part $u_{di}(r,t)$. The quasi-static part $u_{si}(r,t)$ satisfies the static-state equilibrium equation, the imposed boundary tractions and the interface continuity conditions. The dynamic part $u_{di}(r,t)$ satisfies the motion equation, the free boundary surface conditions and the interface continuity conditions. As a result, the $u_i(r,t)$ can be expressed in a series of eigenfunctions (i.e., wave modes) [33] as follows:

$$u_i(r,t)=u_{si}(r,t)+\sum_{m=1}^{\infty} U_m^i(r)q_m(t) \tag{3}$$

where $a_i \leqslant r \leqslant b_i$, $i=1,2,\ldots,$ and $N$; $U_m^i(r)$ is the $m$th wave mode of the $i$th layer; and $q_m(t)$ is the unknown time-dependent coefficient associated with $U_m^i(r)$.

In order to obtain the exact solution of the radial displacement, it is necessary to have the governing equations of the wave modes and the unknown time-dependent coefficients, and the orthogonal conditions of the wave modes.

The wave modes $U_m^i(r)$ are governed by the following eigenvalue problem:

$$\frac{d^2U^i(r)}{dr^2}+\frac{1}{r}\frac{dU^i(r)}{dr}-\frac{U^i(r)}{r^2}+\frac{\omega^2}{c_i^2}U^i(r)=0 \tag{4a}$$

$$\sigma_r^i(a_1)=0 \tag{4b}$$

$$\sigma_r^i(b_N)=0 \tag{4c}$$

$$\sigma_r^i(b_i)=\sigma_r^{i+1}(a_{i+1}) \tag{4d}$$

$$U^i(b_i)=U^{i+1}(a_{i+1}) \tag{4e}$$

where $a_i \leqslant r \leqslant b_i$; $k^i=\omega/c_i$ is the wave number of the $i$th layer. It can be shown that the eigenvalue $\omega^2$ is real and non-negative [34].

It can be shown that the general solution of wave modes (the eigenvalue problem) for the $i$th layer is expressed in terms of Bessel functions as follows:

$$U^i(r)=A\varepsilon_1^i(k^ir) \tag{5a}$$

$$\varepsilon_j^i(k^ir)=a_1^iJ_j(k^ir)+a_2^iY_j(k^ir) \tag{5b}$$

where $A$, $a_1^i$, and $a_2^i$ are unknown coefficients; and $J_j$ and $Y_j$ are, respectively, the Bessel functions of the first and second kinds of the $j$th order, where $j=0,1$, and 2.

Substituting the general solution (5) into the boundary and interface continuity conditions (4$b$)–(4$e$), a set of linear algebraic equations can be obtained as the following matrix form:

$$\begin{bmatrix} C_{1,1} & C_{1,2} & 0 & 0 & 0 & 0 & \cdots & \cdots & 0 & 0 & 0 & 0 \\ C_{2,1} & C_{2,2} & C_{2,3} & C_{2,4} & 0 & 0 & \cdots & \cdots & 0 & 0 & 0 & 0 \\ C_{3,1} & C_{3,2} & C_{3,3} & C_{3,4} & 0 & 0 & \cdots & \cdots & 0 & 0 & 0 & 0 \\ 0 & 0 & C_{4,3} & C_{4,4} & C_{4,5} & C_{4,6} & \cdots & \cdots & 0 & 0 & 0 & 0 \\ 0 & 0 & C_{5,3} & C_{5,4} & C_{5,5} & C_{5,6} & \cdots & \cdots & 0 & 0 & 0 & 0 \\ \cdots & \cdots & \cdots & \cdots & \cdots & \cdots & \cdots & \cdots & \cdots & \cdots & \cdots & \cdots \\ \cdots & \cdots & \cdots & \cdots & \cdots & \cdots & \cdots & \cdots & \cdots & \cdots & \cdots & \cdots \\ 0 & 0 & 0 & 0 & 0 & 0 & \cdots & \cdots & C_{2N-2,2N-3} & C_{2N-2,2N-2} & C_{2N-2,2N-1} & C_{2N-2,2N} \\ 0 & 0 & 0 & 0 & 0 & 0 & \cdots & \cdots & C_{2N-1,2N-3} & C_{2N-1,2N-2} & C_{2N-1,2N-1} & C_{2N-1,2N} \\ 0 & 0 & 0 & 0 & 0 & 0 & \cdots & \cdots & 0 & 0 & C_{2N,2N-1} & C_{2N,2N} \end{bmatrix} \begin{bmatrix} a_1^1 \\ a_2^1 \\ a_1^2 \\ a_2^2 \\ \cdots \\ \cdots \\ a_1^{N-1} \\ a_2^{N-1} \\ a_1^N \\ a_2^N \end{bmatrix} = \begin{bmatrix} 0 \\ 0 \\ 0 \\ 0 \\ \cdots \\ \cdots \\ 0 \\ 0 \\ 0 \\ 0 \end{bmatrix} \tag{6a}$$

In the coefficient matrix $[C]$, the four nonzero components in the first and last rows are related to the traction boundary conditions at the inner and outer boundary surfaces.

$$C_{1,1}=M_1(\lambda_1,\mu_1,k^1,a_1) \tag{6b}$$

$$C_{1,2}=M_2(\lambda_1,\mu_1,k^1,a_1) \tag{6c}$$

$$C_{2N,2N-1}=M_1(\lambda_N,\mu_N,k^N,b_N) \tag{6d}$$

$$C_{2N,2N}=M_2(\lambda_N,\mu_N,k^N,b_N) \tag{6e}$$

The eight nonzero components in each of the next two rows are results from the fully continuous conditions of the radial stress and displacement at the interface between two connected coaxial layers. For the interface between the $i$th layer and the $(i+1)$th layer, we have

$$C_{2i,2i-1}=M_1(\lambda_i,\mu_i,k^i,b_i) \tag{6f}$$

$$C_{2i,2i}=M_2(\lambda_i,\mu_i,k^i,b_i) \tag{6g}$$

$$C_{2i,2i+1}=-M_1(\lambda_{i+1},\mu_{i+1},k^{i+1},a_{i+1}) \tag{6h}$$

$$C_{2i,2i+2}=-M_2(\lambda_{i+1},\mu_{i+1},k^{i+1},a_{i+1}) \tag{6i}$$

$$C_{2i+1,2i-1}=J_1(k^ib_i) \tag{6j}$$

$$C_{2i+1,2i}=Y_1(k^ib_i) \tag{6k}$$

$$C_{2i+1,2i+1}=-J_1(k^{i+1}a_{i+1}) \tag{6l}$$

$$C_{2i+1,2i+2}=-Y_1(k^{i+1}a_{i+1}) \tag{6m}$$

where $i=1,2,\ldots,N-1$ and

$$M_1(\lambda,\mu,k,r)=(\lambda+2\mu)k\frac{dJ_1(kr)}{d(kr)}+\lambda\frac{J_1(kr)}{r} \tag{6n}$$

$$M_2(\lambda,\mu,k,r)=(\lambda+2\mu)k\frac{dY_1(kr)}{d(kr)}+\lambda\frac{Y_1(kr)}{r} \tag{6o}$$

To facilitate the subsequent analyses, the Eq. (6$a$) is rewritten in a compact form below:

$$[C][a]=[0] \tag{7}$$

where $[C]$ is the $2N\times 2N$ square matrix; $[a]$ is the column matrix of the eigenvectors with $2N$ elements, i.e., coefficients $a_1^i$ and $a_2^i$ $(i=1,2,\ldots,N)$; and $[0]$ is the zero column matrix.

The existence of nontrivial solutions leads to that the determinant of the coefficient matrix $[C]$ is zero, which forms a transcendental equation. This transcendental equation is also called as the frequency equation governing the axisymmetrical plane-strain radial vibration:

$$\mathrm{Det}[C]=0 \tag{8}$$

Equation (8) is called a characteristic equation (or the frequency equation) of axisymmetrical plane-strain radial vibration of an elastic cylinder with $N$ number of coaxial layers. It has been shown generally that an elastic body has an infinite growth of the positive characteristic values (Gurtin [35], p. 270). So, Eq. (8) has infinite number of positive roots. The positive root solutions of Eq. (8) then provide the values of $\omega_m$ $(m=1,2,\ldots)$ which represent the circular frequencies or eigenvalues. The circular frequencies can be determined accurately from the frequency Eq. (8) by numerical techniques, such as Newton method.

The particular wave mode of the $i$th layer $U_m^i(r)$ associated the $m$th circular frequency $\omega_m$ can be expressed as follows using the general solution (5):

$$U_m^i(r)=A_m\varepsilon_1^i(k_m^ir) \tag{9a}$$

$$\varepsilon_j^i(k_m^ir)=a_{1m}^iJ_j(k_m^ir)+a_{2m}^iY_j(k_m^ir) \tag{9b}$$

The wave mode $U_m^i(r)$ can form an orthogonal set. The set is derived directly from the Eq. (4) and follows the orthogonal condition below (see Appendix A):

$$\sum_{i=1}^{N}\int_{a_i}^{b_i}\rho_i U_m^i(r)\cdot U_n^i(r)2\pi r dr=\delta_{mn} \tag{10}$$

where $\delta_{mn}$ is the Kronecker delta.

The coaxial layers can have different values for the mass density $\rho_i$. The term $\rho_i$ in Eq. (10) cannot be put outside the summation. For a circular cylinder with a single layer, this term can always be eliminated by the techniques of normalization, which results in the well known orthogonal condition without the term of mass density.

The coefficient $A_m$ in Eq. (9*a*) applicable to all the coaxial layers are given below according to the orthogonal condition (10) (see Appendix B).

$$A_m^{-2}=\sum_{i=1}^{N}\rho_i\{\pi b_i^2[\varepsilon_1^{i\,2}(k_m^i b_i)-\varepsilon_0^i(k_m^i b_i)\varepsilon_2^i(k_m^i b_i)] \\ -\pi a_i^2[\varepsilon_1^{i\,2}(k_m^i a_i)-\varepsilon_0^i(k_m^i a_i)\varepsilon_2^i(k_m^i a_i)]\} \tag{11}$$

The corresponding nonzero eigenvector $[a]$, i.e., coefficients $a_{1m}^i$ and $a_{2m}^i$, can be determined by the arbitrary $2N-1$ linear algebraic equations of the matrix Eq. (7) pulse the orthogonal condition (10).

Furthermore, by substituting Eq. (3) into Eq. (1) in conjunction with the equations governing $u_{di}(r,t)$ and $u_{si}(r,t)$, we have

$$\sum_{m=1}^{\infty}\left[\frac{d^2q_m(t)}{dt^2}+\omega_m^2 q_m(t)\right]U_m^i(r)=\frac{d^2u_{si}(r,t)}{dt^2} \tag{12}$$

By using the orthogonal condition (10), we can obtain the ordinary differential equations governing $q_m(t)$ below:

$$\frac{d^2q_m(t)}{dt^2}+\omega_m^2 q_m(t)=\frac{d^2Q_m(t)}{dt^2} \tag{13a}$$

$$Q_m(t)=-\sum_{i=1}^{N}\int_{a_i}^{b_i}\rho_i u_{si}(r,t)U_m^i(r)2\pi r dr \tag{13b}$$

Using Laplace transforms and the initial conditions (2*e*) and (2*f*), we can obtain a formal solution of the unknown time-dependent coefficients from Eq. (13*a*) as follows:

$$q_m(t)=q_m(0)\cos\omega_m t+\frac{1}{\omega_m}\frac{dq_m(0)}{dt}\sin\omega_m t \\ +\frac{1}{\omega_m}\int_0^t\frac{d^2Q_m(\tau)}{d\tau^2}\sin\omega_m(t-\tau)d\tau \tag{14a}$$

where $q_m(0)$ and $dq_m(0)/dt$ are defined as follows:

$$q_m(0)=\sum_{i=1}^{N}\int_{a_i}^{b_i}\rho_i u_{0i}(r)U_m^i(r)2\pi r dr+Q_m(0) \tag{14b}$$

$$\frac{dq_m(0)}{dt}=\sum_{i=1}^{N}\int_{a_i}^{b_i}\rho_i v_{0i}(r)U_m^i(r)2\pi r dr+\frac{dQ_m(0)}{dt} \tag{14c}$$

Finally, the quasi-static radial displacement for the *i*th layer in the form of Lame's solution is

$$u_{si}(r,t)=\frac{a_i^2p_1^i(t)-b_i^2p_2^i(t)}{2(\lambda_i+\mu_i)(b_i^2-a_i^2)}\cdot r+\frac{b_i^2a_i^2}{2\mu_i(b_i^2-a_i^2)}\frac{1}{r} \\ \times[p_1^i(t)-p_2^i(t)] \tag{15}$$

where $p_1^i(t)$ is the quasi-static inner pressure and $p_2^i(t)$ the quasi-static outer pressure of the *i*th layer. Two external applied pressures are known, i.e., the pressure $p_1^1(t)$ of the first layer is the imposed pressure $p_1(t)$ and the pressure $p_2^N(t)$of the *N*th layer is the applied pressure $p_2(t)$. The other $p_1^i(t)$ and $p_2^i(t)$ are the unknown quasi-static interfacial pressures and can be determined by the full continuity condition of the radial displacement in Eq. (2*d*).

It is noted that although the different coaxial layers may have different wave modes, they should vibrate at the same circular frequencies $\omega_m$ and depend upon the same unknown time-dependent coefficients functions $q_m(t)$. Furthermore, the solution given above satisfies the Navier's motion Eq. (1) and the initial and boundary conditions and the radial stress and displacement continuity conditions at the interfaces (2*a*) to (2*f*). Therefore, the above solution is an exact solution for the transient response of an infinite long and multilayered circular elastic cylinders subject to uniformly distributed pressures in the inner and outer boundaries. The computational procedure to obtain the radial displacement and stresses using the above exact solution can be summarized as follows.

At first, we will calculate the circular frequencies using Eq. (8). We then determine the coefficients of wave modes using Eq. (6), (10) and the results of the corresponding circular frequency. Next, we determine the quasi-static radial displacement using Eqs. (2*c*), (2*d*), and (15). Moreover, we calculate the time-dependent coefficient functions $q_m(t)$ using Eq. (14). Finally, we calculate the transient radial displacement according Eq. (3) and then the stress components using the strain and displacement relationship and the linear stress and strain relationship in elasticity.

**2.3 Approximate Solution.** An approximate solution can be obtained by following the approach given in Eringen and Suhubi [33]. At first, we perform the integration in Eq. (14*a*) successively by parts and obtain a new expression for the time-dependent coefficient function $q_m(t)$. As a result, Eq. (3) for the transient radial displacement can be re-expressed in the following form:

$$u_i(r,t)=u_{si}(r,t)-\sum_{m=1}^{\infty}Q_m(t)U_m^i(r) \\ +\sum_{m=1}^{\infty}\left[\alpha_m\cos\omega_m t+\frac{1}{\omega_m}\beta_m\sin\omega_m t \right. \\ \left. -\omega_m\int_0^t Q_m(\tau)\sin\omega_m(t-\tau)d\tau\right]U_m^i(r) \tag{16}$$

where $\alpha_m=\sum_{i=1}^N\int_{a_i}^{b_i}\rho_i u_{0i}(r)U_m^i(r)2\pi r dr$ and $\beta_m=\sum_{i=1}^N\int_{a_i}^{b_i}\rho_i v_{0i}(r)U_m^i(r)2\pi r dr$.

Following the suggestion by Eringe and Suhubi [33], the quasi-static displacement, $u_{si}(r,t)$ can be expressed in the following series of the eigenfunctions $Q_m(t)U_m^i(r)$.

$$u_{si}(r,t)=\sum_{m=1}^{\infty}Q_m(t)U_m^i(r) \tag{17}$$

Consequently, the transient radial displacement in Eq. (16) can be approximately expressed as follows:

$$u_i(r,t)=\sum_{m=1}^{\infty}\left[\alpha_m\cos\omega_m t+\frac{1}{\omega_m}\beta_m\sin\omega_m t-\omega_m \right. \\ \left. \times\int_0^t Q_m(\tau)\sin\omega_m(t-\tau)d\tau\right]U_m^i(r) \tag{18}$$

It is noted that the above solution does not satisfy the nonzero stress boundary conditions. This is because the wave mode $U_m^i(r)$ is determined using the zero-traction boundary conditions. Therefore, the solution in (18) is an approximate solution. Gong and Wang [25] gave a similar conclusion for transient radial displacement in a single-layer hollow cylinder subject to dynamic boundary traction. Furthermore, by using the approximate method described above, Eringen and Suhubi [33] examined the initial and boundary value problems for finite strip fixed at one end and in single spherical and cylindrical domains. Liu and Qu [36] examined the transient wave propagation in a circular annulus.

## 3 Numerical Results

**3.1 General.** In the numerical calculations, the following partial sums with finite number of wave modes are adopted to represent the exact solution and the approximate solution given in Eqs. (3) and (18), respectively,

(a) For the exact solution, we have

$$u_i(r,t)=u_{si}(r,t)+\sum_{m=1}^{n} U_m^i(r)q_m(t) \tag{19}$$

(b) For the approximate solution, we have

$$u_i(r,t)=\sum_{m=1}^{n}\left[\alpha_m \cos\omega_m t+\frac{1}{\omega_m}\beta_m \sin\omega_m t-\omega_m \times\int_0^t Q_m(\tau)\sin\omega_m(t-\tau)d\tau\right]U_m^i(r) \tag{20}$$

In Eqs. (19) and (20), the $n$ is the total number of the wave modes used in the calculations. Furthermore, the following nondimensional parameters are used to show numerical results:

- the non-dimensional displacement and stresses components: $u(\lambda_1+\mu_1)/a_1/p_0$, $\sigma_r/p_0$, and $\sigma_\theta/p_0$.
- the nondimensional structural and material parameters for multilayered circular cylinder: the ratio of acoustic impedance of the $i$th layer to that of the first layer $\rho_i c_i/\rho_1 c_1$; the ratio of the wall thickness of the $i$th layer to that of the first layer, $h_i/h_1$; the ratio of the time of wave traveling throughout the wall of the $i$th layer to that throughout the first layer $(h_i/c_i)/(h_1/c_1)$; and the ratio of the wall thickness to inner radius of the first layer $h_1/a_1$.
- the nondimensional independent variables: $\bar{r}=(r-a_1)/(b_N-a_N)$ and $\bar{t}=t/\Sigma_{i=1}^N(b_i-a_i)/c_i$.

**3.2 Comparison Between the Exact and Approximate Solutions.** In this section, we give a numerical comparison between the exact solution and the approximate solution presented above. Using the two solutions, we estimate the transient response of a circular cylinder with two coaxial layers subjected to a step pressure suddenly imposed at the inner boundary surface. The imposed pressures at the inner and outer boundary surfaces can then be expressed as follows:

$$p_1(t)=p_0H(t) \tag{21a}$$

$$p_2(t)=0 \tag{21b}$$

where $p_0$ is the amplitude of the imposed step pressure, and $H(t)$ is the Heaviside step function.

For this comparison, we consider that the inner and outer coaxial cylindrical layers are made of steel and aluminum, respectively. The structural and material parameters are chosen to be $h_1/a_1=1$, $h_2/h_1=1$, $(h_2/c_2)/(h_1/c_1)=1.1$, $\rho_2c_2/\rho_1c_1=1/3$ and the Poisson ratios $\upsilon_1=\upsilon_2=0.25$.

Figure 2 shows the variations of the radial displacement, the radial stress, and the circumferential stress with the radial distance in the cylinder at the nondimensional time $\bar{t}=1$. Three $n$ values (i.e., $n=1$, 3, and 2000) are used in the partial sums for the exact solution (19) and the approximate solution (20). Parametric studies indicate that the results obtained using $n=2000$ can be considered as the converged values of the infinite sums in equations (3) and (18). From Fig. 2, one can have the following four observations:

1. The converged results of the two stresses indicate that the exact solution can be used to simulate the propagations of the transient waves in the cylinder. At the time $\bar{t}=1$, the compressive cylindrical wave, initiated at the inner boundary surface, travels in the radial direction and its front arrives exactly at the external boundary surface. Before this time, as the compressive wave traveled across the interface, a reflected tensile wave and a transmitted compression wave were generated. The transmitted wave front has reached at the external boundary surface. The reflected wave backed from the interface, reflected again at the inner boundary surface, traveled towards the outside and its front has just arrived at $\bar{r}=0.0555$. The wave fronts can be identified easily from the jumps in the stress curves.
2. The converged results of the two stresses from the exact solution and the approximate solution have the only differences at the boundary surfaces with nonzero stresses. In other words, the approximate solution cannot satisfy the nonzero stress conditions at the boundary surfaces. The maximum shear stress at the inner boundary surface of the two-layered circular cylinder at the time $\bar{t}=1$ is estimated to be $0.9876p_0$ using the exact solution and $1.3580p_0$ using the approximate solution. The difference is large.
3. The converged results of the radial displacements from the exact solution and the approximate solution are the same.
4. The exact solution and the approximate solution result in substantially different results if only one or three wave modes are used in the partial sums (i.e., $n=1$ or 3). The substantial difference between the first several modes of the two solutions indicates that the nonzero traction boundary condition has a strong influence on the wave propagation and more wave modes shall be used in the analysis of forced vibration. The largest difference in the radial stress occurs near the nonzero inner boundary surface. The largest differences in the circumferential stress and radial displacement occur near the two boundary surfaces. It is noted that the boundary stresses play an essential role in the failure evaluation of cylinders under external dynamic forces.

**3.3 Discussions on the Solution Convergence.** The convergence of the exact and approximate solutions is supported theoretically by the completeness of eigenfunctions for general elastic body (Gurtin [36], p. 271). In particular, the eigenvalue problem (4) is a typical Sturm-Liouville problem (Titchmarsh [37], p. 17). Because the quasi-static radial displacement (15) is continuous and bounded with the interval $(a_1,b_N)$ and can be integrated over the radial distance $(a_1,b_N)$, its eigenfunction expansion (17) converges to $u_s(r,t)$ at any fixed time (Titchmarsh [37], p. 12). Hence the converged results of the radial displacement associated with the two solutions are the same in the interval $(a_1,b_N)$. Similar conclusions can be obtained for the eigenfunction expansions of the quasi-static stresses.

In the theory of eigenfunction expansion, at the boundaries (in the paper, at $r=a_1$ and $r=b_N$), the expansion results can converge; however, it may not converge to the real values of the expanded functions. According to the boundary conditions (4$b$–4$c$), it is clear that the expansion of the quasi-static radial stress converges to zero at the two boundary surfaces. It is therefore that the approximate solution would result in the radial stress zero at the two boundary surfaces.

The differences in the stresses between the exact and approximate solutions concentrate at the two boundary surfaces since we

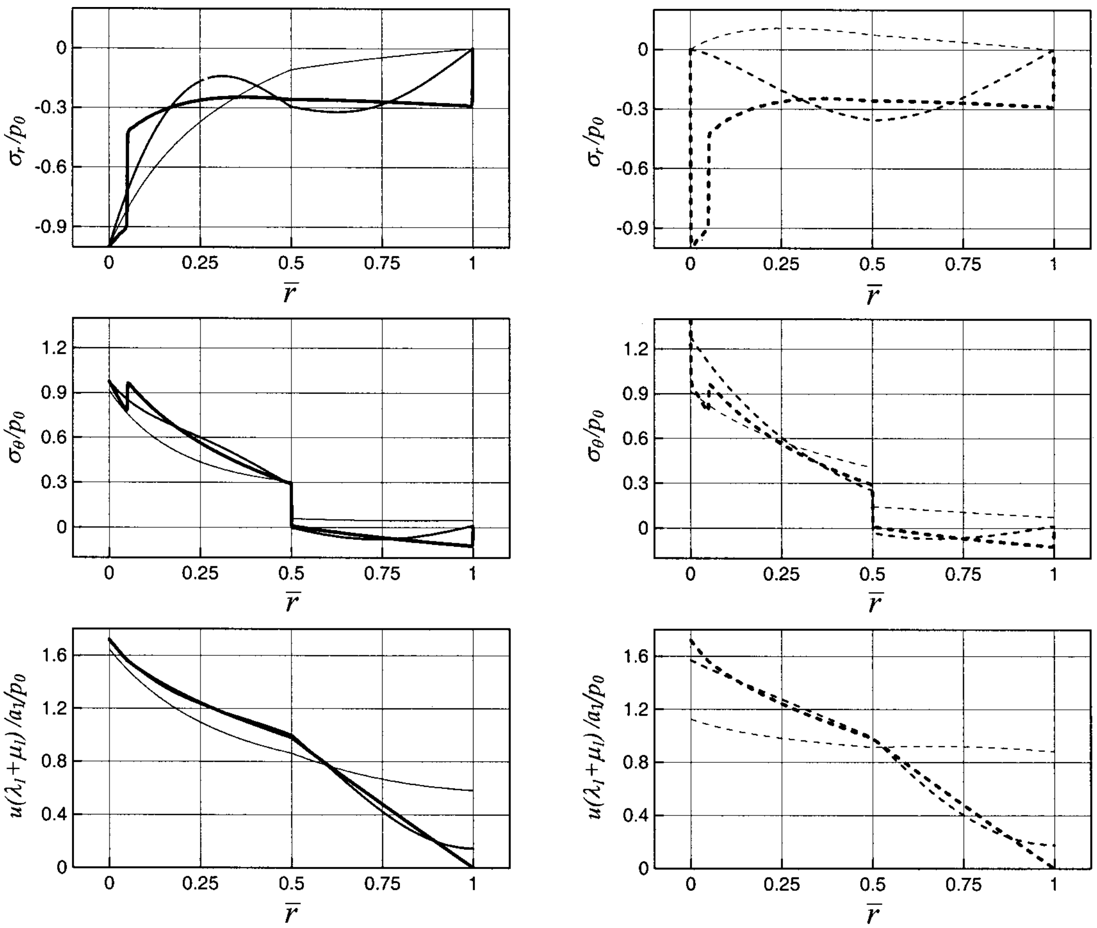

**Fig. 2 Spatial variations of the radial displacement and the radial and circumferential stress obtained using the exact solution (19) (solid line) and the approximate solution (20) (dashed line) at the time $\bar{t}=1$ for a two-layered circular cylinder (the thick line for $n=2000$; the moderately line for $n=3$; and the thin line $n=1$)**

use a large number of eigenfunctions in the numerical calculations. The differences would be large and occur at other locations if we use a small number of eigenfunctions.

The quasi-static radial displacement can be expressed as an integral function of the quasi-static stresses. So, the limited differences in the stresses at the two boundary surfaces would not cause any meaningful effect on the displacement. The full continuity of the quasi-static radial displacement at the closed interval $[a_1, b_N]$ holds that its eigenfunction expansion converges to its real values at the two boundary surfaces. Then the observation (3) above is valid over the closed interval $[a_1, b_N]$.

In addition, in Fig. 2, the $n$ value was selected to be 2000 for showing the propagation of waves more clearly. Usually, $n=50$ can generate accurate results in the numerical calculation. It is noted that we used less than 20 minutes to complete the calculation of the 2000 frequencies on a 300 MHz Pentium II PC and less than five minutes were needed to calculate the three curves shown in Fig. 2.

**3.4 Interfacial Stresses for a Seven-Layered Circular Cylinder.** A circular cylinder with seven coaxial layers subject to a step pressure at its inner boundary surface is used to examine the behavior of the interfacial stresses. The circular cylinder has the following structural dimensions and material constants in the nondimensional forms: $h_1/a_1=1$; $\upsilon_i=0.25$ for $i=1,2,\ldots,7$; $(h_i/c_i)/(h_1/c_1)=1$ and $\rho_i c_i/\rho_1 c_1=1$ for $i=1$, 3, 5, and 7; $(h_i/c_i)/(h_1/c_1)=4$ and $\rho_i c_i/\rho_1 c_1=0.15$ for $i=2$, 4, and 6. The odd layers are harder layers and the even layers as softer layers.

Figure 3 illustrates the variations of the stresses at the seven interfaces with time obtained using the partial sum (19) for the exact solution in equation, where $n=2000$. From Fig. 3, the following can be observed.

As a cylindrical wave is generated at the inner boundary surface by the step impulse pressure, the interfaces begin to response in sequence. The circumferential stress $\sigma_\theta/p_0$ at each interface is negative initially and then positive and so on. The stresses have their peak values when the cylindrical waves including the transmitted and reflected waves reach the corresponding interfaces. The trails of the transmitted and reflected wave fronts can be traced from the peaks. From Fig. 3, it seems impossible to represent the time histories of the interfacial pressures in a simple form.

## 4 Applications

**4.1 Verification of Assumptions in Classical Thin Shell Theories.** As pointed out by Loy and Lam [17], the classical thin shell theories and their refinements (so-called higher-order shell theories) may be inadequate for the analysis of the steady-state response of moderately thick and thick shells. It could be argued that the thin shell theories may also be inadequate for the transient responses of multilayered shells and cylinders. The exact solution presented above for the transient response of a multilayered circular cylinder under impose loading can be used as a benchmark to verify the classical thin shell theories for the axisymmetric plane-stain transient response of multilayered circular cylindrical shells.

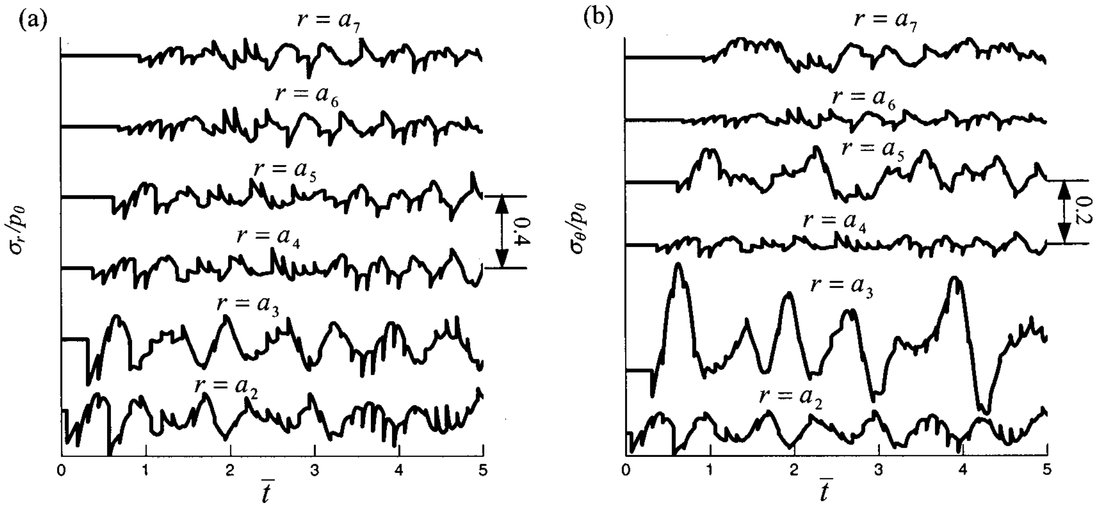


**Fig. 3 Time histories of the radial stress (*a*) and the circumferential stress (*b*) at the interfaces of a seven-layered circular cylinder ($n=2000$)**

Such verification usually needs substantial numerical data and accountable cases, as shown by Noor and Burton [1] for the linear static and free vibration problems of multilayered composite shells. On the other hand, the classical thin shell theories adopt two main assumptions: (a) the radial stress is small compared with other stress components and may be negligible and, (b) the radial displacement varies constantly or linearly in the radial direction. Therefore, the present investigation focuses on the distributions of the transient displacement and stress components in the radial direction for three types of seven-layered circular cylinders subjected to the step impulse pressure. The three types of the seven-layered circular cylinders are defined by $h_1/a_1=0.1$, $h_1/a_1=1$, and $h_1/a_1=10$, respectively. The other nondimensional structural and material parameters are as same as those given in Section 3.4. Because each of the seven coaxial hollow cylinder layers has a wall thickness equal to either $0.1a_1$, $1a_1$, or $10a_1$, we can call the corresponding composite circular cylinder with thin, moderately thick or thick layers, respectively.

The numerical results are shown in Figs. 4, 5, and 6, where the horizontal coordinate uses the layer thickness as its unit. As a result, the seven layers can be identified easily from the horizontal coordinate. All the numerical results in Figs. 4, 5, and 6 are calculated by using the number of wave modes $n=2000$.

Figure 4 shows the radial displacements at different time in the seven layered cylinder associated with $h_1/a_1=1$ or $h_1/a_1=10$. From Fig. 4, one can have the following observations:

- The radial displacement decreases nonlinearly and significantly with increasing in the radial distance in the first layer (0 to 1 and a hard layer) for the two types of composite cylinders.
- The radial displacement oscillates significantly with the increasing in the radial distance in the second layer (1 to 2 and a soft layer) for the $h_1/a_1=10$ type of composite cylinders.
- The radial displacement increases or decreases significantly at different with the increasing in the radial distance in the second layer (1 to 2) for the $h_1/a_1=1$ type of composite cylinders.

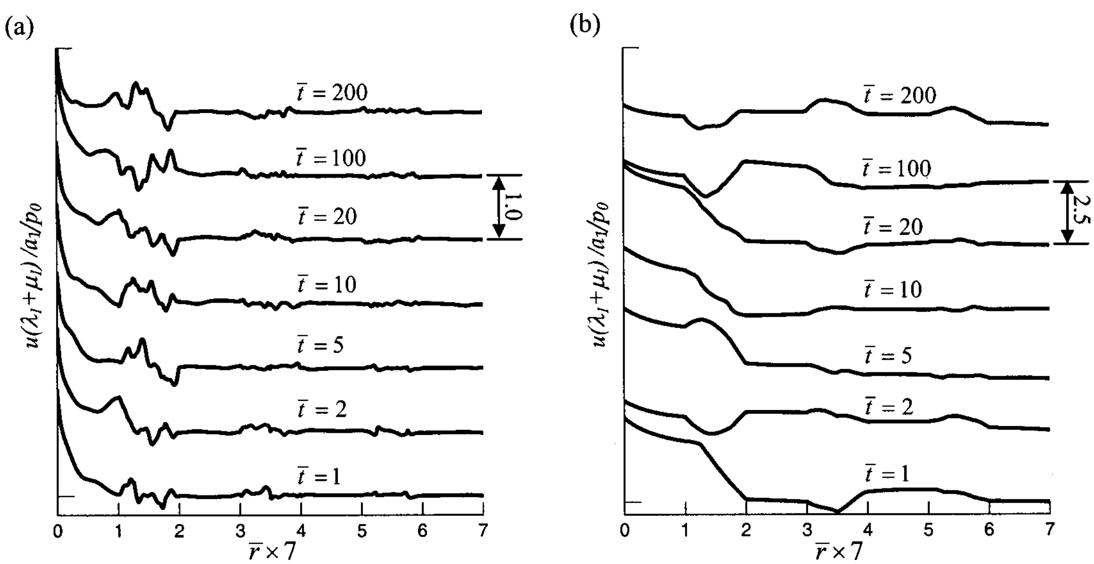


**Fig. 4 Spatial distributions of the radial displacements at different time for seven-layered circular cylinders where (*a*) for $h_1/a_1=10$ and (*b*) for $h_1/a_1=1$ ($n=2000$)**

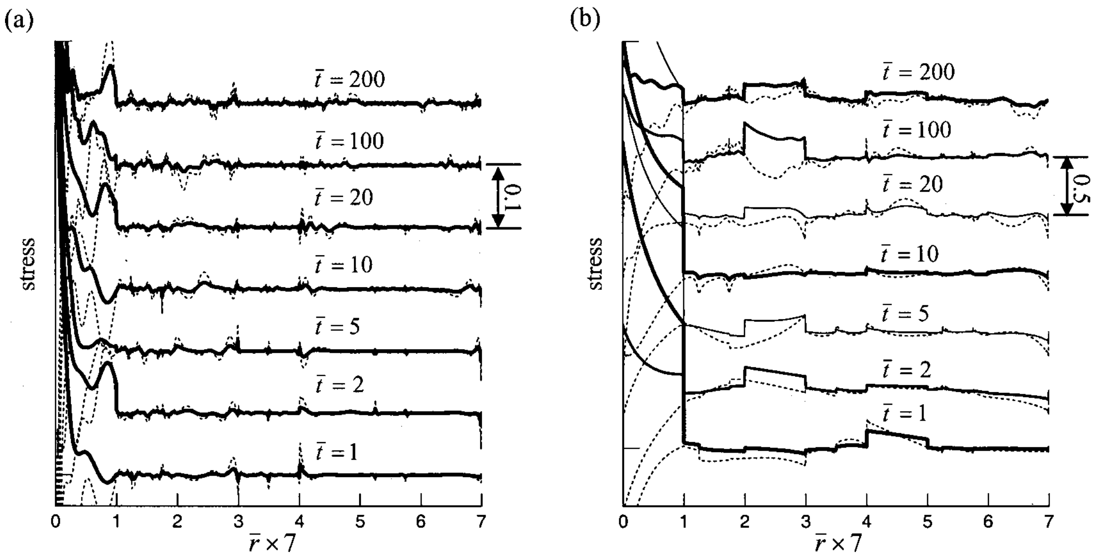


**Fig. 5 Spatial distributions of the stresses at different time for seven-layered circular cylinders where (*a*) for $h_1/a_1=10$, and (*b*) for $h_1/a_1=1$; the solid lines for the circumferential stress and the dashed lines for the radial stress**

- The radial displacement also varies with the radial distance in the fourth layer (3 to 4) for both the two types of composite cylinders.
- The radial displacement is almost constant or has linear variations with the radial distance in the other layers for both the two types of composite cylinders.

The above results indicate that the second assumption in the thin shell theories, i.e., the radial displacement varies constantly or linearly in the radial direction, may be not adequate for the thick and moderately thick composite cylinders.

Figure 5 shows the radial and circumferential stresses at different time in the seven-layered composite cylinder associated with $h_1/a_1=1$ or $h_1/a_1=10$. From Fig. 5, one can have the following observations:

- The stresses have much more complicated patterns of distributions along the radial direction and at different time.
- The radial stress in the soft coaxial layers has the magnitude similar to the corresponding circumferential stress.
- The oscillated distributions of the stresses along the radial direction mainly occur in the softer coaxial layers and do not exhibit significant decreasing with the time.

The above results show that it may not be adequate to neglect the radial stress component in the failure analysis, especially in the soft layers, for the multilayered shells with thick or moderately thick layers.

Figure 6 shows the radial displacement and the radial and circumferential stresses at different time in the seven-layered com-

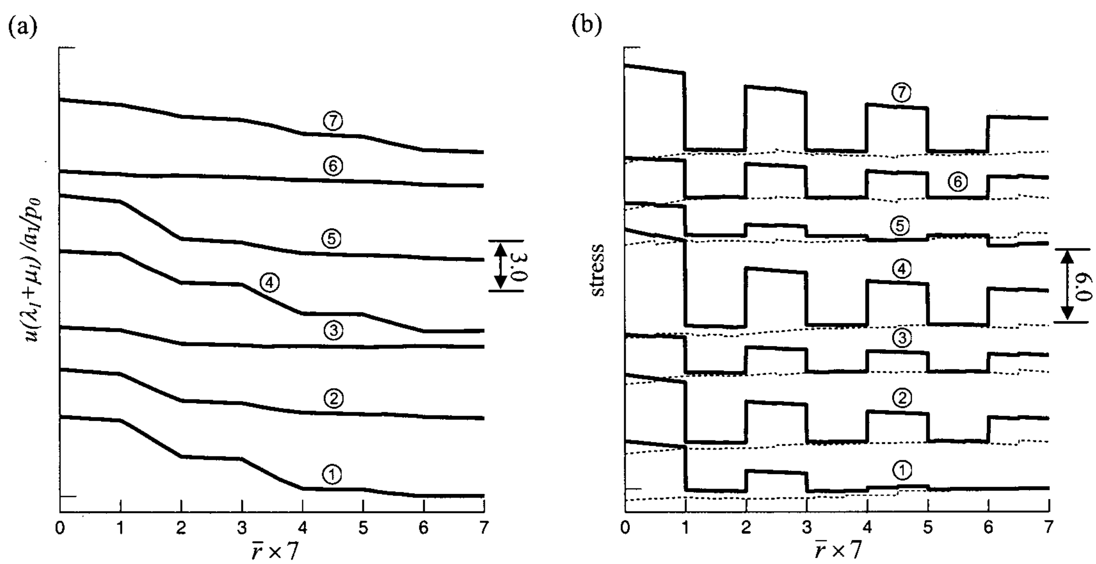


**Fig. 6 Spatial distributions of the radial displacement and the stresses for a seven-layered circular cylinder with $h_1/a_1=0.1$ where the solid lines for the circumferential stress and the dashed lines for the radial stress; $\bar{n}=2000$; ①: $\bar{t}=1+1/32$, ②: $\bar{t}=2+1/32$, ③: $\bar{t}=5+1/32$, ④: $\bar{t}=10+1/32$, ⑤: $\bar{t}=20+1/32$, ⑥: $\bar{t}=100+1/32$, ⑦: $\bar{t}=200+1/32$**

posite cylinder associated with $h_1/a_1=0.1$ (the thin layer thickness case). From Fig. 6, one can have the following observations:

- The radial displacement and the two stresses are piecewisely linear functions of the radial distance.
- The radial stress has a magnitude significant smaller than and similar to that of the corresponding circumferential stress in the hard layers and the soft layers, respectively.
- The radial stress has small jumps at some internal points of the seven-layered composite cylinder.
- The circumferential stress has jumps at both internal points and the interfaces of the seven-layered composite cylinder.

The total wall thickness of the composite cylinder is $(b_7-a_1)/a_1=0.7$, which may not be treated as a thin shell. The linear distributions of the radial displacement with each layer show that the assumption of linear radial displacement distribution in the thin shell theories is adequate such composite cylinders.

In Fig. 6, the nondimensional time is specified to be an integer plus 1/32. As a result, some reflected and transmitted wave fronts may locate not at the boundaries of layers and the wave fronts can be identified as the slight jumps in the distribution curves of stress components along the radial distance.

The relatively jumping amplitudes of stress components at these wave fronts reflect both the influences of transient wave propagations and the capability of the application of the thin shell theories. From Fig. 6($b$), the relatively jumped amplitudes in the stresses are very small. Furthermore, the radial stress has magnitudes much less than those of the circumferential stress in the hard layers. Therefore, the other assumption in the thin shell theories that the radial stress is small compared with other stress components and may be negligible may be adequate for the transient response of the composite cylinders with thin layers although the thin shell theories cannot model the relative stress jumps at the internal points.

**4.2 Effects of Layer Acoustic Impedance.** Because of the common use of multilayered composite shells with substantially different acoustic impedance layers, it is valuable to examine the changes of the linear characteristics in Fig. 6 with the distribution of the layer acoustic impedances. We consider two extreme cases for the seven-layered cylinders with different changeable acoustic impedances in Fig. 6.

The first case is that the two neighbor layers have the same acoustical impedances. The second case is that the acoustic impedances of the soft layers are very small. In the first case, the multilayered cylinder behaves as a single moderately thick cylinder with the total thickness of the seven layers. In the second case, few quantities of the wave disturbance can transmit from the first (hard) layer to the second (soft) layer. The multilayered cylinder behaves as a thin cylinder consisting of only the first hard layer.

Figure 7 shows the quantitative comparisons in attempt to describe the change of the linear characteristics with the distribution of acoustic impedances. In Fig. 7, the horizontal coordinate represents the ratio of the acoustic impedance of the soft layers over that of the hard layers. The vertical coordinate represents the relative wavefront height: i.e., the relative maximum jump height at wavefronts with respect to the divergence of the circumferential stresses at the two boundaries within the first (hard) layer. The corresponding values of $(h_2/c_2)/(h_1/c_1)$ are also list in the figure. The smaller the relative wavefront height is, the stronger linear characteristics are. Figure 7 shows the relative wavefront height descends quickly with the decreasing of the acoustic impedance ratio. This result means that the applicability of the thin classic shell theories to the multilayered circular cylindrical shells strongly depends upon the material properties.

## 5 Conclusions

The paper has presented an exact solution and an approximate solution for the transient response of an infinite long and multilayered circular cylinder subject to uniform distributed dynamic pressure at the inner and outer boundaries. Numerical results show that the present solutions are suitable for the analysis of the transient responses. From the numerical results presented in the paper, one can observe that the interfacial pressures are complicated and cannot be represented in a simple form. The approximate solution is inadequate for the calculations of the nonzero stresses at the boundaries. Furthermore, it is found that the two solutions may not be able to give converged results for the analysis of forced vibration if a small number of the eigenfunctions is used. The applicability of the thin shell theories to the transient response of multilayered cylinders strongly depends upon both the geometrical and material properties of the cylinders.

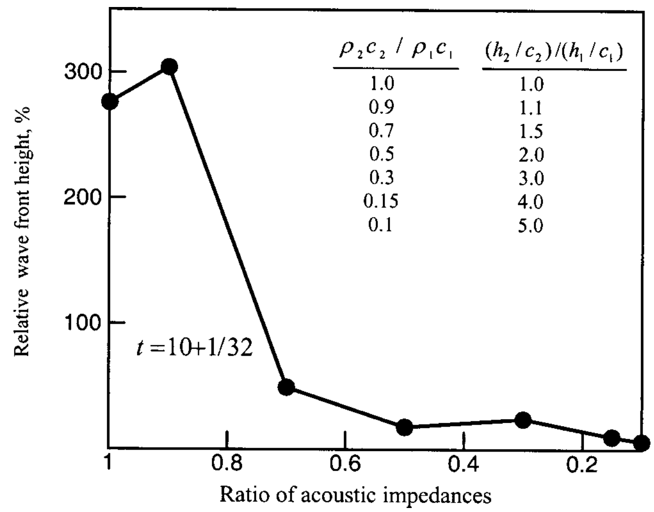


**Fig. 7 Variation of the relative wave front height with the decreasing of the acoustic impedance ratio for a seven layered cylinder ($n=2000$)**

## Acknowledgments

The study is financially supported by the Research Grants Council of Hong Kong. The authors would also like to thank the two peer reviewers, and the Associate Editor, Professor Ajit Mal for their valuable comments and suggestions which have greatly improved the presentation of the manuscript.

## Appendix A

**Mathematical Derivation for Eq. (10).** We consider two wave modes $U_n^i(r)$ and $U_m^i(r)$ corresponding to the eigenvalues $\omega_n$ and $\omega_m$, respectively. They satisfy the equations below:

$$\frac{d}{dr}\left(r\frac{dU_n^i}{dr}\right)+\left[(k_n^i)^2r-\frac{1}{r}\right]U_n^i=0 \qquad (A1)$$

$$\frac{d}{dr}\left(r\frac{dU_m^i}{dr}\right)+\left[(k_m^i)^2r-\frac{1}{r}\right]U_m^i=0 \qquad (A2)$$

We multiply $(A1)$ by $U_m^i(r)c_i^2\rho_i$ and $(A2)$ by $U_n^i(r)c_i^2\rho_i$. We then subtract the two results, integrate the remaining over the layer thickness, then make the summation of all the layers. We can obtain the following equation.

$$(\omega_m^2-\omega_n^2)\sum_{i=1}^{N}\int_{a_i}^{b_i}\rho_i U_n^i(r)U_m^i(r)2\pi r dr=\sum_{i=1}^{N}2\pi\rho_i c_i^2\int_{a_i}^{b_i}\left[U_m^i\frac{d}{dr}\left(r\frac{dU_n^i}{dr}\right)-U_n^i\frac{d}{dr}\left(r\frac{dU_m^i}{dr}\right)\right]dr$$

$$=\sum_{i=1}^{N}2\pi\rho_i c_i^2\left[rU_m^i\frac{dU_n^i}{dr}-rU_n^i\frac{dU_m^i}{dr}\right]_{a_i}^{b_i}-\sum_{i=1}^{N}2\pi\rho_i c_i^2\int_{a_i}^{b_i}\left[r\frac{dU_n^i}{dr}\frac{dU_m^i}{dr}-r\frac{dU_m^i}{dr}\frac{dU_n^i}{dr}\right]$$

$$=\sum_{i=1}^{N}2\pi\rho_i c_i^2\left[rU_m^i\frac{dU_n^i}{dr}-rU_n^i\frac{dU_m^i}{dr}\right]_{a_i}^{b_i}=2\pi\rho_N c_N^2 b_N\left[U_m^N(b_N)\frac{dU_n^N(b_N)}{dr}\right.$$

$$\left.-U_n^N(b_N)\frac{dU_m^N(b_N)}{dr}\right]-2\pi\rho_1c_1^2a_1\left[U_m^1(a_1)\frac{dU_n^1(a_1)}{dr}-U_n^1(a_1)\frac{dU_m^1(a_1)}{dr}\right]$$

$$+2\pi\sum_{i=1}^{N-1}\left\{\rho_i c_i^2 b_i\left[U_m^i(b_i)\frac{dU_n^i(b_i)}{dr}-U_n^i(b_i)\frac{dU_m^i(b_i)}{dr}\right]\right.$$

$$\left.-\rho_{i+1}c_{i+1}^2a_{i+1}\left[U_m^{i+1}(a_{i+1})\frac{dU_n^{i+1}(a_{i+1})}{dr}-U_n^{i+1}(a_{i+1})\frac{dU_m^{i+1}(a_{+1i})}{dr}\right]\right\}. \quad (A3)$$

Rewrite the conditions (4*b*)–(4*c*) in the manuscript in the following forms:

$$\left[(\lambda_1+2\mu_1)\frac{dU^1}{dr}+\lambda_1\frac{U^1}{r}\right]_{r=a_1}=0 \quad (A4)$$

$$\left[(\lambda_N+2\mu_N)\frac{dU^N}{dr}+\lambda_N\frac{U^N}{r}\right]_{r=b_N}=0. \quad (A5)$$

By using (*A*4) and (*A*5) and expressing the wave modes with their derivations, we can show the first two terms in the right-hand side of Eq. (*A*3) to be vanished.

As a result, we obtain

$$(\omega_m^2-\omega_n^2)\sum_{i=1}^{N}\int_{a_i}^{b_i}\rho_i U_n^i(r)U_m^i(r)2\pi r dr$$
$$=2\pi\sum_{i=1}^{N-1}\left\{\rho_i c_i^2 b_i\left[U_m^i(b_i)\frac{dU_n^i(b_i)}{dr}-U_n^i(b_i)\frac{dU_m^i(b_i)}{dr}\right]\right.$$
$$-\rho_{i+1}c_{i+1}^2a_{i+1}\left[U_m^{i+1}(a_{i+1})\frac{dU_n^{i+1}(a_{i+1})}{dr}\right.$$
$$\left.\left.-U_n^{i+1}(a_{i+1})\frac{dU_m^{i+1}(a_{+1i})}{dr}\right]\right\} \quad (A6)$$

We then use the condition (4*e*) $U^{i+1}(a_{i+1})=U^i(b_i)$, $\rho_i c_i^2=(\lambda_i=2\mu_i)$ and $a_{i+1}=b_i$. So, we can reduce (*A*6) as the following result:

$$(\omega_m^2-\omega_n^2)\sum_{i=1}^{N}\int_{a_i}^{b_i}\rho_i U_n^i(r)U_m^i(r)2\pi r dr$$
$$=2\pi\sum_{i=1}^{N-1}\left\{b_iU_m^i(b_i)\left[(\lambda_i+2\mu_i)\frac{dU_n^i(b_i)}{dr}\right.\right.$$
$$\left.-(\lambda_{i+1}+2\mu_{i+1})\frac{dU_n^{i+1}(a_{i+1})}{dr}\right]-b_iU_n^i(b_i)$$
$$\left.\times\left[(\lambda_i+2\mu_i)\frac{dU_m^i(b_i)}{dr}-(\lambda_{i+1}+2\mu_{i+1})\frac{dU_m^{i+1}(a_{i+1})}{dr}\right]\right\} \quad (A7)$$

From the condition (4*d*) and the condition (4*e*), we have

$$(\lambda_i+2\mu_i)\frac{dU^i(b_i)}{dr}-(\lambda_{i+!}+2\mu_{i+1})\frac{dU^{i+1}(a_{i+1})}{dr}$$
$$=(\lambda_i-\lambda_{i+1})\frac{U^i(b_i)}{b_i} \quad (A8)$$

By substituting (*A*8) into the expression (*A*7), we have

$$(\omega_m^2-\omega_n^2)\sum_{i=1}^{N}\int_{a_i}^{b_i}\rho_i U_n^i(r)U_m^i(r)2\pi r dr$$
$$=2\pi\sum_{i=1}^{N-1}\{(\lambda_i+\lambda_{i+1})U_m^i(b_i)U_n^i(b_i)$$
$$-(\lambda_i+\lambda_{i+1})U_n^i(b_i)U_m^i(b_i)\}=0 \quad (A9)$$

If $\omega_n$ and $\omega_m$ are distinct, then we have

$$\sum_{i=1}^{N}\int_{a_i}^{b_i}\rho_i U_n^i(r)U_m^i(r)2\pi r dr=0 \quad (A10)$$

For simplicity, we can normalize the set of eigenfunctions by requiring

$$\sum_{i=1}^{N}\int_{a_i}^{b_i}\rho_i|U_m^i(r)|^2 2\pi r dr=1 \quad (A11)$$

Finally, we can obtain the orthogonal condition in the form of summation as Eq. (10) below:

$$\sum_{i=1}^{N}\int_{a_i}^{b_i}\rho_i U_n^i(r)U_m^i(r)2\pi r dr=\delta_{mn} \quad (A12)$$

## Appendix B

**Mathematical Derivation for Eq. (11).** As shown in Eq. (9*b*), $\varepsilon_j^i(k_m^i r)$ is a linear function of the Bessel functions of the first and second kinds of the $j$th order, i.e., $J_j$ and $Y_j$. So, $\varepsilon_j^i(k_m^i r)$ has the following properties as those of the Bessel functions $J_j$ and $Y_j$:

$$\varepsilon_{j-1}(x)-\varepsilon_{j+1}(x)=2\frac{d}{dx}(\varepsilon_j(x)) \tag{B1}$$

$$\frac{d}{dx}(x^j\varepsilon_j(x))=x^j\varepsilon_{j-1}(x) \tag{B2}$$

$$\frac{d}{dx}\varepsilon_0(x)=-\varepsilon_1(x) \tag{B3}$$

where $x$ stands for $k_m^i r$ and $\varepsilon_j(x)$ for $\varepsilon_j^i(k_m^i r)$.

If $m=n$, the orthogonal condition (10) becomes

$$\sum_{i=1}^{N}\int_a^b \rho_i A_m^2\varepsilon_1^2(x)2\pi x dx/(k_m^i)^2=1 \tag{B4}$$

where $a$ is $k_m^i a_i$ and $b$ is $k_m^i b_i$.

So, the coefficient $A_m$ is

$$A_m^{-2}=\sum_{i=1}^{N}\frac{\pi\rho_i}{(k_m^i)^2}\int_a^b \varepsilon_1^2(x)d(x^2) \tag{B5}$$

Performing the integration by parts, we obtain

$$\int_a^b \varepsilon_1^2(x)d(x^2)=[x^2\varepsilon_1^2(x)]_a^b-\int_a^b x^2 2\varepsilon_1(x)\frac{d}{dx}(\varepsilon_1(x))dx. \tag{B6}$$

Using ($B1$), ($B2$), and ($B3$), one can show the following is valid:

$$\begin{aligned}\int_a^b x^2 2\varepsilon_1(x)\frac{d}{dx}(\varepsilon_1(x))dx &=\int_a^b x^2\varepsilon_1(x)[\varepsilon_0(x)-\varepsilon_2(x)]dx\\ &=\int_a^b\{[x^2\varepsilon_1(x)]\varepsilon_0(x)+[x^2\varepsilon_2(x)][-\varepsilon_1(x)]\}dx\\ &=\int_a^b\left\{\frac{d}{dx}[x^2\varepsilon_2(x)]\varepsilon_0(x)+[x^2\varepsilon_2(x)]\frac{d}{dx}[\varepsilon_0(x)]\right\}dx\\ &=\int_a^b d[x^2\varepsilon_2(x)\varepsilon_0(x)]=[x^2\varepsilon_2(x)\varepsilon_0(x)]_a^b.\end{aligned} \tag{B7}$$

Substituting ($B7$) into ($B6$) and ($B5$), the coefficient $A_m$ is defined by

$$\begin{aligned}A_m^{-2}=\sum_{i=1}^{N}\rho_i\{&\pi b_i^2[\varepsilon_1^{i\,2}(k_m^i b_i)-\varepsilon_0^i(k_m^i b_i)\varepsilon_2^i(k_m^i b_i)]\\ &-\pi a_i^2[\varepsilon_1^{i\,2}(k_m^i a_i)-\varepsilon_0^i(k_m^i a_i)\varepsilon_2^i(k_m^i a_i)]\}\end{aligned} \tag{B8}$$

## References


[1] Noor, A. K., and Burton, W. S., 1990, ''Assessment of Computational Models for Multilayered Composite Shells,'' Appl. Mech. Rev., **43**, pp. 67–97.

[2] Noor, A. K., 1990, ''Bibliography of Monographs and Surveys on Shells,'' Appl. Mech. Rev., **43**, pp. 223–234.

[3] Soldatos, K. P., 1994, ''Review of Three Dimensional Dynamic Analyses of Circular Cylinders and Cylindrical Shells,'' Appl. Mech. Rev., **47**, pp. 501–516.

[4] Valle, C., Qu, J., and Jacobs, L. J., 1999, ''Guided Circumferential Waves in Layered Cylinders,'' Int. J. Eng. Sci., **37**, pp. 1369–1387.

[5] Nayfeh, A. H., Abdelraman, W. G., and Nagy, P. B., 2000, ''Analyses of Axisymmetric Waves in Layered Piezoelectric Rods and Their Composites,'' J. Acoust. Soc. Am., **108**, pp. 1496–1504.

[6] Habip, L. M., 1965, ''A Review of Recent Work on Multilayered Structure,'' Int. J. Mech. Sci., **7**, pp. 589–593.

[7] Christoforou, A. P., and Swanson, S. R., 1990, ''Analysis of Simply-Supported Orthotropic Cylindrical Shells Subjected to Lateral Impact Loads,'' ASME J. Appl. Mech., **57**, pp. 376–382.

[8] Chonan, S., 1984, ''Response of a Pre-Stressed Orthotropic Thick Cylindrical Shell Subjected to a Pressure Pulse,'' J. Sound Vib., **93**, pp. 31–38.

[9] Humphreys, J. S., and Winter, R., 1965, ''Dynamic Response of a Cylinder to a Side Pressure Pulse,'' AIAA J., **3**, pp. 27–32.

[10] Sivadas, K. R., and Ganesan, N., 1993, ''Dynamic Analysis of Circular Cylindrical Shells With Material Damping,'' J. Sound Vib., **166**, pp. 103–116.

[11] Nachbar, P. M., 1962, ''On the Role of Bending in the Dynamics Response of Thin Shells to Moving Discontinuous Loads,'' J. Aerosp. Sci., **29**, pp. 648–657.

[12] Jones, J. P., and Bhuta, P. G., 1964, ''Response of Cylindrical Shells to Moving Loads,'' ASME J. Appl. Mech., **31**, pp. 105–111.

[13] Mangrum, E., and Burns, J. J., 1979, ''Orthotropic Cylindrical Shells Under Dynamic Loading,'' ASME J. Mech. Des., **101**, pp. 322–329.

[14] Lindberg, H. E., 1964, ''Buckling of a Very Thin Cylindrical Shell due to an Impulsive Pressure,'' ASME J. Appl. Mech., **31**, pp. 267–272.

[15] Goodier, J. N., and McIvor, I. K., 1964, ''The Elastic Cylindrical Shell Under Nearly Uniform Radial Impulse,'' ASME J. Appl. Mech., **31**, pp. 259–266.

[16] Lovell, E. G., and McIvor, I. K., 1969, ''Nonlinear Response of a Cylindrical Shell to an Impulsive Pressure,'' ASME J. Appl. Mech., **36**, pp. 277–284.

[17] Loy, T. C., and Lam, K. Y., 1999, ''Vibration of Thick Cylindrical Shells on the Basis of Three-Dimensional Theory of Elasticity,'' J. Sound Vib., **226**, pp. 719–737.

[18] Svärdh, P. A., 1984, ''Three-Dimensional Analysis of Axisymmetric Transient Waves in Hollow Elastic Cylinders,'' ASME J. Appl. Mech., **51**, pp. 792–797.

[19] Chong, K. P., Lee, P. C. Y., and Cakmak, A. S., 1969, ''Propagation of Axially Symmetric Waves in Hollow Elastic Circular Cylinders Subjected to a Step-Function Loading,'' J. Acoust. Soc. Am., **49**, pp. 201–210.

[20] Heimann, J. H., and Kolsky, H., 1958, ''The Propagation of Elastic Waves in Thin Cylindrical Shells,'' J. Mech. Phys. Solids, **14**, pp. 121–130.

[21] Fitch, A. H., 1963, ''Observation of Elastic-Pulse Propagation in Axially Symmetric and Nonaxially Asymmetric Longitudinal Modes of Hollow Cylinders,'' J. Acoust. Soc. Am., **35**, pp. 706–708.

[22] Kley, M., Valle, C., Jacobs, L. J., Qu, J., and Jarzynski, J., 1999, ''Development of Dispersion Curves for Two-Layered Cylinders Using Laser Ultrasonics,'' J. Acoust. Soc. Am., **106**, pp. 582–588.

[23] Rabern, D. A., and Lewis, M. W., 1992, ''Two and Three-Dimensional Simulations of Moving Pressure Fronts in Gun Tubes,'' ASME J. Pressure Vessel Technol., **114**, pp. 181–188.

[24] Cinell, G., 1966, ''Dynamic Vibrations and Stresses in Elastic Cylinders and Spheres,'' ASME J. Appl. Mech., **33**, pp. 825–830.

[25] Gong, Y. N., and Wang, X., 1991, ''Radial Vibrations and Dynamic Stress in Elastic Hollow Cylinders,'' *Structural Dynamic: Recent Advances*, Elsevier Science Publications, Elsevier, London, pp. 137–147.

[26] Wang, X., and Gong, Y. N., 1992, ''An Theoretical Solution for Axially Symmetric Problem in Elastodynamics,'' Acta Mech. Sin., **7**, pp. 275–282.

[27] Wang, X., 1995, ''Thermal Shock in a Hollow Cylinder Caused by Rapid Arbitrary Heating,'' J. Sound Vib., **183**, pp. 899–906.

[28] Cho, H., Kardomateas, G. A., and Valle, C. S., 1998, ''Elastodynamic Solution for the Thermal Shock Stresses in an Orthotropic Thick Cylindrical Shell,'' ASME J. Appl. Mech., **65**, pp. 184–193.

[29] Yin, X. C., 1997, ''Multiple Impacts of Two Concentric Hollow Cylinders With Zero Clearance,'' Int. J. Solids Struct., **34**, pp. 4597–4616.

[30] Yin, X. C., and Wang, L. G., 1999, ''The Effect of Multiple Impacts on the Dynamics of an Impact System,'' J. Sound Vib., **228**, pp. 995–1015.

[31] Wang, X., and Gong, Y. N., 1992, ''An Elastodynamic Solution for Multilayered Cylinders,'' Int. J. Eng. Sci., **30**, pp. 25–33.

[32] Wang, X., 1993, ''Stress Wave Propagation in a Two-Layered Cylinder With Initial Interface Pressure,'' Int. J. Solids Struct., **30**, pp. 1693–1700.

[33] Eringen, A. C., and Suhubi, E. S., 1975, *Elastodynamics, Vol. 2, Linear Theory*, Academic Press, New York.

[34] Love, A. E. H., 1944, *A Treatise on the Mathematical Theory of Elasticity*, Dover, New York.

[35] Gurtin, M. E., 1984, ''The Linear Theory of Elasticity,'' *Mechanics of Solids*, C. Truesdell, ed., Springer-Verlag, Berlin, **II**, pp. 1–295.

[36] Liu, G., and Qu, J., 1998, ''Transient Wave Propagation in a Circular Annulus Subjected to Transient Excitation on Its Outer Surface,'' J. Acoust. Soc. Am., **104**, pp. 1210–1220.

[37] Titchmarsh, E. C., 1962, *Eigenfunction Expansions, Part I*, Oxford University Press, London.

**J. M. Horton**
Reflecting Roadstuds, Ltd.
Boothtown,
Halifax HX3 6TR, UK

**G. E. Tupholme**

**M. J. C. Gover**

School of Computing and Mathematics,
University of Bradford,
Bradford BD7 1DP, UK

# Axial Loading of Bonded Rubber Blocks

*Axially loaded rubber blocks of long, thin rectangular and circular cross section whose ends are bonded to rigid plates are studied. Closed-form expressions, which satisfy exactly the governing equations and conditions based upon the classical theory of elasticity, are derived for the total axial deflection and stress distribution using a superposition approach. The corresponding relations are presented for readily calculating the apparent Young's modulus, $E_a$, the modified modulus, $E_a'$, and the deformed lateral profiles of the blocks. From these, improved approximate elementary expressions for evaluating $E_a$ and $E_a'$ are deduced. These estimates, and the precisely found values, agree for large values of the shape factor, S, with those previously suggested, but also fit the experimental data more closely for small values of S. Confirmation is provided that the assumption of a parabolic lateral profile is invalid for small values of S.* [DOI: 10.1115/1.1507769]

## 1 Introduction

Extensive use is made of rubber bearings in a wide range of modern engineering environments. The important applications include the reduction of traffic-induced movement and the seismic isolation of vulnerable buildings, the flexure of bridges with expansion bearings and the protection of vibration-sensitive instruments. They often involve rubber blocks bonded to rigid metallic end plates and it is therefore necessary to be able to predict the stiffness and stress distribution created when loads are applied.

The approximate expressions developed by Gent and Lindley [1] and Gent [2] for the apparent Young's modulus, $E_a$, of bonded incompressible rubber blocks subjected to compression are still widely quoted and used in the engineering industry for assessing their axial stiffnesses. They depend upon the so-called shape factor, $S$, which is defined as the ratio of the loaded bonded area to the force-free lateral surface area. The Gent and Lindley [1] approximations, $E_a^{(\mathrm{GL})}$, take the forms

$$E_a^{(\mathrm{GL})}=\frac{4E}{3}(1+S^2), \tag{1}$$

for blocks of rectangular cross section whose length is large compared to its width, and

$$E_a^{(\mathrm{GL})}=E(1+2S^2), \tag{2}$$

for blocks of circular cross section, where $E$ denotes the Young's modulus of the material of the block. As rubber is generally regarded as incompressible, the expressions (1) and (2) are often written ([3]) with $3\mu$ replacing $E$, where $\mu$ is the shear modulus which along with $K$, the bulk modulus, are fundamental material constants.

To account for the bulk compression of the block, Gent and Lindley [1] reasoned that for blocks of high shape factor, the modified modulus, $E_a'$, should be introduced according to the formula

$$\frac{1}{E_a'}=\frac{1}{E_a}+\frac{1}{K}, \tag{3}$$

Contributed by the Applied Mechanics Division of THE AMERICAN SOCIETY OF MECHANICAL ENGINEERS for publication in the ASME JOURNAL OF APPLIED MECHANICS. Manuscript received by the ASME Applied Mechanics Division, October 30, 2001; final revision, May 22, 2002. Associate Editor: E. Arruda. Discussion on the paper should be addressed to the Editor. Prof. Robert M. McMeeking, Department of Mechanical and Environmental Engineering University of California–Santa Barbara, Santa Barbara, CA 93106-5070, and will be accepted until four months after final publication of the paper itself in the ASME JOURNAL OF APPLIED MECHANICS.

where $E_a$ is approximated appropriately by either (1) or (2). They suggested that $E_a'$ should then be used to predict the small deflections of rubber blocks bonded to rigid end plates under the influence of an axial load.

In fact, Gent and Lindley [1] found that the predicted values of the apparent Young's modulus calculated using the relations (1), (2), and (3) agree well with their experimental measurements, except for small values of $S$ when they fall below the experimental values.

In deriving the approximations (1) and (2) it was assumed that the block material is incompressible, that cross sections of the block normal to the direction of the applied load remain plane and normal and also that the free lateral surfaces have parabolically deformed shapes. In the published subsequent discussions of the Gent and Lindley [1] study, Payne [4] observed that the discrepancy "relating to the technically important range of shape factors less than unity" might be accounted for by "the fact that the profile of the compressed block was not quite parabolic," and Hirst [5] hoped that the next step "would be an improved method of estimating the 'bulgeability.' " However, it appears that no further progress has been made.

The present paper derives easily calculable expressions for the apparent Young's modulus of blocks of long, thin rectangular and circular cross sections, and for the deformed profiles of their lateral surfaces, which satisfy exactly the governing equations based upon the classical theory of linear elasticity. The analytical techniques used here are fundamentally similar to those which Horton, Gover, and Tupholme [6,7] presented in deriving expressions for the radial stiffness and tilting stiffness of a rubber bush mounting of finite length. Improved approximations for $E_a'$ are also deduced. These give values that agree with those predicted by the relations (1), (2), and (3) for large values of $S$, but which appear to fit more closely the experimental data for the smaller values of $S$. The shapes of the deformed free surfaces are shown to be parabolic only for large values of $S$, and it is confirmed therefore that for small values of $S$ the previously used assumption of a parabolic profile is indeed invalid.

The analyses of Sections 2 to 5 incorporate the effects of bulk compressibility using the principle of superposition for two loading situations. The total axial deflection of the loaded block and the stress distribution within it are evaluated, in addition to presenting expressions for the apparent Young's modulus, the modified modulus and the deformed profile, for blocks having long, thin rectangular or circular cross sections. Finally, in Section 6, some numerical results are displayed and discussed. Interesting comparisons are made particularly with the recent experimental

  

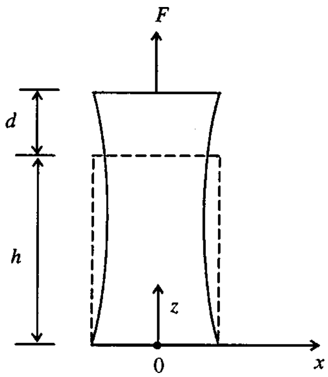


**Fig. 1 Cross section of the block through the $y=0$ plane: undeformed (dashed), deformed (solid)**

measurements of Mott and Roland [8], and a finite element analysis of the stress distribution of laminated elastomeric bearings by Imbimbo and De Luca [9].

## 2 Formulation

Consider a right-prismatic rubber block of axial height $h$ and uniform cross-sectional area $A$. Relative to an origin $O$, a rectangular Cartesian coordinate system $(x, y, z)$ is established with $Oz$ along the axis of the block, and its plane ends at $z=0$ and $z=h$, as depicted in Fig. 1.

It is assumed throughout that the rubber is homogeneous and isotropic, and that during the subsequent deformations the displacement gradients are sufficiently small for the classical linear theory of elasticity to be applicable (see, for example, Sokolnikoff [10], Spencer [11], or Hunter [12]). The rubber is bonded to rigid end plates at $z=0$ and $z=h$ which prevent all distortions of its end surfaces.

Suppose the end $z=0$ of the block is held in a fixed position and the other end, $z=h$, is subjected to a load of constant magnitude $F$ along the $z$-axis, which causes it to extend or compress a distance $d$. The force-free lateral surfaces will be drawn inwards if the loading is tensile, as illustrated in Fig. 1, but will bulge outwards under compressive loading. The resulting displacement is calculated here by the superposition of the displacements arising in two separate specified loading situations, as represented diagrammatically in Fig. 2.

First, in Case A the block is subject to an axial tensile load and at the same time the lateral surfaces are prevented from distorting by the application of a tensile stress of magnitude $\sigma_L$. The slight bulk distortion creates an extension of the block with the face $z=h$ being displaced a distance $d_A$. Then, in Case B, the same block is loaded on its lateral surfaces alone with a compressive stress equal and opposite to that in Case A. Treating the rubber as incompressible, this applied loading axially extends the block by a distance $d_B$. By superposition the total displaced distance, $d$, is then given by $d_A+d_B$, with the effects of the lateral loadings canceling out.

## 3 Case A: Axial End Load With Undistorted Lateral Surfaces

Suppose that the block of uniform cross-sectional area $A$ is subjected to bulk dilation by an axial tensile load $F$ applied on the plane end face $z=h$ with the lateral faces restrained to remain undistorted and parallel to the $z$-axis by tensile stresses of magnitude $\sigma_L$ applied normally to these faces.

The magnitude of the imposed axial stress is $F/A$ and, with $\sigma_L=F/A$, the block material is everywhere in a state of hydrostatic tensile stress, whose magnitude, $\sigma$, is given by

$$\sigma=\sigma_L=\frac{F}{A}. \tag{4}$$

The bulk dilation, $\delta V$, is given by

$$\frac{\delta V}{V}=\frac{F}{AK} \tag{5}$$

where $K$ is the bulk modulus of the rubber. Since the cross-sectional area remains unchanged during the distortion and the end of the block at $z=0$ is fixed, the resulting deflection, $d_A$, of the end at $z=h$ is given by

$$d_A=\frac{Fh}{AK}. \tag{6}$$

The consequences of the Case B loadings are now analyzed in detail; first when the block has a long, thin rectangular cross section and then secondly when it has a circular cross section.

## 4 Block of Long, Thin Rectangular Cross Section

**4.1 Case B: Loaded Lateral Surfaces.** Now consider an incompressible block of rectangular cross section of width $b$ and length $l$ with $l \gg b$, bounded by the planes $x=\pm b/2$ and $y=\pm l/2$. In the literature, this is often called an "infinitely long rectangular block." Suppose that it is subjected only to lateral loading on the faces $x=\pm b/2$ by a normal stress $-\sigma_L$ $(=-F/A)$, which is equal and opposite to that in Case A.

Relative to the rectangular Cartesian axes, the displacement components at a point $P=(x,y,z)$ are denoted by $u$, $v$, and $w$, the strain components by $\varepsilon_{xx}$, $\varepsilon_{yy}$, $\varepsilon_{zz}$, $\varepsilon_{xy}$, $\varepsilon_{xz}$, and $\varepsilon_{yz}$, and the

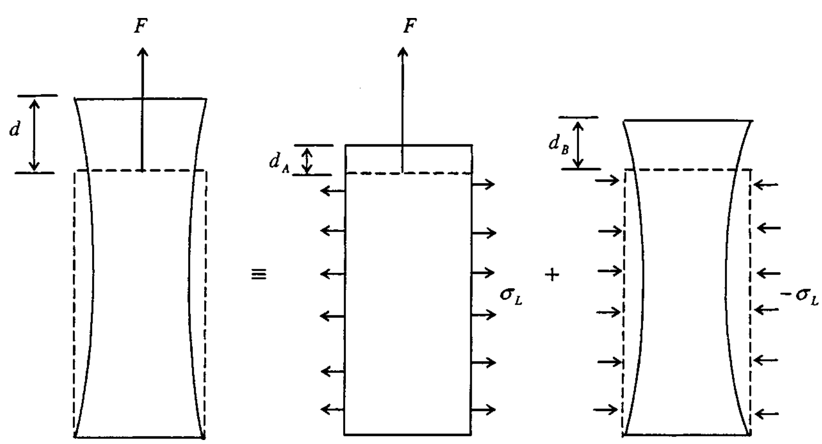


**Fig. 2 Superposition of Cases A and B**

stress components by $\sigma_{xx}$, $\sigma_{yy}$, $\sigma_{zz}$, $\sigma_{xy}$, $\sigma_{xz}$, and $\sigma_{yz}$ in the usual notation. For small strains, the assumption of incompressibility implies that

$$\varepsilon_{xx}+\varepsilon_{yy}+\varepsilon_{zz}=0 \tag{7}$$

and that

$$\nu=\frac{1}{2}, \quad \mu=\frac{E}{3}, \tag{8}$$

with $\nu$, $\mu$, and $E$ denoting the Poisson's ratio, shear modulus and Young's modulus of the rubber, respectively. The constitutive equations relating the stress and strain components then become

$$\varepsilon_{xx}=\frac{1}{E}\left[\sigma_{xx}-\frac{1}{2}(\sigma_{yy}+\sigma_{zz})\right], \quad \varepsilon_{yy}=\frac{1}{E}\left[\sigma_{yy}-\frac{1}{2}(\sigma_{xx}+\sigma_{zz})\right],$$

$$\varepsilon_{zz}=\frac{1}{E}\left[\sigma_{zz}-\frac{1}{2}(\sigma_{xx}+\sigma_{yy})\right], \tag{9}$$

$$\varepsilon_{xy}=\frac{3}{2E}\sigma_{xy}, \quad \varepsilon_{xz}=\frac{3}{2E}\sigma_{xz}, \quad \varepsilon_{yz}=\frac{3}{2E}\sigma_{yz}, \tag{10}$$

and the equilibrium equation which must be fulfilled in the $x$-direction is

$$\frac{\partial\sigma_{xx}}{\partial x}+\frac{\partial\sigma_{xy}}{\partial y}+\frac{\partial\sigma_{xz}}{\partial z}=0. \tag{11}$$

The block is of very large extent in the $y$-direction and it is supposed that each rectangular plane $z=$constant within the block remains plane and rectangular during the deformation. Therefore

$$v=0, \quad \frac{\partial u}{\partial y}=\frac{\partial w}{\partial x}=\frac{\partial w}{\partial y}=0 \tag{12}$$

and it follows from the incompressibility condition (7) that

$$\frac{\partial u}{\partial x}=-\frac{dw}{dz}. \tag{13}$$

By symmetry, $u=0$ at $x=0$ for all values of $z$, and hence

$$u=-x\frac{dw}{dz}. \tag{14}$$

Representations for the nonzero stress components at any point $P$ within the rubber can now be derived in terms of $w$ and its derivatives. Using Eqs. (9), (10), and (14) yields

$$\sigma_{yy}=\sigma_{xx}+\frac{2E}{3}\frac{dw}{dz}, \quad \sigma_{zz}=\sigma_{xx}+\frac{4E}{3}\frac{dw}{dz}, \quad \sigma_{zx}=-\frac{E}{3}x\frac{d^2w}{dz^2} \tag{15}$$

and the equilibrium Eq. (11) reduces to

$$\frac{\partial\sigma_{xx}}{\partial x}=\frac{E}{3}x\frac{d^3w}{dz^3}. \tag{16}$$

Integrating Eq. (16), and applying the boundary condition that $\sigma_{xx}=-F/A$ when $x=\pm b/2$, and substituting into Eq. $(15)_2$ results in

$$\sigma_{zz}=\frac{E}{3}\left[4\frac{dw}{dz}-\frac{1}{2}\left(\frac{b^2}{4}-x^2\right)\frac{d^3w}{dz^3}\right]-\frac{F}{A}. \tag{17}$$

In this loading case there is no imposed force in the $z$-direction per unit length in the $y$-direction and so

$$\int_{-b/2}^{b/2}\sigma_{zz}dx=0, \tag{18}$$

which, upon evaluation using Eq. (17), gives the differential equation governing $w$ as

$$\frac{d^3w}{dz^3}-\frac{48}{b^2}\frac{dw}{dz}=-\frac{36F}{EAb^2}. \tag{19}$$

Its general solution can be written as

$$w=c_1\cosh\alpha z+c_2\sinh\alpha z+\frac{3Fz}{4EA}+c_3, \tag{20}$$

with $c_1$, $c_2$, and $c_3$ being arbitrary constants, and

$$\alpha^2=\frac{48}{b^2}. \tag{21}$$

The constants $c_1$, $c_2$, and $c_3$ can be determined to fulfill the boundary conditions imposed at the two ends of the block. Since the block is assumed to be bonded to rigid end plates, $u=0$ at $z=0$ and $z=h$ for all $x$, and hence, from Eq. (14),

$$\frac{dw}{dz}=0 \quad \text{at } z=0 \text{ and } z=h. \tag{22}$$

Also,

$$w=0 \quad \text{at } z=0, \tag{23}$$

since the end at $z=0$ is regarded as fixed. When the general solution (20) is subjected to the conditions (22) and (23) it is found that the required solution can be written as

$$w=\frac{3F}{4EA}\left\{z-\frac{2}{\alpha}\frac{\sinh\frac{\alpha z}{2}\cosh\left[\frac{\alpha}{2}(h-z)\right]}{\cosh\frac{\alpha h}{2}}\right\}. \tag{24}$$

The magnitude of the axial displacement, $d_B$, of the end of the block at $z=h$ being sought is thus given by

$$d_B=\frac{3Fh}{4EA}\left(1-\frac{2}{\alpha h}\tanh\frac{\alpha h}{2}\right). \tag{25}$$

**4.2 Apparent Young's Modulus and Deformed Profile.** The apparent Young's modulus can now be determined. By superposition of the displacements (6) and (25) obtained above in Cases A and B, the axial end deflection $d=d_A+d_B$ of the block when it is subjected only to the axial load $F$ is given by

$$d=\frac{Fh}{A}\left[\frac{3}{4E}\left(1-\frac{2}{\alpha h}\tanh\frac{\alpha h}{2}\right)+\frac{1}{K}\right]. \tag{26}$$

Adopting the notation of Gent and Lindley [1], this can be written in terms of the "apparent Young's modulus," $E_a'$, as

$$d=\frac{Fh}{AE_a'}. \tag{27}$$

Recalling Eq. (21) yields the representation

$$\frac{1}{E_a'}=\frac{3}{4E}\left(1-\frac{S}{\sqrt{3}}\tanh\frac{\sqrt{3}}{S}\right)+\frac{1}{K}, \tag{28}$$

where, for a block of rectangular cross section in which the length is much greater than the width, the shape factor $S$ is approximately given by

$$S=\frac{b}{2h}. \tag{29}$$

When the material of the block is incompressible ($K=\infty$), it follows from Eq. (28), or by comparison with Eq. (3), that the apparent Young's modulus, $E_a$, for a block of incompressible rubber can be calculated exactly from the compact relationship

**Table 1 Percentage errors in using approximations for $E_a$**

| $S$ | 0.4 | 0.8 | 1.2 | 1.6 | 2.0 | 2.4 | 2.8 |
|---|---|---|---|---|---|---|---|
| Error in $E_a$ using relation (1), % | 10.78 | 9.78 | 7.19 | 5.16 | 3.77 | 2.83 | 2.19 |
| Error in $E_a$ using relation (32), % | −4.60 | −1.22 | −0.41 | −0.17 | −0.08 | −0.04 | −0.02 |

$$E_a=\frac{4E}{3\left(1-\frac{S}{\sqrt{3}}\tanh\frac{\sqrt{3}}{S}\right)}. \tag{30}$$

Numerical values of $E_a'$ and $E_a$ can be easily derived from Eqs. (28) and (30) with modern software. However, it is interesting to cite even more readily accessible elementary estimates, $E_a'^{\text{approx}}$ and $E_a^{\text{approx}}$, which can be deduced for them.

By expanding the hyperbolic tangent using the series representation given by Abramowitz and Stegun [13], Eq. (4.5.64), it can be shown that the relations (28) and (30) are approximated by

$$\frac{1}{E_a'^{\text{approx}}}=\frac{3}{4E(1.2+S^2)}+\frac{1}{K}, \tag{31}$$

$$E_a^{\text{approx}}=\frac{4E}{3}(1.2+S^2). \tag{32}$$

These are of the same form as, but are more accurate than, the relationships given by Eqs. (1) and (3) which were proposed by Gent and Lindley [1]. For example, $E_a^{\text{approx}}$ approximates increasingly more closely to the exact representation (30) for values of $S$ greater than about 0.23. Specifically, the percentage errors in using Eqs. (1) and (32), rather than Eq. (30), when $S=0.4$ are 10.8% and −4.6%, respectively, while when $S=2$ the corresponding errors are 3.8% and −0.1%. Further values are presented in Table 1.

Most of the analyses in previous papers have been founded on the assumption that the unloaded lateral surfaces will deform to have parabolic profiles. However, it follows from Eqs. (14) and (24) that in fact

$$u=-\frac{3Fx}{2EA}\,\frac{\sinh\frac{\alpha z}{2}\sinh\left[\frac{\alpha}{2}(h-z)\right]}{\cosh\frac{\alpha h}{2}}, \tag{33}$$

which when $x=\pm b/2$ gives an expression for the exact deformed shapes of the free edges of the block.

**4.3 Stresses.** The stress components created within the block by the application of the load $F$ alone can be calculated by the superposition of those in Cases A and B. These are derived explicitly from Eqs. (4), (17), (24), and (15) as

$$\sigma_{xx}=\frac{3F}{2A}\left(1-\frac{4x^2}{b^2}\right)\frac{\cosh\left[\alpha\left(z-\frac{h}{2}\right)\right]}{\cosh\frac{\alpha h}{2}},$$

$$\sigma_{yy}=\frac{F}{A}\left\{\frac{1}{2}-\left(\frac{6x^2}{b^2}-1\right)\frac{\cosh\left[\alpha\left(z-\frac{h}{2}\right)\right]}{\cosh\frac{\alpha h}{2}}\right\},$$

$$\sigma_{zz}=\frac{F}{A}\left\{1-\left(\frac{6x^2}{b^2}-\frac{1}{2}\right)\frac{\cosh\left[\alpha\left(z-\frac{h}{2}\right)\right]}{\cosh\frac{\alpha h}{2}}\right\},$$

$$\sigma_{zx}=\frac{F\alpha x}{4A}\,\frac{\sinh\left[\alpha\left(z-\frac{h}{2}\right)\right]}{\cosh\frac{\alpha h}{2}}. \tag{34}$$

Their maximum values occur on the bonded ends $z=0$ and $z=h$, where

$$\sigma_{xx}=\sigma_{yy}=\sigma_{zz}=\frac{3F}{2A}\left(1-\frac{4x^2}{b^2}\right),\quad \sigma_{zx}=\mp\frac{F\alpha x}{4A}\tanh\frac{\alpha h}{2}. \tag{35}$$

## 5 Circular Block

**5.1 Case B: Loaded Lateral Surface.** A similar analysis can be applied to study an incompressible block of circular cross section of radius $a$, with the cylindrical polar coordinates $(r,\theta,z)$ of a point $P$ related to its rectangular Cartesian coordinates by $x=r\cos\theta$, $y=r\sin\theta$, $z=z$. Suppose that it is subjected only to lateral loading on the surface $r=a$ by a radial stress $-\sigma_L$.

The displacement components at $P$ are denoted by $u_r$, $u_\theta$, and $u_z$, and the strain and stress components by $\varepsilon_{ij}$ and $\sigma_{ij}$, where $i$, $j=r$, $\theta$ or $z$, with the corresponding constitutive equations relating them. The loading is axisymmetrical and plane cross sections normal to the $z$-axis are assumed to remain plane. Therefore,

$$u_\theta=0,\quad \frac{\partial u_r}{\partial\theta}=\frac{\partial u_z}{\partial\theta}=\frac{\partial u_z}{\partial r}=0. \tag{36}$$

The incompressibility condition implies that

$$\varepsilon_{rr}+\varepsilon_{\theta\theta}+\varepsilon_{zz}=0, \tag{37}$$

and the equilibrium equation which must hold in the radial direction ([11], Eq. (11.39)) is

$$\sigma_{rr}-\sigma_{\theta\theta}+r\frac{\partial\sigma_{rr}}{\partial r}+r\frac{\partial\sigma_{rz}}{\partial z}=0. \tag{38}$$

It follows from Eqs. (36) and (37) that

$$\frac{\partial}{\partial r}(ru_r)=-r\frac{du_z}{dz}, \tag{39}$$

and hence, since $u_r=0$ at $r=0$ for all values of $z$,

$$u_r=-\frac{r}{2}\frac{du_z}{dz}. \tag{40}$$

The nonzero stress components within the block can now be written in terms of $u_z$ and its derivatives. Equation (40) and the constitutive equations yield

$$\sigma_{rr}=\sigma_{\theta\theta},\quad \sigma_{zz}=\sigma_{rr}+E\frac{du_z}{dz},\quad \sigma_{zr}=-\frac{E}{6}r\frac{d^2u_z}{dz^2} \tag{41}$$

and the equilibrium Eq. (38) gives

$$\frac{\partial\sigma_{rr}}{\partial r}=\frac{E}{6}r\frac{d^3u_z}{dz^3}. \tag{42}$$

Imposing the boundary condition that $\sigma_{rr}=-F/A$ when $r=a$ on the integral of Eq. (42) and substituting into Eq. $(41)_2$ yields

**Table 2 Percentage errors in using approximations for $E_a$**

| $S$ | 0.4 | 0.8 | 1.2 | 1.6 | 2.0 | 2.4 | 2.8 |
|---|---|---|---|---|---|---|---|
| Error in $E_a$ using relation (2), % | 10.92 | 7.61 | 4.77 | 3.11 | 2.15 | 1.56 | 1.18 |
| Error in $E_a$ using relation (56), % | $-2.57$ | $-0.50$ | $-0.14$ | $-0.05$ | $-0.02$ | $-0.01$ | $-0.01$ |

$$\sigma_{zz}=E\left[\frac{du_z}{dz}-\frac{1}{12}(a^2-r^2)\frac{d^3u_z}{dz^3}\right]-\frac{F}{A}. \tag{43}$$

However, as there is no externally applied axial force,

$$\int_0^a \sigma_{zz} r\,dr=0, \tag{44}$$

which leads to the governing differential equation for $u_z$ as

$$\frac{d^3u_z}{dz^3}-\frac{24}{a^2}\frac{du_z}{dz}=-\frac{24F}{EAa^2}. \tag{45}$$

Since the rubber is bonded to rigid end plates, $u_r=0$ at $z=0$ and $z=h$ for all $r$, and thus, from Eq. (40)

$$\frac{du_z}{dz}=0 \quad \text{at } z=0 \text{ and } z=h. \tag{46}$$

Moreover the end at $z=0$ is fixed, so

$$u_z=0 \quad \text{at } z=0. \tag{47}$$

The solution of Eq. (45) which satisfies the conditions (46) and (47) can be written as

$$u_z=\frac{F}{EA}\left\{ z-\frac{2}{\beta}\frac{\sinh\frac{\beta z}{2}\cosh\left[\frac{\beta}{2}(h-z)\right]}{\cosh\frac{\beta h}{2}}\right\}, \tag{48}$$

where

$$\beta^2=\frac{24}{a^2}. \tag{49}$$

The distance, $d_B$, through which the end of the block at $z=h$ is displaced is therefore given by

$$d_B=\frac{Fh}{EA}\left(1-\frac{2}{\beta h}\tanh\frac{\beta h}{2}\right). \tag{50}$$

**5.2 Apparent Young's Modulus and Deformed Profile.** Representations for the apparent Young's modulus can now be determined analogously to those for the rectangular block above. By superposition of the distances (6) and (50), the axial end deflection $d$ of the circular block when subjected to the axial load $F$ is

$$d=\frac{Fh}{A}\left[\frac{1}{E}\left(1-\frac{2}{\beta h}\tanh\frac{\beta h}{2}\right)+\frac{1}{K}\right]. \tag{51}$$

Equations (27) and (49) then yield the representation

$$\frac{1}{E_a'}=\frac{1}{E}\left(1-S\sqrt{\frac{2}{3}}\tanh\frac{1}{S}\sqrt{\frac{3}{2}}\right)+\frac{1}{K}, \tag{52}$$

where, for a block of circular cross section, the shape factor $S$ is

$$S=\frac{a}{2h}. \tag{53}$$

The apparent Young's modulus, $E_a$, for a circular block of incompressible rubber can consequently be written as

$$E_a=\frac{E}{1-S\sqrt{\frac{2}{3}}\tanh\frac{1}{S}\sqrt{\frac{3}{2}}}. \tag{54}$$

Gent and Lindley [1] presented the expressions (2) and (3) for $E_a$ and $E_a'$. However, the series expansions of Eqs. (54) and (52) yield refined approximations, $E_a^{\text{approx}}$ and $E_a'^{\text{approx}}$, for them. It is found that the results (52) and (54) are closely approximated by

$$\frac{1}{E_a'^{\text{approx}}}=\frac{1}{E(1.2+2S^2)}+\frac{1}{K}, \tag{55}$$

$$E_a^{\text{approx}}=E(1.2+2S^2). \tag{56}$$

The relation (56), for example, provides a better estimate to the exact representation (54) than that given by Gent and Lindley for values of $S$ greater than about 0.16. Comparative values for the percentage errors in using Eq. (56) as opposed to (2) for evaluating $E_a$, which is given exactly by the relation (54), are displayed in Table 2.

It follows from Eqs. (40) and (48) that

$$u_r=-\frac{Fr}{EA}\frac{\sinh\frac{\beta z}{2}\sinh\left[\frac{\beta}{2}(h-z)\right]}{\cosh\frac{\beta h}{2}}. \tag{57}$$

Obviously, the deformed profile of the curved outer surface of the block can then be deduced by putting $r=a$. This has previously been assumed to be parabolic. However, it is shown in Section 6 that this is only appropriate for large values of $S$.

**5.3 Stresses.** By superposition of those in Cases A and B, the stress components within the block that are created by the applied load $F$ alone can be determined from Eqs. (4), (40), (48), and (41) in the forms

$$\sigma_{rr}=\sigma_{\theta\theta}=\frac{2F}{A}\left(1-\frac{r^2}{a^2}\right)\frac{\cosh\left[\beta\left(z-\frac{h}{2}\right)\right]}{\cosh\frac{\beta h}{2}},$$

$$\sigma_{zz}=\frac{F}{A}\left\{1+\left(1-\frac{2r^2}{a^2}\right)\frac{\cosh\left[\beta\left(z-\frac{h}{2}\right)\right]}{\cosh\frac{\beta h}{2}}\right\},$$

$$\sigma_{rz}=\frac{F\beta r}{6A}\frac{\sinh\left[\beta\left(z-\frac{h}{2}\right)\right]}{\cosh\frac{\beta h}{2}}. \tag{58}$$

Their maximum values occur on the bonded ends $z=0$ and $z=h$, where

$$\sigma_{rr}=\sigma_{\theta\theta}=\sigma_{zz}=\frac{2F}{A}\left(1-\frac{r^2}{a^2}\right), \quad \sigma_{rz}=\mp\frac{F\beta r}{6A}\tanh\frac{\beta h}{2}. \tag{59}$$

It is also interesting to note that at the central cross section, where $z=h/2$, $\sigma_{rz}=0$ and as the height $h$ of the block becomes large $\sigma_{rr}=\sigma_{\theta\theta}\rightarrow 0$ and $\sigma_{zz}\rightarrow F/A$, indicating a uniform stress.

## 6 Numerical Results and Conclusions

There is clearly a close similarity between the techniques and analyses presented in Sections 4 and 5. However, in this section the discussion is concentrated on the implications of the circular block results for easy comparison with the available experimental and finite element approach investigations.

The deformed profiles of the curved lateral sides of circular blocks are given precisely by Eq. (57) when $r=a$. But it is convenient to introduce the non-dimensionalized fractional radial displacement component of the free surface per unit axial strain, $u_a/ae$, as a suitable measure for the comparison of the profiles of blocks having various shape factors. Here the fractional radial displacement component of the free surface at a height $z$ is $u_a/a$ with $u_a=u_r$ evaluated at $r=a$, and $e=d/h$ is a measure of the axial strain. Recalling Eqs. (57), (51), (49), and (53) leads to the representation, in terms of the shape factor $S$,

$$\frac{u_a}{ae}=-\frac{\sinh\left[\frac{1}{S}\sqrt{\frac{3}{2}}\left(\frac{z}{h}\right)\right]\sinh\left[\frac{1}{S}\sqrt{\frac{3}{2}}\left(1-\frac{z}{h}\right)\right]}{\left(1+\frac{E}{K}\right)\cosh\left(\frac{1}{S}\sqrt{\frac{3}{2}}\right)-S\sqrt{\frac{2}{3}}\sinh\left(\frac{1}{S}\sqrt{\frac{3}{2}}\right)}. \tag{60}$$

As expected, the values of $u_a/ae$ are clearly symmetrical about $z/h=0.5$. The multiplicative negative sign indicates that for a tensile load the profile will be waisted inwards. However, for a compressive load it will analogously bulge outwards.

Graphs of $-u_a/ae$ as a function of $z/h$ are presented in Figs. 3(*a*) and 3(*b*) for a range of values of $S$ with $E/K$ having the value $19\times10^{-4}$. Its maximum value is found to occur on the central cross-sectional plane $z=h/2$ when $S\approx1.6$. It is obvious that the graphs when $S=0.1$ and $S=0.2$ cannot be approximated at all reasonably by parabolic curves. Careful analysis, in fact, shows that the accuracy of fit between the graphs and the exact parabolic curves drawn through the points $z=0$, $z=h$ and the apices of the graphs increases as $S$ increases. Comparisons of these are displayed in Figs. 4(*a*) and 4(*b*) for illustration when $S=0.1$ and $S=1.6$.

Gent and Lindley [1], and other authors, derived relations for the apparent Young's modulus based upon the assumption of a parabolic profile. It was found experimentally, however, by Mott and Roland [8] that slender rubber circular cylinders (with $S$ between about 0.11 and 0.27) assume a much flatter profile. A comparison of the Gent and Lindley prediction with the experimental results is given by Mott and Roland in their Fig. 2, and they conclude that "the assumption of a parabolic profile is erroneous." There is a striking resemblance between the flattish curves in Fig. 3(*a*) here and the pattern of their experimental values. Thus the analysis of Section 5 and the graphs presented therein demonstrate theoretically for the first time that it is indeed not adequate for small values of $S$ to assume parabolic profiles for circular blocks. The assumption can be shown to be similarly invalid for rectangular blocks from the results of Section 4.

Gent and Lindley [1] (Fig. 1) compared their predicted values of the apparent Young's modulus, $E_a'^{(\mathrm{GL})}$, as given by Eqs. (2) and (3), for a circular block in compression with experimental measurements. They observed that for the smaller values of $S$ "the measured values of $E_a'$ are seen to fall somewhat below those predicted." Bearing in mind the above discussion, it is reasonable to presume that this discrepancy is due to the assumption of a parabolic profile. This is indeed confirmed by comparing the values of $E_a'$ given exactly by the representation (52) with those, $E_a'^{(\mathrm{GL})}$, calculated from Eq. (3) using the Gent and Lindley approximation $E_a^{(\mathrm{GL})}$ of Eq. (2). The realistic data used here are $E=19$ kg/cm$^2$ and $K=10^4$ kg/cm$^2$, as adopted by Gent and Lindley [1]. The values using Eq. (52) are found to be significantly greater than those using the approximation (2) for values of $S$ less than 2. They are presented in Fig. 5 when plotted on a logarithmic scale for direct comparison with Fig. 1 of Gent and Lindley [1]. It is assumed throughout that blocks of small shape factor do not experience instability when in compression.

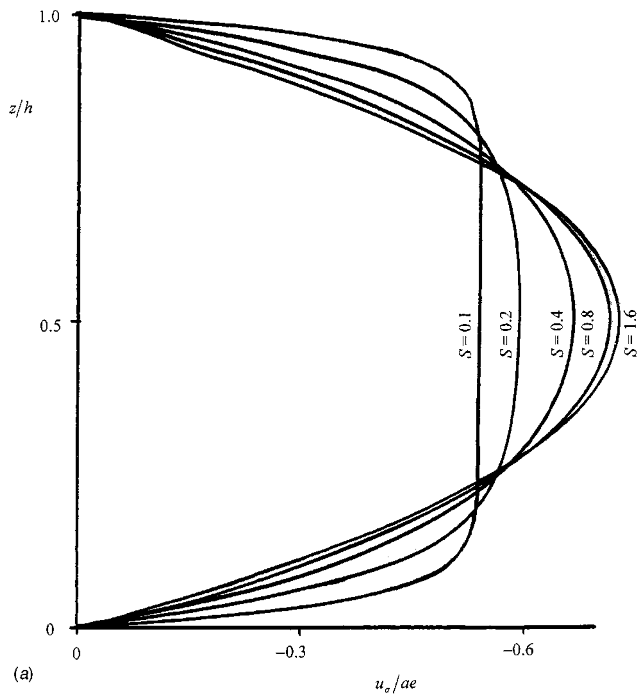


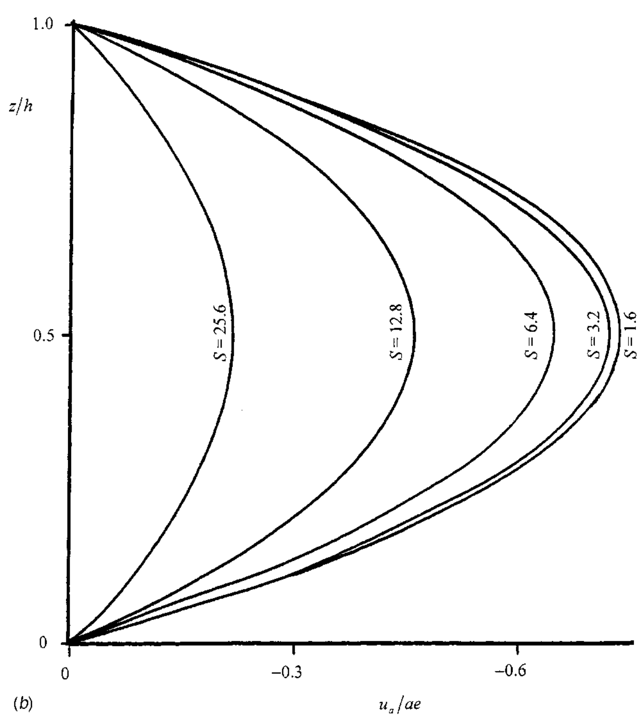


**Fig. 3 Comparison of the deformed profiles (*a*) when $S=0.1$, 0.2, 0.4, 0.8 and 1.6 (*b*) when $S=1.6$, 3.2, 6.4, 12.8 and 25.6**

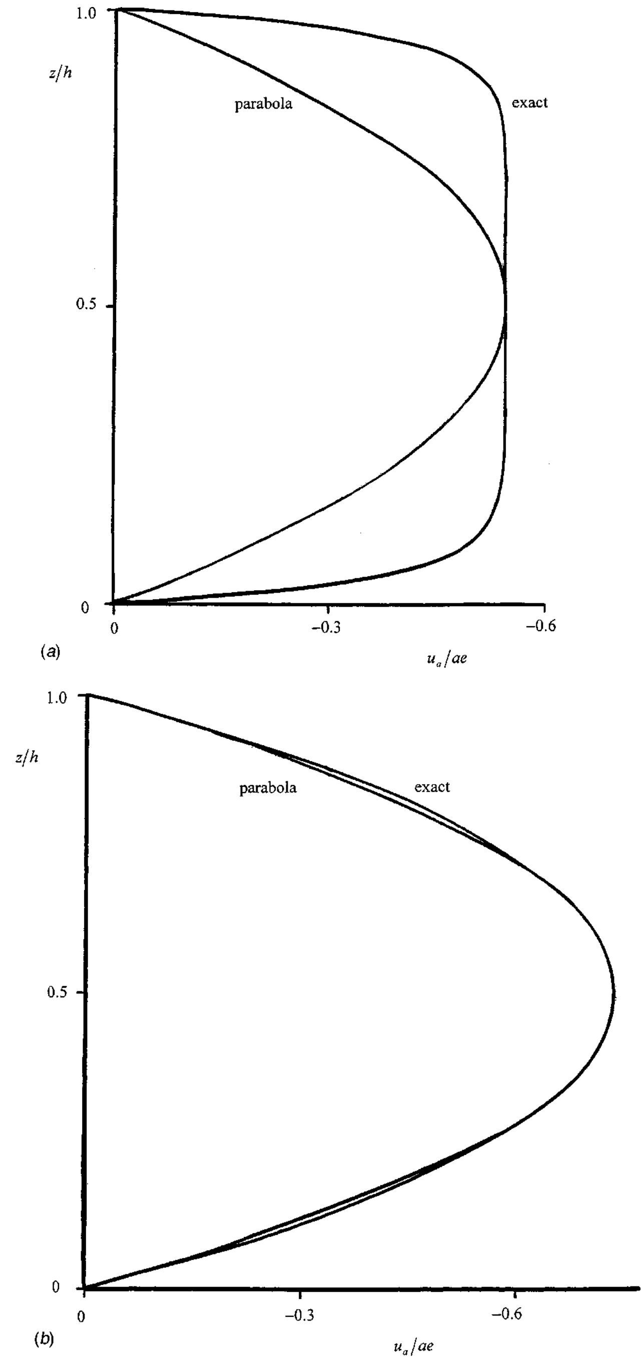


**Fig. 4 Comparison of the deformed profiles with parabolic curves (*a*) when $S=0.1$ (*b*) when $S=1.6$**

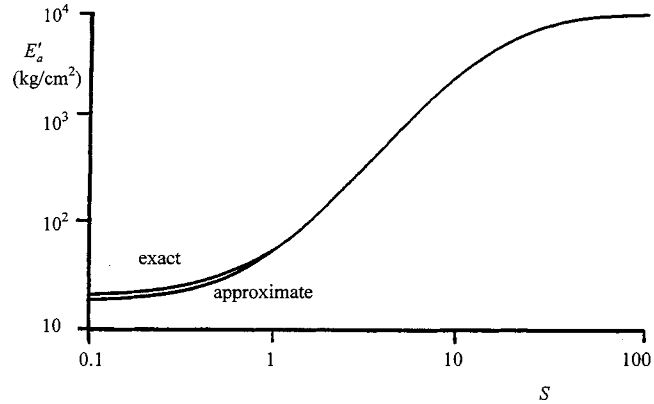


**Fig. 5 Comparison of the exact values of $E'_a$ with the approximate values $E'^{(GL)}_a$ as $S$ varies**

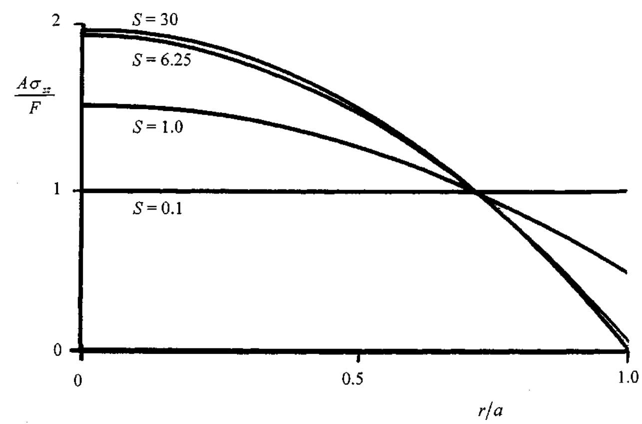


**Fig. 6 Variation of $A\sigma_{zz}/F$ with $r/a$ at the mid-height section**

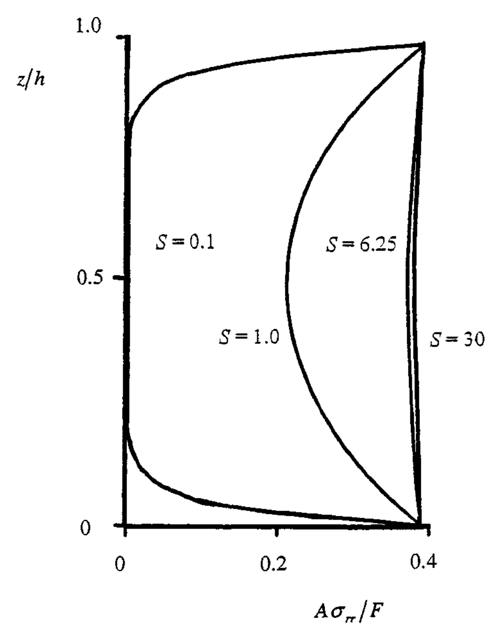


**Fig. 7 Variation of $A\sigma_{rr}/F$ with $z/h$ at $r/a=0.9$**

Imbimbo and De Luca [9] provided a comparison of the influence of varying the shape factor upon the stress distribution within a circular block between a finite element model and one based upon the approximation (2) of Gent and Lindley [1]. They concluded that the approximate solution only "gives a satisfactory estimation for defining all the stress distributions within the device" for values of $S>20$. Particular emphasis is given to studying the normal stresses in the central rubber layer and at the rubber-steel interfaces in their Figs. 4 and 8. The corresponding graphs of the nondimensional normal stresses $\sigma_{zz}/(F/A)$ at $z=h/2$ and $z=0$ or $z=h$ plotted against $r/a$ can readily be drawn using the exact representations (58) and (59) in Section 5 for a range of values of $S$.

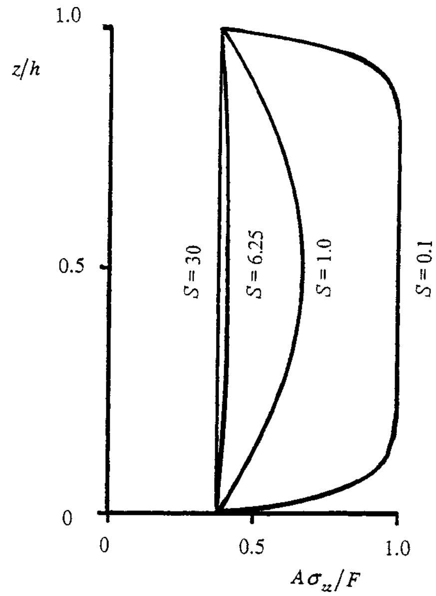


**Fig. 8 Variation of $A\sigma_{zz}/F$ with $z/h$ at $r/a=0.9$**

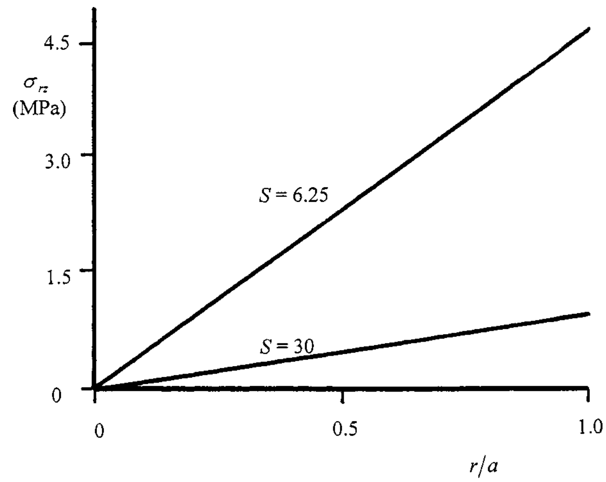


**Fig. 9 Variation of $\sigma_{rz}$ with $r/a$ at the bonded ends**

At the bonded ends, the variation of $A\sigma_{zz}/F$ $(=A\sigma_{rr}/F$ $=A\sigma_{\theta\theta}/F)$ with $r/a$ is given by the parabolic curve $(59)_1$. This, in fact, is clearly independent of the shape factor $S$, although Imbimbo and De Luca [9] (Figs. 5–8) apparently failed to realize this in presenting their virtually identical graphs.

The variation of $A\sigma_{zz}/F$ with $r/a$ at the mid-height section $z=h/2$ is illustrated in Fig. 6, using Eq. $(58)_2$ for $S=0.1$, 1.0, 6.25 and 30. For larger values of $S$ (as presented by Imbimbo and De Luca [9] (Fig. 4)), the curves become indistinguishable from those for $S=30$. For $S=0.1$ the stress distribution has become constant across the section.

In Figs. 7 and 8, the variation of $A\sigma_{rr}/F$ and $A\sigma_{zz}/F$ with the height, $z/h$, up the block are depicted for illustration at the radial position $r/a=0.9$, for $S=0.1$, 1.0, 6.25, and 30. Again it is clear that the curves virtually coalesce for the larger values of $S$. The prerequisite for a parabolic distortion of the lateral surfaces is that $\partial\sigma_{rr}/\partial z=0$. This can be seen from Fig. 7 to be satisfied approximately for the larger values of $S$, giving further confirmation of the comments made above about the validity of the parabolic surface assumption. Additionally Figs. 7 and 8 demonstrate that $\sigma_{zz}\approx\sigma_{rr}$ $(=\sigma_{\theta\theta})$ for the larger values of $S$. From Figs. 6, 7, and 8 it can be inferred that for a block with $S=0.1$ when $0.2<z/h<0.8$ the radial and tangential stresses are approximately zero and the axial stress is approximately uniform across the section and equal to $F/A$.

The variation with $r/a$ of the shear stress, $\sigma_{rz}$, at the bonded end $z=h$, as calculated from the expression $(59)_2$, is shown in Fig. 9. The graphs are drawn for $S=6.25$ and $S=30$, with $F/A=30$ MPa for direct comparison with those provided by the model of Imbimbo and De Luca [9], (Figs. 11 and 12). It should, of course, be pointed out here that the theoretically predicted maximum values of the shear stress occurring at the force-free outer lateral surface cannot physically exist, and must actually decay rapidly to zero very near to this surface. They arise as a consequence of assuming that, during axial strain, plane sections of the block remain plane. This cannot be valid at the free outer surfaces.

## References


[1] Gent, A. N., and Lindley, P. B., 1959, "The Compression of Bonded Rubber Blocks," Proc. Inst. Mech. Eng., **173**, pp. 111–122.

[2] Gent, A. N., 1994, "Compression of Rubber Blocks," Rubber Chem. Technol., **67**, pp. 549–558.

[3] Muhr, A. H., and Thomas, A. G., 1989, "Allowing for Non-linear Stress-Strain Relationships of Rubber in Force-Deformation Calculations. Part 1: Compression Stiffness of Bonded Rubber Blocks," N R Tech., **20**, pp. 8–14.

[4] Payne, A. R., 1959, communications, "The Compression of Bonded Rubber Blocks," Proc. Inst. Mech. Eng., **173**, pp. 120–121.

[5] Hirst, A. J., 1959, communications, "The Compression of Bonded Rubber Blocks," Proc. Inst. Mech. Eng., **173**, p. 119.

[6] Horton, J. M., Gover, M. J. C., and Tupholme, G. E., 2000, "Stiffness of Rubber Bush Mountings Subjected to Radial Loading," Rubber Chem. Technol., **73**, pp. 253–264.

[7] Horton, J. M., Gover, M. J. C., and Tupholme, G. E., 2000, "Stiffness of Rubber Bush Mountings Subjected to Tilting Deflection," Rubber Chem. Technol., **73**, pp. 619–633.

[8] Mott, P. H., and Roland, C. M., 1995, "Uniaxial Deformation of Rubber Cylinders," Rubber Chem. Technol., **68**, pp. 739–745.

[9] Imbimbo, M., and De Luca, A., 1998, "F. E. Stress Analysis of Rubber Bearings Under Axial Loads," Comput. Struct., **68**, pp. 31–39.

[10] Sokolnikoff, I. S., 1956, *The Mathematical Theory of Elasticity*, McGraw-Hill, New York.

[11] Spencer, A. J. M., 1980, *Continuum Mechanics*, Longman, London.

[12] Hunter, S. C., 1983, *Mechanics of Continuous Media*, 2nd Ed., Halsted, New York.

[13] Abramowitz, M., and Stegun, I. A., Eds., 1965, *Handbook of Mathematical Functions*, Dover, New York.

**Z. Q. Qian**
School of Mechanical, Materials, Manufacturing Engineering and Management, University of Nottingham, University Park, Nottingham NG7 2RD, UK

**A. R. Akisanya[1]**
e-mail: a.r.akisanya@eng.abdn.ac.uk

**D. S. Thompson**

Department of Engineering, University of Aberdeen, Aberdeen AB24 3UE, UK

# Stress Behavior at the Interface Junction of an Elastic Inclusion

*The stress distribution at the interface junction of an elastic inclusion embedded in a brittle matrix is examined. Solutions are derived for the stress and displacement fields near the junction formed by the intersection of the interfaces between the inclusion and the matrix. The stress field consists of symmetric (mode I) and skew-symmetric (mode II) components. The magnitude of the intensity factor associated with each mode of deformation is determined using a combination of the finite element method and a contour integral. The numerical results of the stresses near the interface junction of two different inclusion geometries show that the asymptotic solutions of the stresses are in agreement with those from the finite element prediction when higher-order terms are considered. The implications of the results for the failure of particle-reinforced and two-phase brittle materials are discussed.* [DOI: 10.1115/1.1507765]

## Introduction

Particulate composites, consisting of particles of one or more materials imbedded in a matrix of another material, are used for a wide range of engineering applications. In civil engineering, for example, aggregate-bitumen composite is used to accommodate the lateral movement of highway bridges while mortar-aggregate composite is widely used in building and construction. The use of plastic encapsulated microcircuits in surface mount technology and in avionics is becoming increasingly popular; the microcircuit is encapsulated with epoxy resin filled with fused silica.

In these applications, and many others, the integrity of the interfaces between the inclusion and the matrix material is paramount to the performance of the product. The debonding of the aggregates from the bitumen matrix, for example, reduces the tensile strength of the composite and can lead to the ingress of water and a further acceleration of the failure because of the freezing and thawing of the condensed moisture. Similarly, debonding at the microchip-encapsulant interface can cause immediate or intermittent electrical failure and can have negative effect on the long-term performance of the microchip by providing a site for the collection of moisture and ionic contaminants.

The mismatch in the elastic and thermal properties of an inclusion and a matrix may lead to the development of stress singularity at the corners of nonspheroid inclusions embedded in an elastic matrix. The corners are the intersection of two or more interfaces between an inclusion and the matrix, hereafter referred to as *interface junctions*. The debonding of the inclusions from the matrix is a combined effect of the stress singularity at the interface junctions and relatively low inclusion/matrix interfacial strength. A detailed characterization of the stress field near the junctions is needed to understand the role of material properties and inclusion geometry on the initiation of debonding in particulate composites.

The analysis of stress singularities at a wedge tip and at an interface corner (i.e., the intersection of an interface with a traction-free surface) of bimaterial joints has been examined by various authors, see for example, Refs. [1–4]. In many cases, the stress field at a traction-free edge is of the form $K_f r^{\lambda-1}$, where $K_f$ is the free-edge stress intensity factor, $(\lambda-1)$ is the order of the stress singularity and $r$ is the radial distance from the singular point. Both $K_f$ and $\lambda$ depend on the elastic and thermal properties of the materials and on the joint geometry. In addition, $K_f$ depends on the magnitude of the applied load. The solution of $\lambda$ and the calibration for $K_f$ for a wide range of bimaterial joint geometries exist in the literature ([1–5]). The magnitude of $\lambda$ is obtained from the asymptotic analysis of the elastic problem while the free-edge intensity factor $K_f$ is determined either by matching the theoretical solution to the finite element solution ([3]) or using a combination of finite element solution and a contour integral ([4,6]).

In contrast to the detailed discussion in the literature on the characteristics of the stress singularity at the free-edge of various bimaterial joint geometries, the analysis of the stress distribution near the interface junctions of inclusions imbedded in another material is relatively nonexistence in the literature. Chen and Nisitani [7] have used the body force method to determine the stress field near the interface junction of an inclusion embedded in an infinite plate, and subjected to a wide range of remote mechanical loading; including uniaxial tension, in-plane shear, and biaxial tension. The stress field was expressed as a sum of two deformation modes, one of which is symmetric and the other skew-symmetric about a line bisecting the inclusion wedge angle. Chen and Nisitani [7] considered only the stress field associated with the smallest eigenvalue; higher-order terms and the stress field associated with temperature change were not considered. Pahn and Earmme [8] have recently examined the stress field near the interface junction of a partially debonded inclusion within a brittle matrix. Following an approach originally proposed by Akisanya and Fleck [9], Pahn and Earmme [8] determined the crack-tip stress intensity factors as a function of the intensity of the singularity at the junction. More recently, Reedy and Guess [10] have analyzed the stress field near the interface junction of a square *rigid* inclusion embedded within an epoxy resin and subjected to an axisymmetric loading. The solution presented by Reedy and Guess [10] is applicable, for example, to plastic encapsulated microcircuits where the matrix is more compliant than the inclusion. However, the assumption of a rigid inclusion may not be appropriate for cases where the stiffness of the inclusion is of the same order of magnitude as that of the matrix.

In this paper we investigate the stress distribution at the interface junction of an elastic inclusion embedded in an elastic matrix and subjected to both mechanical and thermal loading (Fig. 1(*a*)). Closed-form solution of the stress field is obtained as a function of the inclusion wedge angle $\gamma$ and of the inclusion elastic and thermal properties relative to those of the matrix material. The intensity of the singularity at the interface junction is determined for both the dominant and higher-order terms using the contour integral approach. The solution is compared with the few cases in the literature, obtained by the body force method ([7]) and by the

[1]To whom correspondence should be addressed.

Contributed by the Applied Mechanics Division of THE AMERICAN SOCIETY OF MECHANICAL ENGINEERS for publication in the ASME JOURNAL OF APPLIED MECHANICS. Manuscript received by the ASME Applied Mechanics Division, July 25, 2001; final revision, July 4, 2002. Associate Editor: D. A. Kouris. Discussion on the paper should be addressed to the Editor. Prof. Robert M. McMeeking, Department of Mechanical and Environmental Engineering University of California–Santa Barbara, Santa Barbara, CA 93106-5070, and will be accepted until four months after final publication of the paper itself in the ASME JOURNAL OF APPLIED MECHANICS.

  

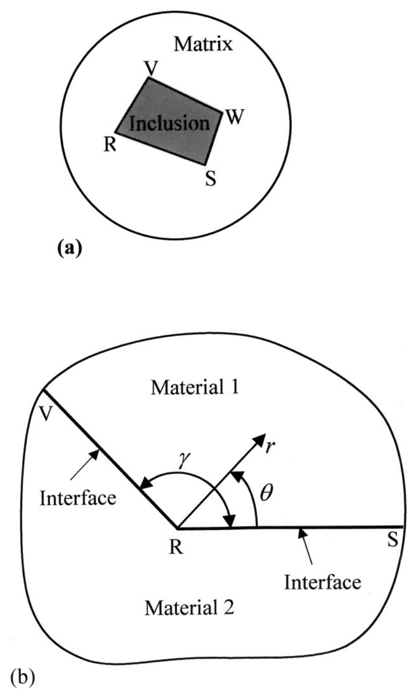


**Fig. 1 (*a*) A quadrilateral elastic inclusion embedded in a brittle matrix; (*b*) a magnified view of interface junction R, showing the local coordinates**

extrapolation method ([10]). The consideration of thermal loading and higher-order terms for a wide range of inclusion/matrix properties will fill the gap that presently exists in the analysis of the stress field near interface junctions. Although the integral method has been used in the past to evaluate the free-edge stress intensity factors ([6,9,11]), a different methodology is needed for the method to be applied to the analysis of stress singularity at interface junctions because the stress distribution at an interface junction is different from that near a free-edge.

## Asymptotic Solution

A schematic diagram of an inclusion embedded in another material is shown in Fig. 1(*a*). For simplicity the inclusion is assumed to have a quadrilateral cross section and the wedge angle at the interface junction of interest is denoted by $\gamma$. Both the inclusion and the matrix material are assumed to be elastic, isotropic and homogeneous, and the two materials are perfectly bonded. When the composite (i.e., inclusion and matrix material) is subjected to a remote mechanical loading and/or a uniform change in temperature, a stress singularity may develop at each of the interface junctions of the inclusion depending on the relative properties of the materials.

A magnified view of one of the interface junctions, labeled R, is shown in Fig. 1(*b*). Plane polar coordinate system ($r$, $\theta$) centred at interface junction R is used to describe the local stresses and displacements. The region $0 \leqslant \theta \leqslant \gamma$ is occupied by the inclusion (material 1) while the region $\gamma < \theta < 2\pi$ is occupied by the matrix (material 2). Plane-strain conditions are assumed in the analysis, however, the equivalent plane stress solution can be obtained from the results presented in this paper by making appropriate substitution for the modulus and the Poisson's ratio.

It is shown in the Appendix that when the geometry of the two-phase material is symmetric about the plane $\theta = \gamma/2$, the stresses and displacements near junction R can be decoupled into symmetric (mode I) and skew-symmetric (mode II) components. For a wide range of material combinations, these stresses and displacements are given by

$$\sigma_{kl} = \sum_{p=1}^{N} K_j^{(p)} r^{\omega_p - 1} f_{kl}^{(p)} + \sum_{q=1}^{M} K_j^{(q)} r^{\delta_q - 1} f_{kl}^{(q)} + \sigma_{klo}$$

$$u_k = \sum_{p=1}^{N} K_j^{(p)} r^{\omega_p} g_k^{(p)} + \sum_{q=1}^{M} K_j^{(q)} r^{\delta_q} g_k^{(q)} + u_{ko} \qquad (1)$$

where $(k,l) \equiv (r,\theta)$, $\omega_p$ is the eigenvalue of the symmetric stress field with a corresponding interface-junction stress intensity factor $K_j^{(p)}$, and $\delta_q$ is the eigenvalue of the skew-symmetric stress field with interface-junction stress intensity factor $K_j^{(q)}$. Note that subscript $j$ denotes *junction*; this distinguishes the interface-junction stress intensity factor from the free-edge stress intensity factor $K_f$ for characterizing the singularity where an interface intersects a traction-free surface. $f_{kl}^{(p)}$, $f_{kl}^{(q)}$, $g_k^{(p)}$, and $g_k^{(q)}$ are nondimensional functions of material properties, polar coordinate $\theta$ and wedge angle $\gamma$, while parameters $N$ and $M$ are the number of eigenvalues associated with the modes I and II fields, respectively. The full expressions for these functions are given in the Appendix.

The eigenvalues $\delta_q (q=1,M)$ is always real while $\omega_p (p=1,N)$ may be complex depending on the wedge angle $\gamma$ and the material properties. However, $\omega_p$ is real when $\beta(\alpha-\beta)>0$, where $\alpha$ and $\beta$ are the Dundurs [12] elastic mismatch parameters defined in Eq. (14). The stress field in Eq. (1) is only applicable to material combinations with real eigenvalues, and this is the focus of the present study. The stress field is singular when $0.5<\omega_p<1$ for the symmetric field (or $0.5<\delta_q<1$ for the skew-symmetric field) and nonsingular when $\omega_p>1$ (or $\delta_q>1$). In addition to the stress field associated with each eigenvalue, it is possible to have a nonsingular constant stress near the interface junction depending on the inclusion geometry and the mismatch in the thermal properties of the materials. The nonsingular constant stress field and the corresponding displacement are denoted, respectively, by $\sigma_{klo}$ and $u_{ko}$ in Eq. (1). These terms are zero when the two-phase material is subjected only to remote mechanical loading and finite when subjected to a uniform change in temperature.

For a wedge angle $\gamma=0$ and inclusion shear modulus $\mu_1=0$ and Poisson's ratio $\nu_1=0$, the eigenvalues are $\omega_1=\delta_1=0.5$. Consequently, Eq. (1) reduces to the conventional mixed-mode crack-tip fields for a crack in a monolithic material.

The interface-junction stress intensity factors $K_j^{(p)}$ and $K_j^{(q)}$ ($p=1,N$; $q=1,M$) are the only unknown parameters in Eq. (1). Each of these intensity factors is defined such that the tangential stress associated with a particular eigenvalue is given by

$$\sigma_{\theta\theta}^{(p)} = K_j^{(p)} r^{\omega_p - 1} \quad (\text{at } \theta=0 \text{ for the mode I field}) \qquad (2a)$$

$$\sigma_{\theta\theta}^{(q)} = K_j^{(q)} r^{\delta_q - 1} \quad (\text{at } \theta=0 \text{ for the mode II field}). \qquad (2b)$$

Note that the interfaces which form the inclusion wedge of interest are along $\theta=0$ and $\theta=\gamma$, where $\gamma$ is the inclusion wedge angle. The definition in Eq. (2) is different from that used by Chen and Nisitani [7] and by Reedy and Guess [10], where the intensity factors are defined relative to the tangential stress along the plane that bisects the inclusion wedge angle. The magnitude of the interface-junction stress intensity factors depends on the inclusion wedge angle $\gamma$, elastic and thermal properties of the inclusion and matrix, and on the magnitude of the applied loading. The full description of the stress field in the vicinity of an interface junction requires knowledge of both the eigenvalues and the associated intensity factors. In addition, the onset of failure at a junction can be predicted based on a critical value of the intensity factor at the interface junction ([13,14]).

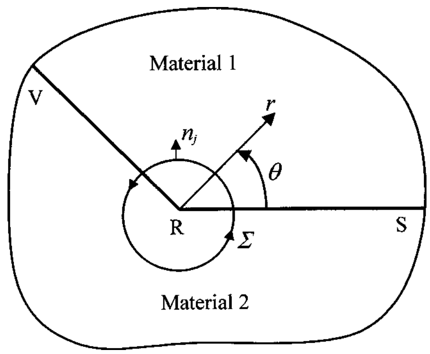


**Fig. 2 A closed integration path Σ around interface junction R**

## Evaluation of the Interface Junction Stress Intensity Factors

The interface-junction stress intensity factor associated with each of the eigenvalues is determined using a combination of a path-independent contour integral and the finite element solution. This method has been applied in the past to bonded joint geometries with single eigenvalue ([4]). The stresses in the vicinity of the interface junction of the two-phase material under consideration are not just singular with higher-order terms; they are also mixed-mode, consisting of symmetric and skew-symmetric fields. A summary of how the path-independent integral approach can be used to evaluate the interface-junction stress intensity factor in such situation is given below.

In order to evaluate the interface-junction stress intensity factor $K_j^{(p)}$ associated with an eigenvalue $\omega_p$ for the symmetric field, consider an integral around a path $\Sigma$ enclosing the interface junction, as shown in Fig. 2,

$$I(\omega_p)=\oint_{\Sigma}[\sigma_{kl}u_k^{(p)*}-\sigma_{kl}^{(p)*}u_k]n_k ds. \tag{3}$$

Here, $(k,l)\equiv(r,\theta)$ are the plane polar coordinates centred at the interface junction R of interest, $(\sigma_{kl},u_k)$ are the total stresses and displacements given in Eq. (1), $(\sigma_{kl}^{(p)*},u_k^{(p)*})$ are auxiliary stress and displacement fields associated with the eigenvalue $\omega_p$, $n_k$ is the outward unit normal to $\Sigma$, and $ds$ is an infinitesimal line segment of $\Sigma$.

It is known from the asymptotic analysis described in the Appendix that if $\omega_p$ is an eigenvalue for given material properties and inclusion wedge angle $\gamma$ thereby satisfying the characteristic Eq. (12), $\omega_p^*(=-\omega_p)$ also satisfies the same characteristic equation for the same material properties and angle $\gamma$. Hence, the stress and displacement fields associated with $\omega_p^*$ are used as the auxiliary fields, and are given by

$$\sigma_{kl}^{(p)*}=K_j^{(p)*}r^{\omega_p^*-1}f_{kl}^{(p)*}$$

$$u_k^{(p)*}=K_j^{(p)*}r^{\omega_p^*}g_k^{(p)*}. \tag{4}$$

The nondimensional functions $f_{kl}^{(p)*}$ and $g_k^{(p)*}$ are obtained simply by replacing $\omega_p$ by $\omega_p^*(=-\omega_p)$ in the expressions for functions $f_{kl}^{(p)}$ and $g_k^{(p)}$ given in the Appendix.

By substituting Eq. (1) and Eq. (4) into Eq. (3), we obtain

$$\begin{aligned}I(\omega_p)=&\oint_{\Sigma}[\sigma_{klo}u_k^{(i)*}-\sigma_{kl}^{(i)*}u_{ko}]n_k ds\\&+\sum_{p=1}^{N}\left\{K_j^{(i)*}K_j^{(p)}r^{\omega_i^*+\omega_p}\oint_{\Sigma}[f_{kl}^{(p)}g_k^{(i)*}-f_{kl}^{(i)*}g_k^{(p)}]d\theta\right\}\\&+\sum_{q=1}^{M}\left\{K_j^{(i)*}K_j^{(q)}r^{\omega_i^*+\delta_q}\oint_{\Sigma}[f_{kl}^{(q)}g_k^{(i)*}-f_{kl}^{(i)*}g_k^{(q)}]d\theta\right\}\end{aligned} \tag{5}$$

where $\omega_i^*=-\omega_p$ for the evaluation of the intensity factor $K_j^{(p)}$ of the symmetric field with eigenvalue $\omega_p$. The integrals in Eq. (5) have the following characteristics:

$$\oint_{\Sigma}[f_{kl}^{(p)}g_k^{(i)*}-f_{kl}^{(i)*}g_k^{(p)}]d\theta=\begin{cases}0 & \omega_i^*\neq-\omega_p\\ L_p & \omega_i^*=-\omega_p\end{cases}$$

$$\oint_{\Sigma}[f_{kl}^{(q)}g_k^{(i)*}-f_{kl}^{(i)*}g_k^{(q)}]d\theta=0 \tag{6a}$$

where

$$L_p=\oint_{\Sigma}[f_{kl}^{(p)}g_k^{(p)*}-f_{kl}^{(p)*}g_k^{(p)}]d\theta. \tag{6b}$$

Hence, Eq. (5) can be rewritten as

$$I(w_p)=\oint_{\Sigma}[(\sigma_{kl}-\sigma_{klo})u_k^{(p)*}-\sigma_{kl}^{(p)*}(u_k-u_{ko})]n_k ds \tag{7a}$$

$$=L_pK_j^{(p)}K_j^{(p)*} \tag{7b}$$

where the nonsingular constant stress $\sigma_{klo}$ and the associated displacement $u_{ko}$ are subtracted from the corresponding total values near the interface junction.

In order to determine the interface-junction stress intensity factor $K_j^{(p)}$ associated with any eigenvalue $\omega_p$ for the symmetric field, the integral $L_p$ in Eq. (6*b*) is first evaluated using the closed-form expressions given in the Appendix for $f_{kl}^{(p)}$ and $g_k^{(p)}$, and the corresponding auxiliary fields. The integral in Eq. (7*a*) is then evaluated along a chosen integration path using: (i) the finite element solution of $(\sigma_{kl},u_k)$ for the particular inclusion geometry, (ii) the auxiliary fields $(\sigma_{kl}^{(p)*},u_k^{(p)*})$ given in Eq. (4) with the intensity factor $K_j^{(p)*}=1/L_p$, and (iii) the magnitude of $\sigma_{klo}$ and $u_{ko}$ determined from the closed-form expressions given in the Appendix. The definition in Eq. (7*a*) ensures that the resulting value of the integral gives $K_j^{(p)}$.

The process is repeated for each of the $N$ eigenvalues $\omega_p(p=1,N)$ of the symmetric field to obtain the corresponding stress intensity factor, and for each of the $M$ eigenvalues $\delta_q$ $(q=1,M)$ of the skew-symmetric field to obtain the corresponding intensity factor. In the evaluation of the intensity factors for the skew-symmetric field, the parameters associated with the symmetric field in Eq. (3) to Eq. (7) are replaced with the corresponding skew-symmetric parameters. This method allows the interface-junction stress intensity factors for the two modes of deformation to be evaluated independently irrespective of the number of eigenvalues. Two examples are used in the next section to demonstrate the capability of the method.

## Numerical Analysis

The inclusion/matrix geometries considered in this paper are shown in Figs. 3 and 4. Figure 3 shows an elastic square inclusion (wedge angle $\gamma=90$ deg) with a side length $2h$, embedded in a block of elastic material with a $4h$ by $4h$ square cross section; this is equivalent to 25% inclusion volume fraction. The inclusion in the second example, Fig. 4(*a*), has a diamond-shaped cross section

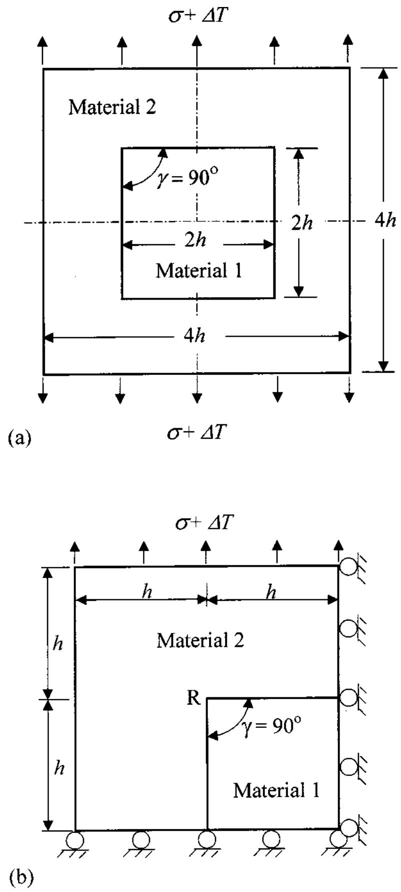


**Fig. 3** (***a***) **The full geometry of the square-shaped inclusion and (*b*) the quarter geometry considered in the finite element analysis. The two-phase material is subject to a remote tension $\boldsymbol{\sigma}$ and a uniform change in temperature $\boldsymbol{\Delta T}$.**

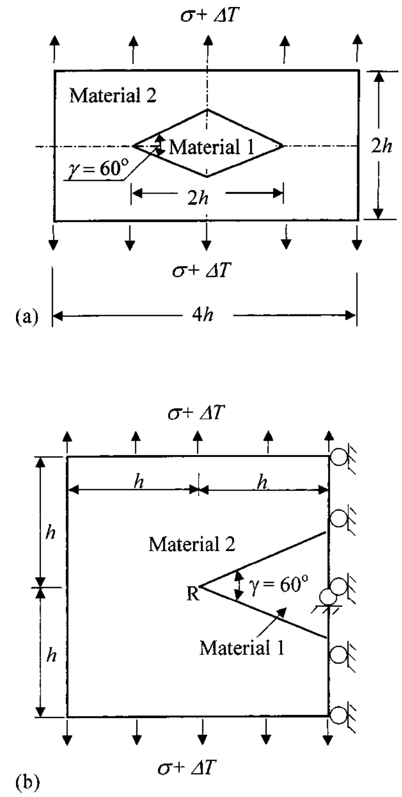


**Fig. 4** (***a***) **The full geometry of the diamond-shaped inclusion and (*b*) the half geometry considered in the finite element analysis. The two-phase material is subject to a remote tension $\boldsymbol{\sigma}$ and a uniform change in temperature $\boldsymbol{\Delta T}$.**

and wedge angles $\gamma=60$ deg and $\gamma=120$ deg; only the stresses near the junction with $\gamma=60$ deg are examined in this paper. The major diagonal of the inclusion is $2h$ long, and it is embedded in a block of elastic material with $4h$ by $2h$ rectangular cross section, see Fig. 4(*a*). The relative dimensions of the diamond-shaped inclusion and the matrix material are equivalent to 17% inclusion volume fraction.

Two loading conditions are considered: a remote uniaxial tension $\sigma$ and a uniform temperature change $\Delta T$ as shown in Figs. 3(*a*) and 4(*a*). The remote tension $\sigma$ is perpendicular to the major axis of the diamond-shaped inclusion, and at 45 deg to the diagonals of the square-shaped inclusion. Because of the symmetry of the geometry and loading, only a quarter of the square-shaped inclusion/matrix geometry and half of the diamond-shaped inclusion/matrix geometry were analyzed, as shown in Figs. 3(*b*) and 4(*b*), respectively. The dimension $h$, which is considered as the characteristic length scale, is taken as $h=1$ unit in the finite element analysis. The finite element mesh used for both geometries is shown in Fig. 5; it consists of eight-node isoparametric plane strain elements. The analysis was carried out using ABAQUS [15] finite element package.

## Results and Discussion

The eigenvalues associated with the symmetric and the skew-symmetric fields are shown in Fig. 6 for the two inclusion geometries. The results in Fig. 6 are shown for Dundurs [12] elastic mismatch parameters $-1<\alpha<1$ and $\beta=\alpha/4$; $\alpha$ and $\beta$ are defined in Eq. (14). $\alpha=1$ when the inclusion is rigid relative to the matrix, $\alpha=-1$ when the inclusion is much more compliant than the matrix, and $\alpha=0$ when the inclusion and the matrix have identical elastic properties. The stress field associated with a particular eigenvalue is singular when the magnitude of the eigenvalue is less than 1. When $\beta=\alpha/4$, there are at most two power-law singular stress fields, one symmetric and the other skew-symmetric. This is consistent with previous study by Chen and Nisitani [16]. For a square rigid inclusion ($\gamma=90$ deg, $\alpha=1$, $\beta=\alpha/4$) there are two eigenvalues for the symmetric field: $\omega_1=0.769$ and $\omega_2=1.169$; and one eigenvalue for the skew-symmetric field, $\delta_1=0.604$. The magnitude of the eigenvalue associated with the singular symmetric stress field, $\omega_1$, is in agreement with that given by Reedy and Guess [10], see Fig. 6(*b*).

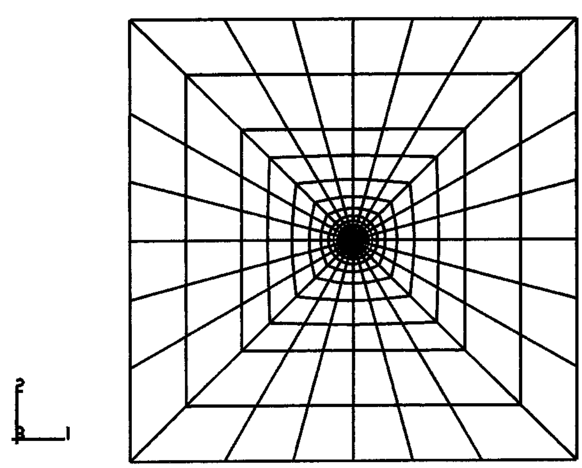


**Fig. 5 The finite element mesh used for the two inclusion geometries**

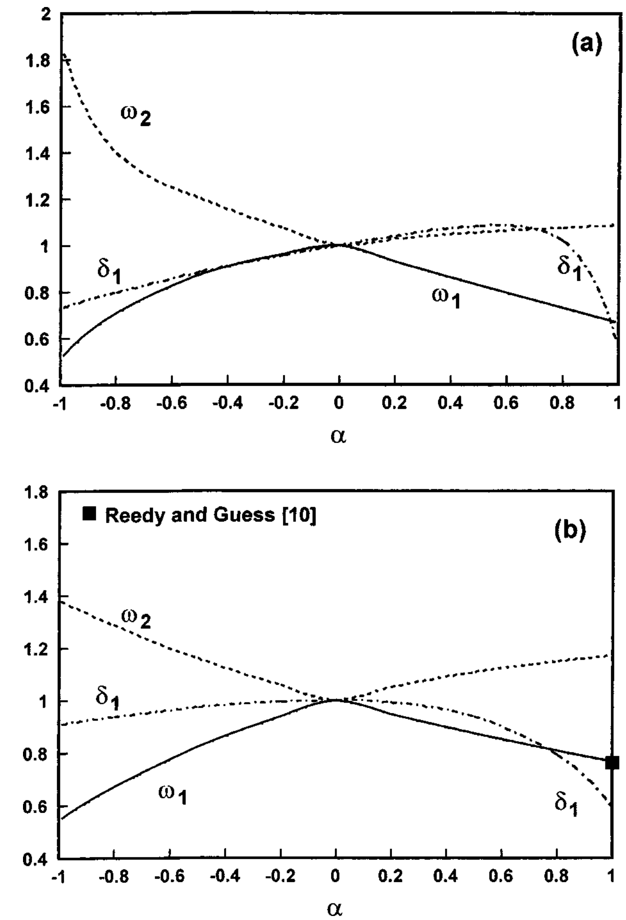


**Fig. 6 The eigenvalues for (*a*) the diamond-shaped inclusion, $\gamma=60$ deg and (*b*) the square-shaped inclusion, $\gamma=90$ deg; both for material elastic mismatch parameters $\alpha$ and $\beta=\alpha/4$. The eigenvalues $\omega_p$ ($p=1,2$) are associated with the symmetric stress field while $\delta_1$ is associated with the skew-symmetric stress field.**

Various authors have suggested that the stress field associated with the smallest eigenvalue dominates the stress near a wedge tip. This suggestion may sometimes by misleading. We shall show later for a diamond-shaped inclusion subjected to remote tension or uniform change in temperature, that the magnitude of the intensity factor associated with the smallest eigenvalue, $\delta_1$, is very small and its contribution to the overall stress field can therefore be neglected. As such, the dominant stress field is that associated with $\omega_1$.

The magnitude of the interface-junction stress intensity factor, $K_j$, associated with each eigenvalue for the two inclusion geometries under consideration is a function of the elastic mismatch parameters ($\alpha$, $\beta$), the inclusion wedge angle $\gamma$, and the magnitude of the applied load. Dimensional considerations dictate that $K_j$ be related to the inclusion geometry and material properties by

$$K_j^{(p)}=\sigma^* h^{1-\omega_p} Q_{\omega_p}(\alpha,\beta,\gamma)$$

$$K_j^{(q)}=\sigma^* h^{1-\delta_q} Q_{\delta_q}(\alpha,\beta,\gamma) \tag{8}$$

where $\sigma^*$ is a representative measure of the applied loading, $h$ is the characteristic length scale and $Q$ is a dimensionless constant function of ($\alpha$, $\beta$) and $\gamma$. Here, $\sigma^*=\sigma$ for a remote uniaxial tension of magnitude $\sigma$ and $\sigma^*=\sigma_o$ for a uniform temperature change, where $\sigma_o$ is a measure of the applied thermal loading defined in Eq. (37). The magnitude of $Q$ associated with each eigenvalue is listed in Table 1 for remote tension and in Table 2 for a uniform change in temperature.

In order to assess the accuracy of the nondimensional constant $Q$ obtained by the integral method, a comparison is made with the two studies in open literature on the subject, which contained the results for some of the material combinations and loading. Chen and Nisitani [7] have used the body force method to determine the intensity factor associated with the dominant symmetric stress field for a diamond-shaped inclusion subjected to remote uniaxial tension; however, the effects of temperature and higher-order terms were not considered. Following the definition of $K_j$ used in the current study, Eqs. (2) and (8), the comparison between the magnitude of $Q_{\omega_1}$ obtained by Chen and Nisitani [7] for remote

**Table 1 The nondimensional constants $Q$ associated with eigenvalues $\omega_1$, $\omega_2$, and $\delta_1$ for inclusion wedge angles $\gamma=60$ deg and $\gamma=90$ deg when the encapsulated inclusion is subjected to remote uniaxial tension. The corresponding magnitude of each eigenvalue is shown in Fig. 6, and the material parameter $\beta=\alpha/4$.**

| | Diamond-Shaped Inclusion, $\gamma=60$ deg | | | Square-Shaped Inclusion, $\gamma=90$ deg | | |
|---|---|---|---|---|---|---|
| $\alpha$ | $Q_{\omega_1}$ | $Q_{\omega_2}$ | $Q_{\delta_1}$ | $Q_{\omega_1}$ | $Q_{\omega_2}$ | $Q_{\delta_1}$ |
| −0.99 | 0.057 | 0.012 | −2.2E-7 | 0.009 | 0.012 | 0.012 |
| −0.8 | 0.490 | −0.020 | −2.5E-7 | 0.106 | 0.151 | 0.172 |
| −0.5 | 0.731 | −0.091 | −5.8E-7 | 0.180 | 0.219 | 0.318 |
| −0.2 | 0.844 | −0.123 | −9.8E-7 | 0.227 | 0.243 | 0.432 |
| 0.2 | −0.288 | 1.108 | −2.1E-6 | 0.253 | 0.268 | 0.558 |
| 0.5 | −0.148 | 0.936 | −1.9E-6 | 0.254 | 0.286 | 0.590 |
| 0.8 | −0.147 | 0.950 | −7.9E-7 | 0.251 | 0.297 | 0.479 |
| 0.99 | −0.145 | 0.955 | −1.9E-8 | 0.248 | 0.301 | 0.318 |

**Table 2 The nondimensional constants $Q$ associated with eigenvalues $\omega_1$, $\omega_2$, and $\delta_1$ for inclusion wedge angles $\gamma=60$ deg and $\gamma=90$ deg when the encapsulated inclusion is subjected to a uniform temperature change. The corresponding magnitude of each eigenvalue is shown in Fig. 6, and the material parameter $\beta=\alpha/4$.**

| | Diamond-Shaped Inclusion, $\gamma=60$ deg | | | Square-Shaped Inclusion, $\gamma=90$ deg | | |
|---|---|---|---|---|---|---|
| $\alpha$ | $Q_{\omega_1}$ | $Q_{\omega_2}$ | $Q_{\delta_1}$ | $Q_{\omega_1}$ | $Q_{\omega_2}$ | $Q_{\delta_1}$ |
| −0.99 | −0.056 | 0.045 | 4.7E-3 | −0.019 | 7.7E-3 | 4.1E-3 |
| −0.8 | −0.519 | −0.054 | 3.7E-3 | −0.263 | −0.345 | 2.7E-3 |
| −0.5 | −1.295 | −0.197 | 2.7E-3 | −0.709 | −0.849 | 1.9E-3 |
| −0.2 | −3.849 | −0.723 | 1.9E-3 | −2.235 | −2.383 | 1.3E-3 |
| 0.2 | 0.913 | 4.266 | 1.1E-3 | 2.425 | 2.878 | 4.8E-4 |
| 0.5 | 0.395 | 1.777 | −3.5E-4 | 1.008 | 1.1261 | 3.7E-4 |
| 0.8 | 0.255 | 1.141 | −2.6E-3 | 0.624 | 0.730 | −1.9E-4 |
| 0.99 | 0.206 | 0.935 | −1.2E-3 | 0.499 | 0.599 | −1.7E-4 |

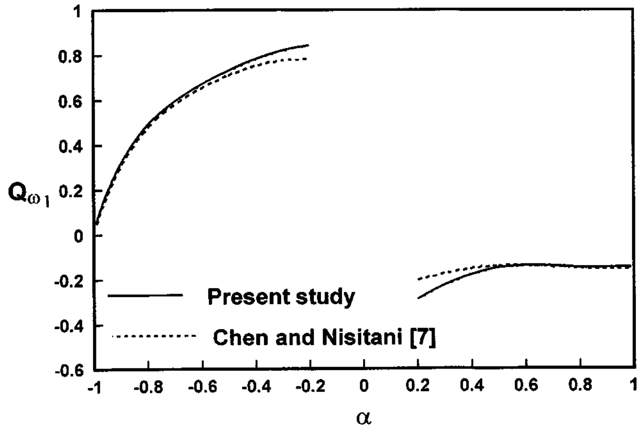


**Fig. 7 Comparison between the nondimensional constant $Q_{\omega_1}$ obtained in the present analysis using the integral method and that obtained by the body force method ([7]), for a diamond-shaped inclusion subjected to remote uniaxial tension. The material parameter $\beta=\alpha/4$.**

uniaxial tension and in the current analysis is shown in Fig. 7; there is good agreement between the two results.

Reedy and Guess [10] have analyzed a square rigid inclusion subjected to a uniform change in temperature. The intensity factor associated with the smallest eigenvalue for the symmetric field was determined by matching the finite element and asymptotic solutions in the vicinity of the interface junction. Using the same definition for $K_j$ as in the current paper, Reedy and Guess [10] result gives a value of $Q_{\omega_1}=0.594$ for $\alpha=1$ and $\beta=0.325$. Using the integral method, a value of $Q_{\omega_1}=0.528$ was obtained for the same loading and material properties ($\alpha=1,\beta=0.325$); this is 11% lower than that obtained by Reedy and Guess [10].

The difference between the two values of $Q_{\omega_1}$ is attributed to the different inclusion volume fraction in the two analyses. The inclusion volume fraction considered by Reedy and Guess [10] was 2.5% and it is 25% in the present analysis. The results of the intensity factor for *unbonded* square rigid inclusion ([10]) show that the magnitude of the intensity factor decreased by 12% when the inclusion volume fraction was increased from 2.5% to 25%. A similar reduction in the intensity factor is anticipated for a fully bonded inclusion.

The results shown in Tables 1 and 2, when used in conjunction with Eq. (8), enable the interface-junction stress intensity factor associated with all the eigenvalues to be determined for an inclusion with wedge angles $\gamma=60$ deg and $\gamma=90$ deg, subjected to remote uniaxial tension and temperature change. The results therefore complement those of Chen and Nisitani [7] for only mechanical loading, and of Reedy and Guess [10] for square *rigid* inclusion subjected to axisymmetric remote tension and temperature change.

For an inclusion with wedge angle $\gamma=60$ deg subjected to remote tension, and with wedge angle $\gamma=90$ deg subjected to uniform temperature change, the magnitude of $Q$ associated with the skew-symmetric field is much smaller than the corresponding magnitude for the symmetric field. For these particular cases where the loading is symmetric about the plane that bisects the wedge angle of interest, a reasonably accurate solution of the stresses near the interface junction can be obtained by neglecting the contribution from the skew-symmetric field. For other cases, however, the stress field associated with all the eigenvalues must be considered to obtain an accurate prediction of the stresses. A comparison of the theoretical asymptotic stress field and the finite element solution is made for an inclusion/matrix combination to demonstrate the need to consider all the stress terms.

Consider, for example, a diamond-shaped inclusion in a matrix as shown in Fig. 4. The shear modulus of the inclusion $\mu_1=3\mu_2$, where $\mu_2$ is the shear modulus of the elastic matrix. The inclusion and the matrix have a Poisson's ratio $\nu_1=\nu_2=0.33$. These relative elastic properties give Dundurs [12] elastic mismatch parameters of $\alpha=0.5$ and $\beta=\alpha/4$. The eigenvalues for the inclusion geometry and material properties are: $\omega_1=0.829$, $\omega_2=1.056$, and $\delta_1=1.082$. Although, only the symmetric stress field associated with the eigenvalue $\omega_1$ is singular, the stress field associated with $\omega_2$ is needed to obtain reasonably accurate results near the interface junction. The stress field associated with $\delta_1$ can be neglected due to the relatively small magnitude of the associated stress intensity factor, as described above.

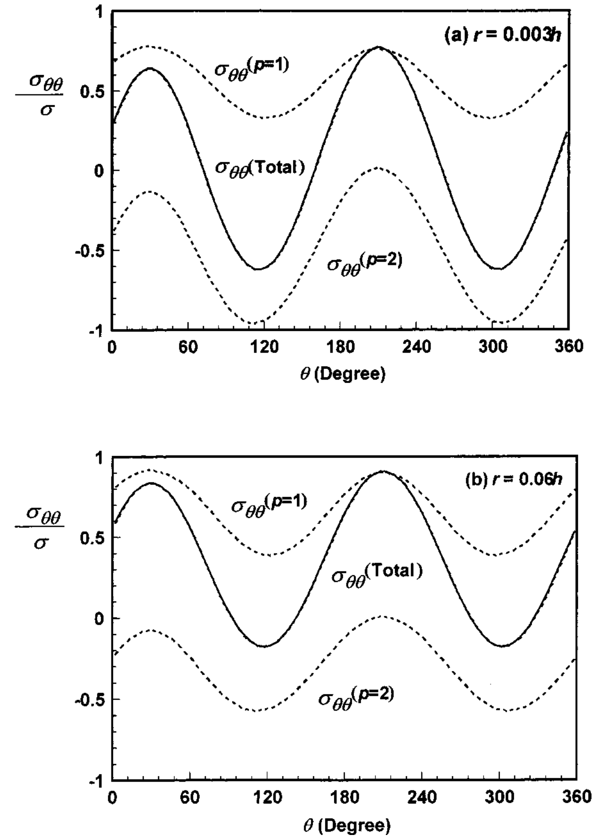


**Fig. 8 The comparison between the asymptotic solution (dashed-dashed line) and finite element prediction (solid line) of $\sigma_{\theta\theta}$ near interface junction R for the diamond-shaped inclusion subjected to a remote uniaxial tension $\sigma$. (*a*) $r=0.003h$ and (*b*) $r=0.06h$; where $r$ is the radial distance from the interface junction and $h$ is half the major diagonal of the inclusion. The elastic mismatch parameters are $\alpha=0.5$ and $\beta=\alpha/4$.**

The asymptotic stresses near the interface junction are compared with the corresponding finite element solution for the inclusion with a wedge angle $\gamma=60$ deg. The asymptotic stresses were calculated using Eq. (1), with the magnitude of the stress intensity factors given by Eq. (8) and the values of $Q$ in Tables 1 and 2. The angular variation of the stress component $\sigma_{\theta\theta}$ at radial distances $r=0.003h$ and $r=0.06h$ from the interface junction is shown in Fig. 8 when the two-phase material is subjected to a remote tension $\sigma$, and in Fig. 9 when it is subjected to a thermal load $\sigma_o$. The magnitude of $\sigma_{\theta\theta}$ is normalized by the applied load: $\sigma$ or $\sigma_o$. Note that the major diagonal of the diamond-shaped inclusion is of length $2h$, and the interfaces that form the inclusion wedge are along $\theta=0$ deg and $\theta=\gamma=60$ deg.

The asymptotic solutions of the symmetric stress field associated with the two eigenvalues $\omega_1(=0.829)$ and $\omega_2(=1.056)$ are shown separately in Figs. 8 and 9 as $\sigma_{\theta\theta}^{(p=1)}$ and $\sigma_{\theta\theta}^{(p=2)}$, respectively, and the asymptotic solution of the nonsingular constant

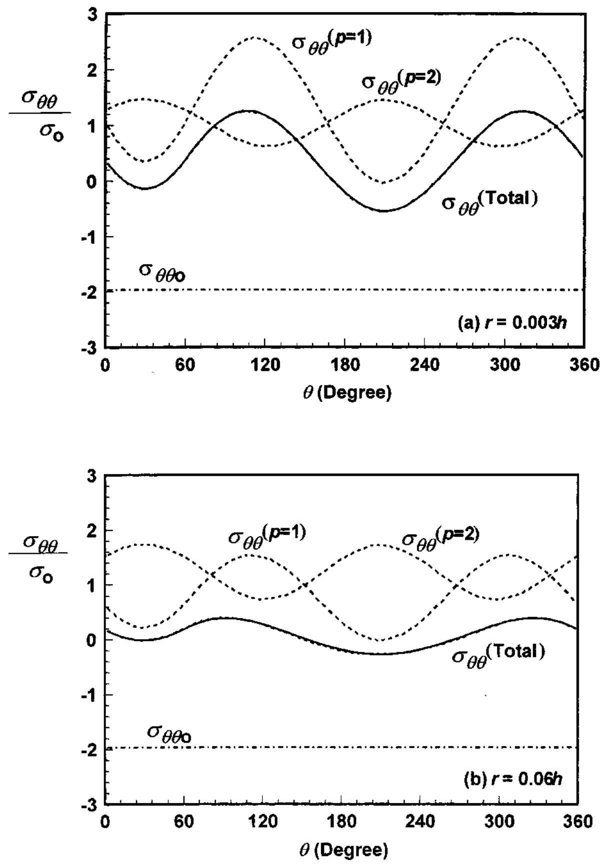


**Fig. 9 The comparison between asymptotic solution (dashed-dashed line) and the finite element prediction (solid line) of $\sigma_{\theta\theta}$ near interface junction R for the diamond-shaped inclusion subject to a thermal load $\sigma_o$. (*a*) $r=0.003h$ and (*b*) $r=0.06h$; where *r* is the radial distance from the interface corner and *h* is half the major diagonal of the inclusion. The elastic mismatch parameters are $\alpha=0.5$ and $\beta=\alpha/4$.**

stress is denoted by $\sigma_{\theta\theta o}$. The nonsingular constant stress is zero when the material is subjected to only remote mechanical loading, Fig. 8, and it is finite for a uniform change in temperature, Fig. 9. As expected the stress fields in Figs. 8 and 9 are symmetric in material 1 (i.e., the inclusion) about $\theta=\gamma/2=30$ deg and in material 2 (i.e., the matrix) about $\theta=210$ deg. The inclusion occupies the region $0<\theta<\gamma$ while the matrix occupies the region $\gamma<\theta<2\pi$.

The stress field $\sigma_{\theta\theta}^{(p=1)}$ is singular at the interface junction since $\omega_1<1$, and $\sigma_{\theta\theta}^{(p=2)}$ is nonsingular since $\omega_2>1$; $\sigma_{\theta\theta}^{(p=2)}=0$ at $r=0$. For the material properties under consideration, $\alpha=0.5$, $\beta=\alpha/4$, the nondimensional constants $Q_{\omega_1}=-0.148$ and $Q_{\omega_2}=0.936$. Therefore, when the inclusion/matrix geometry is subjected to a remote tension, the interface-junction stress intensity factor associated with $\omega_1$, $K_j^{(p=1)}<0$, while that associated with $\omega_2$, $K_j^{(p=2)}>0$. Consequently, the results presented in Fig. 8 for remote tension show that $\sigma_{\theta\theta}^{(p=1)}$ is negative with an absolute value which decreases with increasing radial distance *r* from the junction, while $\sigma_{\theta\theta}^{(p=2)}$ is positive and increases in magnitude with increasing distance *r*. Therefore, the magnitude of the total stress $\sigma_{\theta\theta}$ increases with increasing radial distance *r* from the interface junction.

The asymptotic total stress is compared in Figs. 8 and 9 with the finite element solution. The comparison shows that although the symmetric stress field $\sigma_{\theta\theta}^{(p=2)}$ is nonsingular, its contribution to the near-junction stresses is significant, even at a radial distance $r=0.003h$ from the junction. A good agreement is obtained between the finite element solution and the asymptotic solution only when both the singular and nonsingular symmetric fields, and the nonsingular constant stress associated with temperature change are considered.

The value of the interface junction stress intensity factor characterises the magnitude of the stress state in the vicinity of the interface junction. The solution of the intensity factors and associated eigenvalues for square-shaped and diamond-shaped inclusions embedded in an elastic matrix and subjected to either remote tension or uniform temperature change, as presented in this paper allow the magnitude of the stresses near the junction to be determined. In addition, the magnitude of the interface-junction intensity factor can be used to predict the onset of failure, provided the zone of dominance of the singular fields is much greater than any nonlinear deformation or fracture process zone near the junction. Failure occurs when the magnitude of the interface-junction stress intensity factor, $K_j$, attains a critical value. A $K_j$-based approach has been used successfully to predict the onset of failure in bonded joint geometries where there is only one singular stress term ([2,14]). However, there have been few studies ([10,13]) on the extension of the approach to the prediction of failure in encapsulated inclusions. For this to be successful, the interaction, if any, between the interface-junction intensity factors for the symmetric and skew-symmetric fields at failure must be established.

## Conclusions

The stress behavior at the interface junctions of an elastic inclusion embedded in elastic, brittle matrix has been described. The stresses at an interface junction can be separated into symmetric (mode I) and skew-symmetric (mode II) fields. A contour integral method was used to evaluate the stress intensity factors associated with both modes of deformation, for a two-phase material subjected to a remote tension and a uniform change in temperature. The results of two examples: square-shaped and diamond-shaped inclusions, showed that the asymptotic solution of the stresses at an interface junction is in agreement with the finite element prediction only when all the stress terms including the higher-order terms are considered.

## Appendix

**The Asymptotic Fields Near the Interface Corner.** The asymptotic stress and displacement solution near the interface junction *R* of the inclusion shown in Fig. 1 can be obtained using the complex variable method or the Airy's stress method. We assume there is a symmetry along $\theta=\gamma/2$ and that the inclusion is perfectly bonded to the matrix. When the two-phase material is subjected to a combination of remote mechanical loading and a uniform change in temperature, the stress field can be split into two independent modes: a symmetric (mode I) and skew-symmetric (mode II) fields. The boundary conditions for each of these modes are

$$\sigma_{r\theta}^1=\sigma_{r\theta}^2;\quad \sigma_{\theta\theta}^1=\sigma_{\theta\theta}^2;\quad u_r^1=u_r^2+r\Delta\rho^*\Delta T;$$
$$u_\theta^1=u_\theta^2 \quad (\text{at } \theta=0 \text{ and } \theta=\gamma) \tag{9a}$$
$$\sigma_{r\theta}^1=u_\theta^1=0 \quad (\text{at } \theta=\gamma/2);\quad \text{and}\quad \sigma_{r\theta}^2=u_\theta^2=0$$
$$(\text{at } \theta=\pi+\gamma/2) \tag{9b}$$

for the symmetric field, and

$$\sigma_{r\theta}^1=\sigma_{r\theta}^2;\quad \sigma_{\theta\theta}^1=\sigma_{\theta\theta}^2;\quad u_r^1=u_r^2+r\Delta\rho^*\Delta T;$$
$$u_\theta^1=u_\theta^2 \quad (\text{at } \theta=0 \text{ and } \theta=\gamma) \tag{10a}$$
$$\sigma_{\theta\theta}^1=u_r^1=0 \quad (\text{at } \theta=\gamma/2);\quad \text{and}\quad \sigma_{\theta\theta}^2=u_r^2=0$$
$$(\text{at } \theta=\pi+\gamma/2) \tag{10b}$$

for the skew-symmetric field. The superscripts in the equations above refer to the material number (1 for the inclusion and 2 for the matrix); $\Delta\rho^{*}=(1+\nu_2)\rho_2-(1+\nu_1)\rho_1$ characterizes the thermal expansion mismatch between the two materials under plane-strain conditions; $\rho_1$ and $\rho_2$ are the thermal expansion coefficients of material 1 and material 2, respectively; and $\Delta T$ is the change in temperature from a reference value of $T_o$ to a current value of $T$, i.e., $\Delta T=T-T_o$.

By substituting the stress and displacement equations from the complex variable analysis into the boundary conditions (9) and (10) it can easily be shown that the stresses and displacements near the interface junction are given by

$$\sigma_{kl}=\sum_{p=1}^{N} K_j^{(p)} r^{\omega_p-1} f_{kl}^{(p)}+\sum_{q=1}^{M} K_j^{(q)} r^{\delta_q-1} f_{kl}^{(q)}+\sigma_{klo}$$

$$u_k=\sum_{p=1}^{N} K_j^{(p)} r^{\omega_p} g_k^{(p)}+\sum_{q=1}^{M} K_j^{(q)} r^{\delta_q} g_k^{(q)}+u_{ko} \tag{11}$$

where $(k,l)\equiv(r,\theta)$, $\omega_p$ is the eigenvalue of the symmetric stress field with a corresponding interface junction stress intensity factor $K_j^{(p)}$, and $\delta_q$ is the eigenvalue of the skew-symmetric stress field with a corresponding interface junction stress intensity factor $K_j^{(q)}$. The parameters $N$ and $M$ are the numbers of eigenvalues associated with the mode I and II fields, respectively. The nondimensional functions $f_{kl}^{(p)}$, $f_{kl}^{(q)}$, $g_k^{(p)}$, and $g_k^{(q)}$ depends on the material properties and the inclusion wedge angle $\gamma$. The terms $\sigma_{klo}$ and $u_{ko}$ in Eq. (11) are the nonsingular constant stress and the corresponding displacements which may exist depending on the mismatch in the thermal properties of the material.

The eigenvalues $\omega=\omega_p$ $(p=1,N)$ associated with the symmetric field must satisfy the characteristic equation

$$\begin{aligned}F_1(\alpha,\beta,\gamma,\omega)=1-\alpha^2-(1-\beta^2)\cos 2\omega\pi+(\alpha-\beta)^2\omega^2(1\\-\cos 2\gamma)+(\alpha^2-\beta^2)\cos[2\omega(\gamma-\pi)]+2\omega(\alpha\\-\beta)\sin\gamma\{\sin\omega\gamma+\sin[\omega(2\pi-\gamma)]\}+2\omega(\alpha\\-\beta)\beta\sin\gamma\{\sin[\omega(2\pi-\gamma)]-\sin\omega\gamma\}=0\end{aligned} \tag{12}$$

and the eigenvalue $\delta=\delta_q$ $(q=1,M)$ for the skew-symmetric field must satisfy the characteristic equation

$$\begin{aligned}F_2(\alpha,\beta,\gamma,\delta)=1-\alpha^2-(1-\beta^2)\cos 2\delta\pi+(\alpha-\beta)^2\delta^2(1\\-\cos 2\gamma)+(\alpha^2-\beta^2)\cos[2\delta(\gamma-\pi)]-2\delta(\alpha\\-\beta)\sin\gamma\{\sin\delta\gamma+\sin[\delta(2\pi-\gamma)]\}-2\delta(\alpha\\-\beta)\beta\sin\gamma\{\sin[\delta(2\pi-\gamma)]-\sin\delta\gamma\}=0\end{aligned} \tag{13}$$

where $\alpha$ and $\beta$ are the elastic mismatch parameters between the inclusion and the matrix, given for plane strain condition by [12]

$$\alpha=\frac{\mu_1(\kappa_2+1)-(\kappa_1+1)\mu_2}{\mu_1(\kappa_2+1)+(\kappa_1+1)\mu_2};\quad \beta=\frac{\mu_1(\kappa_2-1)-(\kappa_1-1)\mu_2}{\mu_1(\kappa_2+1)+(\kappa_1+1)\mu_2}. \tag{14}$$

The characteristic Eqs. (12) and (13) are identical to those given by Chen and Nisitani [16] when the appropriate substitution are made for $(\alpha,\ \beta)$ and the wedge angle.

The functions $f_{rr}$, $f_{\theta\theta}$, $f_{r\theta}$, $g_r$, and $g_\theta$ corresponding to an eigenvalue $\lambda$ $(=\omega_p$ or $\delta_q$; $p=1,N$ and $q=1,M)$ are given by

$$\begin{Bmatrix} f_{rr}\\ f_{\theta\theta}\\ f_{r\theta}\\ g_r\\ g_\theta\end{Bmatrix}_m=\begin{bmatrix} \lambda(3-\lambda)\cos(\lambda\theta-\theta) & -\lambda(3-\lambda)\sin(\lambda\theta-\theta) & -\lambda\cos(\lambda\theta+\theta) & \lambda\sin(\lambda\theta+\theta)\\ \lambda(\lambda+1)\cos(\lambda\theta-\theta) & -\lambda(\lambda+1)\sin(\lambda\theta-\theta) & \lambda\cos(\lambda\theta+\theta) & -\lambda\sin(\lambda\theta+\theta)\\ \lambda(\lambda-1)\sin(\lambda\theta-\theta) & \lambda(\lambda-1)\cos(\lambda\theta-\theta) & \lambda\sin(\lambda\theta+\theta) & \lambda\cos(\lambda\theta+\theta)\\ \dfrac{(\kappa_m-\lambda)\cos(\lambda\theta-\theta)}{2\mu_m} & \dfrac{(\lambda-\kappa_m)\sin(\lambda\theta-\theta)}{2\mu_m} & \dfrac{-\cos(\lambda\theta+\theta)}{2\mu_m} & \dfrac{\sin(\lambda\theta+\theta)}{2\mu_m}\\ \dfrac{(\kappa_m+\lambda)\sin(\lambda\theta-\theta)}{2\mu_m} & \dfrac{(\lambda+\kappa_m)\cos(\lambda\theta-\theta)}{2\mu_m} & \dfrac{\sin(\lambda\theta+\theta)}{2\mu_m} & \dfrac{\cos(\lambda\theta+\theta)}{2\mu_m}\end{bmatrix}\begin{Bmatrix} A_m\\ B_m\\ C_m\\ D_m\end{Bmatrix} \tag{15}$$

where $\mu_m$ $(=E_m/2(1+\nu_m))$, $E_m$, and $\nu_m$ denote shear modulus, Young's modulus, and Poisson's ratio for material $m(=1,2)$, respectively, and $\kappa_m=3-4\nu_m$ for plane strain. The nondimensional constants $A_m$, $B_m$, $C_m$, and $D_m$, where $m(=1,2)$ is the material number, are given for the symmetric field by

$$A_1(\omega)=\xi_1(\alpha-\beta)\sin[\omega(\gamma-\pi)]\cos[(\omega-1)\gamma/2] \tag{16}$$

$$B_1(\omega)=-\xi_1(\alpha-\beta)\sin[\omega(\gamma-\pi)]\sin[(\omega-1)\gamma/2] \tag{17}$$

$$\begin{aligned}C_1(\omega)=\xi_1\{\omega(\alpha-\beta)\sin[\gamma-\omega(\gamma-\pi)]+(1-\beta)\sin\omega\pi\}\\ \times\cos[(\omega+1)\gamma/2]\end{aligned} \tag{18}$$

$$\begin{aligned}D_1(\omega)=-\xi_1\{\omega(\alpha-\beta)\sin[\gamma-\omega(\gamma-\pi)]\\+(1-\beta)\sin\omega\pi\}\sin[(\omega+1)\gamma/2]\end{aligned} \tag{19}$$

$$A_2(\omega)=-\xi_2(\alpha-\beta)\sin[\omega(\gamma-\pi)]\cos[(\omega-1)(\pi+\gamma/2)] \tag{20}$$

$$B_2(\omega)=\xi_2(\alpha-\beta)\sin[\omega(\gamma-\pi)]\sin[(\omega-1)(\pi+\gamma/2)] \tag{21}$$

$$\begin{aligned}C_2(\omega)=-\xi_2\{\omega(\alpha-\beta)\sin[\gamma-\omega(\gamma-\pi)]\\+(1+\beta)\sin\omega\pi\}\cos[(\omega+1)(\pi+\gamma/2)].\end{aligned} \tag{22}$$

$$\begin{aligned}D_2(\omega)=\xi_2\{\omega(\alpha-\beta)\sin[\gamma-\omega(\gamma-\pi)]+(1+\beta)\sin\omega\pi\}\\ \times\sin[(\omega+1)(\pi+\gamma/2)]\end{aligned} \tag{23}$$

with

$$\begin{aligned}\frac{1}{\xi_1}=\omega(\omega+1)(\alpha-\beta)\sin[\omega(\gamma-\pi)]\cos[(\omega-1)\gamma/2]\\+\omega\{\omega(\alpha-\beta)\sin[\gamma-\omega(\gamma-\pi)]+(1-\beta)\sin\omega\pi\}\\ \times\cos[(\omega+1)\gamma/2]\end{aligned} \tag{24}$$

$$\xi_2=\xi_1\left\{\frac{(1-\beta)\sin\omega\gamma+(1-\alpha)\sin[\omega(\pi-\gamma)]+\omega(\alpha-\beta)\sin\gamma}{(1+\beta)\sin[\omega(2\pi-\gamma)]+(1+\alpha)\sin[\omega(\gamma-\pi)]+\omega(\alpha-\beta)\sin\gamma}\right\} \tag{25}$$

Similarly, the nondimensional constants $A_m$, $B_m$, $C_m$, and $D_m$ for the skew-symmetric field are given by

$$A_1(\delta)=\xi_3(\alpha-\beta)\sin[\delta(\gamma-\pi)]\sin[(\delta-1)\gamma/2] \tag{26}$$

$$B_1(\delta)=\xi_3(\alpha-\beta)\sin[\delta(\gamma-\pi)]\cos[(\delta-1)\gamma/2] \tag{27}$$

$$C_1(\delta)=\xi_3\{\delta(\alpha-\beta)\sin[\gamma-\delta(\gamma-\pi)]-(1-\beta)\sin\delta\pi\}\times\sin[(\delta+1)\gamma/2] \tag{28}$$

$$D_1(\delta)=\xi_3\{\delta(\alpha-\beta)\sin[\gamma-\delta(\gamma-\pi)]-(1-\beta)\sin\delta\pi\}\times\cos[(\delta+1)\gamma/2] \tag{29}$$

$$A_2(\delta)=\xi_4(\alpha-\beta)\sin[\delta(\gamma-\pi)]\sin[(\delta-1)(\pi+\gamma/2)] \tag{30}$$

$$B_2(\delta)=\xi_4(\alpha-\beta)\sin[\delta(\gamma-\pi)]\cos[(\delta-1)(\pi+\gamma/2)] \tag{31}$$

$$C_2(\delta)=\xi_4\{\delta(\alpha-\beta)\sin[\gamma-\delta(\gamma-\pi)]-(1+\beta)\sin\delta\pi\}\times\sin[(\delta+1)(\pi+\gamma/2)] \tag{32}$$

$$D_2(\delta)=\xi_4\{\delta(\alpha-\beta)\sin[\gamma-\delta(\gamma-\pi)]-(1+\beta)\sin\delta\pi\}\times\cos[(\delta+1)(\pi+\gamma/2)] \tag{33}$$

with

$$\frac{1}{\xi_3}=\delta(\delta+1)(\alpha-\beta)\sin[\delta(\gamma-\pi)]\sin[(\delta-1)\gamma/2]+\delta\{\delta(\alpha-\beta)\sin[\gamma-\delta(\gamma-\pi)]-(1-\beta)\sin\delta\pi\}\times\sin[(\delta+1)\gamma/2] \tag{34}$$

$$\xi_4=\xi_3\left\{\frac{\delta(\alpha-\beta)\sin\gamma-(1-\beta)\sin\delta\gamma-(1-\alpha)\sin[\delta(\pi-\gamma)]}{(1+\beta)\sin[\delta(2\pi-\gamma)]+(1+\alpha)\sin[\delta(\gamma-\pi)]-\delta(\alpha-\beta)\sin\gamma}\right\}. \tag{35}$$

When the inclusion-matrix composite material is subjected to a uniform change in temperature, an additional nonsingular constant stress field $\sigma_{klo}$ and associated displacement $u_{ko}$ given in Eq. (11) must be considered; $(k,l)\equiv(r,\theta)$. The nonsingular constant stress field and the associated displacement field are given by

$$\begin{aligned}
\sigma^1_{rro}=\sigma^2_{rro}=\sigma^1_{\theta\theta o}=\sigma^2_{\theta\theta o}&=-\frac{\sigma_o}{8\beta}\\
\sigma^1_{r\theta o}=\sigma^2_{r\theta o}=u^1_{\theta o}=u^2_{\theta o}&=0\\
u^1_{ro}&=\frac{r}{2\mu_1}(1-\kappa_1)\frac{\sigma_o}{8\beta}+r\rho^*_1\Delta T\\
u^2_{ro}&=\frac{r}{2\mu_2}(1-\kappa_2)\frac{\sigma_o}{8\pi}+r\rho^*_2\Delta T
\end{aligned} \tag{36}$$

where

$$\sigma_o=E^*\Delta\rho^*\Delta T \tag{37}$$

is a measure of the applied thermal loading and $E^*$ is the effective modulus given by

$$\frac{1}{E^*}=\frac{1}{2}\left[\frac{1-\nu_1^2}{E_1}+\frac{1-\nu_2^2}{E_2}\right]. \tag{38}$$

Both $\sigma_{klo}$ and $u_{ko}$ vanish if the material is subjected only to a remote mechanical loading.

## References


[1] Bogy, D. B., and Wang, K. C., 1971, ‘‘Stress Singularity at Interface Corners in Bonded Dissimilar Isotropic Elastic Materials,’’ Int. J. Solids Struct., **7**, pp. 993–1005.

[2] Reedy, E. D., 1993, ‘‘Asymptotic Interface-Corner Solutions for Butt Tensile Joints,’’ Int. J. Solids Struct., **30**, pp. 767–777.

[3] Yang, Y. Y., and Munz, D., 1995, ‘‘Stress Intensity Factor and Stress Distribution in a Joint With an Interface Corner Under Thermal and Mechanical Loading,’’ Comput. Struct., **57**, pp. 467–476.

[4] Qian, Z. Q., and Akisanya, A. R., 1998, ‘‘Analysis of Free-Edge Stress and Displacement Fields in Scarf Joints Subjected to a Uniform Change in Temperature,’’ Fatigue Fract. Eng. Mater. Struct., **21**, pp. 687–703.

[5] Liu, D., and Fleck, N. A., 1999, ‘‘Scale Effects in the Initiation of Cracking of a Scarf Joint,’’ Int. J. Fract., **95**, pp. 67–88.

[6] Carpenter, W. C., and Byers, C., 1987, ‘‘A Path Independent Integral for Computing Stress Intensities for V-Notched Cracks in a Bi-material,’’ Int. J. Fract., **35**, pp. 245–268.

[7] Chen, D. H., and Nisitani, H., 1992, ‘‘Numerical Analysis of Singular Stress Around a Bonded Edge,’’ ASME J. Electron. Packag., **114**, pp. 529–536.

[8] Pahn, L. O., and Earmme, Y. Y., 2000, ‘‘Analysis of Short Interfacial Crack From the Corner of a Rectangular Inclusion’’ Int. J. Fract., **106**, pp. 341–356.

[9] Akisanya, A. R., and Fleck, N. A., 1997, ‘‘Interfacial Cracking From the Free-Edge of a Long Bi-material Strip,’’ Int. J. Solids Struct., **34**, pp. 1645–1665.

[10] Reedy, E. D., and Guess, T. R., 2001, ‘‘Rigid Square Inclusion Embedded Within an Epoxy Disk: Asymptotic Stress Analysis,’’ Int. J. Solids Struct., **38**, pp. 1281–1293.

[11] Sinclair, G. B., Okajma, M., and Griffin, J. H., 1984, ‘‘Path Independent Integral for Computing Stress Intensity Factors at Sharp Notches in Elastic Strips,’’ Int. J. Numer. Methods Eng., **10**, pp. 999–1008.

[12] Dundurs, J., 1968, ‘‘*Elastic Interaction of Dislocations With Inhomogeneities*,’’ *Mathematics Theory of Dislocations*, ASME, New York, pp. 70–115.

[13] Hattori, T., Sakata, S., and Murakami, G., 1989, ‘‘A Stress Singularity Parameter for Evaluating the Interfacial Reliability of Plastic Encapsulated LSI Devices,’’ ASME J. Electron. Packag., **111**, pp. 243–248.

[14] Qian, Z. Q., and Akisanya, A. R., 1998, ‘‘An Experimental Investigation of Failure Initiation in Bonded Joints,’’ Acta Mater., **46**, pp. 4895–4904.

[15] ABAQUS/Standard, User’s Manual, Version 5.8, 2000, Hibbit, Karlsson & Sorensen, Inc, Pawtucket, RI.

[16] Chen, D. H., and Nisitani, H., 1993, ‘‘Singular Stress Field Near the Corner of Jointed Dissimilar Materials,’’ ASME J. Appl. Mech., **60**, pp. 607–613.

Journal of Applied Mechanics

# Brief Notes

A Brief Note is a short paper that presents a specific solution of technical interest in mechanics but which does not necessarily contain new general methods or results. A Brief Note should not exceed 2500 words *or equivalent* (a typical one-column figure or table is equivalent to 250 words; a one line equation to 30 words). Brief Notes will be subject to the usual review procedures prior to publication. After approval such Notes will be published as soon as possible. The Notes should be submitted to the Editor of the JOURNAL OF APPLIED MECHANICS. Discussions on the Brief Notes should be addressed to the Editorial Department, ASME International, Three Park Avenue, New York, NY 10016-5990, or to the Editor of the JOURNAL OF APPLIED MECHANICS. Discussions on Brief Notes appearing in this issue will be accepted until two months after publication. Readers who need more time to prepare a Discussion should request an extension of the deadline from the Editorial Department.

## Penetration Limit Velocity for Ogive-Nose Projectiles and Limestone Targets

**M. J. Forrestal**
Sandia National Laboratories, Albuquerque, NM 87185-1174. Fellow ASME

**S. J. Hanchak**
4701 Theodore Street, Munhall, PA 15120-2934

*We conducted depth-of-penetration experiments with ogive-nose steel projectiles and limestone targets to determine the penetration limit velocity. The penetration limit velocity is defined as the minimum striking velocity required to embed the projectile in the target. For striking velocities smaller than the penetration limit velocity, the projectile rebounds from the target.*
[DOI: 10.1115/1.1480820]

### Introduction

Most studies in the broad field of penetration mechanics focus on penetration depth or residual velocity ([1,2]). In our recent work on penetration into aluminum ([3]) or limestone targets ([4]), we started with striking velocities large enough to embed the projectiles in the targets and increased the striking velocities until the projectiles were defeated by turning within or exiting the sides of the targets. In this study, we define the penetration limit velocity as the minimum striking velocity required to embed the projectiles in the targets. We use the same targets and projectiles as those used by Frew, Forrestal, and Hanchak [4]; however, we obtain data for smaller striking velocities and determine the penetration limit velocity.

For some applications, such as anchors or munitions that carry explosives, the projectiles should be embedded in the targets. Anchors must be embedded in order to transfer loads to the target, and munitions are much more effective when coupled to the target. Thus, another defeat mechanism for some projectiles is rebound from the target.

Contributed by the Applied Mechanics Division of THE AMERICAN SOCIETY OF MECHANICAL ENGINEERS for publication in the ASME JOURNAL OF APPLIED MECHANICS. Manuscript received by the ASME Applied Mechanics Division, June 26, 2001; final revision December 3, 2001. Associate Editor: K. T. Ramesh.

### Experiments and Results

We conducted depth-of-penetration experiments with ogive-nose steel rod projectiles and limestone targets. The 3.0 caliber-radius-head (CRH) rod projectiles were machined from 4340 $R_c$ 45 (VAR) steel and had diameters of 7.11 mm and total lengths of 71.1 mm. The nominal properties for the limestone targets include density ($\rho = 2.31$ Mg/m$^3$), water content ($w = 0.15$ percent), porosity ($n = 15$ percent), and unconfined compressive strength ($\sigma_{cf} = 60$ MPa). Again, these are the same projectiles and targets as used in our previous study ([4]). Other experimental details are reported by Hanchak [5].

We summarize the results from six experiments in Table 1. Three projectiles were embedded in the target and three projectiles rebounded. These data show that the penetration limit velocity is between 289 m/s and 308 m/s or about 300 m/s. For the striking velocity of 308 m/s, the projectile was embedded in the target and the penetration depth was $P = 36.8$ mm; so for the projectile diameter of $2a = 7.1$ mm, $P/2a = 5$.

Figure 1 shows data from this study and the data from Frew, Forrestal, and Hanchak [4]. The data from this study shows the penetration limit velocity at 300 m/s. The data from [4] show results for both 4340 $R_c$ 45 ([6]) and Aer Met 100 $R_c$ 53 ([7]) steel projectiles. For striking velocities greater than those shown in Fig. 1, the projectiles severely bent and turned within or exited the sides of the targets.

### Summary

We conducted a set of experiments with ogive-nose rod projectiles and limestone targets to determine the penetration limit velocity. For striking velocities greater than this limit velocity, the projectiles were embedded in the target, and for striking velocities

**Table 1 Penetration data for the 7.1-mm-diameter, 71-mm-long, 0.0205 kg, 3.0 CRH projectiles. For pitch and yaw: *D* = down, *U* = up, *R* = right, *L* = left.**

| Shot Number | Striking Velocity $V_s$ (m/s) | Pitch, Yaw (degrees) | Penetration Depth P(mm) |
|---|---|---|---|
| 6-3418 | 242 | 0, 0.75 *R* | 30.9 Rebound |
| 6-3420 | 271 | 0.5 U, 1.75 *R* | 35.0 Rebound |
| 6-3423 | 289 | 0, 0.5 *R* | 36.2 Rebound |
| 6-3422 | 308 | 0.5 *D*, 1.0 *R* | 36.8 Embed |
| 6-3421 | 320 | 0.5 *D*, 1.0 *R* | 40.0 Embed |
| 6-3419 | 331 | 0.5 *D*, 0.5 *R* | 44.4 Embed |

  

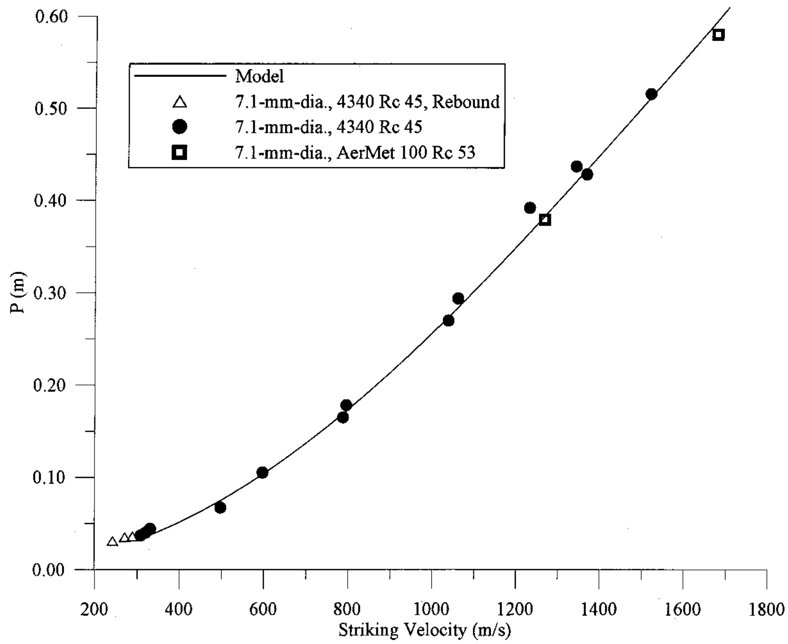


**Fig. 1 Data and prediction for limestone targets**

less than this limit velocity, the projectiles rebounded from the targets. The penetration limit velocity for these experiments was found to be about 300 m/s.

## Acknowledgment


This work was supported by the United States Department of Energy and the Joint DoD/DOE Munitions Technology Development Program. Sandia is a multiprogram laboratory operated by Sandia Corporation, a Lockheed Martin Company, for the United States Department of Energy under Contract DE-AC04-94AL85000.


## References


[1] Zukas, J. A., 1982, "Penetration and Perforation of Solids," *Impact Dynamics*, John Wiley and Sons, New York, Chap. 5.
[2] Zukas, J. A., 1990, "Introduction to Penetration Mechanics," *High Velocity Impact Dynamics*, John Wiley and Sons, New York, Chap. 4.
[3] Piekutowski, A. J., Forrestal, M. J., Poormon, K. L., and Warren, T. L., 1999, "Penetration of 6061-T6511 Aluminum Targets by Ogive-Nose Steel Projectiles With Striking Velocities Between 0.5 and 3.0 km/s," Int. J. Impact Eng., **23**, pp. 723–734.
[4] Frew, D. J., Forrestal, M. J., and Hanchak, S. J., 2000, "Penetration Experiments With Limestone Targets and Ogive-Nose Steel Projectiles," ASME J. Appl. Mech., **67**, pp. 841–845.
[5] Hanchak, S. J., 1999, "Projectile Imbed/Rebound Parameters in Salem Limestone," Interim Letter Report UD-TM-1999-00011, University of Dayton Research Institute, Dayton, OH.
[6] Brown, W. F., Mindlin, H., and Ho, C. Y., 1996, *Aerospace Structural Metals Handbook*, Vol. 1, Code 1206, CINDAS/USAF CRDA Handbooks Operation, Purdue University, West Lafayette, IN.
[7] Dahl, J., 1991, "Aer Met 100—An Advanced Steel for the Aerospace Industry," Adv. Mat. Tech. Int., pp. 40–45.


# One, Two, and Three-Dimensional Universal Laws for Fragmentation due to Impact and Explosion


**A. Carpinteri**
Professor,
e-mail: carpinteri@polito.it

**N. Pugno**
Researcher,
e-mail: pugno@polito.it

Department of Structural Engineering and Geotechnics,
Politecnico di Torino, Corso Duca degli Abruzzi
24, Torino, Italy



*Based on the fractal particle size distribution, a fragmentation theory for quasi-brittle materials is herein developed. The results are three simple and powerful universal laws for the multiscale energy dissipation under impact and explosion fragmentation for one, two, and three-dimensional bodies, respectively. The three-dimensional law unifies the most important and well-known fragmentation theories. As an example, it has been applied to the prediction of the devastated area due to asteroid impacts on earth as a function of the energy released in the collision.*


[DOI: 10.1115/1.1488937]


## 1 Introduction

Since the two pioneering books of Mandelbrot [1] and Feder [2], the noneuclidean, fractal, and multiscale geometry of nature has been observed everywhere. In particular, a fractal size distribution is clearly presented by particles obtained from explosive or impact fragmentation processes, both natural and man-made. The fractal nature of the phenomenon simply means that the fragments are geometrically self-similar at each scale. Engleman et al. [3] show that this particle size distribution (power-law) is a necessary consequence of the maximum entropy principle.

Based on the fractal particle size distribution, a fragmentation theory is herein developed. The results are three simple and pow-


Contributed by the Applied Mechanics Division of THE AMERICAN SOCIETY OF MECHANICAL ENGINEERS for publication in the ASME JOURNAL OF APPLIED MECHANICS. Manuscript received by the ASME Applied Mechanics Division, July 2, 2001; final revision, January 24, 2002. Associate Editor: K. Ravi-Chandar.

erful universal laws for the multiscale energy dissipation under impact and explosion fragmentation for one, two, and three-dimensional bodies, respectively.

The three-dimensional law unifies the most important and well-known fragmentation theories: the surface theory [4], when the dissipation occurs on a surface, the volume theory [5], when the dissipation occurs in a volume and the third comminution theory [6], when the dissipation occurs in a domain exactly intermediate between a surface and a volume (see [7]).

## 2 Three-Dimensional Theory

After comminution or fragmentation, the cumulative distribution of particles with radius ($=3\sqrt{3/4\pi\cdot \text{volume}_{\text{particle}}}$) smaller than $r$ is (see, for example, [8])

$$P(<r)=\frac{N(<r)}{N_0}=1-\left(\frac{r_{\min}}{r}\right)^D, \tag{1}$$

where $N(<r)$ is the number of fragments with radius smaller than $r$, $N_0$ is the total number of fragments, $r_{\min}$ ($\ll r_{\max}$) is the minimum fragment radius, and $D(>0)$ is the fractal dimension.

The probability density function $p(r)$ times the interval amplitude d$r$ represents the percentage of particles with radius comprised between $r$ and $r+\mathrm{d}r$. It is provided by derivation of the cumulative distribution function (1):

$$p(r)=\frac{dP(<r)}{dr}=D\,\frac{r_{\min}^D}{r^{D+1}}. \tag{2}$$

During fragmentation, the energy dissipation due to fracture, d$W_F$, is proportional to the surface area of fragments, d$S$ (Griffith [9]):

$$\mathrm{d}W_F\propto \mathrm{d}S. \tag{3}$$

During impact fragmentation (material in compression), the main dissipation d$W_C$ is due to collisions and friction between particles (converted into heat) and the effect results to be proportional to the same quantity dS (Smekal [10], see [7]):

$$\mathrm{d}W_C\propto \mathrm{d}S. \tag{4}$$

On the other hand, during explosion fragmentation (material in tension) the main dissipation d$W_T$ is proportional to the kinetic energy of fragmented ejecta d$T$. The velocity of fragmented ejecta varies inversely with fragment size as $v\propto r^{-1/2}$ (Nakamura and Fujiwara [11]), so that the kinetic energy, i.e., the main dissipation in explosion, results again in being proportional to the fragment surface d$S$ (of volume d$V$):

$$\mathrm{d}W_T\propto \mathrm{d}T\propto v^2\mathrm{d}V\alpha\mathrm{d}S. \tag{5}$$

Summarizing, the global dissipation in impacts ($W_C+W_F$) or explosions ($W_T+W_F$) surprisingly appears always proportional to the total surface area $S$ of fragments. It can be obtained by integration:

$$\begin{aligned}
S&=\int_{r_{\min}}^{r_{\max}}4\pi r^2\mathrm{d}N\\
&=\int_{r_{\min}}^{r_{\max}}N_0(4\pi r^2)p(r)\mathrm{d}r\\
&=4\pi N_0\frac{D}{D-2}r_{\min}^D\left(\frac{1}{r_{\min}^{D-2}}-\frac{1}{r_{\max}^{D-2}}\right)\\
&\cong\begin{cases}4\pi N_0\dfrac{D}{D-2}r_{\min}^2, & D>2\\[2ex] 4\pi N_0\dfrac{D}{2-D}r_{\min}^D r_{\max}^{2-D}, & D<2.\end{cases}
\end{aligned} \tag{6}$$

If $0<D<2$ it is necessary to specify $r_{\max}$ but not $r_{\min}$ in order to obtain a finite total surface area of fragments. But if $D>2$ it is necessary to specify $r_{\min}$ in order to constrain the total surface area to a finite value. Thus for most observed distribution of fragments the surface area of the smallest fragments dominates.

On the other hand, the total volume of the particles, or total fragmented volume $V$, is

$$\begin{aligned}
V&=\int_{r_{\min}}^{r_{\max}}\frac{4}{3}\pi r^3\mathrm{d}N\\
&=\int_{r_{\min}}^{r_{\max}}N_0\left(\frac{4}{3}\pi r^3\right)p(r)\mathrm{d}r\\
&=\frac{4}{3}\pi N_0\frac{D}{3-D}r_{\min}^D(r_{\max}^{3-D}-r_{\min}^{3-D})\\
&\cong\begin{cases}\dfrac{4}{3}\pi N_0\dfrac{D}{3-D}r_{\min}^3 r_{\max}^{3-D}, & D<3\\[2ex] \dfrac{4}{3}\pi N_0\dfrac{D}{D-3}r_{\min}^3, & D>3.\end{cases}
\end{aligned} \tag{7}$$

If $0<D<3$ it is necessary to specify $r_{\max}$ but not $r_{\min}$ in order to obtain a finite volume of fragments. The volume is predominantly in the largest fragments. This is the case for most observed distributions of fragments. If $D>3$ it is necessary to specify $r_{\min}$ but not $r_{\max}$. the volume of the small fragments dominates.

It is interesting to note that in Eqs. (6) and (7) $D$ equal to 2 and 3 do not represent singular points but indeterminate forms. So, the physical meaning is preserved also for $D$ equal to 2 and 3.

Based on fracture mechanics we can assume a material "quantum" of size $r_{\min}$=constant (Novozhilov [12] and Sammis [13]) and make a statistical hypothesis of self-similarity, i.e., $r_{\max}\propto\sqrt[3]{V}$ (the larger the fragmented volume, the larger the largest fragment; Carpinteri [14]), so that the energy $W$ dissipated in a three-dimensional fragmentation process, which is proportional to the total surface area $S$, can be obtained eliminating $N_0$ from Eqs. (6) and (7) as

$$W\propto S\propto V^{\bar{D}/3},\quad\text{with}\begin{cases}\bar{D}=2, & D<2\\ \bar{D}\equiv D, & 2\leqslant D\leqslant 3\\ \bar{D}=3, & D>3.\end{cases} \tag{8}$$

The universal law of Eq. (8) can be used to predict the multiscale energy dissipation under fragmentation in impacts and explosions of three-dimensional bodies. It represents an extension of the third comminution theory, where $W\propto V^{2.5/3}$ ([6]; see [7]). The extreme cases contemplated by Eq. (8) are represented by $\bar{D}=2$, surface theory ([4]; see [7]), when the dissipation really occurs on a surface ($W\propto V^{2/3}$), and by $\bar{D}=3$, volume theory ([5]; see [7]), when the dissipation occurs in a volume ($W\propto V$). These three laws are substantially experimental, so that the universal law of Eq. (8) is obviously experimentally verified.

## 3 Two-Dimensional Theory

For a two-dimensional body of area $A$ (and thickness $h$), we have

$$S=\int_{r_{\min}}^{r_{\max}}N(2\pi rh)p(r)dr,\quad A=\int_{r_{\min}}^{r_{\max}}N(\pi r^2)p(r)dr,$$

$$r_{\max}\propto\sqrt[2]{A}, \tag{9}$$

so that Eq. (8) becomes

$$W \propto S \propto A^{\bar{D}/2}, \quad \text{with} \begin{cases} \bar{D}=1, & D<1 \\ \bar{D}\equiv D, & 1\leqslant D\leqslant 2 \\ \bar{D}=2, & D>2. \end{cases} \tag{10}$$

The universal law of Eq. (10) can be used to predict the multiscale energy dissipation under fragmentation in impacts and explosions of two-dimensional bodies (e.g., panel or shell structures).

## 4 One-Dimensional Theory

For a one-dimensional body of length $L$ (and cross section $h^2$), we have

$$S=\int_{r_{\min}}^{r_{\max}} Nh^2 p(r)dr = Nh^2, \quad L=\int_{r_{\min}}^{r_{\max}} Nrp(r)dr = N\bar{r},$$

$$r_{\max} \propto L, \tag{11}$$

so that Eq. (8) becomes ($D>0$)

$$W \propto S \propto L^{\bar{D}}, \quad \text{with} \begin{cases} \bar{D}\equiv D, & D\leqslant 1 \\ \bar{D}=1, & D>1. \end{cases} \tag{12}$$

The universal law of Eq. (12) can be used to predict the multiscale energy dissipation under fragmentation in impacts and explosions of one-dimensional bodies (e.g., beams or cables).

## 5 An Example of Application: The Asteroid Collision

As an example, we can apply the three-dimensional law to the prediction of the devastated area due to asteroid impacts on earth as a function of the energy released in the collision. The comparison with the experimental Steel's law ([15]), based on nuclear weapons tests, shows a good correspondence.

Assuming that the destroyed zones (or fragmented volumes $V$) are self-similar at each scale, the area $\Omega_{\text{devasted}}$ devastated by an impact is proportional to $V^{2/3}$ and, being $W \propto V^{\bar{D}/3}$, the theoretical prediction for the devastated area will be

$$\Omega_{\text{devasted}} \propto W^{2/\bar{D}}. \tag{13}$$

Steel [15] provided the following formula (see http://www1.tpgi.com.au/users/tps-seti/spacegd7.html), based on nuclear weapons tests, for estimating the area of destruction due to asteroid impacts:

$$\Omega_{\text{devasted}} = 400W^{0.67}, \quad [\Omega_{\text{devasted}}]=[\text{km}^2], \quad [W]=[\text{megatons}]. \tag{14}$$

Equation (14) appears in good agreement with the theoretical prediction of Eq. (13) and, if we assume $\bar{D}\approx 3$, they practically coincide.

## 6 Conclusions

Summarizing, the universal laws for the energy dissipation in impact and explosion fragmentation of one, two, or three-dimensional bodies can be rewritten as

$$\begin{aligned} &W \propto L^{\bar{D}} \quad (0\leqslant \bar{D}\leqslant 1) \quad \text{one-dimensional} \\ &W \propto A^{\bar{D}/2} \quad (1\leqslant \bar{D}\leqslant 2) \quad \text{two-dimensional} \\ &W \propto V^{\bar{D}/3} \quad (2\leqslant \bar{D}\leqslant 3) \quad \text{three-dimensional.} \end{aligned} \tag{15}$$

The three-dimensional law unifies the experimentally verified and well-known fragmentation theories (surface theory, von Rittinger [4]; volume theory, Kick [5]; and third comminution theory, Bond [6]; see [7]).


## Acknowledgment

The present research was carried out with the financial support of Ministry of University and Scientific Research (MURST), National Research Council (CNR) and EC-TMR Contract No. ERBFMRXCT960062.


## References


[1] Mandelbrot, B. B., 1982, *The Fractal Geometry of Nature*, Freeman, New York.
[2] Feder, J., 1988, *Fractals*, Plenum, New York.
[3] Engleman, R., Rivier, N., and Jaeger, Z., 1988, "Size Distribution in Sudden Breakage by the Use of Entropy Maximization." J. Appl. Phys., **63**, pp. 4766–4768.
[4] von Rittinger, P. R., 1867, *Lehrbuch der Aufbereitungskunde*, Berlin.
[5] Kick, F., 1885, *Das Gesetz der Proportionalen Widerstände*, Leipzig.
[6] Bond, F. C., 1952, "The Third Theory of Comminution," Mining Eng., **4**(5)(Aime Trans 193), pp. 484–494.
[7] Béla Beke, D., 1964, *Principles of Comminution*, Publishing House of the Hungarian Academic of Sciences, Budapest.
[8] Turcotte, D. L., 1992, *Fractals and Chaos in Geology and Geophysics*, Cambridge University Press, Cambridge, UK.
[9] Griffith, A. A., 1921, "The Phenomenon of Rupture and Flow in Solids," Philos. Trans. R. Soc. Lond. Ser. A., **221**, pp. 163–198.
[10] Smekal, A., 1937, *Physikalisches und technisches Arbeitsgesetz der Zerkleinerung*, Zeitschr. VDI, Beiheft Verfahrenstechnik.
[11] Nakamura, A., and Fujiwara, A., 1991, Icarus, **92**, 132.
[12] Novozhilov, V., 1969, "On a Necessary and Sufficient Criterion for Brittle Strength," Prikl. Mat. Mekh., **33**, pp. 212–222.
[13] Sammis, C. G., 1997, "Fractal Fragmentation and Frictional Stability in Granular Materials," *IUTAM Symposium on Mechanics of Granular and Porous Materials*, Kluwer, The Netherlands, pp. 23–34.
[14] Carpinteri, A., 1986, *Mechanical Damage and Crack Growth in Concrete*, Martinuus Nijhoff, Dordrecht, the Netherlands.
[15] Steel, D., 1995, *Rogue Asteroids and Doomsday Comets*, John Wiley and Sons, New York.


# A Note on the Application of the Flamant Solution of Classical Elasticity to Circular Domains


**A. J. Levy**
Department of Mechanical, Aerospace and Manufacturing Engineering, Syracuse University, Syracuse, NY 13244-1240. Mem. ASME



*It is a well known fact that the Flamant solution of classical elasticity cannot be used at an interior point of an elastic body since the resulting displacement field would be multivalued. In this note we demonstrate that the solution to the problem of a concentrated force at a point on an interior circular boundary has a multivalued displacement component but that the exclusion of the point of application of the load from the domain renders the displacement field single-valued everywhere.*


[DOI: 10.1115/1.1480821]


## 1 Introduction

This note contains an analysis of nonuniform convergence of the displacement field in the Flamant solution to the problem of a concentrated force at a point of an interior circular boundary of an unbounded elastic domain. This issue, which does not exist in the Flamant problem for the straight boundary, arose in previous work by the author on cavity nucleation in planar inclusion problems where the inclusion-matrix interface is modeled explicitly by a


Contributed by the Applied Mechanics Division of THE AMERICAN SOCIETY OF MECHANICAL ENGINEERS for publication in the ASME JOURNAL OF APPLIED MECHANICS. Manuscript received by the ASME Applied Mechanics Division, July 12, 2001; final revision, March 4, 2002. Associate Editor: M.-J. Pindera.

nonlinear cohesive zone of vanishing thickness (Levy [1]). In that work the Flamant solution for the boundary displacement is used as a Green's function in an integral equation formulation of the problem. In two interesting papers, Dundurs and Hetényi [2], and Dundurs et al. [3] have considered the problem of a circular inclusion in an unbounded plate subject to a concentrated force at a point of the plate and oriented so that its line of action is along a diametral line.[1] The problem considered in this note is therefore a special case of these studies. The focus of [2,3], however, is on constructing the Airy stress functions and providing formulas for the stress components. Although the nature of the singularity is discussed, and the condition of single-valued displacements is enforced, no explicit consideration is given to the issue of the nonuniform convergence of the tangential displacement at the boundary, which is the subject of this note.

In order to explore this issue, first consider the Flamant solution to the problem of a concentrated force acting at a point on a straight boundary. In that problem the force acts at a point with radius $r=0$ which is situated on a straight boundary which can be defined by the polar angles $\theta=0$, $\theta=-\pi$. For the case where the load is directed along the outward normal to the boundary, it is well known that the displacement normal to the boundary ($u_r$) becomes unbounded, while the displacement tangent to the boundary ($u_\theta$) becomes multivalued, as $r$ approaches zero. Note that each point within the domain $D=\{(r,\theta)|r\in(0,\infty), \theta\in[-\pi,0]\}$ occupied by the half-plane is uniquely represented by one set of coordinates. Only when $r$ is zero, do points coalesce and then multivaluedness becomes an issue. Because it is implicitly assumed that a neighborhood of the point $r=0$ is excluded from the domain the displacement field is therefore bounded and single-valued everywhere in $D$. This contrasts with the Flamant problem for circular domains (Fig. 1). Here, the domain of interest is given by $D=\{(r,\theta)|r\in[a,\infty),\theta\in[0,2\pi]\}$ so that multivaluedness (or continuity if $\theta\in[0,2\pi)$) becomes an issue not just on the boundary $r=a$ but for any $r\in[a,\infty)$. It is a straightforward matter to demonstrate that on the boundary $r=a$ the tangential displacement is multivalued at $\theta=0$ and $\theta=2\pi$. The interesting part of this problem, and the primary concern of this note, is in demonstrating the nonuniform convergence of the tangential displacement component $u_\theta(r,\theta)$ as $r\downarrow a$ to a multivalued limit function for $r=a,\ \theta\in[0,2\pi]$.

A formal statement of the Flamant problem appears, without solution, in the elasticity text of Timoshenko and Goodier [4], for the case of a concentrated load acting normal to the interior circular boundary, and is restated here verbatim:

"*Verify that the stress function*[2]

$$\phi=-\frac{P}{\pi}\left\{\psi r\sin\theta-\frac{1}{4}(1-\nu)r\log r\cos\theta-\frac{1}{2}r\theta\sin\theta+\frac{d}{4}\log r-\frac{d^2}{32}(3-\nu)\frac{1}{r}\cos\theta\right\} \tag{1}$$

*satisfies the boundary conditions for a force P acting in a hole in an infinite plate with zero stress at infinity, and that the circumferential stress round the hole is*

$$\frac{P}{\pi d}[2+(3-\nu)\cos\theta] \tag{2}$$

*except at* A *(Fig. 1). Show that it also corresponds to single-valued displacements."*

Note that the last sentence in the problem statement explicitly refers to the issue of single-valued displacements. This will be analyzed in Section 3. Section 2 contains an outline of the solution for the stresses and displacements.

[1]Reference [2] considers the perfectly bonded interface while [3] treats the smooth interface.

[2]$\phi$ is appropriate for plane stress. For plane strain let $\nu\to\nu/(1-\nu)$.

## 2 The Solution

Because the problem as originally stated provides the stress function, we will proceed directly from it as opposed to using complex potentials. First, note the following geometrical relations (Fig. 1), valid away from the point (A) of application of the load $P$,

$$\begin{aligned}
&R\sin\psi=r\sin\theta,\\
&R^2=a^2+r^2-2ar\cos\theta,\\
&a\sin\psi=r\sin(\psi-\theta),\\
&\cos\psi=-R/2a\quad\text{on}\quad r=a,\\
&\sin\psi=a\sin\theta/R\quad\text{on}\quad r=a,\\
&\cos\psi\sin\psi=-\sin\theta/2\quad\text{on}\quad r=a.
\end{aligned} \tag{3}$$

The stress function $R\psi\sin\psi$ gives rise to the well-known simple radial stress distribution of a force acting at a point of a boundary. The polar components of this stress state, referred to a basis at the hole center, are easily shown to be given by

$$\begin{aligned}
S_{rr}&=\frac{2\cos\psi}{R}\cos^2(\theta-\psi),\\
S_{r\theta}&=-\frac{2\cos\psi}{R}\cos(\theta-\psi)\sin(\theta-\psi),\\
S_{\theta\theta}&=\frac{2\cos\psi}{R}\sin^2(\theta-\psi),
\end{aligned} \tag{4}$$

which may be expressed entirely in terms of $(r,\theta)$ by utilizing geometrical relations (3). This distribution gives rise to nonvanishing tractions on the hole surface which must be removed by superimposing the stress field arising from the stress function

$$-\frac{1}{4}(1-\nu)r\log r\cos\theta-\frac{1}{2}r\theta\sin\theta+\frac{a}{2}\log r-\frac{a^2}{8}(3-\nu)\frac{1}{r}\cos\theta.$$

For this function the polar components of stress follow from the stress table in Barber [5],

$$\begin{aligned}
S_{rr}&=-\frac{1}{4}(1-\nu)\frac{\cos\theta}{r}-\frac{\cos\theta}{r}+\frac{a}{2}\frac{1}{r^2}+\frac{a^2}{4}(3-\nu)\frac{\cos\theta}{r^3},\\
S_{r\theta}&=-\frac{1}{4}(1-\nu)\frac{\sin\theta}{r}+\frac{a^2}{4}(3-\nu)\frac{\sin\theta}{r^3},\\
S_{\theta\theta}&=-\frac{1}{4}(1-\nu)\frac{\cos\theta}{r}-\frac{a}{2}\frac{1}{r^2}-\frac{a^2}{4}(3-\nu)\frac{\cos\theta}{r^3}.
\end{aligned} \tag{5}$$

The complete stress field for the problem follows directly by superimposing like components in (4) and (5) and multiplying each component sum by $-(P/\pi)$. By utilizing the relations in (3) it can be quickly verified that the circumferential stress at $r=a$ is given by (2) while the normal and tangential tractions on the boundary ($S_{rr}(r=a)$, $S_{r\theta}(r=a)$, respectively) vanish away from point A.

The calculation for the polar components of displacement follows from the stress function and the displacement table in Barber [5],

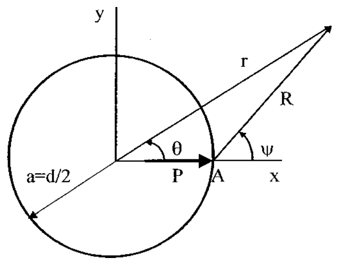


**Fig. 1 Problem geometry**

$$\frac{4\mu\pi u_r}{P}=-(\kappa-1)(\psi-\theta)\sin\theta-(\kappa+1)\log R\cos\theta+2\cos^2\psi\cos\theta+2\cos\psi\sin\psi\sin\theta-\left[\frac{1}{4}(1-\nu)+\frac{3}{2}\right]\cos\theta+(\kappa-1)\log r\cos\theta+\frac{a}{r}+\frac{\kappa}{\kappa+1}\frac{a^2}{r^2}\cos\theta, \tag{6}$$

$$\frac{4\mu\pi u_\theta}{P}=-(\kappa-1)(\psi-\theta)\cos\theta+(\kappa+1)\log R\sin\theta-2\cos^2\psi\sin\theta+2\cos\psi\sin\psi\cos\theta-\left[\frac{1}{4}(1-\nu)-\frac{1}{2}\right]\sin\theta-(\kappa-1)\log r\sin\theta+\frac{\kappa}{\kappa+1}\frac{a^2}{r^2}\sin\theta,$$

where $\kappa$ is $(3-\nu)/(1+\nu)$ for plane stress and $3-4\nu$ for plane strain. Consider the displacement of points initially situated on the boundary $r=a$. By using relations (3) in displacement components (6) we arrive at the form

$$4\mu u_r=\frac{P}{\pi}\left[-\frac{\kappa-1}{2}(\pi-\theta)\sin\theta-\frac{\kappa+1}{2}\log(1-\cos\theta)\cos\theta\right], \tag{7}$$
$$4\mu u_\theta=\frac{P}{\pi}\left[-\frac{\kappa-1}{2}(\pi-\theta)\cos\theta+\frac{\kappa+1}{2}\log(1-\cos\theta)\sin\theta\right],$$

where for compactness we have superimposed an appropriate rigid-body displacement. An interesting feature of this boundary displacement is that it is multivalued. A casual inspection of (7) reveals that the offending term occurs in the expression for $u_\theta$, i.e., $(\pi-\theta)\cos\theta$. This will be discussed in the following section. For now, we note that the boundary displacement behaves correctly in the simple case of a uniform pressure applied to the inner boundary. To see this introduce the kernel functions

$$U_r=\mathbf{e}_r\cdot\mathbf{U}\mathbf{e}_r=-\frac{\kappa+1}{8\pi\mu}\cos\theta\log(1-\cos\theta)-\frac{\kappa-1}{8\pi\mu}(\pi-\theta)\sin\theta, \tag{8}$$
$$U_\theta=\mathbf{e}_\theta\cdot\mathbf{U}\mathbf{e}_\theta=\frac{\kappa+1}{8\pi\mu}\sin\theta\log(1-\cos\theta)-\frac{\kappa-1}{8\pi\mu}(\pi-\theta)\cos\theta.$$

Then the boundary displacement is determined by

$$\mathbf{u}=\int_{\partial\mathbf{R}}\mathbf{U}\mathbf{s}(\mathbf{n})ds, \tag{9}$$

where $\mathbf{s(n)}$ is the traction vector and $\mathbf{n}$ is the unit normal vector pointing away from the boundary $\partial R$. Note that in (9) $\mathbf{U}$ is a function of the difference $\theta-\theta'$,[3] $\mathbf{s(n)}$ is a function of $\theta'$, $\mathbf{u}$ is a function of $\theta$ and integration is carried out with respect to $\theta'$. For a pressure load, $\mathbf{s(n)}=p_0\mathbf{e}_r$ (8) and (9) yield the boundary displacement vector $\mathbf{u}=(ap_0/2\mu)\mathbf{e}_r$.

[3]That is, the difference between field point and source point.

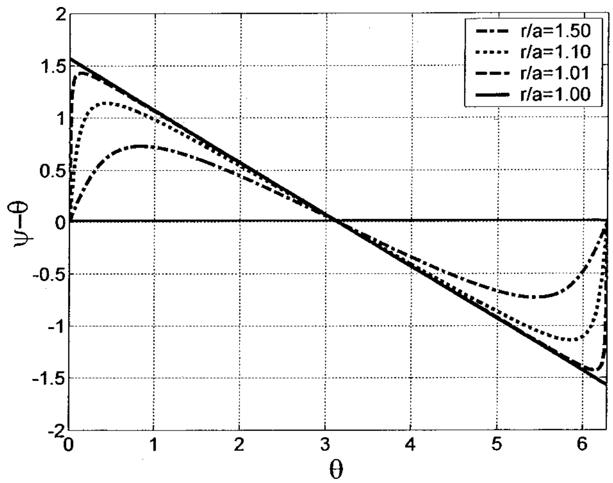


**Fig. 2 Nonuniform convergence of function $\psi-\theta$**

## 3 Discussion

First, the stress components are single-valued and infinitely differentiable at all points within the domain except at point A. This follows directly from (4) and (5). Now consider the displacement field (6) and in particular the terms $(\psi-\theta)\sin\theta$, $(\psi-\theta)\cos\theta$. From Fig. 1 and the first three identities in (3) it follows that

$$\psi-\theta=\sin^{-1}\left(\frac{a\sin\theta}{\sqrt{r^2+a^2-2ar\cos\theta}}\right),\quad \theta\in[0,2\pi],\quad r\in(a,\infty). \tag{10}$$

Now for $r\in(a,\infty)$ the function $\psi-\theta$ is a single-valued and continuous function of $(r,\ \theta)$. Consider the limit as $r\downarrow a$ for $\theta\in(0,2\pi)$. It is not hard to show that

$$\lim[\psi(r,\theta)-\theta]=\frac{\pi-\theta}{2},r\downarrow a \tag{11}$$

which is consistent with boundary displacement (7). Thus we have the fact that, while single-valued and continuous for all $r\in(a,\infty)$, $\theta\in[0,2\pi]$, $\psi-\theta$ converges to a discontinuous limit function on $r=a$, $\theta\in[0,2\pi)$, i.e., the function $\psi-\theta$ is multivalued on $r=a$, $\theta\in[0,2\pi]$. The limit function $(\pi-\theta)/2$ is piecewise continuous and $2\pi$ periodic on $r=a$, the points of discontinuity occurring at $\theta=0$, $\pm2n\pi$, $n$ integer. (A graph of this function is shown in Fig. 2 for values of $r/a$ approaching unity.) The above discussion concerning the function $\psi(r,\theta)-\theta$ implies that the tangential component of displacement $u_\theta(r,\theta)$ has the following properties:

$$u_\theta(r,0)=u_\theta(r,2\pi),\quad r\in(a,\infty),$$
$$\mathrm{Lim}\ u_\theta(r,0)=0\neq u_\theta(a,0),\quad r\downarrow a,$$
$$\mathrm{Lim}\ u_\theta(r,2\pi)=0\neq u_\theta(a,2\pi),\quad r\downarrow a,$$
$$u_\theta(a,0)\neq u_\theta(a,2\pi) \tag{12}$$

where use has been made of (6). Because the point $(r=a,\theta=0,2\pi)$ is excluded from the domain (it coincides with the point A of application of the concentrated force $P$ and the point of singularity for the stresses) the displacement field is single-valued and continuous everywhere in the domain. The equation for the deformed boundary is given by

$$\frac{\tilde{a}}{a}=1-\alpha\left[\frac{\kappa-1}{2}(\pi-\theta)\sin\theta+\frac{\kappa+1}{2}\log(1-\cos\theta)\cos\theta\right],$$
$$\alpha=\frac{P}{4\mu\pi}. \tag{13}$$

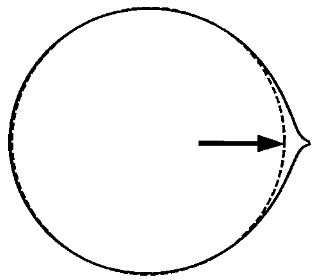

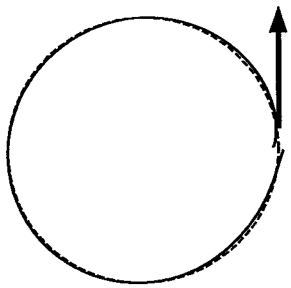

Fig. 3 Boundary distortion; (*a*) normal force ($\alpha=.01, \nu=1/3$), (*b*) tangential force ($\alpha=0.4, \nu=1/3$)

Figure 3(*a*) shows the distortion of the boundary near the point of application of the load for the case of plane strain.

Note that the related problem of a tangential force $F$ acting at a point on the interior boundary of an unbounded domain gives rise to similar behavior. For that problem, it can be shown that the components of boundary displacement are given by

$$4\mu u_r=\frac{F}{\pi}\left[\frac{\kappa-1}{2}(\pi-\theta)\cos\theta-\frac{\kappa+1}{2}\log(1-\cos\theta)\sin\theta\right],$$
$$4\mu u_\theta=\frac{F}{\pi}\left[-\frac{\kappa-1}{2}(\pi-\theta)\sin\theta-\frac{\kappa+1}{2}\log(1-\cos\theta)\cos\theta\right], \tag{14}$$

so that the breakdown in single-valued behavior at the point of application of load $F$ occurs in the expression for the radial component of displacement. This fact gives rise to a more jarring picture of the boundary displacement field (Fig. 3(*b*)).

## References


[1] Levy, A. J., 1998, "The Affect of Interfacial Shear on Cavity Formation at an Elastic Inhomogeneity," J. Elast., **50**, pp. 49–85.
[2] Dundurs, J., and Hetényi, M., 1961, "The Elastic Plane With a Circular Insert, Loaded by a Radial Force," ASME J. Appl. Mech., **28**, pp. 103–111.
[3] Dundurs, J., Fukui, K., and Fukui, T., 1966, "Concentrated Force Near a Smooth Circular Inclusion," ASME J. Appl. Mech., **33**, pp. 871–876.
[4] Timoshenko, S. P., and Goodier, J. N., 1934, *Theory of Elasticity*, McGraw-Hill, New York.
[5] Barber, J. R., 1992, *Elasticity*, Kluwer Academic, Dordrecht, The Netherlands.


# A Closed Contour With No Warping: A Common Feature in all Confocally Elliptical Hollow Sections


**T. Chen**
e-mail: tchen@mail.ncku.edu.tw

**Y. J. Kung**

Department of Civil Engineering, National Cheng Kung University, Tainan 70101, Taiwan



*We show that for a confocally elliptical hollow section under Saint-Venant's torsion, there always exists a confocally elliptical closed contour inside the section that exhibits no warping. This property is generally true without any regard to the thickness or the aspect ratio of the hollow section, as long as the inner and the outer ellipses are confocal. This property allows us to apply Packham and Shail's (Packham, B. A, and Shail, R., 1978, "St. Venant Torsion of Composite Cylinders," J. Elast., **8**, pp. 393–407) superposition method for the torsion solutions of a two-phase elliptical hollow section. Previously, this superposition method is only applicable to symmetric compound sections with respect to a straight line or a circular arc.* [DOI: 10.1115/1.1504095]


## 1 Introduction

Saint-Venant's torsion of a prismatic bar is a classic problem in solid mechanics. For a circular cross-section or circular ring under torsion, it is well known that there is no warping in the section. For a cross section of general shape, typically the absence of warping only occurs at positions which exhibit the symmetry of the geometry. For instance, the warping contour of a square bar under torsion indicates that there are only four straight lines with zero warping, two diagonal, one horizontal, and one vertical (see, for example, [1], p. 133, Fig. 27). In this work, we found, incidentally, that for a confocally elliptical hollow section there always exists a closed elliptical contour inside the section that has no warping. We make use of a mapping function that transforms the confocal ellipses in the $z$-plane onto concentric circles in the $p$-plane. Suppose the outer and the inner ellipses are mapped, respectively, onto circles with radii 1 and $r$, we find, remarkably, that this closed contour with no warping is simply given by $|p|=r^{1/2}$. In other words, this zero warping closed contour is also a confocal ellipse with the same foci as that of the inner and outer ellipses. This existence of the zero-warping contour is found without any regard to the thickness or the aspect ratio of the hollow section, provided that the inner and the outer ellipses are confocal. A recent paper of Chiskis and Parnes [2] proposed a general criterion for closed thin-wall members which exhibit no warping under the condition of constant thickness. By letting $|p|\rightarrow 1$, the present finding serves as a complemental example of the absence of warping for a thin-wall section with *nonconstant* thickness.

The finding makes it possible to extend Packham and Shail's superposition method [3] to find the torsion solution of a *two-phase* confocally elliptical hollow section. This method states that for a certain symmetric two-phase section, the torsion solution can be obtained by a linear superposition of two solutions with homogeneous sections: one is the solution of the whole section and the other is one part of the compound section. Originally, this superposition method was only applicable to a two-phase symmetric section in which the interface is of a straight line or of a circular arc. This finding of the applicability of Packham and Shail's method to elliptical interface is new and may have further implication on solutions of various compound elliptical geometries. In the analysis, we use the complex function theory together with conformal mapping techniques. We start with a brief revisit on the torsion solution of hollow sections and prove the assertion in Section 3. The validity of the superposition method to a special class of elliptical compound section is shown in Section 4.

## 2 A Revisit of Torsion of Hollow Sections

Consider the Saint-Venant's torsion problem of a hollow shaft with shear modulus $\mu$ whose cross-section $R$ is bounded by two single curves $L_i$, $i=1,2$. We use the complex variables approach together with the method of conformal mapping to solve for the


Contributed by the Applied Mechanics Division of THE AMERICAN SOCIETY OF MECHANICAL ENGINEERS for publication in the ASME JOURNAL OF APPLIED MECHANICS. Manuscript received by the ASME Applied Mechanics Division, August 27, 2001; final revision, April 3, 2002. Associate Editor: J. R. Barber.

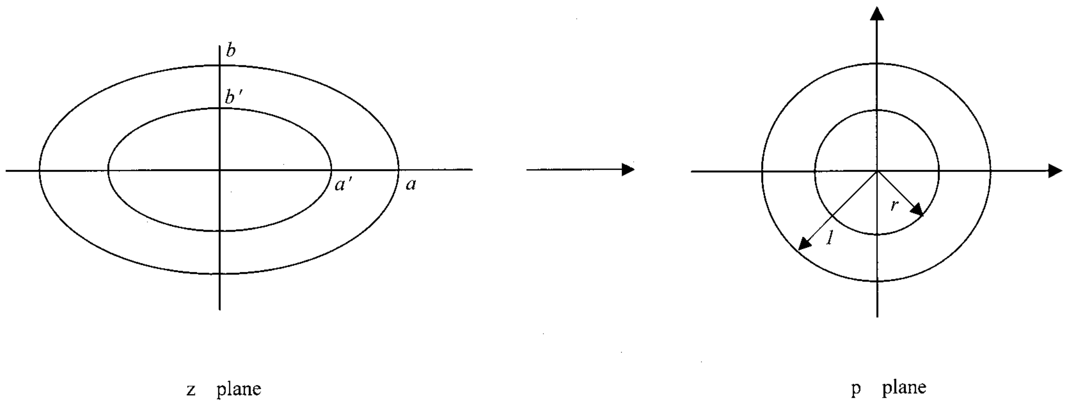


**Fig. 1 A schematic illustration of a confocally elliptical hollow section mapping onto a concentric circle**

warping function to this question. The displacement fields of the Saint-Venant torsion are characterized by $u_x=-\vartheta yz$, $u_y=\vartheta xz$, and $u_z=\vartheta\varphi(x,y)$, where $\vartheta$ is the angle of twist per unit length of the bar and $\varphi$ is the warping function. The equilibrium condition $\sigma_{ij,j}=0$ requires that $\varphi$ be harmonic throughout the cross section of the cylinder. On the traction-free boundary $L_i$, the boundary condition is written in the form

$$\frac{d\varphi}{dn}=-\mathbf{v}\cdot\mathbf{n}|_{L_i}, \tag{2.1}$$

where $\mathbf{v}=-y\ \mathbf{i}+x\ \mathbf{j}$ and $n$ denotes the outward normal to $L_i$. Since $\varphi$ is harmonic, one can construct the analytic function $w(z)=\varphi(z)+i\psi(z)$, of the complex variable $z=x+iy$, in which $\psi$ is the conjugate harmonic function.

Since for any doubly connected region $R$ in the $z$-plane there exists a one-to-one conformal mapping that transform the domain $R$ onto a circular annulus with outer radius 1 and inner radius $r$ in the $p$-plane [4,5]. This mapping function can be written as

$$z(p)=\sum_{n=-\infty}^{\infty}a_np^n,\quad p=\rho e^{i\theta}, \tag{2.2}$$

where $a_n$ are some complex coefficients. The analytic function $w(z(p))$ in the circular annulus can also be expressed as a Laurent series

$$w(p)=\sum_{n=-\infty}^{\infty}b_np^n, \tag{2.3}$$

with unknown coefficients $b_n$, and the boundary conditions (2.1) are now transformed to

$$\begin{aligned}w_c(p)-\overline{w_c}(\overline{p})&=iz(p)\overline{z}(\overline{p})|_{|p|=1}+\text{const.},\\ w_c(p)-\overline{w_c}(\overline{p})&=iz(p)\overline{z}(\overline{p})|_{|p|=r}+\text{const.},\end{aligned} \tag{2.4}$$

where the bar denotes the complex conjugation. We expand the series, using (2.2), [6] (see also [7] for simply connected sections)

$$z(p)\overline{z}(\overline{p})=\sum_{k=0}^{\infty}A_ke^{ik\theta}+\sum_{k=1}^{\infty}\overline{A}_ke^{-ik\theta}, \tag{2.5}$$

where

$$A_k=\sum_{j=-\infty}^{\infty}a_{j+k}\overline{a}_j\rho^{2j+k}. \tag{2.6}$$

Thus, Eq. $(2.4)_1$ provides

$$\sum_{n=-\infty}^{\infty}b_ne^{in\theta}-\sum_{n=-\infty}^{\infty}\overline{b_n}e^{-in\theta}=i\left(\sum_{k=0}^{\infty}A_k|_{\rho=1}e^{ik\theta}+\sum_{k=1}^{\infty}\overline{A_k}|_{\rho=1}e^{-ik\theta}\right)+\text{const.}, \tag{2.7}$$

and $(2.4)_2$ gives

$$\sum_{n=-\infty}^{\infty}b_nr^ne^{in\theta}-\sum_{n=-\infty}^{\infty}\overline{b_n}r^ne^{-in\theta}=i\left(\sum_{k=0}^{\infty}A_k|_{\rho=r}e^{ik\theta}+\sum_{k=1}^{\infty}\overline{A_k}|_{\rho=r}e^{-ik\theta}\right)+\text{const.} \tag{2.8}$$

Equivalently, (2.7) and (2.8) imply that

$$\begin{cases}b_k-\overline{b_{-k}}=iA_k|_{\rho=1},\\ b_kr^k+\overline{b_{-k}}r^{-k}=iA_k|_{\rho=r},\end{cases}\quad\text{for } k=1,2,\cdots,\infty. \tag{2.9}$$

This leads to

$$b_k=\frac{i(r^{-k}A_k|_{\rho=1}-A_k|_{\rho=r})}{r^{-k}-r^k},\quad b_{-k}=\frac{i(r^k\overline{A_k}|_{\rho=1}-\overline{A_k}|_{\rho=r})}{r^k-r^{-k}}, \tag{2.10}$$

and the coefficient $b_0$ is left as arbitrary. Apart from a nonessential constant, Eqs. (2.3) and (2.10) constitute the torsion solutions of any hollow section described by the mapping function (2.2). Various shapes of technological interests can be resolved without any difficulty. For example, one can consider the hollow epitrochoids, hypotrochoids, and many others [8]. A general solution for the stress function which uses conformal mapping for hollow cylinders of general geometry can also be found in Lurie ([9], pp. 405–407). We mention that previous solutions derived by Bartels [10] for eccentric ring and hollow lune can be reconstructed in a simple and unified manner. Instead of seeking warping fields of various geometric shapes, we shall restrict our attention on confocally elliptical hollow section.

## 3 A Contour With No Warping in Confocally Elliptical Hollow Sections

We consider here the hollow section is of a confocally elliptical shape. The outer elliptical boundary is defined by the $(a,\ b)$-axes, and the inner boundary by the $(a', b')$-axes, in which $a$ and $a'$ are the major axes of these ellipses. In the mapping (2.2) we assign (Fig. 1)

$$z(p)=\frac{a+b}{2}p+\frac{a-b}{2}p^{-1}. \tag{3.1}$$

It is well known [8] that the transformation (3.1) maps a confocal elliptical configuration in the $z$-plane onto concentric circles in the $p$-plane. The outer and inner ellipses are mapped, respectively, onto the circles $\rho=1$ and $\rho=r$ in the $p$-plane. The semi-axes of the inner and outer ellipse are interrelated by the following connections:

$$a'=\frac{a+b}{2}r+\frac{a-b}{2}r^{-1}, \quad b'=\frac{a+b}{2}r-\frac{a-b}{2}r^{-1}. \tag{3.2}$$

Thus, the circle of radius $\rho=m^{1/2}$, where $m=(a-b)/(a+b)$, in the $p$-plane is mapped onto a flat ellipse with $a'=c$ and $b'\to 0$ in the physical plane, where $c$ is the common focal distance of all the ellipses given by $c=\sqrt{a^2-b^2}$. This flat ellipse represents here a crack of length $2c$ lying on the $x$-axis. It is therefore seen that the parameter $r$ needs therefore to obey the constraint $m^{1/2}\leqslant r\leqslant 1$.

From the results of (2.10), it can be verified that

$$w=b_2p^2+b_{-2}p^{-2}, \tag{3.3}$$

where

$$b_2=i\frac{c^2}{4}\frac{r^{-2}-1}{r^{-2}-r^2}, \quad b_{-2}=i\frac{c^2}{4}\frac{1-r^2}{r^{-2}-r^2}. \tag{3.4}$$

This suggests that the warping function in the hollow ellipse takes the simple form

$$\varphi(p)=\frac{c^2}{4}\frac{1}{1+r^{-2}}\left(\rho^{-2}-\frac{\rho^2}{r^2}\right)\sin 2\theta. \tag{3.5}$$

Greenhill [11] was the first to solve the solution of hollow confocal ellipse in terms of the conjugate warping function ([12], p. 320) using a different mapping function $z=c\cosh(\xi+i\eta)$. Although tedious, we have verified analytically that both expressions are equivalent. It is also mentioned that the torsion solution for confocally elliptical hollow section can also be found in Lurie ([9], pp. 407–409) in which the solutions are obtained in terms of stress function.

Back to (3.5), letting $\varphi(p)=0$ will give

$$\sin 2\theta=0, \text{ or } \rho^{-2}-\frac{\rho^2}{r^2}=0. \tag{3.6}$$

The first condition is an expected outcome, as they in fact represent the lines of geometric symmetry. The latter is somewhat surprising, which gives exactly

$$\rho=r^{1/2}. \tag{3.7}$$

Since the closed contour $r^{1/2}$ always lies inside the interval of ($r$, 1), (3.7) suggests that there always exists a unique closed contour that exhibits no warping inside the hollow ellipse, without any regard to the value of $r$ (or the thickness of the hollow section). It is mentioned that the contour of $\rho=r^{1/2}$ represents an ellipse with the same foci common to the outer and the inner ellipses. A similar analysis has been carried out for a number of geometries (corresponding to different mapping functions). It turns out that no simple guidelines can be found. For instance, there exists no zero-warping closed contours for any hollow epitrochoid and, for hollow hypotrochoids the existence of the zero-warping contour depends on the dimension as well as the geometric factor.

Back to (3.7), for a thin-wall limitation, we set $r=1-\delta$, where $\delta\to 0$ and the elliptical hollow section becomes a thin ring of variable thickness. It follows from (3.2) that the axes of the inner ellipse are $a'=a-b\delta$ and $b'=b-a\delta$, and the major and minor axes of the zero-warping contour are

$$a|_{\rho=r^{1/2}}=a-\frac{b}{2}\delta, \quad b|_{\rho=r^{1/2}}=b-\frac{a}{2}\delta. \tag{3.8}$$

When $\delta\to 0$, the warping function along the thickness direction is negligible and $\varphi$ is assumed to be a function only of the arc length. Since (3.7) represents a closed curve of zero warping, we conclude that for a limitingly thin confocal elliptical tube, there is no warp. Chiskis and Parnes [3] recently found a general criterion for closed thin-wall members which exhibit no warping, in which their derivation is under the condition of *constant thickness*. The present finding serves as a complemental example of the absence of warping for a thin-wall section with nonconstant thickness. To our knowledge, no such results for nonconstant thickness were reported before. It is mentioned that the existence of such a contour could be very sensitive to the shape of both interfaces. For example, one could fix the outer boundary of the ellipse (with semi-axes $a$ and $b$) and deform the inner boundary of the confocally elliptical hollow section to a geometrically similar ellipse (with semi-axes $ka$ and $kb$, where $k<1$). Since such an elliptical ring has the same warping function as the simply connected elliptic section, namely $\varphi\propto x,y$ (see, for example, Timoshenko and Goodier [13], pp. 328–329), no closed zero-warping contour now exists.

## 4 Packham and Shail's Superpositions for a Two-Phase Confocally Elliptical Hollow Section

A few decades ago, Packham and Shail [3] showed that in Saint-Venant's torsion problem for a two-phase compound section (also in current flow of two immiscible viscous fluids [14]), if the cross section is symmetric about the interface, the stress function (or the warping function) for the compound cylinder can be expressed in terms of two separate solutions for homogeneous cylinders. One corresponds to the torsion of the whole section, and the other to the torsion of a section whose cross section coincides with that of the region occupied by one constituent of the two-phase section. The superposition method was originally applied to the cases that the interfaces are parallel to the $x$ or $y$-axes, and was further modified to the cases of $\theta=$constant or $r=$constant. For the former case, namely $\theta=$const., Chen and Huang [15] generalized the concept to analyze the torsional rigidity of a two-phase circumferentially symmetric compound bar. The aim of this section is to show that, upon the finding of the fact (3.7), Packham and Shail's method is also applicable to a special class of compound section with elliptical interface.

Let us now consider the auxiliary problem of a hollow circular cross-section consisting of two different phases in which the material $\alpha$ lies in the region $r^{1/2}\leqslant\rho\leqslant 1$ and the phase $\beta$ in $r\leqslant\rho\leqslant r^{1/2}$. This belongs to the original context of Packham and Shail with interface being described by $r=$const. Note that for the superposition to be valid, it is necessary that the interface $\rho=r^{1/2}$ be the square root of the radii of the inner and outer boundary. This is analogous to the image method in harmonic problems [16]. Consider the following two boundary value problems for hollow elliptical sections under torsion

$$\nabla^2\varphi_1=0 \text{ in } \Omega_\alpha, \quad \partial\varphi_1/\partial n=-\mathbf{v}\cdot\mathbf{n} \text{ on } \rho=r \text{ and } \rho=1,$$
$$\nabla^2\varphi_2=0 \text{ in } \Omega_\alpha, \quad \partial\varphi_2/\partial n=-\mathbf{v}\cdot\mathbf{n} \text{ on } \rho=r^{1/2} \text{ and } \rho=1. \tag{4.1}$$

The solution $\varphi_1$ has been given in (3.5) and $\varphi_2$, by the same routes in Section 2, is found as

$$\varphi_2(p)=\frac{c^2}{4}\frac{1}{1+r^{-1}}\left(\rho^{-2}-\frac{\rho^2}{r}\right)\sin 2\theta. \tag{4.2}$$

Packham and Shail [3] procedures show that the warping functions in phases $\alpha$ and $\beta$ of this compound configuration can be obtained from those of the two homogeneous sections by the linear superposition

$$\varphi_\alpha(\rho,\theta)=a_1\varphi_1(\rho,\theta)+a_2\varphi_2(\rho,\theta),\quad r^{1/2}\leqslant\rho\leqslant 1,$$

$$\varphi_\beta(\rho,\theta)=b_1\varphi_1(\tfrac{r}{\rho},\theta)+b_2\varphi_2(\tfrac{r}{\rho},\theta),\quad r\leqslant\rho\leqslant r^{1/2},\tag{4.3}$$

where the coefficients $a_1$, $a_2$, $b_1$, $b_2$ are

$$a_1=\frac{2\mu_\beta}{\mu_\alpha+\mu_\beta},\quad a_2=\frac{\mu_\alpha-\mu_\beta}{\mu_\alpha+\mu_\beta},$$

$$b_1=-\frac{2\mu_\alpha}{\mu_\alpha+\mu_b},\quad b_2=\frac{\mu_\alpha-\mu_\beta}{\mu_\alpha+\mu_\beta}.\tag{4.4}$$

The field solutions (4.3), (4.4) can be verified, with some mathematical skills, that they indeed fulfill Laplace equation, the traction-free boundary condition (2.1) as well as the continuity conditions of the warping displacement and traction at interface $\rho=r^{1/2}$, namely

$$w_\alpha-\left(\frac{\mu_\alpha+\mu_\beta}{2\mu_\alpha}w_\beta+\frac{\mu_\alpha-\mu_\beta}{2\mu_\alpha}\overline{w_\beta}\right)=i\,\frac{\mu_\alpha-\mu_\beta}{2\mu_\alpha}z\overline{z}.\tag{4.5}$$

We now consider a special type of two-phase elliptical hollow section. Suppose the geometry of this compound elliptical section is given such a way that, under the transformation (3.1), it is mapped onto the configuration of the auxiliary boundary value problem. We claim that the warping functions of this compound elliptical cross-section in the $p$-plane are given as (4.3) and (4.4). The reasons are simple. Since $\varphi$ is the real part of the analytic function $w$ and the mapping function (3.1), and its inverse, is analytic, thus it satisfies the governing equation (Laplace equations). Also, since for a hollow confocal ellipse, the closed contour $\rho=r^{1/2}$ has zero warping (or equivalently the normal derivative of the conjugate function $\psi$ is zero). Thus, Packham and Shail's superperposition method is applicable to this compound confocally elliptical configurations. Obviously (4.3) and (4.4) are exactly the warping fields of this compound elliptical section in the transformed domain. This perspective is new and may have further implications on chessboard-like elliptical geometry [17]. Of course, the torsion solutions of this compound elliptical section could have been analyzed directly as in the steps in Section 2 together with the satisfaction of interface conditions (4.5). Although much cumbersome than that of (4.3)–(4.4), we have indeed done the analysis and have verified that the superposition is true for this configuration.

## Acknowledgments

This work was supported by the National Science Council, Taiwan, under contract NSC 90-2211-E006-119.

## References

[1] Sokolnikoff, I. S., 1956, *Mathematical Theory of Elasticity*, McGraw-Hill, New York.
[2] Chiskis, A., and Parnes, R., 2000, ''On Torsion of Closed Thin-Wall Members With Arbitrary Stress-Strain Laws: A General Criterion for Cross Sections Exhibiting No Warping,'' ASME J. Appl. Mech., **67**, pp. 460–464.
[3] Packham, B. A., and Shail, R., 1978, ''St. Venant Torsion of Composite Cylinders,'' J. Elast., **8**, pp. 393–407.
[4] Ahlfors, L. V., 1966, *Complex Analysis: An Introduction to the Theory of Analytic Functions of One Complex Variable*, McGraw-Hill, Tokyo.
[5] Caratheodory, C., 1969, *Conformal Representation*, Cambridge University Press, Cambridge, UK.
[6] Chen, T., Benveniste, Y., and Chuang, P. C., 2002, ''Exact Solutions in Torsion of Composite Bars: Thickly Coated Neutral Inhomogeneities and Composite Cylinder Assemblages,'' Proc. R. Soc. London, Ser. A, **458**, pp. 1719–1759.
[7] Wang, C. T., 1953, *Applied Elasticity*. McGraw-Hill, New York.
[8] Muskhelishvili, N. I., 1953, *Some Basic Problems of the Mathematical Theory of Elasticity*, Noordhoff, Groningen.
[9] Lurie, A. I., 1970, *Theory of Elasticity*, Nauka, Moscow (in Russian).
[10] Bartels, R. C. F., 1943, ''Torsion of Hollow Cylinders,'' Trans. Am. Math. Soc., **53**, pp. 1–13.
[11] Greenhill, A. G., 1879, ''Fluid Motion Between Confocal Elliptic Cylinders and Confocal Ellipsoids,'' Q. J. Math., **16**, pp. 227–256.
[12] Love, A. E. H., 1944, *A Treatise on the Mathematical Theory of Elasticity*, Dover, New York.
[13] Timishenko, S. P., and Goodier, J. N., 1970, *Theory of Elasticity*, 3rd Ed., McGraw-Hill, New York.
[14] Packham, B. A., and Shail, R., 1971, ''Stratified Laminar Flow of Two Immiscible Fluids,'' Proc. Cambridge Philos. Soc., **69**, pp. 443–448.
[15] Chen, T., and Huang, Y. L., 1998, ''Saint-Venant Torsion of a Two-Phase Circumferentially Symmetric Compound Bar,'' J. Elast., **53**, pp. 109–124.
[16] Kellogg, O. D., 1953 *Foundations of Potential Theory*, Dover, New York.
[17] Chen, T., 2001, ''Torsion of a Rectangular Checkerboard and the Analogy Between Rectangular and Curvilinear Cross-Sections,'' Q. J. Mech. Appl. Math., **54**, pp. 227–241.

# Are Lower-Order Gradient Theories of Plasticity Really Lower Order?

**K. Yu. Volokh**
Faculty of Civil Engineering, Technion–Israel Institute of Technology, Haifa 32000, Israel

**J. W. Hutchinson**[1]
Division of Engineering and Applied Sciences, Harvard University, Cambridge, MA 02138
e-mail: hutchinson@husm.harvard.edu. Mem. ASME

*An explicit example of one-dimensional shearing is used to illustrate the necessity of extra boundary conditions for a class of incremental theories of plasticity regarded as otherwise conventional apart from a dependence of the tangential moduli on gradients of plastic strain.* [DOI: 10.1115/1.1504096]

Gradient effects may be introduced into plasticity theory by using additional kinematical and work-conjugate stress variables. Such theories enjoy the structure of Cosserat-type continua in the general case. Extra stresses and boundary conditions are inherent in the generalized continuum theories. While very flexible in introducing new quantities, the generalized continuum theories have drawbacks associated with the difficulty of physical interpretation of the higher-order stresses and extra boundary conditions. To avoid such higher-order formulations, a class of theories has been proposed by Bassani [1], which introduces gradients of plastic strain into the instantaneous tangent moduli. Otherwise, conventional equilibrium equations of lower-order theory are retained. The underlying premise of these enhanced conventional theories is that they accommodate only the same types of boundary conditions associated with the conventional theory. In this note it will be shown that this is not always the case. By considering a relatively simple, well-posed problem for one-dimensional shearing of a layer, it will be demonstrated that this class of theories can accommodate extra boundary conditions under special circumstances, and, in fact, are not lower order in this sense. However, the higher-order nature of the theories does not appear to be in accord with basic physical requirements, as will be discussed.

To begin, consider a conventional material whose stress-strain curve in shear is specified by $\gamma\equiv\gamma_e+\gamma_p=\tau/G+\gamma_p$ with

$$\gamma_p=0(\tau\leqslant\tau_Y),\quad \gamma_p=\gamma_0(\tau/\tau_Y-1)^n(\tau>\tau_Y).\tag{1}$$

In the plastic range $\tau/\tau_Y=1+(\gamma_p/\gamma_0)^N$ with $N=1/n$, such that the tangent modulus defined by $\dot\tau=G_t\dot\gamma$ can be expressed as

$$\frac{1}{G_t}=\frac{1}{G}+\frac{1}{H}\ \text{ with }\ \frac{1}{H}=\frac{n\gamma_0}{\tau_Y}\left(\frac{\gamma_p^2}{\gamma_0^2}\right)^{(n-1)/2n}.\tag{2}$$

[1]To whom correspondence should be addressed.

Contributed by the Applied Mechanics Division of THE AMERICAN SOCIETY OF MECHANICAL ENGINEERS for publication in the JOURNAL OF APPLIED MECHANICS. Manuscript received by the ASME Applied Mechanics Division, June 21, 2001; final revision, June 8, 2002. Associate Editor: A. Needleman.

  

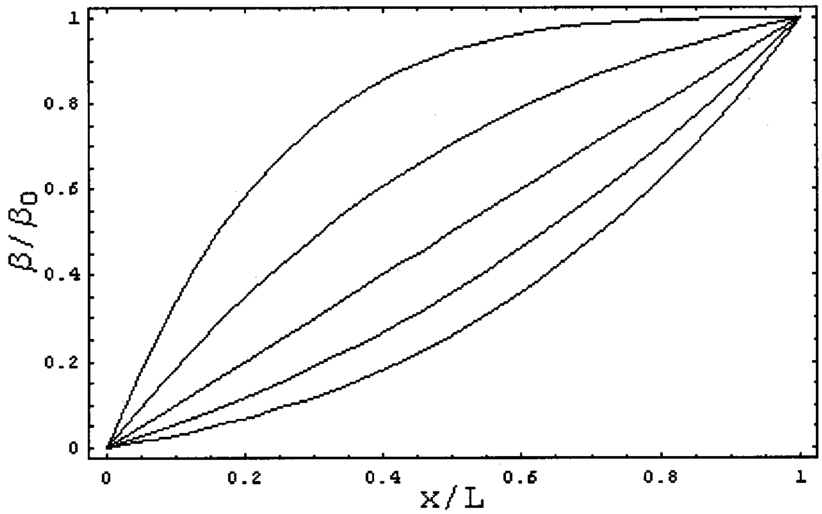


**Fig. 1 Numerical solutions of Eq. (4) with $n=3$ and $m=2$. The curves correspond to the values $\lambda=1/4;1/2;1;2;4$ from the bottom to the top.**

Consider shearing displacements parallel to the $x_2$-axis with $u_2(x_1)\equiv u(x)$ and $\gamma(x)=u'(x)$. With $\sigma_{12}(x_1)\equiv\tau(x)$, conventional incremental equilibrium requires $\dot{\tau}'(x)=0$.

The incremental boundary value problem considered here has displacement boundary conditions: $\dot{u}(0)=0$ and $\dot{u}(L)=\dot{v}$ with $v$ increased monotonically. The solution for the conventional material where the stress satisfies (1) is a uniform state of stress and strain consistent with the incremental relations $\dot{\gamma}=\dot{v}/L$ and $\dot{u}=\dot{\gamma}x$. The plastic strain is also uniform and all details of the solution can be generated as a function of $v$.

Introduce the enhanced material by including the gradient of plastic strain in the tangent modulus in (2) according to

$$\frac{1}{G_t}=\frac{1}{G}+\frac{1}{H} \quad \text{with} \quad \frac{1}{H}=\frac{n\gamma_0}{\tau_Y}\left(\frac{(\gamma_p/\gamma_0)^2}{(1+\ell^2\gamma_p'^2/\gamma_p^2)^m}\right)^{(n-1)/2n} \tag{3}$$

where $\ell$ is the material length parameter. The factor $m$ can be used to adjust the strength of the gradient hardening. In the absence of the gradient this reduces to the original form (2), and it meets requirements outlined for the type of formulation proposed by Bassani [1]. In the plastic range, $\dot{\tau}=G_t\dot{\gamma}$ is precisely equivalent to $\dot{\tau}=H\dot{\gamma}_p$. Assuming conventional equilibrium holds ($\dot{\tau}'(x)=0$), $\dot{\tau}$ is uniform and, thus, $\dot{\gamma}_e$ is uniform in both the elastic and plastic range. In the elastic range ($\tau\leqslant\tau_Y$), $\gamma=\gamma_e=v/L$, $\tau=G\gamma$ and $\gamma_p=0$. In the plastic range ($\tau>\tau_Y$), equilibrium requires $(H\dot{\gamma}_p)'=0$. Because $\gamma_e$ is uniform, the displacement can be written as $u(v,x)=\gamma_e(v)x+u_p(\nu,x)$ with $\gamma_p=u_p'$. Moreover, because $H$ is homogeneous in the plastic strain and its gradient, the equation $(H\dot{\gamma}_p)'=0$ admits a separated solution $u_p=\alpha(v)\beta(x)$ with $\gamma_p=\alpha\beta'$ and $\dot{\gamma}_p=\dot{\alpha}\beta'$ ($\dot{\alpha}=d\alpha/dv$). The equation is third order and homogeneous in $\beta$ and its derivatives:

$$\beta''[(n-1)m\ell^2\beta'''\beta'+[1-(n-1)m]\ell^2\beta''^2+\beta'^2]=0. \tag{4}$$

One solution to (4) is obviously $\beta'=c$ corresponding to a uniform plastic strain distribution. This solution coincides with the solution for the conventional material when the conditions, $\dot{u}(0)=0$ and $\dot{u}(L)=\dot{v}$, are enforced. But there is an entire family of other perfectly acceptable solutions to the problem as posed that satisfy the boundary conditions $\dot{u}(0)=0$ and $\dot{u}(L)=\dot{v}$. These solutions do not have a uniform distribution of plastic strain. They are possible because $\gamma_p'$ is not otherwise determined at the onset of plastic flow. Due to the third-order character of (4), one additional boundary condition can be imposed. The example shown in Fig. 1 was computed numerically from (4) with $\beta(0)=0$, $\beta(L)=\beta_0$ and $\beta'(0)=\lambda\beta_0/L$ for $n=3$, $m=2$, $\ell/L=1$ and several values of $\lambda$. The solution for $\lambda=1$ is that with uniform plastic strain. For each of the solutions, it is a straightforward process to piece together the entire solution to the boundary value problem with $\dot{u}(0)=0$ and $\dot{u}(L)=\dot{v}$ by making an appropriate choice for $\alpha(v)$. The plastic strain distribution will depend on $\lambda$, as will the overall relation between shear stress and shearing displacement $v$.

Uniqueness of solution requires that one extra boundary condition be specified on $\dot{\gamma}_p$ in addition to $\dot{u}(0)=0$ and $\dot{u}(L)=\dot{v}$. The example shown introduces the extra condition at the left end of the interval. One could have equally well imposed the one extra boundary condition at the right end, but not on both simultaneously. Higher order theories (Fleck and Hutchinson [2] and Hutchinson [3]) do involve extra boundary conditions. In a one-dimensional problem such as the present one, they require specification of extra conditions at *both* ends of the interval. An extra condition at each end of the interval would be expected on physical grounds due to the constraint, or lack thereof, on plastic flow that would be expected due to interaction of dislocations with each boundary. Thus, it would appear that the added flexibility associated with the extra boundary condition afforded by the enhanced formulation in the present example is inconsistent with sound physical principles.

The values of parameters chosen for the numerical example in Fig. 1 are not exceptional; solutions can be generated for any choice of the parameters. Similarly, the one-dimensional shearing problem is not an isolated example. Another simple, basic example for which an extra boundary condition must be specified is the deformation well away from the edges of a uniform film attached to a planar substrate. Moreover, the issue arises in this enhanced class of conventional theories whether these problems are approached using a phenomenological theory or a single crystal theory such as that discussed by Bassani [1]. The need for an extra boundary condition in these examples arises because the deformation at the onset of plasticity is uniform and, therefore, the gradient of plastic strain is indeterminant. Consequently the tangent modulus is also indeterminant unless an additional condition is imposed such as the extra boundary condition. At the very least, these basic examples raise questions about enhanced conventional formulations, and they suggest that further conditions must be stated to render unique solutions. Our own view is that higher-order boundary conditions, which specify constraints on plastic deformation at boundaries, interfaces, and free surfaces, should be an integral part of a strain gradient theory of plasticity.

## Acknowledgment

The work of KYV was supported by the Fund for the Promotion of Research at the Technion.

## References

[1] Bassani, J. L., 2001, "Incompatibility and Simple Gradient Theory of Plasticity," J. Mech. Phys. Solids, **49**, pp. 1983–1996.
[2] Fleck, N. A., and Hutchinson, J. W., 2001, "A Reformulation of Strain Gradient Plasticity," J. Mech. Phys. Solids, **49**, pp. 2245–2271.
[3] Hutchinson, J. W., 2000, "Plasticity at the Micron Scale," Int. J. Solids Struct., **37**, pp. 225–238.

# A Note on the Post-Flutter Dynamics of a Rotating Disk

**A. Raman**[1]
School of Mechanical Engineering, Purdue University,
West Lafayette, IN 47907-1288
e-mail: raman@ecn.purdue.edu

**M. H. Hansen**
Wind Energy Department Risø National Laboratory, DK-4000 Roskilde, Denmark

**C. D. Mote, Jr.**
Professor of Engineering and President,
Glenn L. Martin Institute, University of Maryland,
College Park, MD 20742

*The dynamic response of a thin, flexible disk spinning in an enclosed air-filled chamber, beyond the onset of aeroelastic flutter, is investigated experimentally. The results describe the occurrence of new nonlinear dynamic phenomena in the post-flutter regime. A primary instability leads to the Hopf bifurcation of the flat equilibrium to a finite amplitude backward traveling wave. A secondary instability causes this traveling wave to jump to a large-amplitude frequency locked, traveling wave vibration. For a small range of rotation speeds, both types of traveling wave motions co-exist. The results underscore the interplay between structural and fluidic nonlinearities in controlling the dynamic response of the fluttering disk in the post-flutter regime.*
[DOI: 10.1115/1.1504097]

## Introduction

The aeroelastic stability of rotating flexible disks is a significant concern for the engineering design of a diverse class of mechanical systems such as magnetic and optical data storage devices, thin sawblades, and turbomachinery. A majority of the literature on the problem is devoted to linear coupled fluid-structure interaction models aiming to predict accurately the speed and mode at the onset of aeroelastic flutter, [1–9].

To the best of our knowledge, [1,2,4,10] are the only works in the literature that present experimental data on the post-flutter vibration response of a spinning disk. In [1], the disk speed was changed in increments of 100 rpm, which is too large to resolve the transitions in dynamic response we are discussing here. It may be noted that the disk and the experimental apparatus used here were also used in [1]. In [2] and [10] a focus was placed on investigating the onset of solitary waves on a very thin, membrane-like disk spinning over a thin air film. The results in [2] and [10] indicated a transition from harmonic to apparently fixed frequency solitary waves. This is similar to the frequency lock-in phenomenon described in the present work. However, in [2,10] the speed dependence of unstable wave amplitude, and the coexistence of multiple solutions in the post-flutter regime were not presented. The present experiments are performed using a stiff steel disk enclosed in a large sealed chamber, a significantly different experimental regime from [2] and [10].

This note aims to communicate rapidly experimental results, which describe the occurrence of new nonlinear dynamic phenomena occurring at rotation speeds above the onset of the flutter instability. These new results should assist the continuing development of nonlinear fluid-nonlinear structure interaction modeling for this problem.

## Experimental Setup

The experimental apparatus (Fig. 1) utilized here is that used in [1]. The design minimizes sources of experimental error, including bearing noise, rotor imbalance, and unwanted stressing of the disk caused by temperature gradients. The primary elements include a thin disk held between thick collars, a high precision spindle, and vibration measurement instrumentation all placed inside a large, sealed chamber. The disk has a nominal outer diameter 356 mm, and the collar diameter is 106.7 mm. The disk material is 8660 steel, ground to a uniform thickness 0.775 mm and with maximum runout less than 0.10 mm. Residual stresses from manufacture are relieved after the grinding, creating a disk that is substantially stress-free. For further details of the experimental chamber and its functionality, the reader is referred to [1].

The experimental configuration in Fig. 2 shows two inductance-type displacement transducers measuring the transverse motion of the disk at a radial distance of 148 mm. The probes are angularly separated by 18 deg, have a linear range of 2.5 mm and a resolution of 0.20 $\mu$m. The vibration response signals from the two displacement probes are conveyed to a Tektronix 2630MS Modal Analyzer coupled to an IBM PS2/Model 70. A counter connected to an optical probe measures the disk rotation speed. An electromagnetic actuator is driven by amplified signals from the computer and applies a transverse force on the disk. Short duration pulses are applied to the actuator to investigate the stability of the fluttering motions under perturbation. The surrounding chamber is closed during the experiments.

## Experimental Procedure

At pre-flutter speeds, disk vibration is excited randomly by the turbulent boundary layer that develops on the disk surface at high speeds. At each speed the Fourier spectrum of the vibration response is computed and averaged over ten time intervals. The magnitude of each peak is converted through the sensor calibration data to the amplitude of the corresponding traveling wave measured at the sensor location. Each peak in the vibration spectrum is associated with a $(m, n)$ forward or backward traveling wave with $m$ nodal circles and $n$ nodal diameters. Identification of the nodal diameter number is facilitated through computation of the phase of the cross-spectrum of the data from the two displacement probes, [11].

As the disk speed is increased, the first critical speed occurs at 40.5 rev/s rotation speed. At this speed, the backward traveling wave (BTW) frequency of the (0,3) mode vanishes. With further increases in disk speed the (0,2), and (0,4) modes reach their critical speeds in succession. As the disk speed is increased into the supercritical range, the frequency of the (0,3) BTW increases from zero (This is sometimes called a reflected wave.) The amplitude of the peak corresponding to the (0,3) BTW starts to increase rapidly beyond 50 rev/s rotation speed indicating the onset of aeroelastic traveling wave flutter.

[1]To whom correspondence should be addressed

Contributed by the Applied Mechanics Division of THE AMERICAN SOCIETY OF MECHANICAL ENGINEERS for publication in the ASME JOURNAL OF APPLIED MECHANICS. Manuscript received by the ASME Applied Mechanics Division, October 7, 2001; final revision, February 6, 2002. Associate Editor: N. C. Perkins.

  

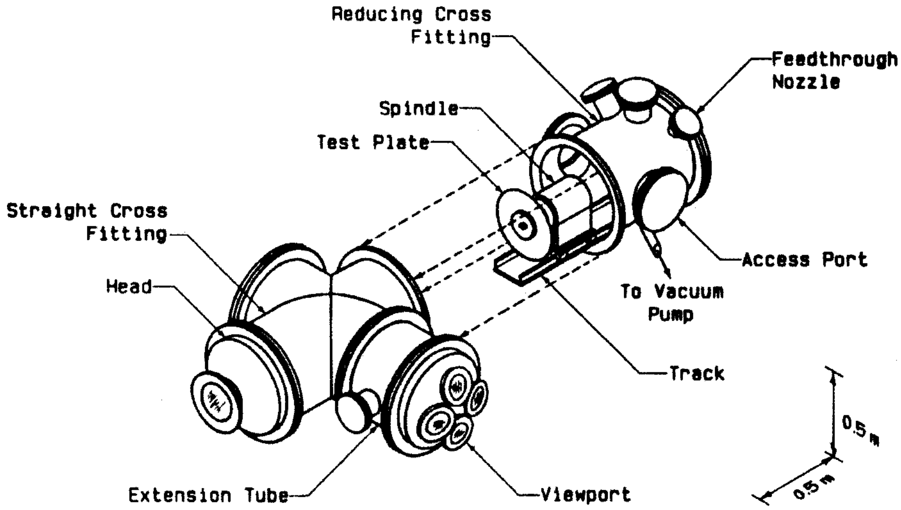


**Fig. 1 A schematic of the chamber (shown open here) and the disk apparatus (from [1])**

At speeds greater than 50 rev/s the disk speed is increased by 1 rev/s increments while increasing and then decreasing the rotation speed across the flutter instability. The fluttering BTW is allowed to stabilize after each speed increment and its frequency and amplitude measured at the sensor locations. Two sets of data are collected while the speed is gradually increased and one set is taken as the speed is decreased from post-flutter speed. The data are collected and presented in Figs. 3(*a*) and (*b*).

## Results

1. As the rotation speed is increased from 50 rev/s, the primary flutter instability of the (0,3) BTW occurs at about 53 rev/s. This point is indicated in Figs. 3(*a*) and (*b*) by the point A. The exact location of point A requires an analysis of the Hopf bifurcation in the presence of colored noise such as that generated by turbulent boundary layer excitation of the disk.

2. As the disk speed is increased above that at point A, the amplitude and frequency of the fluttering (0,3) BTW continue to increase. However, below point B, there is a small, but discernible change in slope of the speed variation of wave frequency, accompanied by a flattening of the amplitude response. The solution branch from A to B is referred to as the *primary instability branch*.

3. The first secondary instability occurs at point B (at approximately 58.5 rev/s). It is characterized by a sudden, large increase in the traveling wave amplitude, and a sudden, simultaneous decrease in frequency of the traveling wave. This instability is quite

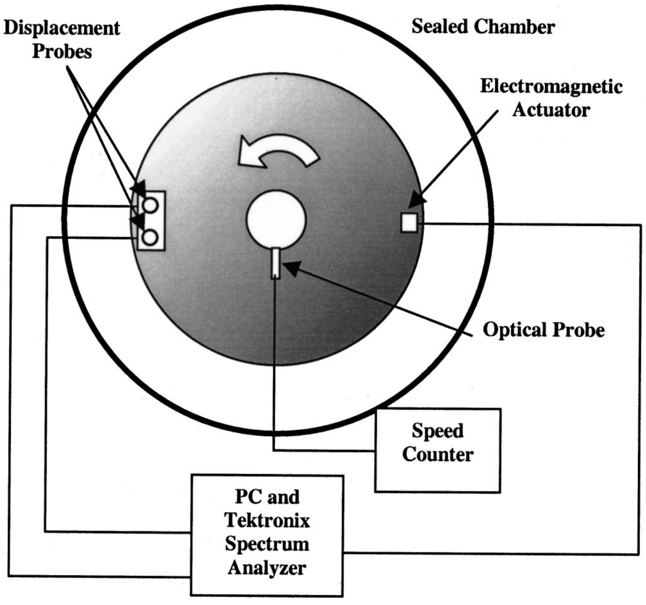


**Fig. 2 A schematic of the experimental configuration**

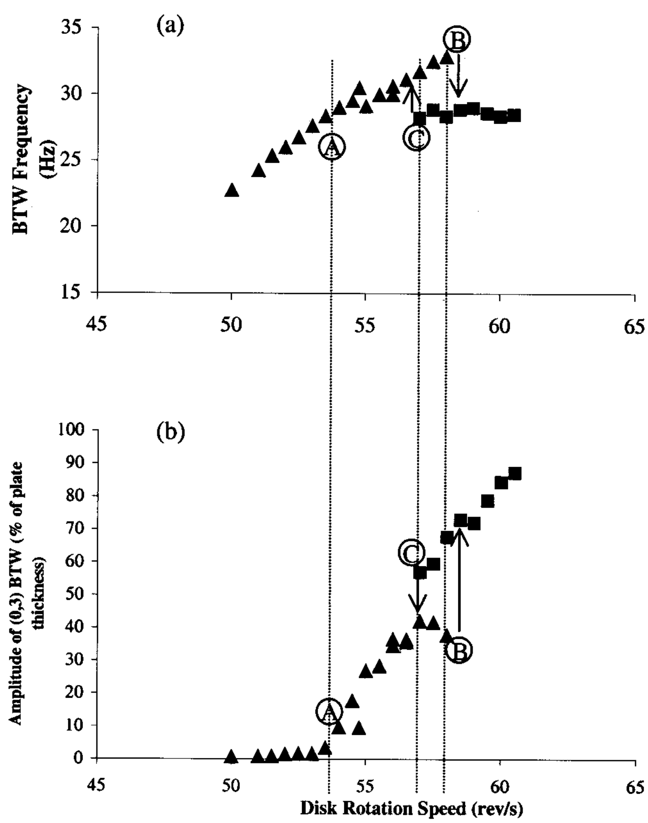


**Fig. 3 (*a*) Frequency of the (0,3) backward traveling wave (BTW) versus disk rotation speed; (*b*) vibration amplitude of the (0,3) BTW measured at the sensor location, versus disk rotation speed. Triangles and squares represent dynamically dissimilar branches.**

dramatic because the amplitude of the traveling wave nearly doubles from about 35% of plate thickness to nearly 80% of plate thickness while its frequency decreases by nearly 20% from nearly 33 Hz to 28 Hz. There is a marked increase in tonal acoustic emission from the enclosure accompanying this secondary instability.

4. As the speed is increased above point B, the amplitude of the traveling wave continues to increase, while the wave frequency remains nearly constant. This new solution branch is referred to as the *locked frequency branch*. The points on this branch are indicated by solid squares in Fig. 3(*a*) and (*b*) while all the other data points including pre-flutter and along the primary instability branch are indicated by solid triangles. At yet greater speeds, the amplitude continues to increase while the wave frequency remains nearly constant.

5. As the speed is decreased from above point B on the locked frequency branch, the amplitude of the (0,3) BTW decreases while its frequency remains nearly constant. As the speed is decreased, the *second secondary instability* occurs at point C (disk speed approximately 56.5 rev/s). At point C, the amplitude of the fluttering (0,3) BTW decreases suddenly while its frequency increases suddenly from about 28 Hz to about 30 Hz. The solution is now on the primary instability branch. As the speed is decreased further the amplitude and frequency of the fluttering (0,3) BTW decrease. Below point A, the zero equilibrium of the disk is stable again.

6. The secondary instability at point B affects all stable traveling waves, and not exclusively the fluttering (0,3) BTW. In particular, while the amplitudes of the stable traveling waves corresponding to other nodal diameter modes remain very small, their frequencies all drop by about 5–15% at point B and remain nearly constant thereafter. Because this effect was also observed in [1] on exactly the same disk, we omit presenting this data for the sake of brevity.

7. One additional test was performed. The disk speed was increased in small increments from below point A to above it while the solution was allowed to stabilize on the primary instability branch. The speed was then adjusted to lie between points B and C while the disk was vibrating on the primary instability branch. A rectangular pulse generated from the signal analyzer was fed to the electromagnetic actuator described earlier to perturb the solution lying on the primary instability branch. For sufficiently large impulse, the response immediately transitioned to the locked frequency branch, demonstrating the coexistence of the primary instability branch and the locked frequency branch over a small range of rotation speeds.

## Discussion

The use of smaller speed increments than in [1] allowed the transitions in the dynamic response of the disk in the post-flutter regime to be clearly resolved. In particular, the results 1 through 7 clearly indicate two distinct solution branches exist beyond the onset of traveling wave flutter. Moreover, secondary instabilities trigger the transitions between the primary instability branch and the locked frequency branch.

Following the onset of primary stability at point A, the response is likely to be dominated by structural geometric nonlinearities such as those modeled by the Von Karman plate. The traveling wave amplitudes grow approximately proportionally to the square root of the speed.

However, as the wave amplitude grows along the primary instability branch, nonlinear coupling to the surrounding air is likely to be the primary trigger for the secondary instabilities. Following the secondary instability, the dynamics of the disk appear to be dominated by fluidic nonlinearities. The nonlinear coupling mechanism leading to the secondary instability may be found amongst the following explanations:

1. The near constancy of BTW frequency along the locked frequency branch indicates a coupling with another oscillating system whose frequencies are unchanged with disk speed. This additional system could be one of the oscillating modes of the acoustic cavity of the enclosure, a suggestion supported by the large acoustic emission along the locked frequency branch. No attempts to alter the cavity were made.

2. Another possible explanation for the near constant frequency on the frequency locked branch could be coupling with an independent vortex shedding frequency near the rim of the disk. Our preliminary investigations using a hotwire anemometer to measure flow fluctuations just outside the disk rim did not support this suggestion. However, we cannot rule out the possibility that flow separation near the rim of the disk at large disk vibration amplitude may be the cause.

3. Another explanation of these results may arise out of the large body of literature concerning the hydrodynamic stability of laminar flows coupled to flexible surfaces. Of particular relevance to the rotating disk problem are the works of Carpenter et al. [12–14]. In these works, the authors investigate the hydrodynamic stability of the three-dimensional Karman swirling flow over rigid disk with a viscoelastic coating. This system features several fluid dominated instabilities leading to time-periodic fluid motions and one structure dominated instability, namely traveling wave flutter of the disk coating. The *nonlinear* interaction of these waves has not been studied in the literature. This may yield important information regarding the post-flutter lock-in phenomenon.

## References


[1] D'Angelo, C., III, and Mote, C. D., Jr., 1993, "Aerodynamically Excited Vibration and Flutter of a Thin Disk Rotating at Supercritical Speed," J. Sound Vib., **168**(1), pp. 15–30.
[2] Boulahbal, D., 1995, "Self Excited Vibrations of a Spinning Disk," Doctoral thesis, MIT, Cambridge, MA.
[3] Stakhiev, Y. M., 1972, "Vibration in Thin Steel Discs," Russ. Eng. J., **52**, pp. 14–17.
[4] Renshaw, A. A., D'Angelo, C., III, and Mote, C. D., Jr., 1994, "Aerodynamically Excited Vibration of a Rotating Disk," J. Sound Vib., **177**(5), pp. 577–590.
[5] Yasuda, K., Torii, T., and Shimuzu, T., 1992, "Self-Excited Oscillations of a Circular Disk Rotating in Air," JSME Int. J., Ser. III, **35**(3), pp. 347–352.
[6] Hansen, M. H., Raman, A., and Mote, C. D., Jr., 2001, "Estimation of Non-Conservative Aerodynamic Pressure Leading to Flutter of a Spinning Disk," J. Fluids Struct., **1**, pp. 39–57.
[7] Kim, B. C., Raman, A., and Mote, C. D., Jr., 2000, "Prediction of Aeroelastic Flutter in a Hard Disk Drive," J. Sound Vib., **238**(2), pp. 309–325.
[8] Hosaka, H., and Crandall, S., 1992, "Self-Excited Vibrations of a Flexible Disk Rotating on an Air Film Above a Flat Surface," Acta Mech. Supple., **3**, pp. 115–127.
[9] Renshaw, A. A., 1998, "Critical Speed for Floppy Disks," ASME J. Appl. Mech., **65**, pp. 116–120.
[10] Choi, J. K., and Crandall, S. H., 1999, "An Experimental Study on Solitary Waves of a Rotating Disk," KSME Int. J., **13**(4), pp. 358–367.
[11] Ahn, T. K., and Mote, C. D., Jr., 1998, "Mode Identification of a Rotating Disk," Exp. Mech., **38**(4), pp. 250–254.
[12] Colley, A. J., Thomas, P. J., Carpenter, P. W., and Cooper, A. J., 1999, "An Experimental Study of Boundary-Layer Transition Over a Rotating, Compliant Disk," Phys. Fluids, **11**(11), pp. 3340–3352.
[13] Cooper, A. J., and Carpenter, P. W., 1997, "The Stability of Rotating-Disc Boundary Layer Flows Over a Compliant Wall.1. Type I and II Instabilities," J. Fluid Mech., **350**, pp. 231–259.
[14] Cooper, A. J., and Carpenter, P. W., 1997, "The Stability of Rotating-Disc Boundary Layer Flows Over a Compliant Wall.2. Absolute Instability," J. Fluid Mech., **350**, pp. 261–270.

Journal of Applied Mechanics

# Discussion

## Discussion: "Computationally Efficient Micromechanical Models for Woven Fabric Composite Elastic Moduli" (Tanov, R., and Tabiei, A., 2001, ASME J. Appl. Mech., 68, pp. 533–560)

**Z.-M. Huang**
Department of Engineering Mechanics, Tongji University, 1239 Siping Road, Shanghai 200092, P. R. China
e-mail: huangzm@mail.tongji.edu.cn

In their paper, Tanov and Tabiei presented two micromechanics-based models to evaluate the elastic moduli of woven fabric reinforced composites. After going through their numerical examples shown in the paper, the present reader has a strong feeling that the accuracy and hence the efficiency of their models is suspect.

The fabric investigated by Tanov and Tabiei is schematically shown in Fig. 1, where $a_f$ and $a_w$ are the fill and warp yarn widths, and $g_f$ and $g_w$ are the inter-yarn gaps between the fill and warp yarns. After the fabric is impregnated with a polymer matrix, the areas in between the inter-yarn gaps have no reinforcement. Namely, they become pure matrix regions in the woven composite. Apparently, these pure matrix regions can significantly reduce the overall stiffness and strength of the woven composite. The amount of reduction depends on the gap-yarn ratios $g_f/a_f$ and $g_w/a_w$. It has been shown by this author (see [1]) that when the gap-yarn ratio $g/a$ (supposing $g_f/a_f = g_w/a_w = g/a$) is only 4%, a reduction of as high as 22% in the in-plane elongation modulus can be recognized. The larger the gap-yarn ratio, the lower the in-plane modulus of the resulting woven composite. Therefore, in order to achieve as high a mechanical performance as possible, the woven composites have been generally fabricated with as small (if not zero) inter-yarn gaps as possible.

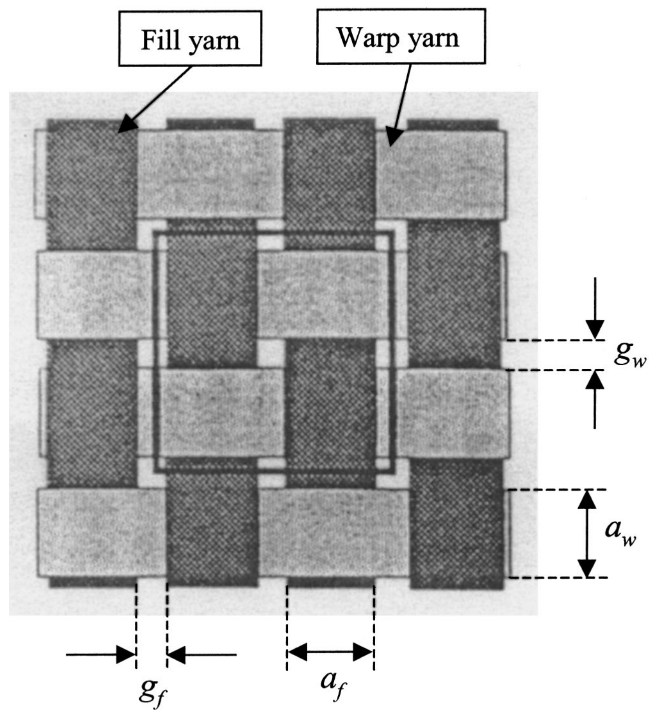


**Fig. 1 Schematic of a plain woven fabric**

However, the three examples of woven fabric reinforced epoxy (with modulus between 3.45 to 4.51 GPa) matrix composites investigated by Tanov and Tabiei were all assumed to have very large gap-yarn ratios (using the term of Ref. [2], the gap-yarn ratio was given by $(1-V_y)/V_y$, see Fig. 1 and Fig. 2 of Ref. [2]), being 85.7%, 284.6%, and 72.4%, respectively. From the input data of the yarns, epoxy matrices, and the yarn volume fractions provided in Ref. [2], we can easily estimate the maximum possible in-plane moduli for the three woven composites without any inter-yarn gaps, which are given by those of the corresponding cross-plied laminates [0 deg/90 deg]. The estimation for the properties of the unidirectional (0 deg) lamina is made based on the bridging micromechanics model (Ref. [3], with bridging parameters $\beta=0.35$ and $\alpha=0.45$) by assuming that it is fabricated from the yarn (fiber) and the matrix with the given yarn (fiber) volume fraction. The classical lamination theory is then applied to obtain the in-plane modulus of the cross-plied laminate. The maximum possible in-plane moduli for the three woven composites thus obtained are: 18.21 GPa, 11.77 GPa, and 45.1 GPa, respectively. In light of the fact reported in Ref. [1] that a 50% gap-yarn ratio would cause nearly 300% reduction in the in-plane modulus of a woven composite, the predicted moduli of the woven composites with the aforementioned very large gap-yarn ratios, i.e., 17.85 GPa, 11.86 GPa, and 45.08 GPa from Tanov and Tabiei's four-cell model, or 18.21 GPa, 11.93 GPa, and 45.17 GPa from their single-cell model, would be hardly possible.

### References

[1] Huang, Z. M., 2000, "The Mechanical Properties of Composites Reinforced With Woven and Braided Fabrics," Compos. Sci. Technol., **60**, pp. 479–498.
[2] Tanov, R., and Tabiei, A., 2001, "Computationally Efficient Micromechanical Models for Woven Fabric Composite Elastic Moduli," ASME J. Appl. Mech., **68**, pp. 553–560.
[3] Huang, Z. M., 2001, "Simulation of the Mechanical Properties of Fibrous Composites by the Bridging Micromechanics Model," Composites, **A32**, No. 2, pp. 143–172.

  

# Closure to "Discussion of 'Computationally Efficient Micromechanical Models for Woven Fabric Composite Elastic Moduli'" (2002, ASME J. Appl. Mech., 69, p. 867)

**R. Tanov**[1]

**A. Tabiei**
Associate Professor and Director

Center for Excellence in DYNA3D Analysis, Department of Aerospace Engineering and Engineering Mechanics, University of Cincinnati, Cincinnati, OH 45221-0070

It is with great embarrassment and humiliation that we write these lines. We, the authors of the above paper, do strongly believe that truth is born through doubt and dispute. However, we were very disappointed to read the "Discussion of 'Computationally Efficient Micromechanical Models for Woven Fabric Composite Elastic Moduli by R. Tanov and A. Tabiei (*J. Appl. Mech.*, **68**, pp. 553–560, 2001)'" by Zheng-Ming Huang. We do not believe that raising trivial questions in front of a large audience as the readers of this journal would contribute in any way to science in general, and computational mechanics in particular. We think that the normal and less embarrassing for both sides way to address such issues is through personal communication, but since this did not happen we see these lines as our only opportunity to defend our work. As much as we want to say, replying to the above discussion, we will limit our response to only pointing the answers to the questions therein raised. We apologize for trying to explain what we think is obvious and trivial and what the reader might have already deduced if reading the referenced lines.

In his writing Huang is questioning the accuracy and therefore the applicability of our work on composites micromechanics, published in this journal. Needless to say, in developing this work we ourselves have gone through a long and rigorous process of questioning, testing, and comparing, to get enough confidence in the presented approaches and their assumptions and formulations. To illustrate that, we have compared our results to previously published data from theoretical, finite element, and experimental studies. However, the author of the above discussion felt that the data presented in our work is "hardly possible" based on his notions for woven composites. He has tried to illustrate his point by first using a micromechanics-based homogenization scheme to determine the values of the moduli presented by us. The values he has come up with, come within a reasonable proximity to our results. However, after determining these values, he further references a woven composite "parameter," which he calls "gap-yarn ratio," and based on which he claims that the above calculated moduli should additionally undergo a "nearly 300% reduction." If the reader is to read Ref. [1] of his discussion he would immediately recognize that what is referenced there as "gap-yarn ratio" is just a different way of expressing the composite yarn volume fraction, the ratio of the volume of the yarns to the volume of the entire composite layer. By homogenizing the composite constituent yarns and matrix in his initial calculations Huang has already taken into consideration this ratio. In this process he, as most micromechanical approaches including ours do, has arrived to a fictitious continuous and homogeneous composite layer. The continuity and homogeneity of this layer would, of course, imply no gaps within it, whatsoever. However, Huang has failed to recognize that by claiming that due to gaps in the initial yarn periodic arrangement the properties should further be significantly reduced. At this point of the analysis, after the homogenization is complete, there is no yarn, no matrix, no gaps, but only one continuous and homogeneous layer, which, to repeat yet again, excludes the presence of any gaps. These gaps, used as basis for Huang's suspect in our work, make his claims incorrect and ungrounded. Another proof of which is that he failed to determine any definite value of the parameters he states as inaccurate apart from that "nearly 300% reduction," which even from a strictly arithmetical point of view makes no sense whatsoever.

We would hereby like to thank the Editor of the *Journal of Applied Mechanics* for the provided opportunity to defend our work. And finally, we would like to again express our confidence in the methods in subject that we have previously developed and published.

[1] Presently at IMMI, Westfield, IN.

  